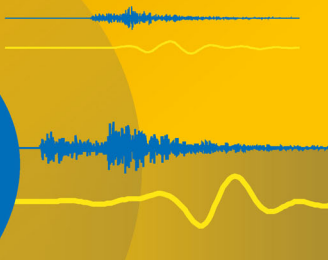


Jens Havskov
Lars Ottemöller



Routine Data Processing in Earthquake Seismology

With Sample Data,
Exercises and Software



 Springer

Routine Data Processing in Earthquake Seismology

Routine Data Processing in Earthquake Seismology

With Sample Data, Exercises and Software

Jens Havskov · Lars Ottemöller

Department of Earth Science
University of Bergen, Norway



Springer

Jens Havskov
Department of Earth Science
University of Bergen
Allegaten 41
5007 Bergen
Norway
jens.havskov@geo.uib.no

Lars Ottemöller
Department of Earth Science
University of Bergen
Allegaten 41
5007 Bergen
Norway
lars.ottemoller@geo.uib.no

Exercises, test data and public domain software (SEISAN) can be downloaded from
<http://extras.springer.com>

ISBN 978-90-481-8696-9 e-ISBN 978-90-481-8697-6
DOI 10.1007/978-90-481-8697-6
Springer Dordrecht Heidelberg London New York

Library of Congress Control Number: 2010923101

© Springer Science+Business Media B.V. 2010

No part of this work may be reproduced, stored in a retrieval system, or transmitted in any form or by any means, electronic, mechanical, photocopying, microfilming, recording or otherwise, without written permission from the Publisher, with the exception of any material supplied specifically for the purpose of being entered and executed on a computer system, for exclusive use by the purchaser of the work.

Cover illustration: The illustration is based on the results shown in Figure 7.38. The fault plane solution and seismograms are from an earthquake in California on 12 August 1998 at 14:10.

Printed on acid-free paper

Springer is part of Springer Science+Business Media (www.springer.com)

Preface

The purpose of this book is to provide a practical description of the most common processing techniques in earthquake seismology. The book will deal with manual methods and computer assisted methods. The idea is that each topic will be introduced with the basic theory followed by practical examples and exercises. There will be manual exercises entirely based on the printed material of the book, as well as computer exercises based on public domain software. However, most exercises are computer based. The software used, as well as all test data will also be available via <http://extras.springer.com>.

This book is intended for everyone processing earthquake data, both in the observatory routine and in connection with research. Using the exercises, the book can also be used as basis for a university course in earthquake processing. Since the main emphasis is on processing, the theory will be dealt with to the extent needed to understand the processing steps, however references will be given to where more extensive explanation can be found.

Currently there is one extensive book dealing with, among other topics, earthquake data processing. This is the “New Manual of Seismological Observatory Practice” (NMSOP) written by many authors (including the authors of this book) and edited by Peter Bormann (2002). The complete manual is available at www.seismo.com/msop/msop_intro.html. NMSOP provides the most extensive background for our book and the intention is to build on NMSOP. In signal processing, the most extensive work is the “Of poles and zeros” by Scherbaum (2001) while the instrumental aspects are covered in “Instrumentation in Earthquake Seismology” by Havskov and Alguacil (2006). As a general textbook on earthquakes and seismology, the book “An introduction to seismology, earthquakes and structure” by Stein Wysession (2003) provides plenty of material and we significantly refer to it. So why another book? We feel that there is a need for one book dealing exclusively with the practical aspects of processing in more details, with more examples and exercises than it was possible in these books, however they will provide extensive background material for our book and will often be referenced.

Our goal is to combine the principles behind earthquake processing and practical examples and exercises in a way not done before so that the reader should be able to get answers to most question in connection with processing earthquake data through

hands on experience with an included set of data and software i. e. “A how to do book”.

The book will be based on the author’s experience of many years of processing data from seismic networks, writing processing software and teaching processing of earthquake data using both NMSOP and other books. The author’s software, SEISAN, has been around for 20 years and is used globally. The almost daily questions and feedback from the many users have provided us with valuable insight into the most important aspects of processing earthquake data and helped to select the most relevant topics.

We have got input and corrections from several people including students who had to suffer the initial versions of the book. Peter Voss, Gerado Alguacil and Mohammad Raeesi provided comments for most of the book. Tim Sonnemann checked the whole book for inconsistencies and references and also checked the formulas. Mathilde B. Sørensen did a detailed review of the focal mechanism chapter. Klaus Klinge and Klaus Stammle pointed our attention to the use of apparent velocity determined by regional arrays, particularly for PKP identification. Peter Bormann provided a very thorough revision of the book, and for the magnitude chapter (his favorite topic) provided almost as much comments as we had written of text ! We are grateful to you all. Most of the book was written during one of the authors (JH) sabbatical stay at the Geological Survey of Denmark and Greenland, Copenhagen and the British Geological Survey, Edinburgh with support from the University of Bergen.

In our examples we use data from a number of seismic networks, too many to mention them here. However, credit to the data sources is given with the examples in the figure captions. As this book heavily relies on the examples, we very much appreciate the support from the data providers.

Contents

1	Introduction	1
1.1	Earthquakes	2
1.2	Recording Seismic Events and Picking Phases	6
1.3	Locating Earthquakes	9
1.4	Magnitude	10
1.5	Fault Plane Solution	11
1.6	Further Data Analysis	12
1.7	Software	13
2	Earth Structure and Seismic Phases	15
2.1	Earth Structure	15
2.2	Seismic Rays	18
2.3	Seismic Phases	21
2.4	Travel Times	28
2.5	Seismic Phases at Different Distances	33
2.6	Determination of Structure	45
2.7	Exercises	48
3	Instruments and Waveform Data	53
3.1	Seismic Sensors	53
3.2	Seismic Recorders	58
3.3	Correction for Instrument Response	61
3.3.1	How to Store the Response Information	65
3.3.2	Response in Practice	66
3.3.3	Using Response	67
3.3.4	How to Make Response Files	67
3.4	Waveform Formats	68
3.4.1	GSE	69
3.4.2	SEED	70
3.4.3	SAC	71
3.4.4	SEISAN	71
3.4.5	CSS	72
3.4.6	Common Points to Consider with Waveform Formats	72
3.4.7	Format to Use	76

3.5	Seismic Noise	76
3.6	Exercises	80
4	Signal Processing	83
4.1	Filtering	83
4.2	Spectral Analysis and Instrument Correction	86
4.3	Reading Seismic Phases	91
4.3.1	First Onset	91
4.3.2	Filtering and Phase Shift	91
4.3.3	Plotting Resolution	93
4.4	Correlation	94
4.5	Particle Motion and Component Rotation	94
4.6	Resampling	98
4.7	Software	99
4.8	Exercises	99
5	Location	101
5.1	Single Station Location	103
5.2	Multiple Station Location	107
5.3	Computer Implementation	110
5.3.1	Grid Search	110
5.3.2	Location by Iterative Methods	112
5.3.3	Example of Location in a Homogeneous Model	115
5.4	Error Quantification and Statistics	116
5.4.1	Example of Error Calculation	118
5.5	Relative Location Methods	120
5.5.1	Master Event Technique	120
5.5.2	Joint Hypocenter Location	122
5.5.3	Double Difference Earthquake Location	123
5.6	Practical Considerations in Earthquake Locations	124
5.6.1	Phases	126
5.6.2	Hypocentral Depth	127
5.6.3	Starting Location	134
5.6.4	Identification of P for Teleseismic Events	138
5.6.5	Outliers and Weighting Schemes	138
5.6.6	Timing Errors	139
5.6.7	Example of Outlier and Timing Problems	139
5.7	Software	143
5.8	Exercises	145
6	Magnitude	151
6.1	Amplitude and Period Measurements	153
6.2	Local Magnitude M_L	154
6.3	Coda Magnitude M_c	160
6.4	Body Wave Magnitude m_b	164
6.5	Broad Band Body Wave Magnitude m_B	169

6.6	Surface Wave Magnitude M_s	171
6.7	Broad Band Surface Wave Magnitude M_S	175
6.8	L_g – Wave Magnitude	178
6.9	Moment Magnitude M_W	178
6.10	Energy Magnitude M_e	179
6.11	Comparison of Magnitude Scales	180
6.12	Summary	183
6.13	Average Magnitude and Station Corrections	184
6.14	Adjusting Magnitude Scales to Local or Regional Conditions	185
6.14.1	Select a Scale from Another Region	185
6.14.2	Derive M_L Scale	186
6.14.3	Derive M_c Scale	187
6.14.4	Determine Local Attenuation to Calculate M_w	188
6.15	Exercises	188
7	Focal Mechanism and Seismogram Modeling	193
7.1	Fault geometry	194
7.2	Source Radiation	195
7.3	Fault Plane Solution in Practice	198
7.4	Obtaining Polarity	206
7.5	Fault Plane Solution Using Local Data and Polarity	208
7.6	Composite Fault Plane Solution	209
7.7	Fault Plane Solution Using Global Data	210
7.8	Fault Plane Solution Using Amplitudes	212
7.8.1	Using Amplitude Ratios	214
7.8.2	Example of Using Amplitude Ratios for a Distant Earthquake	216
7.8.3	Using Spectral Amplitudes	219
7.9	Moment Tensor	222
7.10	Moment Tensor Inversion	227
7.10.1	Moment Tensor Inversion at Local and Regional Distance	229
7.10.2	Global Distance	233
7.11	Seismogram Modeling	235
7.11.1	Ray Method	236
7.11.2	Approximation to Complete Seismograms	236
7.11.3	Global Case of Using the Ray Method	236
7.11.4	The Source Time Function	237
7.11.5	Local Case of Using the Ray Method	238
7.11.6	Complete Seismogram	239
7.12	Software	240
7.13	Exercises	241

8 Spectral Analysis	245
8.1 Attenuation	245
8.2 Seismic Source Model	248
8.3 Geometrical Spreading	251
8.3.1 Local and Regional Distances	251
8.3.2 Teleseismic Distances	253
8.4 Self Similarity and Seismic Source Spectra	255
8.5 Spectral Analysis at Local and Regional Distances	257
8.6 Spectral Analysis at Teleseismic Distances	262
8.6.1 Attenuation	262
8.6.2 Geometrical Spreading	263
8.7 Determination of Q	265
8.7.1 Determine κ	265
8.7.2 Q and κ from Spectral Modeling	267
8.7.3 Coda Q	268
8.7.4 Two Station Methods for Q-Determination	273
8.7.5 Multiple Station Method for Q-Determination	276
8.8 Soil Amplification	278
8.9 Exercises	280
9 Array Processing	283
9.1 Basic Array Parameters	283
9.1.1 Example of Calculating p from a Three Station Array	286
9.1.2 Using a Seismic Network as an Array	287
9.2 Beam Forming	288
9.3 Frequency – Wavenumber Analysis (fk)	289
9.4 Array Response	290
9.5 Processing Software	292
9.5.1 Manual Processing	292
9.5.2 FK Processing	293
9.6 Using Array Measurements for Identifying Phases	294
9.7 Exercises	295
10 Operation	299
10.1 Data and Data Storage	299
10.2 Routine Processing	303
10.2.1 Screening of Detections	303
10.2.2 Event Classification	304
10.2.3 Analysis	304
10.2.4 Epi and Hypocenter Maps	307
10.2.5 Felt Earthquakes	308
10.2.6 Quality Control	309
10.2.7 Seismic Bulletin	314

Contents		xi
10.3	Data Exchange	314
10.4	Earthquake Statistics	318
10.5	Software	320
10.5.1	Processing Systems for Routine Operation	321
10.5.2	Mapping Software	323
10.6	Exercises	324
References	327
Index	339

Chapter 1

Introduction

The number of seismic stations has increased rapidly over recent years leading to an even greater increase in the amount of seismic data. The increase is partly due to the general change of recording and storing of continuous data. This requires more processing and good organization of the data. It is very easy to sell new networks and usually some kind of processing software is thrown into the deal with some training. Some manufacturers' software tend to mostly work only with data from their equipment although there is now a trend for standardizing recording formats. Thus most observatories also have a need for other processing systems than the one coming with the equipment. A number of public domain data-processing programs are available as well as a few commercial systems, and a seismic observatory typically makes use of several. However having the programs is not enough since all programs require some basic understanding of the seismological problems to be solved and how to do it in the best way. In the following, a brief introduction will be given to the main topics in this book, which are also the main problems in routine processing:

- Earthquakes and earth structure
- Recording earthquakes
- Picking phases
- Locating earthquakes
- Determining magnitude
- Source mechanism
- Managing data and formats
- Data exchange

All computer exercises, including software, are available via <http://extras.springer.com> and also available on <ftp://ftp.geo.uib.no/pub/seismo/SOFTWARE/SEISAN>, and a short overview of the exercises is given in each chapter. Description of relevant software is given in individual chapters.

Conventions: We will show many seismograms. Unless otherwise noted, they will always be original signals proportional to velocity in the instruments pass band.

Throughout the whole book, log will denote 10 based logarithm.

1.1 Earthquakes

Seismograms are recordings of ground motion. The ground is continuously at unrest mostly due to waves in the ocean (see Section 3.5), changes in the atmosphere and human activity. Sometimes higher amplitude motions are recorded and we talk about a *seismic event* (see Fig. 1.1). Seismic events are caused by a sudden release of energy by seismic sources which are mainly earthquakes, but which also can be explosions, volcanic eruptions, rock-falls etc.

In this book we will mainly deal with the analysis of data from earthquakes and we will therefore give a description of seismic sources and their origin. For a more comprehensive overview, see NMSOP, Lay and Wallace (1995) and Stein and Wysession (2003). The earthquake source can be described as a sudden release of strain energy during the movement along a fault. The reason for the movement is the slow accumulation of strain energy due to relative movement of the two sides of the fault (Figs. 1.2, 1.3, and 1.4). When the breaking strength of the rock along the fault has been reached, the fault will slip suddenly. Faults can be very small (meters) with only a fraction of a mm slip to very large (1,000 km) with tens of meters of slip. The largest faults release much more energy than the largest nuclear explosions while the smallest can be compared to a pistol shot. The earthquake size, related to the energy release, is expressed through the magnitude M (see Section 1.4 and Chapter 6). The magnitude scale is open ended, however, the largest earthquake measured so far (Chile in 1960) had a magnitude of 9.5 and for practical reasons it is hard to measure magnitudes below -3 . The global catalogs of earthquakes for the recent years contain all earthquakes larger than magnitude 4 in most areas. For more on magnitude, see Chapter 6.

For a large fault, the slip will not occur instantaneously along the whole fault, but will start at some point and then propagate (rupture) with the rupture velocity (~ 0.8 times the S-velocity, see Section 1.2 for definition of S-waves) to the end of the fault. The factor 0.8 is a common value and the factor could be in the range

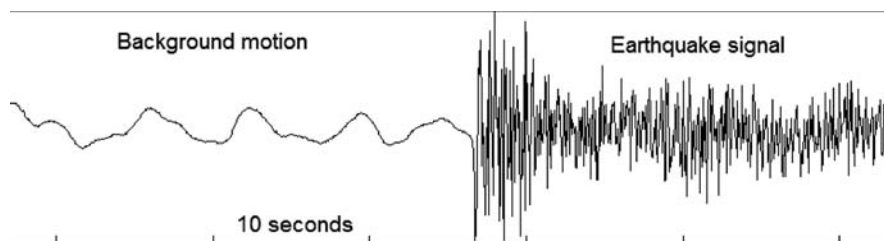


Fig. 1.1 Seismogram from an $M = 3.8$ event in Venezuela. At the left part of the seismogram is seen the natural background motion of the earth and to the right the earthquake signal. The signal amplitude is proportional to ground velocity. The station recording the event is BAUV and the time of the occurrence of the earthquake is 2003 0422 13:29 meaning year 2003, month 04, day 22, hour 13 and minute 29. This notation will be used throughout the book to refer to the time of occurrence of earthquakes

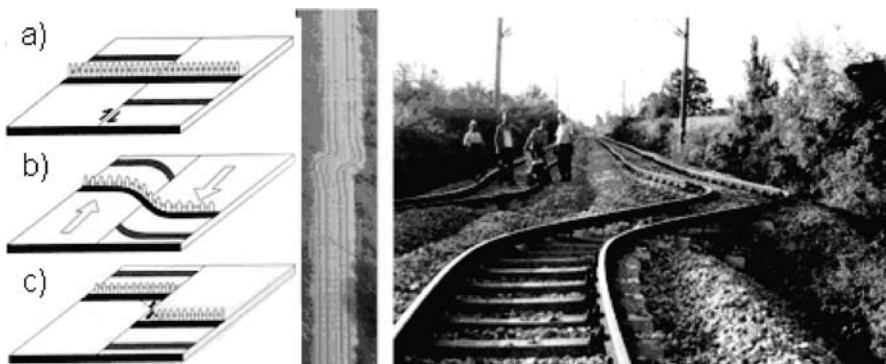


Fig. 1.2 Illustration of the elastic rebound model. *Left:* The arrows show the relative motion across the fault. **(b)** When the two sides move and the fault is locked, the material on the two sides of the fault undergoes complete elastic deformation and linear features in **(a)** become deformed, **(c)** finally the strain becomes so large that the fault slips and we have an earthquake. The deformed material rebounces to its original position and features across the fault are offset. Figure from Stein and Wysession (2003) and copied from http://epscx.wustl.edu/seismology/book/book_no_captions/figures/. *Right:* Displaced railroad tracks due to an earthquake. The earthquake causing this displacement was the 1999 Izmit earthquake of magnitude 7.4 (pictures from Aykut Barka)

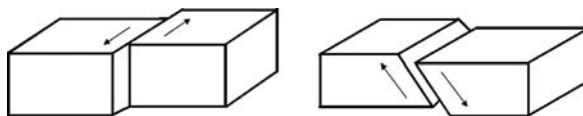


Fig. 1.3 Examples of two faults. *Left:* A vertical fault moving horizontally (strike-slip fault) with left lateral movement. *Right:* An inclined fault moving at an angle to the vertical (a dip-slip fault)

0.2–1.0. In addition there are earthquakes with extreme low rupture velocities which are called “slow”. The slowest earthquakes can last for months, but will not be discussed here as they are practically aseismic. The duration of the seismic signal, generated at the source, will last from a fraction of a second to several minutes depending on the size of the fault. The signal duration at the receiving station will be much longer since all energy does not arrive at the same time due to the internal structure of the earth and different wave speeds of different types of seismic waves (see Chapter 2). So seismograms of small and large earthquakes will look different due to signal duration and frequency content (see Chapter 8).

Faults can have different orientations relative to the earth and the motion on the fault can be in different directions relative to the fault plane. Figure 1.3 shows two simple examples. More examples and a detailed description are given in Chapter 7. At different seismic stations, an earthquake will generate different seismograms which can be used to determine the so-called fault plane solution (orientation of fault plane and slip direction on the fault). This will be described in more detail in Chapter 7.

Fig. 1.4 The El Asnam fault, Algeria, is an example of a fault with a vertical displacement. The earthquake ($M = 7.6$) occurred on October 10, 1980. Picture from <http://www.smate.wwu.edu/teched/geology/GeoHaz/eq-faults/eq-faults-19.JPG>



Some faults are visible along the surface of the earth (Figs. 1.2 and 1.4), however the majority of earthquakes have no surface expression and occur at depths down to 700 km (Frohlich, 2006), although most earthquakes occur in the crust (above Moho, see Chapter 2).

The location of the earthquake is given by latitude, longitude and depth and is called the hypocenter while the projection to the surface (only latitude and longitude) is called the epicenter. Earthquakes do not occur randomly. Figure 1.5 shows world wide epicenters as reported by the International Seismological Center (ISC), which is the main center for collecting parametric earthquake information worldwide, see www.isc.ac.uk.

It is seen that earthquakes mostly occur in particular zones. This has been explained by the theory of plate tectonics. The earth's surface is split into several rigid plates which move with velocities of 2–10 cm per year relative to each other. Along the plate boundaries we find the major faults, which are mainly of four types:

- (a) Transform faults: The plates slide along each other and we have a strike slip fault of which a famous one is the San Andreas fault in California. Another example is the Anatolia fault separating Eurasia from the Anatolian plate (most

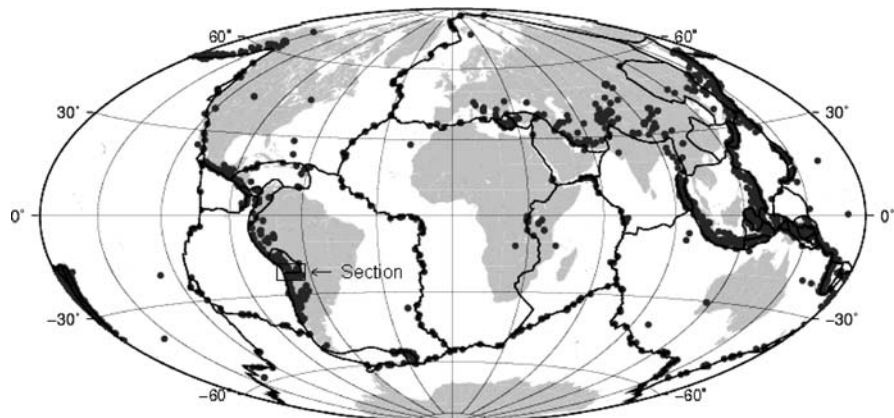
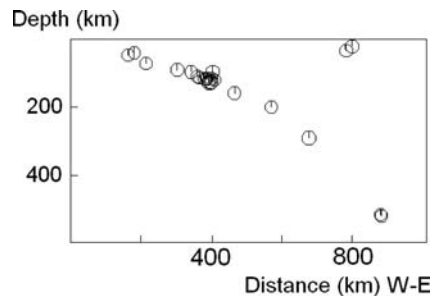


Fig. 1.5 Global epicenters for the time period 2002–2004 (inclusive). The figure shows all epicenters reported by ISC (International Seismological Center) with magnitude $m_b \geq 5.0$. The earthquakes within the square marked with "Section" are plotted on Fig. 1.6. The plate boundaries are indicated with heavy black lines

Fig. 1.6 Depth section of hypocenters across the Chilean subduction zone using the data shown in Fig. 1.5 within the rectangular section area. Note how the subducting plate is clearly indicated by the alignment of the hypocenters



of Turkey). Maximum depth of the events is usually around 20–25 km. The plate is conserved.

- (b) Convergent: The plates collide head on and one plate is sliding under the other in the so-called subduction zones, which produce earthquakes down to about 700 km and volcanic mountain chains. An example is the subduction zone of the coast of Chile (Fig. 1.5), which produced the largest recorded earthquake ($M = 9.5$) in 1960. The plate is destructed when it reaches the lower mantle.
- (c) Convergent: The plates collide without one of them being subducted, or partly subduced, leading to the buildup of mountains as for example in the case of the Himalayas. The resulting faulting is complex, but dominated by thrust and strike-slip movement. The plate is deformed and the rocks undergo changes.
- (d) Divergent: Mid-oceanic spreading centers like the Mid-Atlantic Ridge where adding of fresh ocean crust by upwelling material to the already existing relatively young ocean plate takes place. This generates shallow (< 15 km) earthquakes. The plate is created.

For more details of earthquakes and plate tectonics, see e.g. Stein and Wysession (2003).

The motion of the plates is thus the major generator of strain accumulation and the largest earthquakes occur between or near the plate boundaries. We call such earthquakes interplate earthquakes. However significant earthquakes also occur inside the plates, the intraplate earthquakes, and small earthquakes occur virtually in all regions. Different types of earthquakes also occur at volcanoes. The processing of these earthquakes is similar to that of purely tectonic events, but the identification of the different types requires techniques that are beyond the scope of this book. For more details on volcanic seismology see Zobin (2003), McGuire et al. (1995) and NMSOP.

Seismologists are fond of saying “Give me a sufficiently sensitive seismograph, and I will find earthquakes anywhere” (see Chapter 3). These smaller earthquakes might be caused by secondary effects like uplift during deglaciation (e.g. Muir-Wood, 2000) and geological processes related to erosion and sediment loading (e.g. Bungum et al., 1990). It has also been shown that the stresses generated at the plate boundaries propagate far inside the plates and can generate small earthquakes. There are about one great earthquake ($M > 8$) a year and more than 1,000,000 earthquakes ($M < 2$) a year. Most small seismic networks are able to detect all events larger than magnitude 2 within the network. So there is ample opportunity to study and analyze seismic events at most places on the earth.

1.2 Recording Seismic Events and Picking Phases

The elastic waves sent out by the earthquake can be recorded both locally (small earthquakes) and globally by seismic instruments called seismographs. The principle of the seismograph is seen in Fig. 1.7 which shows a mechanical analog seismograph where there is a direct translation from the ground motion (too small to be felt) to the amplified ground motion recording on the paper.

Today almost all seismographs are based on digital recording where the amplified ground motion is recorded as a series of numbers which can be plotted to look like a traditional seismogram (see Fig. 1.1) or used for more sophisticated digital processing (see Chapter 4 on signal processing).

Using both digital and analog seismic recordings, the gain of the instrument (relation between the amplitude on the seismogram and on the ground) is known and can be related back to the true motion of the ground. The gain together with the seismometer and possibly filter response as function of frequency is the so-called instrument response. It is an important characteristic without which only little analysis can be made and, therefore, should always be supplied with the waveform data. Instruments will be dealt with more extensively in Chapter 3.

Once we have recordings of seismic events, the arrival times of new wave groups with distinctly larger amplitudes than the background motion, called seismic phases, have to be picked, see Figs. 1.9 and 1.10. Several types of phases can be

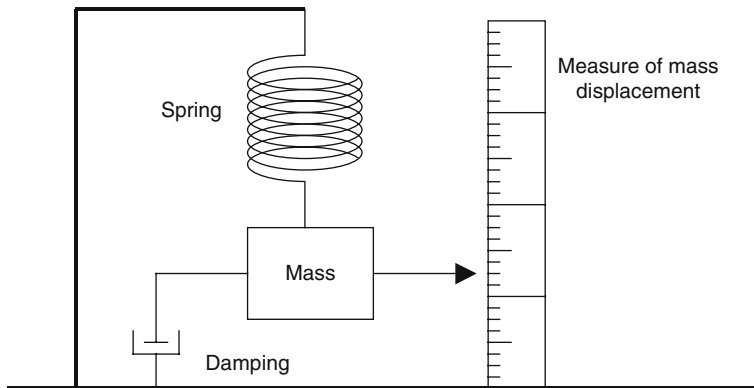


Fig. 1.7 Principle behind the inertial seismometer. It is shown for illustration, but is in little use today. The damping of the motion can be mechanical, but is usually electro-magnetic. This kind of seismograph had a magnification up to a few hundred times, however the instrument shown has a magnification of one (no magnification). Reproduced with kind permission of Springer Science and Business Media. Figure from Havskov and Alguacil (2006), Fig. 1.3

distinguished in a seismogram, mainly due to the different types of seismic waves and the layering of the earth. The principle types of seismic waves are (see Fig. 1.8):

- P-waves: Compressional waves, P stands for primary since these waves are the first to arrive. A typical velocity in the upper crust (depth less than 15 km) is 6 km/s.
- S-waves: Shear waves. S also stands for secondary, since S-waves arrive after the P-wave. A typical velocity in the upper crust is 3.5 km/s.
- Surface waves: Waves traveling along the surface. Multiply reflected and superimposed S-waves (Love waves) or a combination of P and S-waves (Rayleigh waves). Typical velocities are 3.5–4.5 km/s. Surface waves always arrive after the S-waves.

P and S-waves are called body waves since they travel in the interior of the earth as opposed to surface waves.

Theoretically the velocity ratio between P and S velocities, v_p/v_s is equal to $\sqrt{3} = 1.73$. In practice it is often closer to 1.78. The surface wave velocities are quite constant over similar structures (like the ocean), however their speed varies with the frequency such that the lowest frequencies travel faster than the higher frequencies so the lowest frequency surface waves arrive before the higher frequency surface waves (see Fig. 1.10 and examples in Chapter 2). This phenomenon is called dispersion and causes interference between surface waves of slightly different frequencies creating wave groups traveling with the so-called group velocity. This is the velocity with which the surface waves travel from the source to the receiver and we will just use the term velocity for group velocity of surface waves. Surface waves are generated by earthquakes near the surface. As the depth of earthquakes increases the surface amplitudes get smaller and smaller to completely disappear for a source depth of a few hundred km.

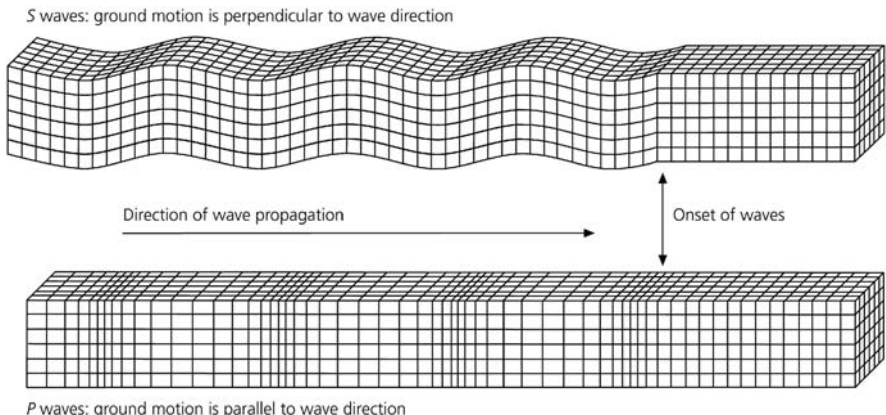


Fig. 1.8 Motion of P and S waves. Figure from Stein and Wysession (2003) and copied from http://epscx.wustl.edu/seismology/book/book_no_captions/figures/

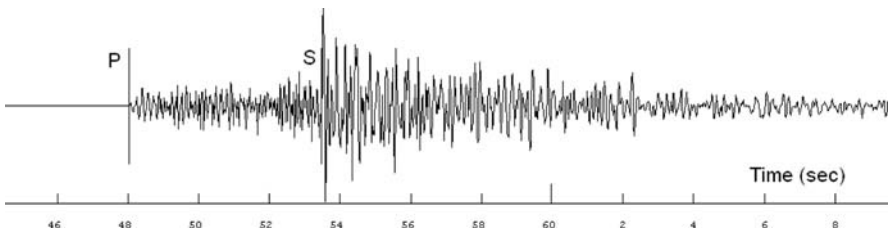


Fig. 1.9 Example of a local earthquake. The P and S arrivals are clearly seen. The seismogram is a recording of the vertical ground motion from station AFUE in the Andalucian seismic network. The time of the earthquake is 2006 0108 15:08, the magnitude is 2.5 and the distance to the earthquake is 40 km

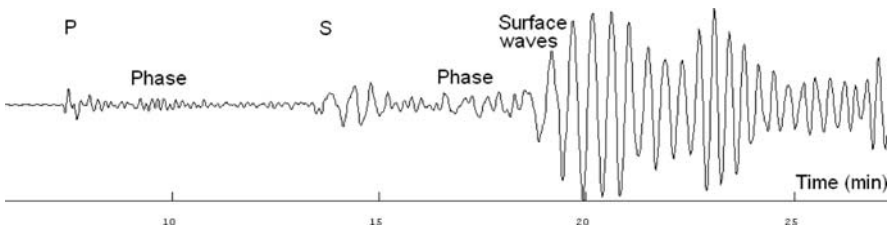


Fig. 1.10 Example of a seismogram recorded at a global distance. The P, S and surface waves are clearly seen. In addition other arrivals are observed (marked as Phase), which are a result of internal reflections in the earth (see Chapter 2). Note the dispersion of the surface waves where the velocity depends on the frequency. The seismogram is a recording of the vertical ground motion from station ERM in the global seismic network. The time of the earthquake is 2007 1002 18:00, the magnitude is 6.2, the depth is 32 km and the distance to the earthquake is 4,200 km. The distance for global earthquakes are mostly measured in degrees and $4,200 \text{ km} = 37.8^\circ$

When starting processing it is necessary to determine the type of event and estimate the distance. For analysis purpose, earthquakes are roughly divided into local earthquakes (distance to stations < 1,000 km), regional earthquakes (distance to stations 1,000–2,000 km) and global earthquakes (terms teleseismic and distant also used) where the distance is > 2,000 km. The distance ranges are not well defined. For earthquake location, the arrival times of P and S are used for local and regional earthquakes and mainly P for global earthquakes, see next section. Figure 1.9 shows a typical seismogram of a local earthquake and Fig. 1.10 a global earthquake.

The first and main task of earthquake analysis is to pick the arrival times of the seismic phases, which is used to locate the earthquake (see next section). In the example above for the local earthquake, we clearly see the P and S-phases and the S-phase usually has the largest amplitude. In this case, the seismogram is simple and P and S are the main phases, but a seismogram for a local earthquake can be more complicated by having phase arrivals from more interfaces, see Chapter 2 for more examples. However, most of the seismograms show scattered waves due to inhomogeneity within the earth and these waves are seen between P and S and at the end of the seismogram.

Earthquakes recorded at large distances can have phases traveling different ways to the station passing all parts of the earth and this can give rise to many different phases, which can be used to study the interior of the earth. Seismology is therefore also the science that has given us the most information about the interior of the earth. In observational seismology, the P-phase is the most common to read but encouragement should be given to read as many phases as possible in order to gain more information of the interior of the earth. For more details on global phases, see Chapter 2.

Picking phases is a skill which requires much practice and the phases observed might be something different than initially assumed. With digital recordings, different filters can be used to enhance certain phases and suppress noise, however this can introduce new problems of phase shift, see Chapter 4 on signal processing.

A seismic array consists of a group of seismic stations placed within an area of a few hundred meters to a few kilometers. Since the stations are so close together, the signals at each station are similar but arriving with a small time delay relative to each other (see Fig. 9.2). By adding the signals with the time delay corresponding to the arrival direction and speed of the seismic waves, the signal to noise ratio can be significantly improved and a seismic array can detect smaller signals than a single seismic station. The time delay can be used to determine the direction and speed of arrival. Basic array analysis techniques will be dealt with in Chapter 9.

1.3 Locating Earthquakes

The next step in the processing of earthquake data is determining the hypocenter. Since the velocity within the earth is known, the travel time as a function of epicentral distance (distance from the station to the epicenter) can be calculated. The arrival

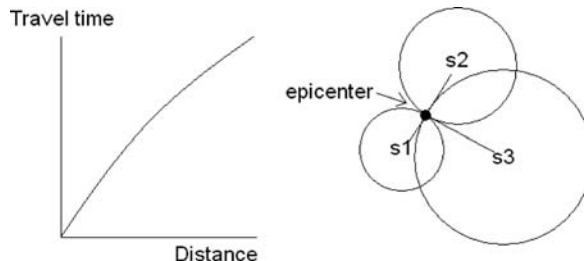


Fig. 1.11 Travel time and location. *Left:* The relation between travel time and distance and to the *right* the principle of location. *Right:* Three stations are located at s_1 , s_2 and s_3 respectively and the P-waves arrive first to s_1 , then to s_2 and finally to s_3 . Thus s_1 must be closest to the epicenter and s_3 furthest from the epicenter. Assuming an origin time, the distance from each station to the epicenter can be calculated and circles drawn. Given a particular travel time-distance relation, there will only be one point and corresponding origin time where all three circles meet

times at the stations can then be used to determine the hypocenter (see Fig. 1.11) and the time of the occurrence of the event (origin time).

The epicenter determined, and particularly the depth, are not giving the exact location due to errors in the arrival time observations and differences between the model and the real earth. Errors of 10 km for local earthquakes and 50 km for global events are common. Earthquake location was earlier done manually, but is now exclusively done by computer. This involves setting up a set of equations as a function of the arrival times and the station locations. These equations are then solved in an iterative process. Most seismic networks will publish a bulletin giving the hypocenters and magnitudes of events recorded by the network. Globally, most observations are collected at the International Seismological Center (ISC) which reprocess all data and publishes a comprehensive global catalog that also includes all local earthquakes reported to the ISC. It is therefore important that all observatories report all their observations to the ISC. For more information on location, see Chapter 5.

1.4 Magnitude

Determining magnitude is an integral part of processing earthquake data and is done routinely with nearly all earthquakes located, whether global or local. The magnitude is an arbitrary number proportional to the size of the event (energy released) and the size of the number is locked to the original definition by Richter (1935) which states that a magnitude 3 earthquake has a maximum amplitude of 1 mm on a Wood-Anderson seismograph (see Chapter 3) at an epicentral distance of 100 km. Obviously, the same earthquake would have a larger amplitude on a Wood-Anderson seismograph at a shorter distance so a distance correction function must be used. Also another seismograph with another gain has a different amplitude. Therefore the general magnitude scale now used is not based on the amplitude on a particular instrument, but rather on the maximum amplitude on the ground measured in

displacement. This therefore requires knowledge of the instrument response. The general relation for determining magnitude M is then

$$M = \log(A_{\max}) + f(\Delta) + c \quad (1.1)$$

where A_{\max} is the maximum ground displacement, $f(\Delta)$ is a correction function depending on distance Δ and C is a constant linking the scale to the original definition. Different magnitude scales are in use, all with similar relations as (1.1), based on different types of seismic waves and epicentral distances. The most important amplitude based magnitude scales are:

- Local magnitudes M_L : Based on the original Richter scale, used for local earthquakes.
- Body wave magnitude m_b : Using the P-wave of distant events.
- Surface wave magnitude M_s : Using the surface waves of distant events.

The earthquake size can also be determined from the seismic moment M_0 defined as

$$M_0 = \mu AD \quad (1.2)$$

where μ is the rigidity, A is the area of the fault and D is the slip on the fault and the so-called moment magnitude M_w is defined as

$$M_w \sim \log(M_0) \quad (1.3)$$

For most observatories, the simplest observation to obtain is the maximum amplitude and it is usually processed routinely. The seismic moment can be obtained either by spectral analysis (any size event, see Chapter 6) or, more reliably, by moment tensor inversion (mostly events larger than magnitude 4, see Chapter 7). For larger events ($M > 5$), this is done routinely by international agencies and M_w is considered the most meaningful magnitude.

1.5 Fault Plane Solution

The orientation of the fault (see Fig. 1.3 and Fig. 1.12) is important information for understanding the nature of the earthquake rupture. The so-called fault plane solution is defined by 3 parameters: Strike, slip and dip of the fault (see Fig. 7.1). The first two parameters are related to the physical orientation of the fault in space and the last parameter, slip, is the direction of movement in the fault plane. The earthquake source can mathematically be described as the radiation from two force double couples (see Chapter 7).

Seismic sources can be more complex than a double couple and for a complete description of the general radiation from a seismic source in any

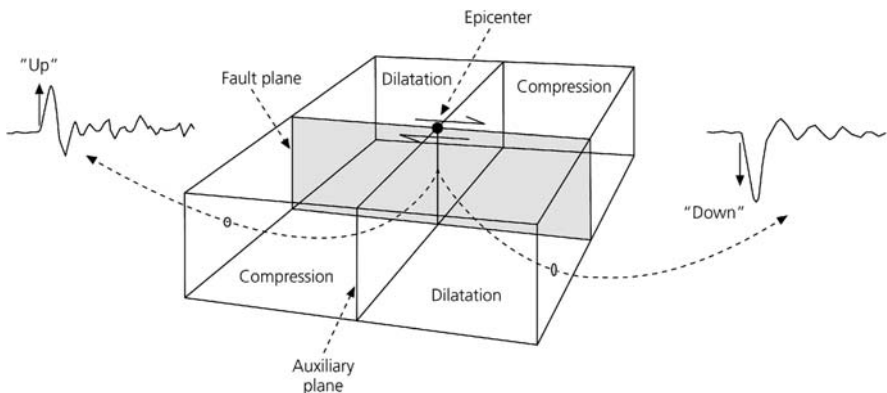


Fig. 1.12 First motion of P observed at different directions relative to the fault plane. The 2 arrows in the fault plane show the relative slip direction in the fault plane. Figure from Stein and Wysession (2003) and copied from http://epscx.wustl.edu/seismology/book/book_no_captions/figures/

coordinate system, a combination of the radiation from 5 double couples and an explosion is used. These parameters are combined in the so-called moment tensor, see Chapter 7.

Fault plane solutions are currently not determined routinely for all events due to a lack of data and the difficulty in computing the fault plane solution. However, more and more events have fault plane solutions determined as it has become easier to do this analysis with increasing quantity and quality of data as well as with more automated analysis techniques. For events larger than magnitude 5, moment tensors are routinely determined by larger agencies. Ideally, it should be a routine parameter like hypocenter and magnitude. The basic information used for fault plane solution is the fact that a seismic event radiates waves with different amplitude and polarity in different direction relative to the slip direction on the fault plane. The most common ways of determining the fault plane solution are then:

- Polarity of the first P-arrival. This is the simplest amplitude information to use, either +1 (compression) or -1 (dilatation), see Fig. 1.12. It can be used with all types of earthquakes and at all distances. Can be done manually.
- Maximum amplitudes of the P and S-waves. In a grid search, the observed amplitudes or their ratio are compared with the theoretical calculated values and a best solution is found.
- Moment tensor inversion (see Chapter 7). The whole or a large part of the seismogram is compared to the theoretical seismograms and an inversion is made for the moment tensor from which the most significant double couple can be extracted.

1.6 Further Data Analysis

The basic analysis described above generates a lot of parameters which are linked to the original data. For a seismic observatory or data agency it is important that the data is stored in a systematic way in some kind of data base. Fortunately some

international standards are emerging for both data storage and data retrieval and some software system are freely available for both processing and storing the data, see software sections in relevant chapters.

Once the data is in a data base and basic parameters have been determined, further analysis and/or presentations might be done for reporting or research purpose.

- Bulletin production: Most observatories and agencies produce a bulletin of observations and basic parameters and distribute to interested parties. While this used to be exclusively in paper form, distribution is now in electronic form. ISC still distributes a paper bulletin for the largest events ($M > 5$). Table 10.4 shows an example.
- Epi-and hypocenter maps: In order to study the spatial distribution of earthquakes, epicenter maps (see Fig. 1.5) in different forms and depth sections of earthquakes are routinely produced. An example of a depth section is seen in Fig. 1.6. In the daily processing, epicenters of single events are often placed on a geographical map to judge the location in relation to places and known earthquake zones (see Chapter 10).
- Earthquake statistics: After accumulating months or years of data, earthquake statistics can be produced. This includes number of event per time unit (e.g. year) and distribution of magnitude sizes used to predict the frequency of occurrence of a given magnitudes, like “statistically a magnitude 5 event will occur every 10 years” in a particular region. see Chapter 10.
- Spectral analysis: Using a displacement spectrum of the P or S-waves, information can be derived of the seismic moment, the size of the fault and the stress drop, all important source parameters. This is part of the routine analysis at some observatories. See Chapter 8.
- Determination of crustal parameters: In general the crustal model including attenuation is required input for routine analysis. In some regions these parameter are uncertain or unknown, so values from other similar regions are used. It is not the purpose of this book to give detailed instruction on how to determine crustal models since this is a well documented field with many text books. However a summary of procedures on how the use earthquake data for determining crustal parameters will be given (see Chapter 2). Simple methods of determining the velocity ratio v_p/v_s (Chapter 5) and Q (Chapter 8) will be dealt with in detail in this book.

1.7 Software

Processing earthquake data without computers is not possible today, not least because practically all data is digital. However most of the important advances in seismology like obtaining travel time curves, determining hypocenters and magnitudes and deriving the internal structure of the earth were done without computers before 1940. Many of the calculations were similar as today, just done by hand! Some of the manual procedures will be used in the exercises in this book.

In seismology there are a large number of programs available and nearly all are non-commercial and the amount of documentation is variable. Some programs are developed locally and only used at one site while others have made their programs available and these public domain programs are found at the institutional home pages. A large collection is found at the ORFEUS (Observatories and Research Facilities for European Seismology) data center <http://www.orfeus-eu.org/Software/software.html>. Some of the most commonly used programs will be described in the relevant chapters. Most of the computer examples in the book are made with the SEISAN software which is available with a manual, test data and a training course via <http://extras.springer.com>.

Chapter 2

Earth Structure and Seismic Phases

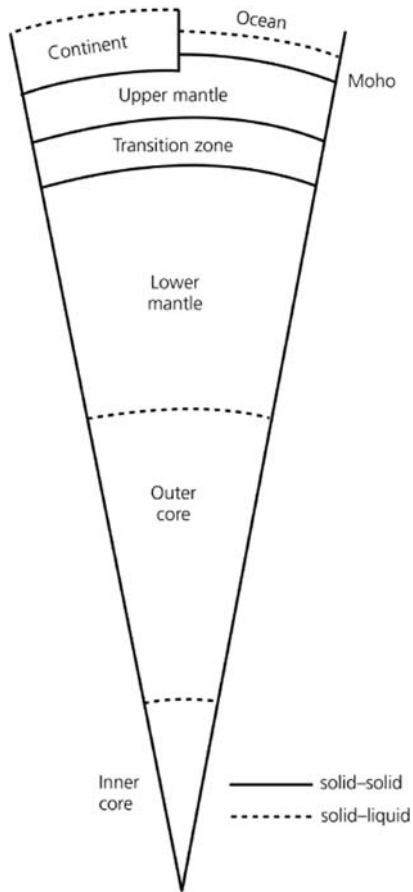
The most basic and most important processing task in seismology is to determine the arrival times of seismic phases. When the first seismic stations with reliable timing appeared more than 100 years ago, they provided, through the observation of travel times, the first real evidence of the internal structure of the earth. Initially there were many unknown wiggles (phases) on the seismogram, however with better and better earth models, we now understand the presence of most of the phases but there are still “abnormal” arrivals to be investigated. In order for the analyst to correctly interpret the seismograms it is therefore important to have a basic understanding, not only of how seismograms look, but also of earth structure, seismic rays and phases. Reading phases is as important as ever since they provide the basic material for improved earth structure (1 and 3D) as well as being used for event location (see Chapter 5). Many phase readings are now done automatically, particularly for the first arriving phase. However, no automatic procedure can for the time being replace the trained analysts who come to know their network and stations. Based on this experience they are able to recognize features in the seismogram by “human pattern recognition”.

In this chapter we will describe the most basic concepts of earth structure, seismic rays and phases and give examples of how to identify phases. These topics have been dealt with extensively in the literature, and text books have been dedicated to this topic. For earth structure and seismic rays, see e.g. NMSOP, Lay and Wallace (1995), Stein and Wysession (2003) and Aki and Richards (2002). Examples of seismograms and guidelines for reading seismic phases are extensively dealt with in NMSOP and Kulhánek (1990). Many good examples with theoretical explanation are found in Kennett (2002).

2.1 Earth Structure

The basic earth structure, as we know it today, is seen in Fig. 2.1. Looking into the earth from the surface, the basic layers are the upper solid crust, solid mantle, liquid core and solid inner core. Most earthquakes occur in the crust, and the crust-mantle boundary is called the Mohorovičić discontinuity, usually just named Moho.

Fig. 2.1 Earth structure showing the main interfaces within the earth (not to scale). Figure from Stein and Wysession (2003) and copied from http://epscx.wustl.edu/seismology/book/book_no_captions/figures/



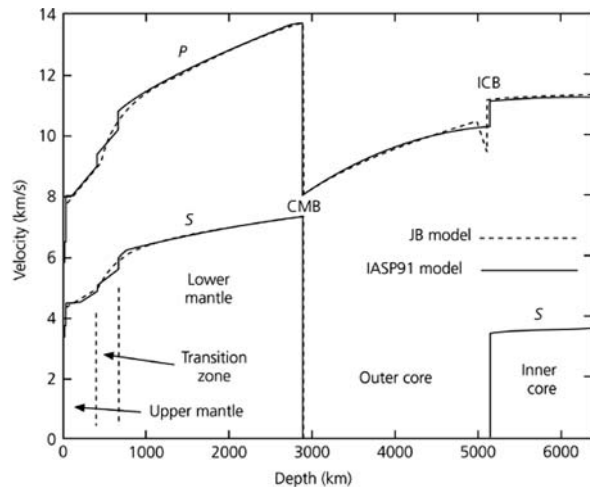
The crust has a P velocity v_p of 5–7 km/s and just below the Moho, v_p is typically around 8 km/s (normally in the range 7.8–8.2 km/s). The thickness of the crust varies globally from 8 km under the Mid-oceanic ridges to 70 km under high mountains. A typical thickness under continents is 30 km. The continental crust is often complicated and needs to be approximated by several layers. A crustal model may include soft and hard sediments, followed by upper, middle and lower crust. In some areas the model may be simpler, consisting only of upper and lower crust, separated by the Conrad discontinuity. A summary of global crustal thicknesses is seen in Fig. 2.2.

The mantle extends to the core-mantle boundary CMB (2,900 km). It is divided into the upper mantle and lower mantle by an area around 660 km's depth (the transition zone) where there are sharp velocity gradients (Fig. 2.3). There is a world wide low velocity layer in the upper mantle in the depth range 100–250 km which is however not well developed or even absent under large Precambrian cratonic areas.



Fig. 2.2 Contour map of thickness of the Earth's crust. The contour interval is 10 km except for the continents where contour 45 km also is included. Figure from <http://earthquake.usgs.gov/research/structure/crust/index.php>

Fig. 2.3 Earth velocity models. The velocity is given for P and S-waves. CMB is core-mantle boundary and ICB is inner core boundary. Figure from Stein and Wysession (2003) and copied from http://epscx.wustl.edu/seismology/book/book_no_captions/figures/



The relatively rigid mantle and crust above the low velocity zone is called the lithosphere while the area below is called the asthenosphere (extending down to about 400 km).

The core is divided into the outer liquid core and the inner solid core with a sharp boundary at 5,100 km.

Earth velocity models are shown in Fig. 2.3. The first modern earth model was made by Jeffreys and Bullen (1940) (JB-model). This was in the days before computers and represented a monumental amount of manual calculations. It is seen that the most pronounced discontinuity is at the core-mantle boundary where the P-velocity decreases drastically and no S-waves can pass due to the outer core being liquid.

The JB-model has later been revised, when much more data and computer power became available and in 1991 the IASP91 model was launched (Kennett and Engdahl, 1991). Notice the small difference with the JB-model. The latest generally recognized model is the AK135 (Kennett et al., 1995), which is an improvement over the IASP91, especially for velocities in the earth's core and it is now considered the best model for global earthquake location.

2.2 Seismic Rays

A seismic ray is defined as a line normal to the wavefront as it travels through the earth. It will only travel in a straight line from A to B if the wave velocity is constant. Since this is not the case in the real earth (Fig. 2.3), the ray will be curved following Snell's law. If for simplicity it is assumed that the earth can be divided into series of flat parallel layers (Fig. 2.4), Snell's law can be written

$$\sin(i_1)/v_1 = \sin(i_2)/v_2 = p \quad (2.1)$$

where i is the angle of incidence and v the wave velocity (the subscript indicates the layer number) and p is the so-called ray parameter. Snell's law can also be used to calculate the ray paths of reflected and critically refracted phases, see Fig. 2.5.

For the reflected ray, the two angles i_1 and i_2 are equal since the velocity is the same for the incoming and reflected ray. As the angle of incidence increases, i_2 will become 90° when $\sin(i_1) = v_1/v_2$ and the ray will be critically refracted along the

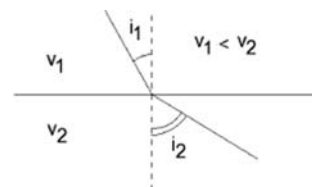


Fig. 2.4 A seismic ray through two layers. v_1 and v_2 are the velocities

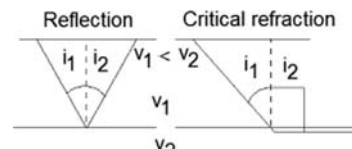


Fig. 2.5 Reflection and critical refraction of rays

interface. When i_1 becomes larger than critical, the ray is totally reflected and not refracted into the second layer.

Due to Snell's law, the ray is thus bending at the interface if the two velocities are different. Since this relation holds for all interfaces, the quantity $\sin(i)/v$ will be constant and the ray parameter is constant. The quantity $1/p$ is also the apparent velocity along the interface (see also Chapter 9). Using Snell's law, it is thus in principle possible to trace the ray through a flat earth from the hypocenter to the seismic station. If the layers are thin, we can consider the velocity as smoothly varying and the ray will be along a smooth curve (see Fig. 2.6).

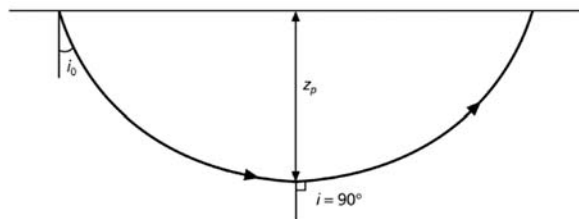


Fig. 2.6 Ray path in an example of linearly increasing velocity with depth. In this case the ray-path is a segment of a circle. The figure is modified from Stein and Wysession (2003) and copied from http://epscx.wustl.edu/seismology/book/book_no_captions/figures

In this case the ray will have a maximum depth z_p at one point. This kind of wave is sometimes called a diving wave.

For distances more than a few hundred kilometers, a spherical earth (Fig. 2.7) model must be used and the ray parameter can be shown to be calculated as (e.g. Stein and Wysession, 2003)

$$p = r_1 \sin(i_1)/v_1 = r_2 \sin(i_2)/v_2 = r \sin(i)/v \quad (2.2)$$

where r is the distance from the center (km). The velocity is mostly smoothly varying and the ray-paths will mostly be curves (see Fig. 2.8) just as the case above (Fig. 2.6). Note that the unit of p is radian/s.

It is seen that in principle, once the velocity structure of the earth is known, a ray can be traced through the earth using a given start ray parameter or angle of incidence at the surface or the earthquake hypocenter.

The radial symmetric earth is a first approximation. In the real earth velocities also vary horizontally, particularly at plate boundaries, so ray tracing becomes more complicated but it follows in principle the methods described above. A further complication can be that the velocity depends on the direction of the ray through the media. This phenomenon is called anisotropy and can result in e.g. S-waves arriving at different times on different components, see an example in Fig. 4.16.

Fig. 2.7 Ray parameter in a spherical earth. v_1 and v_2 are velocities. Modified from http://epscx.wustl.edu/seismology/book/book_no_captions/figures

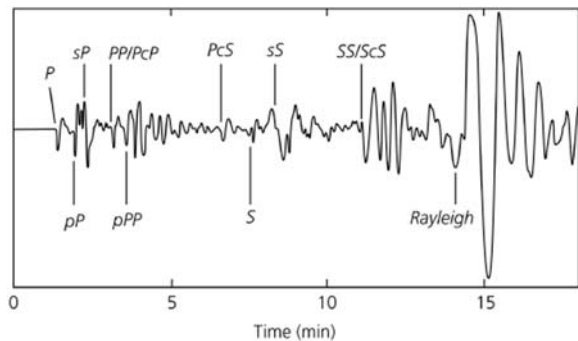
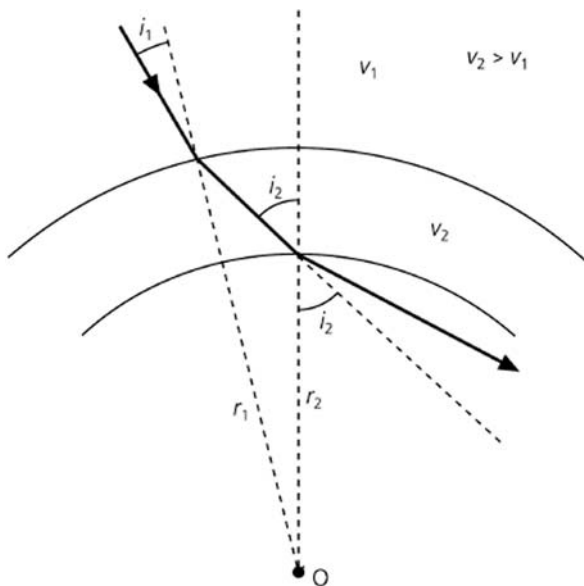
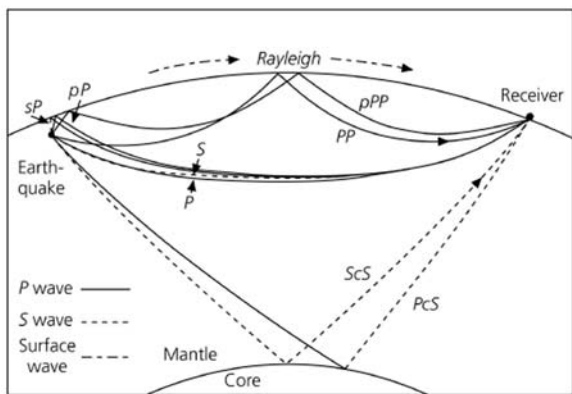


Fig. 2.8 Top: Long period seismogram (Z-component) showing typical global phases; Bottom: Ray paths of some of the phases seen in the seismogram. P-phases are shown as solid lines and S-phases as dotted lines. Notice that the P and S phases do not travel the exact same path since their velocity ratio is not constant. The figure is from Stein and Wysession (2003) and copied from http://epscx.wustl.edu/seismology/book/book_no_captions/figures/



2.3 Seismic Phases

Due to the internal structure of the earth, seismic waves can travel along multiple paths between the source and receiver and this can result in a seismogram containing many more phases than just the P and S as illustrated in Fig. 2.8. The figure shows some of the most important generally observed phases.

Note that the reflection points of ScS and PcS at the CMB and the reflection points of pP and sP at the surface are different. This can be explained by Snell's law due to the difference in P and S-velocity. Figure 2.8 shows a few of the possibilities while Fig. 2.9 shows a more complete picture of the most common body wave phases. At distances larger than 103° there is no longer a direct P due to the earth's core and only at 140° will direct P passing through the core appear (PKP phases). The distance range $103\text{--}140^\circ$ is therefore called the shadow zone and only P-waves, Pdif, diffracted around the core (Fig. 2.10) will be seen as direct arrivals (and corresponding for S).

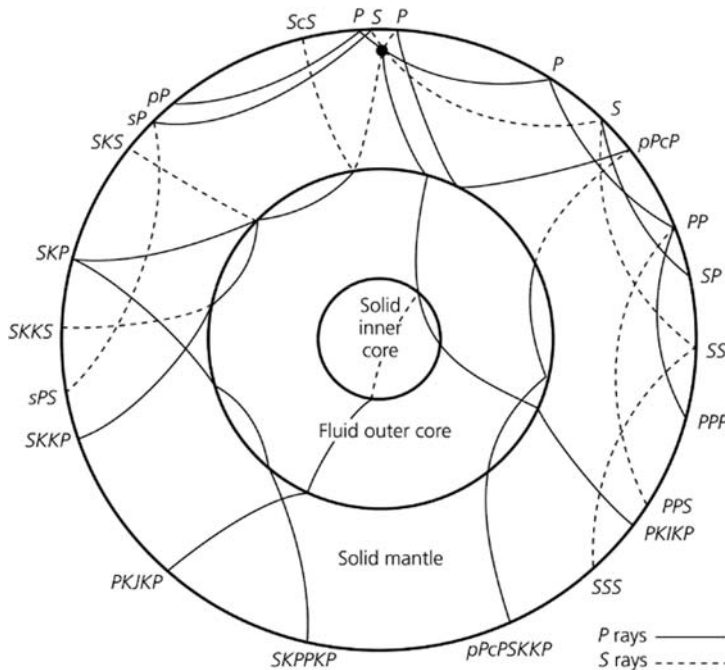
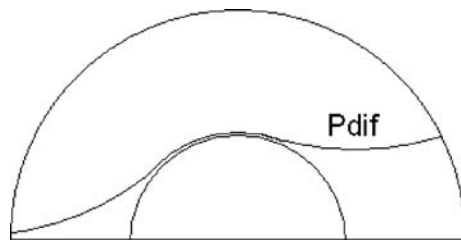


Fig. 2.9 Examples of body wave phases on a global scale. The large figure is from Stein and Wysession (2003) and copied from http://epscx.wustl.edu/seismology/book/book_no_captions/figures/

Fig. 2.10 The Pdif phase

In order to systematically name phases, a few rules apply of which the most important are:

P:	Compressional wave
S:	Shear wave
K:	P wave through outer core
I:	P wave through inner core
PP and SS:	P or S wave reflected once at the surface
PPP:	P wave reflected two times at the surface etc.
SP and PS:	S converted to P or P converted to S during reflection at the surface
pP , pS, sS or sP:	P or S wave upgoing from the focus and reflected or converted at the surface
c:	Denotes a reflections at the core-mantle boundary
Pdif:	P wave diffracted along core-mantle boundary

These phase nomenclatures and several more can endlessly be combined for seismic waves with complicated travel paths and a revised phase list has been adopted by the IASPEI Commission on Seismological Observation and Interpretation. This list (Table 2.1) can be found at the ISC home page. The rationale behind the new phase list is published in Storchak et al., (2003) with figures showing the different ray paths.

In addition to what might be labeled global phases, there is also a series of local phases, where the travel path is approximated to be in a flat earth with plane parallel layers (Fig. 2.11). The crust is simplified to have two layers, a top granitic layer and a bottom basaltic layer and the boundary between them is often called the Conrad discontinuity. This layering is only valid for some continental areas. Under the oceans, the crust is much thinner (10–15 km) and usually only has a basaltic layer. Some phases generated in this model are seen on Fig. 2.11. The most common phases are the direct phases Pg, Sg (g: granite) and the critically refracted phases Pn, Sn, while Pb (b: basalt, sometimes called P*) is harder to observe. The Moho reflections PmP and SmS are only seen at distances where the angle of incidence at Moho is larger than critical (see Fig. 2.5), usually at epicentral distances larger than 70–100 km. Critically refracted phases are theoretically expected to have small amplitudes and direct phases large amplitudes. Sometimes, the converted phase SmP

Table 2.1 IASPEI approved names for seismic phases. The list can be found at ISC (www.isc.ac.uk) where updates also will be available

Crustal phases

Pg	At short distances, either an upgoing P wave from a source in the upper crust or a P wave bottoming in the upper crust. At larger distances also arrivals caused by multiple P-wave reverberations inside the whole crust with a group velocity around 5.8 km/s.
Pb	(alt:P*) Either an upgoing P wave from a source in the lower crust or a P wave bottoming in the lower crust
Pn	Any P wave bottoming in the uppermost mantle or an upgoing P wave from a source in the uppermost mantle
PnPn	Pn free surface reflection
PgPg	Pg free surface reflection
PmP	P reflection from the outer side of the Moho
PmPN	PmP multiple free surface reflection; N is a positive integer. For example, PmP2 is PmPPmP
PmS	P to S reflection from the outer side of the Moho
Sg	At short distances, either an upgoing S wave from a source in the upper crust or an S wave bottoming in the upper crust. At larger distances also arrivals caused by superposition of multiple S-wave reverberations and SV to P and/or P to SV conversions inside the whole crust.
Sb	(alt:S*) Either an upgoing S wave from a source in the lower crust or an S wave bottoming in the lower crust
Sn	Any S wave bottoming in the uppermost mantle or an upgoing S wave from a source in the uppermost mantle
SnSn	Sn free surface reflection
SgSg	Sg free surface reflection
SmS	S reflection from the outer side of the Moho
SmSN	SmS multiple free surface reflection; N is a positive integer. For example, SmS2 is SmSSmS
SmP	S to P reflection from the outer side of the Moho
Lg	A wave group observed at larger regional distances and caused by superposition of multiple S-wave reverberations and SV to P and/or P to SV conversions inside the whole crust. The maximum energy travels with a group velocity around 3.5 km/s
Rg	Short period crustal Rayleigh wave
Mantle phases	
P	A longitudinal wave, bottoming below the uppermost mantle; also an upgoing longitudinal wave from a source below the uppermost mantle
PP	Free surface reflection of P wave leaving a source downwards
PS	P, leaving a source downwards, reflected as an S at the free surface. At shorter distances the first leg is represented by a crustal P wave.
PPP	analogous to PP
PPS	PP to S converted reflection at the free surface; travel time matches that of PSP
PSS	PS reflected at the free surface
PcP	P reflection from the core-mantle boundary (CMB)
PcS	P to S converted reflection from the CMB
PcPN	PcP multiple free surface reflection; N is a positive integer. For example Pcp2 is PcpPcp
Pz+P	(alt:PzP) P reflection from outer side of a discontinuity at depth z; z may be a positive numerical value in km. For example P660+P is a P reflection from the top of the 660 km discontinuity.
Pz-P	P reflection from inner side of discontinuity at depth z. For example, P660-P is a P reflection from below the 660 km discontinuity, which means it is precursory to PP.

Table 2.1 (continued)

Pz+S	(alt:PzS) P to S converted reflection from outer side of discontinuity at depth z
Pz-S	P to S converted reflection from inner side of discontinuity at depth z
PScS	P (leaving a source downwards) to ScS reflection at the free surface
Pdif	(old:Pdif) P diffracted along the CMB in the mantle
S	A shear wave, bottoming below the uppermost mantle; also an upgoing shear wave from a source below the uppermost mantle
SS	Free surface reflection of an S wave leaving a source downwards
SP	S, leaving source downwards, reflected as P at the free surface. At shorter distances the second leg is represented by a crustal P wave.
SSS	analogous to SS
SSP	SS to P converted reflection at the free surface; travel time matches that of SPS
SPP	SP reflected at the free surface
ScS	S reflection from the CMB
ScP	S to P converted reflection from the CMB
ScSN	ScS multiple free surface reflection; N is a positive integer. For example ScS2 is ScSScS
Sz+S	(alt:SzS) S reflection from outer side of a discontinuity at depth z; z may be a positive numerical value in km. For example S660+S is an S reflection from the top of the 660 km discontinuity.
Sz-S	S reflection from inner side of discontinuity at depth z. For example, S660-S is an S reflection from below the 660 km discontinuity, which means it is precursory to SS.
Sz+P	(alt:SzP) S to P converted reflection from outer side of discontinuity at depth z
Sz-P	S to P converted reflection from inner side of discontinuity at depth z
ScSP	ScS to P reflection at the free surface
Sdif	(old:Sdif) S diffracted along the CMB in the mantle
Core phases	
PKP	(alt:P') unspecified P wave bottoming in the core
PKPab	(old:PKP2) P wave bottoming in the upper outer core; ab indicates the retrograde branch of the PKP caustic
PKPbc	(old:PKP1) P wave bottoming in the lower outer core; bc indicates the prograde branch of the PKP caustic
PKPdf	(alt:PKIKP) P wave bottoming in the inner core
PKPpre	(old:PKhKP) a precursor to PKPdf due to scattering near or at the CMB
PKPdif	P wave diffracted at the inner core boundary (ICB) in the outer core
PKS	Unspecified P wave bottoming in the core and converting to S at the CMB
PKSab	PKS bottoming in the upper outer core
PKSbc	PKS bottoming in the lower outer core
PKSdf	PKS bottoming in the inner core
P'P'	(alt:PKPPKP) Free surface reflection of PKP
P'N	(alt:PKPN) PKP reflected at the free surface N-1 times; N is a positive integer. For example P'3 is P'P'P'
Pz-P'	PKP reflected from inner side of a discontinuity at depth z outside the core, which means it is precursory to P'P'; z may be a positive numerical value in km
P'S'	(alt:PKPSKS) PKP to SKS converted reflection at the free surface; other examples are P'PKS, P'SKP
PS'	(alt:PSKS) P (leaving a source downwards) to SKS reflection at the free surface
PKKP	Unspecified P wave reflected once from the inner side of the CMB
PKKPab	PKKP bottoming in the upper outer core
PKKPbc	PKKP bottoming in the lower outer core
PKKPdf	PKKP bottoming in the inner core

Table 2.1 (continued)

PNKP	P wave reflected N–1 times from inner side of the CMB; N is a positive integer
PKKPpre	a precursor to PKKP due to scattering near the CMB
PKiKP	P wave reflected from the inner core boundary (ICB)
PKNIKP	P wave reflected N–1 times from the inner side of the ICB
PKJKP	P wave traversing the outer core as P and the inner core as S
PKKS	P wave reflected once from inner side of the CMB and converted to S at the CMB
PKKSab	PKKS bottoming in the upper outer core
PKKSbc	PKKS bottoming in the lower outer core
PKKSdf	PKKS bottoming in the inner core
PcPP'	(alt:PcPPKP) PcP to PKP reflection at the free surface; other examples are PcPS', PcSP', PcSS', PcPSKP, PcSSKP
SKS	(alt:S') unspecified S wave traversing the core as P
SKSac	SKS bottoming in the outer core
SKSdf	(alt:SKIKS) SKS bottoming in the inner core
SPdifKS	(alt:SKPdifS) SKS wave with a segment of mantle side Pdif at the source and/or the receiver side of the raypath
SKP	Unspecified S wave traversing the core and then the mantle as P
SKPab	SKP bottoming in the upper outer core
SKPbc	SKP bottoming in the lower outer core
SKPdf	SKP bottoming in the inner core
S'S'	(alt:SKSSKS) Free surface reflection of SKS
S'N	SKS reflected at the free surface N–1 times; N is a positive integer
S'z–S'	SKS reflected from inner side of discontinuity at depth z outside the core, which means it is precursory to S'S'; z may be a positive numerical value in km
S'P'	(alt:SKSPKP) SKS to PKP converted reflection at the free surface; other examples are S'SKP, S'PKS
S'P	(alt:SKSP) SKS to P reflection at the free surface
SKKS	Unspecified S wave reflected once from inner side of the CMB
SKKSac	SKKS bottoming in the outer core
SKKSdf	SKKS bottoming in the inner core
SNKS	S wave reflected N–1 times from inner side of the CMB; N is a positive integer
SKIKS	S wave traversing the outer core as P and reflected from the ICB
SKJKS	S wave traversing the outer core as P and the inner core as S
SKKP	S wave traversing the core as P with one reflection from the inner side of the CMB and then continuing as P in the mantle
SKKPab	SKKP bottoming in the upper outer core
SKKPbc	SKKP bottoming in the lower outer core
SKKPdf	SKKP bottoming in the inner core
ScSS'	(alt:ScSSKS) ScS to SKS reflection at the free surface; other examples are: ScPS', ScSP', ScPP', ScSSKP, ScPSKP

Near source surface reflections (Depth phases)

pPy	All P-type onsets (Py) as defined above, which resulted from reflection of an upgoing P wave at the free surface or an ocean bottom; WARNING: The character “y” is only a wild card for any seismic phase, which could be generated at the free surface. Examples are: pP, pPKP, pPP, pPcP, etc
sPy	All Py resulting from reflection of an upgoing S wave at the free surface or an ocean bottom; For example: sP, sPKP, sPP, sPcP, etc
pSy	All S-type onsets (Sy) as defined above, which resulted from reflection of an upgoing P wave at the free surface or an ocean bottom; for example: pS, pSKS, pSS, pScP, etc
sSy	All Sy resulting from reflection of an upgoing S wave at the free surface or an ocean bottom; for example: sSn, sSS, sScS, sSdif, etc

Table 2.1 (continued)

pwPy	All Py resulting from reflection of an upgoing P wave at the ocean's free surface
pmPy	All Py resulting from reflection of an upgoing P wave from the inner side of the Moho
Surface waves	
L	Unspecified long period surface wave
LQ	Love wave
LR	Rayleigh wave
G	Mantle wave of Love type
GN	Mantle wave of Love type; N is integer and indicates wave packets traveling along the minor arcs (odd numbers) or major arc (even numbers) of the great circle
R	Mantle wave of Rayleigh type
RN	Mantle wave of Rayleigh type; N is integer and indicates wave packets traveling along the minor arcs (odd numbers) or major arc (even numbers) of the great circle
PL	Fundamental leaking mode following P onsets generated by coupling of P energy into the waveguide formed by the crust and upper mantle
SPL	S wave coupling into the PL waveguide; other examples are SSPL, SSSPL
Acoustic phases	
H	A hydroacoustic wave from a source in the water, which couples in the ground
HPg	H phase converted to Pg at the receiver side
HSg	H phase converted to Sg at the receiver side
HRg	H phase converted to Rg at the receiver side
I	An atmospheric sound arrival, which couples in the ground
Ip	I phase converted to Pg at the receiver side
Is	I phase converted to Sg at the receiver side
Irg	I phase converted to Rg at the receiver side
T	A tertiary wave. This is an acoustic wave from a source in the solid earth, usually trapped in a low velocity oceanic water layer called the SOFAR channel (SOund Fixing And Ranging)
TPg	T phase converted to Pg at the receiver side
TSg	T phase converted to Sg at the receiver side
TRg	T phase converted to Rg at the receiver side
Amplitude measurement phases (displacement unless otherwise mentioned)	
A	Unspecified amplitude measurement
AML	Amplitude measurement for local magnitude (old)
AMB	Amplitude measurement for body wave magnitude (old)
AMS	Amplitude measurement for surface wave magnitude (old)
IAML	IASPEI standard amplitude (nm) measurement for local magnitude
IAmB	IASPEI standard amplitude (nm) measurement for short period body wave magnitude mb
IVmB_BB	IASPEI standard velocity amplitude (nm/s) measurement for broad band body wave magnitude mB
IAMs_20	IASPEI standard amplitude (nm) measurement for surface wave magnitude at a period of 18–22 s
IVMs_BB	IASPEI standard velocity amplitude (nm/s) measurement for broad band surface wave magnitude
END	Time of visible end of record for duration magnitude
Unidentified arrivals	
x	(old:i,e,NULL) unidentified arrival
rx	(old:i,e,NULL) unidentified regional arrival
tx	(old:i,e,NULL) unidentified teleseismic arrival
Px	(old:i,e,NULL,(P),P?) unidentified arrival of P-type
Sx	(old:i,e,NULL,(S),S?) unidentified arrival of S-type

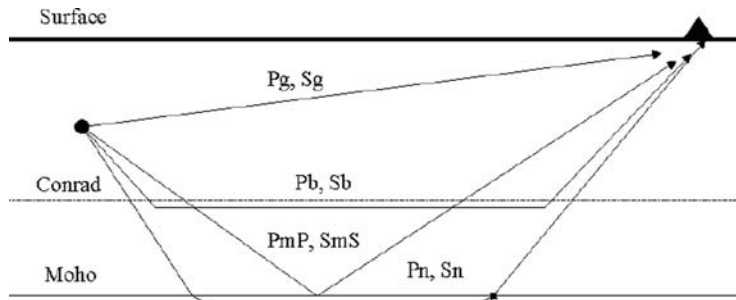


Fig. 2.11 A simplified model of the crust showing the most important crustal phases observed at local and regional distances (from NMSOP)

may be the strongest P-wave arrival after Pg. This simple model of Pg and Pn mostly serves to calculate travel times (see Section 2.4) and to get a simple understanding of the phases seen on the seismogram. The real crust will have uneven layering and velocity gradients so it is likely that the crustal phases, except at very short distances (< 50–100 km), are diving waves (see Fig. 2.6), and although travel times fit Pn, the amplitude may be larger than expected for Pn.

In addition to the crustal body waves, there are also crustal surface waves. The most important is Lg which follows the Sg arrival. Lg propagates as a guided wave multiply reflected within the crust with a typical velocity of 3.5 km/s and a typical frequency of 1 Hz. It is seen from a few hundred to more than 1,000 km distance and on regional seismograms, it often has the largest amplitude. Near surface events, particularly explosions or rock bursts, produce a short period surface wave of Rayleigh type, called Rg which propagates with a velocity close to 3.0 km/s, see Fig. 2.12. If the distance is less than 100 km, the rather monotonic Rg wave can dominate the seismogram and it is a good indication of a shallow source. Rg is limited to distances of a few hundred km due to its high damping.

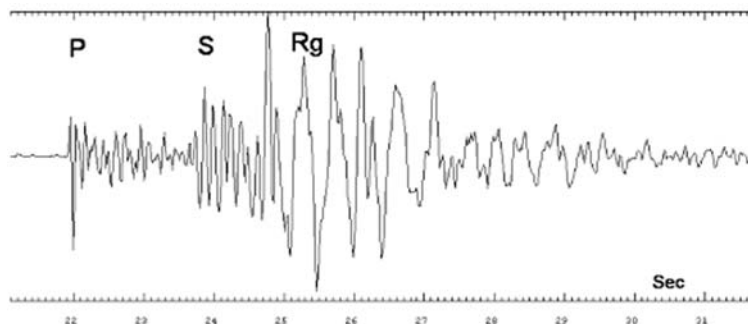


Fig. 2.12 An example of Rg waves for a local explosion. The station is the vertical component ASK, origin time is 1990 1213 11:09, magnitude M_L is 0.6 and epicentral distance is 16 km. The explosive charge was 220 kg fired in water

In Fig. 2.12 we also see seismic waves long time after the Rg waves. They are so-called coda waves and consist mostly of S-waves scattered by inhomogeneities in the crust. This means that the waves can arrive at the station from all directions and might have been scattered more than once although single scattering is the most common model. Scattered P-waves will also been seen between the P and S arrival. See also Fig 8.18.

T-waves are guided high frequency (>1 Hz) P-waves trapped in a water low velocity layer, propagating with a speed of around 1.5 km/s and recorded on ocean bottom seismographs or at seismographs near the coast (see Figs. 2.22 and 2.23). Due to little damping, T-waves can travel large distances ($> 2,000$ km).

2.4 Travel Times

We have now defined the major phases. In order to identify theses phases in the seismogram, as well as locating earthquakes based on the observations, it is essential to know the travel time defined as the time it takes to travel from the hypocenter to the station. In other words, the travel time is the difference between origin and arrival time. Although the waves travel in the interior of the earth, the distance is measured in degrees along the surface of the earth. For local earthquakes, distance in km is usually used. The first travel time tables were constructed from observations of arrival times at given stations from which a preliminary hypocenter and origin time could be estimated (see Chapter 5). In reality the travel time and hypocenter and origin time should be determined simultaneously but this was initially done in an iterative process which culminated in the famous JB tables (example in Table 2.2) and corresponding JB model (see above). Today, travel time observations are used to construct earth models (like AK135, see above) from which travel time tables are calculated. Figures 2.13 and 2.14 show some global travel times calculated using IASP91.

It is seen that the travel time curves are not linear (except for surface waves), as the earth is spherical and velocity changes with depth. As the distance increases, the difference in arrival time of the different phases generally increases and this is particularly used for the most prominent P and S- phases to calculate the epicentral distance. For example if the S-P arrival difference is 8.5 min, then the epicentral distance is about 64° for a surface focus earthquake (Fig. 2.13). The global travel time curves are very similar for all regions of the earth indicating that the earth in a first approximation can be described with a 1D model. Figure 2.14 shows the approximate travel time for the first arriving surface waves up to a distance of 120° . An approximate relationship is distance in degrees = $2 \cdot$ travel time in minutes. Their largest amplitudes arrive somewhat later.

For earthquake location, the most important phases are the first arrivals (always P-type) since they are usually clear and unambiguous (see examples below). Up to about 100° , the first arrival is P, then Pdif and from 115° , PKP is theoretically the first arrival. It is seen that the travel time curve for the first arrival is not continuous with a jump from Pdif to PKP. The PKP travel time has 3 branches as seen

Table 2.2 Extract of the JB travel time tables for P-waves. Δ is the epicentral distance in degrees. Hypocentral depth is given as a fraction a of earth radius minus the crust ($6370-33)a+33$, so the depths 0.0, 0.01, 0.02 etc correspond to 33, 96, 160, 223, 286 and 350 km respectively. Travel time differences in 0.1 s/deg are given for interpolation (*right* part of column). Retyped from JB tables, Jeffreys and Bullen, 1967.

TIMES OF P—*continued*

Depth $h =$																					
Δ	Surface		0.00		0.01		0.02		0.03		0.04		0.05								
$^\circ$	m	s	m	s	m	s	m	s	m	s	m	s	m	s							
30	6	12.5	88	6	07.7	89	6	01.6	88	5	55.7	88	5	49.9	87	5	44.4	87	5	39.2	86
31	6	21.3	88	6	16.6	88	6	10.4	87	6	04.5	87	5	58.6	87	5	53.1	86	5	47.8	86
32	6	30.1	87	6	25.4	87	6	19.1	87	6	13.2	86	6	07.3	86	6	01.7	86	5	56.4	85
33	6	38.8	87	6	34.1	86	6	27.8	86	6	21.8	85	6	15.9	85	6	10.3	85	6	04.9	85
34	6	47.5	86	6	42.7	86	6	36.4	85	6	30.3	85	6	24.4	85	6	18.8	84	6	13.4	84
35	6	56.1	85	6	51.3	85	6	44.9	85	6	38.8	84	6	32.9	84	6	27.2	84	6	21.8	84
36	7	04.6	84	6	59.8	84	6	53.4	84	6	47.2	84	6	41.3	84	6	35.6	84	6	30.2	83
37	7	13.0	84	7	08.2	84	7	01.8	83	6	55.6	84	6	49.7	83	6	44.0	83	6	38.5	83
38	7	21.4	84	7	16.6	83	7	10.1	83	7	04.4	83	6	58.0	83	6	52.3	82	6	46.8	82
39	7	29.8	83	7	24.9	83	7	18.4	83	7	12.3	82	7	06.3	82	7	00.5	82	6	55.0	82
40	7	38.1	82	7	33.2	83	7	26.7	82	7	20.5	82	7	14.5	82	7	08.7	82	7	03.2	81
41	7	46.3	82	7	41.5	82	7	34.9	82	7	28.7	82	7	22.7	81	7	16.9	81	7	11.3	81
42	7	54.5	82	7	49.7	82	7	43.1	82	7	36.9	81	7	30.8	81	7	25.0	80	7	19.4	80
43	8	02.7	81	7	57.9	81	7	51.3	81	7	45.0	80	7	38.9	80	7	33.0	80	7	27.4	80
44	8	10.8	81	8	06.0	80	7	59.4	80	7	53.0	80	7	46.9	79	7	41.0	79	7	35.4	79
45	8	18.9	79	8	14.0	80	8	07.4	79	8	01.0	79	7	54.8	79	7	48.9	78	7	43.3	78
46	8	26.8	79	8	22.0	78	8	15.3	79	8	08.9	78	8	02.7	77	7	56.7	78	7	51.1	77
47	8	34.7	79	8	29.8	79	8	23.2	78	8	16.7	78	8	10.4	78	8	04.5	77	7	58.8	77
48	8	42.6	77	8	37.7	77	8	31.0	77	8	24.5	77	8	18.2	76	8	12.2	76	8	06.5	76
49	8	50.3	77	8	45.4	77	8	38.7	77	8	32.2	76	8	25.8	76	8	19.8	75	8	14.1	75
50	8	58.0	76	8	53.1	76	8	46.4	76	8	39.8	76	8	33.4	75	8	27.3	74	8	21.6	74
51	9	05.6	76	9	00.7	75	8	54.0	75	8	47.4	75	8	40.9	74	8	34.7	74	8	29.0	74
52	9	13.2	75	9	08.2	75	9	01.5	75	8	54.9	74	8	48.3	74	8	42.1	73	8	36.4	73
53	9	20.7	73	9	15.7	74	9	09.0	73	9	02.3	73	8	55.7	73	8	49.4	72	8	43.7	72
54	9	28.0	74	9	23.1	73	9	16.3	73	9	09.6	73	9	03.3	72	8	56.6	72	8	50.9	71
55	9	35.4	72	9	30.4	72	9	23.6	72	9	16.9	72	9	10.2	71	9	03.8	71	8	58.0	71
56	9	42.6	72	9	37.6	72	9	30.8	71	9	24.1	70	9	17.3	71	9	10.9	70	9	05.1	69
57	9	49.8	70	9	44.8	70	9	37.9	70	9	31.1	70	9	24.4	70	9	17.9	70	9	12.0	69
58	9	56.8	70	9	51.8	70	9	44.9	69	9	38.1	70	9	31.4	69	9	24.9	69	9	18.9	69
59	10	03.8	69	9	58.8	69	9	51.8	69	9	45.1	68	9	38.3	68	9	31.8	68	9	25.8	67
60	10	10.7	68	10	05.7	68	9	58.7	68	9	51.9	68	9	45.1	67	9	38.6	67	9	32.5	66
61	10	17.5	68	10	12.5	67	10	05.5	67	9	58.7	67	9	51.8	67	9	45.3	66	9	39.1	66
62	10	24.3	66	10	19.2	67	10	12.2	67	10	05.4	66	9	58.5	66	9	51.9	65	9	45.7	65
63	10	30.9	66	10	25.9	65	10	18.9	65	10	12.0	65	10	05.1	65	9	58.4	65	9	52.2	64
64	10	37.5	65	10	32.4	65	10	25.4	65	10	18.5	65	10	11.6	64	10	04.9	64	9	58.6	64
65	10	44.0	64	10	38.9	64	10	31.9	64	10	25.0	64	10	18.0	64	10	11.3	63	10	05.0	63
66	10	50.4	64	10	45.3	63	10	38.3	63	10	31.4	63	10	24.4	63	10	17.6	63	10	11.3	63
67	10	56.8	63	10	51.6	63	10	44.6	62	10	37.7	62	10	30.7	62	10	23.9	62	10	17.6	61
68	11	03.1	62	10	57.9	62	10	50.8	62	10	43.9	61	10	36.9	61	10	30.1	61	10	23.7	61
69	11	09.3	61	11	04.1	61	10	57.0	61	10	50.0	61	10	43.0	61	10	36.2	61	10	29.8	61
70	11	15.4		11	10.2		11	03.1		10	56.1		10	49.1		10	42.3		10	35.9	

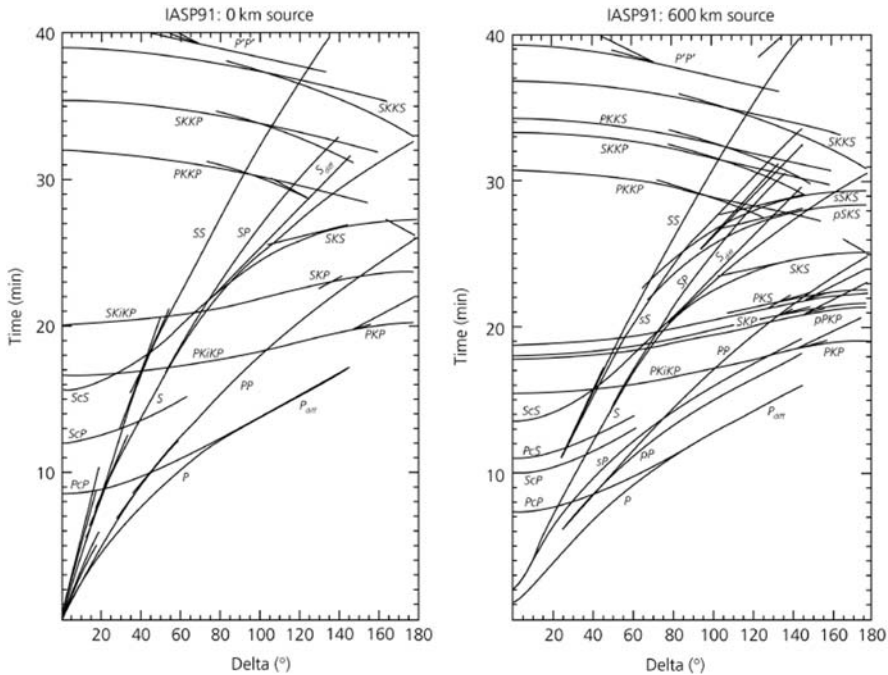


Fig. 2.13 Travel times for body waves using the IASP91 model. Delta is distance in degrees. To the *left* is shown travel times for a surface focus and to the *right* travel times for a focal depth of 600 km. Figure from Stein and Wysession (2003), and copied from http://epscx.wustl.edu/seismology/book/book_no_captions/figures/

in Fig. 2.15 and labeling the phase PKP means that a detailed detection and discrimination of these 3 branches has not been possible. One should strive to correctly identify and report these phase names (see Fig. 2.15). Detailed guidelines and record examples are found in NMSOP. The ray paths corresponding to the 3 branches are seen in Fig. 2.15.

Figure 2.14 gives an indication of the frequency content of the different seismic phases, and it is seen that particularly P-type seismic phases usually have higher frequency than S- type phases due to the higher attenuation of S. In other cases phases are more attenuated due to a particular travel path. This difference in attenuation implies that some phases are best observed on long period type records (frequency < 0.1 Hz) while others are better seen on short period (SP) type records (frequency > 1 Hz). So knowledge of the frequency content might help in identifying a particular seismic phase.

The crust has large tectonic variations with widely varying Moho depths (see above) so travel time curves at local and regional distances must be adjusted to the local conditions. In most cases, particular for location of local earthquake (see Chapter 5), a flat 1D model is used.

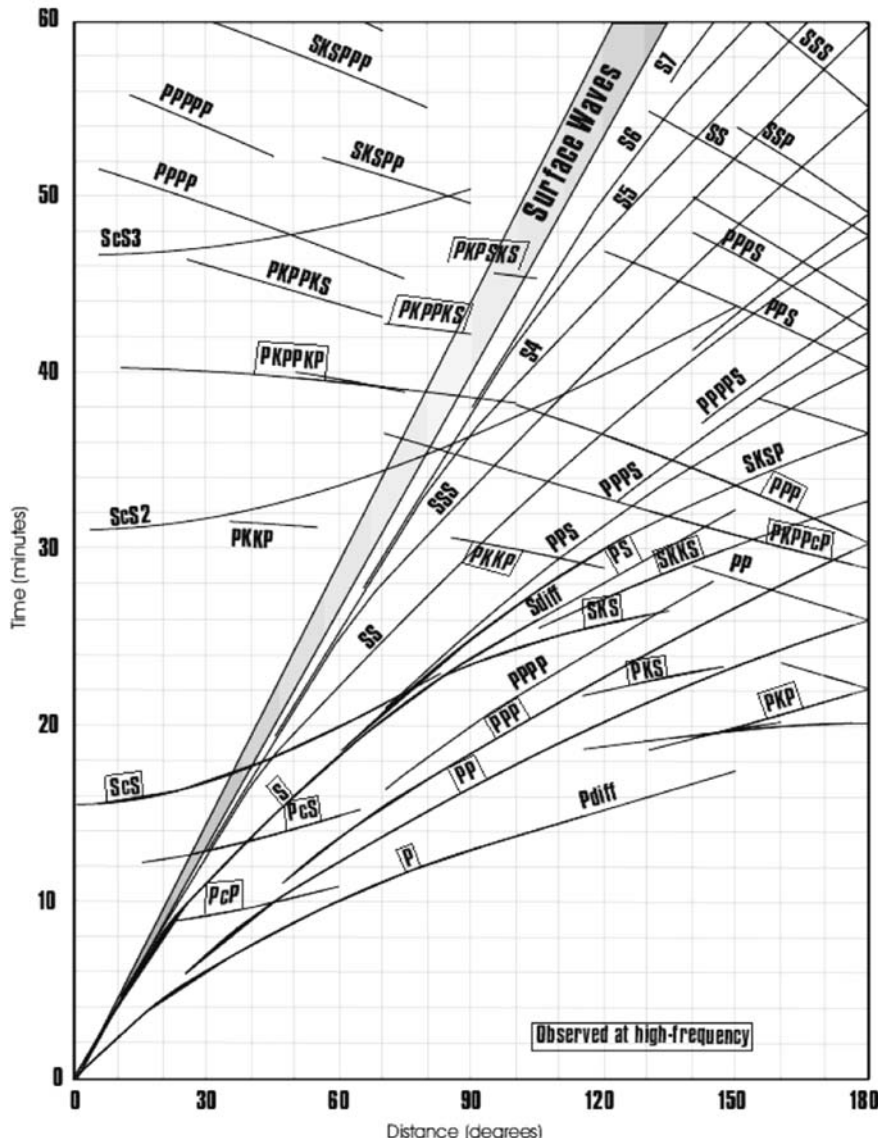
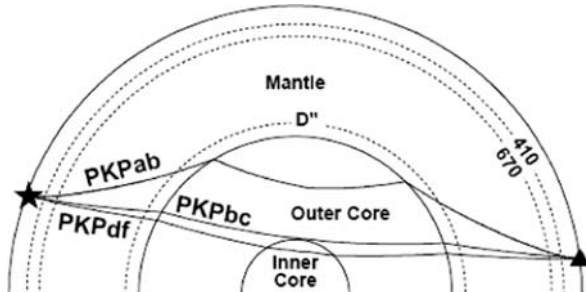


Fig. 2.14 This figure also shows the IASP91 travel times (surface focus), but with the additional information of the surface waves travel times and the frequency content of the different types of phases. The names of the high frequency phases are encased in brackets. Figure modified from http://neic.usgs.gov/neis/travel_times/ttgraph.pdf

Fig. 2.15 Raypaths of the different branches of PKP.
Figure from http://www.scec.org/news/01news/es_abstracts/romano2.pdf



Using a simple one layer over Moho (Fig. 2.16), the travel time of Pn for a surface focus can be calculated as (e.g. Stein and Wysession, 2003):

$$TPn(\Delta) = \Delta/v_2 + 2h \left(1/v_1^2 - 1/v_2^2 \right)^{1/2} \quad (2.3)$$

where v_1 and v_2 are the layer velocities and h the layer thickness.

The Pg travel time for a surface focus is

$$TPg = \Delta/v_1 \quad (2.4)$$

The corresponding travel time curves are seen in Fig. 2.17. The slopes of the travel time curves are the inverse of the velocities and, since the angle of incidence for Pn in the half space is 90° , p for the Pn ray is $1/v_2 = 1/v_{app} = dT/d\Delta$ where v_{app} is the apparent horizontal velocity. For a spherical earth, the corresponding relation is (e.g. Stein and Wysession, 2003)

Fig. 2.16 A simple model with one layer over a half space simulating the Moho interface. The extra time to travel $d\Delta$ is dT

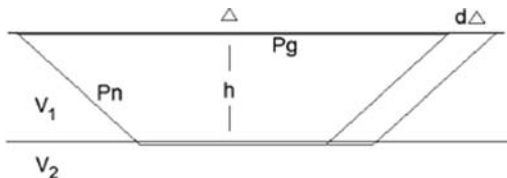
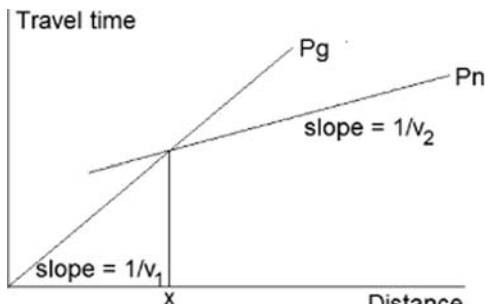


Fig. 2.17 Travel time curves for Pg and Pn, the crossover distance x , is the distance from which Pn comes before Pg



$$dT/d\Delta = p = r \sin(i)/v = 1/v_{app} \quad (2.5)$$

Note that the unit of $dT/d\Delta$ is seconds/radian. Since the travel time curves for global phases are not straight lines, there is a relationship between the slope of the travel time curves and the epicentral distance so if the apparent velocity can be determined for a seismic arrival, then the travel time curve can be used to determine the distance. This is used when locating earthquakes using seismic arrays (see Chapters 5 and 9). In addition, seismic phases arriving close in time might have very different apparent velocities (like PP and Pcp at 45°, see Figs. 2.13 and 9.11) and knowing the apparent velocity will help to identify the phase.

2.5 Seismic Phases at Different Distances

In practice most observatories read very few different phases, which is a pity, since reading more phases would greatly contribute to a better location of the source and to the improvement of the earth model. On the other hand it takes more time, even with modern technical help. Reading seismograms has for some operators become almost an art where the analysts are able to identify where the earthquake is located and even identify several phases without consulting travel time tables. This was often the case when only one or a few stations were processed and the analyst had been processing the data for many years. New operators often only read the P phase for teleseismic events and P and S for local and regional events. In the routine operation it may not be expected that many exotic phases are read, however an effort should be made to identify and read the clearest phases and leave the more exotic ones for research related projects. In the following we will try to give some simple guidelines for the most basic phase identification at different epicentral distances. For a much more detailed discussion with examples of phases at different distances, see Kulhánek (1990), NMSOP, Kennett (2002) and (in Spanish) Payo (1986). Earlier examples are given by Simon (1968) and Lehmann (1954). Together these books have more than 900 pages of examples and explanations so it is a well studied topic.

The most important phases relevant for daily processing are:

Local/regional: P, S, Pg, Sg, Pn, Sn, Rg, Lg, T

Distant: P, PP, PPP PKP, pPKP, S, SS, SSS, pP, sP, Pcp, ScS, Pdif

Examples of these phases will be given in the following.

The appearance of seismograms is very distance dependent and partly also dependent on the magnitude of the events. The further the events travel, the more high frequency energy is filtered away and the signals appear more low frequency. This effect is compounded by the fact that recording an earthquake at e.g. 60° requires a certain minimum magnitude (4–5) and larger events generate relatively

more low frequency energy than small earthquakes (see Chapter 8). In general, analysis of seismic events is divided into groups depending on the epicentral distance:

- Local : Distance 0–1,000 km.
- Regional: 1,000–2,000 km.
- Distant or teleseismic: Distance > 2,000 km.

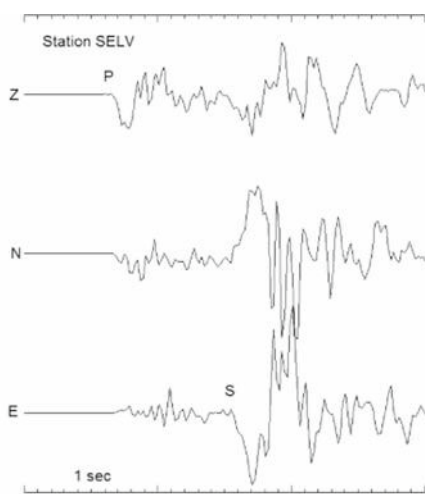
There is no absolute agreement about these distance boundaries. It is particularly difficult to define a regional event. In some instances regional events are defined to have a distance up to 30° since only beyond this distance will the ray-path be little affected by the crust and upper mantle transition zone and in many types of analysis (spectral analysis (Chapter 8), modeling, magnitudes (Chapter 6)), reliable results for teleseismic events are only obtained at distances beyond 30° . The regional events can potentially present the most difficult seismograms to interpret since the ray can pass a varying crustal structure and the transition zone. The classification is also important for earthquake location since local events normally are located using a flat layered model while distant events use a global model for a spherical earth and regional events can use either or a combination. Beyond 2,000 km a spherical model should be used.

In the following, a few examples of digital seismograms will be shown for the different distance ranges and recommendations of which phase observations could be made. The interpretation will not necessarily give the correct phase identification but rather give the most likely initial interpretation which later might have to be modified following more processing. To see correctly interpreted seismograms, we refer to Kulhánek (1990), NMSOP, Kennett (2002) and Payo (1986). Some general recommendations for phase readings are:

- Read only clear phases if possible (maybe unclear if needed for location).
- Read on unfiltered traces if possible (see Chapter 4), broadband data has to be filtered in many cases, short period records are already high-pass filtered while long-period records are low-pass filtered.
- Preferably read P-phases on vertical component and S-phases on horizontal components.
- First arriving P and S phases should be labeled only P and S even if they might be Pg, Pn, PKP, since it is difficult to initially know the phase type and location programs will use the calculated first arrival. Later processing might require name changes (e.g. to Pdif, PKP).

Fig. 2.18 Seismogram of a local event ($M_L = 3.4$) at station SELV recorded with the Andalucian Seismic Network. The sensor is broadband and the traces are not filtered. Each trace has the same scale. The hypocentral depth is estimated to 2.5 km and the origin time is 2007 0104 23:32. The epicentral distance is 6 km

Epicentral distance 6 km, depth 2.5 km and magnitude 3.4
Phases Pg and Sg



This very local earthquake (Fig. 2.18) is an example of the simplest analysis possible. The P-phase is very clear on the Z-component and the S-phase on the horizontal components and less so on the vertical component. The phases should be labeled only P and S although they are Pg and Sg.

Summary: Read only P and S.

Epicentral distance 20–96 km, depth 5 km and magnitude 1.5
Phases Pg, Sg and PmP

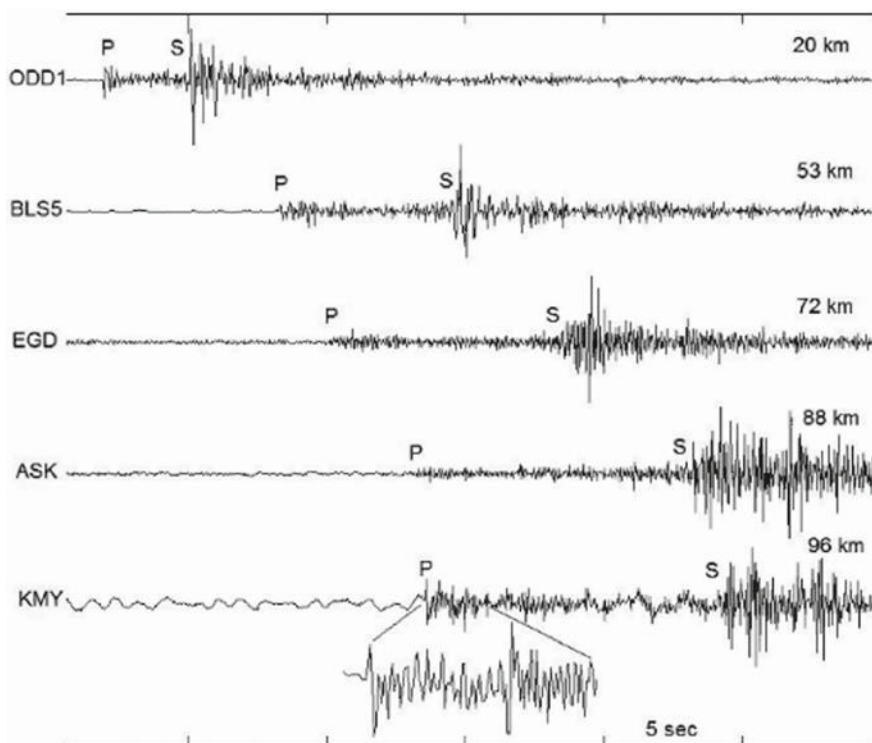


Fig. 2.19 Seismogram of a local event ($M_L = 1.5$) at 5 stations recorded with the Norwegian National Seismic Network. Sensors are short period and the traces are not filtered. Each trace is auto scaled. The hypocentral depth is estimated to 5 km and the origin time is 2004 0502 19:24. The epicentral distances are given above the traces to the right. To save space, only vertical components are shown, however, the S-phases looked very similar on horizontal components in this example

This event (Fig. 2.19) is a typical local event. The phases are very clear on some stations and less so on others. The phases should be read as P and S although they are likely to be Pg and Sg. Within the P and S-wave train, there is a tendency to see other arrivals. This is clearly seen on station KMY where there is a clear phase 1.5 s after the P. Since at this distance, the first arriving phase is expected to be Pg, this phase cannot be Pg. A likely interpretation could be a reflection from Moho which was verified by modeling. Moho reflections are usually not used in location programs and without prior knowledge of local conditions it is not advised to identify it as such. Since it is likely to be a P-phase, it could be identified as Px for future reference (Fig. 2.19).

Summary: Read only P and S and possibly label other clear phases.

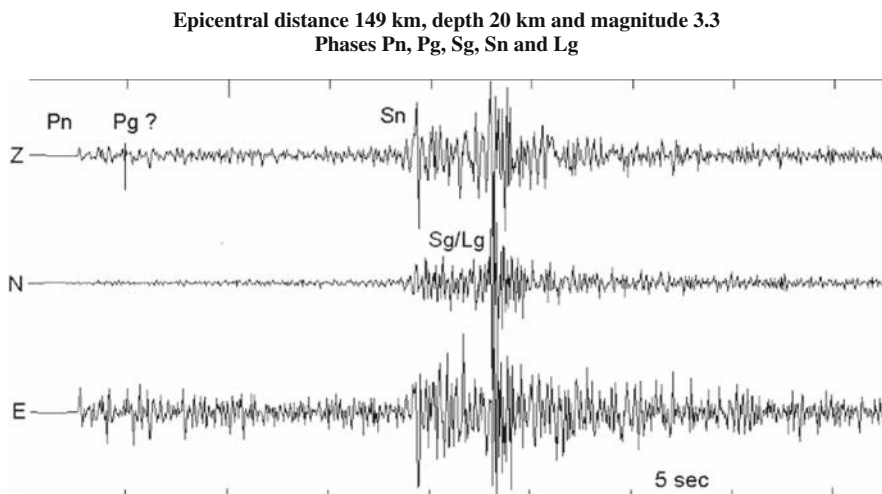


Fig. 2.20 Seismogram of a local event ($M_L = 3.3$) recorded with the Danish-Greenland network, station SFJD1. The sensor is broadband and the traces are not filtered. Each trace is auto scaled. The hypocentral depth is estimated to 20 km and the origin time is 2005 0723 13:23. The epicentral distance is 149 km

In this example (Fig. 2.20), due to the distance and depth, the first arrival is most likely Pn. In the S-wave train, two very clear S arrivals are seen which are interpreted as Sn and Sg/Lg. Whether the first arrival is Pn or a diving wave cannot be decided, however the Sn amplitude seems to be rather too large for Sn so most likely this is a diving wave. The Pn and Sn travel times are used for processing. The second S-wave fits with both Lg and Sg and again it is difficult to judge which one it is. If an Sg, a Pg should be expected where the “Pg?” is marked (difference Sg–Sn is 1.78 times the difference Pg–Pn), but no clear phase is seen. So most likely the second S-phase is Lg. In many cases, both Pn and Pg are seen but not Sn, see example in Fig. 5.16. The Lg phase, being a surface type wave, will never have a clear onset but is nevertheless often used for location purposes since it could be the first significant onset in the S-wave train.

Summary: Read first phase as P, first S as S and second S as Lg and check by location whether or not the first S really is a first arrival (Sn).

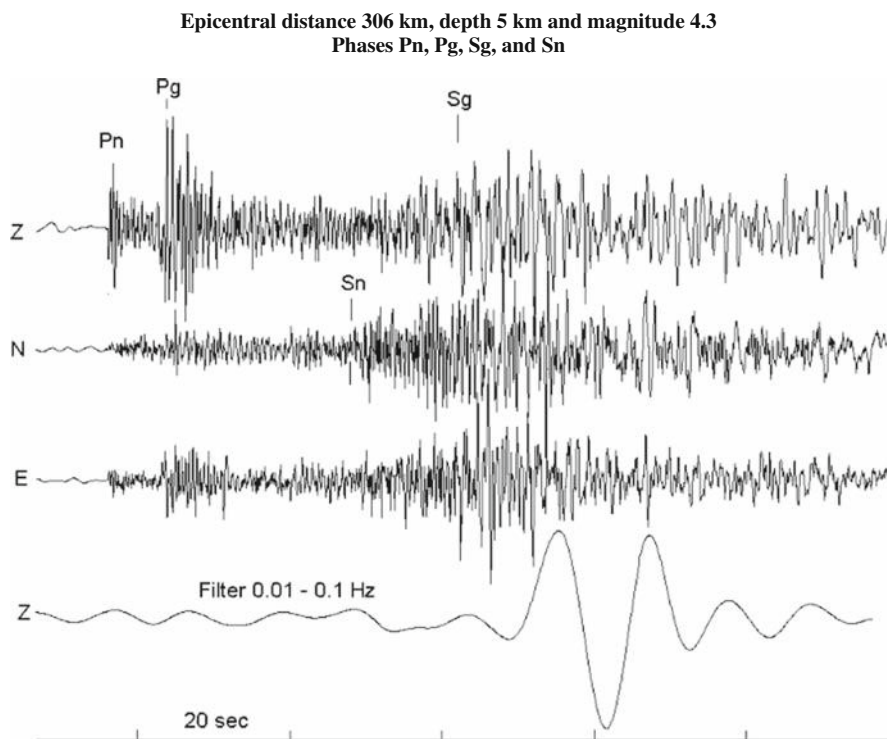


Fig. 2.21 Seismogram of a local event ($M_L = 4.3$) recorded with the UK network, station MCH. The sensor is broadband and the *top 3* traces are not filtered while the *bottom* trace is filtered as indicated. Each trace is auto scaled. The hypocentral depth is estimated to 5 km and the origin time is 2007 0428 07:18. The epicentral distance is 306 km

This event (Fig. 2.21) is typical of a local event at intermediate distance. The Pn and Pg are clear, while there are some phase arrivals seen at the theoretical arrival times for Sn and Sg but none of them are very clear. Filtering or component rotation (see Chapter 4) does not improve the sharpness of these phase arrivals. The unclear arrivals are probably caused by the complexity of the crustal structure giving rise to both scattering and arrivals having traveled different paths. Ideally, only P should be read for this event, however S might have to be read if needed for location, but the phase reading would have a few seconds uncertainty. The bottom trace shows that the event is large enough to generate a clear low frequency surface wave (not Lg), which is not seen in the unfiltered trace.

Summary: At this distance first arrival is Pn, but read as P. Only read S if it is clear.

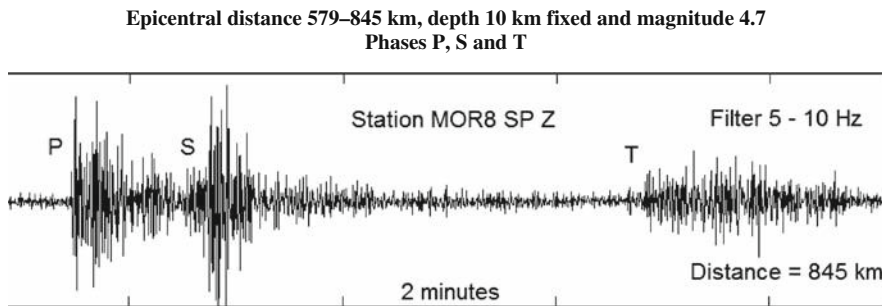


Fig. 2.22 Earthquake on the Mid-Atlantic ridge in the Greenland Sea recorded on the west coast of Norway. The signal is filtered 5–10 Hz. The origin time is 1997 1006 23:45 and the magnitude is $3.2 M_L(\text{BER})$ and $m_b 4.7$ (ISC). The depth is fixed to 10 km

The event shown in Fig. 2.22 is on the Mid-Atlantic ridge and recorded near the coast of Norway so almost the entire travel path is under the ocean. The P-wave is quite clear while the S is less clear. The event also has a clear T-phase, which however in the initial processing was considered a new event, see next example. M_L is low compared to m_b since the secondary arrival is not as strong as it would have been along a continental path for which the magnitude scale was developed. Both P and S are refracted or diving waves and, particularly due to the oceanic path, it is difficult to identify a phase type so the best is to leave the identification as P and S.

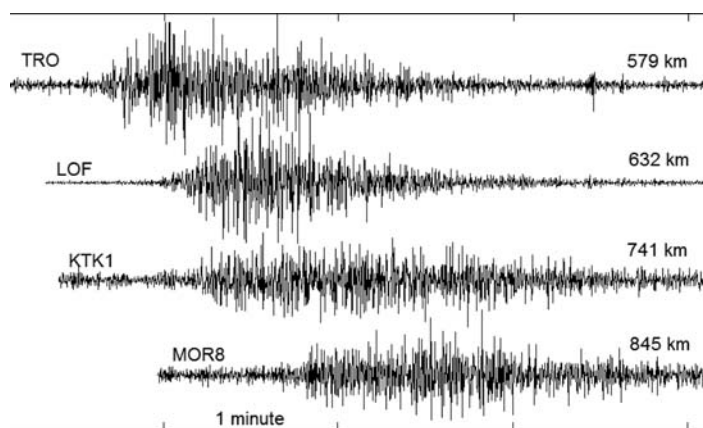


Fig. 2.23 T-waves on 4 land stations in the Norwegian National Seismic Network. The signals are filtered in the 5–10 Hz range. The origin time is 1997 1006 23:45 and the magnitude is $3.2 M_L(\text{BER})$ and $m_b 4.7$ (ISC). The depth was fixed to 10 km

At a first glance this event (Fig. 2.23) could look like a separate event where only S-waves are seen. However trying to locate in this way gives an unrealistic location due to the difference in apparent velocity, large residuals and it also appears strange

that similar S-waves are not found on other stations. The two coastal stations TRO and LOF also have too large arrival time difference (about 30 s) for the waves to be S-waves. A closer inspection of the signal reveals high frequency signals of a rather monochromatic nature and since the “event” is only recorded on stations at or relatively near the coast, this is a good indication of T-waves. The signals seen are not directly T-waves since the stations are on land and in the case of KTK1, situated 200 km from the coast. So the T-waves are either converted to TPg, TSg or TRg. In order to identify one of these phases, more detailed analysis is required involving calculating travel path in the ocean and on land. For routine analysis it is sufficient to label the phases T to indicate their presence in the data. They are not used routinely for location due to the uncertain onset and uncertain average velocity over the ocean-continent path.

Summary: Read first phases and P and S. If clear T-phases are present, they should be reported and only labeled as T.

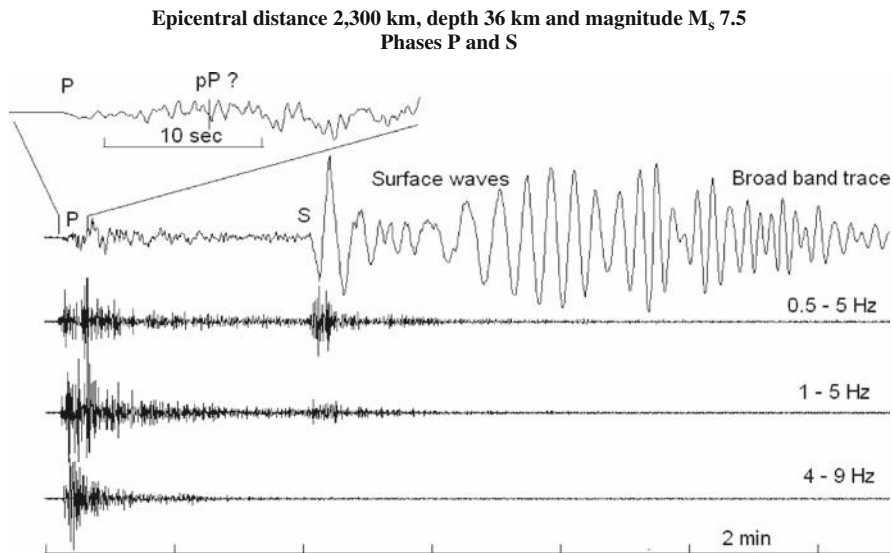


Fig. 2.24 Seismogram of the global network broadband station YAK, vertical component. The origin time is 2009 0115 17:49. The zoom of the P shows the theoretical arrival time of the pP. The 3 lower traces have been filtered as indicated. Notice the surface wave dispersion on the top trace

At this distance and for such a large event (Fig. 2.24), the only clear phases to read in this example are P and S. At the time where the pP (and sP) should arrive there is no clear arrival to be seen (see Table 5.7) and pP is in most cases more clearly seen at teleseismic distances. However, exceptions are possible as the next figure shows. The filtered traces show that there is no S (or surface waves) to be seen for frequencies above 4 Hz. At this regional distance, the S is therefore often not seen on short period records.

Summary: P and S clearly seen at this distance but S only on the broadband record.

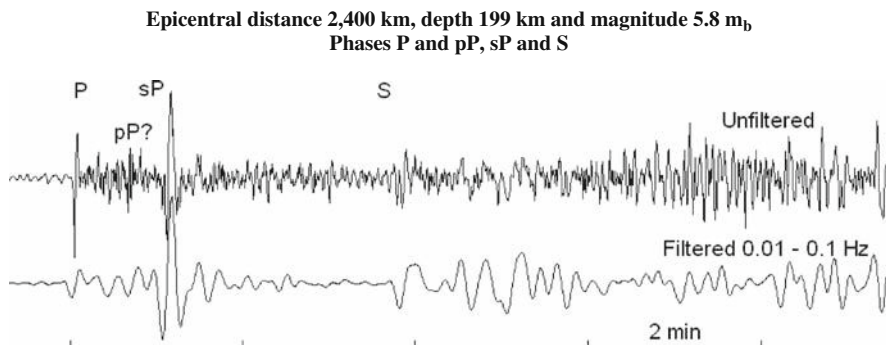


Fig. 2.25 Seismogram of the global network broadband station BDFD, *vertical* component. The origin time is 1993 0616 18:41. The *lower* trace has been filtered as indicated

This earthquake (Fig. 2.25) is clearly deep due to the lack of surface waves. S is best seen on the filtered trace. The largest phase after P is not pP but sP and it is doubtful whether pP is seen. This is probably due to the focal mechanism (see how this can happen in Chapter 7).

Summary: Read P and S. Lack of surface waves indicates a deep earthquake. The first large phase observed after P could be sP and not pP.

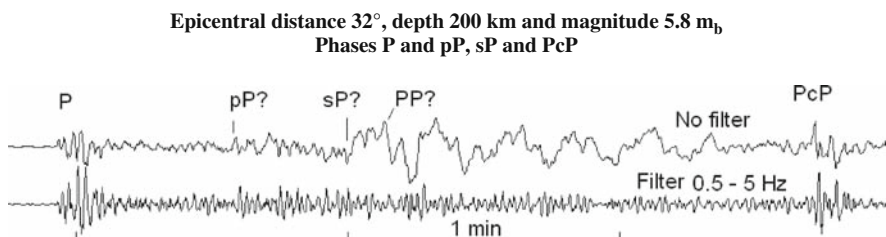


Fig. 2.26 Seismogram of the global network broadband station WRAB, *vertical* component. The origin time is 1996 0610 01:04. The *bottom* trace is filtered 0.5–5 Hz

The PcP phase of this event (Fig. 2.26) has a rather small amplitude and is therefore most clearly seen on records of deep earthquakes, where the P-coda is small, as in this example. Since PcP is also clearly seen on the filtered trace, it is expected to also be observed on short period seismograms. The PcP travel time curve crosses several other travel time curves (Fig. 2.13) so at certain distance ranges, the PcP will mix with other phases. In this example of a deep earthquake, the theoretical arrival times of pP, sP and PP are indicated. Although there is an indication of phase arrivals at these times, the onsets are not clear enough to be read in a first analysis. However, the depth phase onset could be read and reported after a final location indicating a deep earthquake.

Summary: PcP is best observed for deep earthquakes in certain distance ranges.

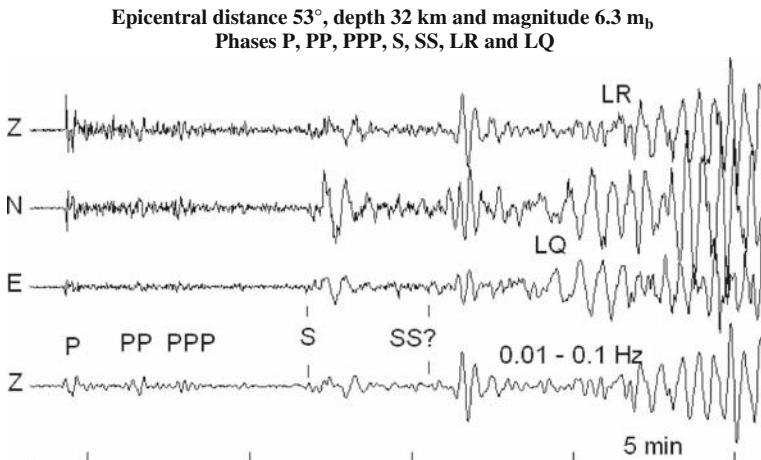
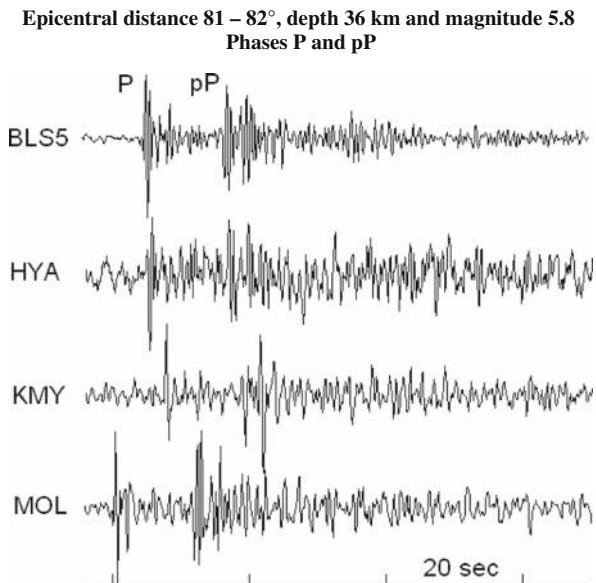


Fig. 2.27 Seismogram of the global network broadband station TLY. The components are indicated and the *bottom* trace has been filtered as indicated. The origin time is 2007 1002 18:00

This seismogram (Fig. 2.27) is typically observed at many stations with respect to epicentral range, depth and size. The event has clear surface waves, note how the Love waves (LQ) on horizontal components come before the Rayleigh waves (LR) on the vertical component. It is again seen that the phases PP and PPP are commonly observed while the SS may be less obvious. Note that the phases are more clearly seen using a filter. The S starts with a rather small amplitude and the maximum S amplitude is about a minute after the initial S (most clearly seen on NS component) so the large amplitude phase seen after the theoretical arrival time of SS is probably the same maximum amplitude SS. This means that in this case the SS arrival time should not be read and definitely not where the maximum amplitude is seen. Using theoretical arrival times is essential in correctly identifying some phase arrivals.

Summary: P and PP are clear phases while the SS may not show initial onset and should not be read.

Fig. 2.28 The P-phases recorded on short period seismograms. A clear P and pP is seen. The origin time is 2003 0326 04:22



On short period seismograms (Fig. 2.28), the pP is often clearly seen and reading the pP arrival time helps to constrain the hypocentral depth (see example described in Table 5.15). Newcomers to reading seismograms will often mistake the above seismogram for the recordings of P and S of a local earthquake since, plotted in this time scale, the recording might appear as that from a local event. A simple way to discard this possibility is to look at the frequency content (a zoom would reveal a frequency near 1 Hz for the P) or note the near constant pP-P (interpreted otherwise as S-P) times for stations several hundred kilometers apart (MOL and KMY).

Summary: Check frequency content of a recording to make sure event is correctly identified.

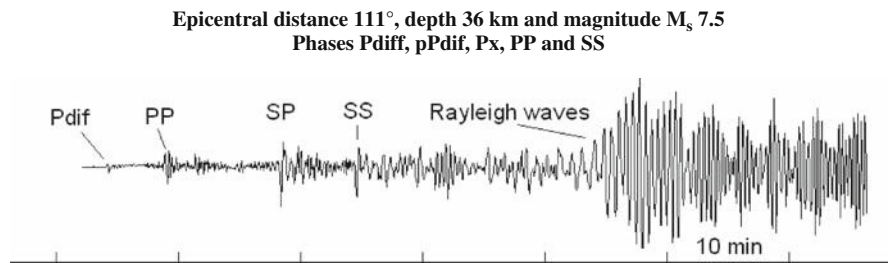


Fig. 2.29 Seismogram of the global network broadband station SDV, *vertical* component. The origin time is 2009 0115 17:49

This event (Fig. 2.29) presents very clear phases. It is obviously recorded at a large distance as indicated by the difference in arrival time of the surface waves relative to the first arriving P-phase. The first arrival, therefore, cannot be P and has actually been clearly identified as Pdif. However it should still be read as P. The Pdif phase is often very weak so for smaller events or noisier stations, the first clear arrival to be seen might be PP. Consequently, for events in this distance range, a careful evaluation should be made whether the first phase observed is a P or PP. This is most simply done by comparing with theoretical arrival times. Note that PS and SP arrive at similar times (within 5 s) so it is not obvious whether the phase is SP or PS. A zoom of Pdif is seen in Fig. 2.30.



Fig. 2.30 Seismogram on the global network broadband station SDV, *vertical* component. The origin time is 2009 0115 17:49

The theoretical arrival times of Pdif and pPdif are shown on the figure and it seems likely that the second arrival is pPdif. However, in routine observations it would not be clear enough for reading. It is seen that the Pdif is a rather low frequency signal due to the low Q near the CMB and filtering the trace (0.8–5 Hz) makes it disappear in the noise so the arrival would not be seen on a short period record.

Summary: At large distances, read first arrivals as P. If the first arrival could be Pdif, check if a first arrival is not PP.

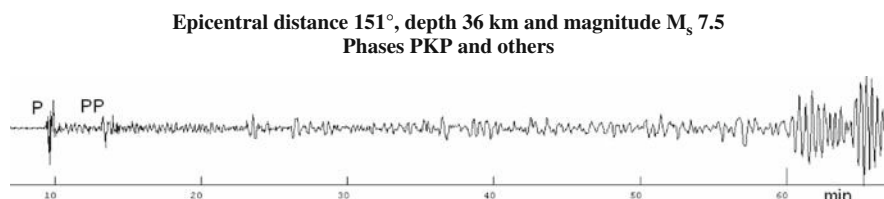


Fig. 2.31 Seismogram of the global network broadband station TRQA, *vertical* component. The origin time is 2009 0115 17:49

This seismogram (Fig. 2.31) is recorded at a large distance which can be seen on the large difference in arrival time on the P and the surface waves (see Fig. 2.14). The P is not a direct P, most likely a PKP, but it is very difficult to decide which type of P-phase it is, and without further analysis the first arrival should simply be read as a P. See Fig. 2.32 for some possibilities of arrivals near the PKP. A common

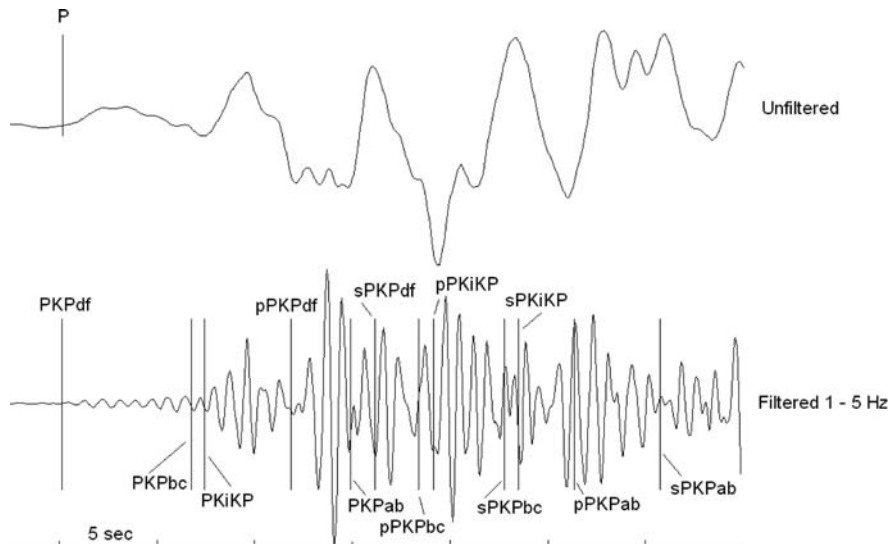


Fig. 2.32 PKP and other phases near the initial P-phase from the event shown in Fig. 2.31. The *top* trace shows unfiltered data and the *bottom* trace the data filtered 1–5 Hz. The location program has identified the first arrival to PKP_{df}. Theoretical arrival times are shown for other phases in the following 35 s

arrival seen at this distance is PP and it sometimes happens that PP is seen as the first phase on the seismogram when PKP is weak.

It is seen from Fig. 2.32 that many phases have theoretical arrival times close to the initial PKP and without also modeling the amplitudes, it is not simple to judge which are actually seen. It seems quite clear that the first arrival is PKP_{df} and it is likely that pPKP_{df} is the arrival with the largest amplitude. The filtering shows that PKP phases are rather high frequency in nature and are expected to be clearly seen on short period records. The ray paths of the different PKP phases are seen in Fig. 2.15.

Summary: At large distances, read the first arrival as P and possibly identify pP. Check if a first arrival is not PP. Filtering out low frequencies might make the arrival more clear and assist in phase identification.

2.6 Determination of Structure

Determining earth structure from travel time observations is a topic in itself and is not the purpose of this book. However, processing of earthquake data is critically dependent on a correct model. While the global model for processing purposes is well known and has seen small gradual improvements, the local crustal models are often less well known. Once data has been accumulated, it might be possible to check and improve on the local model. We will therefore describe a few simple methods for some local model parameter determination.

Travel-time curve slope: The method consists of plotting e.g. the P-arrival times versus distance and get curves of the type seen in Fig. 2.17. From the slope of the linear sections and the intercept of the lines, a layered structure can be deduced. See Stein and Wysession (2003) for more information.

Determine v_s/v_p velocity ratio: Models often give only the v_p velocity so a velocity ratio must be specified. The simplest method to determine v_p/v_s is to make a Wadati diagram by plotting observed S-P arrival times versus P-arrival times. See Chapter 5.

Inversion of arrival times: When a large number of well determined hypocenters are available, this data set can be inverted to improve the local structure and the hypocenters as well as the global model. At the local scale one normally starts with the inversion for a minimum 1D model, which is then used as a starting model in the 3D inversion. Commonly used software for the 1D inversion is VELEST (Kissling et al., 1994) and SIMULPS for the 3D inversion (Evans et al., 1994). Tomographic inversions on a global scale are used to refine the 3D image of the earth. Global models such as *ak 135* were found by computing smoothed empirical travel times and then finding a radial model that best explains the empirical travel times (Kennett et al., 1995).

Surface wave inversion: For both regional and global structure, the velocity model can be determined by studying the dispersion curves of surface waves. As mentioned in Chapter 1, the velocity of surface waves depends on the frequency of the seismic waves since longer period surface waves penetrate deeper and therefore “feel” higher velocity layers. The velocity versus frequency relation is called the dispersion curve and the shape of the dispersion curve will therefore depend on the crustal and mantle structure. The dispersion curve can be measured by different methods of which the simplest is to measure the travel time between the source and the station for different frequency surface wave groups (in practice this is often done by using spectral analysis and measuring phase differences, see Chapter 4). The dispersion curve would then be representative of the average structure between the station and the event. A slightly more difficult approach is to measure arrival time difference of identified phase positions for different frequencies between two sufficiently close stations as to enable phase correlation and then phase velocity measurements. The dispersion curve would then be representative for the structure between the two stations and thus have a better spatial resolution than velocity models determined by the group velocity method. However, this requires the station to be aligned with the event. For more information see Stein and Wysession (2003). There are standard programs available for determining crustal structure from surface waves, e.g. Computer Programs in Seismology by Herrmann (2004).

Receiver function method: By studying the phase conversion in the crust from teleseismic arrivals, the local crustal structure can be determined, see Fig. 2.33.

The so-called receiver function is derived by de-convolving (see Chapter 4) the vertical component from a horizontal component and the receiver function can be inverted for the crustal and upper mantle structure (Langston, 1979; Ammon, 1991). The analysis uses a number of teleseismic recordings which are grouped

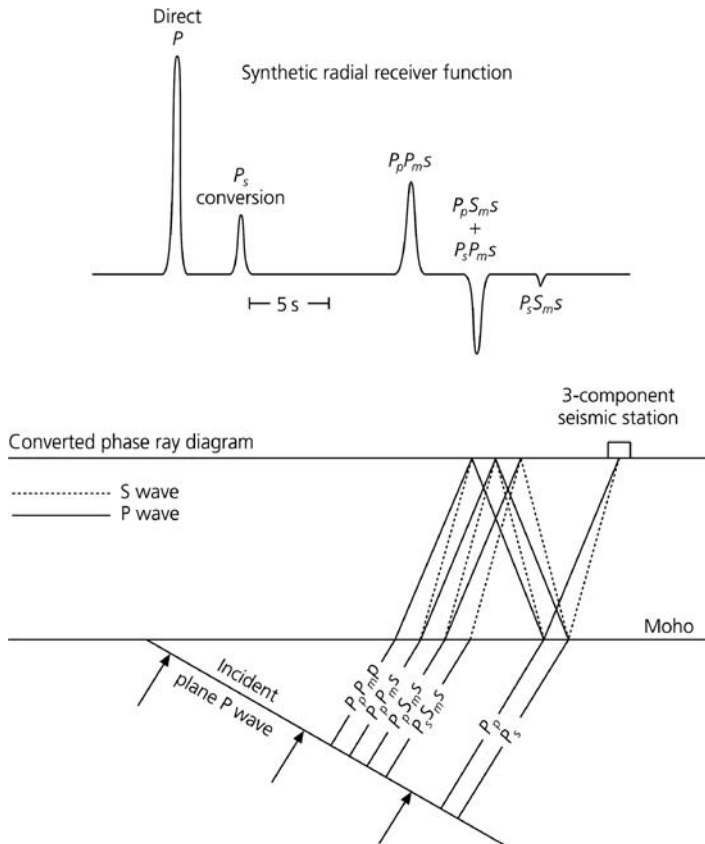


Fig. 2.33 Overview of the receiver function method. The diagram shows (bottom) the ray paths for some converted phases in a one layer model and the corresponding arrival times and receiver function (top). The figure is from Stein and Wysession (2003) and copied from <http://epscx.wustl.edu/seismology/book/>

into distance and azimuth bins and then stacked before the inversion of the velocity structure. Broadband signals from teleseismic events are used, however good short period records can also be used. The method has been used extensively in recent years. Software for the computation and inversion of received functions has been made available by Charles Ammon (<http://eqseis.geosc.psu.edu/~cammon/HTML/RftnDocs/rftn01.html>).

Crustal conversions: In a simpler approach, crustal conversions observed for local earthquakes below Moho are used to model the crustal structure, particularly the crustal thickness. The clearest converted phase to observe is the S to P seen just before the S (Fig. 2.34), however also P to S is often seen. The best earthquakes to use are deep events due to their clear S-phase and relatively steep incidence angle.

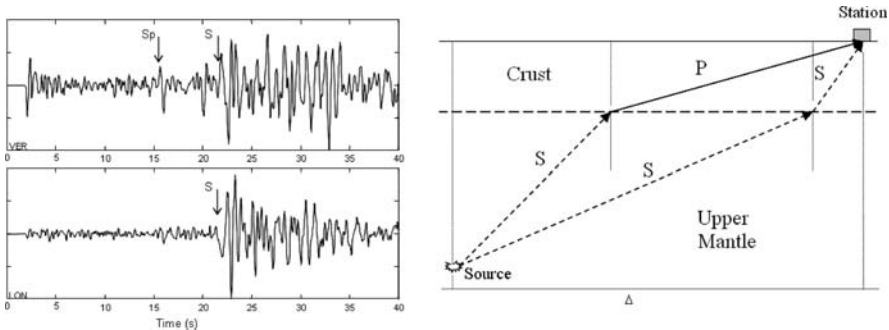


Fig. 2.34 Example of a converted S-phase Sp. The figure to the *left* shows the vertical channel seismogram and the figure to the *right* the schematic ray-path. Figure modified from Narcia-Lopez et al. (2004). The event had a depth of 174 km and epicentral distance Δ of 174 km and was located in S. Mexico

2.7 Exercises

Exercise 2.1 Travel time tables for local earthquakes

Table 2.3 shows a travel time table for crustal phases in Sweden. The aim of the exercise is to determine the corresponding layer velocities for Pg, Pb and Pn, Sg, Sb and Sn.

Table 2.3 Travel times for local earthquake in Sweden. P^* is Pb. Table is from Kulhánek (1990) and originally made by Båth (1979b).

Travel times for $h = 0$

Δ km	Pg m	P* m	Pn m	Sg m	S* m	Sn m	Sg m	-Pg m	Pm m	P s	Rg m	s
0	0				0			0			0	
10	1.6				2.8			1.2			3.3	
20	3.2				5.6			2.4			6.6	
30	4.8				8.4			3.6			9.9	
40	6.4				11.2			4.8		13.7	13.2	
50	8.0				14.0			6.0		14.2	16.6	
60	9.6				16.8			7.2		15.1	19.9	
70	11.3				19.6			8.3		16.1	23.2	
80	12.9				22.3			9.4		17.2	26.5	
90	14.5				25.1			10.6		18.3	29.8	
100	16.1				27.9			11.8		19.5	33.1	
110	17.7	18.7	20.8	30.7			36.8	13.0	20.8		36.4	
120	19.3	20.2	22.1	33.5			39.0	14.2	22.1		39.7	
130	20.9	21.7	23.3	36.3			41.2	15.4	23.4		43.0	
140	22.5	23.2	24.6	39.1			43.4	16.6	24.8		46.4	
150	24.1	24.7	25.9	41.9			45.6	17.8	26.1		49.7	
160	25.7	26.2	27.2	44.7	45.9		47.7	19.0	27.5		53.0	

Table 2.3 (continued)

Travel times for $h = 0$																		
Δ	Pg			P*		Pn		Sg		S*		Sn		Sg	-Pg	Pm	P	Rg
km	m	s	m	s	m	s	m	s	m	s	m	s	m	s	m	s	m	s
170	27.3		27.7		28.5		47.5		48.6		49.9		20.2		28.9		56.3	
180	28.9		29.2		29.7		50.3		51.4		52.1		21.4		30.3		59.6	
190	30.6		30.8		31.0		53.1		54.1		54.3		22.5		31.8	1	02.9	
200	32.2		32.3		32.3		55.9		56.8		56.5		23.7		33.2	1	06.2	
210	33.8		33.8		33.6		58.7		59.5		58.7		24.9		1		09.5	
220	35.4		35.3		34.8	1	01.4	1	02.2	1	00.9		26.0		1		12.8	
230	37.0		36.8		36.1	1	04.2	1	04.9	1	03.1		27.2		1		16.2	
240	38.6		38.3		37.4	1	07.0	1	07.6	1	05.3		28.4		1		19.5	
250	40.2		39.8		38.7	1	09.8	1	10.3	1	07.5		29.6		1		22.8	

- Plot the travel time curves for the 6 mentioned phases.
- Calculate the velocities from the travel time curves using the slope.
- Calculate the velocities directly from the travel time table as $d\Delta/dt$, how do they compare to the above calculated velocities?
- Calculate v_p/v_s for the 3 layers, are they reasonable?
- At 160 km distance, calculate the average velocity for Pg, Pb and Pn assuming a travel path along the surface. How do they compare to the true velocities?

Exercise 2.2 Travel time table for teleseismic earthquakes

Table 2.2 shows an extract of the Bullen tables. The aim of the exercise is to calculate apparent velocity and ray parameter from the travel time table.

The JB table gives the travel time in one degree interval and the difference between each entry in the table is given for interpolation. This difference corresponds to $dt/d\Delta$ where distance is measured in degrees (see (2.2)). At an epicentral distance of 30° and surface focus:

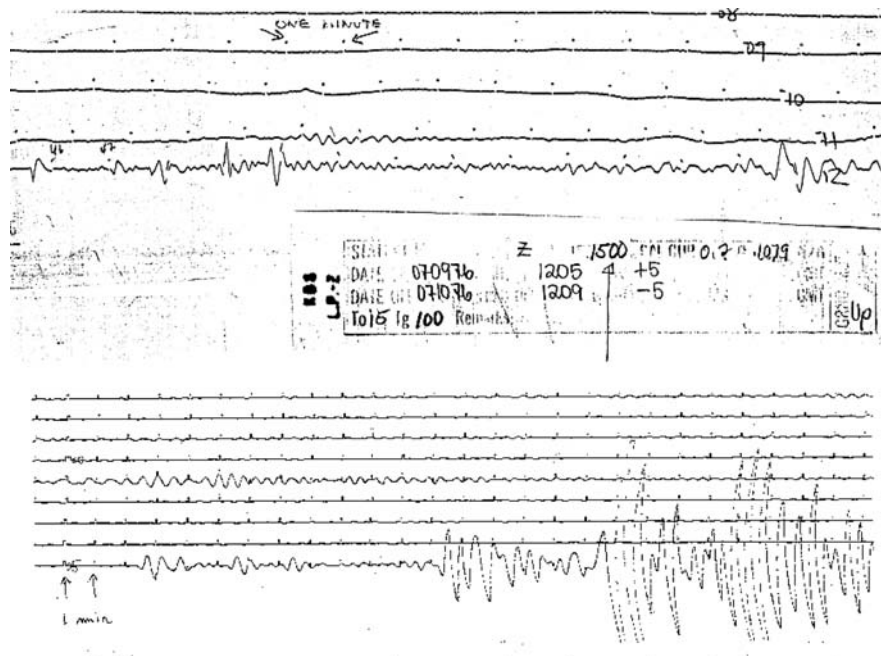
- Calculate the ray parameter p in s/deg and s/km. What is the apparent velocity at the surface? How does that compare to the true velocity at the surface?
- Calculate the angle of incidence at a surface station for an event at epicentral distance of 30° and for depths of 0 and 350 km respectively. Velocities as a function of depth are found in Fig. 2.3. Draw a sketch of the two rays. Does the difference in angle of incidence seem reasonable?

Note: For an exercise in reading local phases, see Exercise 5.2.

Exercise 2.3 Reading phases on a global seismogram

Figure 2.35 shows LP Z-seismograms for 2 different events. The goal of the exercise is to determine as many phases as possible using the travel-time curves. One event is shallow and one is deep. Some idea of the depth might be obtained by comparing the surface waves, since a shallow event will have larger amplitude surface waves relative to P and S waves than a deep event.

- For the shallow event, identify prominent phases on the seismograms and transfer the arrival times to a strip of paper which has the same time scale as one of the figures of the travel time curves (Fig. 2.13). Slide the strip of paper to different distances in order to fit as many phases as possible, see Fig. 2.36 for an example. Once the best fit is obtained, write the names of the identified phases on the seismograms.
- Determine the distance and origin time of the event.
- For the deep event, identify the pP phase (assuming it to be the first phases after P) and find the depth using Table 5.7 (assume a distance of 60°).



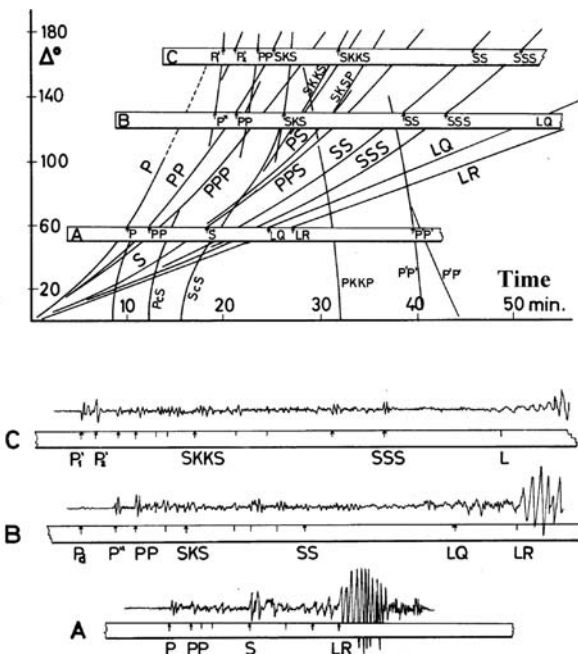


Fig. 2.36 Identification of seismic phases using the strip method. On *top* is shown the travel time curves and on *bottom* the seismograms. Note that the time axis is on horizontal axis in contrast to Fig. 2.13. For phase names, see Table 2.1. Note that PKP is labeled P' on the figure. The method is: (1) Use strips of paper (A, B and C for three different seismograms) to mark arrival times of clear phases (bottom figure). The time scale on the seismogram should be the same as the time scale on the travel time curve, if not the arrival times must be manually plotted on the paper strip using the same time scale as used for the travel time curve. (2) Move the paper strip on to the travel time curves and move the strip along the distance axis in order to fit as many phases as possible. A good starting point is to assume that the first arriving phase is P or PKP. This method will give both the phase names and the epicentral distance, while, ideally different hypocentral depths, would require different travel time curves. Thus the method is mostly useful for shallow events. Figure from Payo (1986)

Computer exercises

- Pick phases
- Compare travel time tables
- Use IASP91 travel time tables to identify phases

Chapter 3

Instruments and Waveform Data

Although it is possible to process earthquake data without knowing much about instruments, it certainly helps to have a basic understanding on how the data is produced and in which way the instruments limit the kind of analysis that can be done. In this chapter we will deal with the sensors and the digitizers since they are the only units that affect the processing of data.

A very important part of the analysis is to have the correct instrumental response and although many data centers provide that information as part of the data, in many other cases the user will have to collect this information and set it up for the processing system used. This again requires some minimal understanding of instruments and will also be dealt with in this chapter.

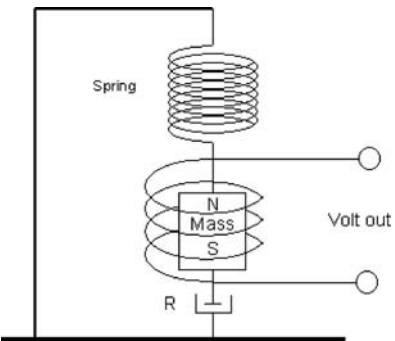
Finally the data is provided in some kind of format. In recent years a large degree of standardization has taken place but different processing systems still use different formats and older data is available in many different formats, often to be interpreted differently on different computer platforms (byte swapping). The following section on instruments partly follows Chapter 1 in Havskov and Alguacil (2006).

3.1 Seismic Sensors

The seismic sensor measures the ground motion and translates it into a voltage. Ground motion can mathematically be described as displacement, velocity or acceleration. Since the measurement is done in a moving reference frame (the sensor is moving with the ground), the principle of inertia dictates that only motions that cause acceleration (change in velocity) can be measured. Thus the principle of all sensors is that a mass must move relative to the reference in response to ground acceleration, see Fig. 3.1.

This simple seismometer will detect vertical ground motion. It consists of a mass suspended from a spring. The motion of the mass is damped using a damping device so that the mass will not swing excessively near the resonance frequency of the system. Intuitively the mass will move relative to the ground when subjected to

Fig. 3.1 Principle behind a seismometer. A magnetic mass is suspended in a spring and the motion (velocity) is detected by a coil, which gives a voltage output proportional to the velocity of the mass. R is a damping device



acceleration. The system has a natural frequency f_0 depending on the spring stiffness k and the weight of the mass m

$$f_0 = \frac{1}{2\pi} \sqrt{k/m} \quad (3.1)$$

The sensitivity of the system to measure ground motion decreases quickly when the frequency is below the natural frequency of the seismometer. If the mass is magnetic and a coil is added around the mass, an electric output is obtained which is proportional to the velocity of the mass. This is the principle in the traditional passive seismometers. This sensor is characterized by 3 parameters: *Natural frequency* f_0 of the free swinging system, *damping constant* h , which is a measure of how much the system is damped ($h = 1$ means the system will not oscillate) and *generator constant* G (V/ms^{-1}), which is a measure of the sensitivity of the coil to ground velocity. With these parameters, the response of the seismometer (relationship between the output and input), the so-called frequency displacement response function, can be calculated:

$$A_d(\omega) = \frac{G\omega^3}{\sqrt{(\omega_0^2 - \omega^2)^2 + 4h^2\omega^2\omega_0^2}} \quad (3.2)$$

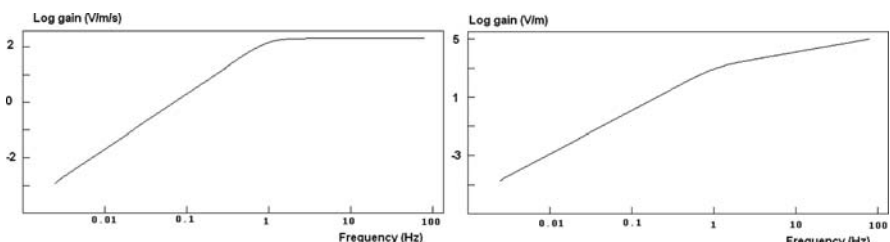


Fig. 3.2 Displacement amplitude response (right) and velocity response (left) of a short period seismometer with natural period of 1 s, damping of 0.7 and a generator constant of $200 \text{ V}/\text{ms}^{-1}$

where $\omega_0 = 2\pi f_0$ and $\omega = 2\pi f$. Displacement response means that when the signal is corrected, the output is displacement. Fig. 3.2 shows an example from a standard short period (SP) seismometer with the following characteristics: $f = 1\text{Hz}$, $h = 0.7$ and $G = 200\text{V}/(\text{ms}^{-1})$. Since this sensor gives an output which is linearly proportional to velocity, when the frequency is above f_0 , this kind of sensor is often called a velocity sensor and its response to velocity is often shown instead of its response to displacement. To obtain the response to velocity A_v , (3.2) is divided by ω and is then

$$A_v(\omega) = \frac{G\omega^2}{\sqrt{(\omega_0^2 - \omega^2)^2 + 4h^2\omega^2\omega_0^2}} \quad (3.3)$$

The response curves for velocity and displacement are shown in Fig. 3.2. For acceleration, one more division with ω is needed.

It is seen that the sensitivity drops drastically when the frequency is below 1 Hz. At 1 Hz the output from the seismometer, when the ground displacement is 1 nm (typical low noise seismic noise), would be $10^3\text{V/m} \times 10^{-9}\text{m/nm} \times 1\text{nm} = 10^{-6}\text{V} = 1\mu\text{V}$ while at 0.01 Hz the theoretical output is 10^{-12} V . While 10^{-6}V easily can be handled by modern recorders, there is no equipment that can handle 10^{-12}V . This should be compared to what the seismologist needs and Table 3.1 shows the frequencies of interest.

Table 3.1 Typical frequencies generated by different seismic sources

Frequency (Hz)	Type of measurements
0.00001–0.0001	Earth tides
0.0001–0.001	Earth free oscillations, earthquakes
0.001–0.01	Surface waves, earthquakes
0.01–0.1	Surface waves, P and S waves, earthquakes with $M > 6$
0.1–10	P and S waves, earthquakes with $M > 2$
10–1000	P and S waves, earthquakes, $M < 2$

This indicates that in the general observatory there is a need to measure signals down to at least a frequency of 0.01 Hz and that can obviously not be done with the SP seismometer. From (3.1) it is seen that by increasing the mass or lowering the stiffness of the spring, the natural frequency can be lowered. In principle this is the way long period seismometers (LP) were made, but the low limit for f_0 was around 0.03 Hz and more commonly around 0.05 Hz. The World Wide Standard Seismic Network (WWSSN) operated standard SP and LP sensors of this passive type for more than 40 years. The response curves are shown in Chapter 6.

When the ground moves, the motion of the sensor mass will be shifted in time relative to the motion of the ground and this is described by the phase shift. If we use a function $\sin(x)$, where x is time, the phase shift ϕ is defined as the number added to x so the phase shifted signal will be $\sin(x + \phi)$, see Fig. 3.3. The original 5 Hz ground displacement is shifted in time by 0.059 s. The period of the signal

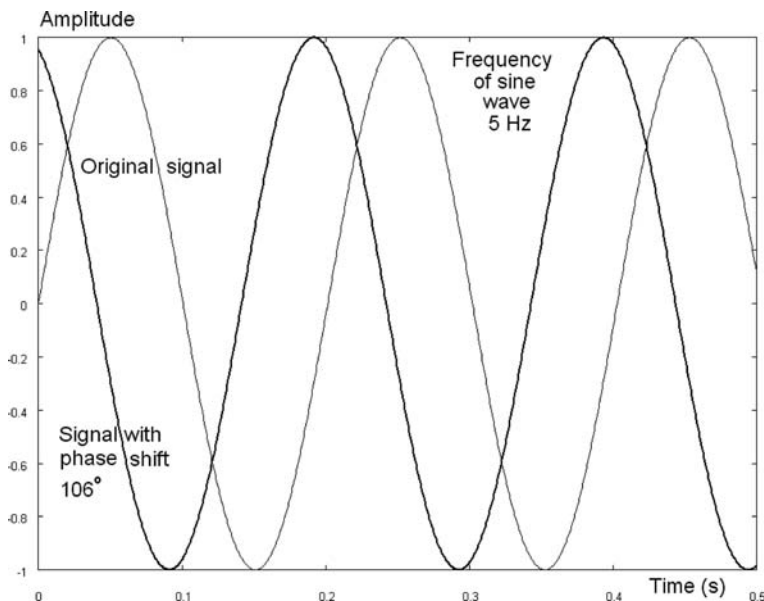


Fig. 3.3 The principle of phase shift. A 5 Hz sine wave is shown together with a 5 Hz sine wave with time shift of 0.059 s caused by a phase shift of 106°

is 0.2 s which corresponds to 360° so the phase shift of 106° degree corresponds to $106/360 \cdot 0.2\text{ s}$. This is the phase shift for a 1 Hz seismometer (see Fig. 3.9). The figure shows what would be seen in case of a steady state motion. It should be noted that the seismometer phase response does not affect the polarity of the first impulse of the P-wave.

Today, purely mechanical sensors are only constructed to have resonance frequencies down to about 1.0 Hz (SP), while sensors that can measure lower frequencies are based on the Force Balance Accelerometer (FBA) Principle of measuring acceleration directly, see Fig. 3.4. The FBA instrument has a feedback coil, which can exert a force equal and opposite to the inertia force due to any desired acceleration range. The displacement transducer sends a current through this force coil through a resistor R in a negative feedback loop. The polarity of the current is such that it opposes any motion of the mass, and it will try to prevent the mass from moving at all with respect to the frame. A small permanent acceleration on the mass will therefore result in a small permanent current and a large acceleration will need a large current. The current is in fact linearly proportional to the ground acceleration, so the voltage over the resistor gives a direct measure of acceleration. FBA sensors were first used to make insensitive strong motion instruments (accelerometers) used in engineering seismology.

The FBA principle is also the heart of nearly all modern broadband sensors (sensors recording in a large frequency band like 0.01–50 Hz). By connecting an integrating circuit, either in the feedback loop or after, the sensor can give out a

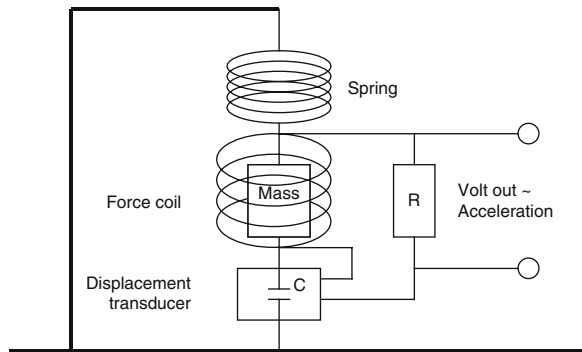


Fig. 3.4 Simplified principle behind the Force Balanced Accelerometer. The displacement transducer normally uses a capacitor C , whose capacitance varies with the displacement of the mass. A current, proportional to the displacement transducer output, will force the mass to remain stationary relative to the frame. Reproduced with kind permission of Springer Science and Business Media. Figure from Havskov and Alguacil (2006), Fig. 1.4

voltage linearly proportional to velocity. However, due to the inertial principle, there must be a low frequency limit (velocity is zero at zero frequency!) and this limit is set by the mechanical-electrical qualities of the sensor. Currently, the best broadband sensors have a limit of about 0.0025 Hz, much lower than it was ever possible with purely mechanical sensors. The broadband sensors have response functions similar to Fig. 3.2 except that the natural frequency is lower and the generator constant is usually higher. There will also be a high cut filter for electronic stabilization.

The accelerometer has a very simple response since its output is linearly proportional to the acceleration and there is no phase shift. The accelerometer is now so sensitive that it can be used to record earthquakes down to at least magnitude 2 at 100 km distance and can therefore in some cases replace the SP sensor, see Fig. 3.5. Some accelerometers use a built-in high pass filter to remove the low frequency noise and consequently they are no longer linearly proportional to acceleration at low frequencies.

The accelerometer (Fig. 3.5) has more instrument noise as seen from the noise in front of the P. The signals are similar although the accelerometer has a bit more high frequency content than the seismometer (seen in spectral content). So why not use an accelerometer as a broadband sensor? The broad band sensor has to record in a large frequency band and the dynamic range of the acceleration signal over the large frequency band is simply too large for any recorder while the integrated acceleration signal (velocity) has a much smaller dynamic range. E.g. a signal with constant velocity amplitude in the range 0.001–10 Hz (dynamic ratio 1) will have a 10^4 dynamic range in acceleration.

Seismic stations usually have 3 sensors, one for measuring the vertical motion (Z, positive up), north–south motion (NS, positive north) and east–west motion (EW, positive east). With active sensors, the three sensors are usually combined in one box for easy orientation and installation.

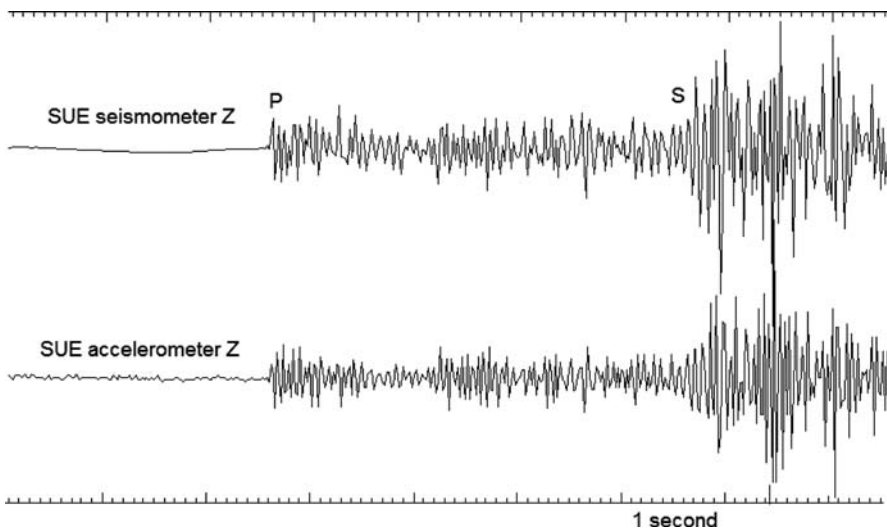


Fig. 3.5 A local earthquake recorded at the same station on an SP seismometer (velocity) and a medium sensitive accelerometer (acceleration). The origin time of the event is 1996 0705 02:20. $M_L = 1.9$ and the hypocentral distance is 27 km

Summary of main sensors used

- Passive SP sensors with an electromagnetic coil: Used for local earthquakes, global observations of P and in exploration seismology. Linear bandwidth to velocity is 1.0–100 Hz. Gain 30–300 V/ms⁻¹.
- Active broadband sensors (BB): The most common sensor today. Used for all kinds of seismological observations, but particularly for global observations. Linear bandwidth for velocity: 0.01–50 Hz. Gain 100–5,000 V/ms⁻¹.
- Accelerometers: Used to get unclipped observations near the earthquake and also sometimes replacing the SP sensor for local earthquakes. Sensors are linear for acceleration in frequency band 0–100 Hz. Gain 1–100 V/g where g is the gravity constant (9.8 ms⁻²).

3.2 Seismic Recorders

The signals from the sensor must be recorded to make a seismogram (Fig. 3.6). In the old systems this was done by amplifying and filtering the signal and recording it on paper on a drum. The WWSSN system was working this way. Now the signals are exclusively recorded digitally.

Common to both systems is that the signal might be amplified and filtered before being recorded which will influence the response function. The digitizer is the unit converting the analog signal to a series of discrete numbers to be read into the computer, processed and stored. The digitizer is usually also the unit time stamping the

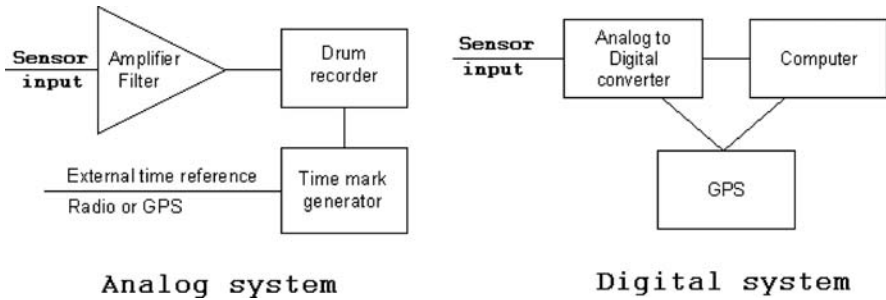


Fig. 3.6 *Left:* A complete analog recorder. The time mark generator is an accurate real time clock which might be synchronized with an external time reference. *Right:* Main units of a digital recorder. The GPS (Global positioning system) gives accurate time and can be connected to the digitizer or the recorder

signal, now exclusively with a GPS. One should think that earlier timing problems at seismic stations do not exist any more. However, a GPS can lose synchronization (maybe it is located at an unfavorable site) or fail. So even today, digital data will sometimes be recorded without proper time synchronization. It is then important that the digital data has an indication of uncertain time.

For most digital systems the amplification and filtering of the signal takes place in the digitizer. Ideally we want as little filtering as possible in order to get the original signal from the sensor. An example of a simple filter is an RC filter, see Fig. 3.7.

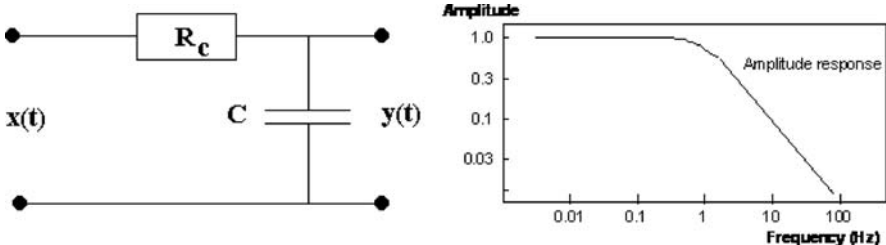


Fig. 3.7 *Left:* An RC high cut filter consisting of a capacitor C and a resistor R_c . The resistance of the capacitor decreases with increasing frequency so the effect of the RC combination is to filter out higher frequencies. The input signal is $x(t)$ and the output signal $y(t)$. *Right:* The amplitude response (output $y(f)$ divided by input $x(f)$) of the RC filter. Reproduced with kind permission of Springer Science and Business Media. Figure modified from Havskov and Alguacil (2006), Figs. 6.3 and 6.5

In this example we have a low pass (or high cut) filter with a corner frequency (frequency at which the level has reached $1/\sqrt{2} = 0.707$ or -3 dB) f_0 of 1.0 Hz (dB is defined as $20 \log(\text{ratio})$ where ratio here is 0.707). The response function is

$$A(\omega) = \frac{1}{\sqrt{1 + \omega^2/\omega_0^2}} = \frac{Y(\omega)}{X(\omega)} \quad (3.4)$$

where $\omega_0 = 1/RC$ and R is measured in Ohm and C in Farad. We call this a 1 pole filter since the amplitude decays proportional to ω^{-n} or f^{-n} , $n = 1$. An RC filter is a passive filter (no amplifier involved). A common example of an active filter (using amplifiers) is a Butterworth filter, which easily can be made to have many poles (e.g. $n = 8$). A drawback with both these filters is that they give a phase shift of the signal which often involves a large part of the pass band and the phase shift increases with the number of poles.

A digitizer samples the data a certain number of times a second (the sample rate), typically at 100 Hz for recording of local earthquakes and 20 or 40 Hz for recording of regional and global earthquakes. The sampling limits the highest frequency which can be used to half the sampling frequency (the Nyquist frequency f_{Ny}) and all signals with frequency above f_{Ny} must be removed before digitizing the signal in order to avoid aliasing effects which can result in distortion of the low frequency signals from the high frequency signals, see example in Chapter 4 (see e.g. Scherbaum 2001). Aliasing occurs as the discrete sampling in time results in a periodic spectrum in the frequency domain. The periodicity in the frequency domain occurs with $2f_{Ny}$ and if the signal contains energy above f_{Ny} , the digitized signal at frequencies below f_{Ny} will be contaminated.

Since the antialiasing filter should remove all energy above the Nyquist frequency and as little as possible below the Nyquist frequency and ideally not provide a phase shift, a Butterworth filter cannot be used and digital filtering with a very sharp cutoff is required. Most digitizers use so-called FIR (Finite Impulse Response Filters) which is specified by a series of filter constants and used in the time domain, see e.g. Scherbaum (2001). If the input signal is x_i , the output signal y_i , where i goes from minus infinity to infinity, the filter operation is simply a convolution (Chapter 4)

$$y_i = \sum_{k=0}^{N-1} x_{i-k} \cdot w_k \quad (3.5)$$

where w_k indicates the N filter constants. The constants w determine the shape of the filter. Fig. 3.8 shows an example of a FIR filter. As it can be seen, the FIR filter corner frequency is at 45 Hz, so the filter is extremely sharp. Fig. 3.8 also shows two Butterworth filters for comparison. The 25 Hz filter has an attenuation of 42 dB at 50 Hz, while the 10 Hz filter has an attenuation of 112 dB. So, we obviously get a much larger bandwidth using FIR filters compared to using Butterworth filters and in addition there is no phase shift in the pass band. A disadvantage is that linear phase FIR filters are acausal, which means that after applying the filter, part of signal energy is shifted and seen in time before the signal arrives. This is known as precursory ringing that can be a problem when reading phases, see Scherbaum (2001) for details and how to correct for it. An example is shown in Fig. 4.3.

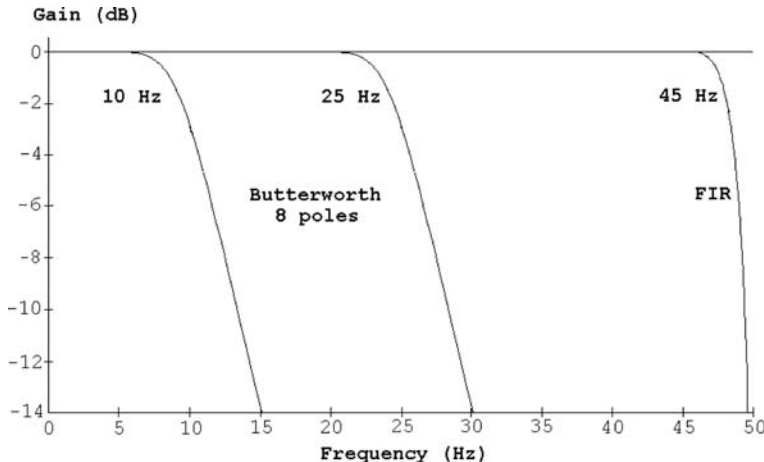


Fig. 3.8 A FIR filter compared to Butterworth filters. The FIR filter has a gain of -150 dB at the 50 Hz Nyquist frequency, while the 10 and 25 Hz Butterworth filters have gains of -42 and -112 dB respectively. Figure from and Havskov and Alguacil (2006)

3.3 Correction for Instrument Response

We have now defined all the elements of the seismic station and it is obvious that raw seismograms do not record the ground motion in displacement, velocity or acceleration directly. In general, the seismologist wants to get the measurements in displacement. Remember that

$$v = 2\pi f d \text{ and } a = 2\pi f v \quad (3.6)$$

where d is displacement, v is velocity and a is acceleration. The seismograph can be understood as a linear system where the input is the ground motion (displacement) and the output is the displacement on the seismogram or the number (count) in the digital recording. For a given instrument, the amplitude frequency response function can be determined, such that for given harmonic ground displacement $U(\omega)$, the output $Z(\omega)$ can be calculated as

$$Z(\omega) = U(\omega) A_d(\omega) \quad (3.7)$$

where $Z(\omega)$ can be the amplitude on a mechanical seismograph, voltage out of a seismometer or amplifier or count from a digital system, and $A_d(\omega)$ is the displacement amplitude response. $A_d(\omega)$ is the combined effect of all elements in the seismograph meaning the sensor, amplifier, filter and digitizer. Let us make an example. A seismograph has the following characteristics:

- $G = 200 \text{ V/ms}^{-1}$.
- $f_0 = 1.0 \text{ Hz}$.

- Amplifier gain = 100.
- An 8 pole low pass filter at 25 Hz (Fig. 3.8).
- A digitizer with a gain of 10^5 count/V.

The gain of the system for velocity, at 30 Hz can then be calculated as

$$200 \text{ V/ms}^{-1} (\text{sensor}) \times 100 \text{ V/V} (\text{amplifier}) \times 0.2 \text{ V/V} (\text{filter}) \times 10^5 \text{ Count/V} (\text{digitizer}) = 4 \times 10^8 \text{ Count/ms}^{-1}$$

The gain of the sensor is 200 V/ms^{-1} since the frequency is above the sensor natural frequency and the gain of the filter is $-14 \text{ db} = 10^{-14/20} = 0.2$ times at 30 Hz (Fig. 3.8). To convert the gain to gain for displacement, we have to multiply with $\omega = 2\pi f$

$$4 \times 10^8 \text{ Count/ms}^{-1} \times 2 \times \pi \times 30 \text{ s}^{-1} = 7.5 \times 10^{10} \text{ count/m} = 75 \text{ count/nm}.$$

Similarly, to convert the gain to gain for acceleration, we have to divide with $\omega = 2\pi f$. At 2 Hz, the seismometer would have a gain of 200 V/ms^{-1} (Fig. 3.2), there would be no effect of the filter and the gain would now be 25 count/nm. This is a reasonable gain considering that the natural background noise, (see Section 3.5 below). Figure 3.9 shows the complete curve as well as the phase response.

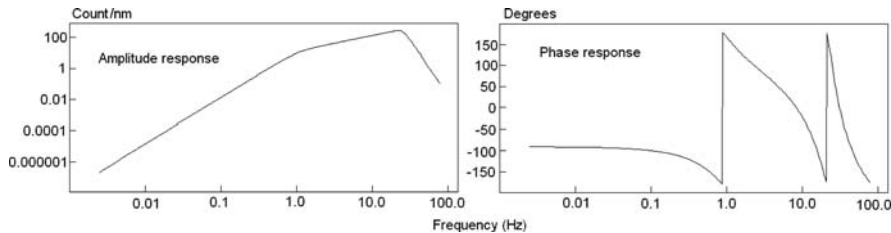


Fig. 3.9 *Left:* Displacement response of the system described above; *Right:* Phase response

Since we now have $A_d(\omega)$ for all frequencies, the ground displacement $U(\omega)$ can simply be calculated as

$$U(\omega) = Z(\omega) / A_d(\omega) \quad (3.8)$$

$A_d(\omega)$ has traditionally been called the magnification or gain since for an analog recorder it gives how many times the signal is magnified. Typical gain curves of classical analog WWSSN seismographs are seen in Fig. 6.10 and Fig. 6.15, respectively. For examples of corrections for response, see Exercise 6.2. The relation (3.8) only corrects for the amplitude. Sensors and filters will also give phase shifts of the signal as shown above (Fig. 3.3), see e.g. Havskov and Alguacil (2006). This cannot be corrected for with analog signals but with digital processing, correction for phase can be done. In practice, the simplest way to deal with the complete instrument response is to work with the complex system response $T(\omega)$. For (3.2) the complex relation for displacement, would be (Havskov and Alguacil, 2006)

$$T_d(\omega) = \frac{-i\omega^3 G}{\omega_0^2 - \omega^2 + i2\omega\omega_0 h} \quad (3.9)$$

Obtaining the corresponding velocity response would be a question of dividing by $i\omega$ and the acceleration response to divide by $(i\omega)^2$. We can define the complex spectra of the input and output signals $x(t)$ and $y(t)$ as $X(\omega)$ and $Y(\omega)$, respectively. Knowing the complex output spectrum we can determine the complex input spectrum as

$$X(\omega) = Y(\omega) / T(\omega) \quad (3.10)$$

We have now obtained the instrument corrected complex ground motion spectrum and since $X(\omega)$ is complex, this also includes the correction for phase. The separate amplitude and phase spectra can then be obtained as

$$A(\omega) = \sqrt{\text{Re}(X(\omega))^2 + \text{Im}(Y(\omega))^2} \quad (3.11)$$

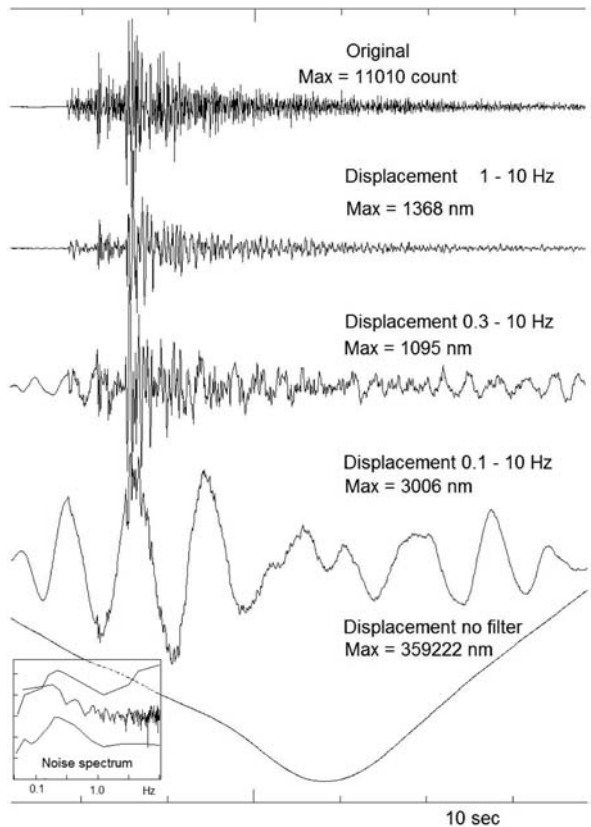
$$\Phi(\omega) = \tan^{-1} \left(\frac{\text{Im}(X(\omega))}{\text{Re}(X(\omega))} \right) \quad (3.12)$$

Usually only the amplitude spectrum is used in practice and (3.10) then gives the principle for correcting for amplitude spectra used in Chapter 8. The true ground displacement time signal is then obtained by taking the inverse Fourier transform of $X(\omega)$, see Chapter 4. For more details, see Scherbaum (2001) and Havskov and Alguacil (2006).

In theory, we can then recover the ground displacement at any frequency knowing the instrument response. In practice, one has to be careful to only do this in the frequency band where the instrument records real ground motion and not just electronic noise since the instrument correction then becomes unstable and the output has nothing to do with the real seismic signal. Fig. 3.10 shows an example. It is seen that the maximum ground displacement is similar for the frequency bands 1–10 Hz and 0.3–10 Hz so the 0.3 Hz waves seen in the 0.3–10 Hz band are likely to be the true microseismic noise (see Section 3.5). In the band 0.1–10 Hz the signal is dominated by 0.1 Hz waves, which could look like seismic background noise, although the amplitude seems very high. However, real background noise rarely has its maximum amplitude at 0.1 Hz (see Fig. 3.12). Looking at the noise spectrum shows that the spectral level increases below 0.3 Hz, while it is expected to decrease (see Section 3.5). So it can be concluded, that this instrument cannot resolve seismic signals below 0.3 Hz and the 0.1 Hz waves are an artifact of the instrument correction. Trying to convert to displacement without using a filter results in a completely unrealistic signal.

In practice we need $T(\omega)$ for every channel of digital signal we have in our processing system. T can be specified as the product of complex functions (like (3.9) for sensor) for sensor and filter or it can be given as discrete numbers giving amplitude gain and phase response for discrete frequencies. When using complex functions, it turns out that, for the components used in seismic systems, the response function can be written as

Fig. 3.10 Instrument correction in different filter bands. The *top* trace is the original recording of a small earthquake in Tanzania with a 1 Hz seismometer. The 3 *bottom* traces have been converted to displacement using different filters. The amplitudes (Max) are maximum amplitudes. The inset at *bottom left* is the noise spectrum (see Section 3.5). The data is from station ITB, vertical channel and the origin time is 1992 1112 12:50



$$T(\omega) = c \frac{(i\omega - z_1)(i\omega - z_2)(i\omega - z_3)\dots}{(i\omega - p_1)(i\omega - p_2)(i\omega - p_3)\dots} \quad (3.13)$$

where c is a scale factor, z are the zeros (or roots) of the nominator polynomials while the zeros of the denominator polynomials are the so-called poles p . Some formats include a normalization constant that normalizes the poles and zeroes at a given frequency to 1. The scale factor c is then separated into normalization factor n and another scale factor s , and $c = ns$ (see also SEED manual, SEED 2007). This so-called poles and zeros representation has become the most standard way of specifying the response function of a seismic system. As an example, the standard displacement response of the velocity transducer (3.9) can be written as

$$T_d(\omega) = \frac{(i\omega - 0)(i\omega - 0)(i\omega - 0)}{(i\omega - p_1)(i\omega - p_2)} \quad (3.14)$$

where all zeros are zero and the poles are calculated as

$$p_1 = -\omega_0(h + \sqrt{h^2 - 1}) \text{ and } p_2 = -\omega_0(h - \sqrt{h^2 - 1}) \quad (3.15)$$

Note that the scale factor is 1.0 for the equation for the seismometer. For the seismometer example shown in Fig. 3.2, the complex poles are $(-4.398, 4.487)$ $(-4.398, -4.487)$ and the complex zeroes are $(0,0)$, $(0,0)$ and $(0,0)$. The unit of frequency used here is radian/s (by definition when using ω instead of f) as used by most processing systems.

In order to convert poles and zeros from units of Hz to units of radian/s, they must be multiplied by 2π . The scale factor in radian/s is the scale factor in Hz multiplied by $2\pi^{(\text{number of poles} - \text{number of zeros})}$. The same is the case for the normalization constant.

Accelerometer: The complex velocity response is $i\omega$ and the displacement response is $(i\omega)^2$. Thus the displacement response in terms of poles and zeros for an accelerometer has two zeroes at $(0,0)$ and a scale factor of 1.0.

Filters: Similar equations can be written for Butterworth filters (and other analog type filters). For digital filters it is in theory also possible to represent the response in terms of poles and zeros, but it generally requires very many poles and zeros and the correction is usually done in the time domain using filter coefficients (Scherbaum, 2001). As the FIR filters are normally very steep, it is practically not possible to correct the amplitude spectrum for FIR filters. However, as mentioned the filters can be acausal and affect the actual signal.

3.3.1 How to Store the Response Information

Response information can be stored in files separate from the digital data or as part of the data headers. The response can be given both as velocity and displacement response and sometimes even as acceleration response. Most processing systems use displacement response.

Commonly available processing systems use one of the accepted response formats which are: SEED, SAC, GSE and SEISAN (see Section 3.4). The information itself is mostly stored using one of the following parameters or a combination of them:

- Poles and zeros (PAZ)
- Discrete amplitude and phase values (FAP)
- Individual parameters (free period, ADC gain etc)
- Time domain filter coefficients
- Combination of the above

Using poles and zeroes is the most common way to store the response information. The two most common international formats are SEED and GSE, both created with the help of many experts. In SEED the response is normally given as velocity while it is displacement in GSE. For the example in Fig. 3.9, the poles and zeros given by SEISAN are:

10	3
0 . 3187E+29	

-4.398	4.487
-4.398	-4.487
-36.77	184.9
-104.7	156.7
-156.7	104.7
-184.9	36.77
-184.9	-36.77
-156.7	-104.7
-104.7	-156.7
-36.77	-184.9
0.000	
0.000	
0.000	

The first number gives the number of poles (10) and the next the number of zeroes (3) and then follows a constant (0.3187E+29). This constant provides the scaling to meters. Next follow the poles (pairs for complex numbers) and it is seen that the first 2 poles belong to the seismometer (compare to example above) so the remaining 8 poles belong to the filter. The 3 zeros belong to the seismometer. For specific examples of formats and how to convert from one to the other, see Havskov and Alguacil (2006).

3.3.2 Response in Practice

When operating more than a few stations, it is common to have changes in response information and it is unfortunately not always updated when station parameters are changed. In that case it is an advantage to be able to add and modify response information afterwards and keep a data base of changing response information with time. If this is too complicated to do, it will often not be done and there are many networks without proper calibration records generally available for processing. It is therefore a help to have a processing system that easily can generate calibration files from any kind of instrumental information.

SEED: The response is always part of the data headers. It is given as a number of stages corresponding to the components of the seismometer and recording system. Some processing system will read SEED response directly from the headers while in other systems the headers must be extracted from the binary data files and stored as local ASCII files. Usually this is done with the IRIS (Incorporated Research Institutions for Seismology, www.iris.edu) official SEED reading program RDSEED. Note that the poles and zeros are given for velocity so if a displacement response is needed, one more zero at (0,0) must be added. The SEED response file will contain the response history so only one file is needed for the particular channel. In SEED the response can also be stored without data, the so-called dataless SEED volume, which can have the response information for a network.

SAC: The response is given as PAZ with a gain factor in individual ASCII files.

GSE: The response can be described in stages, similar to SEED. It is possible to describe all common components of the sensor and recording system. In GSE it is possible to have one file for the whole network, or single files for each channel.

SEISAN: The response can be part of the data but is usually distributed as separate response files for each channel. The response is always in displacement. The response history is taken care of through different files for each time period with a particular history.

3.3.3 Using Response

If a response file is provided with the data and it is the right kind for the system, all should be ok. There is still a possibility that the response file is not correct, so some simple checks can be made to investigate if a response is “reasonable”:

Noise spectrum: The simplest test is to make the noise spectrum as shown in the examples in Fig. 3.16. Within a rather large area with similar distance to the ocean, the noise spectra should be very similar and large errors will be seen immediately.

Shape of the response curve: Plotting the given response curve and comparing to other similar station will indicate significant errors.

Calculate m_b : The m_b magnitude is determined around 1 Hz (see Chapter 6) and is therefore not much affected by local noise. Determine m_b for e.g. 10 events, calculate the average and compare to m_b at a recognized data center like ISC or United States Geological Survey (USGS). The difference should be less than 0.2 magnitude units. Similar tests can be made with surface wave magnitude M_s .

3.3.4 How to Make Response Files

Different processing systems require response files in different formats as described above. In order to make a response file, the system parameters must be collected. Many manufacturers will give the complete poles and zeros for their instruments and it is then just the case of formatting these to the requirements of the processing system used, making sure that the response is correct in terms of displacement or velocity and that the gain factor is correct. In other cases, the instrument parameters are given and the response file must be made from scratch. Response files can be very large and complicated to make manually. Fortunately most processing systems will have a program to create the response files given instrumental parameters. Examples are given in the computer exercises.

Passive sensor: Natural frequency, damping and generator constant are needed.

BB sensors: While strictly not a standard velocity sensor, most BB sensors will have a response function very close to that of a standard velocity sensor and most manufacturers give the corresponding natural frequency and damping. The exact response is given by poles and zeros but the approximated response is often sufficient so the same parameters, as for the passive sensor, are needed. However BB

sensors typically have a built-in low pass filter with a corner frequency that might be lower than the digitization frequency and will have to be taken into account.

Accelerometer: The response in acceleration is usually very simple since both phase and acceleration response is independent of frequency, usually up to well above 50 Hz so if a correction is to be done in acceleration, it is just a question of multiplying with a constant. The complex displacement response is $(i\omega)^2$ as given earlier.

Digitizer: The main number needed is the gain in terms of count/V. Most digitizers have very sharp digital filters and for most processing needs, the antialiasing filter can be disregarded. As mentioned above, the FIR filters are rarely corrected for in the frequency domain and only if correction is to be made in the time domain (e.g. to correct for ringing at the onset) will the filter coefficients be needed. However, it is best practice to include the FIR filters as part of the response information and this is a requirement by the larger data centers (e.g., IRIS and ORFEUS).

3.4 Waveform Formats

Each channel of seismic waveform data consists of a series of samples (amplitude values of the signal) that are normally equally spaced in time (sample interval). Each channel of data is headed by information with at least the station and component name (see below for convention on component name), but often also network and location code (see below). The timing is normally given by the time of the first sample and the sample interval or more commonly, the sample rate. Some waveform formats (e.g. SAC) can store the timing of each sample. Waveform data has been recorded and is stored in a large variety of formats making life difficult for the end user. In this section, a brief overview of waveform formats will be given with recommendation of what to use. A more complete discussion is found in NMSOP, Chapter 10. Waveform data files are nearly exclusively stored in binary form (except GSE format) in order to save space as compared to the ASCII form. Since there are so many different waveform formats, only the ones in common use for data exchange and by public domain processing systems will be mentioned.

Different formats have arisen mainly for 3 purposes:

Recording format: In the past the recording format was often designed for that specific purpose, which usually was not very suitable for processing. Now it is more usual to use a common data format that can be used for data processing directly without conversion.

Processing format: A processing system develops a format convenient for processing. This is usually a more complete format than the recorder format. Examples are SAC and SEISAN.

Data exchange format: A format developed by international collaboration to be used for data exchange. This is the most complete format and often also the most complex since it must contain all information about the data. Examples are SEED and GSE.

In addition to the format being different, the same data file will be read differently (byte order) on big endian computers (Unix systems, e.g. Sun) and small endian computers (PC). This requires the processing software to be able to recognize where the data file was written and correct the numbers read.

3.4.1 GSE

The format proposed by the Group of Scientific Experts (GSE format) has been extensively used by the Comprehensive Test Ban Treaty Organization (CTBTO) projects on disarmament and is also widely used in the seismological community. The format is a pure ASCII format, which makes it easy to transmit by conventional email and from one type of computer to another. The format has a compression facility so that, despite being in ASCII, it can still be stored in almost the same space as a compressed binary format. The GSE2.1, now renamed IMS1.0, is the most recent version. The manual can be downloaded from (http://www.seismo.ethz.ch/autodrm/downloads/provisional_GSE2.1.pdf) or International Monitoring System (www.ctbto.org) web pages.

Below is an example of a GSE file.

```

WID2 1996/07/15 21:29:30.521 HRV     BH      CM6      2452    20.000000  0.10E+01
STA2          42.51000   -71.56000           0.000  0.000
DAT2
WY-nX3UQkR012WD1+m8X1kQ1DkR0V2kQV8ke1FVNkTkkSVBkH0KSV5kT7V-19UQUR16USOQV2NUEkPF33
UMRD9kGkKPv23lQ8DS-D8RGkIV9VHmIkHwOSkH0kHUGUM126kP1X7Nr+U1V4IDkG10VAJkJLUE8S6NU
FkR2UQ1EULVL1HkRVSUHkRPDV1+18V6W1kH1D7V6kJ1F4V091-R148UOk00kG18+v01NUMIn9WBUTm30
0kF5kEIBJv51+FBkV7l3VM517V-7TW51G1-VfkM291+UQV51MkPV1VBQm23V2ULKq1CVFCSo1DV+UMkQ
-1I+s831DBUmkOKD1-4VK181KVAKLW7163V13-4kTVr-UImaw7VP1615UOVNjQ10UHUTkMkj4359hkMC
UQ161HVDFV1o+F47kPVl17UJ+1NVQULk1HPWJ+1EUOkLUHUM1TVMQk0V4m1ULV71TCV1m+V0V1mBL12F
WS121LUGUK1DOWBQ1-UFUHV6UsMf+W01C10FHW9V+1DkLV+UP1G1Fv8CkTUHm9V7UMm0WOK19VEkP1-W
+UH14CMV3UL111-UFVJ-1GkICA91311W3VBmK14W+UG1PV+V310WT1Cn4WPV8kL117UQUkks1Fk0WLUS
o0V9W3kTm0UHUn10VFmDkEXQkNm2UHPVSSS16hkGVAV-1MVAfkHV9115VlmBJVMVFURnLSW1kE21311
VGkELUH1QAUL1CVJUF1GkL-VOK1TUPW515URam8W391PUR16J1DBV4Qk12kNVJUHS18U1V2m6V6VOST8
kNGViKRF1MDX11AK4kEVQFn3VNVLm0+V8kG40kLVC1nkGUQ6ULk06RIPUGUK1NUHVQkLkNI7915AUS1+
k109UHR18V+V7m4KWKMNV4HUMTkF2HUNMkPkKSV271DP58kGUFUFkOP-V3+1EUMUECV91F1-V8UHUL+1
...
CHK2  5342683

```

A GSE2.1 waveform data file consists of a waveform identification line (WID2) followed by the station line (STA2), the waveform information itself (DAT2), and a checksum of the data (CHK2) for each DAT2 section. In this example the waveform has been compressed with the algorithm CM6, which means that all numbers have been replaced by printable characters. The response data type allows the complete response to be given as a series of response groups that can be cascaded. The waveform identification line WID2 gives the date and time of the first data sample; the station, channel and auxiliary codes; the sub-format of the data, the number of samples and sample rate. Line STA2 contains the network identifier, latitude and longitude of the station, reference coordinate system, elevation and emplacement depth.

Since the data comes in one block with timing information for the first sample only, it is assumed that there are no time gaps. If there is more than one channel in the file, they come one after the other. Data files are limited in size, usually not written for more than a few hours duration. The GSE format is not suitable for direct access reading so reading a particular channel in a large file will be slow.

3.4.2 SEED

The Standard for the Exchange of Earthquake Data (SEED) format was developed within the Federation of Digital Seismographic Networks (FDSN) and in 1987 it was adopted as its standard. It is by far the most complete format available for seismological data. It is also the most complicated and was ONLY intended for data exchange. In that respect it has been very successful and all major data centers store and offer data in SEED format. SEED can be used on all computer platforms and has response information (and much more) included in its headers. For a complete description of the SEED format, see SEED manual found at www.iris.edu/manuals/SEEDManual_V2.4.pdf. Here we will give a brief summary.

SEED is a binary format and the data is written as a series of main headers followed by the waveform data. Irrespective of number of channels stored in the file, all the main headers come first.

Main headers: These describe all kinds of general information about the seismic channels in the file including station location, format of data and response information. The main headers have many options for giving information, but the main information used in processing is the response information.

Data blocks: All data blocks have sizes between 256 and a multiple of 256 bytes and one block contains data from only one channel. A data block starts with the standard information about channel name, sample rate, start time etc, followed by the waveform data. There are many formats for the waveform data defined in the SEED standard, but fortunately only 3 are generally used: Integers, integers compressed with Steim1 (up to 2 times compressed) and integers compressed with Steim2 (up to 3 times compressed). The data blocks can come in any order, but data from data centers are usually demultiplexed, so all the blocks of one channel come first followed by blocks from the next channel etc.

Since a seismic trace consists of a series of data blocks, each with its own header time, there is a possibility of having time gaps in the data, either intentionally (large gaps) or because a digitizer is drifting (small gaps). The data blocks contain all that is needed for processing, except response information, and consequently, SEED files without the main headers are commonly used and the format is officially called MiniSEED. The size of a SEED file is only limited by the storage device and what is practical. It is common practice to use SEED files of one day duration for continuous data storage while event files might be a few minutes to a few hours long.

Since SEED was intended for data storage and exchange and due to its complexity, very few processing systems use SEED directly. So the current practice has been to download SEED, convert it to some other format like GSE and start processing.

Fortunately, MiniSEED, being easier to read and write, has gained wide acceptance on a lower level and much more software is available for MiniSEED than for SEED. An important factor contributing to this is that nearly all commercial recorders now record directly in MiniSEED (or can convert to MiniSEED) and a de facto standard has been established. As a consequence some processing systems can now use MiniSEED.

A MiniSEED file can only be checked with a program, however the first 20 character are written in ASCII and can be viewed without a program, which can be useful for a simple check of an unknown file, see Table 3.2.

Table 3.2 Content of first 20 bytes of a MiniSEED file, see later for explanation

Field name	Length (bytes)
Sequence number	6
Data header/quality indicator: D, R, Q or M	1
Reserved byte (a space)	1
Station code	5
Location identifier	2
Channel identifier	3
Network code	2

3.4.3 SAC

Seismic Analysis Code (SAC) is a general-purpose interactive program designed for the study of time sequential signals (Goldstein et al., 2003; Goldstein and Snoke, 2005). Emphasis has been placed on analysis tools used by research seismologists. A SAC data file contains a single data component recorded at a single seismic station. Each data file also contains a header record that describes the contents of that file. Certain header entries must be present (e.g., the number of data points, the file type, etc.). Other headers are always present for certain file types (e.g., sampling interval, start time, etc. for evenly spaced time series). Other header variables are simply informational and are not used directly by the program. The SAC analysis software runs on several platforms (Unix, Linux, Mac, Cygwin) and it has both binary and ASCII formats. SAC has a number of ways to correct for instrumentation, e.g. for predefined instruments, response by the program EVALRESP (by IRIS) and the response given as PAZ in a text file per channel.

3.4.4 SEISAN

The SEISAN binary format is used in the seismic analysis program SEISAN and other programs (<ftp://ftp.geo.uib.no/pub/seismo/SOFTWARE/SEISAN/>). The format consists of a main header describing all channels. Each channel then follows with a channel header with basic information including response. SEISAN can read binary SEISAN files written on any platform, as well as SEED, MiniSEED, GSE and SAC.

Since the data comes in one block per channel with timing information for the first sample only, it is assumed that there are no time gaps. If there is more than one channel in the file, they come one after the other. Data files are limited in size, usually not more than a few hours. There is no built in compression. A channel can be read direct access.

3.4.5 CSS

The Center for Seismic Studies (CSS) Database Management System was designed to facilitate storage and retrieval of seismic data for seismic monitoring of test ban treaties. The format (Anderson et al., 1990) is mainly used within the Comprehensive Testband Treaty community and GEOTOL uses CSS. However, large amount of data is stored in CSS format.

The description of waveform data is physically separated from the waveform data itself and can be maintained within a relational database. Data are stored in files, which are indexed by a relation that contains information describing the data and the physical location of the data in the file system. Each waveform segment contains digital samples from only one station and one channel. The time of the first sample, the number of samples and the sample rate of the segment are noted in an index record. The index also defines in which file and where in the file the segment begins, and it identifies the station and channel names. A calibration value at a specified frequency is noted.

3.4.6 Common Points to Consider with Waveform Formats

Data compression: Data compression is needed for large data sets. Data compression can be done with an external program like gzip, but compression is mostly built into the recording format itself like for SEED and GSE. While external and internal compression might achieve similar compression rate, it is preferable, in terms of reading speed, to use built in compression which takes place on the fly. SEED and GSE compression algorithms are also a bit more effective than other external compression programs since they are designed specifically for seismic data.

Reading speed and direct access: Binary files can be read faster than ASCII files and being able to read direct access to any channel or even to a part of a channel speeds up the reading process. As mentioned above, built in compression is also important for speed.

Timing: Correct timing seems to be a never ending problem despite progress in timing systems, although it has improved a lot with the introduction of GPS timing. *The first and worst problem* is when the data has no information that a timing problem is present. Ideally it should be possible to have this information with the waveform data and it should be part of the format. Having a flag in the format is no guarantee that the timing flag is active since the acquisition software might not set a time flag or the data has been converted from a format without timing

error information. *The second problem, less common*, is when the time of the first sample in the file is correct, but the digitizer has a drift so the indicated digitization rate is not correct. This means that the last sample in the file might have a timing error. Timing problems are better controlled with the SEED format than other formats since one data block commonly is 4,096 bytes long which approximately corresponds to a maximum of 4,000 samples. Large timing errors are easy to spot automatically or by the operator but timing errors under 5 s can be difficult to spot (see Section 5.6). See Table 3.5 which lists formats that have a time error flag.

Continuous data: The data can be written to files of constant length, e.g. 1 hour, 1 day, 1 month. Of the formats mentioned, long files can only be written in MiniSEED, while the other format types have limited size. When writing discrete files with formats other than SEED, the length should be long enough to avoid getting very many files (e.g. 1 h) but short enough to exclude problems of digitizer time drift or other timing problems (like loss of GPS synchronization) within the length of the file.

Time gaps: There can be time gaps between files, either because of the mentioned clock or digitizer drift or due to missing data. While modern acquisition systems are very accurate, with older systems one may observe a few samples tolerance. Usually time gaps are positive (meaning that the next file starts after the end of the previous file), however negative time gaps (overlap) can also occur. *In processing we can deal with time gaps in 3 ways:* (1) If positive, add zeros (or the DC level) to fill the time gaps under the assumption that real data is missing and the clock is correct. This is the most common approach. (2) Let the time gap remain whenever possible in the processing (e.g. plot data with time gaps or with overlap). (3) Apparent gaps can be introduced by incorrect timing of consecutive data blocks. In this case, it may be possible to ignore the gaps under the assumption that it is not real (known if it can be verified that no samples are missing). It is unfortunately not always clear and well documented how processing software deals with time gaps.

Station codes: The station code can be up to 5 characters long.

SEED and other formats channel naming: A few years ago, naming a channel BZ, LZ or SZ was enough to understand which kind of system was used. Now a large variety of sensors and digitizers exist and the FDSN has set up a recommendation for channel naming that is used in the SEED format. The SEED component code consists of 3 letters: A frequency *band* code (the sensor-digitizer), an *instrument* code (the family to which the sensor belongs) and the third code is the *orientation* (usually Z, N or E). It is strongly recommend to use these codes with all formats, where it is possible, in order to standardize channel code names. The most common codes used are given below, for a complete list see the SEED manual (SEED, 2007) (Tables 3.3 and 3.4).

Examples:

SHZ corresponds to the traditional SZ and could be a 1 Hz sensor with 50 Hz sample rate. However if the sample rate is 100 Hz, the code is EHZ.

HHZ would be used for a broadband seismometer with a sample rate of 100 Hz.

Table 3.3 The most common band codes for channel naming. There is no corner period specified in the SEED manual for sample rates lower than 1 Hz, however it is assumed to be more than 10 s

Band code	Band type	Sample rate	Corner period (s)
E	Extremely short period	≥ 80 to < 250	< 10
S	Short period	≥ 10 to < 80	< 10
H	High broadband	≥ 80 to < 250	≥ 10
B	Broad band	≥ 10 to < 80	≥ 10
M	Mid period	> 1 to < 10	
L	Long period	≈ 1	
V	Very long period	≈ 1	
U	Very long period	≈ 0.01	

Table 3.4 The most common instrument and orientation codes used for channel naming

<i>Instrument code</i>	
H	High gain seismometer
L	Low gain seismometer
G	Gravimeter
M	Mass position seismometer
N	Accelerometer
<i>Orientation code</i>	
Z N E	Traditional (Vertical, north–south, east–west)
A B C	Triaxial (Along the edges of a cube turned up on a corner)
T R	For formed beams (Transverse, Radial)

ENZ would be used for an accelerometer with a sampling rate of 200 Hz. Here, the corner frequency criterion does not apply, but it can be assumed that the instrument does not record much beyond a period of 10 s.

In addition to the channel name, each channel also has a *location code*. This code is needed if more than one instrument of the same type or two different digitizers recording the same signal are used in parallel at one site. This is the case at a number of GSN stations where a very broadband sensor (360 s) and a broadband sensor (120 s) are operated at one site. The location code consists of 2 characters and usually the location codes used are the numbers 00 and onwards (there does not seem to be a definition given in SEED manual), with 00 normally being used if only one instrument is recording. Finally there is the possibility to record the same channel with 2 different networks so a 2 letter network code is also added to each channel. For example the IRIS/USGS network is called IU. Assignment of station codes and network codes is done by USGS or the ISC which jointly operate the global register of codes (<http://www.iris.edu/stations/networks.txt>). The channel codes are assigned by the user.

The combination of station, component, network and location code is known as the SCNL code. The SCNL code is the most complete identifier for a channel of seismic data and used by the larger data centers to access data. However, with an

Table 3.5 Comparing seismic formats and public domain processing systems. Abbreviations are: T: Has time error flag, C: Use SEED channel code, N: Use SEED network code, SH seismic handler, SE SEISAN, A: All platforms, W: Windows, U: Unix, Prog: Processing software. Note that SAC does not run under Windows directly since it must use the Unix simulation software Cygwin

Format	Platform	Com	Multi channel	Direct access	T	C	N	File size	Time gaps	Reading speed	Prog
SEED	All	Yes	Yes	Yes	Yes	Yes	Yes	No limit	Yes	Fast	SE:A
MiniSEED	All	Yes	Yes	Yes	Yes	Yes	Yes	No limit	Yes	Fast	SE:A
GSE	All	Yes	Yes	No	No	Yes	No	Limit.	No	Slow	SH:U
SAC	All	No	Yes	No	No	Yes	No	Limit.	No	Medium	SE:A
SEISAN	All	No	Yes	Yes	Yes	Yes	Yes	Limit.	No	Medium	SH:U

increase in the exchange of waveform data there is also a need to use the complete code in the data processing and for reporting of phases.

3.4.7 Format to Use

The format to use will partly depend on the processing system the user chooses and the format of the incoming data. However it seems that MiniSEED is fast becoming the standard to use for both processing and storage. Table 3.5 compares the capability of the common formats and lists some of the public domain processing system that can use the formats and on which platforms. From the table it is seen MiniSEED scores on all points and it is strongly recommended to use MiniSEED for both storage and processing.

3.5 Seismic Noise

All seismic traces contain noise, which can have two origins: Instrumental noise and “real” seismic noise from the ground. Normally the instrumental noise should be well below the seismic noise, but this might not be easy to see unless one is familiar with the characteristics of the noise at a particular station. However, in the following we will deal with what we characterize as seismic noise. Fig. 3.11 shows a noise record at a typical SP station.

It is seen that the unfiltered noise is dominated by 0.3 Hz waves, (typically generated from standing waves in the ocean) which is not so surprising considering

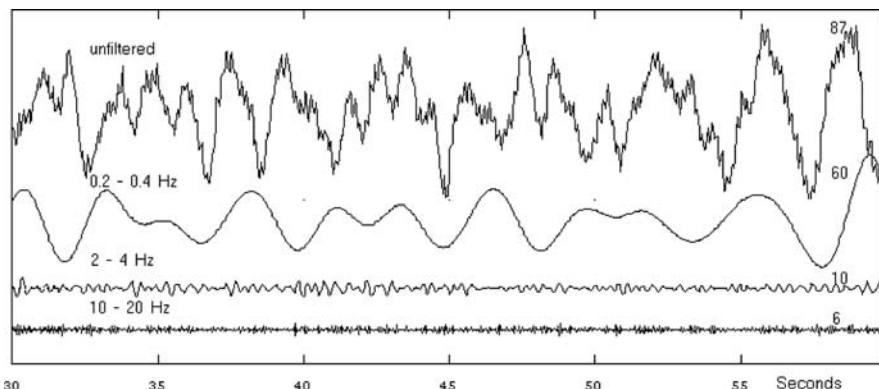


Fig. 3.11 Seismic noise in different filter bands at station MOL in the Norwegian National Seismic Network. The short period station (1 Hz) is situated about 40 km from the North Sea and the unfiltered trace clearly shows the high level of low frequency noise (~ 0.3 Hz) generated by the sea. All traces are plotted with the same scale and the numbers to the right above the traces are the maximum amplitude in count. Reproduced with kind permission of Springer Science and Business Media. Figure is from Havskov and Alguacil (2006), Fig. 3.1

the short distance to the ocean. Fig. 3.12 shows another 30 s time window from a broadband station in North America.

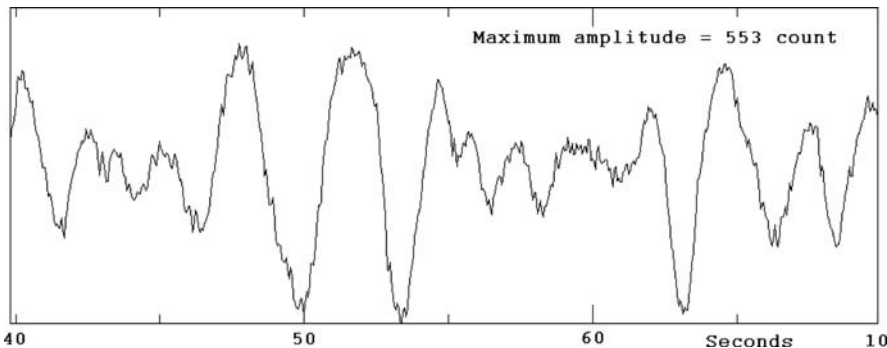


Fig. 3.12 Unfiltered signal from broad band station HRV, vertical component

It is seen that this seismogram also is dominated by 0.3 Hz waves, which actually is seen on all good stations in the world. So observing the 0.3 Hz seismic noise is an indication that the station is working correctly. So what is the real absolute noise level? Fig. 3.13 shows an example.

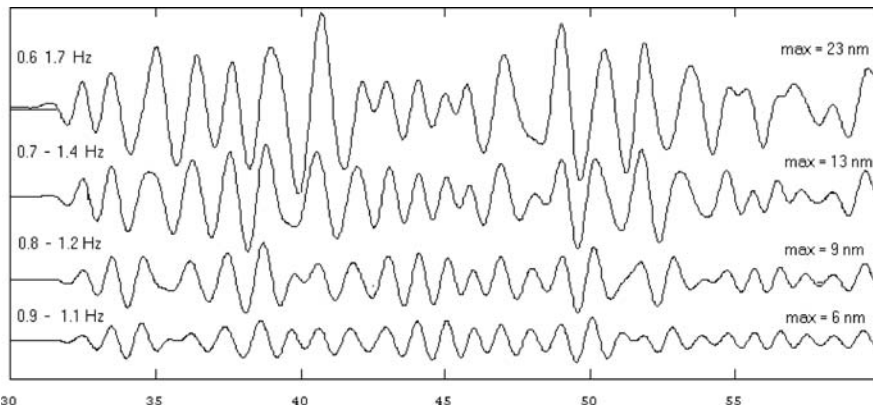


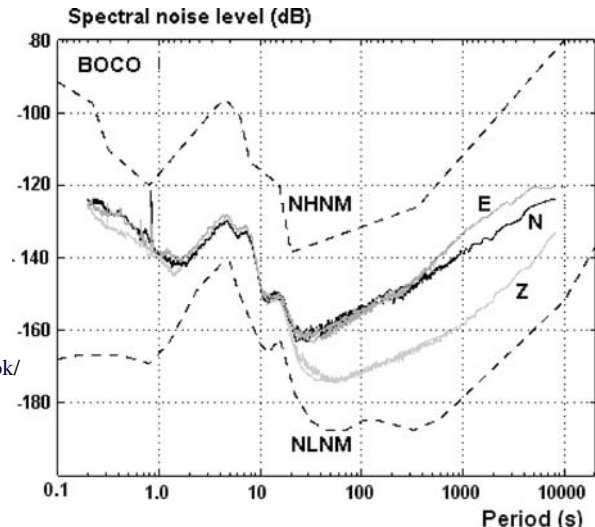
Fig. 3.13 The signal from Fig. 3.11 band pass filtered with different filter widths. The signals have been corrected for instrument response to show displacement. The maximum amplitude in nm is shown to the right on top of the traces. Reproduced with kind permission of Springer Science and Business Media. Figure from Havskov and Alguacil (2006), Fig. 3.2

Depending on filter width, we get noise amplitudes around 1 Hz between 6 and 12 nm and a good seismic station should have a noise level of 1 nm at 1 Hz. Measuring in another filter band would give a different noise level. In order to get the complete picture of the noise level at a station, independent of the filter used, the power spectrum of the noise is calculated. It has become the convention to represent the noise spectra as the noise power density acceleration spectrum $P_a(f)$, commonly in units of dB referred to 1 $(\text{m/s}^2)^2/\text{Hz}$. *Noise Level* is thus calculated as

$$\text{Noise Level} = 10 \log \left[P_a(f) / \left(m/s^2 \right)^2 / \text{Hz} \right] \quad (3.16)$$

Fig. 3.14 shows the new global high (NHNM) and low noise models (NLNM) (Peterson, 1993) and an example of noise spectra at a seismic station.

Fig. 3.14 The Peterson noise curves and noise spectral level for the IRIS station BOCO. The noise level is in dB relative to $1 (\text{ms}^{-2})^2/\text{Hz}$. The Peterson high and low noise models are shown with dashed lines. The noise spectra are shown for all 3 components. Note the lower noise level for the vertical (Z) component. Figure modified from IRIS station book, http://www.fdsn.org/station_book/ (note that x-axis represents decreasing frequency)



The NHNM and NLNM curves represent upper and lower bounds of a cumulative compilation of representative ground acceleration power spectral densities determined for noisy and quiet periods at 75 worldwide distributed digital stations. These so-called Peterson curves have become the standard by which the noise level at seismic stations is evaluated. Note that a power density spectrum can be defined in different ways and it is important that the definition used is identical to the one used originally by Peterson in order to compare the spectra, see Havskov and Alguacil (2006) for the exact definition.

Intuitively it is not easy to understand what the curve means physically (unlike Fig. 3.13). It is possible to convert from power spectral density to displacement provided the filter bandwidth is known and assumptions are made about the statistical noise distribution (Havskov and Alguacil, 2006). Assuming a one octave filter (like 5–10 Hz) and using the relationships given in Havskov and Alguacil (2006), an approximate relationship can be calculated between the noise power density $N(\text{dB})$ given in dB (Fig. 3.14) and the ground displacement d in m

$$d = \left(1/(38f^{1.5}) \right) 10^{N(\text{dB})/20} \quad (3.17)$$

or going the other way

$$N(\text{dB}) = 20 \log(d) + 30 \log(f) + 32 \quad (3.18)$$

where f is the average frequency of the filter. Looking at the example in Fig. 3.13, the one octave filter (0.7–1.4 Hz) gives a noise amplitude of 13×10^{-9} m which using (3.18), assuming $f = 1.0$ Hz, gives a spectral density level of -126 dB, which seems quite reasonable compared to Fig. 3.14.

The noise spectra for a particular station will change over the day (diurnal variation, at frequencies above 1 Hz) due to changes in cultural noise and weather and it will also change over the year (seasonal variation). The noise at low frequencies is typically higher on the horizontal components than on the vertical component due to the difficulty of stabilizing the station for small tilts.

In order to evaluate the seismic noise at a station it is necessary to record for a long enough time. If noise is measured to find a suitable site for a new station this is normally done for at least several days. If one is interested in the seasonal changes, one needs to use much longer time intervals. It is common practice to compute noise spectra from continuous data and to use the results to check the quality of the data. If noise is computed over a longer time, it is necessary to average the spectra from shorter time intervals with some overlap. It is also useful to look at the distribution of the noise levels as function of frequency, which can be done by computing probabilities of the observations. A method for this has been suggested by McNamara and Buland (2004) in which probability density functions (PDF) are computed from the power spectral density (PSD) data. This approach was implemented in the PQLX software (McNamara and Boaz, 2005) that is now widely used. A similar approach is implemented within SEISAN (Fig. 3.15). Noise curves and other quality control measures for GSN stations are found at <http://www.iris.edu/servlet/quackquery/>.

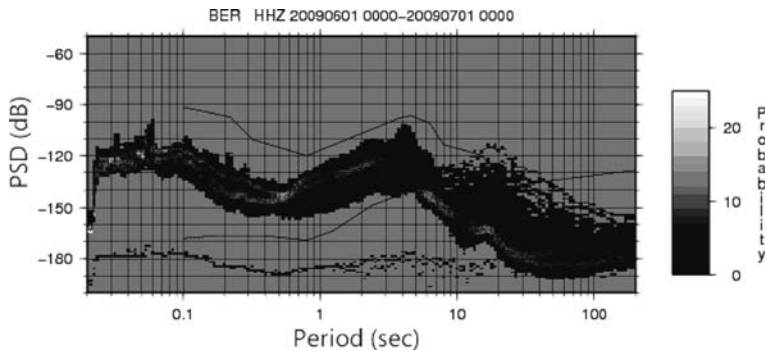


Fig. 3.15 Probability density function of seismic noise recorded on station BER from one month of data between 20090601 and 20090701

So what is the importance of seismic noise when processing earthquake data? For most seismic stations, the seismic noise remains stable over time so a noise spectrum indicates how the station is supposed to be operating. If some analysis results look strange and there is suspicion of instrument malfunction or errors in the response information, then calculating a noise spectrum and comparing it to the standard spectrum will immediately tell of any significant modifications in the system.

A second help in processing is to evaluate the quality of an unknown station. Fig. 3.16 shows some examples.

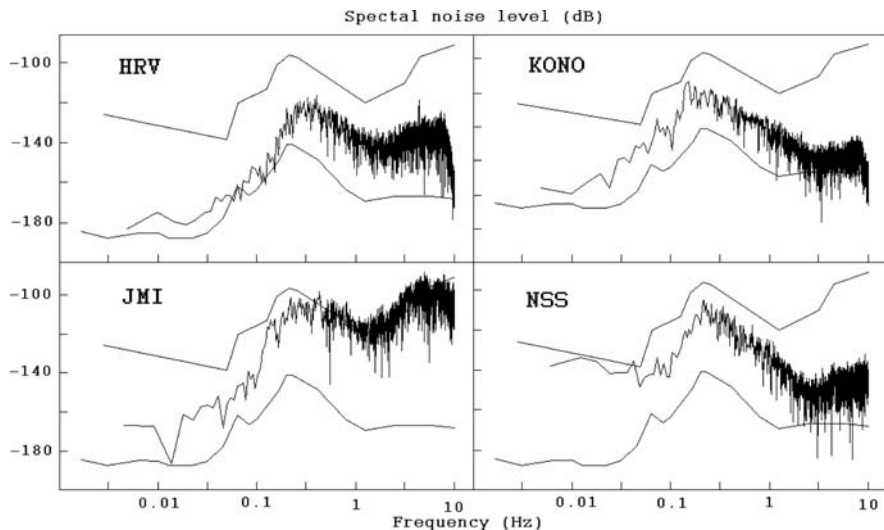


Fig. 3.16 Noise spectra (dB relative to $1 \text{ (ms}^{-2}\text{/Hz)}^2$) for 4 different stations. The time window is 120 s and the vertical components are used. Station NSS uses a 30 s broadband sensor while the rest have 120 s sensors

Station HRV (eastern USA) has a very small low frequency noise level and average high frequency noise. JMI is on the small volcanic island of Jan Mayen, so the high frequency level is very high while the low frequency level seems ok. KONO has a typical noise level for a Norwegian station and the other Norwegian station NSS should have had a similar noise level. However due to a more noisy sensor with 30 s period, the seismic noise is not resolved below 0.1 Hz. So just by looking at the noise spectra, we gain much information of the quality of the seismic station.

3.6 Exercises

Exercise 3.1 Calculate gain and noise

Given a seismic broadband station with the following characteristics:

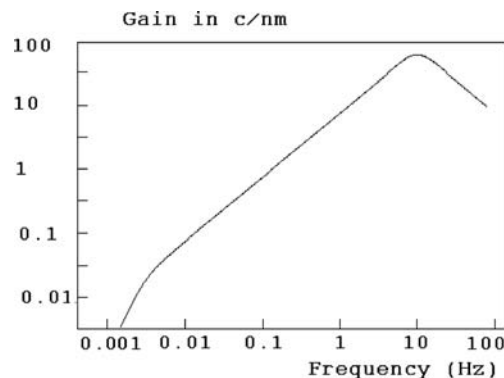
Seismometer free period:	60 s
Damping ratio:	0.7
Generator constant:	2000 V/m/s
Filter:	8 pole Butterworth filter at 10 Hz (see Fig. 3.8)
Digitizer gain:	100,000 count/V

- Calculate manually the system gain at Hz and at 10 Hz in terms of count/m, count/(m s⁻¹) and count/(m s⁻²).
- Calculate the noise level in m of the NLNM (Fig. 3.14) at 1 Hz and 0.2 Hz assuming a 1 octave filter using (3.17).
- Will this seismic station be able to detect signals at the NLNM level at 1 Hz and 0.2 Hz respectively under the assumption that the smallest signal that can be recorded is one count?

Exercise 3.2

Fig. 3.17 shows the displacement response curve for station HRV corresponding to the seismogram shown in Fig. 3.12. The response has been extracted from the SEED header.

Fig. 3.17 Response curve for station HRV. This is the vertical component from a broadband station



- What is the equivalent natural frequency of this sensor?
- Read the maximum amplitude and corresponding frequency from the seismogram in Fig. 3.12.
- Calculate the corresponding ground displacement using Fig. 3.17.
- Convert to noise amplitude (N-db) and compare to Fig. 3.16.
- If the sample rate is 50 Hz, what should the channel code be for the vertical channel?

Computer exercises

- Use response programs to calculate response functions, calculate both discrete values and poles and zeroes.
- Noise spectra, see Chapter 8 on spectral analysis.
- Test file conversion.

Chapter 4

Signal Processing

Earthquake data are today mostly digital which gives the analyst many options for viewing the data in different ways (filtering etc) and perform advanced signal processing tasks. The data itself often requires signal processing in order to do simple tasks like filtering when picking phases. In the analog world it was common to have high gain SP records and a low gain LP record (see Chapter 3), which can be considered recording the signal with 2 fixed filters. However, even a simple operation like filtering is not without problems since filtering can change the arrival time of a particular phase. One of the most used possibilities with digital data is being able to correct the data for the effect of the instrument and thereby being able to view the signals (time or frequency domain) as ground displacement, velocity or acceleration within the bandwidth where they have a signal level above the background noise (see Chapter 3). Many books have been written on general signal processing e.g. Oppenheim et al. (1998). In geophysics there is e.g. Kanasewich (1973). For digital seismology the most relevant is Scherbaum (2001) and Stein and Wysession (2003). Some examples are also found in NMSOP and Havskov and Alguacil (2006). In this chapter we will deal with the most common methods of signal processing except spectral analysis which is dealt with in Chapter 6.

4.1 Filtering

The most common signal processing operation is to filter the signals to enhance certain features and suppress others and numerous examples of filtered traces are seen throughout this book. A filter has the purpose of removing part of the signal in a particular frequency range and 3 types of filters are generally used:

- High pass filter (or low cut) at frequency f_1 : Removes signals below frequency f_1 .
- Low pass filter (or high cut) at frequency f_2 : Removes signals above frequency f_2 .
- Bandpass filter at frequencies f_1 to f_2 : Removes signals above f_2 and below f_1 .

The frequencies f_1 and f_2 are called corner frequencies of the filter and are defined as the point where the amplitude has decreased to 0.7 relative to the unfiltered part of the signal. The filters are shown schematically in Fig. 4.1.

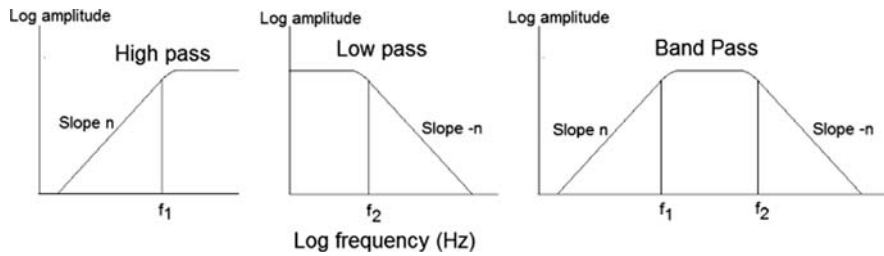


Fig. 4.1 Schematic representation of filters

In the log-log domain, filters are usually represented by straight line segments. The ratio of the output amplitude to the input amplitude, the gain, is often given in decibel (dB) defined as

$$dB = 20 \log (\text{gain}) \quad (4.1)$$

This means that the corner frequency is $20 \log (0.7) = -3$ relative to the flat part of the filter response (below the flat part). The sharpness of the filter is determined by the slope n , often given as the number of poles for the filter. In processing, n is usually between 1 and 8 and typically 4. The sharpness of the filter is sometimes also given as amplitude decay in dB/octave. One octave is a doubling of the frequency meaning, for a one pole filter, the amplitude is halved or reduced by 6 dB/octave whereas a 4 pole filter corresponds to 24 dB/octave.

There are many types of filters (Scherbaum, 2001), however in practical analysis, Butterworth filters are used almost exclusively since they have nice properties: No ringing (or ripples) in the pass band and the corner frequency remains constant for any order of the filter. The amplitude response of a low pass Butterworth filter is (e.g. Kanasewich, 1973)

$$B(\omega) = \frac{1}{\sqrt{1 + (\omega/\omega_0)^{2n}}} \quad (4.2)$$

It is seen from the equation and Fig. 3.8 that this filter has a very smooth response. Filters have, in addition to reducing the amplitude outside the pass band, also the effect of changing the phase which can have serious implications when reading arrival times of seismic phases. Seismic signals are usually filtered in the time domain by creating the filter coefficients corresponding to the filter specifications and passing the signal through the filter as shown in (3.5). Since the filtering starts in one end and works through the signal, energy will be moved backwards in the signal or in other words, there will be a phase shift (Fig. 4.2). Note that the initial onset is still seen with the same polarity as before filtering, however the onset is less

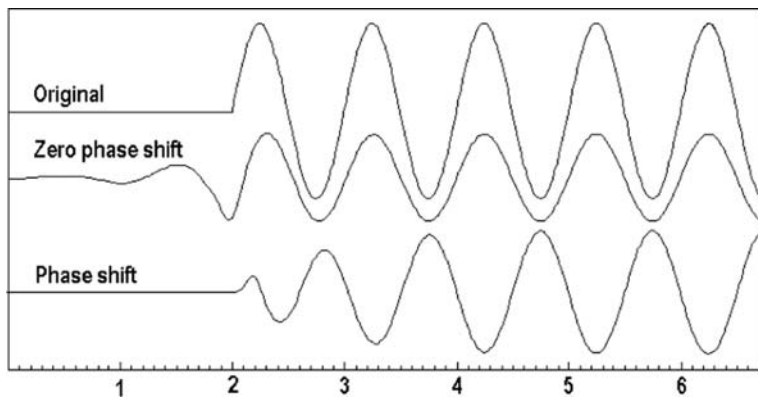


Fig. 4.2 The effect of using filters on a sharp onset. The signal is a 1 Hz sine wave with an onset at 2 s (*top* trace). The *middle* trace shows the signal filtered with a zero phase shift Butterworth filter while the *bottom* trace shows the signal filtered with a Butterworth filter with a phase shift. Both filters are band pass with corners 1 and 5 Hz. Reproduced with kind permission of Springer Science and Business Media. From Havskov and Alguacil, (2006), Fig. 6.12

clear and it is likely that it would have been read later on the filtered trace, especially in the case of a low signal to noise ratio.

The phase shift can be annulled by passing the filter backwards through the time series, however then energy might be moved to a point earlier than the initial onset and polarity and arrival time cannot be read with any confidence.

It is important to be aware of the filters that are applied as part of the digitization process. Most modern digitizers produce the data through resampling, and digital anti-alias filters are applied. The most common anti-alias filter is a linear phase finite impulse response filter (FIR). This type of filter is acausal, which means signal energy can be shifted backward in time resulting in precursory ringing see example in Fig. 4.3.

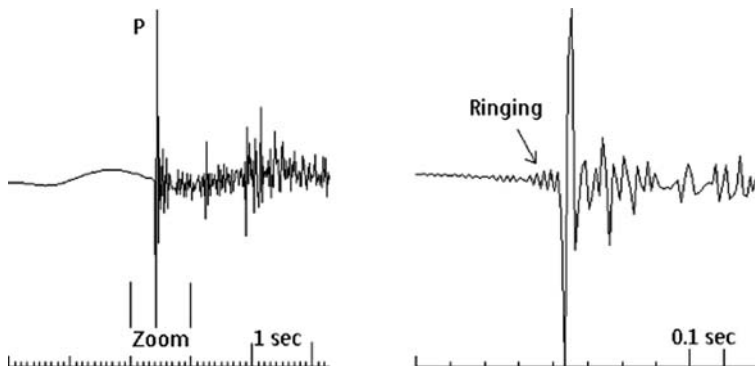


Fig. 4.3 The effect of precursory ringing from a digitizer. The *left* hand figure shows the signal in a low resolution and the *right* hand figure shows a zoom of the P. The data is from station MCH in the UK network and the component is HHZ. The origin time is 2005 0605 13:06 and the magnitude is $M_L = 0.7$

This example shows clear ringing for a digitizer. It is not clearly seen in the low resolution figure but clearly seen when zooming in. More details of this problem are given in Scherbaum (2001).

4.2 Spectral Analysis and Instrument Correction

The basis for many digital analysis techniques is using spectral methods: Instrument correction and simulation, source spectral analysis, surface wave analysis etc. The Fourier transformation allows us to move signals between the time and frequency domain, which makes it possible to choose either of them for a particular operation on the data. A brief overview of the theory will therefore be given. For a more complete overview, see e.g. Oppenheim et al. (1998).

The seismic signal x is defined as a function of time t as $x(t)$. The complex Fourier spectrum $X(\omega)$ is then given as

$$X(\omega) = \int_{-\infty}^{\infty} x(t)e^{-i\omega t} dt \quad (4.3)$$

where $\omega = 2\pi f$. Note that the unit of spectral amplitudes is amplitude times second or amplitude/Hz and consequently it is called the amplitude density spectrum. Since the energy has been distributed over an infinite number of cycles with different frequencies, it is not possible to talk about the amplitude at a particular frequency, but rather about the energy per cycle with unit of frequency. Similarly we can define the power density spectrum $P(\omega)$ as

$$P(\omega) = |X(\omega)|^2 \quad (4.4)$$

The power spectrum is real and an expression for the power in the signal. In seismology, it is mostly used for analyzing noise, see Chapter 3.

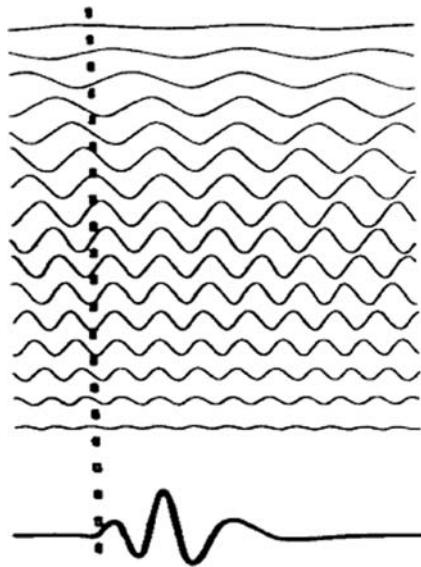
To illustrate the concept of Fourier transformation, Fig. 4.4 shows an example of a sum of harmonics that gives a short wavelet by constructive and destructive interference. Note that the individual signals are determined through their amplitude, frequency and phase.

The corresponding inverse Fourier transform is given by

$$x(t) = \frac{1}{2\pi} \int_{-\infty}^{\infty} X(\omega)e^{i\omega t} d\omega \quad (4.5)$$

The spectrum is complex and can be separated into the amplitude and phase spectra:

Fig. 4.4 Sum of harmonic functions (*top*) that become the wavelet seen at the *bottom*. The figure is from Lay and Wallace (1995), Fig. 5B1.2, copyright Elsevier



$$A(\omega) = \sqrt{Re(X(\omega))^2 + Im(X(\omega))^2} \quad (4.6)$$

$$\Phi(\omega) = \tan^{-1} \left(\frac{Im(X(\omega))}{Re(X(\omega))} \right) \quad (4.7)$$

where $A(\omega)$ is the amplitude spectrum and $\Phi(\omega)$ is the phase spectrum. Note that using a complex spectrum and positive and negative frequencies simplifies the calculations. It is possible to do the same spectral analysis by separately calculating amplitude and phase spectra without using negative frequencies, see e.g. Havskov and Alguacil (2006). Figure 4.5 shows an example of an amplitude spectrum.

This example shows the spectrum of a nearly monochromatic surface wave train where the maximum amplitude signal has a frequency close to 0.04 Hz. The monochromatic nature of the surface wave can also be seen on the seismogram. However, even for this very monochromatic signal, there is also energy in the signal at other frequencies, particularly at higher frequencies. The P-wave spectrum shows that the energy is spread out among a large frequency range corresponding to the more complex P-wave signal. Note that the spectra are not corrected for instrument response and the y-axis is linear, while normally, displacement spectra are show in a log-log diagram (see Chapter 8).

If $x(t)$ is the signal recorded by a seismograph, then $X(\omega)$ is not the true ground motion spectrum and to obtain the true ground motion spectrum $Y(\omega)$, $X(\omega)$ must be divided by the complex instrument response $T(\omega)$. The true ground motion spectrum can then be obtained as $X(\omega) / T(\omega)$. The ground motion amplitude and phase spectra are then obtained by using (4.6) and (4.7). In order to obtain the true ground

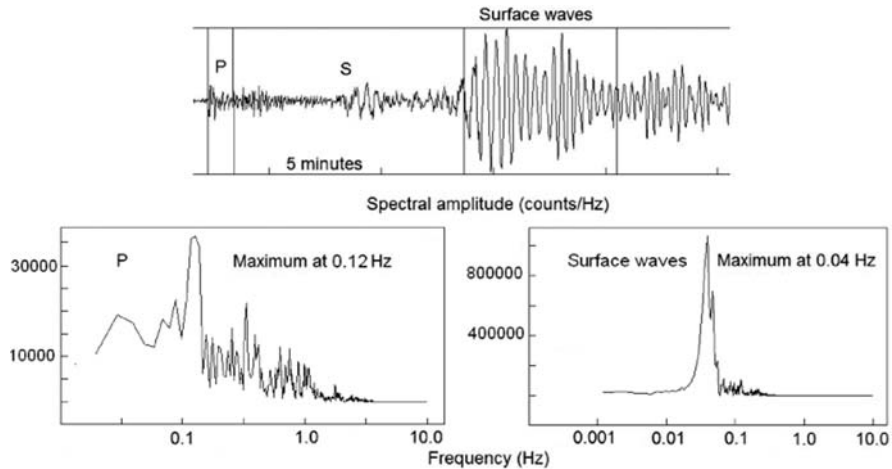


Fig. 4.5 Spectra of surface waves (bottom right) and P-waves (bottom left). The windows used for the spectra are indicated (top). The event ($m_b = 6.2$ (PDE)) is recorded with the Global Seismic Network, broadband station ERM, vertical channel. The origin time is 2007 1002 17:59

signal in time domain, the inverse Fourier transform is used and the corresponding instrument corrected signal is

$$y(t) = \frac{1}{2\pi} \int_{-\infty}^{\infty} X(\omega)/T(\omega) \cdot e^{i\omega t} d\omega \quad (4.8)$$

In magnitude determinations (Chapter 6), amplitudes are not read on true ground motion traces but on traces simulating some standard response like WWSSN SP and LP seismographs with an instrument response $I(\omega)$. The simulated seismogram $x_s(t)$ is then obtained as

$$x_s(t) = \frac{1}{2\pi} \int_{-\infty}^{\infty} (X(\omega)/T(\omega))I(\omega) \cdot e^{i\omega t} d\omega \quad (4.9)$$

In theory, we now have a procedure to recover the ground motion at any frequency knowing the instrument response, however care must be taken to do so only in the frequency band where real seismic signals are present, see the example in Fig. 3.10. Both the amplitude and phase components of the spectrum have to be used when correcting for the effects of instrumentation.

The Fourier and inverse Fourier transform allow us to move signals between the time and frequency domain. Operators on signals in one domain have an equivalent operator in the other domain. For example the multiplication in the frequency domain corresponds to the so-called convolution in the time domain. The convolution $c(t)$ of signals $x(t)$ and $y(t)$ in the time domain is defined as

$$c(t) = x(t) * y(t) = \int_{-\infty}^{\infty} x(\tau)y(t - \tau)d\tau \quad (4.10)$$

where $*$ signifies the convolution operator. The modification of ground signals due to the instrument has been described as an operation needing spectral analysis. However it can also be done directly in the time domain through convolution. The signal $x(t)$ recorded by a seismograph can then be described as the outcome from the convolution of ground motion $y(t)$ and instrument response $i(t)$

$$x(t) = y(t) * i(t) = \int_{-\infty}^{\infty} y(\tau)i(t - \tau)d\tau \quad (4.11)$$

So what is instrument response in the time domain? It turns out that it is simply the response of the instrument in time domain to an impulse so $i(t)$ can be obtained by recording the signal from the instrument due to an impulse (Fig. 4.6).

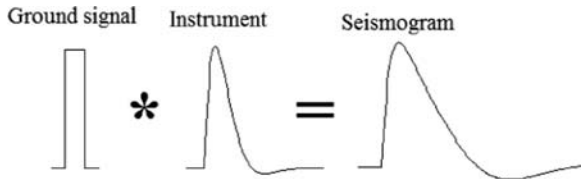


Fig. 4.6 The seismogram is obtained as a convolution of the input signal with the impulse response of the instrument. The impulse has no time duration and is infinitely high, but in the figure it is symbolized with a short pulse

Usually the need is to get the ground signal from the seismogram so the inverse of $i(t)$, $i^{-1}(t)$ has to be constructed as

$$y(t) = x(t) * i^{-1}(t) \quad (4.12)$$

This operation is called deconvolution. The inverse operator is not so easy to make. Fortunately the concept of Fourier transformation allows us to look at signals in both the time and frequency domain and we have seen that the de-convolution in time domain corresponds to a division in the frequency domain (4.8). Similarly a convolution in the time domain corresponds to a multiplication in the frequency domain and (4.10) becomes

$$C(\omega) = X(\omega) \cdot Y(\omega) \quad (4.13)$$

In practice, correction for instrument is mostly done in the frequency domain.

In real life we do not have an infinite continuous signal but a time series of N discrete values $x_k, k = 0, N - 1$ covering a time window T , and the continuous Fourier transform can be replaced by the discrete Fourier transform

$$X_n = \Delta t \sum_{k=0}^{N-1} x(k\Delta t) e^{-i\omega_n k \Delta t} = \Delta t \sum_{k=0}^{N-1} x_k e^{-i2\pi n k / N} \quad (4.14)$$

where Δt is the sample interval, $x_k = x(k\Delta t)$ and $\omega_n = 2\pi n / T$ ($f_n = n/T$). The frequencies sampled are therefore $f = 0, 1/T, 2/T, \dots$. The amplitudes are now given at a finite number of frequencies depending on the sample rate and window length. The first frequency is at $f = 0$ and seen from (4.14), $X_0 = T \cdot \text{average}(x)$ or an expression for the average signal level (DC level). The next frequencies are $1/T, 2/T, 3/T$ etc so no spectral information is available for periods longer than the length of the time window. If the signal contains frequencies higher than half the sampling frequency, aliasing will occur, see Fig. 4.7.

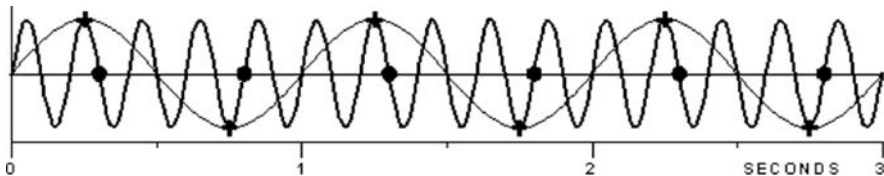


Fig. 4.7 A 5 Hz signal is digitized with a rate of 2 Hz. The digitization points are indicated with black dots. Depending on where the samples are taken in time, the output signal can either be interpreted as a straight line (points in middle) or a 1 Hz sine wave. Thus the highest frequency which should be used with a 2 Hz sample rate is 1 Hz. Reproduced with kind permission of Springer Science and Business Media. Figure from Havskov and Alguacil (2006), Fig. 4.10

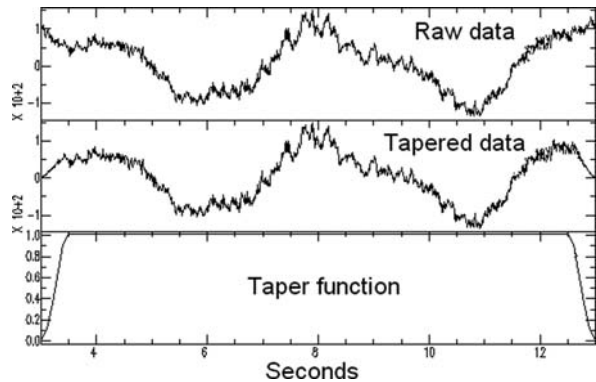
Due to aliasing, the highest frequency available is therefore $N/2T$. The spectral components corresponding to $k > N/2$ are where the negative frequencies spectral amplitudes are stored. The unit of the amplitude spectrum is still amplitude/Hz which can be seen from the factor Δt in (4.14). This is also a normalizing factor. If e.g. the sample rate doubles, then the spectral estimates X_k also double, but are then normalized to half the value as Δt is halved.

The inverse discrete Fourier transform can similarly to (4.14) be written

$$x_k = \frac{1}{T} \sum_{n=0}^{N-1} X_n e^{i2\pi n k / N} \quad (4.15)$$

This is how Fourier transformation is implemented in most computer programs. The implementation assumes that the signal repeats itself outside the window, so if e.g. at the start of the window $t = 0$, the signal is different from the signal at the end of the window $t = T$, an artificial step is introduced in the signal. This will contaminate the spectrum and the signal is usually tapered which means multiplying

Fig. 4.8 Example of a 10% cosine taper. On the *top* is seen the original signal, in the *middle* the tapered signal and on the *bottom* is seen the tapering function. The figure is generated with SAC (see end of this chapter)



the signal with a function to reduce the signal level to zero at each end of the signal. One of the most popular taper functions is the cosine taper (see Fig. 4.8) where a certain fraction of the signal (usually 5% at each end) is multiplied with a cosine function w

$$w_k = \frac{1}{2} \left(1 - \cos \frac{k\pi}{M+1} \right) \quad (4.16)$$

where $k = 0$ to $M+1$ and M (for a 10% taper) is 5% of the total number of samples. This function will taper the first part of the signal and a similar function is used for the end. It is seen that for $k = 0$, $x_k = 0$ and for $k = M+1$, $w_k = 1$.

Most programs will have different tapering functions. For more information on this problem, see e.g. Press et al. (1995).

4.3 Reading Seismic Phases

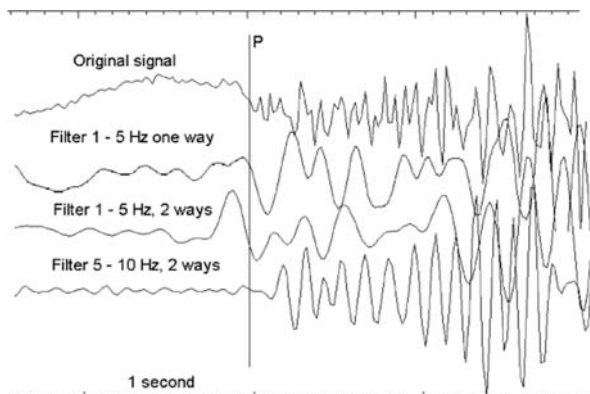
4.3.1 First Onset

The predominant phase read on seismograms is the first onset since it can be observed without doubt and usually also identified unambiguously as P, which also includes Pdif and PKP. In case of a noisy record, later arriving phases (like PP) might appear to arrive first, particularly at distances where Pdif is the theoretical first arrival (see Chapter 2). In most cases, there is no doubt where the first onset (whatever phase it is) is observed, however a first onset might have a bad signal to noise ratio, be very emergent or completely hidden in the noise so let us look at some of these “difficult” examples.

4.3.2 Filtering and Phase Shift

Figure 4.9 shows a small local event recorded on a broadband station.

Fig. 4.9 Effect of using filters for picking a P-phase. The station is ANER in Southern Spain, Z-component of a broadband sensor. The event has an epicentral distance of 60 km, depth of 10 km, magnitude $M_c = 2.5$. Origin time is 2006 01 08 15:08



Since this local event is recorded on a broadband station with a small signal, filtering may be required. Since it is a small event, a relatively high frequency filter is used. By using a 1–5 Hz filter one way, the first arrival is clearly seen at about the same position as the original P on the unfiltered trace. Passing the filter both ways would push the P-observation too early. Using a 5–10 Hz filter both ways result in a too late identification of P so apparently the first P has a relatively low frequency for an event of this magnitude, see Chapter 8. Ideally, all stations should be read with the same instrument response and filter to avoid difference in phase shift between stations.

Figure 4.10 shows a small regional event on a broadband station.

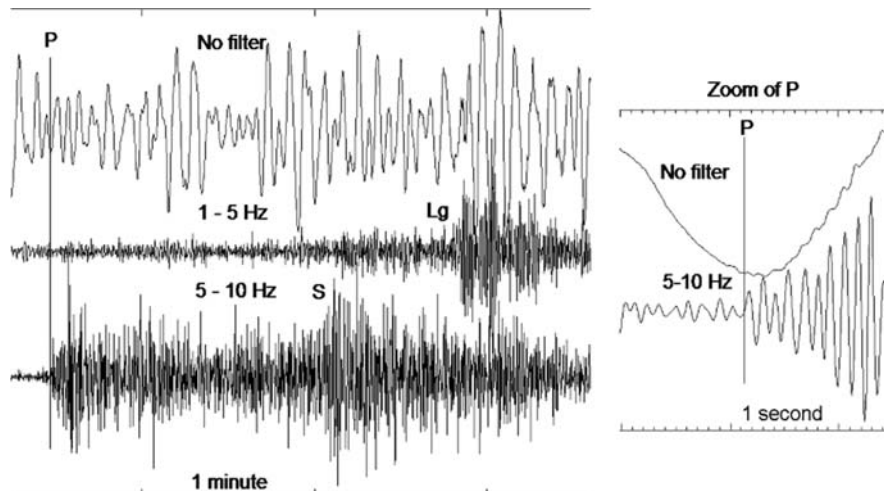


Fig. 4.10 Effect of filtering of weak signals. *Left:* The signal using different filters. *Right:* Zoom of P – phase. The event is from the Greenland seismic network, broadband station NRS, vertical component. The magnitude is $M_L = 3.2$, epicentral distance 970 km and origin time 2005 0102 10:24. The filters used are 4 pole Butterworth filters passed forward, thus one way only

On the original signal, the event is not seen since it is masked by the microseismic noise. The 1–5 Hz filter barely indicates the presence of P and S while the Lg is clearly seen due to its frequency content near 1 Hz. The 5 – 10 Hz signal clearly shows both P and S while even on the zoomed unfiltered trace, P cannot be seen clearly. The uncertainty in reading P is probably less than 0.2 s. So in this case phases cannot be read unless filtering is done.

4.3.3 Plotting Resolution

When looking for seismic phases in a record, it is important that the plotting is done with sufficient resolution on the screen, otherwise the phase onset might not be detected, see example in Fig. 4.11.

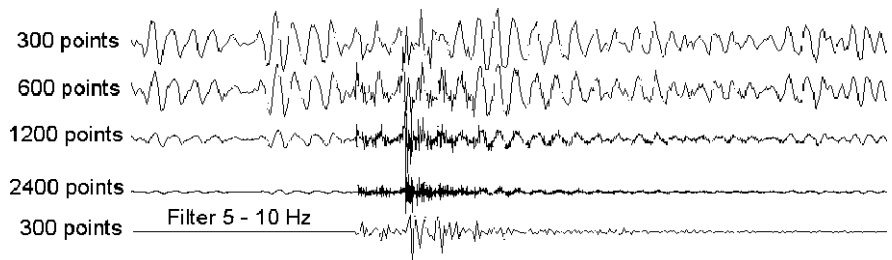


Fig. 4.11 Plotting aliasing. The traces have been plotted with different resolution in terms of number of points plotted across the screen

The example shows that if too few points are plotted, only the low frequency signals are seen and the event might be missed and we can consider that an effect of plotting aliasing. By eliminating the low frequencies by filtering, the signal would have been seen, but appears too low frequency due to few sample points. By zooming, the signal would have been seen since more points are used to plot the signal.

Summary

- Read arrival times on unfiltered traces if possible. Filters can be used to initially find the phase, then zoom in and read on unfiltered trace.
- To read the phases of small earthquakes using broadband data, filtering is often needed.
- High frequency energy ($f > 5\text{--}10 \text{ Hz}$) can often travel far regional distances so a high frequency filter should be used to identify short period body-wave phases.
- Only causal filters (passing forward) should be used. Be aware that a few digitizers might produce precursory signals.
- Only read polarity on unfiltered traces.

- When inspecting large time intervals manually for events, make sure enough plotting points are used or use an appropriate filter.

4.4 Correlation

A common problem in seismology is to investigate the similarity of two signals. An example is seeing a phase on one station and wanting to find the same phase on another station. To do this we identify the part of the signal we want to identify as $y(t)$ and the signal we want to investigate for this signal as $x(t)$. A measure of the similarity of the two signals is obtained by computing the so-called cross correlation function between two signals $x(t)$ and $y(t)$ as

$$\phi_{xy}(\tau) = x(t) \circ y(t) = \int_{-\infty}^{\infty} x(t)y(t + \tau)dt \quad (4.17)$$

where “ \circ ” symbolizes the correlation operator. Convolutions and cross correlations are similar operations and the only difference is the sign of the time shift. The correlation of a signal with itself is the auto-correlation. Often the cross correlation function is normalized by the auto-correlation functions

$$\phi_{xy}^N(\tau) = \frac{\int_{-\infty}^{\infty} x(t)y(t + \tau)dt}{\sqrt{\phi_{xx}(\tau)\phi_{yy}(\tau)}} \quad (4.18)$$

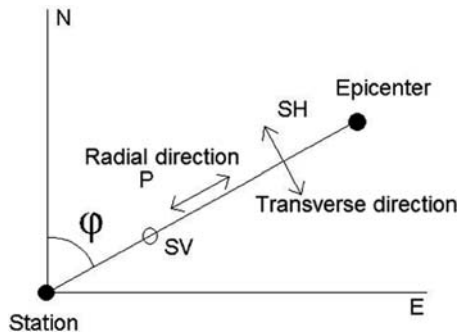
The maximum amplitude of the cross-correlation function can be used to determine the relative time for which the two signals are most similar. In practice this can be used to very accurately determine relative arrival times of e.g. P-waves for one earthquake. This can be useful when the P (or other phases) is very clear on one trace and partly disappears in the noise on other traces. Some programs (like Seismic Handler) have a built in tool where a signal segment from one trace can be selected and then used to automatically read the same phase on other traces. This is most useful for teleseismic P-phases, which often are similar over a regional network.

Another common use is to determine relative arrival times for the same station for different similar earthquakes with the purpose of doing very accurate relative locations, see Fig. 5.12.

4.5 Particle Motion and Component Rotation

Different kinds of seismic waves have their particle motion (or amplitude) in different directions (Fig. 4.12). Analysis of the particle motion can thus be used to identify the different wave types. Particle motion or polarization of the waves is

Fig. 4.12 Definition of the radial and transverse directions



best looked at in a coordinate system that points from the earthquake to the seismic station. Through a simple rotation we can change the two horizontal components into the radial (R) and transverse (T) components. The radial direction is along the line from the station to the event and the transverse direction is in the horizontal plane at a right angle to the radial direction. For example, the P wave is polarized in the direction from source to receiver, and particle motion is in the vertical-radial plane. The wave motions of the different kinds of waves are:

- P-waves: Linear in radial and vertical plane.
- SH waves: Linear in the transverse direction.
- SV waves: Linear in the radial and vertical plane.
- Rayleigh waves: Elliptical in the radial and vertical plane.
- Love waves: Linear in the transverse direction.

The rotation is computed using

$$\text{Radial} = -NS \cos(\varphi) - EW \sin(\varphi) \quad (4.19)$$

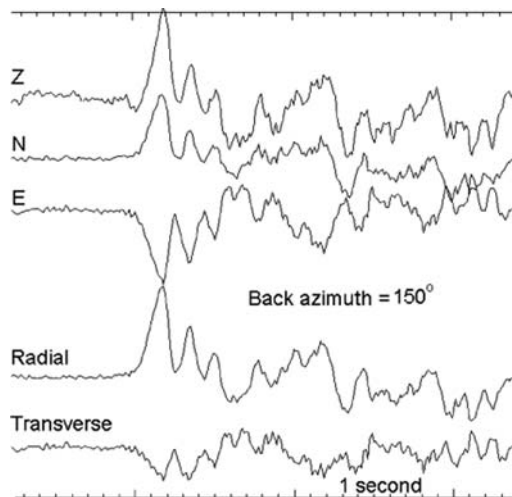
$$\text{Transverse} = NS \cdot \sin(\varphi) - EW \cdot \cos(\varphi) \quad (4.20)$$

where φ is the back azimuth angle defined as the angle between the north and the radial direction towards the source (Fig. 4.12) and *Radial*, *Transverse*, *EW* and *NS* are the amplitudes in the respective directions. Using an angle of 90° , it is seen that *Radial* = $-EW$ and *Transverse* = *NS*. This means that when the observer faces the station from the event, the radial motion is positive towards the station and the motion to the right is positive on the T-component. The component rotation can be carried one step further by rotating the R and Z-components into the direction of the incident seismic ray (the Q-component) using the angle of incidence at the surface. This is usually not done in routine operation, partly due to the uncertainty in obtaining a correct angle of incidence which depends on the wavelength, see NMSOP.

While we can look at the amplitudes on three component rotated seismograms oriented in R and T directions, an alternative way to visualize the particle motion is by producing particle motion plots. These can be either two dimensional plots (which we show here in Fig. 4.14) where the amplitude of one component is plotted against the amplitude of the other or three dimensional plots showing all components at the same time. For the identification of wave types plotting transverse component against radial component is the most useful approach.

While in theory analyzing particle motion (either by rotating seismograms or making particle motion plots) sounds attractive, the real world is more complicated. In practice, the effect is often less clear due to lateral inhomogeneities which have the effect that the rays do not always arrive with the same back azimuth as indicated by the P or the event location. A simple test is to observe how it works on the P-phase on a rotated seismogram (Fig. 4.13).

Fig. 4.13 Rotation of the P-phase of a local earthquake. The event is recorded with the Mexican seismic network, broadband station CAIG, epicentral distance 194 km, depth 15 km, $M_L = 4.5$, origin time 1995 1219 22:04. The scale on all traces is the same



In theory the P-phase should only be seen on the radial component. As it is seen on the figure, this is not quite the case although the radial component has a significantly larger P-amplitude than the transverse component. We observe the same when looking at the horizontal component particle motion plot where there is some scattering around a radially polarized P wave (Fig. 4.14). While identification of P and S is obvious in most cases, particle motion plots can help to confirm that what is seen is indeed P or S.

Particle motion plots can be used to determine the back azimuth from a P wave particle motion plot of NS and EW components. This is an alternative to use the amplitudes of NS and EW components as shown in Chapter 5. Figure 4.14 shows an example. The figure shows clearly how the P-motion in the horizontal plane is in the NW-SE direction, however, from this plot, it cannot be seen if the earthquake is in the NW or SE direction.

Particle motion plots can be useful to distinguish teleseismic phases with different polarization. Figure 4.15 shows an example of the different polarization between

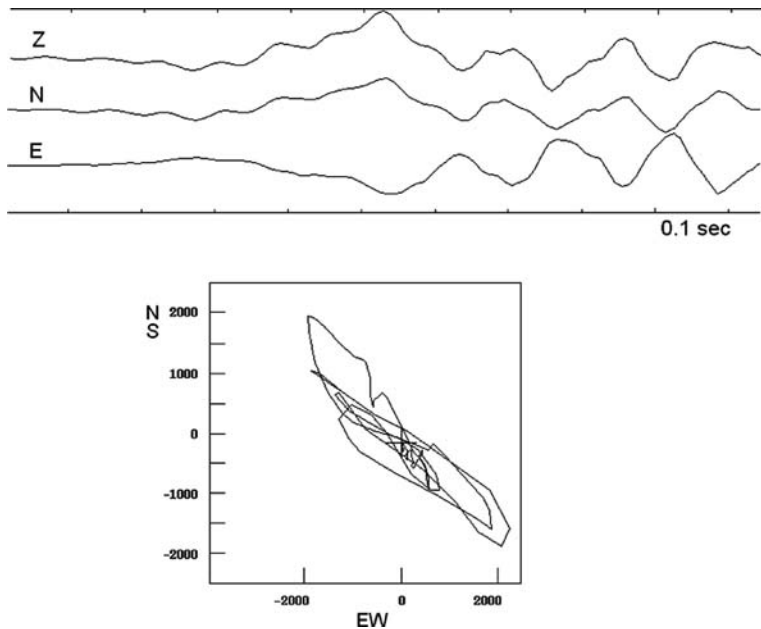


Fig. 4.14 Horizontal component particle motion plot for the P wave of an earthquake in the south-east of England. The top figure shows the window around P-phases used for the particle motion plot (bottom). The event is recorded with the UK seismic network, broadband station CWF, epicentral distance 249 km, depth 5 km, $M_L = 4.3$, origin time 2007 0428 07:18. The back azimuth is 318°

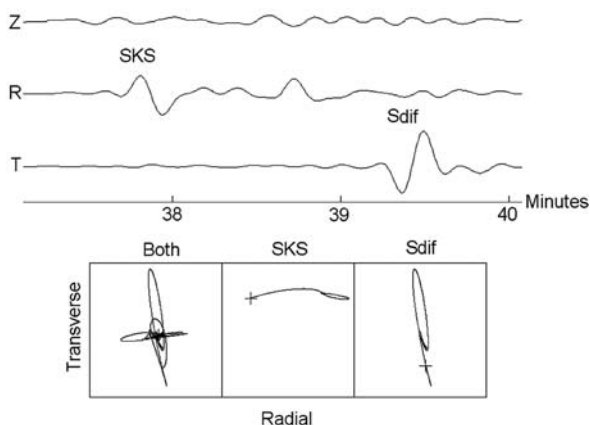
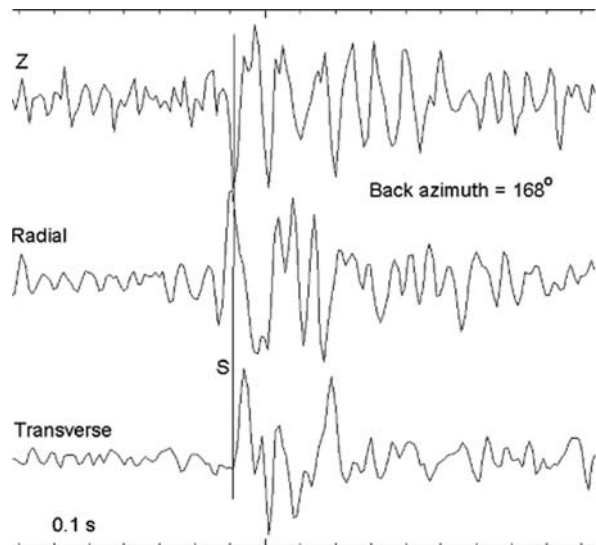


Fig. 4.15 Example of particle motion plot for an earthquake in Ecuador, origin time is 2007 1116 03:13. The earthquake is recorded on a GSN broadband station in Uganda. The horizontal components are rotated into radial and transverse components (R and T respectively). The scaling is the same on all 3 traces and they are filtered in the band 0.01–0.1 Hz. The bottom plot shows the particle motion of transverse versus radial component in different windows where “Both” indicates that the whole trace above has been used

SKS and Sdif. In this example, the difference in polarization between SKS with particle motion in the vertical-radial plane and Sdif with particle motion in transverse direction is clearly seen in both the seismograms and the particle motion plots.

By separating the SH and SV waves, the effect of anisotropy can also be observed (Fig. 4.16). Notice that the SH waves on the transverse component arrives later than the SV wave on the radial component indicating a lower SH velocity than SV velocity (S-wave splitting). This is an indication of anisotropy, which means different velocity in different directions. The effect of anisotropy can also be studied using particle motion diagrams (see section above).

Fig. 4.16 Component rotation of a local earthquake. It is observed that SH on the transverse component arrives later than SV on the vertical and radial components. The event is recorded with the Norwegian National Seismic Network, short period station STOK1, epicentral distance 18 km, depth 4 km, $M_L = 1.6$, origin time 2005 0731 15:44



4.6 Resampling

Resampling is the procedure in which the sampling rate gets changed. The sampling rate can be both decreased and increased. The sampling rate increase requires an interpolation between data points and is not much used in routine operation. We, therefore, deal with the reduction in sampling rate only.

The main reason for decreasing the sampling rate is to reduce the data volume to what is required for a given analysis task. If speed and memory were no issue, there would be no need to resample except where programs require all channels to have the same sample rate. Typical sampling rates used for the GSN are 80 sps for local data and 20 sps for regional and teleseismic data. When working with surface waves, a sampling rate of 1 sps is sufficient. Global data centers typically provide various sampling rates, but local networks store their data with the original sampling rate and resampling may be required.

Resampling consists of two steps, first the data is low-pass filtered to avoid aliasing. This low-pass filtering is done with digital FIR filters that drop off sharply

below the Nyquist frequency (see Chapter 3). The second step is the actual resampling, reducing the sampling rate by an integer number, but can also be done by any factor which might require interpolation between samples.

4.7 Software

The following gives some the independent phase picking and data processing programs. Many other programs have been developed at individual observatories but they are generally not available or are not general enough for users at other observatories. Thus there are surprisingly few generally used free standing public domain programs available. For complete systems which include plotting software, see Chapter 10.

SAC: SAC is probably the most popular free standing display program, however it is also a system of programs and has therefore been described in Chapter 10.

PITSA: PITSA – in its current version written by Frank Scherbaum, Jim Johnson and Andreas Rietbrock – is a program for interactive analysis of seismological data. It contains numerous tools for digital signal processing and routine analysis. PITSA is currently supported on SunOS, Solaris and Linux and uses the X11 windowing system. PITSA is not just for plotting traces, but has been used for that purpose. It is also the main plotting tool in GIANT. See http://www.geo.uni-potsdam.de/arbeitsgruppen/Geophysik_Seismologie/software/pitsa.html

SeisGram2K Seismogram Viewer: SeisGram2K Seismogram Viewer is a platform-independent Java software package for interactive visualization and analysis of earthquake seismograms. SeisGram2K runs and reads data files locally and over the Internet. The software is developed by Anthony Lomax (<http://alomax.free.fr/seisgram/SeisGram2K.html>). The program supports several standard waveform file formats like MiniSEED and SAC.

PQL II: PQL II is a program for viewing time-series data and reading phases in any of four formats: MSEED, SEGY, SAC, or AH. The program operates on MAC OS X, Linux, and Solaris platforms. The program has many options for trace manipulation and filtering. See <http://www.passcal.nmt.edu/content/pql-ii-program-viewing-data>.

4.8 Exercises

Since signal processing means processing digital data, so there are no manual exercises.

Computer exercises

- Reading seismic phases with and without filter.
- Component rotation.

Chapter 5

Location

Earthquake location is one of the most important tasks in practical seismology and most seismologists have been involved in this task from time to time. The intention with this chapter is to describe the most common methods without going into too much mathematical details, which has been described in numerous text books, and to give some practical advice on earthquake location.

The earthquake location is defined by the earthquake hypocenter (x_0, y_0, z_0) and the origin time t_0 . The hypocenter is the physical location, usually longitude (x_0), latitude (y_0) and depth below the surface (z_0). The epicenter is the projection of the earthquake location on the earth's surface (x_0, y_0) . For simplicity, the hypocenter will be labeled x_0, y_0, z_0 with the understanding that it can be either geographical latitude (deg), longitude (deg) and depth (km) or Cartesian coordinates. The epicentral distance Δ is the distance from the epicenter to the station (x, y, z) along the surface of the earth. For a local earthquake where a flat earth is assumed, it is simply calculated as

$$\Delta = \sqrt{(x - x_0)^2 + (y - y_0)^2} \quad (5.1)$$

and, it is usually given in km. For a spherical earth, the epicentral distance in degrees is calculated along a great circle path and it can be shown to be (e.g. Stein and Wysession, 2003)

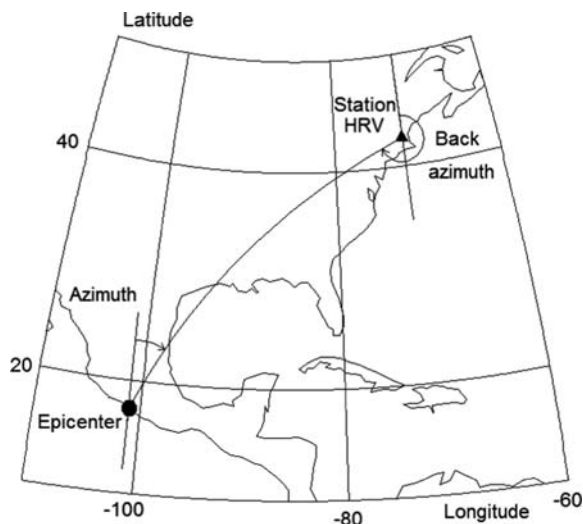
$$\Delta = \cos^{-1}(\sin(\theta_0) \sin(\theta) + \cos(\theta_0) \cos(\theta) \cos(\lambda - \lambda_0)) \quad (5.2)$$

where θ_0 and θ are the latitude of the epicenter and station respectively and λ_0 and λ are the corresponding longitudes. For local earthquakes, the hypocentral distance is also used and calculated as

$$\Delta = \sqrt{(x - x_0)^2 + (y - y_0)^2 + (z - z_0)^2} \quad (5.3)$$

while for distant earthquakes, the term hypocentral distance is not used. The equivalent distance would be the distance along the raypath (see e.g. Fig. 2.8). In connection with earthquake location we also use the terms azimuth and back azimuth (Fig. 5.1).

Fig. 5.1 Definition of the terms azimuth and back azimuth. Here, the azimuth is 39° and the back azimuth is 234°



The azimuth is calculated using the epicenter and the station location. The back azimuth can be calculated, but it can also be observed on three component stations (see next section) and arrays (see Chapter 9). Azimuth is the angle at the epicenter between the direction to the north and the direction to the station measured clockwise. The back azimuth is the angle at the station between the direction to the north and the direction to the epicenter measured clockwise. For local earthquakes (flat earth assumed), back azimuth and azimuth are 180° apart, while for global distances, this is not the case (Fig. 5.1) and the angles must be measured on a spherical triangle.

In addition to calculating on a spherical earth, the effect of ellipticity must be taken into account (see e.g. Stein and Wysession, 2003). This is usually built into most global location programs so travel times are automatically corrected for ellipticity.

Finally, seismic stations are in general not at sea level while epicentral distances and corresponding travel times are calculated on the sea level surface. So the effect of the station elevation on the travel time is calculated and added to the travel time.

The origin time is the time of occurrence of the earthquake (start of rupture). The physical dimension of a fault can be several hundred kilometers for large earthquakes and the hypocenter can in principle be located anywhere on the rupture surface. Since the hypocenter and origin time are determined by arrival times of seismic phases initiated by the first rupture, the computed hypocenter will correspond to the point where the rupture initiated and the origin time to the time of the initial rupture. This is also true using any P or S-phases since the rupture velocity is smaller than the S-wave velocity so that P or S-wave energy emitted from the end of a long rupture will always arrive later than energy radiated from the beginning of

the rupture (see 7.41). Standard earthquake catalogs (such as from the International Seismological Center, ISC) report location based primarily on arrival times of high frequency P-waves. This location can be quite different from the centroid origin time and location obtained by moment tensor inversion of long period waves (see Chapter 7). The centroid location represents the average time and location for the entire event.

Most of the theory for this chapter was originally written by Havskov for the European Seismological Commission meeting young seismologist training course in Lisbon in 2001. It was later slightly modified by Havskov et al. (2002) and incorporated in an Information sheet 11.1 in NMSOP, where the original text is found. It is further modified for this text.

For a good general overview of earthquake location methods, see Thurber and Engdahl (2000).

5.1 Single Station Location

In general, epicenters are determined using many arrival times from different seismic stations and phases. However, it is also possible to locate an earthquake using a single 3-component station. Since the P-waves are vertically and radially polarized, the vector of P-wave amplitude can be used to calculate the back azimuth to the epicenter (see Fig. 5.2). The radial component of P will be recorded on the 2 horizontal seismometers north and south and the ratio of the amplitudes A_E/A_N on the horizontal components can be used to calculate the back azimuth of arrival ϕ

$$\phi = \tan^{-1} A_E/A_N \quad (5.4)$$

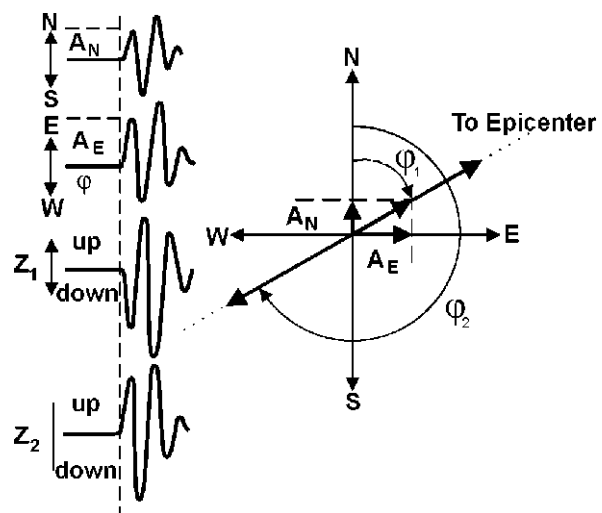


Fig. 5.2 Example of P-wave first motions in 3-component records (left) from which the back azimuth ϕ can be derived. ϕ_1 corresponds to, in this example, a first motion down (Z_1) on the vertical channel and ϕ_2 to a first motion up (Z_2). Copyright granted by IASPEI. Figure from NMSOP, IS 11.1

There is an ambiguity of 180° , but the first polarity can be up or down so the polarity must also be used in order to get the correct back azimuth. If the first motion on the vertical component of the P is upward, then the radial component of P is directed away from the hypocenter. The opposite is true if the P-polarity is negative, see Table 5.1.

Table 5.1 Combination of polarities and cases where 180° has to be added to the calculation according to (5.4)

Z	+	-	+	-	+	-	+	-
N	+	+	-	-	-	-	+	+
E	+	+	+	+	-	-	-	-
Add	180	0	0	180	0	180	180	0

The amplitude A_Z of the Z-component can, together with the amplitude $A_R = \sqrt{(A_E^2 + A_N^2)}$ on the radial components, also be used to calculate the *apparent angle of incidence* $i_{app} = \tan^{-1} A_R/A_Z$ of a P-wave. However, according already to Wiechert (1907) the true incidence angle i_{true} of a P-wave is

$$i_{true} = \sin^{-1} \left(\frac{v_p \sin(0.5i_{app})}{v_s} \right) \quad (5.5)$$

with the difference accounting for the amplitude distortion due to the reflection at the free surface. Knowing the incidence angle i and the local seismic P-velocity v_p below the observing station, we can calculate the apparent velocity v_{app} (see Chapter 2) of this seismic phase with

$$v_{app} = \frac{v_p}{\sin(i_{true})} \quad (5.6)$$

With high frequency data it might be difficult to manually read the amplitudes of the original break or sometimes the first P-swings are emergent. Since the amplitude ratio between the components should remain constant, not only for the first swing of the P-phase, but also for the following oscillations of the same phase, we can, with digital data, use the method of cross correlation between channels (see Chapter 4) (Roberts et al., 1989) to automatically calculate back azimuth as well as the angle of incidence. Since this is much more reliable and faster than using the manually readings of the first amplitudes, calculation of back azimuth from 3-component records of single stations has again become a routine practice (e.g., Saari, 1991). In case of seismic arrays, apparent velocity and back azimuth can be directly measured by observing the propagation of the seismic wavefront with array methods (see Chapter 9). As we shall see later, back azimuth observations are useful in restricting epicenter locations and in associating observations to a seismic event. Knowing the

incidence angle and implicitly the ray parameter of an onset helps to identify the seismic phase and to calculate the epicentral distance.

With a single station we have now the direction to the seismic source. The distance can be obtained from the difference in arrival time of two phases, usually P and S. If we assume a constant velocity, and origin time t_0 , the P and S-arrival times can then be written as

$$t_p^{arr} = t_0 + \Delta/v_p \quad t_s^{arr} = t_0 + \Delta/v_s \quad (5.7)$$

where t_p^{arr} and t_s^{arr} are the P and S-arrival times (s) respectively, v_p and v_s are the P and S-velocities respectively and Δ is the epicentral distance (km). If the event is not at the surface, Δ should be replaced by hypocentral distance. By eliminating t_0 from (5.7), the distance can be calculated as

$$\Delta = (t_p^{arr} - t_s^{arr}) \frac{v_p v_s}{v_p - v_s} \quad (5.8)$$

But (5.8) is applicable only for the travel-time difference between Sg and Pg, i.e., the direct crustal phases of S and P, respectively (see Chapter 2). They are first onsets of the P- and S-wave groups of local events only for distances up to about 100–250 km, depending on crustal thickness and source depth. Beyond these distances the Pn and Sn, either head waves critically refracted at the Mohorovičić discontinuity or waves diving as body waves in the uppermost part of the upper mantle, become the first onsets. At smaller distances we can be rather sure that the observed first arrival is Pg. The distance at which Pn comes before Pg depends on the depth of the Moho as well as the hypocentral depth, see Chapter 2.

In the absence of local travel-time curves for the area under consideration one can use (5.8) for deriving a “rule of thumb” for approximate distance determinations from travel-time differences Sg-Pg. For an ideal Poisson solid $v_s = v_p/\sqrt{3}$. This is a good approximation for the average conditions in the earth’s crust. With this follows from (5.8)

$$\text{Normal crust, } v_p = 5.9 \text{ km/s} \quad \Delta(\text{km}) = (t_{Sg} - t_{Pg}) \times 8.0 \quad (5.9)$$

$$\text{old crust, } v_p = 6.6 \text{ km/s} \quad \Delta(\text{km}) = (t_{Sg} - t_{Pg}) \times 9.0 \quad (5.10)$$

However, if known, the locally correct v_p/v_s ratio should be used to improve this “rule of thumb”. If the distance is calculated from the travel-time difference between Sn and Pn another good rule of thumb is

$$\text{Pn and Sn} \quad \Delta(\text{km}) = (t_{Sn} - t_{Pn}) \times 10 \quad (5.11)$$

It may be applicable up to about 1,000 km distance. For distances between about $20^\circ < \Delta < 100^\circ$ the relationship

$$\text{Teleseismic distance} \quad \Delta(^{\circ}) = \{(t_s - t_p)_{\min} - 2\} \times 10 \quad (5.12)$$

still yields reasonably good results with errors $< 3^\circ$. The arrival times are in minutes. However, beyond $\Delta = 10^\circ$ the use of readily available global travel-time tables such as IASP91 (Kennett and Engdahl, 1991; Kennett, 1991), SP6 (Morelli and Dziewonski, 1993), or AK135 (Kennett et al., 1995) is strongly recommended for calculating the distance.

With both azimuth and distance, the epicenter can be obtained by measuring the distance along the azimuth of approach. Finally, knowing the distance, we can calculate the P-travel time and thereby get the origin time using the P-arrival time.

Figure 5.3 shows an example. The seismogram has amplitudes of 7, -4 and 10 mm on Z, N and E components, respectively. Using (5.4) gives $\phi = \arctan(10/-4) = -68^\circ = 292^\circ$. According to Table 5.1, this is also the correct back azimuth. The S-P time is 7.8 s and using $\Delta = (t_{Sg} - t_{Pg}) \times 8.0$ gives an epicentral distance of 62 km. The location can then be made as shown on fig. 5.3. It is seen that this simple location, done without knowing the velocity structure, gives a good first estimate of the epicenter location.

If the first half cycle (0.06 s) is used with the cross correlation technique, the result is 293° , apparent velocity of 6.7 km/s and a correlation coefficient of 0.7. The P-velocity in the surface layer is set to 5 km/s. This seems quite reasonable considering the epicentral distance of 60 km. This example is clear and with good correlation between components. In practice this is often not the case. The first onset

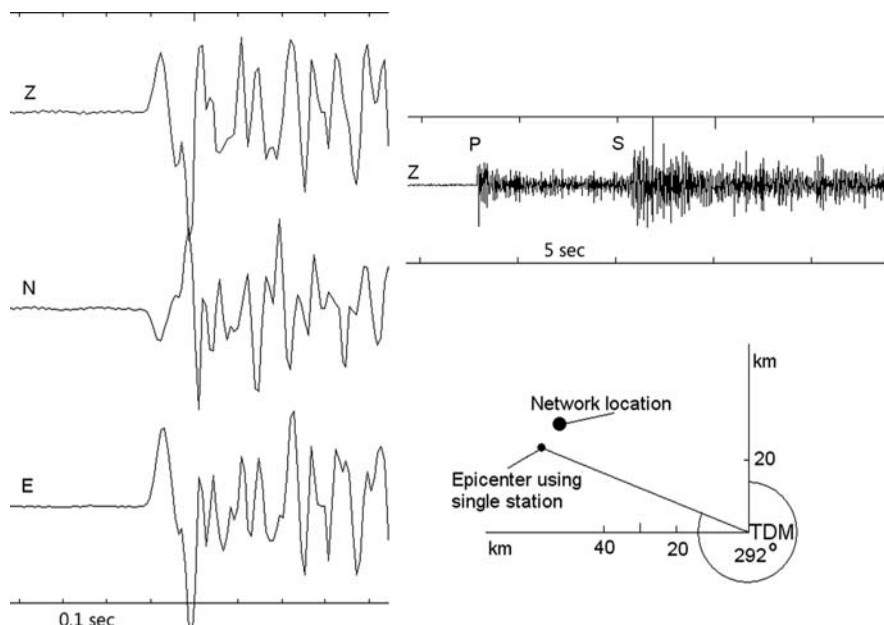


Fig. 5.3 Example of a three component recording and location by using the back azimuth. Bottom right: Location of the event using only station TDM. The data is from the Tanzanian network. The origin time is 1992 1015 00:16, epicentral distance is 60 km, depth is 16 km and $M_L = 2.0$

might be very emergent, or the signals are quite different and it will be hard to get a good correlation between components. Sometimes later arrivals will give better correlation and filtering will often help. Table 5.2 shows the calculation of back azimuth, apparent velocity and correlation coefficient for different time windows, start times and filters.

Table 5.2. Calculation of back azimuth ϕ , apparent velocity V and correlation coefficient Corr for different time windows W, start times (Start) and filter. The start times are at the P-onset (P) and at the following whole second following the P. The signal is seen in Fig. 5.3

	Start	P	49	50	51	52	53	54	55
W = 0.2 s	Φ	299	255	268	242	255	219	263	260
No	V	7.0	13.0	17.7	12.1	11.7	11.3	14.5	22.3
Filter	Corr	0.6	-4.8	-0.1	-1.2	0.2	-0.5	-0.3	-3.8
W = 0.2 s	Φ	294	246	267	270	268	162	327	260
5–10 Hz	V	6.3	13.5	5.7	10.1	6.6	18.8	8.8	5.7
Filter	Corr	0.8	0.6	0.8	-0.8	0.4	-1.3	0.8	0.1
W = 0.1 s	Φ	301	256	276	247	273	228	254	240
No	V	7.3	22.2	17.7	7.8	12.2	10.4	15.1	28.8
Filter	Corr	0.8	-19.9	0.4	0.2	-0.1	-1.0	-1.7	-9.7

In this example it is seen that a shorter time window generally gives better results than a longer time window in terms of correlation coefficient and a “reasonable” apparent velocity. It is also seen that in the entire P-wave train, the back azimuth generally gives a good indication of the arrival direction of the waves despite bad correlation coefficients, however most of these results give a smaller back azimuth than obtained with the first P. It is to be expected that the arrival direction and apparent velocity will change in the P-wave train due to inhomogeneities, layering and scattering but not as much as observed here (this would be better tested with array measurements, see Chapter 9). The back azimuth calculated from the first P is consistently around 300° as also calculated manually. From the event location, the back azimuth should have been 280° . This difference can be ascribed to local inhomogeneities, wrong instrument alignment or error in the calculated epicenter. This “good” example illustrates the type of errors to be expected with a back azimuth determination for small events. The accuracy cannot be expected to be better than $\pm 20^\circ$.

Teleseismic events have lower frequency and therefore better correlation and the accuracy will typically be $\pm 5^\circ$ (see NMSOP).

5.2 Multiple Station Location

When at least 3 stations are available, a simple manual location can be made from drawing circles (the circle method) with the center at the station locations and the radii equal to the epicentral distances calculated from the S-P times (Fig. 5.4).

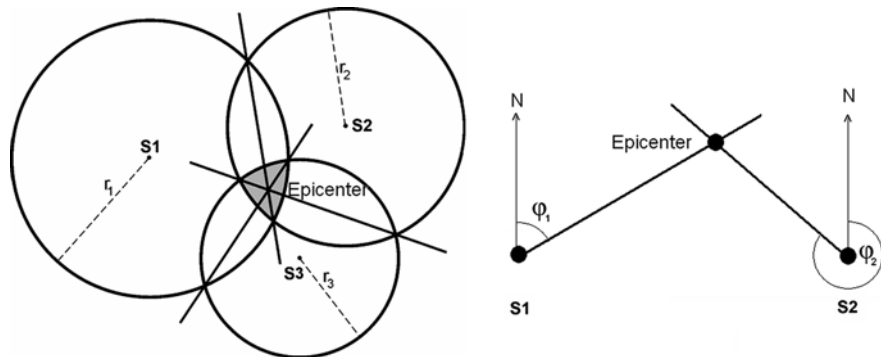


Fig. 5.4 *Left:* Location by the circle method. The stations are located in S1, S2 and S3. The epicenter is found within the shaded area where the circles overlap. The best estimate is the crossing of the chords, which connect the crossing points of the different pairs of circles. *Right:* Location by two stations and back azimuth. Copyright granted by IASPEI. Figure redrawn from NMSOP, IS 11.2

In this case six observations are used, but in principle three P arrivals and one S arrival are enough from three stations. The origin time is then given through the distance determined from the S-P observation. The distances from the other stations can then be computed from the P travel times for the other two stations, and the epicenter found from the intersection of the circles.

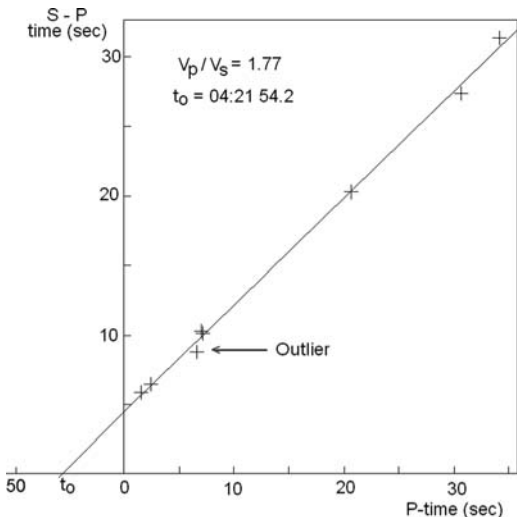
These circles will rarely cross in one point which indicates errors in the observations and/or that we have wrongly assumed a surface focus. In fact, $t_s - t_p$ is the travel-time difference for the hypocentral distance r which is, for earthquakes with $z > 0$ km, generally larger than the epicentral distance Δ . Therefore, the circles drawn around the stations with radius r will normally not be crossing in a single point at the epicenter but rather “overshoot”. One should therefore fix the epicenter either in the “center of gravity” of the overshoot area (black area in Fig. 5.4) or draw straight lines passing through the crossing point between two neighboring circles. These lines intersect in the epicenter. Still other methods exist (e.g., Båth, 1979a) to deal with this depth problem (e.g., the hyperbola method which uses P-wave first arrivals only and assumes a constant P-wave velocity), however since they are rarely used, they will not be discussed here.

With back azimuth available, for a local earthquake, epicenter and origin time can also be calculated with two stations with back azimuth and one P or S-reading (Fig. 5.4). In order to get the depth, at least one P and S-reading must be available.

With several stations available from a local earthquake, the origin time can be determined by a very simple technique called a Wadati diagram (Fig. 5.5) (Wadati, 1933). Assuming a constant v_p/v_s , equation (5.7) can be written in a more general case for any travel time function $t^{tra}(\Delta)$ as

$$t_p^{arr} = t_0 + t_p^{tra}(\Delta) \quad t_s^{arr} = t_0 + t_p^{tra}(\Delta) \cdot \frac{v_p}{v_s} \quad (5.13)$$

Fig. 5.5 An example of a Wadati diagram. The intercept on the x-axis gives the origin time. The slope of the line is 0.77 so the v_p/v_s ratio is 1.77. Note that the points do not exactly fit the line indicating model or observation errors. In particular one station has suspicious readings (marked with outlier). The event is from the Andalucian network, origin time 2006 0122 04:21



and, eliminating $t_p^{tra}(\Delta)$, the S-P time can be calculated as

$$t_s^{arr} - t_p^{arr} = \left(\frac{v_p}{v_s} - 1 \right) (t_p^{arr} - t_0) \quad (5.14)$$

The S-P times are plotted against the absolute P-time. Since $t_s^{arr} - t_p^{arr}$ goes to zero at the hypocenter, a straight line fit on the Wadati diagram gives the origin time at the intercept with the P-arrival axis, and from the slope of the curve we get v_p/v_s . Note that it is thus possible to get a determination of both the origin time and v_p/v_s without prior knowledge of the crustal structure. The only assumption is that v_p/v_s is constant and that the P and S-phases are of the same type like Pg and Sg or Pn and Sn. Independent determination of these parameters can be very useful when using other methods of earthquake location.

The example in Fig. 5.5 illustrates the use of a Wadati diagram for a local event. The v_p/v_s ratio determined seems quite reasonable and the readings, except for one, look acceptable. The origin time determined with the Wadati diagram is only 1 s different from the origin time determined by location. As we shall see in Section 5.6, it can sometimes be difficult to find the one station with the bad reading when locating, and the Wadati diagram can then be very useful in making independent checks of the observed arrival times. Any points not fitting the linear relationship might be badly identified, either by not being of the same type or misread.

By making Wadati diagrams of many events, an accurate v_p/v_s – ratio for a region can be determined. This is a simple way of getting information on crustal structure without any prior knowledge of a region. This is also in most cases sufficient information for location purposes since an average v_p/v_s ratio is normally used.

5.3 Computer Implementation

Manual location methods provide insight into the location problem, however in practice computer methods are used. In the following, the most common ways of calculating hypocenter and origin time by computer will be discussed.

The calculated arrival time t_i^{arr} at station i can be written as

$$t_i^{arr} = t_i^{tra}(x_i, y_i, z_i, x_0, y_0, z_0) + t_0 = t_i^{tra} + t_0 \quad (5.15)$$

where t_i^{tra} is the calculated travel time as a function of the known station location (x_i, y_i, z_i) , an assumed hypocenter location (x_0, y_0, z_0) and the velocity model. This equation has 4 unknowns, so in principle 4 arrival time observations from at least 3 stations are needed in order to determine the hypocenter and origin time. If we have n observations ($n > 4$), there will be n equations of the above type and the system is over-determined. A solution has to be found in such a way that the overall difference between the observed and calculated travel times (the residuals) are minimized. The residual r_i for station i is defined as the difference between the observed and calculated arrival times, which is the same as the difference between the observed and calculated travel times

$$r_i = t_i^{obs} - t_i^{arr} \quad (5.16)$$

where t_i^{obs} is the observed arrival time. Thus the problem seems quite simple in principle. However, since the travel time function t_i^{tra} is a nonlinear function of the model parameters, it is not possible to solve (5.15) with any analytical methods. So even though t_i^{tra} can be quite simple to calculate, particularly when using a 1D earth model or travel time tables, the non linearity of t_i^{tra} greatly complicates the task of inverting for the best hypocentral parameters. The non linearity is evident even in a simple 2D location where the travel time t_i^{tra} from the point (x, y) to a station (x_i, y_i) can be calculated as

$$t_i^{tra} = \frac{\sqrt{(x - x_i)^2 + (y - y_i)^2}}{v} \quad (5.17)$$

where v is the velocity. It is obvious that t_i^{tra} does not scale linearly with either x and y so it is not possible to use any set of linear equations to solve the problem. In the following, some of the methods of solving this problem will be discussed.

5.3.1 Grid Search

Since it is easy to calculate the travel times to any point in the model, a very simple method is to perform a grid search over all possible locations. For each point in the grid there will be n equations of the type

$$r_i = t_i^{obs} - (t_i^{tra} + t_0) \quad (5.18)$$

and the only unknown is t_0 , which then is determined in some average way using all observations. The most common approach is to use the least squares solution which is to find the minimum of the sum of the squared residuals e from the n observations

$$e = \sum_{i=1}^n (r_i)^2 \quad (5.19)$$

The hypocentral location would then be the point with the best agreement between the observed and calculated times which means the lowest e . The root mean squared residual RMS , is defined as $\sqrt{e/n}$. RMS is given in almost all location programs and commonly used as a guide to location accuracy. If the residuals are of similar size, the RMS gives the approximate average residual. As will be seen later, RMS only gives an indication of the fit to the data, and a low RMS does not automatically mean an accurate hypocenter determination, see section below on errors.

The average squared residual e/n is called the variance of the data. Formally, n should here be the number of degrees of freedom, ndf , which is the number of observations – number of parameters in fit (here 4). Since n usually is large, it can be considered equal to the number of degrees of freedom. This also means that RMS^2 is approximately the same as the variance.

The least squares approach is the most common measure of misfit since it leads to simple forms of the equations in the minimization problems (see later). A particularly problem is individual large residuals also called outliers. A residual of 4 will contribute 16 times more to the misfit, e , than a residual of 1. This problem could partly be solved by using the sum of the absolute residuals as a norm for the misfit

$$e1 = \sum_{i=1}^n |r_i| \quad (5.20)$$

This is called the L1 norm and is considered more robust when there are large outliers in the data (Menke, 1989). It is not much used in standard location programs since the absolute sign creates complications in the equations. This is of course not the case for grid search. Most location programs will have some scheme for weighting out large residuals (see later).

Once the misfits (e.g. RMS) have been calculated at all grid points, one could assign the point with the lowest RMS as the “solution”. For well behaved data, this would obviously be the case, but with real data, there might be several points, even far apart, with similar RMS and the next step is therefore to estimate the probable

uncertainties of the solution. The simplest way to get an indication of the uncertainty, is to contour the *RMS* as a function of x and y (2D case) in the vicinity of the point with the lowest *RMS*, see Fig. 5.6.

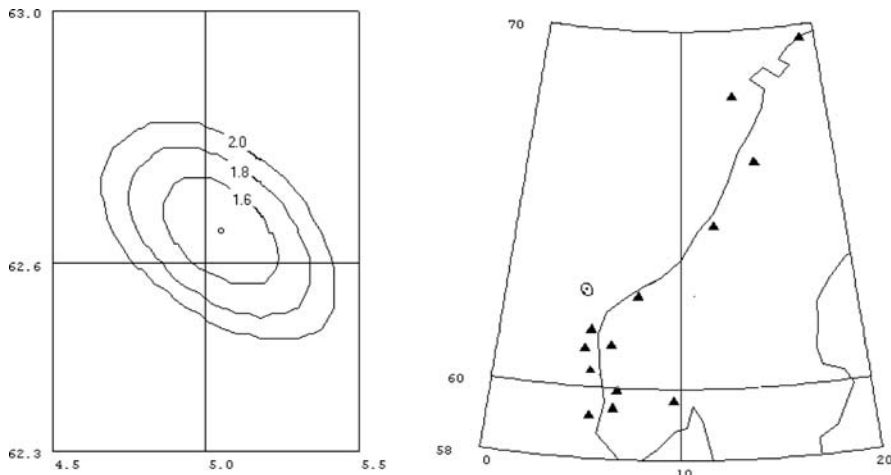


Fig. 5.6 *Left:* RMS contours (s) from a grid search location of an earthquake off western Norway (*left*). The grid size is 2 km. The circle in the *middle* indicates the point with the lowest RMS (1.4 s). *Right:* The location of the earthquake and the stations used. Note the elongated geometry of the stations. The RMS ellipse from the figure on the *left* is shown as a small ellipse. Latitudes are degrees north and longitudes degrees west. Copyright granted by IASPEI. Figure from NMSOP, IS 11.1

Clearly, if *RMS* is growing rapidly when moving away from the minimum, a solution with lower uncertainties has been obtained than if *RMS* grows slowly. If *RMS* is contoured in the whole search area, other minima of similar size might be found indicating not only large errors but a serious ambiguity in the solution. Also note in Fig. 5.6 that networks with irregular aperture have reduced distance control in the direction of their smallest aperture but good azimuth control in the direction of their largest aperture.

Location by grid search is up to 1,000 times slower than location by iterative methods (see next section). Probabilistic earthquake location uses a variation of the grid search method by performing a so-called “directed random walk” within the x,y,z volume, meaning that the whole volume does not have to be searched and this method is only 10 times slower than iterative methods (Lomax et al., 2000).

5.3.2 Location by Iterative Methods

Despite increasing computer power, earthquake locations are mainly done by other methods than grid search. These methods are based on linearizing the problem. The first step is to make a guess of hypocenter and origin time (x_0, y_0, z_0, t_0). In its

simplest form, e.g., in case of events near or within a station network, this can be done by using a location near the station with the first arrival time and using that arrival time as t_0 . Other methods also exist (see later). In order to linearize the problem, it is now assumed that the true hypocenter is close enough to the guessed value so that travel-time residuals at the trial hypocenter are a linear function of the correction we have to make in hypocentral distance.

The calculated arrival times at station i , t_i^{arr} from the trial location are, as given in (5.15), $t_i^{arr} = t_i^{arr}(x_0, y_0, z_0, x_i, y_i, z_i) + t_0$. We now assume that the residuals are due to the error in the trial solution and the corrections needed to make them zero are Δx , Δy , Δz , and Δt . If the corrections are small, we can calculate the corresponding corrections in travel times by approximating the travel time function by a Taylor series and only using the first term. The residual can now be written

$$r_i = \frac{\partial t_i^{tra}}{\partial x_i} \Delta x + \frac{\partial t_i^{tra}}{\partial y_i} \Delta y + \frac{\partial t_i^{tra}}{\partial z_i} \Delta z + \Delta t \quad (5.21)$$

In matrix form we can write this as

$$\mathbf{r} = \mathbf{G} \mathbf{x} \quad (5.22)$$

where \mathbf{r} is the residual vector, \mathbf{G} the matrix of partial derivatives (with 1 in the last column corresponding to the source time correction term) and \mathbf{x} is the unknown correction vector in location and origin time. Except for very simple models with constant velocity, see (5.26), the derivative cannot be obtained from a simple function and must be calculated by interpolation of travel time tables (see Chapter 2). This means that the method of earthquake location is decoupled from the complexity of the model. Any model for which a travel time can be obtained can be used for earthquake location, including 3D models.

Our problem to solve is then a set of linear equations with 4 unknowns (corrections to hypocenter and origin time), and there is one equation for each observed phase time. Normally there would be many more equations than unknowns (e.g., 4 stations with 3 phases each would give 12 equations). The best solution to (5.22) is usually obtained with standard least squares techniques. The original trial solution is then corrected with the results of (5.22) and this new solution can then be used as trial solution for a next iteration. This iteration process can be continued until a predefined breakpoint is reached. Breakpoint conditions can be either a minimum residual r , a last iteration giving a smaller hypocentral parameter changes than a predefined limit, or just the total number of iterations. This inversion method was first invented and applied by Geiger (1910) and is called the Geiger method of earthquake location. The iterative process usually converges rapidly unless the data are badly configured or the initial guess is very far away from the mathematically best solution (see later). However, it also happens that the solution converges to a local minimum and this would be hard to detect in the output unless the residuals are very bad. A test with a grid search program could tell if the minimum is local or tests could be made with several starting locations.

So far we have only dealt with observations in terms of arrival times. Many 3-component stations and arrays now routinely report back azimuth ϕ . It is then possible to locate events with less than 3 stations (Fig. 5.4). However, the depth must be fixed. If one or several back azimuth observations are available, they can be used together with the arrival time observations in the inversion and the additional equations for the back azimuth residual are

$$r_i \phi = (\partial\phi/\partial x_i)\Delta x + (\partial\phi/\partial y_i)\Delta y \quad (5.23)$$

Equations of this type are then added to (5.22). The Δx and Δy in (5.23) are the same as for (5.22), however the residuals are now in degrees. In order to make an overall *RMS*, the degrees must be “converted to seconds” in terms of scaling. For example, in the location program HYPOCENTER (Lienert and Havskov, 1995), a 10 deg back azimuth residual is optionally made equivalent to 1 s travel time residual. Using e.g., 20 deg as equivalent to 1 s would lower the weight of the back azimuth observations. Schweitzer (2001) used a different approach in the location program HYPOSAT. In this program the measured (or assumed) observation errors of the input parameters are used to weight individually the different lines of the equation system (5.21) before inverting it. Thereby, more uncertain observations will contribute much less to the solution than well-constrained ones and all equations become non-dimensional.

Arrays (see Chapter 9) or single stations do not only measure the back azimuth of a seismic phase but also its ray parameter (or apparent velocity). Consequently, the equation system (5.21) and (5.22) to be solved for locating an event, can also be extended by utilizing such observed ray parameters $p = 1/v_{app}$ (see Chapter 2). In this case we can write for the ray parameter residual

$$r_i p = (\partial p / \partial x_i) \Delta x + (\partial p / \partial y_i) \Delta y + (\partial p / \partial z_i) \Delta z \quad (5.24)$$

This equation is independent of the source time and the partial derivatives are often very small. However, in some cases, in particular if an event is observed with only one seismic array, the observed ray parameter will give additional constraint for the event location. In case only a P-observation is available from the array, p must be included to calculate a location.

Relation (5.21) is written without discussing whether working with a flat earth or a spherical earth. However, the principle is exactly the same and using a flat earth transformation (e.g., Müller, 1977), any radially symmetric earth model can be transformed into a flat model. The travel times and partial derivatives are often calculated by interpolating in tables and in principle it is possible to use any earth model including 2D and 3D models to calculate theoretical travel times. In practice, 1D models are mostly used, since 2D and 3D models are normally not well enough known and the travel-time computations are much more time consuming (which is why 3D times are pre-computed). For local seismology, it is a common practice to specify a 1D crustal model and calculate arrival times for each ray while for global models an interpolation in travel-time tables such as IASPEI91 is the most common. However, as Kennett and Engdahl (1991) pointed out, the preferred and

much more precise method for obtaining travel times from the IASP91 model or other 1D global earth models is to apply the tau-p method developed by Buland and Chapman (1983).

5.3.3 Example of Location in a Homogeneous Model

The simplest case for earthquake location is a homogeneous medium (example from Stein and Wysession, 2003). The travel times can be calculated as

$$t_i^{tra} = \frac{\sqrt{(x - x_i)^2 + (y - y_i)^2 + (z - z_i)^2}}{v} \quad (5.25)$$

where v is the velocity. The partial derivatives can be estimated from (5.25) and e.g., for x , assuming the station is at the surface ($z_i = 0$), the derivative is

$$\frac{\partial t_i^{tra}}{\partial x} = \frac{(x - x_i)}{v} \frac{1}{\sqrt{(x - x_i)^2 + (y - y_i)^2 + z^2}} \quad (5.26)$$

A similar expression can be made for y and for z it is

$$\frac{\partial t_i^{tra}}{\partial z} = \frac{z}{v} \frac{1}{\sqrt{(x - x_i)^2 + (y - y_i)^2 + z^2}} \quad (5.27)$$

Table 5.3 gives an example of locating an earthquake with 10 stations in a model with constant velocity (from Stein and Wysession, 2003). The stations are from 11 to 50 km from the hypocenter. The earthquake has an origin time of 0 s at the point (0, 0, 10) km. The starting location is at (3, 4, 20) km at 2 s. The exact travel times were calculated using a velocity of 5 km/s and the iterations were done as indicated above. At the initial guess, the sum of the squared residuals were 92.4 s², after the first iteration it was reduced to 0.6 s² and already at the second iteration, the “correct” solution was obtained. This is hardly surprising, since the data had no errors. We shall later see how this works in the presence of errors.

Table 5.3 Inversion of error free data. Hypocenter is the correct location, Start is the starting location, and the location is shown for the two following iterations. Units for x , y and z are km, for t_0 s and for the misfit e according to (5.19) it is s²

	Hypocenter	Start	1. Iteration	2. Iteration
$X(\text{km})$	0.0	3.0	-0.5	0.0
$Y(\text{km})$	0.0	4.0	-0.6	0.0
$Z(\text{km})$	10.0	20.0	10.1	10.0
$t_0(\text{s})$	0.0	2.0	0.2	0.0
$e(\text{s}^2)$		92.4	0.6	0.0
$RMS(\text{s})$		3.0	0.24	0.0

5.4 Error Quantification and Statistics

Since earthquakes are located with arrival times that contain observational errors and the travel times are calculated assuming a velocity model, all hypocenter estimates will have errors. Contouring the grid search *RMS* (Fig. 5.6) gives an indication of the uncertainty of the epicenter. Likewise it would be possible to make 3D contours to get an indication of the 3D uncertainty. The question is now how to quantify this measure. The *RMS* of the final solution is very often used as a criterion for “goodness of fit”. Although it can be an indication, *RMS* depends on the number of stations and does not in itself give any indication of errors and *RMS* is not reported by e.g., PDE (preliminary determination of epicenters from USGS) and ISC. From Fig. 5.6 it is seen that the contours of equal *RMS* are not circles. We can calculate an ellipsoid within which there is a 67% probability equal to one standard deviation (or any other desired probability) of finding the hypocenter (see below). We call this the error ellipse. It is not sufficient to give one number for the hypocenter error since it varies spatially. Standard catalogs from PDE and ISC give the errors in latitude, longitude and depth, however that can also be misleading unless the error ellipse has the minor and major axis NS or EW. In the example in Fig. 5.6, this is not the case. Thus the only proper way to report error is to give the full specification of the error ellipsoid.

Before going into a slightly more formal discussion of errors, let us try to get a feeling for what elements affect the shape and size of the epicentral error ellipse. If we have no arrival time errors, there are no epicenter errors so the magnitude of the error (size of error ellipse) must be related to the arrival time uncertainties. If we assume that all arrival time reading errors are equal, only the size and not the shape of the error ellipse can be affected. So what would we expect to give the shape of the error ellipse? Fig. 5.6 is an example of an elongated network with the epicenter off to one side. It is clear that in the NE direction, there is a good control of the epicenter since S-P times control the distances in this direction due to the elongation of the network. In the NW direction, the control is poor because of the small aperture of the network in this direction. We would therefore expect an error ellipse with the major axis NW as observed. Note, that if back azimuth observations were available for any of the stations far north or south of the event, this would drastically reduce the error estimate in the NW direction.

Another geometry of the stations would give another shape of the error ellipse. It is thus possible for any network to predict the shape and orientation of the error ellipses, and, given an arrival error, also the size of the ellipse for any desired epicenter location. This could e.g., be used to predict how a change in network configuration would affect earthquake locations at a given site.

In all these discussions, it has been assumed that the errors have Gaussian distribution and that there are no systematic errors like clock error. It is also assumed that there are no errors in the theoretical travel times, back azimuths, or ray parameter calculations due to unknown structures. This is of course not true in real life, however error calculations become too difficult if we do not assume a simple error distribution and that all stations have the same arrival time error.

The previous discussion gave a qualitative description of the errors. We will now show how to calculate the actual hypocentral errors from the errors in the arrival times and the network configuration. When earthquake location is based on the least squares inversion and a Gaussian distribution of the arrival time errors the statistics are well understood.

The errors in the hypocenter and origin time can formally be defined with the variance – covariance matrix σ_X^2 of the hypocentral parameters. This matrix is defined as

$$\sigma_X^2 = \begin{pmatrix} \sigma_{xx}^2 & \sigma_{xy}^2 & \sigma_{xz}^2 & \sigma_{xt}^2 \\ \sigma_{yx}^2 & \sigma_{yy}^2 & \sigma_{yz}^2 & \sigma_{yt}^2 \\ \sigma_{zx}^2 & \sigma_{zy}^2 & \sigma_{zz}^2 & \sigma_{zt}^2 \\ \sigma_{tx}^2 & \sigma_{ty}^2 & \sigma_{tz}^2 & \sigma_{tt}^2 \end{pmatrix} \quad (5.28)$$

The diagonal elements are variances of the location parameters x_0 , y_0 , z_0 and t_0 while the off diagonal elements give the coupling between the errors in the different hypocentral parameters. For more details, see e.g. Stein and Wysession (2003). The nice property about σ_X^2 is that it is simple to calculate

$$\sigma_x^2 = \sigma^2(\mathbf{G}^T \mathbf{G})^{-1} \quad (5.29)$$

where σ^2 is the variance of the arrival times multiplied with the identity matrix. \mathbf{G} is the known matrix of partial derivatives (5.22) which relates changes in travel time to changes in location. \mathbf{G}^T is \mathbf{G} transposed. The standard deviations of the hypocentral parameters are thus given by the square root of the diagonal elements. Within one standard deviation, there is a 68% probability of finding the solution and within 2 standard deviations there is a 95% probability. Often the errors are reported with 90% probability which then is a bit less than 2 standard deviations. So how can we use the off diagonal elements? Since σ_X^2 is a symmetric matrix, a diagonal matrix in a coordinate system, which is rotated relatively to the reference system, can represent it. We now only have the errors in the hypocentral parameters, and the error ellipse simply has semi axes σ_{xx} , σ_{yy} , and σ_{zz} . The main interpretation of the off diagonal elements is thus that they define the orientation and shape of the error ellipse. A complete definition therefore requires 6 elements. Equation (5.28) also shows, as earlier stated, intuitively that the shape and orientation of the error ellipse only depends on the geometry of the network and the crustal structure, while the standard deviation of the observations is a scaling factor. Figure 5.7 shows examples of error ellipses. The figure shows how the error ellipses are larger for events outside the network than inside the network. The error in depth is also generally larger than the error in the epicenter as expected (see later).

The critical variable in the error analysis is thus the arrival-time variance σ^2 . This value is usually larger than would be expected from timing and picking errors alone, however it might vary from case to case. Setting a fixed value for a given data set

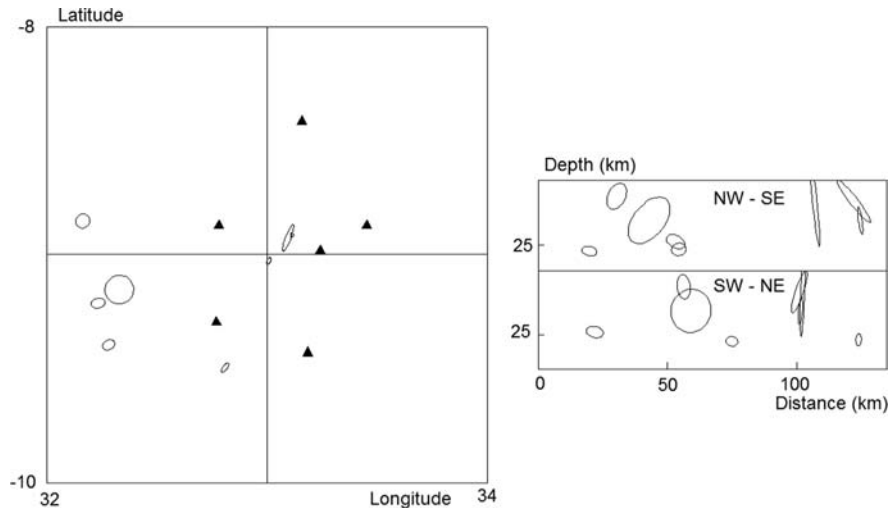


Fig. 5.7 Hypocenters plotted with error ellipses. *Left:* Epicenter error ellipses. Triangles are station locations. *Right:* Hypocenter error ellipses. Two profiles are shown. The data is from the Tanzanian network from October and November, 1992

could result in unrealistic error calculations. Most location programs will therefore estimate σ from the residuals of the best fitting hypocenter:

$$\sigma^2 = \frac{1}{ndf} \sum_{i=1}^n (r_i^2) \quad (5.30)$$

Division by ndf rather than by n compensates for the improvement in fit resulting from the use of the arrival times from the data. However, this only partly works and some programs allow setting an a priori value, which is only used if the number of observations is small. For small networks this can be a critical parameter.

5.4.1 Example of Error Calculation

We can use the previous error free example (Table 5.3) and add some errors (example from Stein and Wysession (2003)). We add Gaussian errors with a mean of zero and a standard deviation of 0.1 s to the arrival times. Now the data are inconsistent and cannot fit exactly. As it can be seen from the results in Table 5.4, the inversion now requires 3 iterations (2 before) before the locations do not change anymore. The final location is not exactly the location used to generate the arrival times and the deviation from the correct solution is 0.2, 0.4, and 2.2 km for x_0 , y_0 ,

Table 5.4 Inversion of arrival times with a 0.1 s standard error. Hypocenter is the correct location, Start is the starting location, and the locations are shown after the three following iterations. e is the misfit according to (5.19)

	Hypocenter	Start	1. Iteration	2. Iteration	3. Iteration
x (km)	0.0	3.0	-0.2	0.2	0.2
y (km)	0.0	4.0	-0.9	-0.4	-0.4
z (km)	10.0	20.0	12.2	12.2	12.2
t_0 (s)	0.0	2.0	0.0	-0.2	-0.2
e (s^2)		93.7	0.33	0.04	0.04
RMS (s)		3.1	0.18	0.06	0.06

and z_0 respectively and 0.2 s for origin time. This gives an indication of the location errors.

It is now interesting to compare to what is obtained with the formal error calculation. Table 5.5 gives the variance – covariance matrix. Taking the square root of the diagonal elements we get a standard deviation of x_0 , y_0 , z_0 and t_0 of 0.2, 0.3 and 1.1 km and 0.1 s respectively. This is close to the “true” error so the solution is quite acceptable. Also note that the RMS is close to the standard error.

The variance – covariance matrix shows some interesting features. As seen from the diagonal elements of the variance – covariance matrix, the error is much larger in the depth estimate than in x_0 and y_0 . This clearly reflects that the depth is less well constrained than the epicenter which is quite common unless there are stations very close to the epicenter and thus $|r - \Delta| / \Delta >> 1$ (r is hypocentral distance). We have for simplicity calculated the standard deviations from the diagonal terms, however since the off diagonal terms are not zero, the true errors are larger. In this example it can be shown that the semi-major and semi-minor axis of the error ellipse have lengths (standard deviation) of 0.29 and 0.24 km respectively and the semi-major axis trends N22°E so the difference from the original diagonal terms is small.

The covariance between depth and origin time is negative indicating a negative trade-off between the focal depth and the origin time. An earlier source time can be compensated by a larger source depth and vice versa. This is commonly observed in practice and is more prone to happen if only first P-phase arrivals are used such that there is no strong limitation of the source depth by P-times at different distances.

Table 5.5 Variance – covariance matrix for the example in Table 5.4

	x	y	z	T
x(km)	0.06	0.01	0.01	0.00
y(km)	0.01	0.08	-0.13	0.01
z(km)	0.01	-0.13	1.16	-0.08
t(s)	0.00	0.01	-0.08	0.01

A parameter often used to get an indication of the reliability of the epicentral solution is what is called the azimuthal gap. This is defined as the largest gap in azimuth from the event to any two seismic stations. A gap of 180° or larger indicates that all the stations are on one side of the event. Most location programs will display the gap as part of the results.

Note that error calculation only estimate errors related to reading errors and station geometry. In addition, there are systematic errors related to the model. Error calculation is a fine art, there are endless variations on how it is done and different location programs will usually give different results. Error estimates critically depend on input parameters and should not be considered absolute. Testing with different configurations of stations and phases will often give an indication of the true errors.

A good way of testing the estimated errors and location accuracy is using reference (or ground truth) events. One expects the true location to be within the error ellipsoid around the computed hypocenter. A reference event is defined as an event for which the location and origin time are well known (e.g. a nuclear explosion) or an earthquake for which the location is known to a given precision as obtained e.g. from a local network. Global data bases of explosion have been collected by the CTBTO (Yang et al., 2000). A list of well located earthquakes have been collected by Engdahl et al. (1998) and currently a working group under IASPEI is building a public data base of reference events (<http://www.iaspei.org/commissions/CSOI.html>). The data base is maintained by ISC, see <http://www.isc.ac.uk/reference/reference.html>.

5.5 Relative Location Methods

5.5.1 Master Event Technique

The relative location between events within a certain region can often be made with a much greater accuracy than the absolute location of any of the events. This is the case when velocity variations outside the local region are the major cause of the travel-time residuals such that residuals measured at distant stations will be very similar for all of the local events. Usually, the events in the local area are relocated relative to one particularly well-located event, which is then called the master event. It should be clear that the Master Event Technique only can be used when the distance to the stations is much larger than the distance between the events, since it is assumed that the residuals caused by the structure are the same for all event-station pairs for different events.

Most location programs can be used for a master event location. For this, travel-time anomalies outside the source region are assumed to cause all individual station residuals after the location of the master event. By using these station residuals as station corrections, the location of the remaining events will be made relative to

the master event since all relative changes in arrival times are now entirely due to changes in location within the source region. It is obvious that only stations and phases for which observations are available for the master event can be used for the remaining events. Ideally, the same stations and phases should be used for all events.

The master event technique will be illustrated with an example. Using a local network of three stations (Fig. 5.20), two events have been identified to have the same location within 100 m when located with only the 3 nearest stations and the depth is 7.8 km. Figure 5.8 shows that the two events have nearly identical signals at stations hundreds of kilometers away, which is another evidence that they are at the same location and in addition also have the same focal mechanism. The signals are quite different between the stations NSS and LOF (both at a similar distance from the source) due to the radiation pattern and possible lateral changes in the structure (Fig. 5.8).

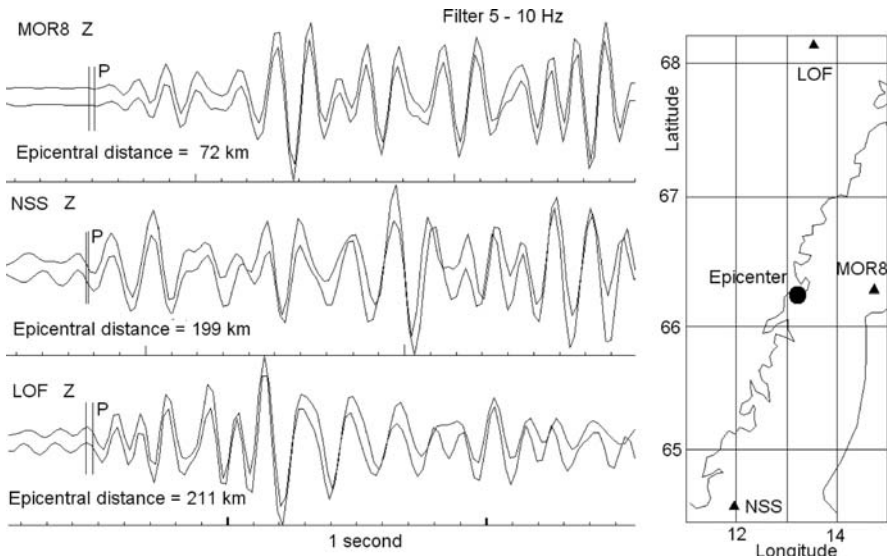


Fig. 5.8 *Left:* The first couple of seconds of the P-waves for the two events analyzed with master event technique. The top trace is the master event. The two vertical lines indicate where the P has been read manually. Master event origin time is 2005 1023 20:01 ($M_L = 1.8$) and second event origin time is 2005 1106 21:00 ($M_L = 1.6$). *Right:* Location of the two events and the 3 stations used

These are then good test events since we know they are collocated. Using the larger regional network, the events are located a few kilometers apart (Table 5.6). The steps for making a relative location are:

Fix the location of the master events. In our case the event was fixed to the network location and the depth fixed to 10 km since this a common depth in the area.

Table 5.6 Relocation by master event technique. The “*” indicates that depth has been fixed. Latitude and longitude are in degrees north and east, respectively and depth is in km

	Latitude	longitude	Depth	RMS
Master event located with MOR8, NSS and LOF	66.247	13.147	10*	0.64
Second event located with MOR8, NSS and LOF	66.236	13.182	10*	0.84
Master event located with nearest 3 stations	66.234	12.972	7.8	0.03
Master event located with MOR8, NSS and LOF using residual corrections	66.247	13.144	10*	0.01
Second event located with MOR8, NSS and LOF using residual corrections	66.245	13.151	10*	0.00

Select stations and phases that are common among the events to be used. Only use clear phases which can be identified in a similar way on all events. Ideally get relative times by cross-correlation, see Chapter 4. In our case only P on 3 stations were selected (this is the minimum number with fixed depth), see Fig. 5.8.

Locate the master event at the fixed location with the selected phases and stations only and observe the residuals at the stations. In our example, the P-residuals at stations MOR8, NSS and LOF were -0.48 , 0.15 and 0.34 respectively.

Add the residuals to the readings for all events to be located relative to the master event. This can usually be done in a configuration file under station corrections. Some programs can use both P and S corrections while others only use P-corrections and calculate S-corrections from the v_p/v_s ratio and the P-correction.

Relocate all events including the master event without any fixing (possibly fix depth). A good test of checking that residuals have been added correctly is to check the location and RMS of the master event. The RMS should be 0 and the location the same as before. In practice there will always be some round off errors so the master event moves a bit. In our case it moved 0.13 km (Table 5.6).

The difference in location was 2.0 km before using the master technique, while it was 0.3 km after correction. In this case a very simple correction was made with only 3 P-phases and not very sharp arrivals (Fig. 5.8), however a significant improvement in the relative location was made in a simple way. From the figure it is seen that the manual picks are not as accurate as what could have been obtained by cross correlation so even a higher accuracy could have been obtained.

5.5.2 Joint Hypocenter Location

In the Master Event Technique, it was assumed that true structure dependent residuals could be obtained absolutely correct from the master event, however other errors

could be present in the readings for the master event. A better way is to determine the most precise station residuals using the whole data set. This is what Joint Hypocenter Determination (JHD) is about. Instead of determining one hypocenter and origin time, we will jointly determine m hypocenters and origin times, and n station corrections (for simplicity, it is assumed there is one observation per station). This is done by adding the station residuals Δt_i to (5.21) and writing the equations for all m earthquakes (index j):

$$r_{ij} = \frac{\partial t_i^{cal}}{\partial x_{ij}} \Delta x + \frac{\partial t_i^{cal}}{\partial y_{ij}} \Delta y + \frac{\partial t_i^{cal}}{\partial z_{ij}} \Delta z + \Delta t_i^S + \Delta t_j \quad (5.31)$$

The JHD method was first proposed by Douglas (1967). Since the matrix \mathbf{G} of (5.22) is now much larger than the $n \times 4$ matrix for a single event location, efficient inversion schemes must be used. If we use e.g., 20 stations with 2 phases (P and S) each for 10 events, there will be $20 \times 10 \times 2 = 400$ equations and 80 unknowns (10 hypocenters and origin times, and 20 station residuals (P and S are different)).

The relative locations obtained by the Master Event Technique or the JHD are usually more reliable than individually estimated relative locations. However, only if we have the absolute location of one of the events (e.g., a known explosion), will we be able to convert the relative locations of a Master Event algorithm to absolute locations, while for JHD, “absolute” locations are obtained for all events, if the assumed velocity model is correct. Accurate relative locations are useful to study e.g., the structure of a subduction zone or the geometry of an aftershocks area, which might indicate the orientation and geometry of the fault. Pujol (2000) gave a very detailed outline of the method and its application to data from local seismic networks. Figure 5.9 shows an example for increased location accuracy after applying JHD.

5.5.3 Double Difference Earthquake Location

The problem of locating seismic events has recently experienced a lot of attention and new procedures have been developed such as the double-difference earthquake location algorithm (Waldbauer and Ellsworth, 2000). In this method, the difference between observed and calculated travel time differences of event pairs (called double difference) is minimized, rather than the difference between observed and calculated travel times for single events. An advantage of this technique is that it works with the combination of catalogue and relative times (e.g. measured through cross-correlation), where the absolute locations are given through the catalogue of arrival times and relative locations are given through travel time differences between event pairs. Use of this technique has resulted in reduced clustering of epicenters, which leads to clearer identification of fault lines (e.g., Waldbauer and Ellsworth, 2000; Hauksson and Shearer, 2005). A comparison of location results

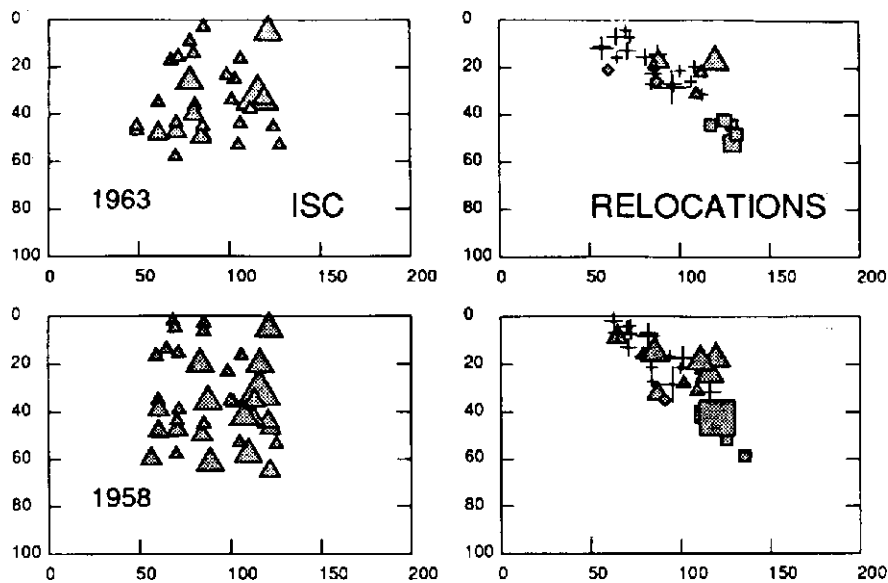


Fig. 5.9 Comparison of earthquake locations using the normal procedure at ISC (left) and JHD relocations (right). The events are located in the Kurile subduction zone along the rupture zones of large thrust events in 1963 and 1958. The vertical cross sections shown traverse the thrust zone from *left* to *right*. Note that the JHD solutions reduce the scatter and make it possible to define a dipping plane. Figure reproduced by permission from the American Geophysical Union. From Schwartz et al. (1989)

using either JHD or double difference is given in Fig. 5.10. It is seen that the results are similar, but clustering is slightly more reduced when using the double difference method.

Several location techniques including recent developments are summarized in a monograph edited by Thurber and Rabinowitz (2000). Event location related to the special requirements for monitoring the CTBT is described by Ringdal and Kennett (2001). An example how much the accuracy of location within earthquake clusters on a regional scale can be improved by applying the above mentioned double-difference earthquake location algorithm is given in Fig. 5.11.

5.6 Practical Considerations in Earthquake Locations

This section is intended to give some practical hints on earthquake location. The section does not refer to any particular location program, but most of the parameters discussed can be used with the HYPOCENTER program (Lienert and Havskov, 1995) or with HYPOSAT (Schweitzer, 2001). Most examples are made with HYPOCENTER.

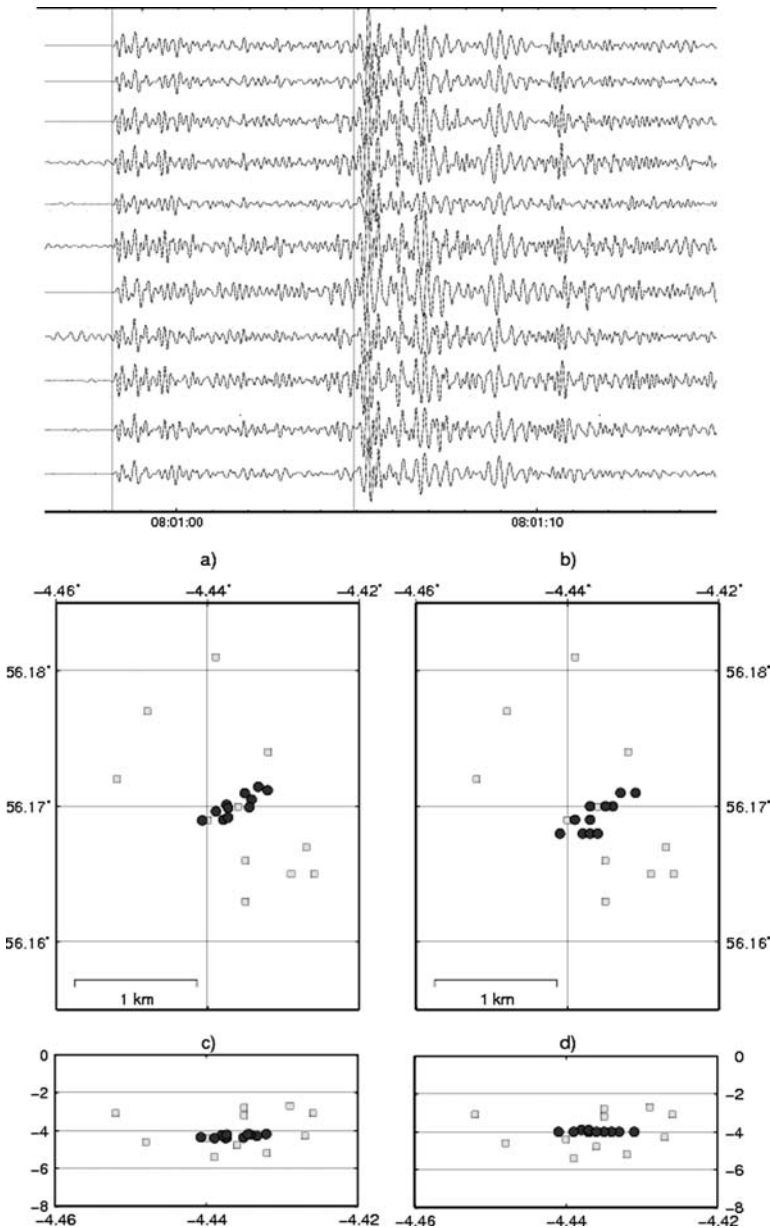


Fig. 5.10 Top: Seismograms recorded from a small swarm of earthquakes showing that the waveforms were highly correlated. Bottom: Improved relative locations using **a)** double difference algorithm and **b)** joint hypocenter determination, **c)** and **d)** are cross sections east-west. The open squares are the original locations. From Ottemöller and Thomas, 2007

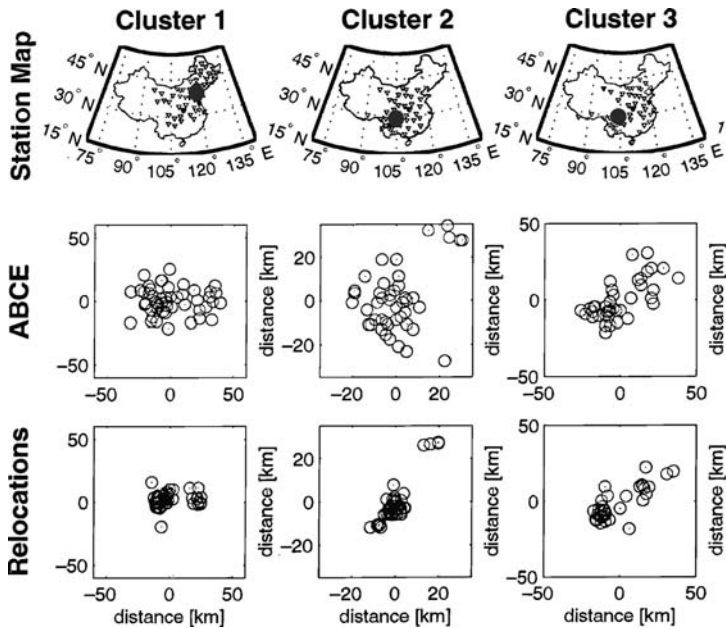


Fig. 5.11 Examples of improving locations for earthquake clusters with the double-difference location. The data is clusters of earthquakes (large black dots) from regional networks of seismic stations (triangles) in China (top figure). The middle row shows the original locations and the bottom row the relocations using double-difference location algorithm. Courtesy of Paul G. Richards

5.6.1 Phases

The most unambiguous phase to pick is usually P, and P is the main phase used in most teleseismic locations. For local earthquakes, usually S-phases are also used. Using phases with different velocities and slowness has the effect of better constraining the distances and there is then less trade-off between depth and origin time or epicenter location and origin time if the epicenter is outside the network. The focal depth is best controlled (with no trade-off between depth and origin time) when phases are included in the location procedure which have different sign of the partial derivative $\partial T/\partial z$ in (5.21) such as for very locally observed direct up-going Pg (positive) and down-going Pn (negative). In general, it is thus an advantage to use as many different phases as possible under the assumption that they are correctly identified, see Schöffel and Das (1999) for an example (see Fig. 5.12).

Many location programs for local earthquakes only use first arrivals (e.g., HYPO71, Lee and Lahr, 1975). This is good enough for many cases. In some distance ranges, Pn is the first arrival, and it usually has a small amplitude. This means that the corresponding Sn phase, which is then automatically used by the program, might also have a small amplitude and is not recognized while actually the phase

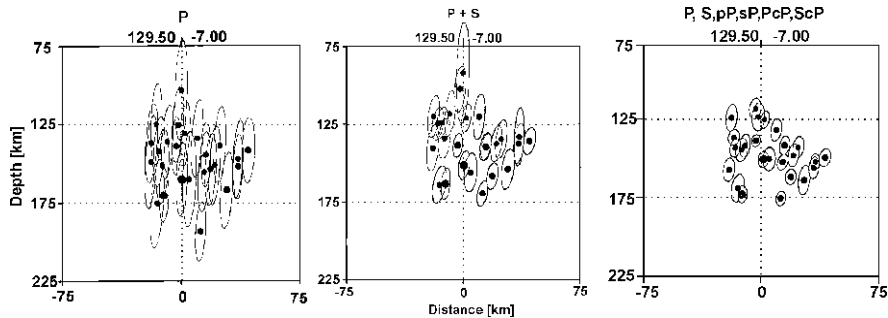


Fig. 5.12 Examples of significant improvement of hypocenter location for teleseismic events by including secondary phases. *Left:* hypocenter locations using only P-phases; *middle:* by including S-phases; *right:* by including also depth phases and core reflections with different sign of $\partial T/\partial z$. Reproduced by permission of the American Geophysical Union. From Schöffel and Das (1999)

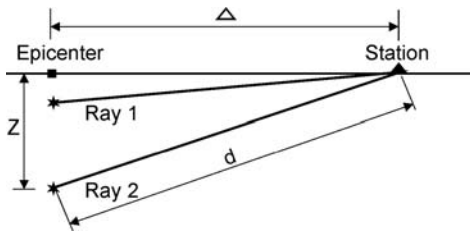
read is Sg or Lg instead. Since the program automatically assumes a first arrival, a wrong travel time curve is used for the observed phase, resulting in a systematic location error. This error is amplified by the fact that the S-phase, due to its low velocity, has a larger influence on the location than the P-phase. It is therefore preferable to use location programs where all crustal phases can be specified.

It is generally possible to give different phase arrivals different weights. As mentioned above, the S-phases will get more weight in the location due to its low velocity while it is often a less certain phase and should have less weight than P. Ideally all phases should be read with an indication of the reading uncertainty, which then would be used to set a phase weight that would be used by the location program. This is usually assigned manually without displaying the uncertainty in the pick time.

5.6.2 Hypocentral Depth

The hypocentral depth is the most difficult parameter to determine, particularly for regional events, due to the fact that the travel-time derivative with respect to depth changes very slowly as function of depth (see Fig. 5.13) unless the station is very close to the epicenter. In other words, the depth can be moved up and down without much change in the travel time. Figure 5.13 shows a shallow (ray 1) and a deeper event (ray 2). It is clear that the travel-time derivative with respect to depth is nearly zero for ray 1 and but not for ray 2 as it follows from (5.27). In this example, it would thus be possible to get an accurate depth estimate for the deeper event but not for the shallower one. Unfortunately, at larger distances from the source, most rays are more like ray 1 than like ray 2 and locations are therefore often made with a fixed “normal” starting depth. Only after a reliable epicenter is obtained will the program try to iterate for the depth. Another possibility is to locate the event with several starting depths and then using the depth that gives the best fit to the data.

Fig. 5.13 The depth – distance trade off in the determination of focal depth. Copyright granted by IASPEI. Figure from NMSOP, IS 11.1



Although one depth will give a best fit to all data, the depth estimate might still be very uncertain and the error estimate must be checked.

For teleseismic events, the best way to improve the depth determination is to include readings from the so-called depth phases such as pP, pwP (reflection from the ocean free surface), sP, sS or similar but also reflections from the earth's core like Pcp, ScP or ScS (see Fig. 5.12). The travel-time differences (i.e., depth phase – direct phase) as pP-P, sP-P, sS-S, and pS-S are quite constant over large range of epicentral distances for a given depth so that the depth can be determined nearly independently of the epicenter distance, see Table 5.7.

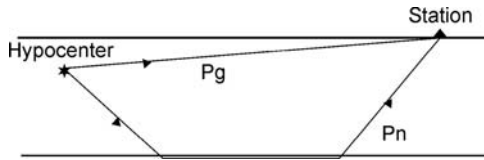
Table 5.7 The pP–P travel time (s) as a function of epicentral distance (degrees) and depth (km). From IASP91 tables

Distance ($^{\circ}$) ↓ Depth (km) →	20	50	100	200	400
20	5	10	19	42	—
30	6	13	21	41	73
40	6	13	23	42	76
50	6	14	24	44	80
60	6	14	25	46	84
70	7	14	25	47	87
80	7	14	26	48	90
90	7	15	26	49	92

Another way of getting a reliable depth estimate for teleseismic locations is to have both near and far stations available. However, this is unfortunately not possible for many source regions.

For local events, a rule of thumb is that at least several near stations should be closer than 2 times the depth in order to get a reliable estimate (Fig. 5.13). This is very often not possible, particularly for regional events. At a distance larger than $2 \times$ depth, the depth depending partial derivative changes very little with depth if the first arriving phase is the more or less horizontally propagating Pg. But at distances where the critically refracted (so-called head-waves) Pb or Pn arrive, there is again some sensitivity to depth due to the steeply down going rays of Pb or Pn (Fig. 5.14) and because of the different sign of the partial derivatives of their travel times with depth, which is negative, as compared to Pg, which is positive. So, if stations are available at distances with both direct and refracted rays as first arrivals, reasonably

Fig. 5.14 Example of both Pg and Pn rays in a single layer crustal model



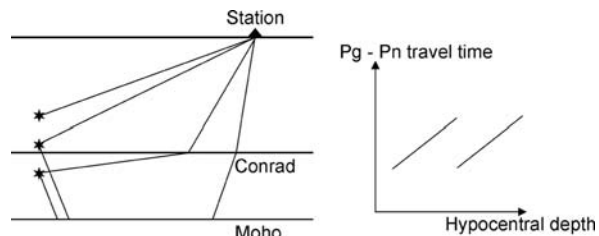
reliable solutions might be obtained. An even better solution is when both Pg and Pn are available at the same station and the location capability could be similar to using P and pP for teleseismic events. The problem is that it might be difficult to identify correctly secondary P-phases and a wrong identification might make matters worse.

The depth estimate using a layered crustal model remains problematic even with a mix of phases. Checking catalogs with local earthquakes, it will often be noted that there is a clustering of hypocenters at layer boundaries. This is caused by the discontinuities in the travel-time curves of the direct phase Pg as a function of depth at layer boundaries; see Fig. 5.15 for an example. The Pg travel time suddenly decreases when the hypocenter crosses a boundary (here Conrad) since a larger part of the ray suddenly is in a higher velocity layer, while the Pn travel time continuously decreases as the depth increases as long as the event is still within the crust. This gives rise to the discontinuities in the Pg travel time curve and therefore also in the Pg-Pn travel-time curve. So one Pn-Pg travel-time difference is not enough to ensure a reliable depth estimate, several such phase arrivals must be available.

Even when several Pg and Pn phases are available, depth estimates still remain a problem at regional distances due to the uncertainty in the crustal models. Since the depth estimates are critically dependent on the accurate calculation of Pg and Pn travel times, small uncertainties in the model can quickly throw off the depth estimate.

Many location programs give the *RMS* of the travel-time residuals in a grid around the calculated hypocenter. This, in addition to the error estimates, gives an idea about the accuracy and a local minimum might be found in this way. A more direct way of estimating the quality of the depth estimate is to calculate the *RMS* as a function of depth in order to check if a local minimum has been reached.

Fig. 5.15 Ray paths of Pg and Pn phases in a two-layer crustal model (left). On the right side the travel-time curve of Pg-Pn as a function of depth is sketched. For a specific example, see Fig. 5.17



This is particularly relevant for crustal earthquakes at shallow depth and can also be used as a complementary tool for better discriminating between quarry blasts and earthquakes.

The following example (Table 5.9) illustrates the use of crustal phases and depth of local earthquakes. The local model is seen in Table 5.8.

Table 5.8 Crustal model used for locating Norwegian earthquakes. The v_p/v_s ratio used is 1.74

Interface	1	2	3	Conrad	4	5	6
				Moho			
Depth (km)	0	12	23		31	50	80
V_p velocity (km/s)	6.20	6.60	7.10		8.05	8.25	8.50

Table 5.9 Location of an earthquake in Western Norway. The origin time is given in the table. The abbreviations are: hrmn: Hour and minute of origin time, sec: Second of origin time, lat: latitude in degrees and minutes, long: Longitude in degrees and minute, no: number of phases, m: degrees of freedom, damp: damping, erln, erlt and errdp: Error estimates (km) of longitude, latitude and depth respectively, stn: Station code, dist: Epicentral distance in km, azm: Azimuth from event to station, ain: Angle of incidence at the source, w: user given weight of phase (0: full weight, 1: .75, 2: 0.5, 3: 0.2 4: 0, 9: differential), phas: User given phase, calcphas: Phase used by program, hrmn: Hour minute of phase, tsec: Seconds of phase, tsec: Observed travel time, t-obs: Calculated travel time, res: Residual (s) = t-obs-t-cal, wt: Weight used by program (0–1) and di: % importance of each observation in the solution. Note the high importance of the S-phases in the solutions (di-values)

date	hrmn	sec	lat	long	depth	no	m	rms	damp	erln	erlt	errdp
96	7	5	220	46.21	6118.07N	4	52.8E	0.0	16	3	0.79	0.000 16.3 3.5 9.2
stn	dist	azm	ain	w	phas	calcphas	hrmn	tsec	t-obs	t-cal	res	wt di
SUE	28	193.3	90.0	0	P	PG	220	51.5	5.34	4.51	0.83	1.00 6
SUE	28	193.3	90.0	0	S	SG	220	55.7	9.46	7.84	1.62	1.00 10
FOO	34	14.6	90.0	0	P	PG	220	51.6	5.39	5.51	-0.12	1.00 9
FOO	34	14.6	90.0	0	S	SG	220	55.9	9.67	9.58	0.09	1.00 16
HYA	72	101.7	90.0	0	P	PG	220	57.7	11.52	11.54	-0.02	1.00 4
HYA	72	101.7	90.0	0	S	SG	221	6.7	20.45	20.08	0.37	1.00 24
ASK	94	169.2	90.0	0	P	PG	221	0.5	14.27	15.17	-0.90	1.00 1
ASK	94	169.2	90.0	0	S	SG	221	12.4	26.15	26.39	-0.24	1.00 4
BER	105	166.2	90.0	0	S	SG	221	15.2	28.97	29.52	-0.55	1.00 4
BER	105	166.2	90.0	0	P	PG	221	2.3	16.12	16.96	-0.85	1.00 1
EGD	116	170.6	90.0	0	P	PG	221	4.1	17.93	18.77	-0.84	1.00 1
EGD	116	170.6	90.0	0	S	SG	221	18.3	32.10	32.66	-0.56	1.00 4
ODD1	182	147.5	50.4	0	P	PN4	221	13.6	27.40	28.13	-0.73	1.00 0
ODD1	182	147.5	50.4	0	S	SN4	221	36.9	50.66	48.94	1.72	1.00 3
ODD1	182	147.5	90.2	4	Pg	PG	221	15.0	28.82	29.37	-0.55	0.00 0
MOL	199	43.6	50.4	0	P	PN4	221	16.2	29.96	30.17	-0.21	1.00 4
MOL	199	43.6	50.4	0	S	SN4	221	39.1	52.89	52.49	0.40	1.00 8
1996	7	5	0220	46.2tL*	61.301	4.880	0.0	TES	8 0.8			1.9LNAAO
The iterations												
iter	origin	lat	long	depth	no	m	rms	damp.	erlg	erlt	erdp	
	(sec)	(dg mn)	(dg mn)	(km)			(sec)		(km)	(km)	(km)	
1	42.83	6123.23N	417.22E	15.0	16	2	1.84	0.005	0.0	0.0	0.0	
2	46.00	6118.16N	442.45E	15.0	16	2	1.25	0.005	44.6	10.2	0.0	
3	46.14	6118.55N	445.05E	15.0	16	2	1.24	0.005	28.5	5.4	0.0	
			444.92E	15.0	16	2	1.24	0.005	26.8	5.3	0.0	
							depth freed:	icd=				
4	46.03	6118.66N	450.90E	1.0	16	3	0.84	0.005	32.6	6.1	12.7	
5	46.02	6118.58N	451.00E	0.2	16	3	0.81	5.120	2.6	0.6	1.4	
6	46.02	6118.57N	451.03E	0.0	16	3	0.81	20.480	0.7	0.2	0.4	
7	46.02	6118.56N	451.03E	0.0	16	2	0.81	0.005	0.0	0.0	0.0	
8	46.18	6118.11N	452.41E	0.0	16	2	0.79	0.005	14.6	3.1	0.0	
9	46.21	6118.08N	452.72E	0.0	16	2	0.79	0.005	13.8	3.0	0.0	
10	46.21	6118.07N	452.78E	0.0	16	2	0.79	0.005	13.7	3.0	0.0	

Initially the phases have been read as P and S. In this case the location program will simply find the fastest phases for the corresponding distance and the phases used by the program are identified. For the nearest station (SUE) the phase is Pg and then we get PN2 and PN4. This means refracted phases from layer 2 and 4 respectively. Layer 4 also corresponds to the Moho interface so PN4 is the same as Pn. Table 5.9 also shows that 10 iterations are needed before the change becomes smaller than the limit set by the program. The program first iterates with the depth fixed to the starting depth and when a stable solution has been obtained (in this case after 3 iterations) it continues with the depth also being a variable. A depth of 0 km is not reasonable for an earthquake in this area and the option could be to fix it to e.g. 15 km. However, let us first look at bit closer at the phase identification. There is a large residual for station SUE. Since it is unlikely that the depth of a local earthquake is 0 km, this might be caused by a wrong depth due to bad phase identification of stations further away or a wrong model. The depth could be fixed, but first lets us look at the phase identification at stations further away. In the example, the S-phase on station ODD1 has a large positive residual. Since it is unlikely that the depth of a local earthquake is 0 km, this might be caused by a wrong depth due to bad phase identification of stations further away or a wrong model. The depth could be fixed, but first lets us look at the phase identification at stations further away. In the example, the S-phase on station ODD1 has a large positive residual. Considering the distance (185 km) this seems reasonable for first arrivals and observing the small amplitude P on the ODD1 seismogram (Fig. 5.16), the P seems likely to be a Pn. However, a similar small Sn would not be seen in the P-coda and the large phases read as S is more likely to be Sg or Lg.

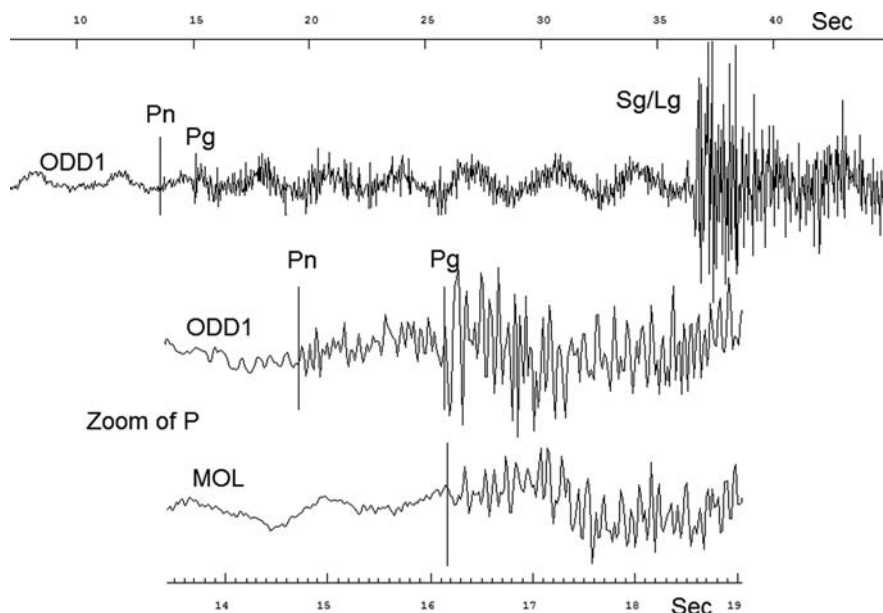


Fig. 5.16 Seismogram of a local earthquake. The *top* shows the signal from station ODD1 and the *bottom* two traces, a zoom around the P for stations ODD1 and MOL which both have an epicentral distance of about 200 km. All traces are unfiltered vertical SP channels. The data is from Western Norway and the origin time is 1996 0705 02:20. Magnitude is $M_L = 1.8$

Changing the phase to Lg results in a significantly better fit for ODD1, the RMS has been reduced and the depth is now more reasonable at 6 km (still a bit shallow for the area) (Table 5.10).

Table 5.10 Location of event in Table 5.9 with new phase identification on ODD1 now using Lg instead of S. For abbreviations, see Table 5.9

date	hrmn	sec	lat	long	depth	no	m	rms	damp	erln	erlt	erdp	I
stn	dist	azm	ain	w	phas	calcphs	hrmn	tsec	t-obs	t-cal	res	wt	di
<hr/>													
SUE	27	194.5	101.9	0	P	PG	220	51.5	5.21	4.47	0.74	1.00	5
..... Stations not shown													
ASK	93	169.3	93.5	0	S	SG	221	12.4	26.02	26.16	-0.14	1.00	3
BER	104	166.3	70.0	0	S	SN2	221	15.2	28.84	29.22	-0.39	1.00	5
BER	104	166.3	70.0	0	P	PN2	221	2.3	15.99	16.80	-0.81	1.00	1
EGD	115	170.7	70.0	0	P	PN2	221	4.1	17.80	18.49	-0.69	1.00	1
EGD	115	170.7	70.0	0	S	SN2	221	18.3	31.97	32.18	-0.21	1.00	5
ODD1	181	147.5	50.4	0	P	PN4	221	13.6	27.27	27.41	-0.15	1.00	3
ODD1	181	147.5	0.0	0	LG	Lg	221	36.9	50.53	50.29	0.23	1.00	6
MOL	199	43.3	50.4	0	P	PN4	221	16.2	29.83	29.63	0.19	1.00	5
MOL	199	43.3	50.4	0	S	SN4	221	39.1	52.76	51.56	1.19	1.00	14
<hr/>													
1996	7	5	0220	46.3	tL*	61.293	4.887	5.7	TES	8	0.7		1.9LNAA

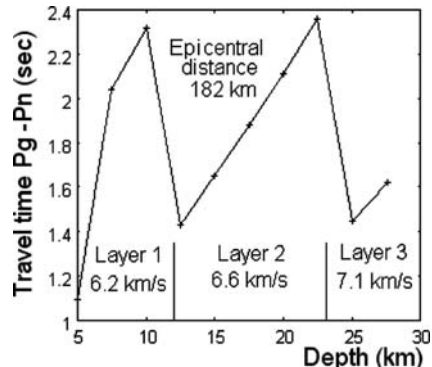
On the seismogram for ODD1, there is a first small phase identified as Pn and a larger phase 1.3 s later. This is most likely Pg. On the seismogram for MOL, at a similar distance (198 km) where we don't see two phases (maybe a hint of a Pn) and the first phase might be Pg and the Pn is lost in the noise. As for ODD1, the S-phase is most likely Lg or Sg. Making these changes again reduces the RMS and the depth now comes out reasonably at 16 km and the residuals at the nearest station SUE is "reasonable" (Table 5.11)

Table 5.11 Location of event in Table 5.9 with new phase identification on MOL now using Pg and Sg instead of P and S. For abbreviations, see Table 5.9

date	hrmn	sec	lat	long	depth	no	m	rms	damp	erln	erlt	erdp	i
stn	dist	azm	ain	w	phas	calcphs	hrmn	tsec	t-obs	t-cal	res	wt	di
<hr/>													
SUE	30	190.3	3113.4	0	P	PG	220	51.5	5.72	5.39	0.32	1.00	5
SUE	30	190.3	3113.4	0	S	SG	220	55.7	9.84	9.39	0.45	1.00	12
FOO	32	17.4	1111.4	0	P	PG	220	51.6	5.77	5.72	0.05	1.00	6
..... Stations not shown													
BER	108	165.9	93.1	0	P	PG	221	2.3	16.50	16.99	-0.49	1.00	1
EGD	119	170.3	55.1	0	P	PN4	221	4.1	18.31	18.60	-0.29	1.00	6
EGD	119	170.3	55.1	0	S	SN4	221	18.3	32.48	32.37	0.11	1.00	13
ODD1	185	147.6	55.1	0	P	PN4	221	13.6	27.78	26.84	0.94	1.00	5
ODD1	185	147.6	0.0	0	LG	Lg	221	36.9	51.04	51.26	-0.22	1.00	7
ODD1	185	147.6	91.6	4	Pg	PG	221	15.0	29.20	28.67	0.53	0.00	0
MOL	198	44.2	91.4	0	PG	PG	221	16.2	30.34	30.69	-0.35	1.00	3
MOL	198	44.2	91.4	0	SG	SG	221	39.1	53.27	53.40	-0.13	1.00	8

Finally, it can be tested if the second phase on ODD1 is Pg. From Table 5.12 it is seen that neither Pg or Pn fits very well at ODD1. This could be caused by the model since it is known that the Moho depth is larger under ODD1 than what is used in the location. On the other hand, the Pg–Pn travel time is not a continuous function and very sensitive to the exact depth (Fig. 5.14) and for this case the exact travel times have been calculated, see Fig. 5.17.

Fig. 5.17 The travel time Pg–Pn as a function of depth for station ODD1 with location as shown in Table 5.12



In this case the observed travel time difference between Pg and Pn was 1.4 s which can fit several depths of which the determined 16 km is not far off.

Table 5.12 Location of event in Table 5.9 with new phase identification on ODD1 now using Pg instead of P. For abbreviations, see Table 5.9

date	hrmn	sec	lat	long	depth	no	m	rms	damp	erln	erlt	erdp	i	
96 7 5	220	45.89	6119.24N	4	51.7E	15.2	17	3	0.39	0.000	8.7	1.9	7.5	
<hr/>														
stn	dist	azm	ain	w	phas	calcp	phs	hrmn	tsec	t-obs	t-cal	res	wt	di
SUE	30	190.6111.5	0	P	PG			220	51.5	5.66	5.33	0.33	1.00	4
<hr/>														
Stations not shown														
ODD1	184	147.6	55.1	0	P	PN4		221	13.6	27.72	26.91	0.82	1.00	18
ODD1	184	147.6	0.0	0	LG	Lg		221	36.9	50.98	51.22	-0.24	1.00	6
ODD1	184	147.6	91.2	0	Pg	PG		221	15.0	29.14	28.65	0.50	1.00	0
MOL	198	44.2	91.1	0	PG	PG		221	16.2	30.28	30.68	-0.40	1.00	4
MOL	198	44.2	91.1	0	SG	SG		221	39.1	53.21	53.39	-0.17	1.00	8

The solution obtained here is not unique, however the example illustrates some of the possibilities of using different phases for local and regional earthquakes and it also illustrates how sensitive the depth is to phase selection when using all data. An alternative, as mentioned earlier, is to use only the nearest stations (Table 5.13) to get a reliable solution. This gives a much better fit and the depth now moves down to 22 km, which is probably more correct than 16 km.

Table 5.13 Location of event in Table 5.9 with only stations within 100 km distance. For abbreviations, see Table 5.9

date	hrmn	sec	lat	long	depth	no	m	rms	damp	erln	erlt	erdp	i	
96 7 5	220	45.38	6119.97N	4	49.0E	22.3	8	3	0.16	0.000	7.7	1.8	3.1	
<hr/>														
stn	dist	azm	ain	w	phas	calcp	phs	hrmn	tsec	t-obs	t-cal	res	wt	di
SUE	31	185.6123.4	0	P	PG			220	51.5	6.17	5.97	0.20	1.00	5
SUE	31	185.6123.4	0	S	SG			220	55.7	10.29	10.39	-0.10	1.00	23
FOO	32	22.1122.5	0	P	PG			220	51.6	6.22	6.10	0.13	1.00	9
FOO	32	22.1122.5	0	S	SG			220	55.9	10.50	10.61	-0.11	1.00	16
HYA	76	103.7	68.4	0	P	PN3		220	57.7	12.35	12.25	0.10	1.00	4
HYA	76	103.7	68.4	0	S	SN3		221	6.7	21.28	21.31	-0.03	1.00	23
ASK	98	167.6	68.4	0	P	PN3		221	0.5	15.10	15.43	-0.33	1.00	10
ASK	98	167.6	68.4	0	S	SN3		221	12.4	26.98	26.84	0.14	1.00	11

We can check this fit by the output of the minimum RMS test, see Table 5.14. As it is seen, the RMS increases in all direction at 5 km distance from the hypocenter. This is of course no guarantee that there are no local minima at other locations, however it gives an indication of the reliability of the inversion.

Table 5.14 Minimum RMS test. This is the change in RMS relative to the hypocenter when the hypocenter is moved a distance d up, down east and west. Abbreviations are: DRMS: Change in RMS, lon: Longitude, lat: Latitude and pos indicates that all RMS values are larger than the RMS value at the hypocenter. In this case $d=5$ km. Example from HYPOCENTER

DRMS:	lon+d	lon-d	lat+d	lat-d	depth-d	depth+d
DRMS pos	0.29	0.25	0.58	0.59	0.25	0.19

At some observatories, it is the practice to label most local phases Pg, Pb or Pn and similarly for S. Without calculation and knowledge of distance and/or apparent velocity and local knowledge, it can be very difficult and misleading to give local phases an a priori identification. Due to the model, there might not be any clear distinction between Pg and refracted phases and the first arrival might be from a diving wave. Lg waves might not be observed due to the local structure as e.g. in the North Sea (Kennett et al., 1985).

Guidelines for identifying phases of local and regional earthquakes

- In general only use first arrivals and label them P and S.
- If a first arrival P is refracted, S observations are likely to be Sg or Lg unless clear Sn and Sg are seen.
- In noisy conditions, a first Pn might not be seen and the first observed phase could be Pg.
- Only use both Pg and Pn and Sn and Sg if very clear.

5.6.3 Starting Location

Iterative location programs commonly start at a point near the station recording the first arrival. This is good enough for most cases, particularly when the station coverage is good and the epicenter is near or within the network. However, this can also lead to problems when using least squares techniques, which converge slowly or sometimes not at all for events outside the limits of a regional network (Buland, 1976). Another possibility is that the solution converges to a local minimum, which might be far from the correct solution. For small-elongated networks, two potential solutions may exist at equal distance from the long axis. A starting location close to the first arrival station can then bias the final solution to the corresponding side of such a network. Although this bias usually is on the correct side, any systematic error in the first-arrival station's time can have a disproportionately large effect on the final location. Thus in many cases, it is desirable to use a better starting location than the nearest station. There are several possibilities:

- (a) The analyst may know from experience the approximate location and can then manually give a start location. Most programs have this option.
- (b) Similar phases at different stations can be used to determine the apparent velocity and back azimuth of a plane wave using linear regression on the arrival times with respect to the horizontal station coordinates. With the apparent velocity and/or S-P times, an estimate of the start location can be made. This method is particularly useful when locating events far away from the network (regionally or globally).
- (c) Back azimuth information is frequently available from 3-component stations or seismic arrays and can be used as under b.
- (d) If back azimuth observations are available from different stations, a starting epicenter can be determined by calculating the intersection of all back azimuth observations (see Fig. 5.4).
- (e) S-P and the circle method can be used with pairs of stations to get an initial location.
- (f) A coarse grid search is a simple method sometimes used.
- (g) The Wadati approach can be used to determine a starting origin time.

The starting depth is usually a fixed parameter and set to the most likely depth for the region. For local earthquakes usually the depth range 10–20 km is used, while for distant events, the starting depth is often set to 33 km. If depth phases like e.g., pP are available for distant events, these phases can be used to set or fix the depth (see next section and earlier).

Figure 5.18 and Table 5.15 show an example of a global location using 4–14 stations where both problems of starting locations and hypocentral depth are illustrated.

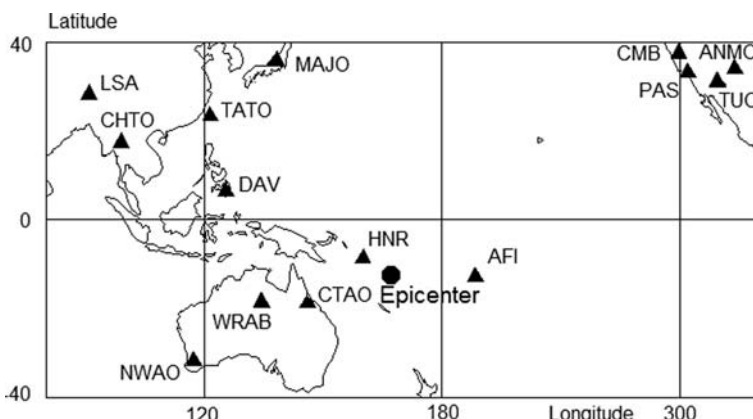


Fig. 5.18 Location of 14 stations and epicenter (calculated by PDE) used for the example in Table 5.15. The origin time of the event is 1996 0610 01:04 and $M_w=6.7$ (PDE)

Table 5.15 Locating the event shown in Fig. 5.19 under different conditions. The table gives the PDE location for comparison. The locations are made by Hypocenter. Abbreviations are: t_0 : Origin time (s), Lat: Latitude (degrees), Long: Longitude (degrees), h: Depth (km), elat; Error estimate in latitude (km), elon: Error estimate in longitude (km) and eh: Error estimate in depth (km). A * means error > 1,000 km. For “Location conditions”, see text

Location conditions	t_0	Lat	Long	h	rms	elat	elon	eh
PDE	47	-13.48	167.13	200				
14 P, all stations	48	-13.52	167.19	198	0.7	17	10	19
14 P+S at HNR, all stations	49	-13.63	167.24	210	0.9	20	13	23
4 P, stations far away	24	-13.53	167.38	0	0.1	9	11	121
4 P, 3 stations far, 1 near	54	-13.50	167.03	258	0.0	6	9	22
4 P California	10	-14.11	163.49	15	0.3	*	*	*
4 P+pP California	35	-13.75	163.97	198	0.3	350	874	9
4 P+pP California, P NWAO	48	-13.26	166.95	199	0.3	226	156	8

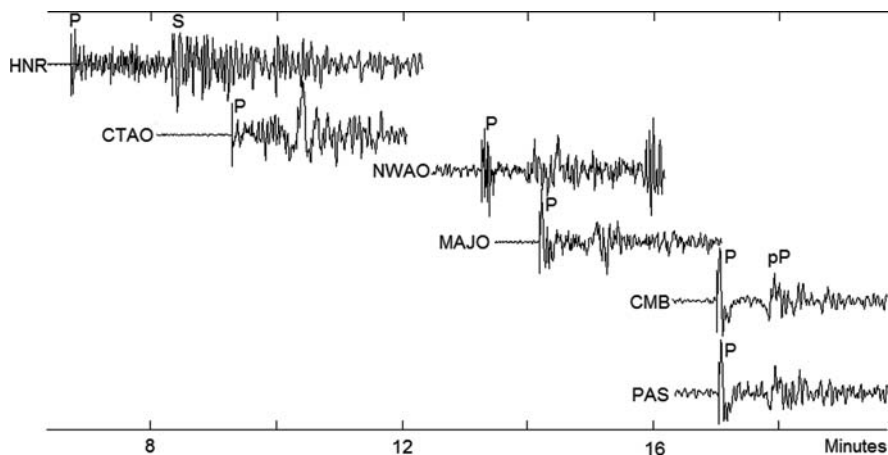


Fig. 5.19 Seismograms of the event used for testing global location (Table 5.17, Fig. 5.18). All stations are broadband Z. The phases pP (and also sP) are seen on most of the stations, but only indicated for the station used (CMB)

Originally this event was located with more than 300 stations. 14 stations have been selected for testing relocation. The model used is the IASP91.

14 stations using only P: The location is well constrained (Table 5.15) and the depth is also well determined since there are both near and far stations. The location is close to the “correct” location and the error estimate is of the order of the difference in location between the PDE solution and the 14 station solution. Any starting location works.

14 stations using P and S at station HNR: The S does not improve the solution, rather the opposite since for this nearest station, S has a disproportional large weight.

This is also the distance at which the travel time is the most uncertain due to possible local inhomogeneities. Any starting location works.

4 stations far away (CHTO, NWAO, MAJO, CMB) using P: The azimuth control is good so the location is quite close to PDE, but there is little depth control, due to the distances, so the depth is wrong (zero), which also affects the epicenter. The event cannot be located using nearest station nor using the apparent velocity estimation and a manual starting location must be used. Notice how the origin time has been traded off versus the depth (see also next example).

4 stations (CTAO, NWAO, MAJO, CMB), 3 far away and one near using P: Although CTAO is not the nearest station, it still has sufficiently different travel time derivative (angle of incidence) to be much better able to constrain the solution and now both depth and origin time are much closer to the PDE than the previous case with 4 stations far away. With only 4 stations and 4 unknowns, the location is critically dependent on accurate readings. E.g. changing the arrival time for CTAO by 1 s, will change the depth by 45 km. Any starting location works.

4 stations close to each other but far away (California: CMB, PAS, ANMO, TUC) using P: In this case, with all stations on one side far away, there is little distance and depth control since both distance and depth can be traded off versus origin time. It is seen that the direction to the event is close to being correct, while the distance is off by about 400 km and the origin time is off by more than 30 s. Although there are 4 stations and 4 unknowns, the depth is restricted to 0–700 km so a perfect fit cannot be made and the RMS is 0.3 s and not close to 0 as in the previous two 4-station cases and error estimates are not realistic (error > 1,000 km). Nearest station does not work as starting location, so azimuth and apparent velocity is used. Notice that the 4 stations in California can almost be considered a seismic array.

4 stations close to each other but far away (California: CMB, PAS, ANMO, TUC) and pP on CMB: The depth control can be improved by reading just one pP (Fig. 5.19). The depth is now correct and the trade off of depth versus origin time has reduced the origin time error to 12 s. However, the distance is still as bad as the previous case due to the use of the one sided array. The error estimate for depth is reasonable while the estimate for latitude and longitude are too large despite the small rms. However, they do indicate correctly that the error in longitude is larger than the error in latitude. Any starting location can be used.

4 stations in California (CMB, PAS, ANMO, TUC), one station opposite (NWAO), using P and one station (CMB) using pP: The distance control can be obtained by reading an S or adding one station on the other side of the event. In this case P from station NWAO has been added. The location is now back to the correct area with correct origin time. The error estimates, except for depth are too large. The nearest station cannot be used for starting location (event iterates to Africa!), while the azimuth derived from apparent velocity works.

Points to consider for global locations:

- It is possible to locate globally with few stations, whether the stations are globally or locally distributed. Best results with a global distribution.
- Starting location is essential when using few stations.

- Depth is only reliable if pP, sP can be read or phases from near stations are available.
- With few stations, error estimates can be misleading.

5.6.4 Identification of P for Teleseismic Events

A first arriving P phase can be P, Pdif or PKP. When reading phases and reporting to ISC, most stations will just report P and the correct identification will then be done by the ISC. Most location programs will assume that the P is the first arriving P for the particular distance and might not re-identify the phase to anything other than the first arrival. Unfortunately this is not always correct. Pdif arrives before PKP (see 2.13), however it often has so small amplitude that the first phase seen is PKP. Additionally there are several possibilities for PKP. If the location is made with few stations, the phase identification will affect the location and vice versa. It is therefore important, for phase arrivals beyond the shadow zone, that the phase is identified. One simple tool for identifying the different PKP phases (and also other phases) is to measure the apparent velocity. This can be done with a regional network or an array, see Chapter 9 for examples.

5.6.5 Outliers and Weighting Schemes

The largest residuals have disproportionately large influence on the fit of the arrival times due to the commonly used least squares fit. Most location programs will have some kind of residual weighting scheme in which observations with large residuals are given lower or even no weight. Bisquare weighting is often used for teleseismic events (Anderson, 1982). This weighting is calculated using the spread s which is defined as

$$s = A \times \text{median} \{ |r_i| \} \quad (5.32)$$

where $A = 1/0.6745$. Since for some data s can be close to zero (resulting in down-weighting of good phases, see (5.34)) s is not allowed to be smaller than s_{\min} , a parameter set by the user, and s is redefined as

$$s = \max (A \times \text{median} \{ |r_i| \}, s_{\min}) \quad (5.33)$$

The residual weight is then calculated as

$$w = \left(1 - \left(\frac{r_i}{s \times c} \right)^2 \right)^2 \text{ if } r_i/(sc) < 1 \\ w = 0 \quad \text{if} \quad r_i/(sc) \geq 1 \quad (5.34)$$

where $c = 4.685$. If the residual is small, no down weighting is done, while large residuals will have weight close to zero.

The residual weighting works very well if the residuals are not extreme since the residual weighting can only be used after a few iterations so that the residuals are close to the final ones. Individual large residuals can often lead to completely wrong solutions, even when 90% of the data are good, and residual weighting will not help in these cases. Some programs will try to scan the data for gross errors (like minute errors) before starting the iterative procedure. If an event has large residuals, try to look for obvious outliers. A Wadati diagram can often help in spotting bad readings for local earthquakes (see Fig. 5.5).

The arrival-time observations will by default always have different weights in the inversion. A simple case is that S-waves may have larger weights than P-waves due to their lower velocities. An extreme case is the T-wave (a guided waves in the ocean, see Chapter 2), which with its low velocity (1.5 km/s) can completely dominate the solution. Considering, that the accuracy of the picks is probably best for the P-waves, it should therefore be natural that P-arrivals should have more importance than S-arrivals in the location. However, the default parameter setting in most location programs is to leave the original weights unless the user actively changes them. Table 5.9 illustrates how the S-phases have almost twice as much importance as the P-phases. It is normally possible to give “a priori” lower weight for all S-phases and in addition, all phases can be given individual weights, including being totally weighted out.

5.6.6 Timing Errors

Seismic stations are critically dependent on correct time. Unfortunately, even today with GPS timing, stations can occasionally experience timing problems, which can have a large influence on earthquake location. In many cases the operator knows about the timing error and can weight out the readings. Even with a timing error, differential readings can be used (like pS-S, Pg-Pn, P-PP). Large timing errors are often easy to spot, particularly when many stations are available, while smaller errors (a few seconds) can be much harder to find since the error tends to spread out over all residuals, see below and Table 5.16.

5.6.7 Example of Outlier and Timing Problems

Table 5.16 shows an example of a well behaved event with a reliable location. Adding a 1 min error to one of the stations (ITB) creates large residuals at all stations although station ITB has the largest residual. This illustrates how an outlier can change all the residuals.

With the plot of the data available, the bad station is easy to spot. Even without the waveform data, it is clear that ITB is the anomalous station with a large positive

Table 5.16 Location of a small event in the local Tanzanian network. The origin time is given in the table. The abbreviations are: hrmn: Hour and minute of origin time, sec: Second of origin time, lat: latitude in degrees and minutes, long: Longitude in degrees and minute, no: number of phases, m: degrees of freedom, damp: damping, erln, erlt and errdp: Error estimates (km) of longitude, latitude and depth respectively, stn: Station code, dist: Epicentral distance in km, azm: Azimuth from event to station, ain: Angle of incidence at the source, w: user given weight of phase (0: full weight, 1: .75, 2: 0.5, 3: 0.2 4: 0, 9: differential), phase: User given phase, calcphs: Phase used by program, hrmn: Hour minute of phase, tsec: Seconds of phase, t-obs: Observed travel time, t-cal: Calculated travel time, res: Residual (s) = t-obs-t-cal, wt: Weight used by program (0-1) and di: % importance of each observation in the solution

Original location														
	date	hrmn	sec	lat	long	depth	no	m	rms	damp	erln	erlt	errdp	i
stn	dist	azm	ain	w	phas	calcphs	hrmn	tsec	t-obs	t-cal	res	wt	di	
PDH	15	111.3135.9	0	S	SG	1250	35.0	6.43	6.42	0.01	1.00*19			
PDH	15	111.3135.9	0	P	PG	1250	32.4	3.74	3.69	0.05	1.00*11			
ITK	37	280.4110.9	0	P	PG	1250	35.2	6.59	6.73	-0.14	0.99*10			
ITK	37	280.4110.9	0	S	SG	1250	40.3	11.65	11.71	-0.06	0.99*21			
TDM	55	223.2102.7	0	P	PG	1250	38.3	9.71	9.51	0.19	0.99* 2			
TDM	55	223.2102.7	0	S	SG	1250	45.3	16.64	16.55	0.08	0.99*17			
ITB	55	171.8102.4	0	P	PG	1250	38.3	9.66	9.54	0.12	0.99* 3			
ITB	55	171.8102.4	0	S	SG	1250	45.0	16.35	16.59	-0.25	0.99*18			
Location with 1 minute error at station ITB														
	date	hrmn	sec	lat	long	depth	no	m	rms	damp	erln	erlt	errdp	
stn	dist	azm	ain	w	phas	calcphs	hrmn	tsec	t-obs	t-cal	res	wt	di	
ITK	36	170.5	92.5	0	P	PG	1250	35.2	-0.70	6.15	-6.85	1.00* 8		
ITK	36	170.5	92.5	0	S	SG	1250	40.3	4.36	10.69	-6.34	1.00*12		
PDH	74	130.4	91.1	0	S	SG	1250	35.0	-0.86	21.85	-22.71	0.99*26		
PDH	74	130.4	91.1	0	P	PG	1250	32.4	-3.55	12.56	-16.11	0.99*14		
TDM	83	176.7	91.1	0	S	SG	1250	45.3	9.38	24.39	-15.01	0.99*15		
TDM	83	176.7	91.1	0	P	PG	1250	38.3	2.42	14.01	-11.60	0.99*11		
ITB	109	152.7	72.1	0	P	PN2	1251	38.3	62.37	18.55	43.82	0.98* 5		
ITB	109	152.7	72.1	0	S	SN2	1251	45.0	69.06	32.28	36.78	0.98*10		
Location when using only P-S arrival time of station ITB leaving 1 min error														
	date	hrmn	sec	lat	long	depth	no	m	rms	damp	erln	erlt	errdp	
stn	dist	azm	ain	w	phas	calcphs	hrmn	tsec	t-obs	t-cal	res	wt	di	
PDH	16	110.1129.5	0	S	SG	1250	35.0	6.15	6.09	0.05	1.00*21			
PDH	16	110.1129.5	0	P	PG	1250	32.4	3.46	3.50	-0.04	1.00*10			
ITK	36	280.8106.7	0	P	PG	1250	35.2	6.31	6.52	-0.21	0.99* 8			
ITK	36	280.8106.7	0	S	SG	1250	40.3	11.37	11.34	0.03	0.99*22			
TDM	55	222.8	99.2	0	S	SG	1250	45.3	16.39	16.28	0.10	0.99*17		
TDM	55	222.8	99.2	0	P	PG	1250	38.3	9.43	9.36	0.07	0.99*11		
ITB	55	171.1	98.7	9	P	PG	1251	38.3	69.38	9.46	59.91	0.00 0		
ITB	55	171.1	98.7	0	S	S -P			6.7	7.0	-0.31	0.99*11		
Location with 1 timing error of 1 s on ITB (1 sec added)														
	date	hrmn	sec	lat	long	depth	no	m	rms	damp	erln	erlt	errdp	
stn	dist	azm	ain	w	phas	calcphs	hrmn	tsec	t-obs	t-cal	res	wt	di	
PDH	17	111.8118.6	0	S	SG	1250	35.0	5.79	5.74	0.05	1.00*20			
PDH	17	111.8118.6	0	P	PG	1250	32.4	3.10	3.30	-0.20	1.00*11			
ITK	35	279.6	72.1	0	P	PN2	1250	35.2	5.95	6.16	-0.21	0.99*11		
ITK	35	279.6	72.1	0	S	SN2	1250	40.3	11.01	10.72	0.29	0.99*21		
TDM	54	221.2	72.1	0	P	PN2	1250	38.3	9.07	9.28	-0.22	0.99* 2		
TDM	54	221.2	72.1	0	S	SN2	1250	45.3	16.00	16.15	-0.15	0.99*17		
ITB	56	170.1	72.1	0	P	PN2	1250	39.3	10.02	9.59	0.43	0.99* 2		
ITB	56	170.1	72.1	0	S	SN2	1250	46.0	16.71	16.69	0.02	0.99*17		

residual which is offset by negative residuals on the other stations. The error can also be found using a Wadati diagram. Another method is to compare the time difference between the stations with the distance between the stations and from Table 5.16 it is obvious that ITB is the station with the error since with such a small network there cannot be such a large arrival time difference between ITB and the other stations. If the error is not exactly one minute, it might be a timing error. This means that the absolute time cannot be used, however the S-P time can be used as shown in Table 5.16. The residual for P now gives a very good estimate of the timing error, while S-P indicates the residual in S-P time. Other differential times can also be used like Pg–Pn etc. Most location programs (global and local) have options for using differential travel times. Finally, residual weighting could have been used to find the error, however, in general, residual weighting is not recommended for local earthquakes as it significantly reduces the domain of convergence of the least squares inversion.

If the timing error is smaller, it is much harder to find. In the table, the last example shows the location with a 1 s timing error on ITB. All stations now have similar residuals and it is in practice almost impossible to detect that ITB has this timing error without other information, however a Wadati diagram would spot the error.

When working with local earthquakes, the nearest stations will usually provide the most accurate information due to the clarity of the phases. In addition, uncertainty in the local model has less influence on the results at short distances than at larger distances; this is particularly true for the depth estimate. It is therefore desirable to put more weight on data from near stations than on those from distant stations and this is usually done by using a distance weighting function of

$$w_d = \frac{x_{far} - \Delta}{x_{far} - x_{near}} \quad (5.35)$$

where Δ is the epicentral distance, x_{near} is the distance to which full weight is used and x_{far} is the distance where the weight is set to zero (or reduced). The constants x_{near} and x_{far} are adjusted to fit the size of the network. x_{near} should be about the diameter of the network, and x_{far} about twice x_{near} . For a dense network, x_{near} and x_{far} might be made even smaller to obtain more accurate solutions. Table 5.13 shows an example of an improved location by using only stations within 100 km for the epicenter and below there is an example of using a very local network.

Distance weighting is not used for teleseismic locations since the global travel time tables have no particular distance bias and clarity of phases is not distance dependent.

Figure 5.20 shows an example of an event which has been recorded by very local stations as well as stations and arrays up to 800 km away. The model used is the standard Norwegian model with a Moho depth of 31 km, which is mostly appropriate for coastal areas, where also most earthquakes and stations are located in Norway like in this example. Locating with all stations and all station minus the 3 nearest give very similar epicenters (Table 5.17), however the depth is zero,

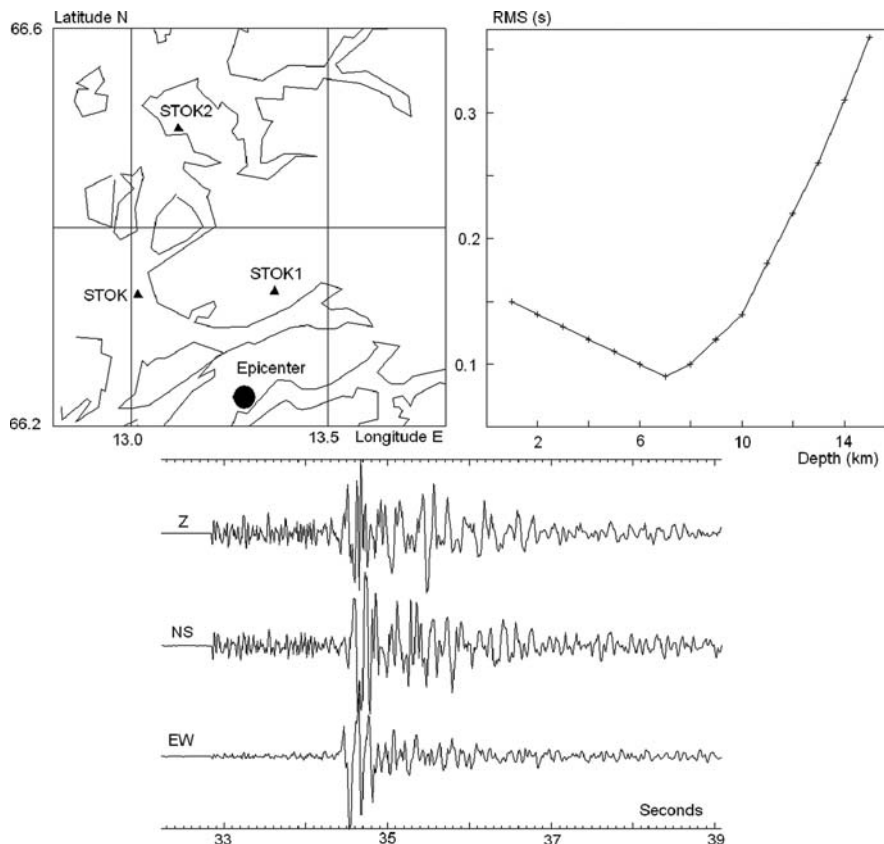


Fig. 5.20 Location of a local event. *Top left:* Three stations used for location. *Top right:* RMS as a function of depth using the 3 stations shown. *Bottom:* Seismogram from the nearest station STOK1. The event origin time is 2006 1220 03:28 and $M_L = 2.2$

which is unrealistic for an earthquake. The seismogram has clear P and S arrivals with a particularly strong EW S- arrival indicating a “deep” event considering the epicentral distance. The RMS versus depth clearly shows a minimum at 7 km which is also the depth calculated when locating with the 3 nearest stations (Table 5.17).

This example clearly shows that in general, hypocentral depths are not to be trusted for local earthquakes unless only local stations are used. Mixing local and regional stations will make the depth unreliable due to strong influence of stations farther away coupled with model inhomogeneities and only a very careful selection of phases coupled with a very reliable local model can avoid this, see also examples in Table 5.8, 5.9, 5.10, 5.11, 5.12, and 5.13. Likewise the epicenter using only the local stations will be the most accurate.

Considering the dimension of the small network, the error estimates seem too large. The reading accuracy of P and S are better than 0.05 s, however the RMS is

Table 5.17 Comparison of the location of an event located with very local stations and regional stations and a combination of local and regional stations. Units are degree for latitude and longitude, seconds for RMS, and km for errors (err). Nearest 3 means the 3 stations shown in Fig. 5.20. “+error means adding 0.1 s error to the readings, shift is shift in km relative to solution with nearest 3 and “minus S” means locating without the S from station STOK1. Location is done with HYPOCENTER

	Origin	Latitude	Err	Longitude	Err	Depth	Err	RMS
All stations	31.9	66.270	4	13.225	12	0.0	9	1.2
Nearest 3 stations	30.5	66.232	5	13.297	9	7.1	9	0.09
Nearest 3+error	30.4	66.228	9	13.303	13	7.0	14	0.15
Shift		0.4		0.3		0.1		
Nearest 3 minus S	30.8	66.261	1	13.297	1	9.2	1	0.02
Shift		0.4		3.3		2.1		
All minus nearest 3	32.4	66.255	5.9	13.416	24	0.0	13	1.2

0.1s so local inhomogeneities or an inaccurate model must have some influence to make the residuals relatively large and consequently making a large error estimate. Intuitively one would expect an error around 1 km. A simple test is adding errors to the readings. Table 5.17 show the shift obtained when adding random 0.1 s errors to the readings. The resulting shift in hypocenter is less than 1 km. Note that the new RMS has not increased to 0.2 s since the shift in the hypocenter and origin time partly accommodates the errors. Another test is to remove one S-reading. This gives a significant shift, however since RMS is smaller, error estimates are now of the order of 1 km. Obviously the location with three S-readings will give a more reliable hypocenter, particularly since the event is a bit outside the network. For other events in the same area, RMS is routinely of the order 0.02 s and the error estimates are also all less than 1 km.

Recommendation when local data is available:

- Locate with the local network only, however, read as many phases as possible as that data is useful, e.g. for tomographic studies.
- Fix the location to the local solution when stations further away are included.
- Be aware that error estimates are very sensitive to residual size and might give very wrong estimate of the real errors.

5.7 Software

There are numerous location programs in use and most are free standing, however in some cases also tightly integrated with the general processing software like HYPOCENTER in SEISAN. Most programs are made for local events. The following gives a short overview of the most used programs in routine processing and we will thus not describe special programs like e.g. for double difference location.

HYP071: The program determines hypocenter, magnitude, and first motion pattern of local earthquakes, and was first released in 1971. This program was the first generally available location program for local earthquakes and has been very widely used due to an early free distribution and a good manual. A lot of data is available in HYP071 format and the program is still quite popular program. For more information, see Lee and Valdez (2003) and Lee and Lahr (1975).

HYPOINVERSE: HYPOINVERSE2000 determines earthquake locations and magnitudes from seismic network data like first-arrival P and S arrival times, amplitudes and coda durations. The present version HYPOINVERSE2000 is in routine use by several large networks and observatories. It is the standard location program supplied with the Earthworm seismic acquisition and processing system (see Johnson et al., 1995) and has thus gotten wide use. Multiple crustal models can be used to cover different regions, and either flat layer or flat layer with linear velocity gradients can be used. For more details, see Klein (2003).

HYPOCENTER is a general purpose location program using a flat layered earth for local earthquakes and the IASP91 travel time tables for global location. HYPOCENTER can use nearly all seismic phases and azimuth of arrival and calculates most magnitudes. It is the main program used in SEISAN for earthquake location and magnitude determination. For more information see Lienert and Havskov (1995).

HYPELLIPSE is a computer program for determining the hypocenters of local or near regional earthquakes and for each event the ellipsoid that encloses the 68% confidence volume. Travel times are determined from a horizontally-layered velocity-structure, from a linear increase of velocity with depth, from a linear increase of velocity over a halfspace, or from a previously generated travel-time table. With the travel-time-table option, gradients are allowed in all layers, but there can be no velocity discontinuities. Arrival times for the first arrival of P waves and S waves, and S-minus-P interval times can be used in the solutions. Arrival times for refractions, such as Pn, even at distances where they do not arrive first, can also be used. Each arrival can be weighted according to the reading clarity, the epicentral distance to the station, and the deviation of its residual from the mean. The magnitude of each event is calculated from the maximum amplitude and/or the signal duration. The program includes a station history database, so that magnitudes will always be computed with the correct response function and gain. First motions can be plotted on the printer using an equal-area, lower-hemisphere, focal projection. The azimuth and apparent velocity of a plane wave crossing the array from a distant source can also be determined. The above description is mainly from <http://pubs.usgs.gov/of/1999/ofr-99-0023/chap1.pdf>. New feature of HYPELLIPSE is the ability to work in areas with large topographic relief, for more information, see Lahr and Snoke (2003).

HYPOSAT: Schweitzer (2001) developed an enhanced routine to locate both local/regional and teleseismic events, called HYPOSAT. The program runs with global earth models and user defined horizontally layered local or regional models. It provides best possible hypocenter estimates of seismic sources by using besides the usual input parameters such as arrival times of first and later onsets (implemented by back azimuth and ray parameters in case of array data or polarization

analyses) also travel-time differences between the various observed phases. If S observations are also available, preliminary origin times are estimated by using the Wadati approach and a starting epicenter with a priori uncertainties by calculating the intersection of all back azimuth observations.

ISCLOC: The ISC is making available source code for a flexible earthquake location program, which is used in day-to-day processing at the ISC. As provided, the program implements the algorithms used at the ISC for phase re-identification, residual calculation using Jeffreys-Bullen travel time tables. It includes routines that calculate depth phase depth and body-wave and surface-wave magnitudes in the way that they have been calculated at the ISC. In addition to current ISC procedures a function is provided for applying a crustal correction to travel times using the 2×2 degree global crustal model made available by Gabi Laski (<http://igppweb.ucsd.edu/~gabi/crust2.html>). All of this functionality is implemented in a modular way so that to change methods it is only necessary to replace the discrete subprograms concerned.

The basic purpose of ISCLOC is to give the best possible source time and location for a seismic event given the arrival data available. This is done using Geiger's method, taking an existing hypocenter as a starting point and iterating to reduce travel time residuals for as many phases as possible. At the moment P and S residuals are used but other phases could be added if desired. A feature of this program is the ability to automatically try different hypocenters as a starting point if the first choice does not result in convergence to a solution. The hypocenters input for an event are ranked in order of their suitability as starting points by a simple algorithm and will be tried in this order unless the operator specifies which starting point to use. If a solution is found for an event body wave and surface wave magnitudes are calculated if suitable amplitude data is available and a depth phase depth is calculated if enough pP phases are reported. Data is input and output from the program as ISF bulletin format text files. The program is fully configurable with all required constants stored in a non-compiled parameter file.

The above description is from <http://www.isc.ac.uk/doc/code/iscloc/> from where the software is also available.

5.8 Exercises

Exercise 5.1 Read local seismic phases and make a Wadati diagram

Figure 5.21 shows a seismogram with traces of some stations. Read the P and S-arrival times for all stations, assume all to be first arrivals (just P and S).

- Make a table of the readings.
- Make a Wadati diagram to determine if the readings are reasonable. Put station names on the plot.
- One of the stations probably has a timing problem (on the plot, the point representing the station is off the line). Which station? How much is the error?

- Determine v_p/v_s , is it reasonable?
- Determine the origin time from the Wadati diagram.

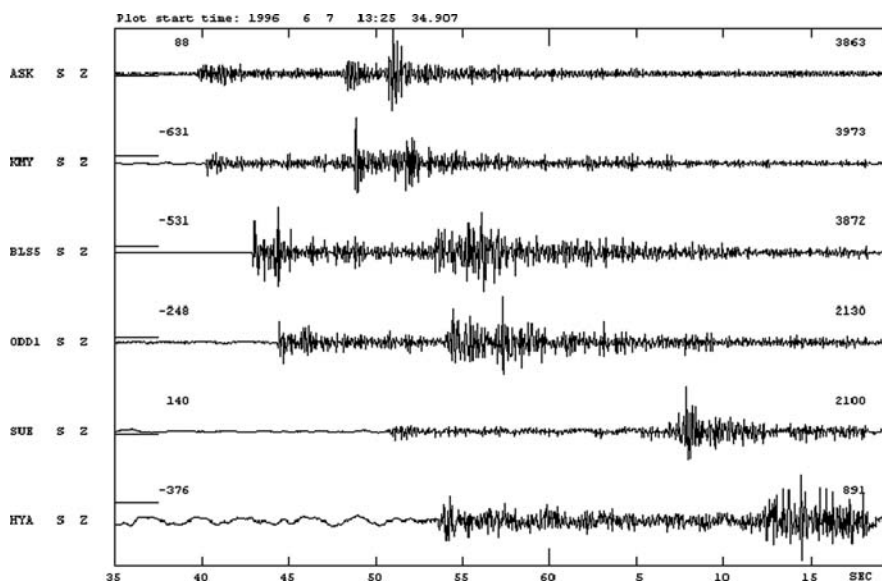


Fig. 5.21 A seismogram of a local earthquake in Western Norway. The numbers above the traces to the right is the maximum count and the numbers to the left are the DC values (count)

Exercise 5.2 Manual location using S-P times

Use the arrival times read for the local event in Exercise 5.1.

- Assuming a P-wave velocity of 7.0 km/s and $v_p/v_s = 1.73$, determine the distance to each station using only first arrivals and the S-P arrival times.
- Locate the earthquake by drawing circles, the station map is found in Fig. 5.22. Give the latitude and longitude of the epicenter.
- Evaluate the error in the epicenter location.
- Will the clock problem found for one of the stations in Exercise 5.1 affect the solution?

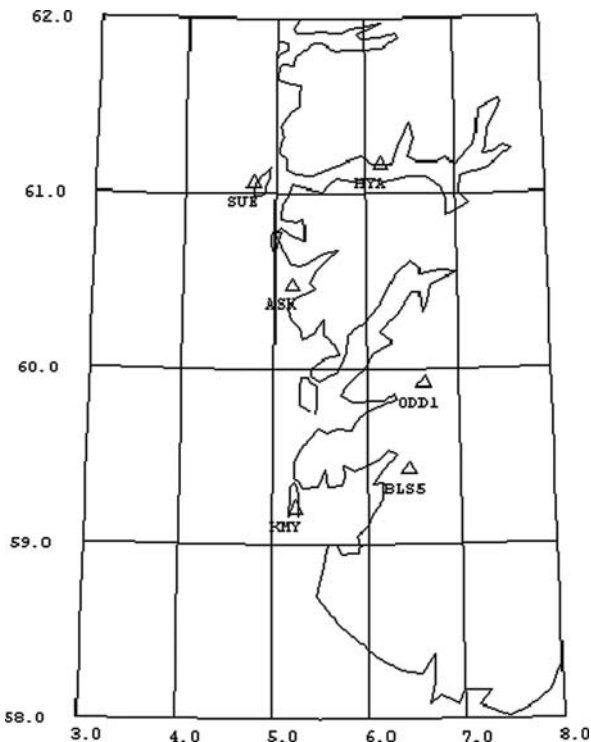
Exercise 5.3 Manual location using origin time and P - arrival time

The origin time was determined in Exercise 5.1

- Using a P-velocity of 7.0 km/s, calculate the epicentral distances from the origin time and the P arrival time. How do they compare to the distances calculated in Exercise 5.2?
- Locate the earthquake as above, how does the location compare to the location in Exercise 5.2?

- Will the clock problem found for one of the stations in Exercise 5.1 affect the solution?

Fig. 5.22 Station map.
Location of some of the stations in Western Norway.
The map has the same scale in y and x and the scale can be determined knowing that one degree latitude is 111.2 km



Exercise 5.4 Three component location

The purpose of this exercise is to determine the epicenter and depth of an earthquake using only one station. Figure 5.23 shows a seismogram with an amplified view of the P-waves at station BRVK

- Read the amplitudes of the first swing on the P-waves and determine back azimuth using (5.4).
- Identify the S- phase, read S-P time and determine distance using (5.12).
- Determined the P-travel time from Fig 5.13.
- Using Fig. 5.24, determine the epicenter. BRVK is at position 53.1°N and 70.3°E .
- From the seismogram, identify the pP phase and read pP-P time. Determine the hypocentral depth from Table 5.7.
- Compare result to data found in international bulletins.

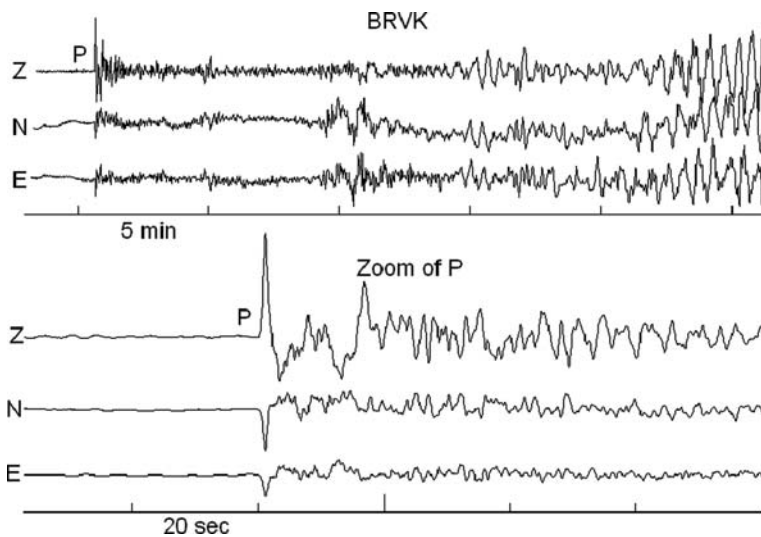


Fig. 5.23 Top: Seismogram of a large ($m_b=6.2$) earthquake at station BRVK. Bottom: A zoom of the P-phase. Note the amplitude scale is the same on the 3 zoomed traces. Origin time: 2007 1002 18:00

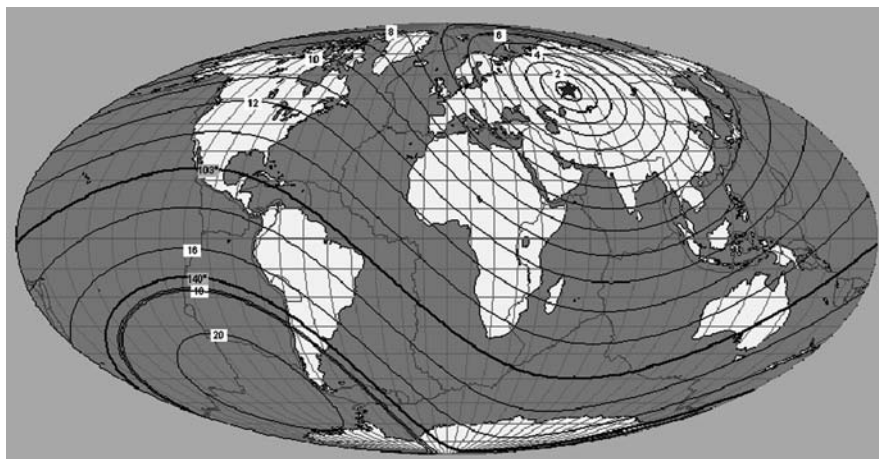
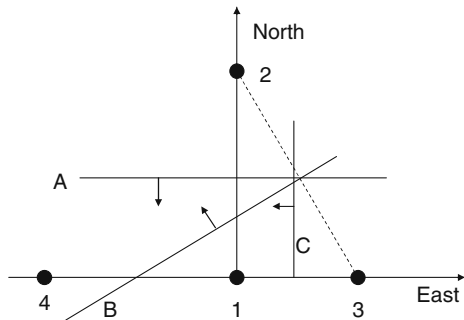


Fig. 5.24 Station BRVK is marked by a star. The great circles indicate P-travel time in minutes from the station. Note, the back azimuth from BRVK can only be measured off approximately on the figure

Exercise 5.5 Location by arrival time order

By just knowing the order of the arrival times to the different stations, it is possible to get an estimate of the epicenter. Figure 5.25 illustrates the principle. The arrival time order is indicated on the figure. When comparing two stations, it is assumed

Fig. 5.25 Location by arrival time order. The arrival times order to the stations (black dots) are given as numbers 1–4 which also is the station numbers. The lines A, B and C are the normal lines in the middle of the lines connecting the stations



that the station with the first arriving phase is located in the same half of the world as the event. Line A is bisecting the line between station 1 and 2 and since the waves arrive at station 1 before station 2, the epicenter must be south of line A as indicated by the arrow. Similarly, lines B and C can be constructed and with 3 stations, the epicenter must be between lines A and B to the west.

- Knowing that the signals arrive last at station 4, find the area in which the epicenter is located.

The assumption of bisecting the distance between the stations is only valid for a constant velocity model and the method can be refined by using real velocity models. With many stations, a quite accurate epicenter can be obtained, see e.g. Anderson (1981).

Computer exercises

- Wadati diagram.
- v_p/v_s in a region.
- Locate locally.
- Locate globally.
- Locate with combination of phases.
- One station location.

Chapter 6

Magnitude

Magnitudes of earthquakes are calculated with the objectives to:

- Express energy release to estimate the potential damage after an earthquake.
- Express physical size of the earthquake.
- Predict ground motion and seismic hazard.

Calculating magnitude is thus a basic and essential task of any seismological network, globally as well as locally. When an earthquake occurs, the first question from the press is about the “Richter magnitude” and the second about location. There are several different magnitude scales in use and, depending on the network and distance to the event, one or several may be used. Most magnitude scales are based on an amplitude measure, mostly in the time domain, but spectral estimates are gaining more widespread use. Due to local variation in attenuation and ground motion site amplification as well as of the station position with respect to the source radiation pattern, large variations in the measured amplitudes might occur, leading to large variance in magnitude estimates at individual stations. Thus, magnitude calculation is not an exact science and in the first hours following an earthquake, the magnitude is often revised several times.

Different magnitude scales are suited for different distance and magnitude size. For global earthquakes at larger distance ($>20^\circ$), magnitude scales have fixed internationally agreed upon parameters, while at local and regional distances the parameters of the magnitude scales will have regional variation due to differences in local attenuation and geometrical spreading. We will therefore also illustrate how to adjust local magnitude scales to the local conditions.

The most general definition of magnitude M is

$$M = \log(A/T)_{\max} + Q(\Delta, h) \quad (6.1)$$

where A is the amplitude of ground displacement which yield together with its related period T the largest ratio A/T , and Q is a distance correction function for the epicentral distance Δ and hypocentral depth h . Since we measure the maximum A/T , proportional to velocity, the magnitude is a measure of energy. Ideally we should then only have one magnitude scale of the form (6.1). However the practice over many years has been to measure A/T on particular instruments leading to different

forms of (6.1) in different frequency bands corresponding to different instruments. This also means that mostly the maximum A is measured instead of maximum A/T . This problem is largely avoided when analyzing unfiltered modern broadband records that are proportional to ground motion velocity V in a very wide range of periods. This allows to measure directly $(A/T)_{\max} = V_{\max}/2\pi$ and has allowed to define new global standards for measuring broadband body- and surface-wave magnitudes (NMSOP, Bormann and Saul, 2008; Bormann et al., 2009). Magnitudes range from less than 0 for very small earthquakes to more than 9 for the largest. We will classify earthquakes according to magnitude as shown in Table 6.1.

Table 6.1 Earthquake size classification by magnitude

Size classification	Magnitude
Great	$M > 8$
Large	$M = 6-8$
Medium	$M = 4-6$
Small	$M = 2-4$
Micro	$M < 2$

In the following the most common traditional magnitude scales as well as the new global measurement standards recommended by the IASPEI (2005) will be discussed.

- Local magnitude M_L for events with magnitude less than 6–7 and distances less than 1,500 km. Frequency band 1–20 Hz.
- Coda magnitude M_c for events with magnitude less than 5 and distance less than 1,500 km.
- Body wave magnitude m_b for teleseismic events of magnitudes less than 7 and distances 20°–100°. Frequency around 1 Hz and >0.3 Hz.
- Broadband body-wave magnitude m_b in agreement with the original definition by Gutenberg and Richter (1956) measuring V_{\max} and its associated period T in a wide period range between 0.2 and 30 s in the same distance range as for m_b . New IASPEI standard.
- Surface wave magnitude M_s for teleseismic events of magnitude up to 8 and distances 20–160°. Period 18–22 s.
- Broadband surface-wave magnitude M_s measuring V_{\max} of shallow seismic events (source depth < 60 km) and its associated period T in a wide range of periods (between 2 s and 60 s) and distances (2–160°) for magnitudes between 4 < $M_s(\text{BB})$ < 9. New IASPEI standard.
- Moment magnitude M_w for any earthquake at any distance.

The distance and magnitude ranges mentioned here are not absolute values, however they are based on common practice. Note that the regional distance range 1,000–2,000 km is particularly difficult to cover reliably with magnitude estimates because of the strong influence of crustal and upper mantle structures

and inhomogeneities. Therefore, neither magnitude scales for local or global earthquakes, with the exception of M_S (BB) and M_w , work well at distances 1,000–2,000 km.

A very serious problem with all magnitude scales mentioned above, except M_w , is magnitude saturation. This means that above a certain magnitude, depending on the magnitude scale, its value no longer increases when the size or energy of the earthquake increases (see Chapter 8 for more information).

A very detailed presentation on the use of different magnitude scales, their benefits and limitations, is given in NMSOP, as well as in several recent review and special publications (Bormann and Saul, 2008, 2009a; Bormann et al., 2009). The IASPEI Commission on Observation and Interpretation has come out with new guidelines, approved by IASPEI (2005), for magnitude determination which will be referenced in the following. These guidelines have lately seen some revision to the naming conventions (not yet published, Dewey (2010), personal communication) which will be followed in this book.

6.1 Amplitude and Period Measurements

Several magnitude scales use the maximum amplitude and often the corresponding period. There are two ways of measuring this (Fig. 6.1):

- Read the amplitude from the base line and the period from two peaks. However this might be difficult, at least when done manually, due to the location of the base line.
- Read the maximum peak-to-adjacent-trough amplitude and divide by 2. This is the most common and IASPEI (2005) recommended practice. It is also the simplest to do both manually and automatically. The period can be read either from two peaks or as half the period from the two extremes. This method will also to some extent average out large variation in the amplitude since it is not certain that one large swing is representative for the maximum amplitude.

The peak to peak method will generally result in a smaller value than the zero to peak. Most display programs will automatically display the maximum amplitude zero to peak (simply the largest number in the offset corrected trace) and for simplicity, unless otherwise noted, this number will be displayed in the following plots.

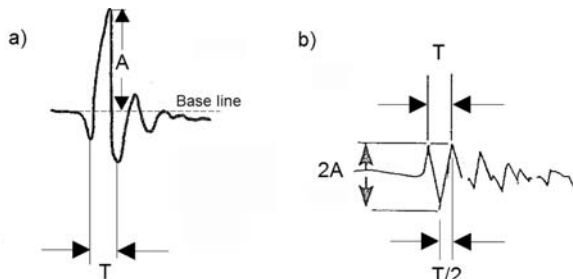


Fig. 6.1 Reading amplitudes.
a) Reading the amplitude A from the base line and the period T from two peaks b)
Reading the amplitude peak to peak ($2A$). Copyright granted by IASPEI. Figure modified from NMSOP, Chapter 3

6.2 Local Magnitude M_L

The first magnitude scale was defined by Richter (1935) for Southern California. All other magnitude scales are related to this scale. The local magnitude M_L is defined as

$$M_L = \log(A) + Q_d(\Delta) \quad (6.2)$$

where A is the maximum amplitude on a Wood-Anderson seismogram (which measures displacement for $f > 2$ Hz), $Q_d(\Delta)$ is a distance correction function and Δ is epicentral distance. The distance correction function, as originally defined for California, is given in Table 6.2. Note that this magnitude scale has no defined frequency dependence.

Table 6.2 Distance correction term $Q_d(\Delta)$ for magnitudes M_L according to Richter (1958). The distance is in km and the correction values assume that the amplitude is measured in mm on a Wood-Anderson horizontal seismograph

Δ	Q_d	Δ	Q_d	Δ	Q_d	Δ	Q_d
0	1.4	90	3.0	260	3.8	440	4.6
10	1.5	100	3.0	280	3.9	460	4.6
20	1.7	120	3.1	300	4.0	480	4.7
30	2.1	140	3.2	320	4.1	500	4.7
40	2.4	160	3.3	340	4.2	520	4.8
50	2.6	180	3.4	360	4.3	540	4.8
60	2.8	200	3.5	380	4.4	560	4.9
70	2.8	220	3.6	400	4.5	580	4.9
80	2.9	240	3.7	420	4.5	600	4.9

It was originally assumed that the gain of the Wood-Anderson seismograph was 2,800. However, it is now recognized that the most likely gain is $2,080 \pm 60$ (Uhrhammer and Collins, 1990). The original short period (SP) Wood-Anderson seismograph (damping 0.8 and natural frequency 1.25 Hz) measured displacement linearly above about 2 Hz and the maximum amplitude was measured as some kind of average (see NMSOP for a discussion) of the amplitudes on the two horizontal components. In order to anchor the scale to some particular number, a magnitude 3 earthquake at 100 km distance was defined to have maximum amplitude of 1 mm on the seismogram. Thus in Table 6.2, the correction term is 3.0 for a distance of 100 km.

In order to use the M_L scale with other instruments than the Wood-Anderson seismometer, the common practice is to generate a displacement trace in the frequency band 2–20 Hz and measure the maximum amplitude. To do it most accurately, the exact response of the Wood-Anderson seismograph should be used, see Table 6.3.

A high pass 2 pole Butterworth filter at 2.0 Hz will approximate the response to within 0.1 magnitude unit.

While, strictly speaking, horizontal components should be used to measure the amplitude, the practice is often to use the vertical component. Experience has shown

Table 6.3 Poles and zeros for the Wood-Anderson response. It is assumed that the free period is 1.25 Hz and the damping is 0.8

Poles, real and imaginary		Zeros, real and imaginary	
-6.283	-4.712	0.0	0.0
-6.283	4.712	0.0	0.0

that on a rock site, the maximum amplitudes on vertical and horizontal components are similar (e.g. Alsaker et al., 1991; Bindi et al., 2005), although there can be small differences (e.g. Siddiqqi and Atkinson, 2002). On soil, horizontal amplitudes are significantly higher than vertical amplitudes due to soil amplification (see Chapter 8). Thus using the vertical component instead of the horizontal components will give more consistent estimates of M_L among stations located on different ground conditions. Alternatively, station corrections can be used to compensate for the site conditions when using horizontal components.

The original M_L scale for California was defined for shallow earthquakes, and the distance correction used the epicentral distance. Since the maximum amplitude usually occurs in the S-waves (and not surface waves), there is no reason to limit the M_L scale to shallow earthquakes since it is simply just a case of replacing the epicentral distance with the hypocentral distance, as also recommended by IASPEI. For a local earthquake, the S-wave amplitude A as a function of hypocentral distance r can be expressed as

$$A(r) = A_0 r^{-\beta} e^{\frac{-\pi f r}{vQ}} \quad (6.3)$$

where A_0 is the initial amplitude at distance 1, β is the geometrical spreading (1 for body waves and 0.5 for surface waves), f is the frequency, v the S-wave velocity and Q the quality factor inversely proportional to the anelastic attenuation. Taking the logarithm gives

$$\log(A(r)) = -\beta \log(r) - 0.43 \frac{\pi f r}{vQ} + \log(A_0) \quad (6.4)$$

We can therefore see that the distance attenuation term is

$$Q_d(\Delta) = -\beta \log(r) - 2.3 \frac{\pi f r}{vQ} \quad (6.5)$$

Assuming a constant f , the M_L scale can then be written as

$$M_L = \log(A) + a \log(r) + br + c \quad (6.6)$$

where a , b and c are constants representing geometrical spreading, attenuation and the base level respectively. We would expect a to be near one assuming body wave spreading and b to be small since it is due to anelastic attenuation ($b = 0.004$ for

$Q = 100$, $f = 1$, and $v = 3.5$ km/s). This is also the case for most M_L -scales, see Table 6.4. The parameter c is then adjusted to anchor the scale to the original definition. The parameters a , b and c can be expected to have regional variation and should ideally be adjusted to the local conditions, see Section 6.14.2 below.

The M_L scale for Southern California has later been improved since it turned out that the distance correction term was not correct at shorter distances (Hutton and Boore, 1987). The modified scale is now the recommended IASPEI (2005) standard:

$$M_L = \log(A) + 1.11 \log(r) + 0.00189 r - 2.09 \quad (6.7)$$

The maximum amplitude A is measured on a ground displacement trace (nm) which has been filtered with the Wood-Anderson response. Thus for frequencies < 2 Hz,

Table 6.4 Parameters a , b and c (equation (6.7)) of the M_L scale at different localities. All parameters are calculated to be used with equation (6.7) and under the assumption of a Wood-Anderson instrument gain of 2,080. Under Dist 50 and 300 km respectively, the magnitudes are calculated for a ground motion of 1,000 nm and at the respective distances

Region	a	b	C	Dist. range (km)	M_L at dist. 50 km	M_L at dist. 300 km	Reference
S. California	1.11	0.00189	-2.09	10–700	2.9	4.2	Hutton and Boore (1987)
C. California	1.00	0.00301	-1.99	0–400	2.9	4.2	Bakun and Joyner (1984)
The Great Basin	1.00	0.0069	-2.38	0–90	2.7	(5.2)	Chávez and Priestley (1985)
Western USA	0.83	0.0026	-1.58	90–600	3.0	4.3	Chávez and Priestley (1985)
Albania	1.66	0.0008	-3.12	10–600	2.7	4.2	Muco and Minga (1991)
Central Europe	1.11	0.00095	-2.00	10–1000	2.9	4.0	Stange (2006)
Norway	0.91	0.00087	-1.68	0–1500	2.9	3.8	Alsaker et al. (1991)
Tanzania	0.776	0.000902	-1.66	0–1000	2.7	3.5	Langston et al. (1998)
S. Australia	1.10	0.0013	-1.99	40–700	2.9	4.1	Greenhalgh and Singh (1986)
N. Italy	1.0	0.0054	-2.22	10–300	2.7	4.9	Bindi et al. (2005)
NW Turkey	1.0	0.00152	-1.61	62–110	3.2	4.3	Baumbach et al. (2003)
Ethiopia	1.20	0.00107	-2.17	200–600	2.9	4.1	Keir et al. (2006)

A will be smaller than the true ground motion. The scale is still anchored to the original definition at 100 km. However, another anchor point at 17 km has also been defined making it easier to adjust the scale to other regions with a significant different attenuation. This means that all M_L scales should give the same magnitude at 17 km, but might be different at 100 km. Inserting an amplitude of $(10^6 \text{ nm})/2,080$ and a distance of 100 km in (6.7), gives a magnitude of 3.0. At 17 km distance and an amplitude of 1 mm on the Wood-Anderson seismogram will give magnitude 2. Equation (6.7) is the IASPEI recommendation for M_L for regions with similar attenuation as California (using horizontal components). For other regions an equation of the same form as (6.7) is recommended, with the coefficients adjusted for the local conditions, and using vertical or horizontal components.

Table 6.4 shows the M_L scale for different regions around the world. M_L scales are presented in many different ways, sometimes with a reference distance built in and sometimes in true ground motion and often in amplitude on a Wood-Anderson seismogram. This can be very confusing and it appears as if the scales have different forms when in reality they have similar parameters. In Table 6.4 they are all presented as given in (6.7).

From the table it is seen that the M_L scales for very different regions give similar magnitudes at 50 km and in most cases also at 300 km except in the case for the relation from The Great Basin, which supposedly is only valid up to 90 km. Also the relation from N. Italy seems to overestimate the magnitude at 300 km. Later in Section 6.14.2, it will be shown how to adjust the M_L scale for a local network, however it seems that, at least for shorter distances, the original Hutton and Boore scale gives a consistent estimate of M_L for many regions.

In order to use M_L , the maximum amplitudes MUST be read on traces which simulate the Wood-Anderson response which can be approximated by using a 2 pole low cut Butterworth filter at 2.0 Hz. Some use the practice of reading amplitude and period on the raw trace and then correcting the amplitude using a response function table or curve for the particular instrument, manually or automatically. However, this might give a wrong value since the maximum amplitude might appear at different times on the raw and Wood-Anderson simulated traces. In addition, if the frequency of the signal is below the Wood-Anderson natural frequency, the ground amplitude will be too large since the filtering of the Wood-Anderson instrument is not included.

M_L for a large event: Figure 6.2 shows an example of calculating M_L for a large regional event recorded with the Mexican seismic network. It is seen that original velocity trace is more low frequency in nature and the Wood-Anderson simulation acts as a high-pass filter. The original trace is close to clipping (at about 8,000,000 count) and for stations closer to the event, clipping occurred. In that case acceleration records can be used so M_L can be calculated for large events at very close distances. According to the Wood-Anderson trace, the maximum ground motion was 0.3 mm. However, calculating the true ground displacement without the Wood-Anderson filter gives 3.3 mm, so the Wood-Anderson ground displacement does not give an accurate amplitude of the true ground displacement for such a large event and M_L is consequently too small (magnitude saturation, see more on this in Chapter 8).

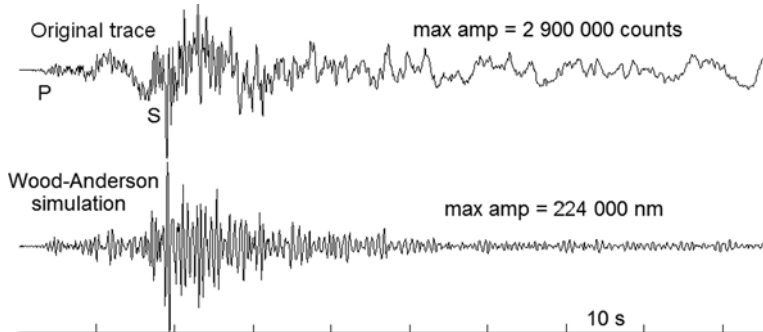


Fig. 6.2 Large regional event from the Mexican network, broadband station CAIG vertical component. The *top* trace shows the original velocity seismogram while the *bottom* trace is the simulated Wood-Anderson displacement trace. The origin time is 1996 0715 21:23. The event is shallow and the hypocentral distance is 107 km. M_L for this station at a hypocentral distance of 107 km was calculated to 6.4

M_L was calculated using the Hutton and Boore relation (6.7). The average M_L for the network was 5.9 using 7 stations in the distance range 100–600 km. ISC reported magnitudes $M_s = 6.7$ and $M_b = 5.7$. So M_L is underestimating the magnitude, as expected, due to magnitude saturation. However, it still gives a reasonable indication of the size of the event.

M_L for a medium magnitude event: The event shown in Fig. 6.3 reported a network M_L of 4.3 and M_L for HPK was calculated to 4.4. Notice the surface waves on the top trace which are filtered out on the bottom trace due to the Wood-Anderson filter. This event will later be used to calculate surface wave magnitude, see Fig. 6.20. This size event is well suited for obtaining M_L .

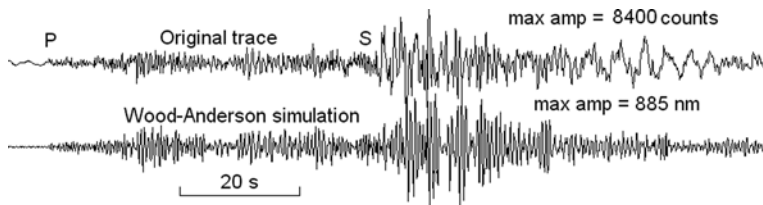


Fig. 6.3 Medium size local event from the UK. The broadband station is HPK, vertical channel. The *top* trace shows the original velocity seismogram while the *bottom* trace is the simulated Wood-Anderson displacement trace. Note the surface waves on the *top* trace. The event origin time is 2007 0428 07:18, epicentral distance is 370 km, the depth is 5.3 km and $M_L = 4.3$

M_L for a small magnitude event: Figure 6.4 shows the seismogram of a deep Venezuelan earthquake. Since the magnitude is small ($M_L = 3.1$), the original and the Wood-Anderson simulated traces are quite similar although the displacement Wood-Anderson trace clearly has a lower frequency content due to the integration from velocity to displacement.

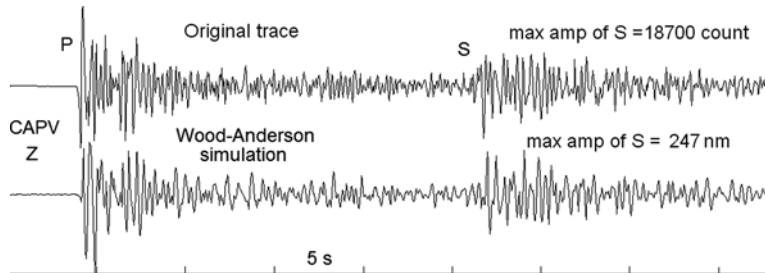


Fig. 6.4 Deep event from the Venezuelan seismic network, broadband station CAPV vertical channel. The origin time is 2003 1127 12:00, hypocentral distance 209 km and depth 154 km. M_L for this station was calculated to 3.1

Since this is a deep event, the P-waves have larger amplitude than the S-waves on the vertical component due to the near vertical incidence, however, the maximum amplitude is still read on the S-waves. It should be emphasized that the M_L scale is only defined for shallow events. For deep events, the attenuation and geometrical spreading will be different (see description in Chapter 8) and the distribution of energy between horizontal and vertical components will be sensitive to the angle of incidence. In principle the M_L scale can be used for deep earthquakes provided the parameters a , b and c have been adjusted to the local conditions.

For very small events and/or weak signals it might not be possible to see the earthquake signal on the Wood-Anderson simulated trace due to the microseismic background noise. A way to get around this problem is to measure the displacement amplitude in a more narrow frequency band. Figure 6.5 shows an example of calculating M_L for a small event. From the figure it is seen that the S-amplitude cannot be seen on the Wood-Anderson simulated trace. Using a filter of 2–20 Hz makes the S-phase visible, but it is still contaminated by the microseismic noise and it seems that the low cut of the filter must be above 3 Hz to remove the microseismic noise. Using low cut filters above 5 Hz reduces the amplitude indicating that energy is removed for the S-signal. So the conclusion is that the low cut of the filter should be just high enough as to remove the effect of the microseismic noise.

For information on how to determine M_L magnitude scale parameters, see Section 6.14.2.

Summary of procedure for M_L

- Calculate the displacement seismogram (nm) for the vertical component and multiply it with the Wood-Anderson filter. An additional low cut filter, typically an 8 pole filter at 1.25 Hz, will often have to be used for events with magnitude smaller than 2–3, see above.
- For very small events ($>$ magnitude 1.0), increase the lower frequency cut until the maximum displacement amplitude is clearly seen above the noise.

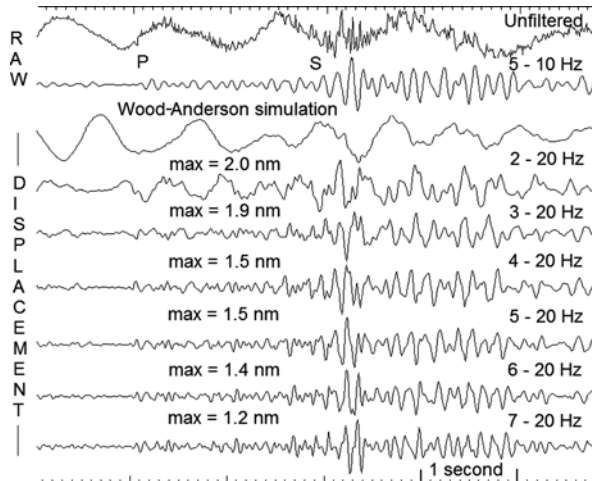


Fig. 6.5 Reading amplitude for M_L for a small event. The *top* trace shows the original raw signal and the next trace the same signal filtered. The third trace gives the Wood-Anderson simulated displacement signal. The following traces give displacement in different frequency bands (8 pole filters). The maximum amplitudes are given *above* the traces. The event is from station STOK, vertical component, the origin time is 2006 1129 00:17 and $M_L = -0.3$

- Read maximum amplitude on the vertical component.
- If an additional low cut filter has been used, the amplitude must be corrected for the gain of this filter.
- When reporting the observations, make sure the corresponding phase ID is reported as IAML.

6.3 Coda Magnitude M_c

The simplest magnitude to use for local earthquakes is the coda magnitude (also called duration magnitude). Coda waves are scattered waves radiating from the earthquake hypocenter and are the last signals to arrive, see Chapter 2. One common definition of the coda length (t_{coda}) is the total duration in seconds of the earthquake recording from the P to the end of the signal defined as the point where the S-coda signal is no longer seen above the noise. It is also possible to estimate magnitudes of large earthquakes at teleseismic distances using the P-coda length (Houston and Kanamori, 1986), however this is not a method used routinely. If the initial amplitude of the signal is larger (a larger earthquake magnitude), the coda length will also be larger as scattered waves from further away reach the station. The strongest amplitude of the earthquake signal is the S-waves (and L_g -waves), so it is the S-wave scattered energy that is observed at the end of the signal.

The decay of amplitude of the scattered signal is inversely proportional to the distance it has traveled. In other words, the theoretical amplitude of the scattered wave will be inversely proportional to the travel time t_c of the coda wave (time from origin time t_0 to end of coda wave arrival time t)

$$t_c = t - t_0 \quad (6.8)$$

and we should use t_c to measure the magnitude, which can be expected to only depend on t_c . The coda magnitude scale could then be expected to have the form

$$M_c = a \log(t_c) + c \quad (6.9)$$

where a and c are constants. This is illustrated in Fig. 6.6, where the coda amplitude is the same at the same time for the 2 stations. The coda length t_{coda} is traditionally measured from the P-arrival time t_p to the end of the signal

$$t_{coda} = t - t_p \quad (6.10)$$

By inserting t from (6.8) in (6.10) we then get

$$t_{coda} = t_c - (t_p - t_0) \quad (6.11)$$

The measured coda length t_{coda} is therefore too short compared to the coda travel time t_c . The further the station is away from the earthquake, the smaller becomes t_{coda} for the same event, since t_p increases approximately linearly with distance. To correct for the use of t_{coda} instead of t_c , a compensation must therefore be made for distance and we can expect the scale to have the form

$$M_c = a \log(t_{coda}) + br + c \quad (6.12)$$

where r is the hypocentral distance and b is a constant.

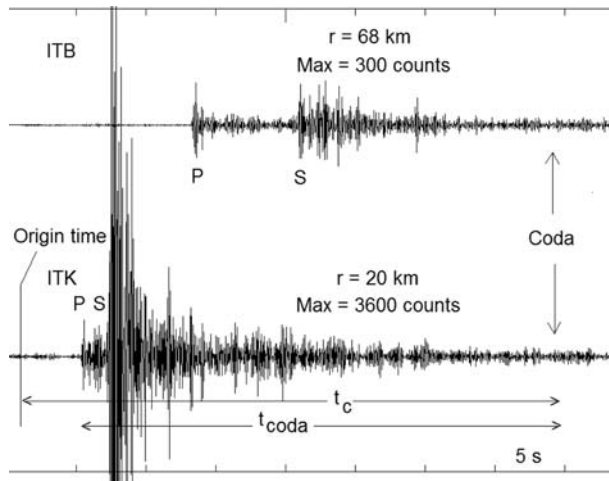


Fig. 6.6 Signals from two stations at different hypocentral distances r shown on plot. The amplitude scale on both seismograms is the same. The signals are filtered 5–10 Hz. The data is from a Tanzanian network. Origin time is 1992 1012 04:49 and $M_L = 1.5$. Notice the equal coda wave amplitude for the 2 stations at the same absolute time, which is what we would expect in an ideal case

The end of the coda indicated on the figure above is defined as the time where the coda amplitude reaches a particular absolute value. Other definitions are also used, see discussion later. For small coda lengths (< 10 s), event duration is not a stable measure of earthquake size since it does not measure energy backscattered from distant points (Aki and Chouet, 1975) and the same linear relation of the type (6.12) cannot be expected to be valid for both small and large events (e.g. Bakun and Lindh, 1977). Most coda wave magnitude relations are given for measured coda lengths larger than 30 s.

Coda magnitude scales are quite different for different regions of the world, partly because of actual differences in attenuation and scattering and partly because of local station conditions like noise level and not least different reading practice. Table 6.5 shows some relations from different regions.

Table 6.5 Coda relations for different areas of the world. The coda magnitude is calculated for a coda length of 100 s and distances of 50 and 300 km respectively

Region	a	b	c	Magnitude range	M_c at 50 km	M_c at 300 km	References
California	2.0	0.0035	-0.87	2–5	3.3	4.2	Lee et al. (1972)
Italy	2.49	0.0	-2.31	1.5–4.5	2.7	2.7	Castello et al. (2007)
E. USA	2.74	0.0	-3.38		2.1	2.1	Viret (1980)
California	0.71	0.0	0.28	0.5–1.5	1.7	1.7	Bakun and Lindh (1977)
Norway	3.16	0.0003	-4.28	1.5–5	2.1	2.1	Havskov and Sørensen (2006)
Mexico	2.40	0.00046	-1.59	3–6	3.2	3.3	Havskov and Macias (1983)
East Africa	1.9	0.0004	-1.2	3–5	2.6	2.7	Dindi et al. (1995)

Comparing the magnitude scales it is seen that the variation in parameters are much larger than seen for M_L . This is probably caused by different ways of measuring coda length combined with different noise levels, and less so different tectonics. Comparing M_c at a distance of 50 km, it is seen that Mexico gives a 1.1 magnitude unit higher magnitude than Norway. This large difference can only partly be explained by the expected difference in attenuation. The Mexican scale was measured on noisy analog records while the Norwegian scale was using low noise digital records so coda length would only for that reason be expected to be larger in Norway.

The magnitude scale by Lee et al. (1972) was one of the first well known M_c scales and used in many places where no local studies had been made. From Table 6.5, it is seen that it is also the scale giving the highest magnitudes and includes the largest distance correction term, so it is probably not a good scale for general use. If no scale has been calibrated for a given area, it is recommended to select a scale for a similar tectonic area.

The coda magnitude is rather discredited since there is no universal scale and the magnitude arbitrarily depends on how the analyst is picking the end of the signal (see below). However, if a scale properly calibrated to an amplitude base magnitude or M_w is available and the coda length observations are made in a systematic way,

the coda magnitude scale has the advantage of being quick and the accuracy is independent of instrument calibration. The scale is also not affected by signal clipping. The M_c scale additional has the advantage of being independent of the source radiation pattern due to the nature of the coda waves. However, the variation in coda magnitude estimation among stations is often larger than variation in M_L , see the example in Table 6.12.

The coda magnitudes critically depend on selecting the correct coda length. There is no well established definition but the most common manual practice is to read the end of the event when the signal level is similar to the noise level. This might be a bit arbitrary and another principle to define the end of the coda at the point where the coda wave amplitude is a given factor (e.g. 2) above the noise amplitude. This can be used in automatic coda length determination, but it is not very easy to use manually. The method also has the drawback that it will depend on the noise level. Below (Fig. 6.7) is an example from a station in the Norwegian National Seismic Network.

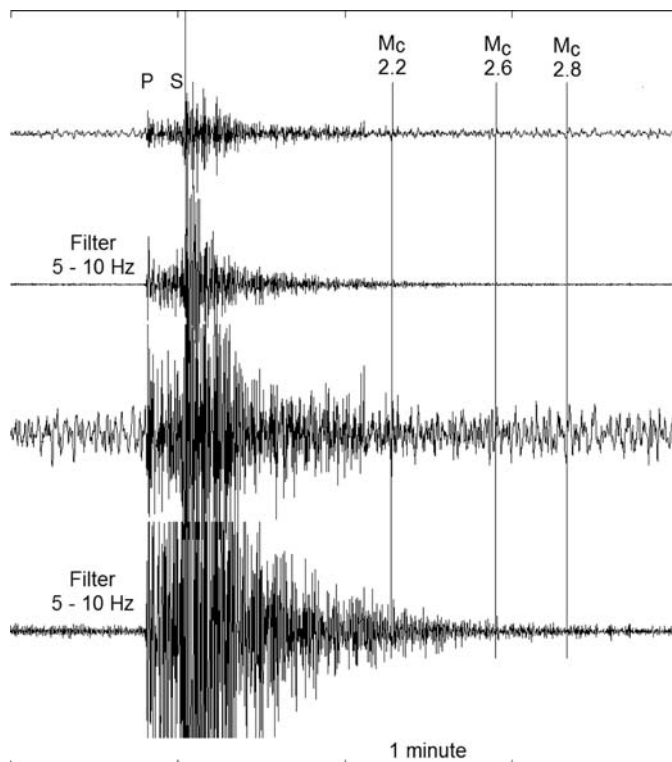


Fig. 6.7 A local event with $M_L = 2.8$ at an epicentral distance of 117 km. The *top* trace (unfiltered signal) shows 3 different locations where the coda has been read and the corresponding coda magnitudes M_c using the scale given in Table 6.5. The 2. trace shows the signal filtered 5–10 Hz, the 3. trace shows the unfiltered signal amplified and the 4. trace shows the signal filtered 5–10 Hz and amplified. The data is from station FOO and the origin time is 1996 0606 06:48

The example illustrates the influence of the coda length on the magnitude. On the top trace it is hard to see where the coda ends and that would be even more difficult with a larger initial amplitude since the end of the signal would appear as a straight line due to the scaling. This problem is not encountered on analog seismograms since the scaling is constant. On the unfiltered amplified signal, it looks like the coda length corresponding to $M_c = 2.6$ could be the end of the coda while on the filtered amplified signal, the coda length, corresponding to $M_c = 2.8$, seems more reasonable. This example illustrates the basic rules to read a reliable coda length.

The best method of measuring the coda length is to fix an absolute noise threshold according to the worst station in the worst noise conditions in the network (using a filter) and measure the end of the coda at this threshold which would be the same amplitude level at all stations (see Fig. 6.6). This would be a more consistent and reproducible defined coda duration than looking for the time when coda amplitudes get below the noise level in station records with varying noise amplitudes. However, this disregards local site effects.

For information on how to determine coda magnitude scale parameters, see Section 6.14.3.

Summary of procedure for M_c

- The signal must be filtered to avoid uneven influence of different background noise levels and different instrument types. Filtering only works if dominant noise frequencies are different from dominant signal frequencies.
- If the maximum amplitude is significantly higher than the background level of the noise, consistent manual reading of coda length requires appropriate scaling of both time and amplitude.
- Ideally, coda lengths should be measured with a fixed filter and a fixed amplitude threshold.

6.4 Body Wave Magnitude m_b

The m_b magnitude is one of the most widely used magnitudes for earthquakes recorded at teleseismic distances. The m_b magnitude is calculated from the maximum amplitude in the P-wave train recorded on a SP seismograph within the entire P-wave train before phase PP (see IASPEI recommendations). Earlier the practice was to measure only within the first few swings, see Bormann and Saul (2009). Note that occasionally the P-wave train of very strong earthquakes may extend even into the time after the first PP arrival. This may necessitate to extend the measurement time window into the PP range based on estimates of total rupture duration from high-frequency (e.g. WWSSN-SP or higher) filtered records (see Bormann and Saul, 2008). The m_b scale was developed from the original body wave magnitude m_B by Gutenberg (1945a) and Gutenberg and Richter (1956), which used instruments with a wider response than SP. For more on m_B , see below. Since many different response curves exist for SP seismographs, some standardization is needed. The measurement of amplitude for m_b in its current standard form was developed

when the WWSSN was in use with a standard SP response. To calculate a correct m_b , the amplitude must consequently be read on a seismogram simulating the standard WWSSN SP response (see Fig. 6.10) and is then corrected for the gain of the WWSSN SP response. This is in principle similar to having to read the amplitude for M_L on a simulated Wood-Anderson seismogram, however no gain correction was needed for M_L since the original M_L was defined as the maximum on the seismogram trace while m_b is the maximum ground displacement. The body wave magnitude scale is defined as

$$m_b = \log(A/T) + Q(\Delta, h) \quad (6.13)$$

where A is the maximum amplitude in nm or μm (depending on which Q -function is used, see later), T the period and Q the attenuation function as a function of epicentral distance Δ and hypocentral depth h . The epicentral distance should be in the range 20–100°. The attenuation function recommended by IASPEI is the original attenuation function developed by Gutenberg and Richter (1956) for P-waves recorded on vertical seismographs, see Fig. 6.8. This function is today used by the ISC and the USGS.

A more recent attenuation function developed with SP recordings of mainly explosions was made by Veith and Clawson (1972), see Fig. 6.9. This function is

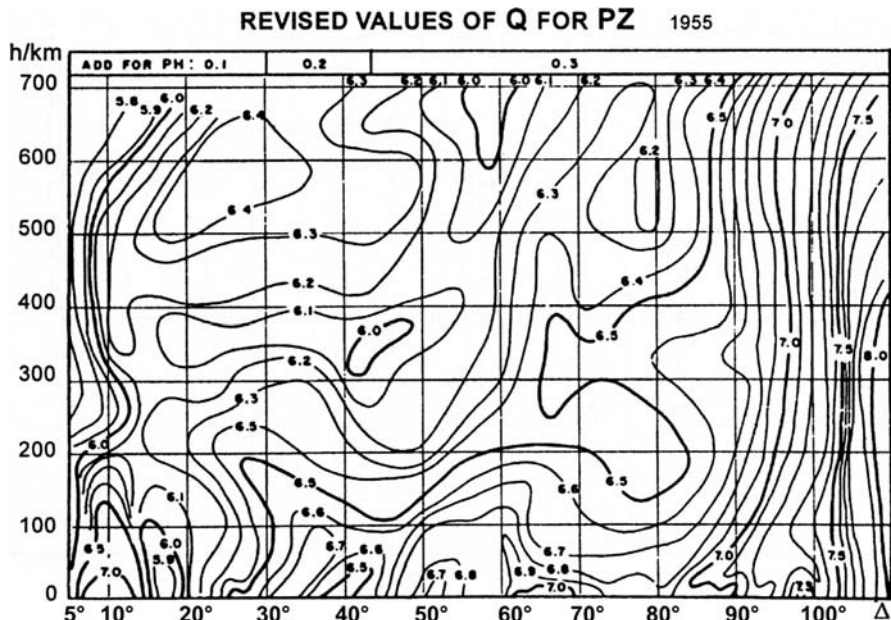


Fig. 6.8 Attenuation functions $Q(\Delta, h)$ for m_b and M_b determination as defined by Gutenberg and Richter (1956). Amplitudes are used according to (6.13) and are measured from zero to peak in μm . Copyright granted by IASPEI. Figure is from NMSOP, DS 3.1

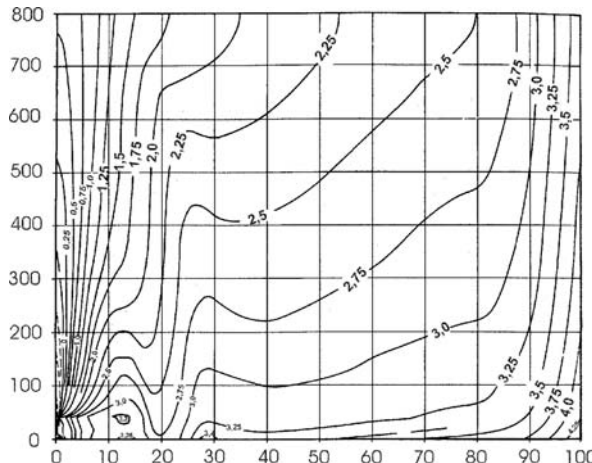


Fig. 6.9 Attenuation functions $Q(\Delta, h)$ for m_b determination from WWSSN type short-period vertical component records (Veith and Clawson, 1972). Amplitudes, according to (6.13), are measured in nm *peak to peak* on a vertical component SP record. Copyright granted by IASPEI. Figure is from NMSOP, Chapter 3.2.

used by the International Monitoring System (IMS). The two functions give systematically different magnitudes, see Table 6.6. For shallow earthquakes, there is little difference, while for deeper events, the Veith and Clawson relation gives smaller magnitudes. The Veith and Clawson function is probably the most accurate attenuation function for shallow earthquakes (NMSOP), but according to K. Veith (personal communication) it is not yet reliable enough for deep earthquakes due to the still rather uncertain global attenuation model used for calculating the corrections for deeper earthquakes.

Table 6.6 Difference in m_b calculated using the Gutenberg and Richter Q-function (Fig. 6.8) and the Veith and Clawson Q-function (Fig. 6.9). The values can be compared by subtracting 3.3 from the Gutenberg values. The factor 3.3 comes from the difference in amplitude measurements (nm to μm and peak to peak versus zero to peak). The numbers in the table have been calculated using the tabulated values for the Gutenberg and Richter function used by USGS (Bob Hutt, personal communication)

Δ degrees	$h = 0 \text{ km}$	$h = 15 \text{ km}$	$h = 100 \text{ km}$	$h = 400 \text{ km}$
10	0.8	-0.3	0.8	1.4
20	0.0	0.1	0.3	0.7
30	-0.1	0.0	0.1	0.3
40	-0.2	0.0	0.2	0.3
50	0.0	0.3	0.5	0.2
60	0.2	0.3	0.5	0.3
70	0.1	0.3	0.1	0.4
80	-0.2	0.1	0.1	0.4
90	-0.1	0.1	0.2	0.2
100	-0.5	-0.3	0.0	0.1

Since the amplitude is measured at a frequency near 1 Hz, the m_b scale will saturate well before magnitude 7 (see Chapter 8). An m_b type magnitude can also be calculated (called m_B) using unfiltered broadband velocity records and the Gutenberg and Richter attenuation relation, see next section. The advantage is that it will saturate at a higher magnitude than m_b . Ideally, m_B is a better magnitude than m_b since it is not limited to a particular instrument response, however it is little used and not routinely reported by USGS or ISC. A problem with both m_b and m_B is that they both underestimate magnitude relative to M_s (Fig. 6.22) (See NMSOP for more details).

From Fig. 6.9, it is seen that the correction function is defined down to zero distance so in principle m_b can be determined for short distances. However, it is also seen that for distances less than 10–15°, the correction function has a strong variation with both distance and depth due to the high degree of inhomogeneity in the earth's crust and upper mantle. The IASPEI recommendation is to determine m_b for distances larger than 20°. For distances larger than 100°, m_b cannot be determined since the P-rays now get into the shadow zone.

Filter to use: Ideally an exact WWSSN filter should be used (Fig. 6.10). However, in case it is not easy to implement poles and zeros in the plotting program, displaying the ground displacement with a “suitable” standard filter will give similar results (maximum error of 0.1 magnitude unit). The poles and zeros for the standard WWSSN SP response are given in Table 6.7 (Bub Hutt, personal communication).

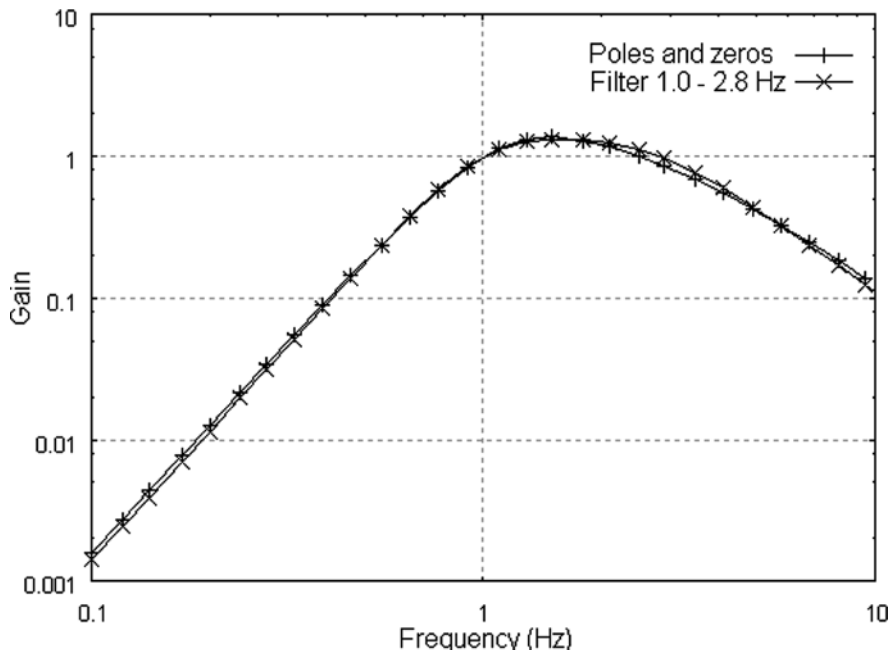


Fig. 6.10 Displacement response of the WWSSN SP seismograph and a Butterworth filter of a 3 pole low cut at 1.0 Hz and a 2 pole high cut at 2.8 Hz. Note that the curve has a nominal gain 1.0 at 1 Hz

Table 6.7 Poles and zeros to describe the WWSSN SP displacement response. The normalization constant giving a gain of 1.0 at the frequency of maximum gain at 1.5 Hz is 384

Poles, real and imaginary		Zeros, real and imaginary	
-3.725	6.22	0.0	0.0
-3.725	-6.22	0.0	0.0
-5.612	0.0	0.0	0.0
-13.24	0.0		
-21.08	0.0		

This response can be simulated very accurately with a Butterworth filter of a 3 pole low cut at 1.0 Hz and a 2 pole high cut at 2.8 Hz, see Fig. 6.10. A gain factor of 1.05 must be used to get a gain of 1.0 at 1.5 Hz.

The most important is the low cut of the filter inherent in the SP response, since lower frequencies, like what is seen with LP or broadband records, would result in significantly higher amplitudes and the assumption of SP response would no longer be valid. Figure 6.11 shows an example of filter use.

Note that in this case the two filters that are wider than the WWSSN SP response both give higher amplitudes. It has been observed that in many cases filters must be used to read phases on broadband seismograms in order to achieve a signal to noise ratio which allows proper phase detection and onset time reading. Similarly it might be difficult to read m_b when strictly using the WWSSN filter since it does not reduce the lower frequency noise sufficiently. This is particularly a problem when the microseismic noise is high, and/or the magnitude is small, see Fig. 6.12.

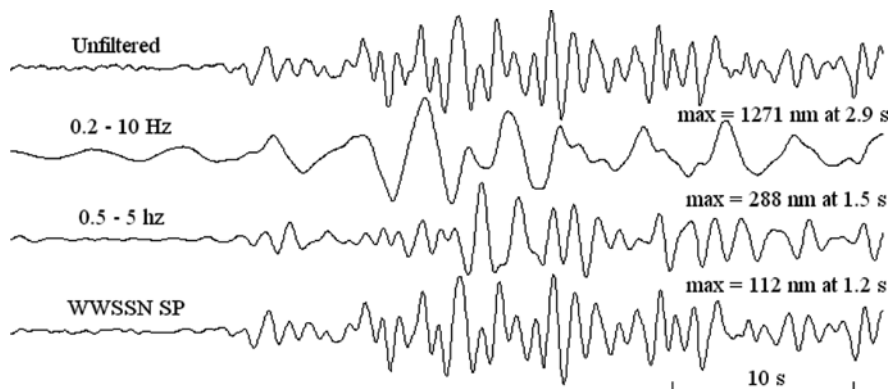


Fig. 6.11 A short period record converted to displacement in two different filter bands (8 pole filters) and the WWSSN SP filter. The event is recorded on station HYA, vertical channel. Origin time is 2008 0415 22:59. The magnitude m_b (PDE) is 6.1 and epicentral distance is 67° . The maximum amplitudes have been read as half the maximum peak to peak amplitude without correction for the filter use. For the WWSSN trace, the true ground motion is 207 nm

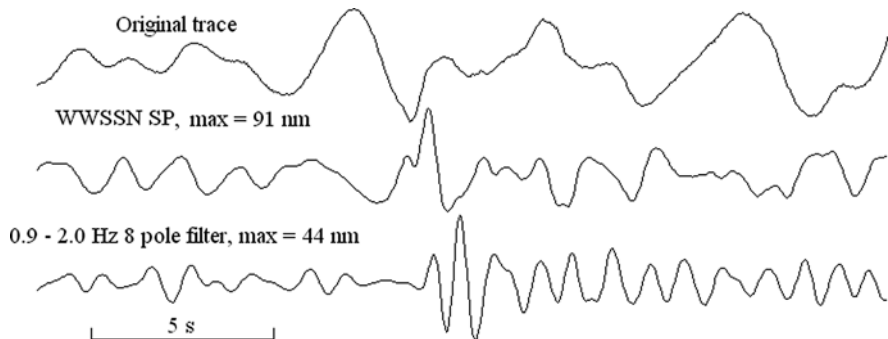


Fig. 6.12 P-wave of a distant earthquake recorded on the vertical component on broadband station TRO. Different filters have been used as shown. The maximum amplitude is from zero to peak. No correction for filter gain is used. Origin time is 2009 0102 07:42 and m_b (PDE) is 4.9. The epicentral distance is 70°

This example shows that without filtering, it is not possible to read the P-phase and it is also impossible to read the P-amplitude with any confidence, when using the WWSSN SP filter. The filter is obviously not sharp enough to cut out the microseismic noise. By using an 8 pole filter 0.9–2.0 Hz instead of the WWSSN filter, the amplitude can be read. This might result in a too small amplitude, but in this case it is the only way to get an amplitude for m_b .

Summary of procedures to calculate m_b

- Calculate the vertical component displacement seismogram, multiply with the WWSSN response function to simulate the WWSSN SP response.
- Read the maximum amplitude (nm) and corresponding period within the whole P-wave train, but before PP. Only use observations with period < 3 s.
- Correct the amplitude for the relative gain of the WWSSN response.
- Make sure reading is not contaminated by microseismic noise.
- Only use stations in the distance range $20\text{--}100^\circ$ to calculate m_b . However, measurements at distance less than 20° can be reported for research purposes.
- When reporting observations, make sure the corresponding phase ID is reported as IAmb.

6.5 Broad Band Body Wave Magnitude m_B

The body wave magnitude m_B is the original body wave magnitude proposed by Gutenberg (1945a, b, 1956) and m_b can be considered a derivative of m_B . The instrument independent definition is:

$$m_B = \log(A/T)_{\max} + Q(\Delta, h) \quad (6.14)$$

where $Q(\Delta, h)$ is the same attenuation function as used above for the standard m_b (Gutenberg and Richter, 1956). Amplitude (μm) is measured on the vertical broadband channel within the entire P-wave train before the phase PP (see IASPEI recommendations) and T should be in the range 0.2–30 s according to the IASPEI recommendations. Like for m_b , the range could be extended to beyond PP for very large events. The epicentral distance should be in the range 20–100°. In practice it is not so easy to measure $(A/T)_{\max}$. Since $A = VT/2\pi$, where V is the velocity amplitude, (6.14) can be written

$$m_B = \log(V_{\max}/2\pi) + Q(\Delta, h) \quad (6.15)$$

and the maximum amplitude, independent of frequency, is read on a velocity trace. This is very convenient since modern broadband instruments record pure velocity in a broad frequency band and thus the maximum amplitude can mostly be read directly from the record. If the instrument is not linear for velocity in the period range 0.2–30 s, instrument correction must be made to produce a true velocity record before the maximum amplitude is read. Figure 6.13 shows an example.



Fig. 6.13 Determination of m_B . The top trace shows the original broadband record from station KBS, the second trace the corresponding band limited velocity. The third trace shows the SP record from HYA which has been extended to simulate broadband velocity and the bottom trace shows the original SP record (same as in Fig. 6.11). To the right are show maximum velocities (peak to peak divided by 2, corresponding periods, displacements and magnitudes, Origin time is 2008 0415 22:59. The magnitude m_b (PDE) is 6.1. The epicentral distances for KBS and HYA are 49° and 67°, respectively and the depth is 10 km

The broadband trace used for m_B is virtually identical in shape to the original broadband record due to the wide filters used. The SP record in the wide band simulation looks very similar to the KBS broadband record despite large difference in distance while the original SP record is much more high frequency. The maximum velocity for KBS is 6,661 nm/s which corresponds to $3.2 \text{ (s)} / 2\pi = 3,392 \text{ nm}$. Thus the corresponding magnitude $m_B = 6.8$ and similarly 6.6 using station HYA. This is substantially higher than the $m_b = 6.1$ and more comparable to the reported $M_w = 6.4$. In this example both the SP and the broadband records can be used for m_B due to the relatively low period for the maximum amplitude wave and this shows that SP records, properly corrected, also in many cases can be used to determine m_B .

m_B is generally a better magnitude to use than m_b since it does not saturate until above magnitude 8 and is instrument independent. It is also not affected by using different attenuation curves as is the case with m_b . The main reason that this has not been used more is probably the widespread dominance of the WWSSN system and corresponding traditional short period m_b magnitude. It also has the drawback that it cannot be used for events smaller than about magnitude 5–5.5 since the microseismic noise usually will be larger than the signal and this can even be a problem with m_b (see Fig. 6.12). There now is a push to start using m_B considering all the drawbacks with m_b and major agencies have started to routinely report m_B , however m_b will continue to be the magnitude for smaller events.

Summary of procedures to calculate m_B

- Calculate the vertical component broadband velocity record in the period range 0.2–30 s.
- Read the maximum velocity amplitude and corresponding period within the whole P-wave train, but before PP.
- Make sure reading is not contaminated by microseismic noise.
- Only use stations in the distance range 20–100°. However, measurements at distance less than 20° can be reported for research purposes.
- When reporting observations, make sure the corresponding phase ID is reported as IVmB_BB.

6.6 Surface Wave Magnitude M_s

At distances greater than about 200 km, the largest ratios $(A/T)_{\max}$ in broadband seismograms and for distances larger than about 600–1,000 km also in long-period seismograms of shallow earthquakes are dominated by surface waves with periods in a wide range from about 3–60 s, yet often around 20 s, see Fig. 6.14

The first surface-wave magnitude scale was developed by Gutenberg (1945a) based on mostly teleseismic recordings of surface waves with oceanic travel path at distances $> 20^\circ$. This led to a formula which proposed measuring A_{\max} in the surface-wave train for periods around 20 s in the distance range $20^\circ < \Delta < 160^\circ$.

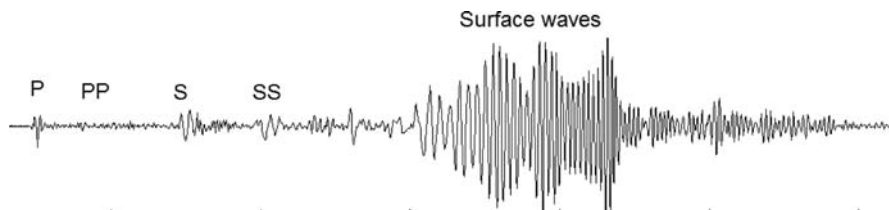


Fig. 6.14 LP seismogram of a large earthquake recorded on KBS, vertical channel. The origin time is 2001 0113 17:33, $m_b(\text{ISC})$ is 6.3 and M_s is 7.8 (PDE). Epicentral distance is 79°

Later, extensive investigations of surface wave propagation along predominantly continental travel path showed that the most stable estimator of the released seismic energy is not A_{\max} at 20 s but rather the ratio $(A/T)_{\max}$ in the mentioned wide range of periods and even at local to regional distances down to 2° (see Bormann et al., 2009). This led Vaněk et al. (1962) to propose the following formula for determining the surface wave magnitude:

$$M_s = \log(A/T)_{\max} + 1.66 \log(\Delta) + 3.3 \quad (6.16)$$

where A is the maximum displacement amplitude in micrometers, T the period in seconds and Δ the distance in degrees. Valid distances are from 20 to 160° and hypocentral depth less than 60 km. This is the Moscow-Prague formula by Karnik et al. (1962), which has been the standard for almost 50 years. In practice there have been some minor variations on how measurements have been carried out and which distance, depth and period ranges should be used (see NMSOP). Similarly as for m_b , measurements have for many years been dominated by readings using the WWSSN LP system (seismometer period 15 sec and galvanometer period 90 sec) with a peak gain for displacement around 15 s. Since this has become the most standard way of measuring M_s (which however might give a different value than calculating m_B), it has been given the IASPEI approved label M_s_20 . Since this is the most common surface magnitude reported, we will label it just M_s . In order to measure standard M_s , the maximum amplitude must be measured on a trace simulating the WWSSN LP response and the amplitude must be corrected for the WWSSN LP gain. Since the maximum amplitude is measured in a narrow period range (18–22 s), (6.16) can be replaced by

$$M_s = \log(A/T) + 1.66 \log(\Delta) + 3.3 \quad (6.17)$$

and the maximum amplitude and corresponding period is measured. The recent IASPEI recommendation is:

Measure the maximum displacement amplitude using the vertical component for surface waves in the period range 18–22 s for earthquakes with hypocentral depth < 60 km and in the distance range 20–160°.

New broadband instrumentation is sensitive to lower frequencies than WWSSN. It is desirable to avoid using the frequency limitation in the WWSSN LP response to avoid magnitude saturation (see Chapter 8) and IASPEI has also given a recommendation to use broadband records. This magnitude is given the IASPEI name M_s_BB (see section below), however in the following we will just label it M_s as in the original definition of surface wave magnitude.

The poles and zeros giving the WWSSN LP displacement response is given in Table 6.8. In case it is not easy to implement poles and zeros in the plotting program, the LP response can be simulated with a Butterworth filter of a low cut 2 pole filter at 0.038 Hz (26 s) and a high cut 1 pole filter at 0.1 Hz (10 s) to be used with the displacement trace. A gain factor of 1.25 must be used to get a gain of 1.0 at 15 sec.

Table 6.8 Poles and zeros for the WWSSN LP response. A normalization constant of 0.83 is needed to get a gain of 1.0 at 15 sec

Poles		Zeros	
-0.40180	0.08559	0.0	0.0
-0.40180	-0.08559	0.0	0.0
-0.04841	0.0	0.0	0.0
-0.08816	0.0		

Figure 6.15 compares the two filters. Using the LP filter means that the maximum amplitude often is in the 18–22 s range, but not always as seen in the example in Fig. 6.16. In this example, the maximum amplitude occurs later in the wave-train with a period of 16 s, while earlier, the 18 s wave arrives with a slightly smaller amplitude. By reading the maximum amplitude, a value of 1,939 nm at 16 s ($A/T = 121 \text{ nm/s}$) would be obtained, while the maximum amplitude in the 18–22 s range is only 1,454 nm at 18 s ($A/T = 81 \text{ nm/s}$). Comparing the A/T values, the difference is even larger. By using the automatically read maximum value, M_s would be 0.2 units larger than using the maximum at 18 s. It is therefore important that any automatic

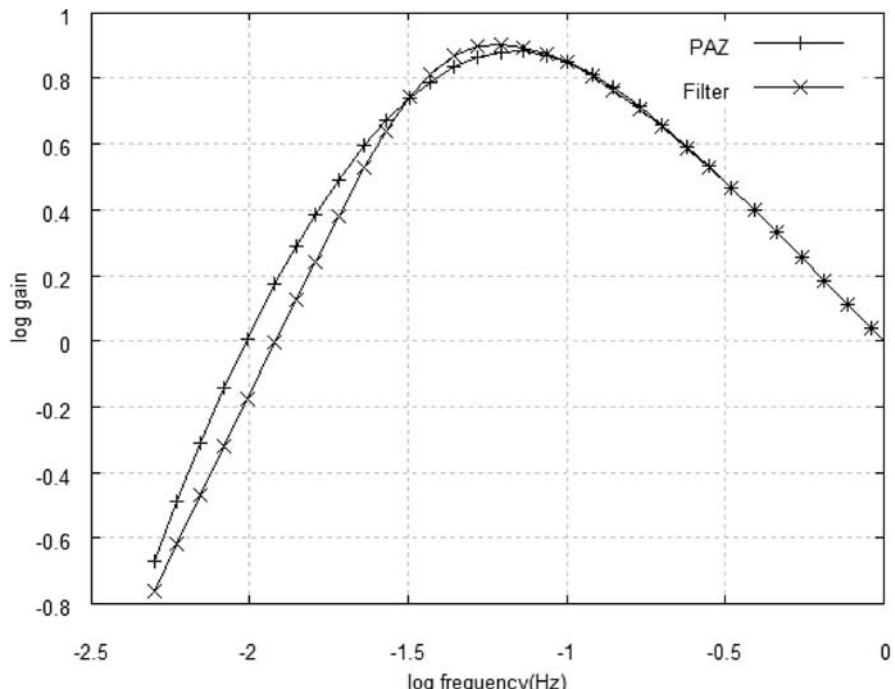


Fig. 6.15 Displacement response of the WWSSN LP seismograph (PAZ) and a Butterworth filter of a 2 pole low cut at 0.038 Hz and a 1 pole high cut at 0.1 Hz. Note that the curves have a nominal gain of 1.0 at 1 Hz. The maximum gain for the PAZ curve is at 0.067 Hz (15 s)

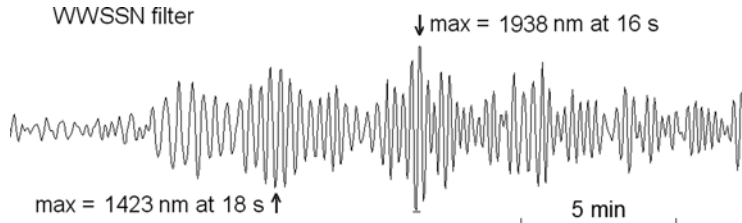


Fig. 6.16 Reading maximum amplitude (peak to peak divided by 2) on a WWSSN LP simulated trace. The seismogram is from station KBS, vertical channel. The origin time is 1996 0603 19:55, $M_s = 5.5$ (ISC) and the epicentral distance is 52° . The amplitude is not corrected for filter gain. The true ground displacement at 18 s is 1454 nm and at 1939 nm at 16 s. Thus the filter gain is small for WWSSN LP

procedure only reads the maximum amplitude in the 18–22 s range. This example illustrates a fundamental problem with M_s which can be solved by using M_S , see next section.

Another practical problem in connection with using broadband data is that the natural background noise might hide the surface waves, see Fig. 6.17. This example illustrates how the surface wave is not seen on the original trace, with the WWSSN LP filter the surface waves are barely seen and only by applying a sharper filter can the surface wave be clearly detected. However, strictly speaking, the 0.038–0.1 Hz 8 pole filter would not be correct to use. With the LP filter, the P is not seen and only by using an SP filter will the P be seen. See also Chapter 4 for examples of reading phases on broadband records.

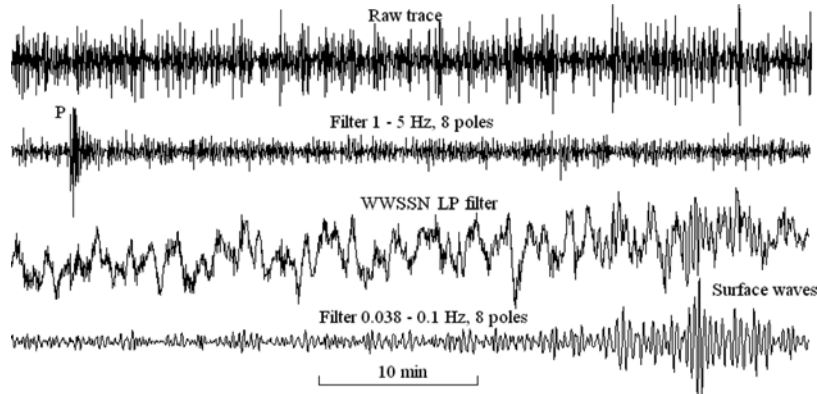


Fig. 6.17 Reading surface wave amplitude in noisy conditions. The *top* trace shows the original trace from a broadband sensor, the second trace is filtered 1–5 Hz, the 3 trace is simulating the WWSSN LP seismogram and the *bottom* trace shows a sharper filter similar to the WWSSN filter. The data is from station NSS, vertical component, the origin time is 2003 0326 04:22, $M_s = 5.3$ (PDE) and the epicentral distance is 79°

Summary of procedures to calculate M_s

- Calculate the vertical component displacement seismogram (nm), multiply with the WWSSN relative response function to simulate the WWSSN LP response.
- Read the maximum amplitude and corresponding period within the period range 18–22 s.
- Correct the amplitude reading for the gain for the WWSSN LP curve.
- Make sure reading is not contaminated by microseismic noise.
- Only use stations in the distance range 20–160° to calculate M_s . However, measurements at distance less than 20° can be reported for research purposes.
- The hypocentral depth must be less than 60 km.
- When reporting observations, make sure the corresponding phase ID is reported as IAMs_20.

6.7 Broad Band Surface Wave Magnitude M_s

The limitation in the practice of determining the current M_s led IASPEI to standardize the original surface wave magnitude relation to using the maximum $(A/T)_{\max}$ on a broadband vertical channel. The new magnitude has the IASPEI label M_s _BB, however we will label it M_s for simplicity. It is defined as

$$M_s = \log(A/T)_{\max} + 1.66 \log(\Delta) + 3.3 \quad (6.18)$$

In practice it is not so easy to measure $(A/T)_{\max}$ (like for m_B). Since $A = VT/2\pi$, where V is the velocity amplitude, (6.18) can be written

$$M_s = \log(V_{\max}/2\pi) + 1.66 \log(\Delta) + 3.3 \quad (6.19)$$

and V_{\max} is reported. This formulation takes into account surface-wave maxima at both lower and higher frequencies than M_s and thus agrees best with the current IASPEI standard M_s calibration formula (see Bormann et al., 2009). The IASPEI recommendations are:

Measure the maximum velocity amplitude using the vertical component for surface waves in the period range 2–60 s for earthquakes with hypocentral depth < 60 km and in the distance range 2–160°.

The 60 s limit is arbitrary, it could really have been any larger period, however in practice periods of 60 s are not encountered on velocity broadband records (Peter Bormann, personal communication). It does mean however, that if the broadband sensor is not linear at the expected frequency of the maximum amplitude, instrument correction must be made. Figure 6.18 shows an example. It is seen that the 3 traces look almost identical. M_s was determined to 8.1 (amp = 891,000 nm at 22 s) and M_s was 8.2 (365,600 nm/s) so in this case the difference is small. Figure 6.19 shows an example of medium size event. The two top traces are again, as expected,

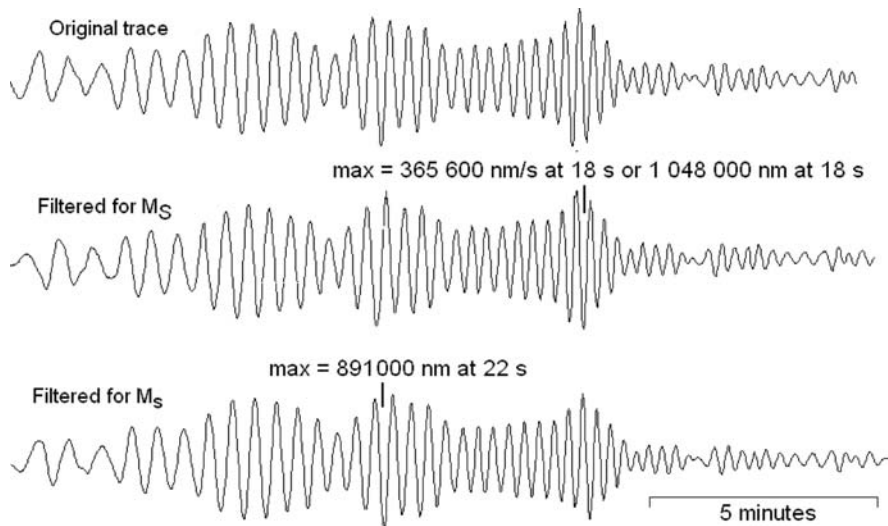


Fig. 6.18 Example of determining M_S . The *top* trace shows the original velocity broadband record, the *middle* trace the record filtered for M_S , the *bottom* the traces filtered for M_S . The station is KBS, vertical channel. The location of the reading is indicated by max and the amplitudes are measured peak to peak divided by 2. The origin time is 2001 0113 17:33, m_b (ISC) is 6.3 and M_S is 7.8 (PDE). Epicentral distance is 79° and depth is 60 km

almost identical, while the M_S trace has less high frequency noise due to the filter in the WWSSN LP response. The magnitudes calculated for this example are $M_S = 4.8$ and $M_S = 5.4$ respectively. Thus M_S is closer to the average ISC M_S than the M_S calculated for KONO and there is a substantial difference between the two magnitudes.

One of the large advantages of using M_S instead of M_S is that there are little limitations of period and distance. This means that M_S also can be used for local

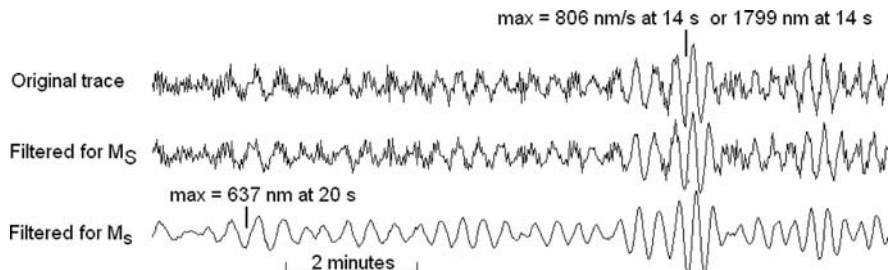


Fig. 6.19 Example of determining M_S . The *top* trace shows the original velocity long period record, the *middle* trace the record filtered for M_S , the *bottom* the traces filtered for M_S . The station is KONO, vertical channel. The location of the reading is indicated by max and the amplitudes are measured peak to peak divided by 2. The origin time is 1996 0623 01:17, m_b (ISC) is 5.4 and M_S is 5.4 (ISC). Epicentral distance is 66° and depth is 33 km

earthquakes and might be an alternative for M_L . For a large number of M_S measurements from earthquakes in China in a wide period and distance range, Bormann et al. (2007) observed an excellent average correlation with M_L . This suggests that using M_S , in the absence of a well calibrated local/regional M_L scale, is a suitable magnitude proxy at distances between 2° and 20° . Since M_S in the local/regional range is measured at significantly longer periods ($T > 3\text{--}15$ s) than M_L ($T < 1$ s) it is much less affected by local/regional differences in crustal structure and attenuation conditions than M_L . This justifies the use of a global average relationship in areas of unknown attenuation. However, depending on local noise conditions, magnitude must be above M_L 3–4 in order for the surface waves to have significant amplitude above the noise, see Fig. 6.20.

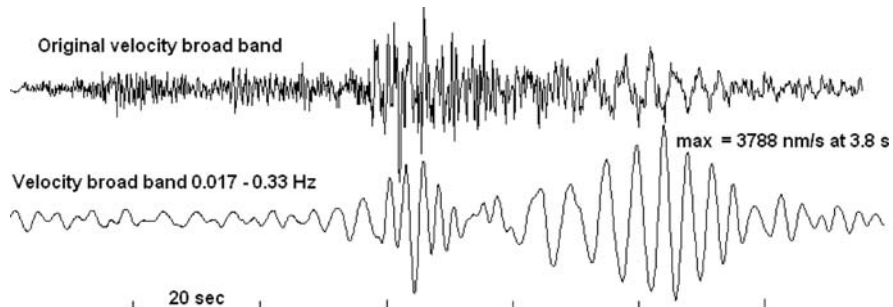


Fig. 6.20 Calculating M_S for a local earthquake. *Top* trace shows the original vertical broadband velocity record from station HPK, the UK network. The *bottom* trace shows the instrument corrected velocity trace using the M_S filter (4 pole filter). The event origin time is 2007 0428 07:18, epicentral distance is 370 km, the depth is 5.3 km and $M_L = 4.3$

This is a local event suitable for M_S . Note that the maximum amplitude surface wave on the original trace appears at higher frequency than the filtered trace due to the high frequency nature of this local event. The M_S calculated was 3.9, similar to M_w of 3.9 (see Chapter 7), but smaller than the M_L of 4.3.

The measurement and reporting of A_{\max} , V_{\max} and T from clearly developed surface waves of earthquakes at larger depths are strongly encouraged for future studies on depth-dependent magnitude corrections and attenuation relationships.

Summary of procedures to calculate M_S

- Calculate the vertical component velocity seismogram in the period range 3–60 s.
- Read the maximum velocity amplitude and corresponding period.
- Make sure reading is not contaminated by microseismic noise.
- Only use stations in the distance range $2\text{--}160^\circ$ to calculate M_S .
- The hypocentral depth must less than 60 km.
- When reporting observations, make sure the corresponding phase ID is reported as IVMs_BB.

6.8 L_g – Wave Magnitude

This scale is using Sg and Lg waves at local and regional distances ($\Delta < 30^\circ$). It is giving similar magnitudes as M_L. It is mostly used in North America. See NMSOP and IASPEI recommendations for more information.

6.9 Moment Magnitude M_w

The moment magnitude M_w, developed by Kanamori (1977) and Hanks and Kanamori (1979) is defined, according to the IASPEI recommended standard form as:

$$M_w = 2/3 \log M_0 - 6.07 \quad (6.20)$$

where the moment M₀ is measured in Nm (see NMSOP). The seismic moment M₀ is a direct measure of the tectonic size (product of rupture area times average static displacement) and therefore does not saturate, provided that it is measured at periods larger than the corner period of the radiated source spectrum (see Chapter 8). The seismic moment can be determined by moment tensor inversion (moderate to large events, see Chapter 7) or spectral analysis (all events, see Chapter 8). If a reliable moment can be determined, it is by far the most objective static measure of earthquake size and it is recommended to determine moment magnitude whenever possible. The moment magnitude was defined through the relation of radiated seismic energy and seismic moment, and energy and surface wave magnitude. However, it should be mentioned that moment magnitude does not correctly reflect total energy released as the moment magnitude scale is defined for a constant stress drop, but energy release depends on the stress drop (see below for energy magnitude). Therefore, moment magnitude is not the most appropriate magnitude for assessing seismic hazard in terms of shaking damage potential, yet well suited for assessing the tsunamigenic potential of large subduction earthquakes. It is also difficult to accurately calculate moment for the very largest earthquake due to the multiple ruptures and a too small moment might be obtained.

Figure 6.21 shows an example of P and S spectra of a large local Mexican earthquake also shown in Fig. 6.2. Recall that the hypocentral distance was 107 km, M_L = 6.4 and M_s = 6.7. Since the station is close to the event, only a short time window can be used for P-analysis. Notice the lower spectral level for the P-spectrum than for the S-spectrum. The average, manually determined M_w for P and S were 6.5 and 6.4 respectively. This example illustrates that P and S spectra give similar magnitude. The teleseismic reported M_w was 6.8 (PDE) and 6.6 (HRV) respectively (See also Chapter 8 on teleseismic spectral determination of M_w). It is thus possible to get a reasonable reliable magnitude estimate for a large local event within seconds of its occurrence provided unclipped records are available. An approximate distance can be calculated from the S-P time. The spectral estimates can be automated and has been shown to work reliable up to magnitude 8 (Ottemöller and Havskov, 2003),

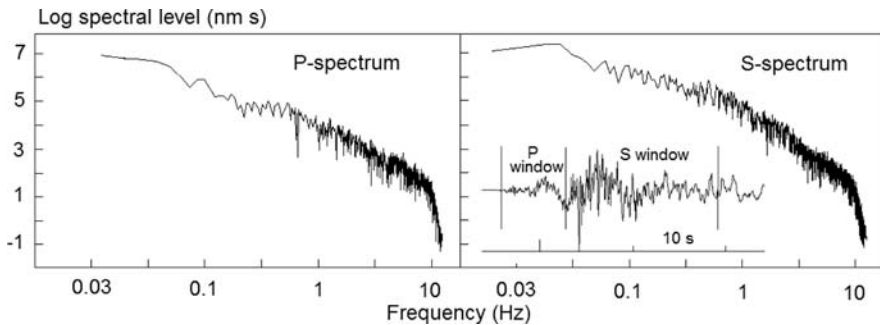


Fig. 6.21 P and S spectra for the event shown in Fig. 6.2. The insert under the S-spectrum shows the time windows used for spectral analysis. The spectra have been corrected for Q using $Q = 204 f^{0.85}$ (Ottemöller et al., 2002)

see Fig. 6.24. Thus calculating M_w using spectral analysis at local and regional distances gives some of the same advantages as using M_S . For larger events ($M > 5$), the corner frequency is quite low so the spectral level is not critical dependent on a correct attenuation like it was the case for M_S . For more details, see Chapter 8 on spectral analysis.

For information on how to determine M_w magnitude scale parameters, see Section 6.14.4.

Summary of procedure for determining M_w using spectra

- Moment magnitude can be determined for earthquakes of any size using P or S-waves.
- The time window used for spectral determination of M_w , must be at least as long as the rupture time to include all the energy. Thus P-spectra of large earthquakes at short distances might not be possible.
- The instruments must be able to record signals with frequencies below the corner frequency.

6.10 Energy Magnitude M_e

Magnitude is proportional to the energy release in earthquakes and there are empirical relations between magnitude and energy (see NMSOP). However, these relations depend on stress drop and the energy can therefore not be calculated correctly from magnitude without knowledge of stress drop. This usually gives large standard deviations when compared with M_w due to the variability of stress drop (Bormann and Saul, 2008). With broadband seismograms, it is possible to calculate the energy directly by integrating the energy flux from the velocity square amplitudes and correcting for geometrical spreading, attenuation and source radiation. The energy magnitude M_e in its current form, as routinely applied at the USGS for selected larger earthquakes, has been developed by Choy and Boatwright (1995).

A few other institutions also routinely calculate M_e , for local earthquakes, see e.g. Dineva and Mereu (2009). M_e is defined (NMSOP, see also Choy and Boatwright (1995) as:

$$M_e = 2/31 \log(E_s) - 2.9 \quad (6.21)$$

where E_s is the energy in J and the constant 2.9 is set so $M_e \approx M_w$ for average stress drop conditions. Calculating energy magnitude is not yet done in any standard procedure and currently only done routinely by the USGS for selected larger events. Also, it is still very difficult to measure reliably E_s for moderate to weak earthquakes in the local and regional range. However, automatic routines for on-line M_e determination in near real-time are currently under development and testing (Di Giacomo et al., 2010). Table 6.9 gives an example, where M_e is smaller than M_w , possibly because of a stress drop lower than the constant stress drop assumed by Kanamori (1977) in developing the M_w formula.

Table 6.9 Example of energy magnitude reported by USGS

Southern Sumatra, Indonesia
Origin time: 2007 09 12 11:10
Moment magnitude: 8.4
Energy: $2.6 \cdot 10^{16}$ J
Energy magnitude: 8.0

6.11 Comparison of Magnitude Scales

With all the different magnitude scales, their different validity ranges and the different use of instruments it is natural to ask how different they are. Figure 6.22 shows a comparison made by Kanamori (1983).

It can be seen that from magnitude 4 to 6.5, there is a reasonable good agreement between M_L , M_s and M_w , but not m_b and m_B . We can thus not expect even m_b and M_s , the two most common magnitude scales, to agree for most earthquakes and, m_B will also be systematically different from M_s and M_w . There are numerous relations between magnitude scales (see NMSOP for an overview) which just illustrates the confusing problem of the different scales. However, the reasons for their disagreement are explained in detail by Bormann and Saul (2008, 2009a, b) and Bormann et al. (2009). So even if the m_B scale does not saturate before magnitude 8–8.5 (M_w), it will for magnitudes > 7 give a too small value compared to the reference M_w and m_B must therefore be corrected if a magnitude compatible to M_w is needed.

There is often a need to convert one magnitude to another, whether of the same type or another type, e.g. if two earthquake catalogs are to be merged. For seismic hazards studies, it is important to convert all magnitudes to one that does not saturate for the given area, which mostly would be M_s or M_w . On the other hand, it can be useful to compare magnitudes within a network or with another network in

Fig. 6.22 Relations between magnitude scales. Reprinted with permission from Elsevier. From Kanamori (1983)

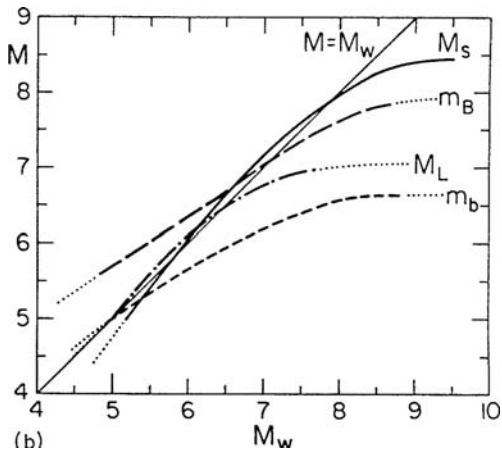
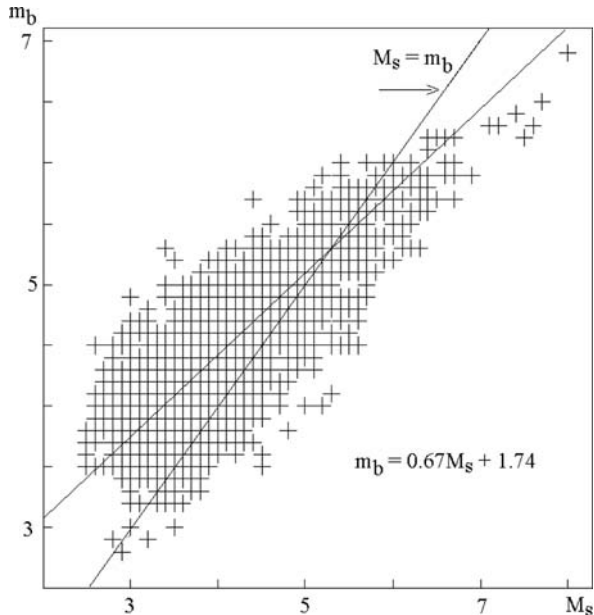


Fig. 6.23 Relationship between m_b and M_s as reported by the ISC for the year 2002. There is a total of 4,427 events. The bimodal relation is shown as well as the 1:1 relationship labeled as $M_s = m_b$



order to find outliers or simply check performance against recognized data centers. This kind of magnitude manipulation can be done with some software packages. Figure 6.23 shows an example from the global network. This is a typical regression made when converting from one magnitude to another. It is preferable to make such a bimodal, or “orthogonal” regression, when there is reason to assume that the uncertainty in the two variables are about the same (see Bormann et al., 2007;

Castellarano and Bormann, 2007). However, usually measurement errors in long-period magnitudes, such as M_s are significantly smaller than in short-period magnitudes, such as m_b . Then also common standard regression will be comparably reliable, provided that the “independent” variable with the likely smaller (or zero) error is put on the x-axis. From the figure, it is seen that m_b is smaller relative to M_s , for $m_b > 5$ and the opposite for $m_b < 5$, as also observed in Fig. 6.22. This kind of relationship between m_b and M_s is also found in many other studies, see Table 6.10 for some examples.

Table 6.10 Constants in the relationship $m_b = aM_s + b$ reported by different studies

a	B	References
0.47	2.79	Gordon (1971)
0.67	2.28	Geller (1976)
0.57	2.25	Ambrasseys (1990)
0.67	1.74	Fig. 6.23

Figure 6.22 does not give information about relationships for magnitudes < 4 and it would be useful to know the relation between M_w and M_L for smaller earthquakes. Table 6.11 summarizes some of the relations available. Some relations give $\log(M_0)$ as a function of M_L and others give the relation between the two magnitudes. All relations have been converted to relations between the two magnitudes using the definition of moment magnitude.

From Fig. 6.22 it is observed that $M_w = M_L$ for $M = 4$ to 6 . However for smaller magnitudes ($M_L < 2 - 4$), this is generally not the case, see Table 6.11. This has been explained by the response of the Wood-Anderson instrument. For small events, which have high frequencies, the amplitude used to measure M_L corresponds to the flat part of the displacement spectrum (see Chapter 8) and the amplitude is therefore linearly proportional to M_0 . So M_L must be linearly proportional to $\log(M_0)$ and we get

$$M_L \propto \log(M_0) \propto 1.5M_w \quad \text{or} \quad M_w \propto 0.67M_L \quad (6.22)$$

Table 6.11 Relationships between M_w and M_L for small earthquakes. $M_w = M_L$ give the magnitude where $M_w = M_L$

Area	Range	Relation	M_w for		References
			$M_L = 1.5$	$M_w = M_L$	
California	1.0–3.5	$M_w = 0.81M_L + 0.61$	1.8	0.6	Bakun and Lindh (1977)
Hawaii	1.0–4.0	$M_w = 0.73M_L + 0.32$	1.4	1.2	Zúñiga et al. (1988)
Germany	1.0–4.5	$M_w = 0.70M_L + 0.51$	1.6	0.2	Scherbaum and Stoll (1983)
Nevada	-2.0–0.0	$M_w = 0.66M_L + 1.21$	–	3.6	Seggern et al. (2003)
N. Italy	0–5	$M_w = 0.64M_L + 0.84$	1.8	2.3	Bindi et al. (2005)

This relation is actually what has been observed (Table 6.11) in many cases. For larger events with significant energy below 1.25 Hz, the maximum amplitude will be more proportional to acceleration. So which magnitude is “the most correct” for small earthquakes? The moment magnitude has no instrumental problem and, provided a correct moment has been calculated, should be considered correct. This does not mean that M_L cannot be used since in an average sense it is observed to give similar magnitude as M_w as seen from the examples in Table 6.11 and Fig. 6.24. However the linear relationship is not one to one for particular data sets.

Fig. 6.24 Comparison of M_w determined from S or Lg spectra to M_L or M_e . The comparison is with M_e for Mexico (triangle), M_L for Norway (circle) and Deception Island (square). The long line shows the one to one relationship. Figure reproduced with permission from Elsevier and modified, from Ottemöller and Havskov (2003)

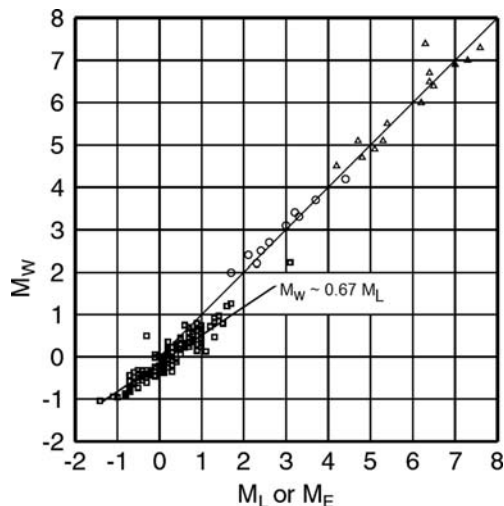


Figure 6.24 shows the relation between M_w determined by spectral analysis at local and regional distances for earthquakes in the magnitude range -1 to 8 . In an average sense, the small magnitude events ($M \sim 0$) also fit the linear relationship. On the other hand, the small events have $M_w - M_L$ relationship which fits quite well with the relationships given in Table 6.11 which is also what we should expect theoretically, see equation (6.22).

6.12 Summary

Ideally we should only calculate M_w and M_e , however it is still easier for most networks to calculate the traditional magnitudes M_L , M_c , m_b , m_B , M_s and M_S . It is recommended to replace the instrument dependent magnitudes m_b and M_s with the instrument independent m_B , and M_S whenever possible. Procedures for calculating M_w might be close to becoming standard and automatic and it is strongly recommended to calculate M_w whenever possible. It might also be possible to calculate M_e in the future.

6.13 Average Magnitude and Station Corrections

For one event, magnitudes from the different stations should ideally be identical. However, this is never the case in practice due to several reasons:

- The radiation pattern will give different amplitudes in different directions. Only coda durations will be independent of the radiation pattern.
- Different noise levels at different stations might affect amplitude measurements if the signal to noise ratio is low. Noise level particularly affects coda length measurements. This will usually result in random errors for a seismic network but may cause systematic errors in M_c for a particular high or low noise station.
- Local or regional geological conditions vary so the free surface amplification might vary and inhomogeneities might cause focusing and defocusing. This could cause systematic errors for a particular station.

The magnitude variation can be dealt with in different ways. It is the normal practice to calculate the average magnitude for all stations in a network. Alternatively, the median could be calculated to exclude outliers. This should average out the effect of radiation pattern if the event is located within the network. Once a large number of magnitude determinations is available, the average deviation of magnitudes measured at a particular station from the average network magnitude, can be calculated. This is called the station correction and is defined as the value that has to be added to the magnitude calculated at that particular station. Most location programs have the possibility to define magnitude station corrections. Table 6.12 gives an example of the variation in magnitudes for a local event.

For this event there is a typical variation in the individual magnitudes. This network has stations with large variation in noise and distances, however the average of M_c and M_L is similar. This is not surprising since M_c has been calibrated from M_L . However, the variability of station M_c values is much larger than of station M_L and M_w estimates. Therefore, one should consider M_c event estimates reliable only when they are based on a sufficiently large number of station estimates. M_w

Table 6.12 Magnitudes for an event in the Norwegian National Seismic Network. r is hypocentral distance. The event origin time is 2004 05 02 19:24

Station	r(km)	M_L	M_L -av.	M_w	M_w -av.	M_c	M_c -av.
ODD1	25	1.6	0.2	1.5	-0.1	0.6	-0.7
BLS5	52	1.5	0.1	1.5	-0.1	1.3	0.0
EGD	71	1.3	-0.1	1.6	0.0	1.1	-0.2
RUND	77	1.6	0.2	1.8	0.2	1.1	-0.2
ASK	87	1.3	-0.1	1.7	0.1	1.6	0.3
KMY	92	1.3	-0.1	1.6	0.0	1.6	0.3
SUE	154	1.4	0.0	1.7	0.1	1.5	0.2
AVERAGE (av.)		1.4		1.6		1.3	

is larger than M_L , but this could be due to a systematic difference of moment magnitude compared to local magnitude, see Section 6.11. This example clearly shows that for a local network, magnitudes should be determined as an average of several magnitudes.

6.14 Adjusting Magnitude Scales to Local or Regional Conditions

A new seismic network might not have any locally adjusted magnitude scales so the question arises how to calculate magnitude. The global magnitude scales, except M_S for larger events, cannot be used for local and regional distances so that leaves M_L , M_w and M_c . There are 4 options: Use a scale from another network, derive M_L , derive M_c or adjust Q for M_w .

6.14.1 Select a Scale from Another Region

Coda magnitude: A common practice has been to use a coda magnitude scale since no instrumental calibration is needed for the readings. Select a scale from an area expected to be tectonically similar to the local area. However, this is quite uncertain since it is not evident how tectonics affect coda length and reading practice is very variable.

Local magnitude: The simplest is to use the California scale since this, at least for the first 100 km, seems to give “reasonable” results in many places. It is also possible to select a scale from a tectonically similar area, see Table 6.4.

Let us illustrate this with an example from the Jamaican seismic network (Fig. 6.25). The standard Hutton and Boore M_L scale was used. For M_c , the Mexican scale was used (Table 6.5) since similar scattering attenuation can be expected at the two localities.

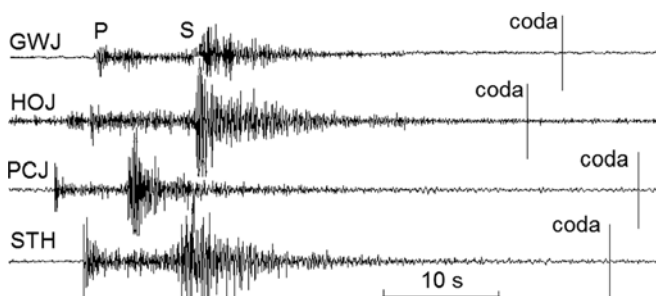


Fig. 6.25 Local event from Jamaican network. The origin time is 2001 03 04 02:11. All channels are vertical. Note that the noise level at station HOJ in front of the P is higher than at the end of the coda. This is caused by some local noise burst and 30 s earlier, the noise level is at the level where the coda reading is made

The local magnitude and coda magnitudes were calculated to 3.1 and 3.1 respectively. The network also reported a moment magnitude of 3.2. In this case it thus seems that selecting magnitude scales M_c and M_L from elsewhere give magnitudes consistent with the supposedly more correct local M_w .

6.14.2 Derive M_L Scale

In order to develop an attenuation function for local magnitude, a good number of amplitude observations in different distance ranges must be collected. Recall the expression for the calculation of local magnitude (6.2).

$$M_L = \log(A) + a \log(r) + br + c \quad (6.23)$$

The objective is to calculate a , b and c . The data can be inverted simultaneously for a number of events by solving the following system of equations

$$\log(A_{ij}) = M_{Li} - a \log(r_{ij}) - br_{ij} - s_j - c \quad (6.24)$$

where i is a counter over m earthquakes and j is a counter over n stations. The station correction is given by s . The system of equations will have $m + n + 2$ unknowns (magnitudes, station corrections, a and b , c is given a fixed value). It is over-determined and can be solved by a standard inversion method, such as linear least-square inversion. The magnitudes will only be correct if a correct c has been used. The constant c can, once a and b are known, be obtained from the definition of the M_L anchor point at 100 km (amplitude of 480 nm gives magnitude 3.0) or 17 km (amplitude of 480 nm gives magnitude 2.0). At the anchor point, c can, using (6.23), be expressed as

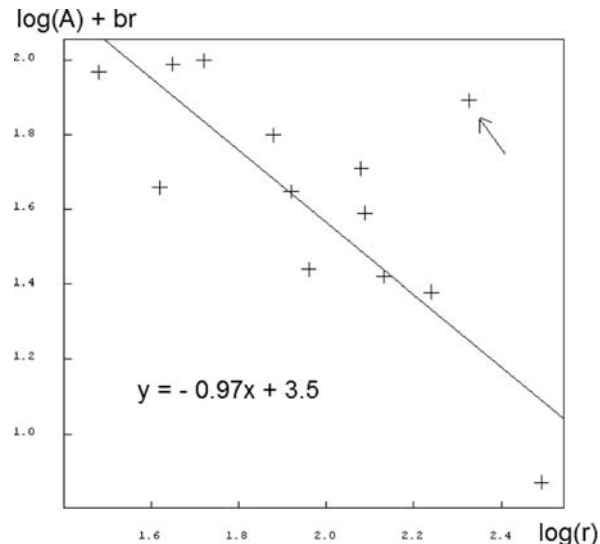
$$c = M_{Lref} - \log(A_{ref}) - a \log(r_{ref}) - br_{ref} \quad (6.25)$$

where M_{ref} , A_{ref} and r_{ref} refer to reference magnitude, amplitude and distance respectively. The anchor point can also be built into (6.24) so as to obtain correct M_L without first calculating a and b . Inserting (6.25) in (6.24) gives

$$\log(A_{ij}) = M_{Li} - a \log(r_{ij}/r_{ref}) - b(r_{ij} - r_{ref}) - s_j - M_{Lref} + \log(A_{ref}) \quad (6.26)$$

In the simplest case, the inversion can be done for one earthquake without determining station corrections. For n stations we then have n equations of type (6.24) with three unknowns a , b and c . If more than 2 observations are available, a , b and $(M_L - c)$ can be determined using just one event. For real data, it is difficult to get reliable results with one event since amplitude variation, as mentioned above, can be large. This procedure can be made more robust by assuming a value for b since this is the most uncertain parameter and also the one with the least importance due to its

Fig. 6.26 Amplitudes (A) in nm plotted as a function of hypocentral distance (r) in km. The origin time of the event is 2004 0511 00:50 and the magnitude is $M_L = 1.8$. The line shows the least squares fit. The observation marked with an arrow (station SNART) is considered an outlier and not used for the least squares



small size. From Table 6.4 it is seen that most values are in the range 0.001–0.003. Equation (6.24) can then be written

$$\log(A) + br = -a \log(r) + (M_L - c) \quad (6.27)$$

and only 2 parameters have to be determined. Figure 6.26 shows an example from an earthquake in Western Norway. Since we know the area, the local value of 0.00087 for b has been chosen (Table 6.4).

The a -value of 0.97 is close to the expected value of 0.91. Considering the large scatter in the data, there is clearly a large uncertainty, however with good data in a large distance range, this simple method, whether determining only a or a and b , can give some insight into the local attenuation. Now that a and b are known, c can be determined. Using the anchor point of 17 km gives, using (6.25), $c = -1.82$

6.14.3 Derive M_c Scale

Coda magnitude scales are calibrated against other known magnitudes, usually M_L but sometimes also m_b . For earthquakes smaller than 3.5, it is usually not a good idea to use m_b since it may be determined for distances shorter than 20° making it unreliable. Recall the coda magnitude scale:

$$M_c = a \log(t_{coda}) + b \Delta + c \quad (6.28)$$

By assuming $M_c = M_L$, we have the equation

$$M_L = a \log(t_{coda}) + b \Delta + c \quad (6.29)$$

For each observation (a coda length and the known magnitude), there is one equation. So for n events of k stations each, there will be nk equations with 3 unknowns a , b and c . These equations look very similar to the equations for M_L , however since magnitudes are known, there are n fewer unknowns and the equations can be solved with a simple least squares inversion. Like for M_L , a station correction term can be added to (6.29), however that also adds k unknowns and the inversion is more complicated. In practice, most networks have an average relation and only 3 unknown have to be found. Even then it is often difficult to reliably determine b due to its small size (weak distance dependence). As seen from Table 6.5, some networks actually chose to set it to zero, in which case only 2 parameters have to be determined. Like for M_L , it is also possible to fix it to some “reasonable” value” and equation (6.29) is

$$M_L - b\Delta = a \log(t_{coda}) + c \quad (6.30)$$

6.14.4 Determine Local Attenuation to Calculate M_w

For local earthquakes, the simplest way to determine the seismic moment is doing spectral analysis of P or S-waves. It is often also the only way since high frequency waveform modelling needed for moment tensor inversion is very difficult for small events ($M < 3$). The spectral analysis is described in Chapter 8. A requirement for doing spectral analysis is to have a correct attenuation in terms of both attenuation Q and near surface attenuation κ (see Chapter 8). If that is not available, it can be determined with either coda waves or using relative spectra, see Chapter 8. The correct geometrical spreading must also be used, see Chapter 8. The advantage of using M_w is that it is a measure which is independent of instrument type and gives a magnitude independent of M_c and M_L . As an example, using the data from the 4 Jamaican stations shown in Fig. 6.25 and using the local attenuation (Wiggins-Grandison and Havskov, 2004), an $M_w = 3.2$ is obtained, which is in reasonable agreement with M_L .

6.15 Exercises

Exercise 6.1 Coda Magnitudes

Figure 6.27 shows a seismogram of a local earthquake from Western Norway.

- Read the S-P times and the coda lengths for all traces and set up in a table.
- Evaluate if it is possible to see the end of the coda on the original trace and the amplified high pass filtered trace.
- Calculate the epicentral distances assuming a constant P-wave velocity of 7 km/s (see Chapter 5) and calculate the coda magnitudes using the relation for Norway (Table 6.5).

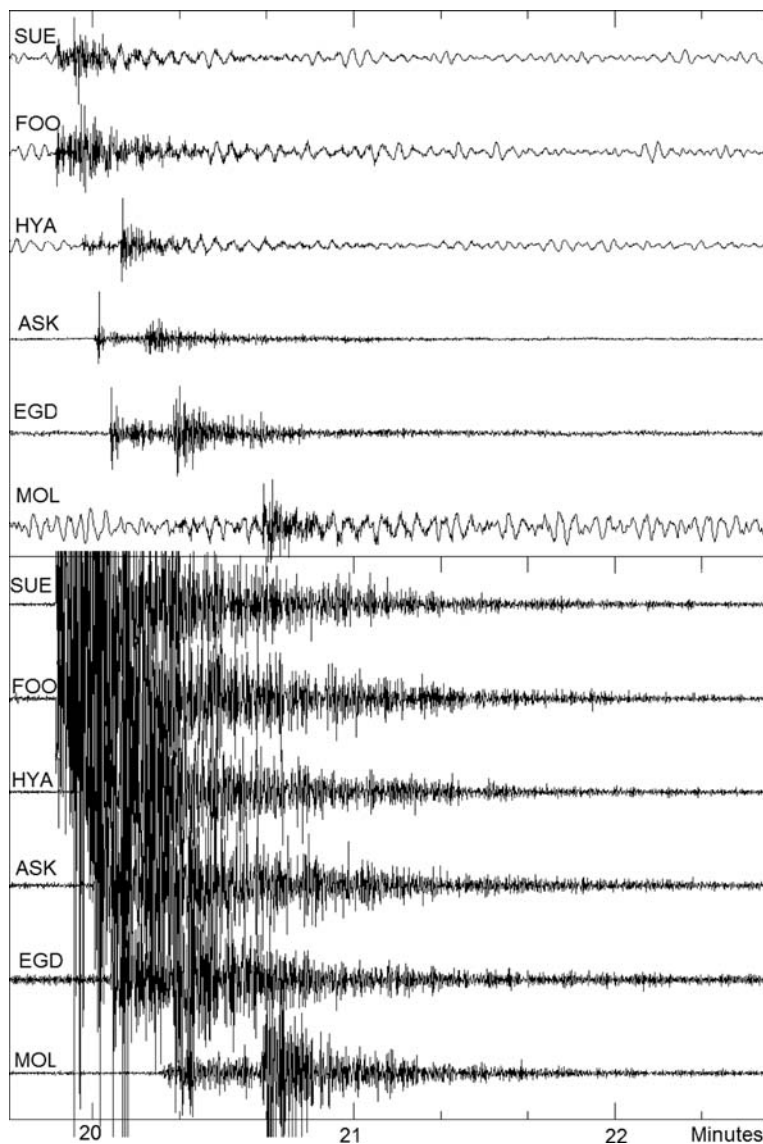


Fig. 6.27 Seismogram of a local earthquake in Western Norway. On *top* is shown the original traces and at the *bottom* the traces amplified and high pass filtered. The time scale is the same for all traces. The origin time is 1996 0705 02:20

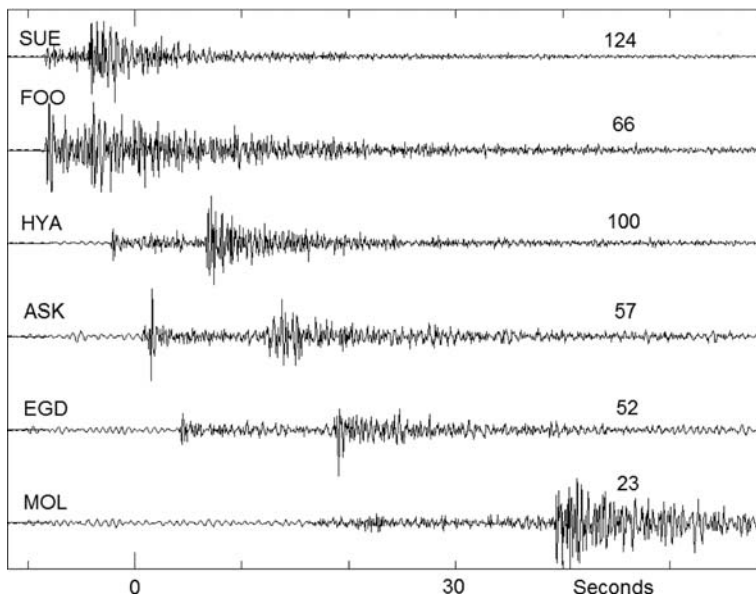


Fig. 6.28 Wood-Anderson simulated displacement seismogram. The number *above* traces to the *right* is maximum amplitude in nm. The origin time is 1996 0705 02:20

Figure 6.28 shows the same seismogram converted to displacement in the frequency band 1.25–20 Hz and it can therefore be considered equivalent to a Wood-Anderson seismogram. This is the kind of conversion some processing systems can do.

- Find the maximum amplitude of each trace and calculate the local magnitude using the relation for Norway (Table 6.4).
- Calculate average M_c and M_L .
- Compare M_c and M_L , both the individual and the average values.

The original local magnitude scale used a tabulated distance correction function (Table 6.2). Assume a gain of 2,080 for the Wood-Anderson seismograph.

- Calculate what the trace amplitudes would have been if recorded on the Wood-Anderson seismogram for the signals in Fig. 6.28.
- Would these amplitudes have been readable on the Wood-Anderson seismogram?
- Calculate the M_L magnitudes using the original definition and attenuation table (Table 6.2) and compare to the magnitudes calculated above.

Exercise 6.2 Body Wave Magnitude m_b

Figure 6.29 shows a copy of a WWSSN SP paper seismogram with a clear P-arrival.

- Read the maximum amplitude (mm) and corresponding period (s) from the seismogram

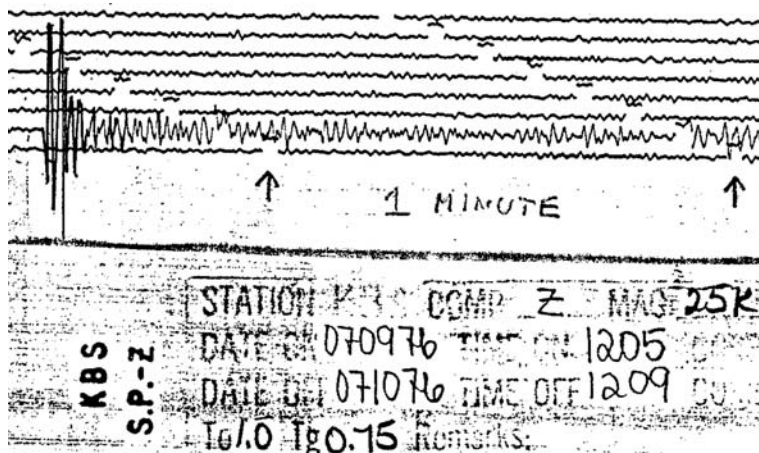


Fig. 6.29 SP seismogram. The figure shows a SP seismogram from the WWSSN. The gain is 25,000. The time scale on printed paper is 60 mm/min like the original seismogram. The origin time is 1976 0710 11:37, depth is 402 km and epicentral distance is 51°

- Convert the amplitude to ground displacement in nm using the gain curve in Fig. 6.10. The gain is 25,000 at 1 Hz.
- Calculate m_b assuming a distance of 85° and a depth of 402 km. For the attenuation function, use both the original relation (Fig. 6.8) and the newer relation (Fig. 6.9) and compare the results and compare to the value of $m_b = 5.8$ reported by ISC. Note that the new attenuation relation is not considered accurate for deeper events.
- Calculate m_b for the event in Fig. 6.11 using the Gutenberg and Richter attenuation relation using both the WWSSN SP simulation and the more broadband signal (0.2–10 Hz). How big is the difference?

Exercise 6.3 Surface Wave Magnitude

Use the seismogram in Fig. 6.17 and calculate M_s . Compare to the reported magnitude.

Computer exercises

- M_L , m_b , and M_s : Read amplitudes manually and automatically and determine magnitudes for all station for one event.
- M_c : Determine coda length manually and test and compare to automatic determination, determine magnitudes.
- M_w : Calculate magnitudes from moments determined by spectral analysis or moment tensor inversion.
- Get average magnitudes of each type and compare to each other and to magnitudes from other agencies.
- Adjust parameters for M_L and M_c magnitudes scales using network observations from several events.
- Merge two catalogs and homogenize magnitudes.

Chapter 7

Focal Mechanism and Seismogram Modeling

The focal mechanism or the fault plane solution describes the orientation of the fault and the slip on the fault relative to a geographical coordinate system. The focal mechanism is the most important parameter to determine once the location and magnitude are known and it is used to determine the actual geometry of the faults as well as inferring the style of faulting and stress regimes of a particular region. All seismological methods of determining fault plane solutions are based on the radiation pattern (see below) that the seismic earthquake source sends out. Seismic waves have different amplitudes and polarities in different directions depending on the relative position of the source with respect to a seismic station. This property can be used in a very simple way by just using the polarities, which is the classical method of using first motion P with analog data. The next level is using amplitudes or amplitude ratios together with polarity data of P and S (can also be used with analog data) while the most advanced methods use the part of or the complete waveforms, either in forward or inverse modeling. A more general description of the seismic source is given by the moment tensor which describes the seismic source radiation as a combination of radiation from several faults. Inversion for the moment tensor can be done from amplitude ratios or full waveform data, which requires the ability to model the seismograms. In this chapter the most common methods will be described. There is a large amount of literature available on seismic sources and how to determine fault plane solutions, see e.g. NMSOP, standard text books, Jost and Herrmann (1989), Kasahara (1981).

Moment tensors solutions for earthquakes at teleseismic distances ($M > 5.5$) based on waveform inversion are usually available within hours of the occurrence of an event. Real-time solutions are also computed routinely for earthquakes at regional distance ($M > 3.5$). However for smaller events, there are generally no routine solutions and one of the methods described in the following may be used if sufficient data is available.

7.1 Fault geometry

The earthquake is assumed to occur on a plane surface and the earthquake can be described as a slip on that surface. In practice, earthquake faults can be much more complicated, however most faults can be described in this simple way. Under this assumption, it is possible to describe the motion causing the earthquake by the orientation of the fault plane (strike and dip) and the direction of slip along the fault plane, slip or rake, see Fig. 7.1. Rake is the most common name for the slip direction and will be used in the following.

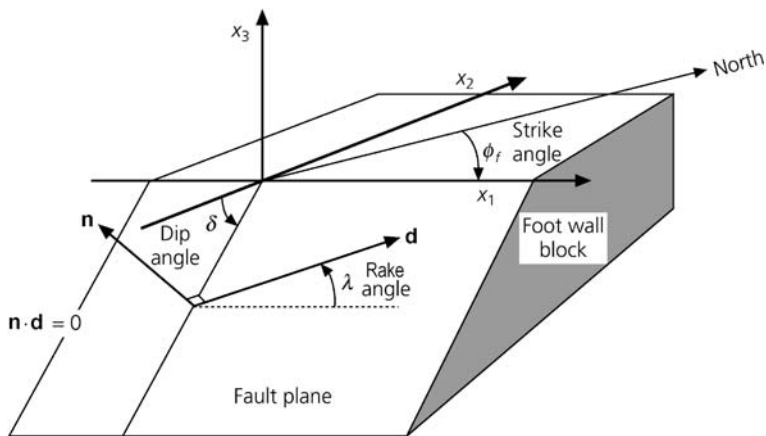


Fig. 7.1 Earthquake fault geometry. The fault orientation is defined by the dip angle δ ($0\text{--}90^\circ$) of the fault and the strike angle Φ measured clockwise from the north ($0\text{--}360^\circ$). The direction of motion in the fault plane is given by the slip vector \mathbf{d} , which is the slip direction and amount with which the hanging wall block moves relative to the foot wall block. The slip is defined with the rake angle λ (-180 to 180°) measured in the fault plane anti clockwise from the strike direction x_1 . The normal vector to the fault is n . Figure from Stein and Wysession (2003) and copied from http://epscx.wustl.edu/seismology/book/book_no_captions/figures/

The geometry of the earthquake faulting can therefore be described by the 3 parameters strike, dip and rake. Different coordinate systems can be used, but the one shown in Fig. 7.1 is the most common. In this coordinate system, x_1 points in the strike direction, x_2 is perpendicular to x_1 and lies in the surface plane and x_3 points up. The strike angle is measured clockwise from north, the rake is measured in the fault plane counter-clockwise from the strike direction and the dip is measured between x_2 and the fault plane. Note that the x_1 axis is chosen so that the dip angle is less than 90° measured from the $-x_2$ axis. The fault and the slip direction can be oriented in many different directions and are named differently relative to the orientation with respect to the surface of the earth, see Fig. 7.2. These examples are the simplest and most faults are a combination of the above as the example in Fig. 7.1, which could be labeled a reverse dip-slip or a thrust fault with a strike slip

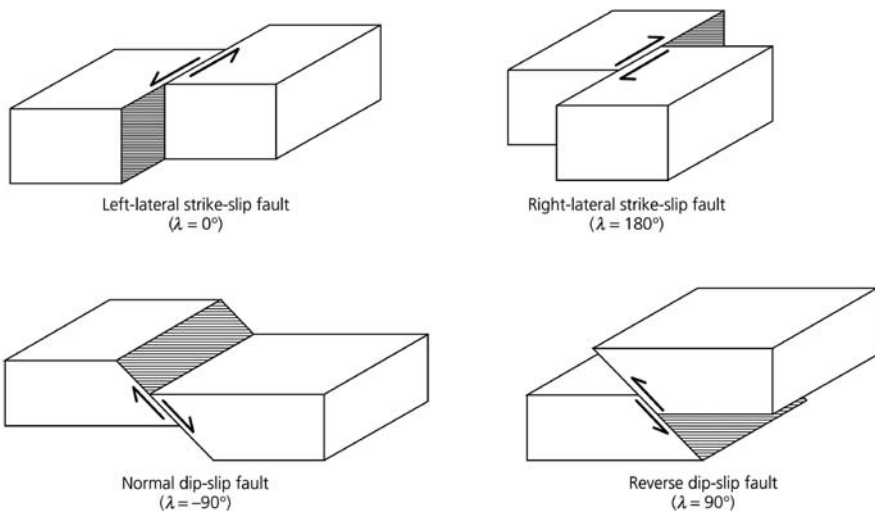


Fig. 7.2 Different orientation of faults with respect to the surface of the earth and corresponding names used. Figure from Stein and Wysession (2003) and copied from http://epscx.wustl.edu/seismology/book/book_no_captions/figures/

component. Such faults are called oblique-slip faults. If the fault breaks the surface, strike, dip and rake can be obtained by geological methods, however the majority of earthquakes do not break the surface so seismological data is used to determine the fault plane solution.

7.2 Source Radiation

When the fault slips, the two sides of the fault move in opposite directions which will create different polarity first motion P in different directions (Fig. 7.3). In this simple example, the surface of the flat earth would be divided into 4 quadrants each of which would have different first motion polarity. If the side of the fault moves towards the station, the first motion is called compression (C) and if it moves away from the station, it is called dilatation (D). On a vertical component sensor this would correspond to motions up or down, respectively. Note that if the slip was on the auxiliary plane, the same observations would be seen. If observations from many uniformly distributed stations were available, the orientation of the two planes could easily be determined by dividing the surface into 4 quadrants with different polarity, however there would be no way of knowing which one was the fault plane without using additional information. For larger earthquakes it is possible to use geology, rupture direction as seen through waveform modeling and aftershock orientation. Thus in principle, we have a simple way of determining the fault plane solution.

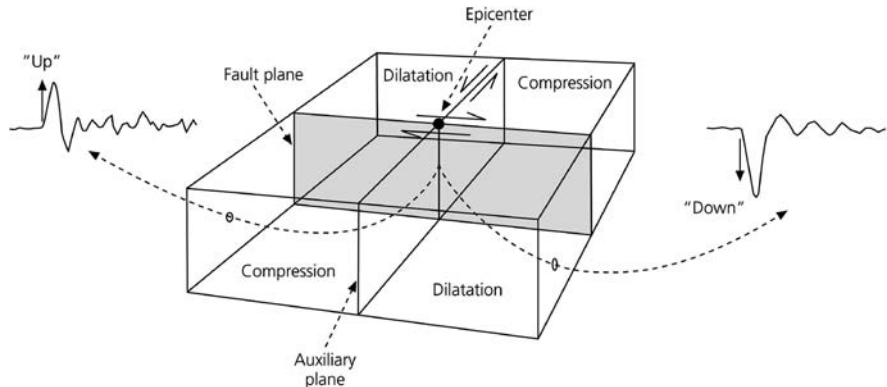


Fig. 7.3 First motion of P observed at different directions relative to the fault plane for a strike-slip fault. The 2 arrows in the fault plane show the relative slip direction in the fault plane. The two arrows in the auxiliary plane show the motion that would give the same seismogram. The arrows can also be considered the forces that drive the motion. Figure modified from Stein and Wysession (2003) and copied from http://epscx.wustl.edu/seismology/book/book_no_captions/figures/

In Fig. 7.3, the motion of the fault is indicated with the arrows, either in the fault plane or the auxiliary plane. The radiation from the underlying forces can be described with a force couple, see Fig. 7.5. Since slip on the fault plane and in the auxiliary plane produces the same polarities, another force couple in the auxiliary plane, with a torque the other way (Fig. 7.3) would create the same polarities. It then turns out that the radiated wave amplitudes from a fault can be described mathematically as the radiation from two force couples, also called a double couple. Having a second couple prevents rotation of the fault system. Considering a simple geometry with the fault plane in the $x_1 - x_2$ plane, the auxiliary plane in the $x_2 - x_3$ plane and a left lateral motion, the normalized P-wave amplitude variation u_r due to the source in the radial direction can, in a spherical coordinate system, and at a constant distance (Fig. 7.4), be expressed as (Stein and Wysession, 2003)

$$u_r = \frac{\sin 2\theta \cos \phi}{4\pi \rho v_p^3} \quad (7.1)$$

where the angles θ and Φ are defined in Fig. 7.4, ρ is the density and v_p is the P-velocity. For SH waves the expression is

$$u_\theta = \frac{\cos 2\theta \cos \phi}{4\pi \rho v_s^3} \quad (7.2)$$

and for SV waves

$$u_\phi = \frac{-\cos \theta \sin \phi}{4\pi \rho v_s^3} \quad (7.3)$$

where v_s is the S-velocity. These equations can be used to generate the radiation patterns seen in Fig. 7.4. It is seen that the ratio between the S amplitude and the P amplitude is theoretically $(v_p/v_s)^3 \approx 5$, which is in agreement with practical observations where S-wave amplitudes are much larger than P-wave amplitudes. The amplitudes will also decrease with distance due to geometrical spreading, see Chapter 8.

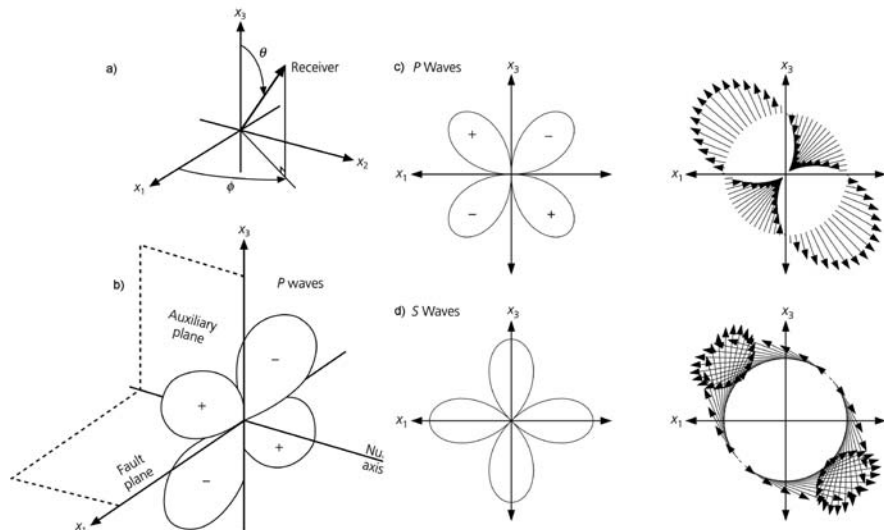


Fig. 7.4 Radiation pattern from a double couple source in the x_1-x_2 plane. (a) The spherical coordinate system, (b) and (c): The P wave radiation pattern, (d): The S wave radiation pattern. Figure b and the two figures in the middle show amplitude and the figures to the right show the direction of motion. For P waves, the amplitude is zero in the fault plane and the auxiliary plane and they are called nodal planes. S waves do not have a nodal plane but the amplitude is zero along the x_2 axis (null axis). Figure from Stein and Wysession (2003) and copied from http://epscx.wustl.edu/seismology/book/book_no_captions/figures/

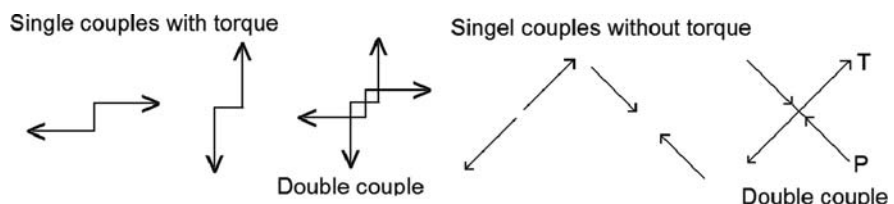


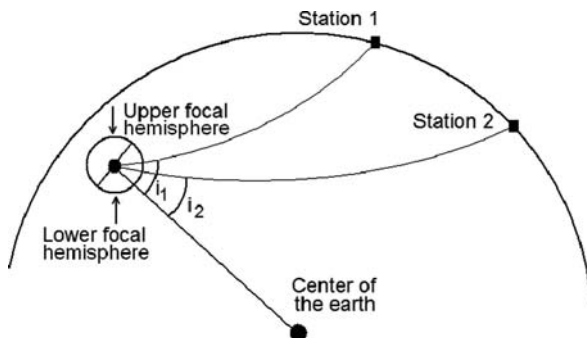
Fig. 7.5 Types of force couples that can generate the far field displacements observed from the fault slip. The force couples without torque are also called dipoles s. Note that the two double couples (middle and right) generate the same far field displacements and either can be used to mathematically describe the fault motion. The maximum and minimum compressive stresses P and T respectively are in directions of 45° to the fault plane and in the same directions as the torque-less single couples

An important use of focal mechanisms is to find the stress orientation in the earth. In an unstressed media we can talk about the compression direction P and tension direction T. However, the interior of the earth is always under compression due to the overburden so we then talk about the direction of maximum and minimum compressive stresses and these directions are also labeled P and T, respectively. From laboratory experiments it is known that new fault planes are oriented at 45° from the maximum and minimum compressive stresses and these stresses are halfway between the nodal planes (Fig. 7.5). However, earthquakes typically occur on pre-existing faults and the angle will be different from 45° (see e.g. Scholtz, 1990; Stein and Wysession, 2003).

7.3 Fault Plane Solution in Practice

The fault geometry is normally not as easy to describe as for the one shown in Fig. 7.3. In order to display the fault planes in two dimensions, the concept of the focal sphere is used (Fig. 7.6).

Fig. 7.6 The focal sphere is a small sphere centered on the hypocenter. The angle of incidence, i , is the angle at which the ray leaves the earthquake focus. It is measured from the vertical direction



The principle of the focal sphere is to observe the motions from the earthquake on the surface of a small sphere centered on the hypocenter. The surface of the sphere will then be divided into 4 quadrants with dilation and compression and again the location of the two possible fault planes can be observed (Fig. 7.7).

Since it is difficult to work on a sphere, one of the hemispheres can be plotted on paper using a stereographic projection (Fig. 7.10). Considering that most observations are on the lower focal sphere and observations on the upper focal sphere can be transferred to the lower focal sphere due to symmetry, the lower focal sphere is mostly used for the projection. Figure 7.8 shows some examples on how different types of faults appear on the stereographic projection.

The simplest fault to imagine is a vertical pure strike slip fault since the fault planes are projected as straight lines. Two examples are shown in Fig. 7.8, (a) with the fault planes N–S or E–W and (b) with a strike of 45° . If example (b) is observed

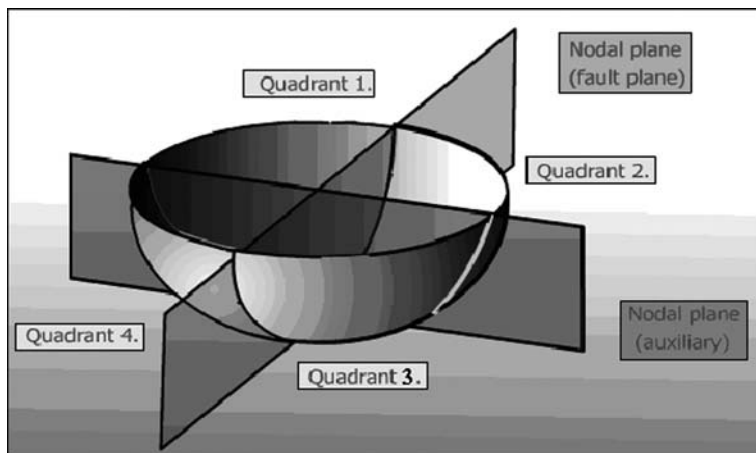


Fig. 7.7 Cutting the focal sphere in 4 parts. The *lower* focal sphere is shown. Figure from www.learninggeoscience.net/free/00071/

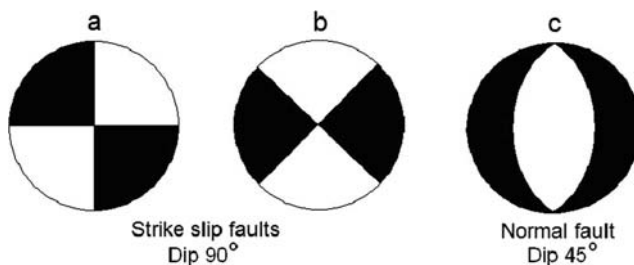


Fig. 7.8 Examples of simple faults. The projections of the *lower* focal sphere are shown

from the top, it looks like example (c). The fault planes in the projections are following the meridians and in example (c) they are no longer straight lines and this is generally the case.

We now describe how to obtain and to plot the observations of polarity on the surface of the focal sphere and measure the strike, dip and rake as defined in the coordinate system of Fig. 7.1. In order to plot an observation point on the focal sphere, the angle of incidence i at the source (Fig. 7.6) and the direction from the earthquake to the station (azimuth, see Chapter 5) must be known. Both of these quantities are calculated when locating an earthquake. Bulletins usually only have the azimuth so when manual fault plane solution are made, the angle of incidence must be calculated manually.

The angle of incidence is always measured from the downward normal to the surface so down-going rays have angle of incidence less than 90° and up-going rays an angle of incidence larger than 90° (see Fig. 7.9). For stations at near distances (Station 1), the first arrival is either Pg or Pn (or another refracted phase).

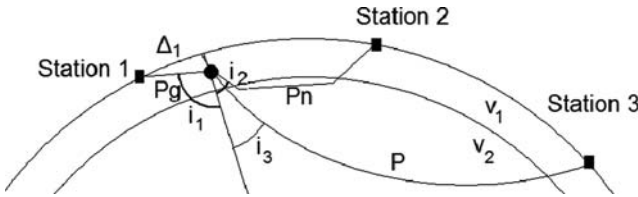


Fig. 7.9 Angle of incidence for different rays. v_1 and v_2 are the P velocities in respective layers and Δ_1 is the epicentral distance to station 1

It is then assumed that the model can be approximated by a flat layer model with constant velocity. For the example in Fig. 7.9, $\tan(180 - i_1) = \Delta_1/h$ (h is hypocentral depth) and it is seen that the angle of incidence is sensitive to the hypocentral depth. Since the angle of incidence has to be projected onto the lower focal sphere, due to symmetry, the angle of incidence to use is $180^\circ - i_1$ and the azimuth to use is $\Phi_1 + 180^\circ$, where Φ_1 is the azimuth for station 1. The angle of incidence used on the lower focal sphere for Pg will then vary with distance from 0 to 90° . For Pn, by Snell's law, $\sin(i_2) = v_1/v_2$. This means the angle of incidence for all Pn phases, irrespective of distance, will be constant. The same will be the case for other refracted phases from one particular layer. In the real earth, velocities vary more continuously so the real angles will vary with distance, but most location programs use layered models so the angles of incidence from refracted phases will plot as concentric circles, see Fig. 7.20.

For teleseismic distances (ray to station 3), the angle of incidence can be calculated from a travel time table (see Chapter 2)

$$r \sin(i)/v = dT/d\Delta \quad (7.4)$$

where r is the distance from the hypocenter to the center of the earth, v the velocity at the hypocenter and $dT/d\Delta$ is the derivative of the travel time curve. In the example above, $\Delta = 65^\circ$ and assuming a normal depth = 33 km, the Bullen Table (Table 2.2), gives $dT/d\Delta = 6.4\text{s}/\text{degree} = 6.4 \cdot (360/2\pi) \text{s}/\text{radian} = 367 \text{s}/\text{radian}$. Using $r = (6371 - 33)$ km and $v = 8\text{km/s}$ gives $\sin(i_3) = 367 \cdot 8.0 / (6371 - 33)$ or $i_3 = 28^\circ$. If the focus had been at the surface and the surface velocity was 6 km/s, $i_3 = 20^\circ$. The angle of incidence is therefore source depth dependent also at teleseismic distances and hypocentral depth is therefore a critical parameter when doing fault plane solutions. As the hypocentral depth is often poorly constrained, it is good practice to investigate the dependency of the solution on depth.

With the observations of azimuth and angle of incidence on the lower focal sphere, the polarity is plotted on the stereographic projection on paper (Fig. 7.10).

An observation is plotted on the line between the center and the observed azimuth (see top observational point). The distance to the point from the center is the angle of incidence. Since the angle of incidence is measured from the vertical, it corresponds to a dip of $90^\circ -$ the dip angle, so it is measured off from the center and out, as

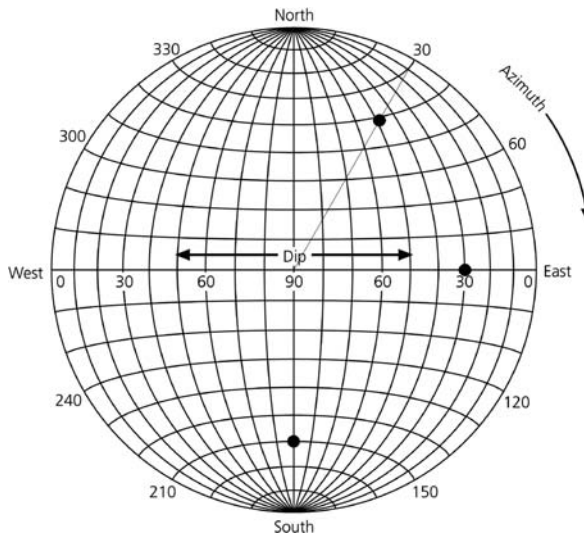


Fig. 7.10 A stereographic projection of the *lower* focal sphere. The azimuth is given by the numbers around the circumference. The meridians (curves going from *top* to *bottom*) are great circles and represent different N–S striking planes with different dips (numbers along the equator). The *top* black point is an observation with an angle of incidence 60° and an azimuth of 30° , the *right* black point is an observation with an angle of incidence of 60° and an azimuth of 90° and the *bottom* black point is an observation with an angle of incidence of 60° and an azimuth of 180° . Figure from Stein and Wysession (2003) and copied (and modified) from http://epscx.wustl.edu/seismology/book/book_no_captions/figures/

indicated by the observation point to the right (azimuth 90° angle of incidence 60°). In the manual practice, this is done by

- Fix a piece of transparent paper at the center over the stereographic grid.
- Trace the rim of the projection and mark the north on the rim of the circle.
- On the rim, mark the azimuth.
- Rotate the paper so the azimuth mark is aligned with the equator (90°).
- Measure off the angle on incidence and plot the point on the transparent paper indicating the observed polarity (usually black circle for compression and open circle for dilatation).
- Rotate paper back to the north and the observation is now at the correct position on the paper.
- Continue with the next point.

The procedure is illustrated in Fig. 7.11. Once all the polarities have been plotted, the next task is to find the fault plane and the auxiliary plane. Figure 7.12 illustrates how it is done manually. The figure shows the process of determining the two fault planes. Figure (a) shows the observations plotted on the stereographic net. The first task is to find the first meridian that separates the dilatations from the compressions.

Fig. 7.11 Principle of plotting an observation point as described above. Az is azimuth and Ain is angle of incidence

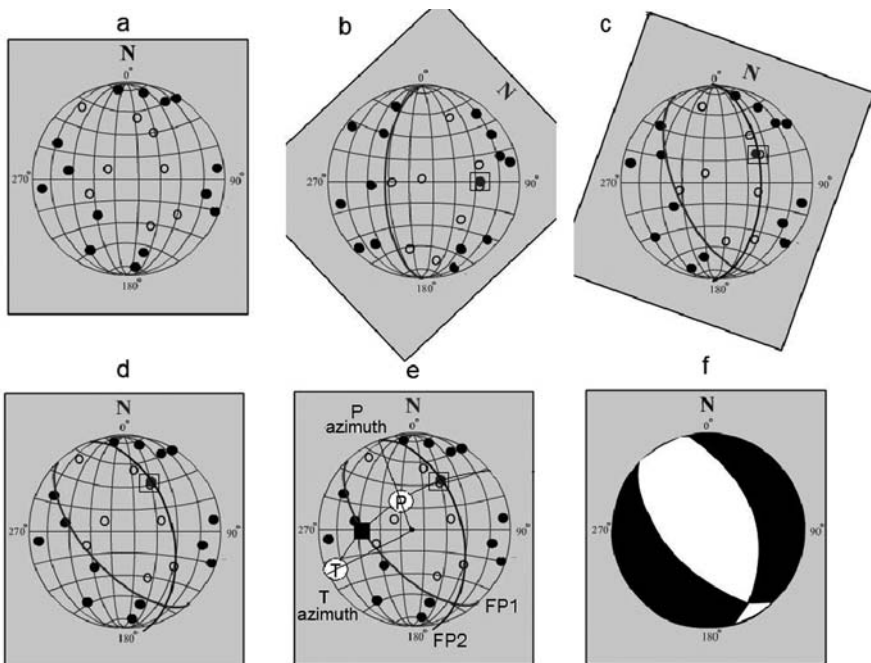
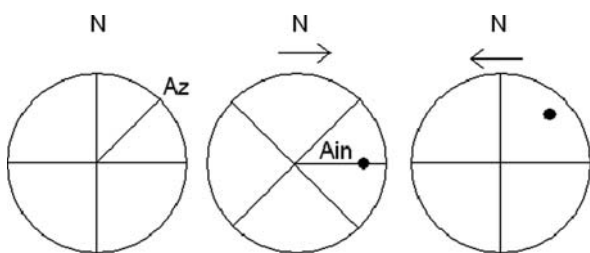


Fig. 7.12 Finding the fault planes. Open circles are dilatation and closed circles compression. The small square indicates the position of the pole of the first fault plane in (b). See text for more explanation. (Modified from www.learninggeoscience.net/free/00071/)

Imagine a piece of transparent paper, on which the observations have been plotted on top of the stereo-net. The observations can now be rotated to find the first meridian that nicely separates the dilatation and compressions (b). The second meridian (fault plane) must now be at a right angle to the first fault plane which means that the second meridian must pass through the pole of the first plane (open square on the figure) as well as separating dilatations and compressions. A pole is found by rotating so that the plane is aligned with a meridian, it is then measured at 90° along the dip axis. So the observation sheet is again rotated to obtain the best fitting meridian (c). The observation sheet then is rotated back to the original position to

see the true orientation of the nodal plane (d). Finally the parameters are read off the plot (e). The above sequence and other fault plane solution information can be seen dynamically at <http://www.learninggeoscience.net/free/00071/>. This example is a “nice” example since there are points all over the focal sphere indicating that the event is surrounded by seismic stations (different azimuths) at a good distribution of distances (different angle of incidence). In many cases networks are more one sided and the focal sphere will only be partly covered with observations making it more difficult to make a reliable fault plane solution.

The next task is to find the strike and dip of the two fault planes. The dip is measured from the outside, along an equatorial line, to the fault plane. In Fig. 7.12 (b), the dip of fault plane 1 (FP1) is seen to be 58° and fault plane 2 (FP2) has a dip of 45° (Fig. 7.12 (c)). Measuring strike presents 2 possibilities, see the example in Fig. 7.13.

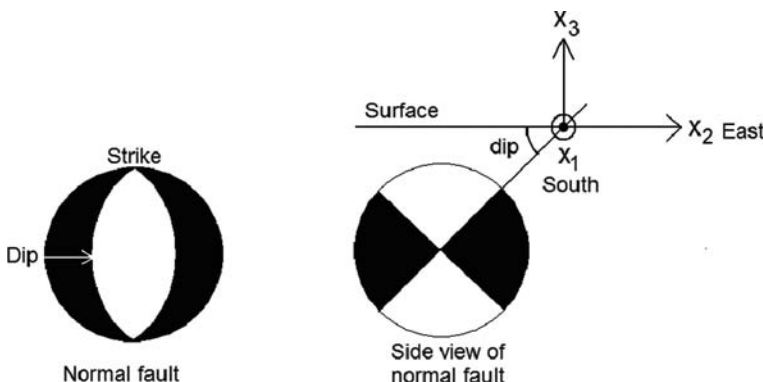


Fig. 7.13 Determining strike and dip of a normal fault from the fault plane solution. The fault plane with the arrow is selected and the length of the arrow shows the dip measurement (from circumference to meridian). The same fault is seen to the right in a side view and the selected fault plane is prolonged to the surface. The orientation of the x_1 , x_2 and x_3 is given in Fig. 7.1 and x_1 is pointing out of the paper

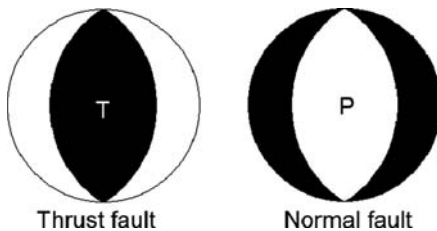
In this example, the normal fault has two planes both in the N–S direction and both with a dip of 45° . The dip is measured from the outside along an equatorial line as described above. The question is now how to determine the correct strike, north or south. The fault plane indicated with an arrow (left) is seen in a side view prolonged to the surface. Since the dip must be less than 90° measured from the $-x_2$ axis, the x_1 axis must be pointing south and the strike is 180° . Similarly the strike of the other plane must be 0° . We can therefore formulate a simple rule on how to correctly measure the strike:

The strike is measured at the point on the circumference from where the fault plane is seen to the left of the center.

In the example in Fig. 7.12, the strike of FP1 is 160° and of FP2 it is 345° . We have now measured the strike and dip of the two fault planes and this almost

describes the fault plane solution. In practice, one of the planes is selected as the fault plane and the strike, dip and rake is given for that plane, which is equivalent to giving the strike, dip and rake for the other plane. Rake can also be obtained geometrically from the above fault plane solution, but this is a bit complicated and difficult to remember (see description in NMSOP) so rake is usually calculated. Unfortunately it cannot be calculated unambiguously from the strike and dip of the two fault planes, see Fig. 7.14.

Fig. 7.14 A pure normal fault and a pure thrust fault



These two faults are defined by the same dip and strike of the two planes, but the rake is in different directions (opposite) since polarities are opposite, so there would be an 180° uncertainty in using only the information about the two fault planes (see examples in Fig. 7.15). The rake of plane 2, λ_2 , is given as function of the dip of plane 1, δ_1 and the two azimuths Φ_1 and Φ_2 as (Stein and Wysession, 2003)

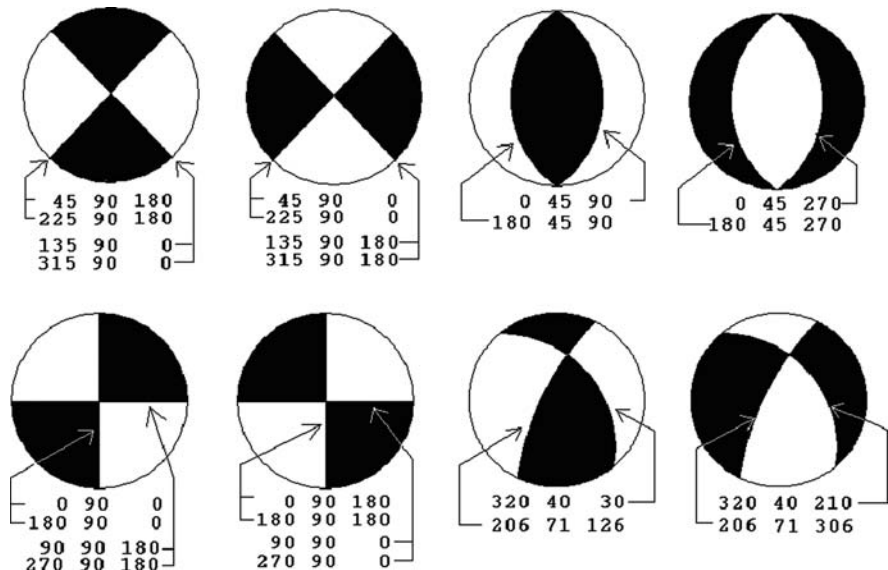


Fig. 7.15 Strike dip and rake for some simple faults. At the *left* is shown strike-slip faults and to the *right* inverse and normal faults. An arrow indicates the strike, dip and rake of the corresponding nodal plane

$$\cos(\lambda_2) = \sin(\delta_1) \sin(\Phi_2 - \Phi_1) \quad (7.5)$$

so flipping Φ_1 and Φ_2 gives a different rake. In order to get the correct rake, information about polarity must be used, which is obtained by using the P and T axis orientation or the type of fault.

Calculating rake using (7.5), the rake can be determined using the following rules:

- If the fault has a reverse component, the rake is between 0° and 180°
- If the faulting has a normal component, the rake is between 180° – 360°
- Pure strike slip: Left lateral: Rake = 0° , Right lateral = 180°

If strike, dip and rake are known for one plane, strike dip and rake can be calculated for the other plane by first calculating δ_2 using (Stein and Wysession, 2003)

$$\cos(\delta_2) = \sin(\lambda_1) \sin(\delta_1) \quad (7.6)$$

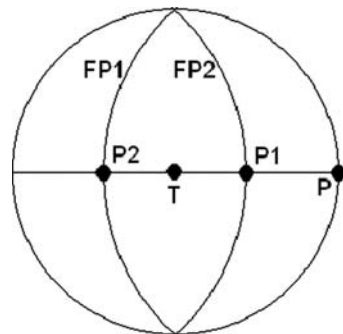
and then Φ_2 using (Stein and Wysession, 2003)

$$\tan(\delta_1) \tan(\delta_2) \cos(\Phi_1 - \Phi_2) = -1 \quad (7.7)$$

and finally λ_2 using (7.5). The ambiguity of the rake must still be resolved as described above.

The P-axis of maximum compression is in the middle of the dilatation quadrant and the T-axis of minimum compression in the middle of the compression quadrant at 45° from the planes (Figs. 7.12 and 7.16).

Fig. 7.16 Illustration of finding P and T of a pure thrust fault. FP1 and FP2 are the 2 fault planes, respectively and P1 and P2 the corresponding poles of the fault planes FP1 and FP2, respectively. The dip and azimuth of T are 90° and 0° (undefined) respectively and the dip and azimuth of P are 90° respectively



The procedure for determining P and T orientations

- Draw a great circle through the two poles P1 and P2 of the two nodal planes.
- Mark the T axis in the middle of the compressional quadrant by measuring of 45° along the great circle connection P1 and P2.

- Mark the P axis in the middle of the dilatational quadrant by measuring of 45° along the great circle connecting P1 and P2.
- Measure the azimuth of P and T respectively (like for polarity observations).
- Measure the dip of P and T respectively (like angle of incidence for polarity observations).

In the example in Fig. 7.12 above, we get approximately

$$\begin{aligned} \text{P axis: } & \text{dip} = 60^\circ, \text{azimuth} = 340^\circ \\ \text{T axis: } & \text{dip} = 10^\circ, \text{azimuth} = 240^\circ \end{aligned}$$

In practice, fault plane solutions are rarely derived by hand, but rather determined using grid search with designated software. In the following we will show some examples of making fault plane solution based on polarity data.

7.4 Obtaining Polarity

Reading polarity will in many cases be clear and simple (see e.g. Fig. 7.19). However, for many seismograms it is not possible to read polarity and for others it is quite uncertain. In the following we will show some examples.

Phases to read: In general only the first arrival P is used since this is usually the only clear phase. However, later arriving P-phases like pP (but not sP), PP and Pg can also be used if they present a clear and unambiguous onset. Note that not all software allows use of these phases. Secondary phases are actually good to use, particularly with a sparse data set, since they usually have very different angles of incidence compared to the first arrival (like Pn and Pg).

Note that polarity should always be read on unfiltered traces since a filter might change the polarity, see Chapter 4.

The example in Fig. 7.17 shows an example of a distant event with very clear P-arrivals.

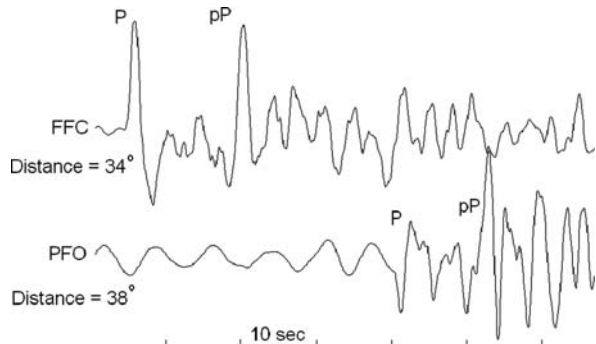


Fig. 7.17 Example of clear polarities of a distant event. The origin time is 2007 1002 18:00, $m_b = 6.2$ (PDE) and the centroid (see later) depth is 41 km. Both traces are vertical broadband

It is seen that the P is very clear, compression on top trace and dilatation on bottom trace. For station FFC, pP can be read as compression with reasonable certainty while the polarity of pP cannot be estimated with confidence for station PFO. The stations here are in a “good” distance range where we can expect clear uncluttered phases. From the same event, Fig. 7.18 shows a near station recording.

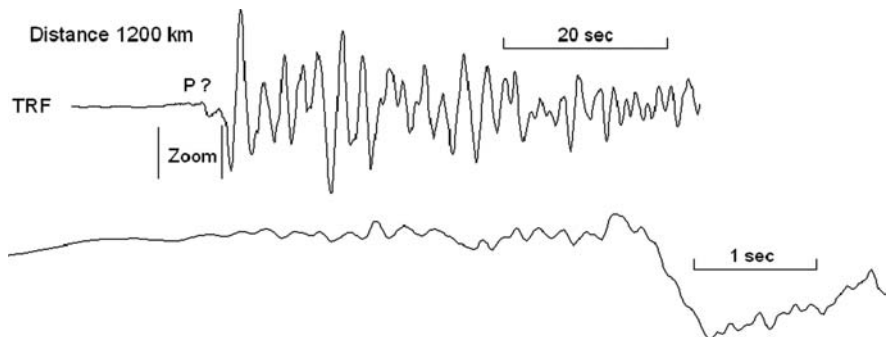


Fig. 7.18 Example of unclear polarity or station TRF, vertical channel broadband. It is the same event as in Fig. 7.17

From the un-zoomed trace it appears that a weak compression is seen (at the question mark) or a stronger dilatation. From the zoomed trace it is clear that some emergent higher frequency signal arrives some seconds before the low frequency signal, which now seems to show clear dilatation. In this case, polarity cannot be read with any confidence despite the short distance and the large magnitude. Figure 7.19 shows a small local event in Tanzania.

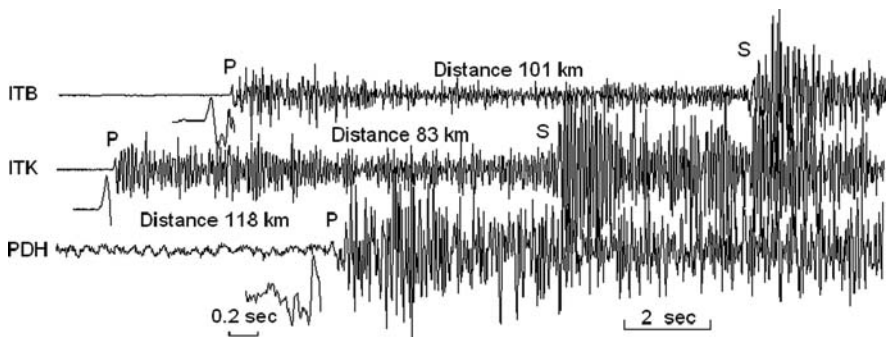


Fig. 7.19 Local event from Tanzania. $M_L = 2.3$, hypocentral depth is 26 km and origin time is 1992 1007 01:13. Zoom of the P is shown *below* the traces. All channels are vertical short period

Since the event is rather deep, the P for ITB and ITK have been identified as Pg and the P-polarities are clearly seen. PDH is further away and the P has been identified as Pn. Since Pn usually has a smaller amplitude than Pg and in addition the signal to noise ratio is poorer on PDH than the other stations, the polarity of the

first arrival P cannot be read with confidence. For local events, it is often the case that refracted arrivals show rather low amplitude emergent P.

Summary of guidelines for reading polarity

- Only read on vertical channel.
- Do not filter.
- Only read clear polarities, could be more than one phase for the same trace.
- Zoom sufficiently to make sure the first P is clearly seen above the background noise.

7.5 Fault Plane Solution Using Local Data and Polarity

The larger globally recorded earthquakes usually get the fault plane solution determined by the global data at some of the larger data centers using moment tensor inversion (see 7.10). For smaller earthquakes recorded locally, the fault plane solution must be determined locally. The method of using polarities is the most common approach and also amplitudes are sometimes used, particularly if few polarity data are available (see 7.8). In this section we will look at examples of using polarity data only in computer based determinations. The most common method is based on grid search. This consists of calculating the theoretical polarities for all observed polarities (using station event parameters) for a particular grid point (strike, dip and rake) and counting how many polarities fit the particular test solution. By systematically checking all possible strike, dip and rake combinations in an equally spaced grid (e.g. 2°), the strike dip and rake with the smallest number of polarity errors can be found. It is quite common that all polarities will not fit and also that the best fit will result in many different solutions giving an indication of the uncertainty of the solutions. It is then up to the user to select one of the solutions. Figure 7.20 shows an example of a local event. This event has stations in the epicentral distance range 1–260 km with most of the stations at less than 100 km distance and the hypocentral depth was well determined to 3 km. The event is within the network so this should potentially give a well restrained solution. With a 5° grid, there are 55 different solutions and Fig. 7.20 shows the range of solutions. So even with relatively good data, as in this case, the uncertainty in the solution is rather high. However the direction of the stress field and type of fault is quite certain (normal fault). There was one polarity from station ARAC that did not fit any of the solutions. From the figure showing the zoom around P, it is seen that the onset is quite emergent and it would not be impossible to interpret the first arrival as dilatation. Probably the onset is too uncertain to be used.

Summary of guidelines for fault plane solutions using polarity and grid search

- Check the location and make sure the depth is as correct as possible, fix depth if needed. It should be checked how stable the solution is to changes in the depth.

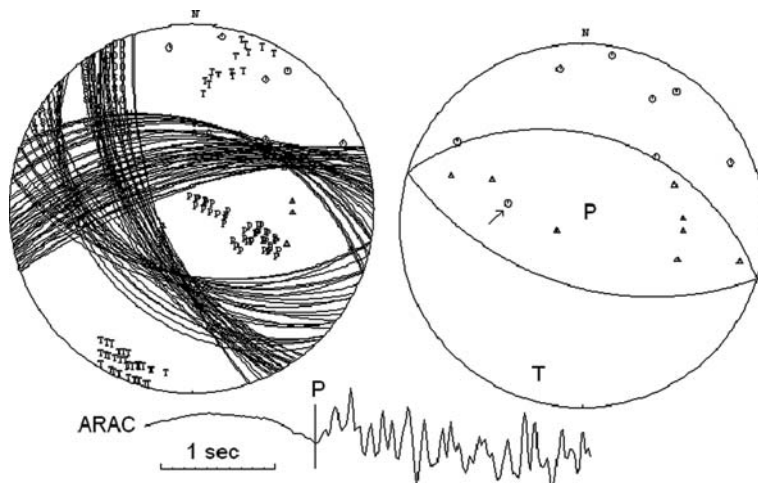


Fig. 7.20 Fault plane solution for a local event in Andalucia, Spain. The *left* figure shows possible solutions within a 5° grid and one polarity error and the figure to the *left* is one of the possible solutions. Compressions are indicated with circles and dilatation with triangles. The *arrow* in the *right* hand figure indicates the polarity that does not fit and the corresponding seismogram is shown at the *bottom*. Note many of the observations in the *right* part of the figure have the same angle of incidence and are therefore plotted at the same distance to the center. P and T indicate P and T axis respectively. Origin time 2007 0104 23:32

- Read polarities on zoomed in traces, the first motion might be quite weak compared to later arrivals.
- Search first in a coarse grid (like 10°) to get an idea of the solution space.
- Refine the grid to find possible solutions.

7.6 Composite Fault Plane Solution

For many small networks, the number of stations is too small to make a fault plane solution using polarities from a single event. Under the assumption that the underlying stress field will generate events with similar fault plane solutions, a group of events can be used together to make one fault plane solution which will represent an average of the supposedly similar solutions. The advantage of using several events with different azimuths and angles of incidence is that the observations will be well spread out on the focal sphere. Figure 7.21 shows an example of using 10 events from a small 5 station network.

Each event has between 2 and 5 polarities and the grid search is performed with a 5° grid and only 2 polarities did not fit. All possible solutions were very close to the one shown. If this had been observations from one event, this solution would have been considered very reliable. In this tectonic regime, it is not unlikely that the events would have similar mechanisms and considering the good fit, this composite solution is probably also reliable. The solution is a normal fault oriented parallel to

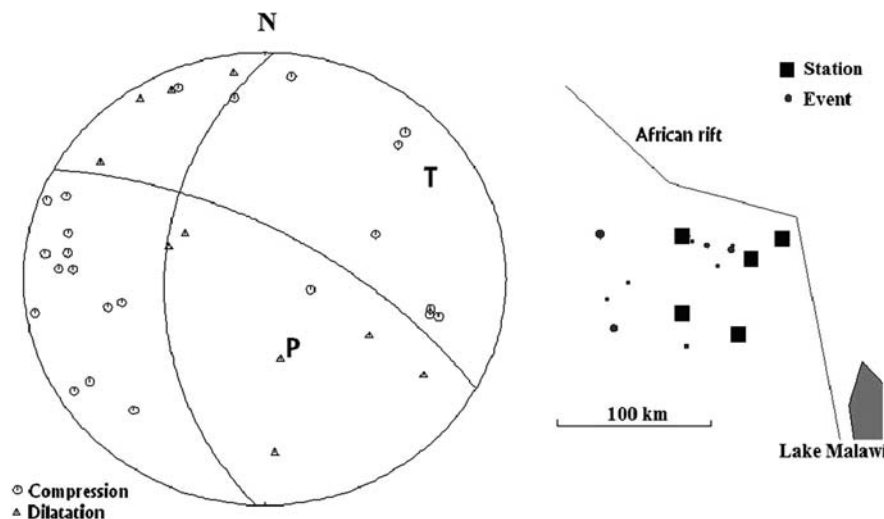


Fig. 7.21 Composite fault plane solution using 10 events. To the *right* is seen a small network in Tanzania near the African rift. The epicenters are marked with circular dots. To the *left* is seen the composite fault plane solution. The data is from October and November, 1992 and the magnitudes are between 1.5 and 3.6. The event depths are between 6 and 36 km

the rift which seems reasonable and very similar to other events with published solutions from the same area (Stein and Wysession, 2003).

7.7 Fault Plane Solution Using Global Data

For all larger events ($M > 5.5$), fault plane solutions are usually available quite quickly from global agencies. It might still be useful to make fault plane solution using polarities and possibly amplitudes for one of the following reasons:

- No global solution available if event is too small or occurring before the moment tensor solutions were generally available.
- Making a moment tensor inversion is more difficult due to lack of digital data for older events.
- Moment tensor and first motion solution might be different so interesting to compare.

If ISC data is available, the first approach can be to just use reported polarities (see example in exercises), however many operators do not read polarities and the quality of the data might be uncertain since the data is not used locally. If little or unreliable ISC data is available, original waveform data must be used, either analog for older data or digital for newer data. In both cases the procedure for doing the fault plane solution is similar:

- Download waveform data from an international data center (see Chapter 10).
- Get hypocenter from an agency, and if using only parameter data, also get all parameters data: Arrival times and polarities of all phases.
- Put data into processing system, make sure depth is correct. If not try to reprocess to improve depth (see Chapter 5). In general, the epicenter should be trusted and fixed to the agency location unless additional data can give a better location.
- Read polarities if using digital data (see Chapter 4), use distance less than 90° to avoid uncertain observations. Use distances less than 30° with caution.
- Locate to make sure P's have been correctly identified (what is thought to be P could be pP or PP).
- Do fault plane solution by computer grid search, try with several combinations of grid sizes and acceptable number of errors.
- Compare to other solutions, if possible, to evaluate quality.

Figure 7.22 shows an example of making a fault plane solution using recent waveform data. The obtained solution is compared to the fault plane solution reported internationally.

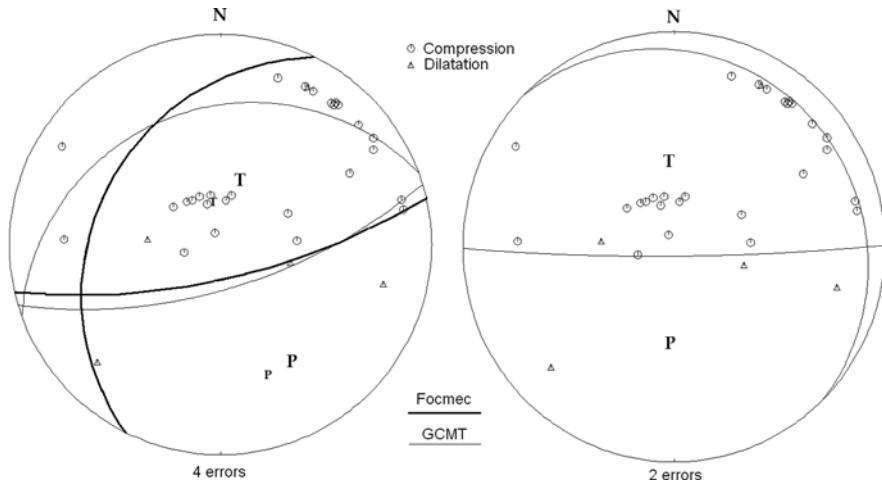


Fig. 7.22 Fault plane solution for an earthquake in Alaska using global data. The solution to the left shows the Global Centroid Moment Tensor (GCMT) solution (thin lines) as well as one of the possible solutions using polarities and the Focmec program (heavy lines). The small P and T's are from GCMT and the large P and T's from our solution. The solution to the right shows an alternative solution using the same polarity data. The origin time is 2007 1002 18:00, $m_b = 6.2$ (PDE) and the centroid depth is 41 km. The angle of incidence is calculated by HYPOCENTER using the IASP91 model

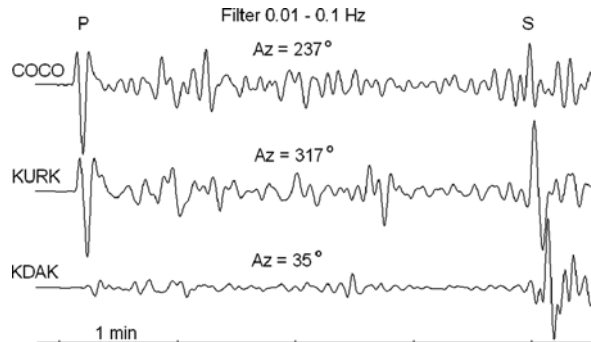
This example is using seismograms obtained from IRIS and a location from USGS (PDE). The depth from USGS was considered reliable due to a large number of both local and distant stations. Not all seismograms were downloaded and there was only a check on the data being reasonably distance distributed so using the

entire data set might have resulted in a different and better constrained solution. See Fig. 7.17 and Fig. 7.18 for examples of reading polarity from this event. Stations were distributed in the distance range 0.3° to 87° . The grid search was performed with a 5° grid and several solutions were possible of which 2 are shown above. The solution is not very well constrained since most observations were compressions so the fault planes are critically dependent on the few dilations. However both solutions show thrust fault with one comparable fault plane and similar direction of P and T. The CMT (Centroid moment tensor, see later) solution is similar to one of the solutions with the polarities, but many observations at short distance (angle of incidence near 90° , plotted near the rim) do not fit the moment tensor solution. This is most likely caused by uncertainty in calculating the angle of incidence at short distances, but might also be caused by the fundamentally different focal solution obtained by the moment tensor than the one obtained by polarities, see Fig. 7.34.

7.8 Fault Plane Solution Using Amplitudes

The radiation pattern has variation in amplitude as a function of the source orientation and a polarity observation can be considered the simplest form of using an amplitude. Obviously the amplitude must have a range of values when changing from positive to negative between stations, see (7.1), so the variation in amplitude holds a lot of information on the source mechanism, which would be desirable to use in determining source mechanism, see Fig. 7.23 for an example.

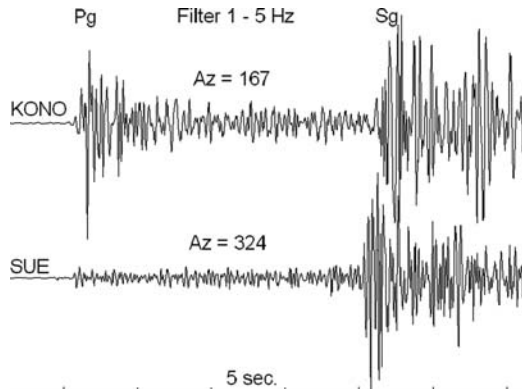
Fig. 7.23 Broadband seismograms of the vertical component showing P and S for a deep earthquake near Japan. The three stations have similar distances ($54\text{--}58^\circ$) but different azimuths (Az) as indicated on the figure. The origin time is 2007 0928 13:38, hypocentral depth is 260 km and $m_b(\text{PDE}) = 6.7$



The figure shows three stations at a similar distance (so amplitude decay due to attenuation is similar), but different azimuths and there is therefore a clear variation in the relative amplitudes of P and S while all three polarities are compression and therefore give relatively less information about the source mechanism than the amplitudes.

A similar example for a local event is shown in Fig. 7.24.

Fig. 7.24 A broadband (KONO) and a SP (SUE) seismogram of the vertical component of a local earthquake. The two stations have similar distances (167–173 km) but different azimuth (Az) as indicated on the figure. The origin time is 1997 0812 08:14, the hypocentral depth is 12 km and $M_L = 2.8$



We also see a clear variation of the relative P and S amplitudes for the local event. In this case the Pg and Sg amplitudes have been compared since the first arrivals Pn and Sn are too small to be clearly seen.

These events will be used to illustrate how to obtain fault plane solution using amplitudes, see below.

There are also drawbacks to using amplitudes since several factors, besides the source mechanism, affect the amplitude observed at a seismic station: Source time function (an earthquake has a finite rupture time so the source time function and the amplitude depends on azimuth due to the rupture propagation, (directivity), see Fig. 7.41), earth structure and instrument characteristics. Particularly the earth structure can complicate the picture. In the following, a simplified overview will be given on how to use amplitudes for determining fault plane solution. In the following, it will be assumed that the amplitude used has a frequency below the corner frequency of the source spectrum (see Chapter 8) so that it is proportional to the seismic moment and we will therefore disregard the effect of the source time function.

In its simplest form we have seen that the earthquake source can be described by a double couple of forces (Fig. 7.5) with a simple mathematical expression (7.1) for the P-amplitude as a function of the spherical coordinates. Relation (7.1) is useful to explain the shape of the radiation pattern for a pure strike-slip fault oriented north-south, but not of much help in determining the fault plane solution for an arbitrary strike, dip and rake in a general coordinate system. In the general case (7.1) is then much more complicated and, assuming a unit distance in a homogeneous medium, (7.1) can be written as (e.g. Aki and Richards, 2002).

$$u_r \sim F(\Phi, \delta, \lambda, x, x_0) \quad (7.8)$$

where F is a function of the source parameters and the position of the event x_0 and the station x . A similar expression can be made for the amplitudes of SV and SH waves u_{SV} and u_{SH} , respectively. The function F is a complicated nonlinear function in terms of Φ , δ and λ as well as distance and azimuth, however it is straight forward

to calculate with known parameters. In practice, the displacement, (at a frequency below the corner frequency (see Chapter 8) so we can assume no time function dependence) is calculated as

$$u_r = M_0 \cdot F(\Phi, \delta, \lambda, x, x_0) \cdot G \cdot A \cdot I \quad (7.9)$$

where M_0 is the seismic moment, G is geometrical spreading including the effect of the free surface (see Chapter 8), I is the effect of the instrument (see Chapter 3), A is the amplitude effect due to the anelastic attenuation (see Chapter 8). Strictly speaking, the effect of attenuation and instrument is frequency dependent, however if it is assumed that u_r represents the maximum amplitude of the first arrival for stations at similar distances, a simple time domain correction can be made. Assuming a known source and receiver position, a known effect of structure and attenuation, then (7.9) contains 4 unknowns: M_0 , Φ , δ , and λ . In principle, only 4 amplitude observations are needed to get the unknowns. This could be 4 P observations at 4 stations or observations of P, SV and SH amplitudes at one station and one amplitude at another station. Normally, many more observations would be available and the problem is over-determined. Since (7.9) is nonlinear, a solution cannot be found by linear methods but using forward modeling and grid search, a best fit of the source parameters can be found (e.g. Slunga, 1981). In the fitting process, absolute amplitudes or amplitudes with polarity can be used. It is often impossible to observe polarity of amplitudes, e.g. for Sg.

In a slightly more complicated approach, a time function can be assumed from the size of the event so instead of just calculating the maximum amplitude, the seismogram of e.g. the P-phase is calculated. By using the well known method of combining the teleseismic phases of P, pP and sP (see below), a complete seismogram for the first part of the seismogram can be calculated (e.g. Stein and Wysession, 2003) and a best fault plane solution obtained by grid search. This is now a standard technique with standard programs available (e.g. QSEIS, Wang and Wang (2007)). Langston (1982) demonstrated that even using a single station, this method was useful in constraining the fault plane solution. The method works reasonably well for the teleseismic distance range 30° to 90° where the effect of the earth structure can be accurately calculated (see Chapters 6 and see 8). For local and regional distances, the path corrections (attenuation and geometrical spreading) for body waves can be complicated and very uncertain and it is difficult to use absolute amplitudes routinely. However, programs are also available that model the local seismogram for selected phases like Pg, Pn and PmP, see below. For very short distances, where only direct rays are used, it is simpler to calculate G and some routine use of amplitudes is seen in practice.

7.8.1 Using Amplitude Ratios

Considering the uncertainty in obtaining absolute amplitudes, using amplitude ratios is more reliable since the effect of moment, geometrical spreading, wave directivity

and instrument cancels out (moment is then not determined) and only the effect of the free surface and possible different attenuation of the two amplitudes u_1 and u_2 (usually P and S) must be corrected for. The observation of the amplitude ratio is then

$$u_2/u_1 = F_r(\Phi, \delta, \lambda, x, x_0) A_r FR \quad (7.10)$$

where F_r is the ratio of the two F 's (ratio of radiation patterns), A_r is the effect of attenuation and FR the free surface effect. *It is assumed that the two amplitudes are of the same type, e.g. Pg and Sg for the assumptions to hold.*

This method has been incorporated into the well known public domain inversion program FOCMEC (Snoke, 2003a) using amplitudes and polarities. The program can also use polarities of SV and SH, however, they are often hard to read and the polarities are very sensitive to the local structure (Snoke, 2003b) so it is in general not recommended to use S-wave polarity data. If used, they are usually read on radial and transverse components to be able to separate SV and SH and the sign convention most often used is as follows (Snoke, 2003b): *When the observer faces the station with the back to the earthquake, motion towards the station is positive on the R component and motion to the right is positive on the T component, see example in Fig. 7.25.*

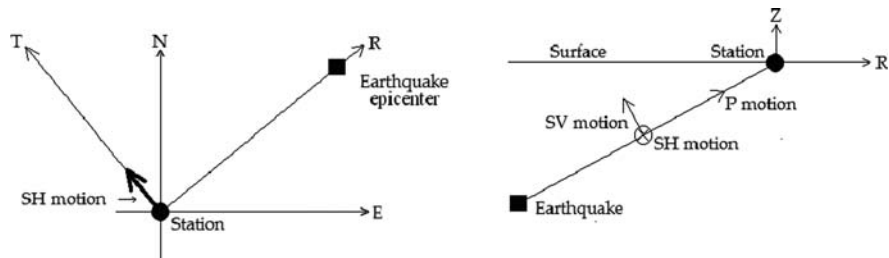


Fig. 7.25 Definition of polarity, see text

In this example the P polarity would be positive on the Z and R components (towards the stations). The SH wave would be positive on the N component and negative on the E component, theoretically zero on the R component and positive on the T component (motion to the right seen from the earthquake). The projection of the SV motion would be recorded on the Z and R components and be positive on the Z component and negative on the R component (motion away from the station).

The method of using amplitude ratios can in principle be used for earthquakes at any distance provided the amplitude ratios can be corrected for the effect of the free surface and attenuation in which case the ratios are what would be expected at the surface of the focal sphere (which is the input to Snoke's program). The correction for the free surface effect only requires v_p/v_s and the angle of emergence (angle from the vertical to the ray), see e.g. Bullen (1963). The angle of emergence can be calculated from the angle of incidence at the source (given by most location

programs) and the velocity at the source and surface. For a local model, Snell's law can be used and for a global model, the ray parameter is used.

The Q-correction for the amplitude ratio of S to P amplitude for local earthquakes is, assuming the same frequency for the case of P and S, (see Chapter 8)

$$e^{-\pi \left(\frac{f_s t_s}{Q_s} - \frac{f_p t_p}{Q_p} \right)} = e^{-\pi f_p \left(\frac{f_s v_p / v_s}{Q_s} - \frac{f_p}{Q_p} \right)} \approx e^{-\pi f_p \frac{v_p / v_s - 1}{Q}} \quad (7.11)$$

where f_p and f_s are the frequencies of P and S, respectively, f is the assumed same frequency of P and S, t_p and t_s are P and S travel times respectively and Q_p , Q_s and Q are Q of P, Q of S and average Q of S and P, respectively. Often only Q of S is known and Q of P is considered to have a similar value (see Chapter 8). For a travel time of 10 s, a frequency of 5 Hz, $v_p/v_s = 1.73$ and a $Q = 300$, the above correction factor is 0.7. This might be considered small compared to other uncertainties in reading amplitudes and is often ignored. At shorter distances the correction would be less.

The Q-correction for the amplitude ratio for distant earthquakes is (see Chapter 8)

$$e^{-\pi \left(f_s t_s^* - f_p t_p^* \right)} \approx e^{-\pi f^3} \quad (7.12)$$

where t_s^* and t_p^* are t^* for P and S respectively and the approximation assumes the same frequency for P and S and the commonly used values of $t_s^* = 4$ and $t_p^* = 1$ for $f < 1$ Hz in the distance range 30–90° (see Chapter 8). At a frequency of 0.1 Hz, this would give a correction in the ratio of a factor of 0.4 and cannot be ignored. Amplitude ratios can be formed between

- S on Z and P on Z or R.
- S on R and P on Z or R.
- S on T and P on Z or R.
- S on R and S on T.

In practice, reading amplitudes on R-components can be very uncertain due to the rapidly changing free surface correction for the amplitudes on R-components and it is recommend only to use Z and T components (Snoke, 2003b). This leaves the ratios S to P on Z, S on T to P on Z and S on Z to S on T and 3 amplitude ratios would then generally be used.

7.8.2 Example of Using Amplitude Ratios for a Distant Earthquake

The event shown in Fig. 7.23 will be used as an example. We now use 13 polarities and except for one, they all fit the CMT solution. Due to their distribution, it is not possible to get a single fault plane solution as shown in Fig. 7.26 (middle) where possible solutions with no polarity error and solutions in a grid of 20° has been

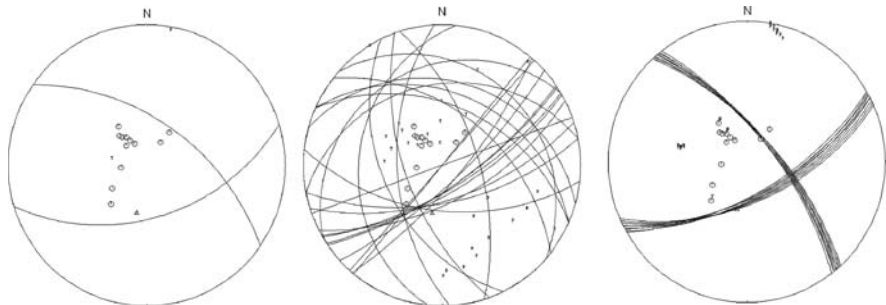


Fig. 7.26 Focal mechanism of a distant earthquake. *Left:* The focal mechanism determined by the GCMT moment tensor inversion together with 13 polarities. *Middle:* Focal mechanisms determined by using the 13 polarities. *Right:* Focal mechanism determined by using 13 polarities and 5 amplitude ratios from 3 stations. Triangle is dilation, hexagon compression and H and V indicate amplitude ratios. The origin time is 2007 0928 13:38, hypocentral depth is 260 km and $m_b(\text{PDE}) = 6.7$

searched. Adding 5 amplitude ratios from 3 stations (KAPI (P and S on Z), TLY (P and S on Z and S on T), ARU (P and S on Z and S on T)) result in the solution in Fig. 7.26 (right) where possible solutions have been checked in a 2° grid, accepting 1 polarity error and no amplitude ratio error and requiring that the amplitude ratios errors are correct within a factor of 1.4. This example clearly shows that using only 5 amplitude ratios makes it possible to obtain a reasonable solution. This example is of course “nice” and in practice the more reliable solution from the moment tensor inversion would be used, however there are cases where the moment tensor solution is not available, particular for smaller events and older data where only analog recordings are available.

Obtaining “correct” amplitudes of local earthquakes can be quite uncertain. The P might be reasonably correct although it can be discussed where the maximum should be read. The S is more difficult since there might be precursors to S (e.g. crustal conversions of S to P) and the polarity of S is rarely seen clearly (see example in Fig. 7.28). Practical observations have shown (Hardbeck and Shearer, 2003) that for high quality local data, the scatter in the S/P ratios can be of a factor 2–3 implying that the scatter in absolute amplitudes might be even higher. All of this tells us that the use of body wave amplitude data for local earthquakes should be done with caution. However, when little polarity data is available, amplitude data can provide a good constraint on the fault plane solution. We will now test this on the data from the small Tanzanian network. Recall Fig. 7.21 showing that a composite solution was made since no individual event had enough polarities to make a solution. One of these events has been selected to be used with amplitudes, see Fig. 7.27. This solution, with only 4 polarities, was obtained by checking in a 1° grid, accepting 0 polarity errors and one amplitude ratio error and requiring that the amplitude ratios errors are correct within a factor of 1.4. This solution is very similar to the composite solution and shows that amplitudes can be used for small earthquakes.

In the next section, we will use a regional earthquake from California later used for testing moment tensor inversion. This same earthquake will now be used for determining a fault plane solution using amplitudes. Some of the traces are seen in Fig. 7.28.

Fig. 7.27 Focal mechanism of a local earthquake from Tanzania (left). The focal mechanism is determined by using 4 polarities and 12 amplitude ratios from 4 stations. Triangle is dilation, hexagon compression and H and V indicate amplitude ratios. The origin time is 1992 1009 06:53, hypocentral depth is 23 km, epicentral distances are from 69 to 120 km and $M_L = 3.4$. The small mechanism to the right is the composite solution from Fig. 7.21

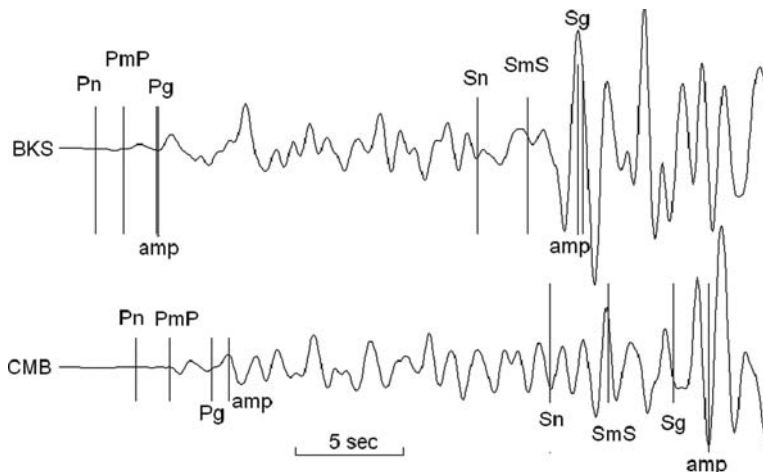
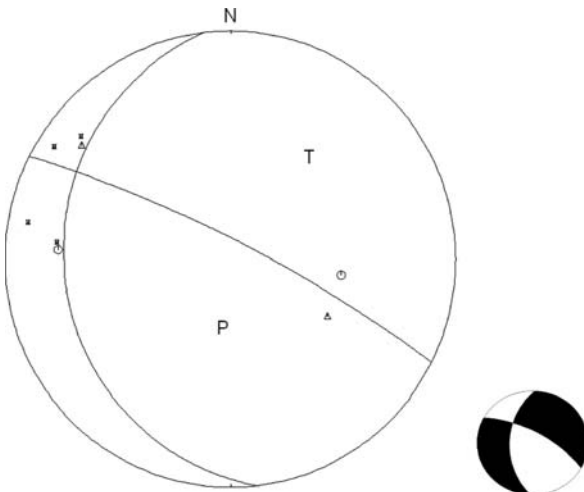


Fig. 7.28 Seismograms for an event from California. The broadband Z-traces have been filtered from 0.1 to 1 Hz. The phase identification gives the theoretical arrival times and “amp” indicates where the amplitudes have been read. The origin time is 1998 0812 14:10 and $M_w = 5.2$

This seismogram does not show very clear phases and ideally, shorter distances (under 100 km) should be used to get clear phases. Without identifying the phases it might be difficult to pick the correct amplitudes and even with the help of theoretical phases, it is not so clear. Theoretically, the largest phase might often be PmP,

however it is not seen so often in practice so it is safe to assume the largest phase after P_n is P_g . The first phase might theoretically be some phase refracted from a layer more shallow than Moho and if first arriving phase is assumed, this will give a wrong angle of incidence.

For the event in Fig. 7.28, amplitude ratios were read on the same 4 stations used for the moment tensor inversion (see Section 7.10.1) and Q_p and Q_s was assumed to be $Q = 100*f$, where f is frequency. Using 4 polarities and 12 amplitude ratios, the inversion was made assuming no polarity error, 2 amplitude ratio errors and a maximum error in amplitude ratio of 1.8. The search was done in a 1° grid. The fault plane solutions are seen in Fig. 7.29.

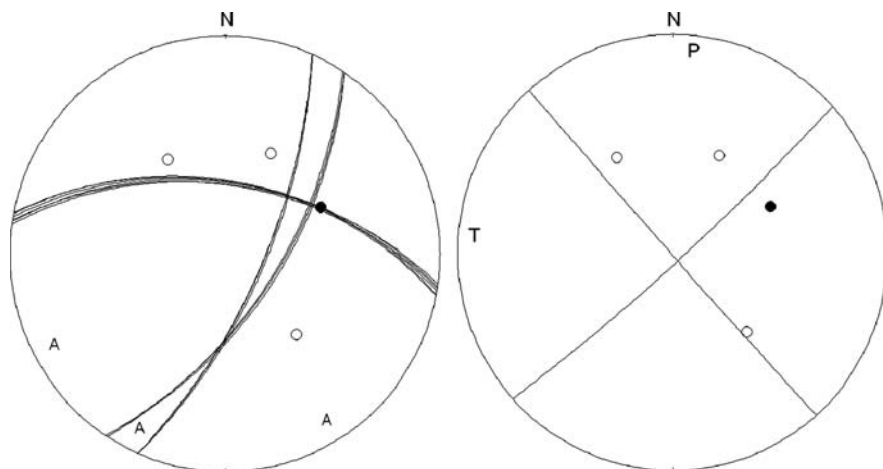


Fig. 7.29 Fault plane solutions of the California event above. The figure to the *left* shows the solutions using amplitudes from 4 stations and polarities from 4 stations and the figure to the *right* shows the CMT solution. The open circles are dilatations and the closed circles compression. Amplitude ratios are marked with A

The amplitudes, amplitude ratios and corrections used are shown in Table 7.1. It is seen that the Q-correction has a significant influence on the amplitudes in this case, due to the distances, even at the low frequencies used (Table 7.1).

In this case a rather high error had to be accepted to get a solution which does resemble the “correct” solution. Using more stations would probably improve the solution.

7.8.3 Using Spectral Amplitudes

An alternative way of using amplitudes is to use the spectral amplitudes. Taking the spectra of the first few seconds of the body waves is a stable way of obtaining an estimate of the amplitude. Recall (8.10) that the displacement source spectrum (instrument and attenuation corrected) for a Brune model can be written as

Table 7.1 Amplitude observation and corrections for the test case in Fig. 7.29. The abbreviations are STAT: Station code, C: Component, PH: Phase, AMP: Amplitude in count, PER: Period in sec, TRTIME: Travel time in sec, QCOR: Log Q-correction, ANGINC: Angle of incidence at the source, ANGEMG: Angle of emergence at the station, AZ: Azimuth from the event to the station, DIST: Epicentral distance in km., Ratio type (see text), T: indicator of ratio type, Amp1 and Amp2: The two amplitudes (count) in the ratio, Fcor is the free surface correction in the amplitude ratio (to be multiplied with ratio) and LogRat is the logarithm of the corrected amplitude ratio used

STAT	C	PH	AMP	PER	TRTIME	QCOR	ANGINC	ANGEMG	AZ	DIST
PKD	Z	PG	13617	1.12	16.4	1.7	96	30	137	100
PKD	T	SG	49001	1.24	29.2	2.5	96	30	137	100
PKD	Z	SG	26751	1.46	29.2	2.5	96	30	137	100
BKS	Z	PG	29029	1.20	24.4	2.2	93	31	330	163
BKS	T	SG	430000	1.36	42.2	3.8	93	31	330	163
BKS	Z	SG	441000	1.57	42.2	3.8	93	31	330	163
CMB	Z	PG	5725	1.16	26.4	2.3	93	31	27	178
CMB	T	SG	73157	1.07	46.9	4.4	93	31	27	178
CMB	Z	SG	41697	1.20	46.9	4.4	93	31	27	178
KCC	Z	PG	9675	1.08	28.4	2.4	93	31	65	193
KCC	T	SG	6707	0.83	50.6	4.9	93	31	65	193
KCC	Z	SG	19872	0.96	50.6	4.9	93	31	65	193
STAT		Ratio type	T	Amp 1		Amp 2		Fcor		LogRat
PKD		SH(T)/P(Z)	H	49001		13617		0.8		0.65
PKD		SV(Z)/P(Z)	V	26751		13617		1.7		0.69
PKD		SV(Z)/SH(T)	S	26751		49001		2.0		0.03
BKS		SH(T)/P(Z)	H	430000		29029		0.8		1.34
BKS		SV(Z)/P(Z)	V	441000		29029		1.7		1.64
BKS		SV(Z)/SH(T)	S	441000		430000		2.0		0.31
CMB		SH(T)/P(Z)	H	73157		5725		0.8		1.31
CMB		SV(Z)/P(Z)	V	41697		5725		1.7		1.36
CMB		SV(Z)/SH(T)	S	41697		73157		2.0		0.05
KCC		SH(T)/P(Z)	H	6707		9675		0.8		0.06
KCC		SV(Z)/P(Z)	V	19872		9675		1.7		0.83
KCC		SV(Z)/SH(T)	S	19872		6707		2.0		0.77

$$D_c(f) = \frac{\Omega_0}{(1 + (\frac{f}{f_0})^2)} = \frac{M_0 * 0.6 * 2.0}{4\pi\rho v^3(1 + (\frac{f}{f_0})^2)} G \quad (7.13)$$

where Ω_0 is the source spectral level (instrument and attenuation corrected), f , the frequency, f_0 the corner frequency, ρ the density and v the P-wave velocity. The factor $0.6*2.0$ account for the free surface effect and source radiation in an average sense. Replacing the source factor 0.6 with the source radiation function from (7.9), assuming the free surface factor 2.0 to be included in G and assuming $f < f_0$, (7.13) can be written

$$\Omega_0 = \frac{M_0 * F(\phi(\delta, \lambda, x, x_0))}{4\pi\pi\rho^3} G \quad (7.14)$$

The observations are now the instrument and attenuation corrected spectral levels which easily can be determined automatically, see Chapter 8. A grid search can now

be made as above for the best strike, dip and rake. In order to also use the polarities, a grid search for the polarities is first performed and then using the range of acceptable solutions, a grid search is then done using the amplitudes. This procedure has successfully been implemented in routine automatic fault plane solutions for the Swedish National Seismic Network and the Icelandic National Seismic network (Rögnvaldsson and Slunga, 1993; Takanami and Kitagawa, 2003) and automatic fault plane solutions are now available for thousands of small earthquakes from these networks (e.g. Bødvarsson et al., 1999). The procedures and assumptions are (Bødvarsson, personal communication):

- Calculate hypocenter.
- Select a time window covering the entire P-wave train and make the instrument corrected P- spectrum.
- Rotate the seismograms.
- Correct the spectrum for attenuation and geometrical spreading assuming direct arrival (Pg).
- Correct the spectrum free surface effect.
- Make an S-wave spectrum of the same length and do the same corrections as for P.
- Make a grid search for the best fault plane solution.
- Use polarity to determine P and T.

Other refracted or reflected arrivals will also be present in the spectral estimate, however, the direct arrivals will dominate, so the spectral estimate will be proportional to the direct arrival amplitudes. The long time window helps to make stable estimates.

The method of using amplitude ratios can also be extended to use spectral ratios with the same benefits as for amplitude ratios.

Summary of using amplitudes

- Using body wave amplitudes for determining fault plane solution is well tested for events at teleseismic distances, while at local and regional distances, body wave amplitudes can provide useful additional constraint on the fault plane solution using polarities
- For small local earthquakes there is often no possibility to make fault plane solutions with polarity data only and because the earthquakes are small, the moment tensor inversion method (see later) cannot be used. It is therefore worth while to use amplitudes whenever possible.
- In all cases, amplitudes must be read at frequencies less than the corner frequency for the assumptions to hold.
- Amplitude ratios are the most reliable since path and instrument effects cancel out.
- Amplitude ratios can in principle be used at any distance provided the attenuation and free surface corrections can be made.

- The uncertainty of picking the right phase and the Q-correction can to some extent be eliminated by using spectral ratios. However, even if Q is assumed the same for P and S, the Q-correction will be different due to travel times difference between P and S.
- Only use P on Z, SV on Z and SH on T components since amplitudes on the R component can be very unreliable.
- There must be at least one polarity reading available. Without polarity, there will always be a 180° ambiguity in the fault plane solution. Do not use S-polarities since they are very unreliable.
- In principle any phase type can be used for amplitude ratios provided the same phase type is identified in both traces.
- The amplitude ratio MUST be corrected for the free surface effect.

7.9 Moment Tensor

So far the fault plane solution has been described by a double couple which mathematically has been calculated as the sum of the radiation from two single couples (or just couples). A seismic source can be more complicated than just one double couple. The radiation from most seismic sources can be shown to be described by a combination of 9 force couples, see Fig. 7.30. Three of these are dipoles along the coordinate axes and the other six force couples can be grouped into three double couples, one in each coordinate plane.

For mathematical reasons, it is an advantage to organize the information in a tensor, the so-called moment tensor

$$M = \begin{Bmatrix} M_{xx} & M_{xy} & M_{xz} \\ M_{yx} & M_{yy} & M_{yz} \\ M_{zx} & M_{zy} & M_{zz} \end{Bmatrix} \quad (7.15)$$

where the moment tensor components are the nine force couples and the scalar moment M_0 of the moment tensor is

$$M_0 = \sqrt{\sum_{ij} M_{ij}^2} / \sqrt{2} \quad (7.16)$$

It can be shown (e.g. Stein and Wysession et al., 2003) that since the force couples are in the coordinate planes, the moment tensor is symmetric. This means that there are only 6 independent moment tensor elements.

If e.g. the source could be explained by only a double couple in the xy plane with a seismic moment M_0 , the moment tensor is simply

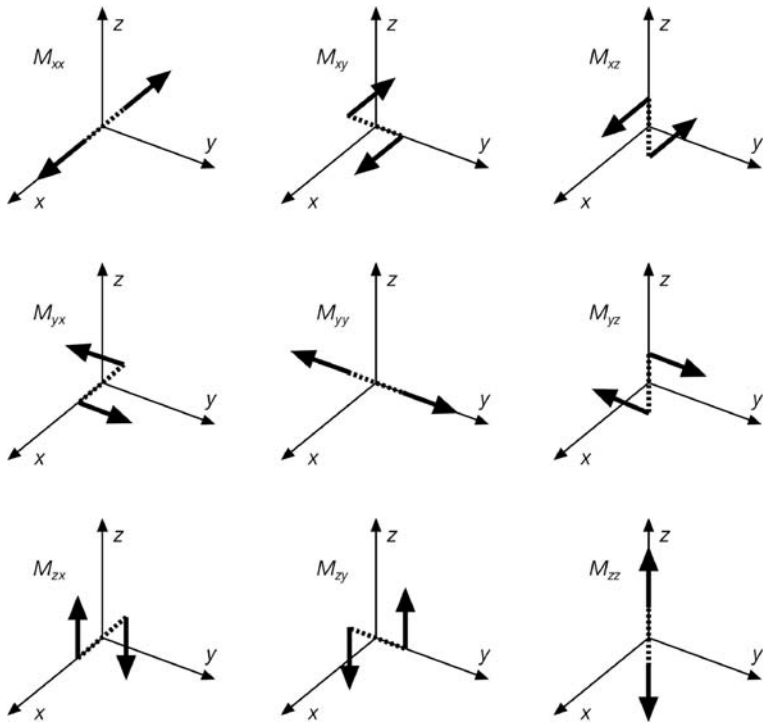


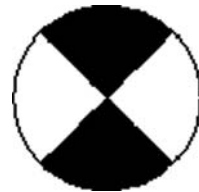
Fig. 7.30 The 9 force couples representing the moment tensor. For example M_{xy} is a force couple in the xy -plane acting in the x -axis direction. All couples are shown with the same strength. In the following, we will use the convention that x , y and z correspond to north, west and up respectively. Figure from Stein and Wysession (2003) and copied from http://epscx.wustl.edu/seismology/book/book_no_captions/figures/

$$M = \begin{Bmatrix} 0 & M_{xy} & 0 \\ M_{yx} & 0 & 0 \\ 0 & 0 & 0 \end{Bmatrix} = M_0 \begin{Bmatrix} 0 & 1 & 0 \\ 1 & 0 & 0 \\ 0 & 0 & 0 \end{Bmatrix} \quad (7.17)$$

and similarly for the fault in the other two planes. We see that $M_{xy} = M_{yx}$. Since the moment tensor is symmetric, there exists a coordinate system where the moment tensor can be represented by a diagonal matrix. The simple moment tensor (7.17) can then be rotated and becomes

$$M = M_0 \begin{Bmatrix} 1 & 0 & 0 \\ 0 & -1 & 0 \\ 0 & 0 & 0 \end{Bmatrix} \quad (7.18)$$

Fig. 7.31 Moment tensor and corresponding pure strike-slip fault corresponding to (7.18). Note that the x-axis points north



where the forces are seen in Figs. 7.30 and 7.5 and in this case simply represents the P and T axis. The corresponding fault plane solution is seen in Fig. 7.31. This illustrates, as it has been demonstrated earlier, that an earthquake can be modeled equally with either two “shear” couples or a tensional and compressional couple (2 dipoles). The diagonal elements can also represent a volume change. If $M_{xx} = M_{yy} = M_{zz}$ we have 3 dipoles with outward forces which model an explosion. This brings us to another property of the moment tensor. In order to have an explosive source, the trace of the moment tensor must be different from zero. The diagonal elements can thus represent both a double couple and an explosion as shown below

$$M = M_0 \left(\begin{Bmatrix} 1 & 0 & 0 \\ 0 & -1 & 0 \\ 0 & 0 & 0 \end{Bmatrix} + \begin{Bmatrix} 1 & & \\ & 1 & \\ & & 1 \end{Bmatrix} \right) = M_0 \begin{Bmatrix} 2 & 0 & \\ & 0 & \\ & & 1 \end{Bmatrix} \quad (7.19)$$

In general, the part of the moment tensor representing the double couples (deviatoric part) will have a trace of zero and the explosive part (isotropic part) will have a non zero trace. This property will be used to decompose the moment tensor. Assuming a deviatoric moment tensor, we can now look at what the diagonal elements represent. Using the property $M_{xx} + M_{yy} + M_{zz} = 0$, it is seen that the diagonal elements can be decomposed to only represent 2 double couples.

$$M = \begin{Bmatrix} M_{xx} & 0 & 0 \\ 0 & M_{yy} & 0 \\ 0 & 0 & M_{zz} \end{Bmatrix} = \begin{Bmatrix} M_{xx} & 0 & 0 \\ 0 & -M_{xx} & 0 \\ 0 & 0 & 0 \end{Bmatrix} + \begin{Bmatrix} 0 & 0 & 0 \\ 0 & -M_{zz} & 0 \\ 0 & 0 & M_{zz} \end{Bmatrix} \quad (7.20)$$

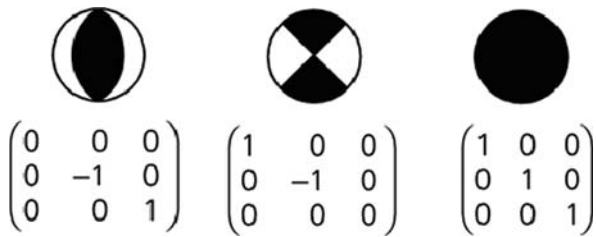
This means that in a general coordinate system, a moment tensor can be represented by an explosive source and 5 double couples and in the coordinates system where the moment tensor is represented by a diagonal tensor, only two double couples and an explosive source are needed, see Fig. 7.32.

For forward modeling, there is no advantage of using the moment tensor since it is possible to just add up the equations of type (7.9). However, the moment tensor allows us to write (7.9) in a much more elegant form

$$u_r = G \cdot A \cdot I \cdot \mathbf{H} \cdot \mathbf{M} \quad (7.21)$$

where \mathbf{H} is a function of matrix form which only depends on known parameters for a given source and receiver. This is a linear equation and can in principle be solved by linear methods to determine the moment tensor and no grid search is needed. This

Fig. 7.32 The fault plane solutions and the explosive source representing the decomposition of the moment tensor into 2 fault plane solutions and an explosive source. Note that the x-axis points north and the y-axis west



means that, in order to find the moment tensor, at least 6 observations must be available or 5 if it is assumed that there is no explosive source ($M_{xx} + M_{yy} + M_{zz} = 0$). The problem now is to interpret the moment tensor in terms of real faults with strike dip and rake. While it is easy to write the moment tensor for any fault or combination of faults as described above, it is more difficult going the other way, since different interpretations can be used. The first step is to simplify the moment tensor by using the coordinate system where it is diagonal matrix.

$$M = \begin{Bmatrix} M_1 & 0 & 0 \\ 0 & M_2 & 0 \\ 0 & 0 & M_3 \end{Bmatrix} \quad (7.22)$$

This can be decomposed in many different ways and above we have already described the decomposition into 2 double couples and an explosive source. Due to the presence of noise, errors in structural model and complex rupture, all three sources will in general be non-zero. A very common assumption for earthquake sources is that the $E = 0$ and the inversion is done with this requirement. The resulting moment tensor elements commonly have one large and a small value (assume it is M_3). A common decomposition is therefore, as described above, into two double couples, the major and minor double couple

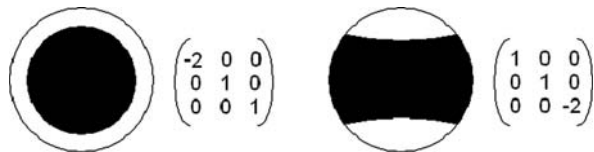
$$M = \begin{Bmatrix} M_1 & 0 & 0 \\ 0 & M_2 & 0 \\ 0 & 0 & M_3 \end{Bmatrix} = \begin{Bmatrix} M_1 & 0 & 0 \\ 0 & -M_1 & 0 \\ 0 & 0 & 0 \end{Bmatrix} + \begin{Bmatrix} 0 & 0 & 0 \\ 0 & -M_3 & 0 \\ 0 & 0 & M_3 \end{Bmatrix} \quad (7.23)$$

A special case of a non-double-couple source is the compensated linear vector dipole (CLVD), where the strength of one of the double couples is twice as large as the strength of the other double couple

$$M = \begin{Bmatrix} M_1 & 0 & 0 \\ 0 & -2M_1 & 0 \\ 0 & 0 & M_1 \end{Bmatrix} = \begin{Bmatrix} M_1 & 0 & 0 \\ 0 & 0 & 0 \\ 0 & 0 & -M_1 \end{Bmatrix} + \begin{Bmatrix} 0 & 0 & 0 \\ 0 & -2M_1 & 0 \\ 0 & 0 & 2M_1 \end{Bmatrix} \quad (7.24)$$

Non double couple sources have particularly been observed for land slides (modeled by a single force) and in volcanic areas. For a summary on this topic, see Julian et al. (1998). For more decompositions, see standard text books and Julian et al.

Fig. 7.33 Example of two CLVD seismic sources and their associated moment tensors



(1998). Non double couple sources can give strange looking focal mechanisms, see Fig. 7.33.

Generally, source mechanism are interpreted in terms of a double couple which is also the only solution possible with polarities, however this can sometimes be misleading, see Fig. 7.34.

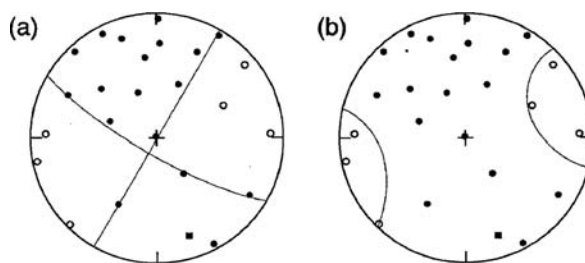


Fig. 7.34 Focal solution for a small earthquake in the Hengill geothermal area on Iceland. Open and solid circles are dilatations and compressions, respectively. Solution **a**) is made with polarities only while solution **b**) is the moment tensor solution made with polarities and amplitude ratios. Figure from Julian et al. (1998). Copyright 1998 American Geophysical Union. Reproduced by permission of American Geophysical Union

This example illustrates that while the traditional first motion solution looks very reliable, there is a completely different solution based on the moment tensor which also fits all the polarities. So a good solution with polarities does not ensure that there is not a strong non double couple component.

The Main Agencies Providing Global Moment Tensor Solutions

NEIC routinely makes near real-time solutions for earthquakes with $M > 5.5$ at the USGS NEIC (<http://earthquake.usgs.gov>) (Sipkin, 2003). This can be done fast since only the P-waveforms are used

The *Global Centroid Moment Tensor (GCMT) project* at Lamont-Doherty Earth Observatory of Columbia University (<http://www.globalcmt.org>) makes solutions for $M > 5.5$ earthquakes with data since 1976. The moment tensor inversions make use of the very long period body waves ($T > 40$ s) and the so-called mantle waves ($T > 135$ s). This catalog was formerly called the Harvard CMT catalog. An example of the information given by the GCMT catalog is seen in Table 7.2.

Table 7.2 Global CMT solution for the event in Fig. 7.22, see text. The information comes from <http://www.globalcmt.org/CMTsearch.html>. The PDE solution for the same event is also shown

Date: 2007/10/ 2	Centroid Time: 18: 0:11.2 GMT
Lat= 54.19	Lon=−161.37
Depth= 41.9	Half duration= 3.5
Centroid time minus hypocenter time: 3.2	
Moment Tensor: Expo=25 2.710 −2.670 −0.046 2.430 0.716 −0.987	
Mw = 6.3 mb = 6.2 Ms = 6.2 Scalar Moment = 3.82e+25	
Fault plane: strike=250 dip=24 slip=87	
Fault plane: strike=73 dip=66 slip=91	
PDE solution	
Date: 2007/10/ 2 Time: 17:59 33.7	
Lat = 54.64 Lon=−161.80	
Depth = 48.4	

It is seen that the complete moment tensor is given as well as the best fitting fault plane solution. The centroid hypocenter and origin time are also given. The centroid location and origin time often differs from the bulletin location since the bulletin location corresponds to the point where the rupture starts (hypocenter), while the centroid location, using the full waveforms, gives the average location in space and time.

7.10 Moment Tensor Inversion

Moment tensor inversion is done routinely at several institution and some examples will be given in the following. Nearly all use the complete seismograms or part of it but different mathematically approaches and software are used. In this book we cannot go into detail with all the methods of moment tensor inversion. For more examples, software and details of how to do it, we refer to others. NMSOP gives a good overview. In general the aim of moment tensor inversion is to set up a set of equations of the form

$$\text{Observations} = \mathbf{GAIH}(\text{known parameters})^* \mathbf{M} \quad (7.25)$$

where known parameters are station and hypocenter locations and crustal model including attenuation. Here \mathbf{M} is the moment tensor. This can be simplified to

$$\text{Observations} = \mathbf{GAIH}(\text{known parameters})^* \mathbf{m} = \mathbf{G}^* \mathbf{m} \quad (7.26)$$

where \mathbf{m} is a vector of the 6 independent moment tensor components and the matrix $\mathbf{G} = \mathbf{GAIH}$ now includes the effect of GAI. The observations can be

- Amplitudes, as defined earlier.
- Spectral levels as defined earlier.

- Seismograms of P.
- Seismograms of surface waves.
- Seismograms of the complete waveforms.

The problem is now how to set up \mathbf{H} as function of the observations used. The simplest approach is to use the amplitudes and spectral levels obtained as described earlier. This method only uses a limited part of the information available in the seismograms and in this case the inversion is often restricted to one double couple and the moment tensor inversion will thus give similar results as using the grid search method described earlier. As we shall see, the most advanced and complete methods use part or all of the seismograms. However this might not be possible for earthquakes smaller than magnitude 3 as the seismograms cannot be realistically modeled at high enough frequencies and amplitudes/spectral levels can be used instead (Ebel and Bonjer, 1990).

The main method of moment tensor inversion is to use part of or the complete seismogram as observations and \mathbf{H} represents the computation of seismograms. The fault geometry and slip direction are included in the moment tensor and \mathbf{H} contains the effect of the structure. The seismograms to be included in \mathbf{H} are therefore the signals that are observed at the stations from a source with a delta source time function, the so-called Green's function. This means that it is necessary to generate a theoretical seismogram in order to do moment tensor inversion using complete seismograms. This can be done with different methods, see Section 7.11. The element of G_{ij} can now be defined as the theoretical seismogram due to moment tensor element m_j at station i and the observed seismograms u_i are given as the linear combination of the Green's functions and a vector of moment tensor elements, m_1 to m_6 , as

$$\begin{Bmatrix} u_1 \\ u_2 \\ u_3 \\ u_4 \\ \vdots \\ u_n \end{Bmatrix} = \begin{Bmatrix} G_{11} & G_{12} & G_{13} & G_{14} & G_{15} & G_{16} \\ G_{21} & G_{22} & G_{23} & G_{24} & G_{25} & G_{26} \\ G_{31} & G_{32} & G_{33} & G_{34} & G_{35} & G_{36} \\ G_{41} & G_{42} & G_{43} & G_{44} & G_{45} & G_{46} \\ \vdots & \vdots & \vdots & \vdots & \vdots & \vdots \\ G_{n1} & G_{n2} & G_{n3} & G_{n4} & G_{n5} & G_{n6} \end{Bmatrix} \begin{Bmatrix} m_1 \\ m_2 \\ m_3 \\ m_4 \\ m_5 \\ m_6 \end{Bmatrix} \quad (7.27)$$

or in matrix form

$$\mathbf{u} = \mathbf{Gm} \quad (7.28)$$

The data vector \mathbf{u} contains the n observed seismograms u_i from a number of seismic stations and components, one after the other, typically with the same number of samples for each seismogram, and the dimension is therefore the total number of samples in all seismograms. The kernel matrix \mathbf{G} has the corresponding Green's functions (6 columns) for the required distances and an assumed source depth.

The number of Green's functions will then be $6n$ and the total number of rows in \mathbf{G} will equal the total number of samples.

The problem is normally over determined (\mathbf{G} is not a square matrix), and the inversion for \mathbf{m} is formulated as a least squares problem. This means that \mathbf{m} is determined to give the smallest mismatch between observed and computed seismograms. At least six seismograms are required to invert for \mathbf{m} , but often more data is available and the problem is over determined. The inversion is done for a single depth, but it is then possible to compute variance as function of a range of fixed depths. In theory, it is straight forward to invert waveform data for the moment tensor. However, it requires high quality data from a number of stations with good azimuthal coverage and the ability to compute synthetic seismograms (see Section 7.11). The computation of synthetic seismograms is easier for larger magnitude earthquakes as the synthetics are less dependent on the physical properties of the model for longer period waves. Therefore, the computation of the moment tensor from earthquakes above M4 is almost routinely practiced at local and regional distances, and for earthquakes above M5.5 at global distances. The computation of synthetics is more problematic for smaller earthquakes where one needs to include higher frequencies, which require better models than are available in most cases. With good models, it may be possible to invert the waveforms for the moment tensor of earthquakes down to M3.

7.10.1 Moment Tensor Inversion at Local and Regional Distance

The moment tensor inversion at local and regional distance for moderate size earthquakes has become routine practice at many observatories due to the availability of high quality data. Apart from the data, the main requirement is good enough knowledge of the model to produce realistic synthetics at the frequency range used depending on the magnitude of the earthquake. In practice this means that clear surface waves must be used since body waves cannot be modeled accurately enough. Automatic moment tensor computation in near real-time has also become feasible and is performed at several institutions around the world. The background and details of the inversion have been well documented (e.g., Jost and Herrmann, 1989; NMSOP). Here, we aim to give an introduction to the topic by giving an example of a regional earthquake and explain the processing steps involved. The data processing and inversion follows the manual on the *tdmt_invc* software (Dreger, 2002) and tutorial by Dreger (2003), where the data processing is done using the Seismic Analysis Code (SAC) software. There is other software to compute the moment tensor from regional data, for example tools are included in the “Computer programs in Seismology” package (Herrmann and Ammon, 2004). As an example we select an earthquake that occurred in the California at origin time 1998 0812 14:10 with a moment magnitude $M_w = 5.1$. The earthquake occurred outside the national network and, therefore, we include data from neighboring networks. In total, data are used from four broadband stations, see Fig. 7.35.

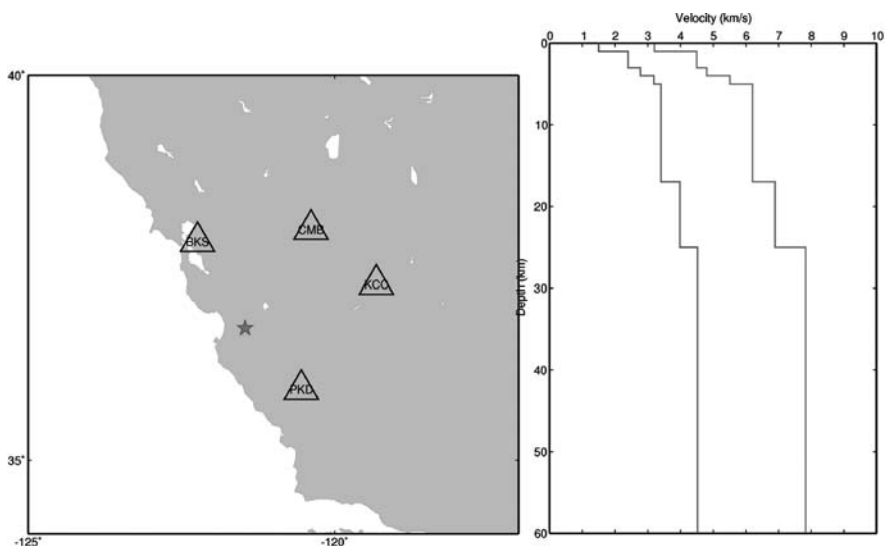


Fig. 7.35 *Left:* Map of stations used in moment tensor inversion. *Right:* Velocity model used. The right curve gives the P-wave velocity and the left curve gives S-wave velocity. The star is the epicenter. The earthquake had a moment magnitude of 5.1 and occurred in California at 1998 0812 14:10

The following are required to perform the moment tensor inversion:

- Waveform data (complete seismograms including P-, S- and surface waves).
- Instrument response and station locations.
- Earthquake location.
- Velocity model (this has to be appropriate for modeling seismograms at the frequencies used in the inversion).

The data needs to be processed before it enters the actual inversion. The main data processing steps are:

- Remove the linear trend, remove mean and taper the signal (see Chapter 4). This is done as preparation for the instrument correction and filtering.
- Remove the instrument response and compute either displacement or velocity seismograms in the frequency range of the sensor. In order to obtain low frequency stability, a highpass filter is often used (see Chapter 3).
- Apply bandpass filter depending on earthquake magnitude, the filters must be the same as applied to the synthetic data (e.g., number of poles, one or two pass filter). This filter is needed to limit the bandwidth to the range where a useful signal (mostly surface waves) is present. Dreger (2002) suggests the filter ranges listed in Table 7.3:

Table 7.3 Recommended frequency bands for moment tensor inversion of local and regional earthquakes

M	Frequency (Hz)
$M < 4.0$	0.02–0.1
$4.0 \leq M < 5.0$	0.02–0.05
$5.0 \leq M < 7.5$	0.01–0.05
$7.5 \leq M$	0.005–0.02

- Decimate data, typically to 1 sps, in order to reduce the number of data for the inversion.
- Cut the data to the required time window that contains the signal of interest. As this mostly contains surface waves, the time window can be determined automatically using the known velocity of the surface waves.
- Rotate horizontal seismograms into radial and transverse components.

An example of pre-processing is shown in Fig. 7.36. The corresponding fit of the synthetic seismograms and the obtained fault plane solution are shown in Figs. 7.37 and 7.38, respectively. Note the filtered trace used for the inversion has no significant body wave signal. Next, the input parameter files have to be setup and the Green's functions are computed. The final step before the inversion is to align in time the observed seismograms with the Green's functions. Due to lateral model inhomogeneities this has to be done for each station individually. The software by Drexler (2002) has the capability to automatically align by computing the cross correlation between the individual Green's function components and the observed seismograms, and then align in time for the highest correlation. However, it is often necessary to manually align the traces and enter this information into the parameter

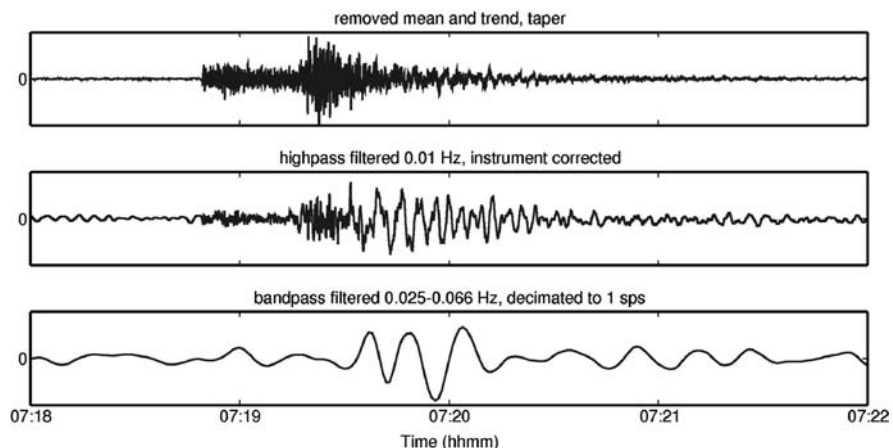


Fig. 7.36 Example of pre-processing applied to vertical broadband data from station CWF. The original data is proportional to velocity, but converted to displacement during the instrument correction. The original sample rate is 100 sps. The event occurred in the UK at 2007 0428 07:18 with $M_W = 4.0$

file for the moment tensor inversion. It is necessary to confirm with polarity readings that the time alignment is correct and that the signals are not shifted by half a period leading to an inverted solution.

It is normally not possible to get the final result with the first run of the moment tensor inversion. It is necessary to inspect the solution and test its stability by inverting using different conditions: Use different sets of stations, exclude individual components with bad signal to noise ratio, change frequency range of data used. There is the possibility that the instrument response for some station is not correct or that the horizontal components are not correctly aligned. This may be a problem in particular when using data from another network. It is often required to refine the choice of stations to possibly improve the azimuthal coverage, but it is not necessary to include as many stations as possible as an even azimuthal distribution is more desirable. Plots of station distribution and trace distance plots can be useful in this process. An attempt to obtain a better velocity model could also be useful.

The quality of the solution can be estimated from the variance reduction defined as (Dreger, 2002)

$$VR = \left[1 - \sum \sqrt{(data_i - synth_i)^2} \right] * 100 \quad (7.29)$$

as well as the ratio of variance to double-couple percentage value. A large CLVD percentage may indicate problems in the inversion, as we expect, for the majority of earthquakes, that the double couple component is dominant. The best depth can be determined by plotting the variance reduction as function of depth. However, generally the solution may not be very sensitive to depth as it mostly relies on surface waves (Fig. 7.37).

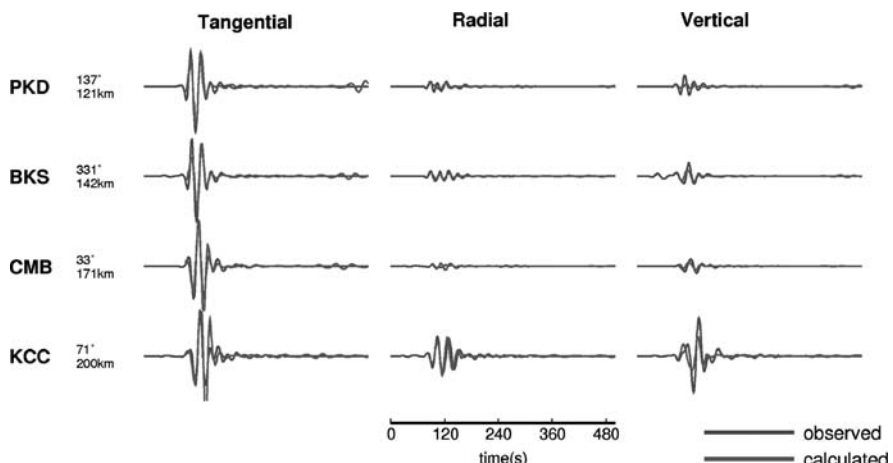
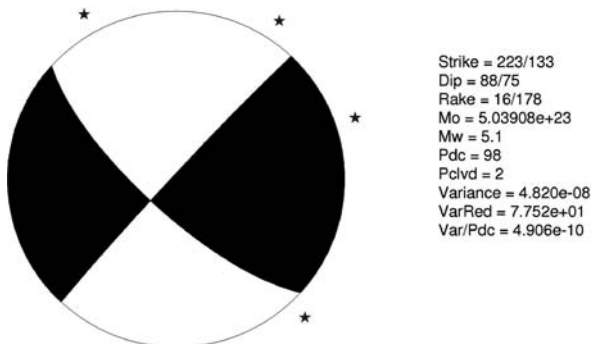


Fig. 7.37 Comparison of observed and calculated seismograms of the surface waves corresponding to the final moment tensor solution for the California event used above. Note that the signals are almost identical

Fig. 7.38 Final results from the moment tensor solution for the California event. The azimuth of the observing stations is given by the stars



7.10.2 Global Distance

Moment tensor solutions are also computed using waveform data recorded at global distances ($30^\circ < \Delta < 90^\circ$). The basic concept of the moment tensor inversion from global data is the same as described in the previous section. The main difference is that due to the size of the events and the global distances (simpler model), it is possible to model the body waves (as also shown in synthetic seismogram section using global ray tracing). The differences can be summarized as:

- The synthetic Green's functions are computed for a global model instead of a local model.
- The model vector can contain the centroid location and time in addition to the moment tensor (e.g., Dziewonski et al., 1981; Aki and Richards, 2002).
- The inversion typically uses body wave signals, however, surface waves can be used in addition while for smaller regional events only surface waves were used since low frequency body waves usually are too small.
- The frequency range used is 0.002 to 1 Hz, larger than for regional studies.
- An extension of the method allows to invert for the slip distribution across the fault (e.g., Kikuchi and Kanamori, 1991).

Open source software for the global moment tensor computation has been made available by Sipkin (2003) and Kikuchi and Kanamori (2003). Figure 7.39 shows an example using the software of Kikuchi and Kanamori with data from the GSN network done by the authors.

The main input data are:

- Earthquake location and origin time.
- Waveform data with instrument response.
- Global velocity model.
- Frequency range to use, typically 0.002–1 Hz.
- Definition of source time function, shape and duration.

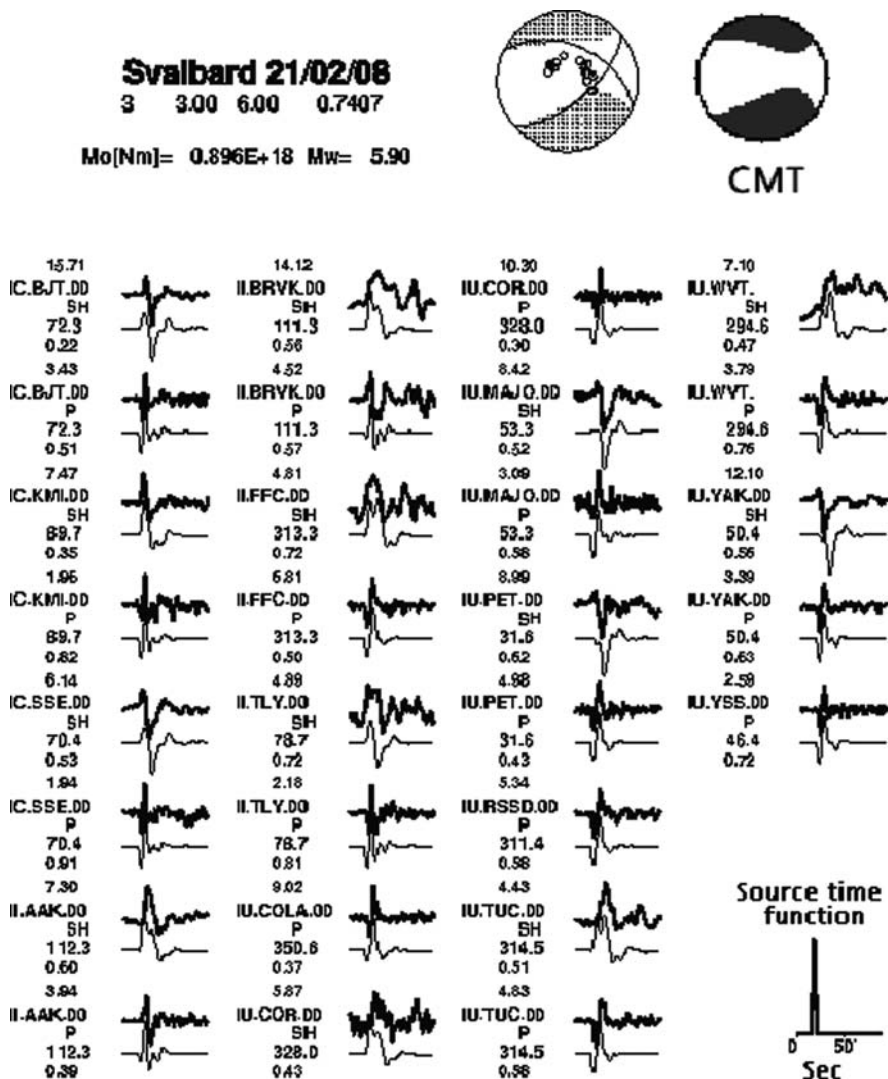


Fig. 7.39 Example of global moment tensor inversion of an earthquake near Svalbard on 2008-02-21. The source time function is shown bottom right. The corresponding double couple solution is shown at the top right together with the CMT solution. The seismograms show the comparison between observed and calculated data for P and SH waves and the stations used

Similar to the regional inversion, the stability of the solution has to be tested and the station configuration may have to be refined. On the global scale, the station distribution of the GSN will normally provide a sufficient coverage.

Figure 7.39 shows an example of moment tensor inversion done by the authors for a moderate size event north of Svalbard using the software by Kikuchi and

Kanamori (2003). In the example, P and SH waves have been used and the synthetics are made with full waveform modeling for a sufficient number of stations. When selecting the stations, good azimuth and distance distribution is more important than the number of stations. As it can be seen, there is a very good fit between the observed and synthetics seismograms.

The solution obtained by GCMT shows a similar solution and both solutions show a significant non double couple element. The complete solution is given below:

```
200802210246A SVALBARD REGION
Date: 2008/ 2/21Centroid Time:2:46:21.9 GMT
Lat=77.02Lon=19.28
Depth= 12.8Half duration= 2.6
Centroid time minus hypocenter time:4.0
Moment Tensor: Expo=25-0.687 1.620 -0.937 -0.424 -0.606 0.032
Mw = 6.1mb = 5.7Ms = 6.1Scalar Moment = 1.58e+25
Fault plane:strike=308 dip=54 slip=-24
Fault plane:strike=53 dip=71 slip=-141
```

Since CMGT uses a different method and a larger data set, a slightly different solution is obtained.

7.11 Seismogram Modeling

The ultimate goal of analyzing seismograms is to extract all the information out of all wiggles in the trace. This means we should also be able to regenerate the trace based on known parameters for the source and the structure. This we call modeling seismograms or making synthetic seismograms and it can be a very useful tool in interpreting seismograms. However as it turns out this is no easy exercise since models are not as simple as what we usually use for calculating travel times and the seismic source will often not be a simple double couple (see moment tensor inversion above). In addition most synthetic seismogram methods are based on approximations that the user must be aware of.

Since the seismogram amplitudes depend on the fault plane solution (see above), a better way of determining fault plane solutions than just read maximum amplitudes is to model the P amplitudes and compare to the observed amplitudes.

Synthetic seismograms are also essential for moment tensor inversion. In order to do a moment tensor inversion, the response of the structure to an impulse (the Green's function) must be known for the particular part of the seismogram used for the moment tensor inversion. This is also the same as generating a synthetic seismogram for an impulse time function from which the seismogram can be generated for any fault orientation and source time function.

We will therefore give a very short overview of methods of generating synthetic seismograms and their use in analyzing seismic data.

7.11.1 Ray Method

We have already dealt with some simple modeling. Calculating travel times for individual phases involves ray tracing in a given earth model (see Chapter 2). In order to generate the seismogram, the amplitudes of the individual phases must be calculated starting with the radiation from the source (see above) and the attenuation and geometrical spreading along the ray path. This is the basis of the so-called ray methods used both locally and globally as shown in two examples below.

7.11.2 Approximation to Complete Seismograms

There are many methods of which some focus on the body waves, some on the surface waves and some on the whole seismograms. Some of the more popular methods for local and regional seismogram generation are based on discrete wave number representation of the wavefields (e.g. Bouchon, 1981). Some of the most used programs are made by Herrmann (<http://www.eas.slu.edu/People/RBHerrmann/CPS330.html>).

It is beyond the scope of this book to describe the different methods in detail as well as the available programs. There is a wealth of literature available on this topic and an overview is given by Doornbos (1988).

7.11.3 Global Case of Using the Ray Method

Seismic first arrivals from events at distances 30–90° travel relatively undisturbed through the earth due to the near vertical incidence and it is relatively simple to calculate the arrival time, geometrical spreading and attenuation of the individual phases. The very first part of the seismogram consists of the phases P, pP and sP and the amplitudes can be calculated. Assuming a source time function and adding the 3 source time functions with the calculated amplitudes a synthetic seismogram can be generated. This is very similar to the observed seismogram and also very sensitive to both the hypocentral depth and the focal mechanism, see Stein and Wysession (2003). Figure 7.40 shows an example

For these two events in Fig. 7.40, with the same depth, the seismograms are very different due to the difference in the focal mechanism. In addition, the seismogram appearance will also depend on the depth since the relative arrival times change with depth. These types of synthetic seismograms are used to determine both the fault plane solution and the focal depth by, automatically, generating synthetic seismogram for combinations of depth and fault plane solutions and comparing to the observed seismogram. See Chapter 5 for using pP for depth determination.

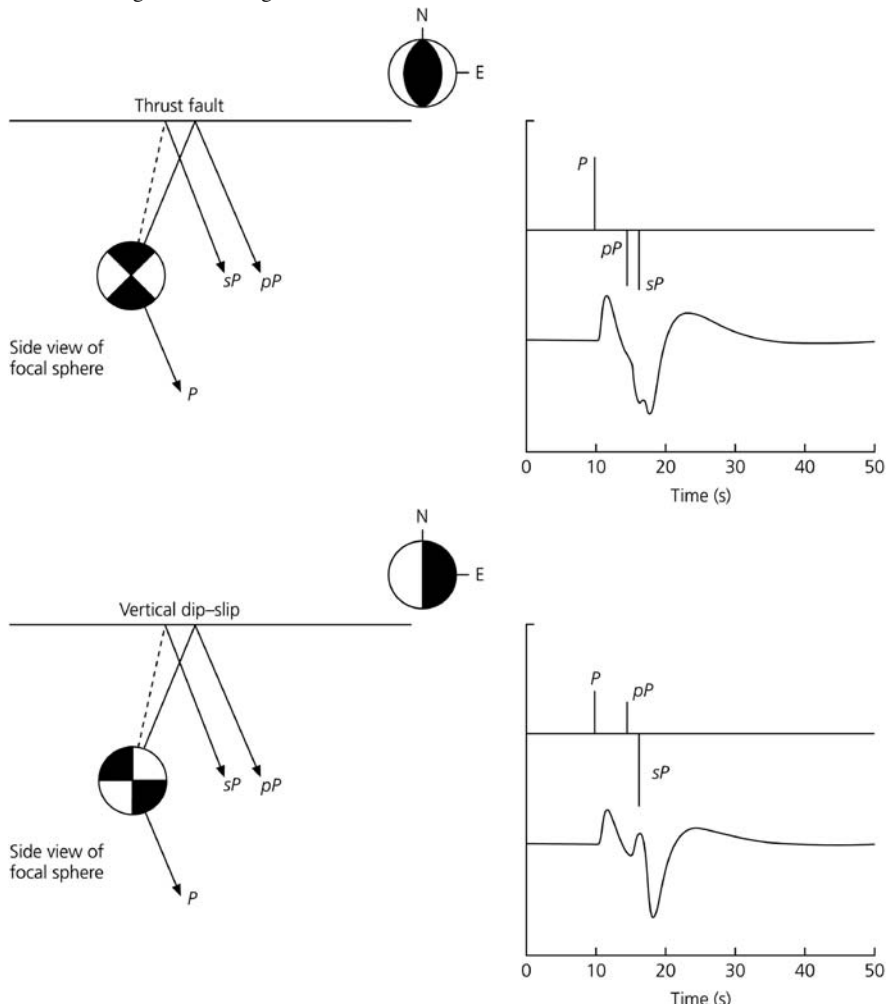


Fig. 7.40 Synthetic seismogram generation from two different fault plane solutions (*top* and *bottom*). The amplitudes are shown as impulses (*top* traces) and the seismic signals including the effect of attenuation and the seismometer (*bottom* traces). The figure is from Stein and Wysession (2003) and copied from <http://epscx.wustl.edu/seismology/book/>

7.11.4 The Source Time Function

When doing fault plane solutions, it is assumed that the seismic source is located in one point which corresponds to the indication of the rupture on the fault. This is also the same point found when calculating the hypocenter. After the initial break on the fault, the rupture will propagate to cover the whole fault (Fig. 7.41). If for simplicity we assume that the rupture starts at one end and propagates along the length L of the fault with rupture velocity v_r , then the rupture process will send out seismic energy for L/v_r seconds (rupture time).

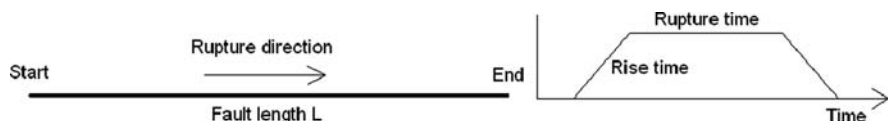


Fig. 7.41 Schematics of a rupturing fault with length L (left) and the resulting time pulse also taking rise time into consideration (right), see text

The source time function is the derivative of the seismic moment as function of time, also called the moment rate function. The length of the source time function is then approximately the rupture time. In addition there is the rise time which is the time it takes to make the rupture at any individual point. The result is that the source time function can be approximated with a trapezoidal time function. The pulse will be shorter and with a larger amplitude to the right of the fault than to the left in the example above due to the Doppler effect. This means that the length of the P-pulse will depend on the station azimuth and this is also called directivity. For more details see e.g. Stein and Wysession (2003).

7.11.5 Local Case of Using the Ray Method

A well known ray tracing method is the so-called WKBJ approach (for an overview, see Doornbos, 1988) which uses an extension of geometrical ray theory. At high frequencies it agrees with geometrical ray theory for direct and turning rays and for partial and total reflections at interfaces. For finite frequencies it remains valid for head waves at plane interfaces. The method can be useful to calculate amplitudes and arrival times of different phases for a given hypocenter and fault plane solution in order to check possible phases and also check fault plane solutions obtained by other methods. Figure 7.42 shows an example. For this event, the depth was

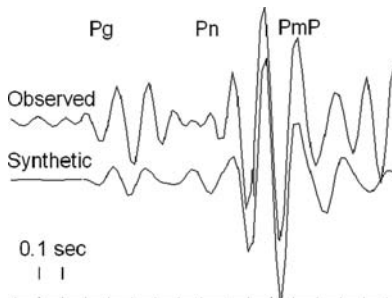


Fig. 7.42 An observed short period vertical seismogram of P compared to the synthetic seismogram modeled with WKBJ as implemented in SEISAN. Only the phases Pg, Pn and PmP are modeled in this case. The trace is from SNART, origin time 2004 0705 18:09, depth 17 km, $M_L = 2.2$, epicentral distance 94 km and strike, dip and rake 147, 17 and 76, respectively. A filter of 5–10 Hz is used

determined by trial and error to make the PmP-Pg travel time fit and the fault plane solutions was determined with the Snode program. In general, PmP is not seen as clearly as in this case although PmP theoretically should have large amplitudes in many cases. However, when PmP is clear, it is a very useful phase to use to restrict the depth. In this case the nearest station was SNART so a normal hypocenter solution would not give a reliable depth due to the distance.

7.11.6 Complete Seismogram

In the moment tensor inversion example for a regional event, the theoretical seismograms were generated with the Herrmann method and the inversion was made primarily with the long period part of the seismogram. Figure 7.43 shows an example of modeling of the complete waveforms for a local event.

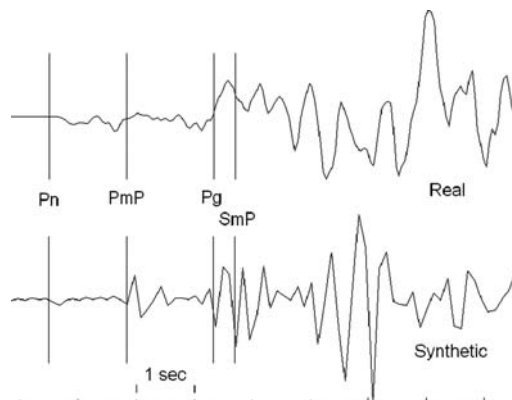


Fig. 7.43 Synthetic and real traces for broadband station BKS, vertical component. The theoretical arrival times for some phases are shown. The synthetic were generated using the Herrmann software (as implemented in SEISAN). A local model for California was used and the focal parameters were taken from the global CMT catalog (Hypocenter latitude 36.61, longitude -121.30, depth 30 km, strike dip and rake: 48,85,-1). The origin time is 1998 0812 14:10, $M_w = 5.2$) and the epicentral distance is 163 km. Both traces are velocity

It is seen that, at a local distance, modeling the complete seismogram does not result in a wiggle for wiggle synthetic seismogram similar to the real signal, however the main elements are there and the polarity is correct. The main reason for this discrepancy is that the model is not detailed enough for local high frequency modeling and also the method only uses a 1D model. A test of the quality of the modeling can be done by inverting for the fault plane solution using synthetic seismogram amplitudes. In the synthetic seismogram, the correct phases can be identified, and Pg and Sg amplitudes were read on 3 stations (BGS, 163 km, CMB 178 km and KCC 193 km) and polarity on 4 stations (in addition PKD). Inverting for the fault plane solution is shown in Fig. 7.44 together with the CMT solution.

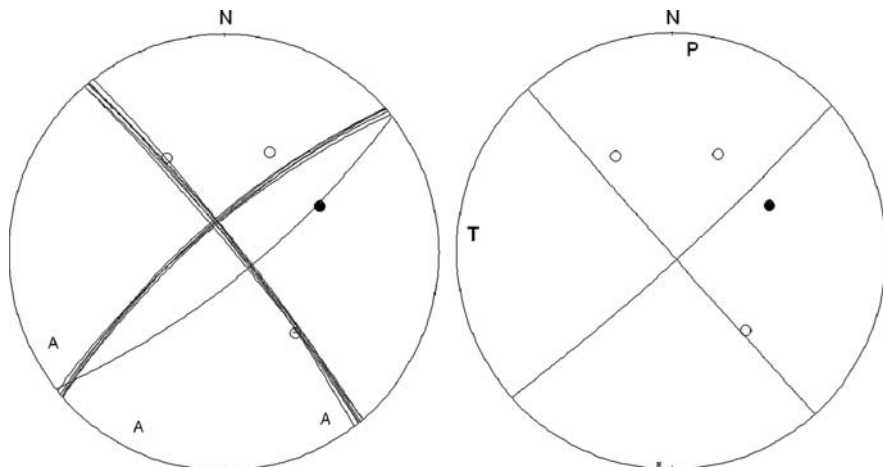


Fig. 7.44 Fault plane solution of event in Fig. 7.43 using amplitudes from 3 stations and polarities from 4 stations (left) and the CMT solution (right). The open circles are dilatations and the closed circles compression. Amplitude ratios are marked with A. See also Fig. 7.29

The amplitude inversion used 3 amplitudes on 3 stations and 4 polarities. The solutions shown on Fig. 7.44 are found using a grid of 2 deg, assuming 1 amplitude ratio error with a factor of 1.4 and no polarity errors. As it can be seen, the synthetic seismograms are good enough to produce the correct amplitudes for the main phases even though the seismogram looks quite different.

7.12 Software

Fault plane solutions can be made with a variety of programs. Here we will only mention the traditional programs using polarities and amplitude ratios since they are the most used in routine operations at smaller centers. Waveform inversion for moment tensor solutions is also done routinely at larger centers and a description of methods and software is found earlier in this chapter.

FOCMEC: This is one of widest used programs having been around since 1984 (Snoke, 2003a). FOCMEC uses polarities and amplitude ratios of local or global earthquakes and a search is made for possible solutions. Graphics software is included for display of the results. FOCMEC uses its own input format, but has also been integrated with SEISAN.

FPPFIT: Another widely used program is FPPFIT (Reasenberg and Oppenheimer, 1985). This is a Fortran program that computes double-couple fault plane solutions from P-wave first motion data using a grid search method. The companion programs FPPLT and FPPAGE plot the results on stereo nets for interactive viewing or for printing. There are additional programs in the package to create summary tables and to plot P&T axes for suites of mechanisms on stereo nets. See <http://earthquake.usgs.gov/research/software/>.

HASH: HASH is a Fortran 77 code that computes double-couple earthquake focal mechanisms from P-wave first motion polarity observations, and optionally S/P amplitude ratios. HASH is designed to produce stable high-quality focal mechanisms, and tests the solution sensitivity to possible errors in the first-motion input and the computed take-off angles. The technique is described by Hardbeck and (2002). Examples are provided for data in FPFIT input format. The code is designed to be as input-format independent as possible, so only minor editing is needed to use data in other formats. See <http://earthquake.usgs.gov/research/software/>.

7.13 Exercises

Exercise 7.1 Fault plane solution of a local event

Table 7.4 shows the observations for a small event in China. The data is from the ISC bulletin and the angles of incidence have been calculated with HYPOCENTER using the IASP91 model. The purpose is to find the fault plane solution.

- Plot the polarities on the stereo net (Fig. 7.45), note that the angles of incidence $> 90^\circ$ for most of the observations so the angles must be corrected as explained in Section 7.3.
- Set up two possible fault planes. Is there more than one possibility?
- Select one fault plane and one auxiliary plane.
- Determine strike and dip of the two planes.
- Determine the rake for the chosen fault plane using (7.5).
- Determine the P and T axis.

This data will also be used in one of the computer exercises which makes it easier to find all possible solutions.

Table 7.4 Polarity and angles for a local event in China. The origin time is 2000 0102 08:33, $M_L = 3.9$ and the location is 23.861 N and 121.004 E

Station	Polarity	Angle of incidence	Azimuth
SMLT	D	156	283
TYC	D	146	288
WDT	C	146	131
WNT	D	123	273
WHF	D	118	40
YUS	C	119	187
ALS	C	115	208
ESL	C	113	97
TCU	D	111	314
TWQ1	C	103	337
TWF1	C	101	152
NSY	C	100	338
NNS	D	98	30
ELDTW	C	98	179
NSTT	C	62	360

Exercise 7.2 Fault plane solution for a global earthquake

This exercise has the goal of determining the fault plane solution for a distant earthquake using a few polarities. The data is from the ISC bulletin (Table 7.5).

- Calculate the angles of incidence from the epicentral distance using the Bullen tables (Table 2.2) and (7.4) for the observations in distance range 40–68°. Assume a depth of 33 km. For the distances 24, 79, 80 and 81° the apparent velocities (s/deg) are 9.7, 5.4, 5.3 and 5.2 respectively.
- Plot the polarities of the stereo net (Fig. 7.45). Set up two possible fault planes. Is there more than one possibility?
- Select one fault plane and one auxiliary plane.
- Determine strike and dip of the two planes.
- Determine the rake for the chosen fault plane using (7.5).
- Determine the P and T axis.

This fault plane solution has few observations, all in the center of the focal sphere due to all observations being at teleseismic distances, so there might be several possibilities. This event also has a moment tensor solution which gives strike = 88°, dip = 6° and rake = 81°.

- Calculate the strike and dip of the other fault plane using (7.5) and (7.6). There might be an ambiguity which can be resolved considering that the two fault planes are at a right angle to each other. Plot the planes on the stereonet. How do the two solutions compare? Is it possible to make the moment tensor solution fit the solution using polarities? If not, what is the most likely explanation?

Computer exercises

- Get ISC data and do FPS.
- Get IRIS data and do FPS.
- Use Snode program for local earthquakes.

Table 7.5 Polarity, distance and azimuth for an earthquake recorded at teleseismic distances. The origin time is 2000 0101 1930, $m_b = 5.0$ and the location is 23.329 N 143.692 E and depth 21 km

Station	Polarity	Epicentral distance, deg.	Azimuth
YSS	D	24	358
NJ2	C	24	297
MDJ	D	24	334
BOD	D	40	336
ZAK	D	41	321
ARU	D	68	323
DAG	C	79	355
OBN	C	80	326
PYA	C	81	314

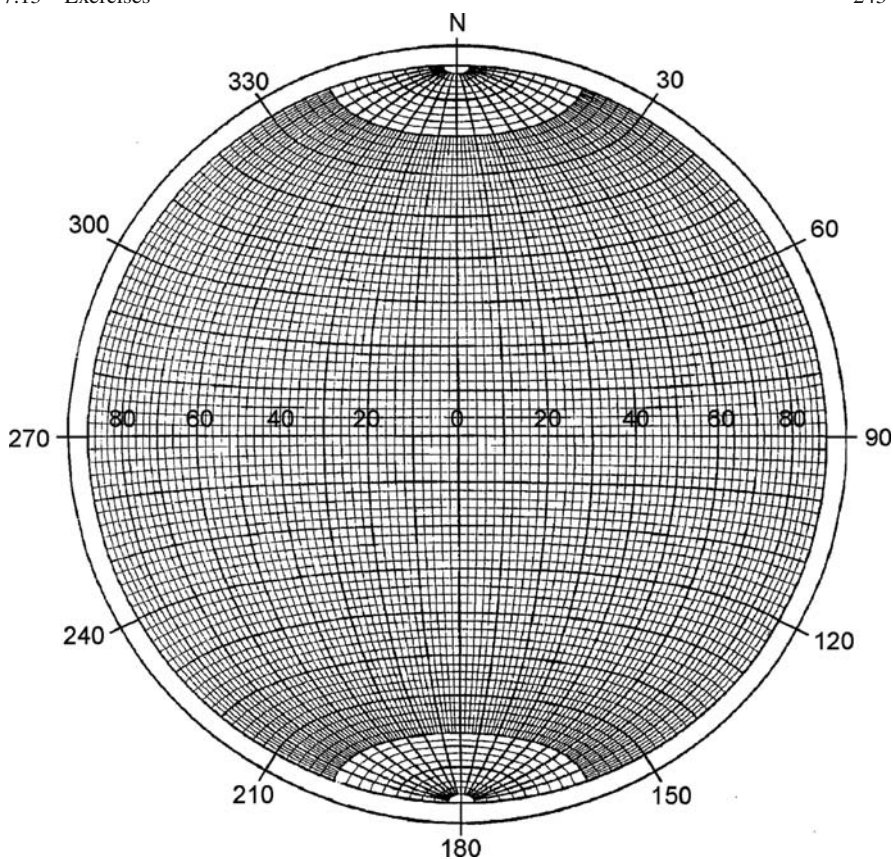


Fig. 7.45 An equal area Lambert-Schmidt net

Chapter 8

Spectral Analysis

As explained in Chapter 4, signals can be looked at in both the time and frequency domain. In seismology both are used and we now describe the spectral analysis of seismic signals. Spectra of seismic signals can be used to do a variety of tasks:

- Calculate seismic moment, source radius and stress drop using P or S-waves.
- Getting moment magnitude M_w from the moment.
- Quantifying the background noise.
- Calculating seismic attenuation Q of body waves or coda waves.
- Calculating the near surface attenuation κ .
- Getting an estimate of the soil amplification.

These tasks are interrelated since, for example, source spectra cannot be determined without knowledge of attenuation. If attenuation is unknown, it has to be estimated. Spectral programs are also used to quantify background noise and investigate soil amplification. All of these tasks can be done with a variety of public domain programs. In the following, the basic theory behind these analysis methods will be described and reference to programs that can do the job will be given. The theory will mainly deal with earthquakes at local and regional distances, however spectral analysis of body waves at teleseismic distances will also be described.

8.1 Attenuation

The amplitude attenuation caused by anelastic attenuation and scattering can be described through the quality factor Q as

$$A(f,t) = A_0 e^{\frac{-\pi f t}{Q(f)}} \quad (8.1)$$

where A_0 is the initial amplitude, $A(t)$ the amplitude after the waves have traveled the time t , f is the frequency and $Q(f)$ is the general frequency dependent Q . Alternatively (8.1) is written

$$A(f, r) = A_0 e^{\frac{-\pi f r}{v Q(f)}} \quad (8.2)$$

where r is the hypocentral distance and v the average velocity along the path. For longer paths, the average velocity might change with hypocentral distance so it is easier (and more correct) to use the travel time, which usually is a precisely known parameter for a given location and origin time.

Q has been observed to have strong regional variation in the lithosphere while it is more stable in the interior of the earth. Q in the lithosphere is most often observed to have a frequency dependency of the form

$$Q(f) = Q_0 f^a \quad (8.3)$$

when $f > 1$ Hz. There is some discussion on the values of Q for $f < 1$ Hz where some studies claim it starts increasing again for $f < 0.1 - 1$ Hz, however the dominant view is that Q is constant for $f < 1.0 - 0.1$ Hz, see e.g. Stein and Wysession (2003). For spectral analysis at regional distances, this has little importance since the effect of Q is small at low frequencies. The amplitude decay caused by Q is due to two mechanisms: Intrinsic Q due to heat loss (also called seismic absorption) and the redistribution of energy due to scattering (see Chapter 2). Q for P and S-waves in the lithosphere are generally expected to be different, see Fig. 8.1 for an overview of observational results.

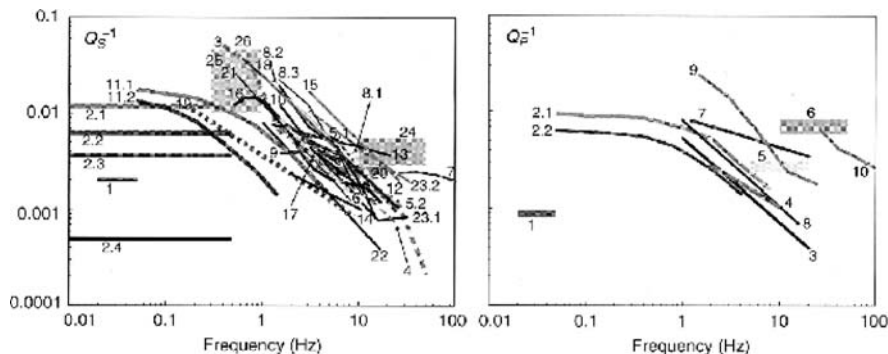
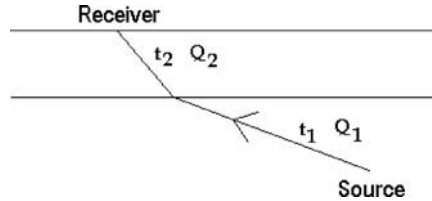


Fig. 8.1 Reported values of Q_s^{-1} (left) and Q_p^{-1} (right) for the lithosphere. 1–2: Surface wave analysis, 3–26: Other methods, see Sato and Fehler (1998) for details. Reproduced with kind permission of Springer Science and Business Media. Figure from Sato and Fehler (1998) and Sato et al. (2002)

From Fig. 8.1 it is seen that there are many more studies of Q_s than Q_p . Other studies of the lithospheric Q have shown Q_p to be smaller than Q_s , approximately $Q_s/Q_p = 1.5$ (e.g. Sato et al., 2002; Carpenter and Sanford, 1985; Kvamme and Havskov, 1989). All studies, except for low frequency surface wave analysis, indicate that Q increases with frequency and the frequency dependence of the scattering Q is stronger than the frequency dependence of the intrinsic Q (e.g., Hoshiba, 1993, overview by Sato et al., 2002). In practice we observe a Q which is a result of

Fig. 8.2 A ray passing two layers with different Q



both intrinsic and scattering attenuation and in practical analysis there is no need to separate the two.

If Q is constant along the path, (8.1) is all we need. If however Q varies along the path, the effect of the different parts of the path must be accounted for. For a two layer case (Fig. 8.2), we get

$$A(f,t) = A_0 e^{\frac{-\pi f t_1}{Q_1(f)}} e^{\frac{-\pi f t_2}{Q_2(f)}} A_0 e^{-\pi f \left(\frac{t_1}{Q_1(f)} + \frac{t_2}{Q_2(f)} \right)} \quad (8.4)$$

For a continuously changing Q we can write

$$A(f,t) = A_0 e^{-\pi f \int_{\text{path}} \frac{dt}{Q(r,f)}} = A_0 e^{-\pi f t^*} \quad (8.5)$$

where t^* is defined as

$$t^* = \int_{\text{path}} \frac{dt}{Q(r,f)} = \frac{T}{Q_{av}(f)} \quad (8.6)$$

and the integration is along the whole path, T is the total travel time along the path and Q_{av} is average Q along the path. For teleseismic body waves, t^* is often nearly constant (near 1 Hz for P-waves) for different travel times, due to increasing Q with depth counteracting the increase in path length (Lay and Wallace, 1995). For ray paths used in local seismology, Q is most often considered constant along the ray path, although some increase of Q with depth has been observed. However, this turns out to be an over simplification since the near surface layers (1–3 km) generally have a much lower Q than the rest of the path and tends to filter out high frequency energy ($f > 10 - 20$ Hz). Thus for local crustal studies, we must at least separate the attenuation into two terms (near surface and the rest) as in (8.4) with a constant Q in each layer. It turns out that the near surface quality factor is nearly frequency independent and limited to the very near surface layers (similar travel time). This has been confirmed by numerous bore hole studies e.g. Horiuchi and Iio (2002). See also summary by Abercrombie (1998). In general the symbol t^* is used for teleseismic ray paths so in order to avoid confusion, we will use $\kappa = t^*$ instead for near surface attenuation. Since $t_1 \gg t_2$, we will replace t_1 with t and Q_1 with Q and the general expression for the amplitude decay to use in local studies is then

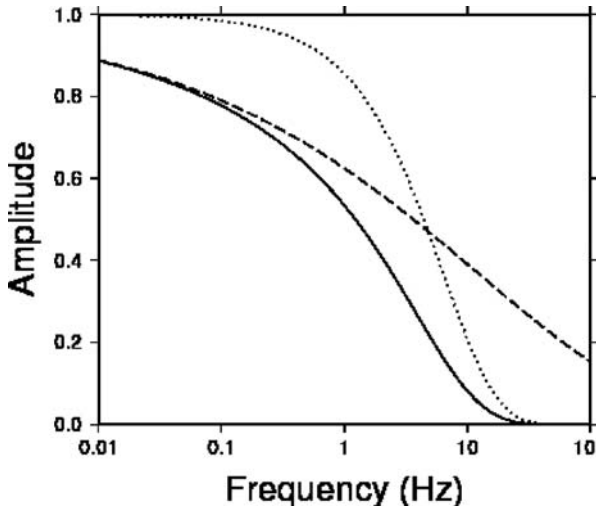


Fig. 8.3 Illustration of equation (8.7) showing the functions $e^{-\pi f t^*}$ (dotted) and $e^{\frac{\pi f t}{Q(f)}}$ (dashed) and the product of the two (solid). In this example we use $Q(f) = 200*f^{0.7}$, $\kappa = 0.05$ and $t = 30$ s

$$A(f, t) = A_0 e^{-\pi f \kappa} e^{\frac{\pi f t}{Q(f)}} \quad (8.7)$$

This general expression for attenuation (8.7) is illustrated in Fig. 8.3 showing the contributions from attenuation along the path and near the surface. Table 8.5 gives Q -values and Table 8.4 κ -values for different areas around the world. A typical κ -value is 0.05 and a typical Q is $Q = 100f^{0.8}$. It should be noted, that the near surface attenuation is not the only phenomenon, which can affect the amplitude at a given site. The so-called site amplification phenomenon is often observed, whereby amplitudes at certain frequencies are enhanced (rarely also reduced) due to local soil structure and/or topographic effects. It is rarely observed at good rock sites while common on sedimentary sites, and is most pronounced on horizontal components. This effect is hard to distinguish from the effect of κ at individual frequencies and it is advised to use vertical component recordings at rock sites, if possible, for Q -determination. See Section 8.6 on soil amplification estimation.

8.2 Seismic Source Model

The most common seismic source model used is the Brune model (Brune, 1970) and no other model will be described here. The model has been used extensively and it has been shown that it gives a good agreement with observations from many different tectonic regions and for a large range of magnitudes, see e.g. Chen and

Atkinson (2002). For a discussion of other models, see NMSOP. The Brune model predicts the following source displacement spectrum $S(f)$

$$S(f) = \frac{M_0}{\left(1 + \left(\frac{f}{f_0}\right)^2\right) 4\pi\rho v^3} \quad (8.8)$$

where M_0 (Nm) is the seismic moment, ρ is the density (kg/m^3), v is the velocity (m/s) at the source (P or S-velocity depending on spectrum) and f_0 is the corner frequency. This expression does not include the effect of radiation pattern (see Chapter 7). The shape of the log-log spectrum is seen in Fig. 8.4. At low frequencies, the spectrum is flat with a level proportional to M_0 while at high frequencies, the spectral level decays linearly with a slope of -2 . At the corner frequency ($f = f_0$), the spectral amplitude is half of the flat level.

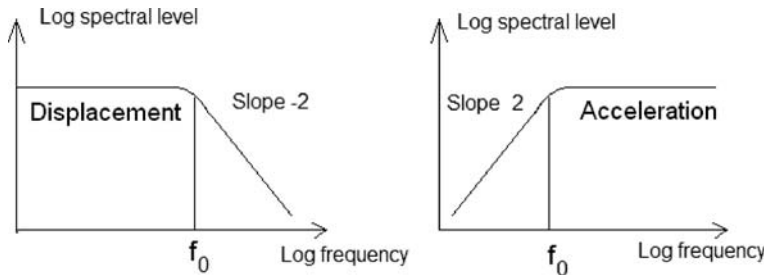


Fig. 8.4 Shape of the seismic source displacement spectrum (left) and source acceleration spectrum (right)

The displacement spectrum at the receiver will be modified by geometrical spreading $G(\Delta, h)$ and attenuation. At an epicentral distance Δ (m) and hypocentral depth h (m), the observed spectrum can be expressed as

$$D(f,t) = \frac{M_0 \times 0.6 \times 2.0}{\left(1 + \left(\frac{f}{f_0}\right)^2\right) 4\pi\rho v^3} G(\Delta, h) e^{-\pi f \kappa} e^{\frac{-\pi f t}{Q(f)}} \quad (8.9)$$

where t is the travel time (equivalent to using the hypocentral distance divided by the velocity), the factor 0.6 account for average radiation pattern effect, the factor 2.0 is the effect of the free surface, ρ is the density (kg/m^3). In practice, the units used are mostly g/cm^3 and km/s .

The spectrum corrected for attenuation is called D_c and is used to obtain the observed parameters corner frequency f_0 and spectral flat level Ω_0 (ms).

$$D_c(f) = \frac{\Omega_0}{\left(1 + \left(\frac{f}{f_0}\right)^2\right)} = \frac{M_0 \times 0.6 \times 2.0}{4\pi\rho v^3 \left(1 + \left(\frac{f}{f_0}\right)^2\right)} G(\Delta, h) \quad (8.10)$$

and the seismic moment can then be calculated as

$$M_0 = \frac{\Omega_0 4\pi \rho v^3}{0.6 \times 2.0 \times G(\Delta, h)} \quad (8.11)$$

If we use the units nm for spectral level, g/cm³ for density, km/s for velocity and km for distance, a multiplication factor of 10⁶ is needed to obtain seismic moment in units of Nm.

In case of simple 1/r body wave spreading (r in m), (8.11) would be

$$M_0 = \frac{\Omega_0 4\pi \rho v^3 r}{0.6 \times 2.0} \quad (8.12)$$

As discussed below, geometrical spreading will in many cases be more complex than just 1/r, so the general expression (8.11) should be used. In the literature, the effect of the average correction for radiation pattern varies between 0.55 and 0.85. According to Aki and Richards (2002), the average is 0.52 and 0.63 for P and S-waves, respectively. The effect of the free surface assumes a vertical incidence, which is an approximation. However, due to the low velocity layers near the surface, the incidence is not far from vertical. The effect is the same for P and S-waves. For simplicity, we will in the following use the values 0.6 and 2.0 for both P and S-waves.

The original Brune spectrum assumed SH waves, which indicate that horizontal components should be used when measuring the source spectrum. On solid rock, experimental studies show that, for S or Lg-waves, there is little difference between the amplitudes on the 3 components (e.g. Alsaker et al., 1991). However near surface amplification, as described above, is common, which mainly affects the horizontal components. So it is safest to always use the vertical component, which in any case is what should be used for the P-wave spectrum. Some studies use an average of all 3 components when making the S-wave spectra.

For a circular fault, the source radius a , is calculated as

$$a = K_s v_s / f_0 \quad (8.13)$$

where the radius is m or km if the S-velocity is m/s or km/s, respectively. The factor K_s has been estimated to different values depending on type of spectrum. Brune (1970) gave the values 0.37 and 0.50 for S and P-waves respectively while Maderiaga (1976) found 0.22 for S-waves and 0.33 for P-waves. This indicates that P and S-spectra will have different corner frequencies as observed in some studies (e.g. Abercrombie, 1995) and predicted theoretically (Maderiaga, 1976). Hanks and Wyss (1972) argues that the relationship between K_s -values for P and S-wave spectra is v_p/v_s , which is the same as a ratio of v_p/v_s between P corner frequency and S-corner frequency. Based on the above K_s -value of Brune and Maderiaga, the ratio

would be 1.35 and 1.50, respectively. Many observed spectra give a ratio between 1 and 2 (Molnar et al., 1973). In order to simplify (8.13), we will assume the ratio between K_s -values = v_p/v_s , use the most common Brune model ($K_s = 0.37$ for S-waves) and (8.13) becomes

$$a = 0.37v/f_0 \quad (8.14)$$

where v is now the P or S velocity for P and S spectra respectively.

The static stress drop (average across fault area) in bar (1 bar = 10^6 dyne/cm 2) is calculated as (Eshelby, 1957)

$$\Delta\sigma = \frac{7}{16}M_0 \frac{1}{a^3} \times 10^{-14} \quad (8.15)$$

where the radius is in km. Since the original formula assumes that moment is in dyne-cm and radius in cm, a conversion factor of 10^{-14} is needed and is calculated as

$$\left((10^7 \text{ dyne cm/Nm}) \times 1 / (10^5 \text{ cm/km})^3 \right) / 10^6 (\text{dyne/cm}^2) / \text{bar} = 10^{-14} \text{ since}$$

$$1 \text{ Nm} = 10^5 \text{ dyne} \times 100 \text{ cm} = 10^7 \text{ dyne cm.}$$

Ideally, all units should be metric and the stress drop measured in MPa (10^6 N/m 2) where one MPa is the same as 10 bar. However it is more practical to use velocity in km/s, density in g/cm 3 and displacement in nm so this is used in the following sections.

8.3 Geometrical Spreading

8.3.1 Local and Regional Distances

Geometrical spreading is dependent on the wave type and the distance and we are describing it with the function $G(\Delta, h)$. Body wave spreading at local distances can simply be described as

$$G(\Delta, h) = 1/\sqrt{\Delta^2 + h^2} = 1/r \quad (8.16)$$

or in a more general expression

$$G(\Delta, h) = r^{-\beta} \quad (8.17)$$

This formulation assumes a constant type of geometrical spreading independent of hypocentral distance. For S-waves, body waves are often assumed for the near field ($\beta = 1$) and surface waves for larger distances ($\beta = 0.5$) under the assumption

that the S-waves are dominated by Lg waves and (8.17) is commonly written as the Herrmann and Kijko (1980) relation

$$G(\Delta) = \frac{1}{\Delta} \quad \text{for } \Delta < \Delta_0 \quad (8.18)$$

$$G(\Delta) = \sqrt{\frac{1}{\Delta \Delta_0}} \quad \text{for } \Delta \geq \Delta_0 \quad (8.19)$$

where Δ_0 often is around 100 km. This works fine for surface focus events and S-Lg waves. However, in spectral analysis, there is no limitation to use only S-Lg waves and shallow events, so (8.18) and (8.19) are not general enough. If e.g. an S-wave is recorded from a deep earthquake at more than Δ_0 epicentral distance, it would not be appropriate to use surface wave spreading. Thus the geometrical spreading will also depend on the hypocentral depth and type of wave. In order to make the transition smooth from shallow to deep earthquakes we will set up a simple formulation for calculating geometrical spreading (Havskov and Ottemöller, 2008) under the assumption that the data to be analyzed predominantly consist of Pg, Sg and Lg. Until depth h_1 and for $\Delta \geq \Delta_0$, surface wave spreading is assumed. Below depth h_2 , body wave spreading is assumed and in between, an interpolation is made. The geometrical spreading is defined as

$$G(\Delta, h) = \frac{1}{g_d} \quad (8.20)$$

where g_d is called the geodistance defined as

P – waves: $g_d = r$	for any Δ and h
S – waves: $g_d = r$	for $\Delta < \Delta_0$ and any h
$g_d = r$	for any Δ when $h \geq h_2$
$g_d = \sqrt{\Delta \Delta_0}$	for $\Delta \geq \Delta_0$ and $h < h_1$
$g_d = \left(1 - \frac{h-h_1}{h_2-h_1}\right) \sqrt{\Delta \Delta_0} + \frac{h-h_1}{h_2-h_1} r$ for $\Delta \geq \Delta_0$ and $h_1 \leq h < h_2$	

The parameters h_1 , h_2 and Δ_0 are regional dependent. The default values used in the example in Fig. 8.5 are $h_1 = 30$ km (Moho), $h_2 = 50$ km and $\Delta_0 = 100$ km. There is no specific theoretical reason for (8.20), however it does provide a smooth transition between surface and body wave spreading as a function of depth and distance and it includes the earlier used relations (8.18) and (8.19).

Relation (8.20) assumes that direct waves always are present, even if the Pn comes before Pg. For some regions and distances, the body wave arrivals consist entirely of Pn and Sn and/or other refracted arrivals and β is no longer 1.0. Theoretically β is expected to have a value larger than 1 (Červaný and Ravindra, 1971). Practical observations have resulted in values in the range 1.2–1.8 (e.g. Allan et al., 2007; Zhu et al., 1991) and β has been observed to be frequency dependent. Even for distances < 100 km, β has been observed to be > 1 (Atkinson, 2004)) and strong focusing can even cause β to be negative (Atkinson, 2004).

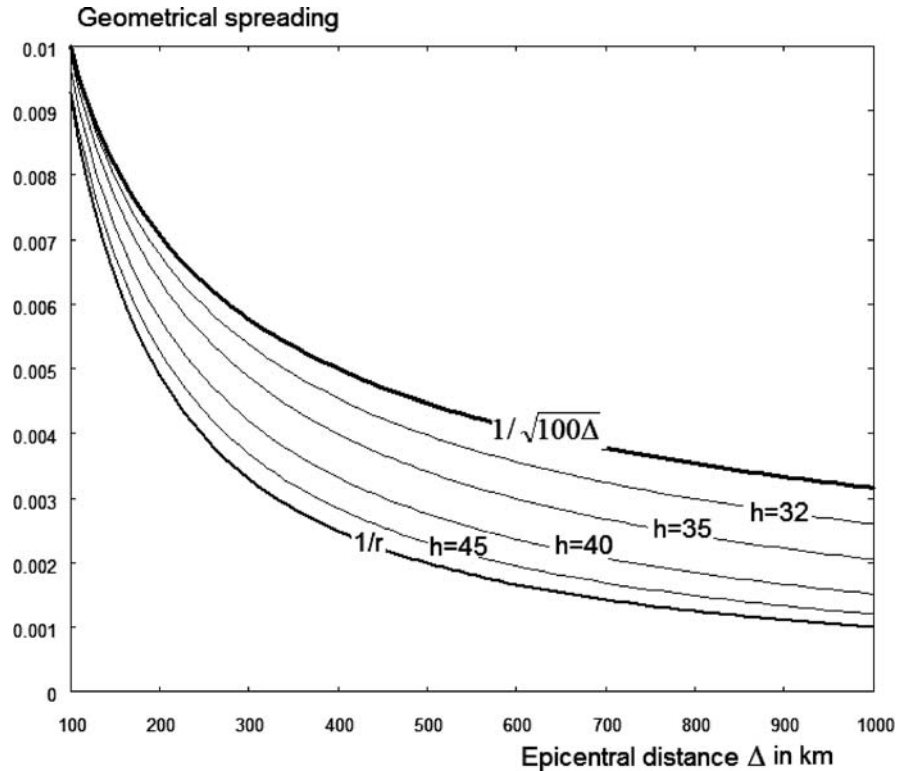


Fig. 8.5 Geometrical spreading using (8.20). The parameters are $h_1 = 30$ km and $h_2 = 50$ km. The bottom curve shows $1/r$ spreading assuming a depth of 40 km. The numbers inside the other curves correspond to hypocentral depth (km)

In summary: Geometrical spreading for local and regional distance depends on phase type, distance and depth and is regional dependent. The most certain relation is for direct waves at short distances where the relationship is $1/r$.

8.3.2 Teleseismic Distances

For larger distances there is no simple expression for geometrical spreading. Theoretically, the geometrical spreading is proportional to the second derivative of the travel time curve (e.g. Stein and Wysession, 2003; Okal, 1992) and it can therefore be calculated from travel time curves and/or earth models. The geometrical spreading (unit km^{-1}) for teleseismic distances is expressed in the same way as for regional distances and we can write

$$G(\Delta, h) = \frac{1}{g_d} \quad (8.21)$$

exactly as for local and regional distances. Calculating geometric spreading curves for real earth models gives very discontinuous curves due to the various discontinuities, particularly, from the upper mantle) (e.g. Dahlen and Tromp (1998), Julian and Anderson (1968)). For practical purposes these curves are often smoothed. Langston and Helmberger (1975) calculated a smoothed g_d based on the Jeffreys-Bullen spherical earth and this function was subsequently used in several modelling studies (e.g. Choy and Boatwright, 1988; Cipar, 1980). The same curve was used for P and S. A curve was also calculated by Dahlen and Tromp (1998) for the PREM model (Dziewonski and Anderson, 1981). Figure 8.6 shows the curves.

A simple relationship can also be estimated from the m_b distance correction tables since they give the amplitude as a function of distance and depth. Recall ((6.13) from Chapter 6)

$$m_b = \log(A/T) + Q(\Delta, h) \quad (8.22)$$

Assuming a constant T and m_b we can write

$$\log(A) = \log(1/g_d) = -Q(\Delta, h) + c \quad (8.23)$$

where c is a constant. For the Gutenberg and Richter attenuation function (Chapter 6), the attenuation term is 6.9 at 60° (Fig. 6.8) for $h = 0$. Assuming $1/g_d$ to

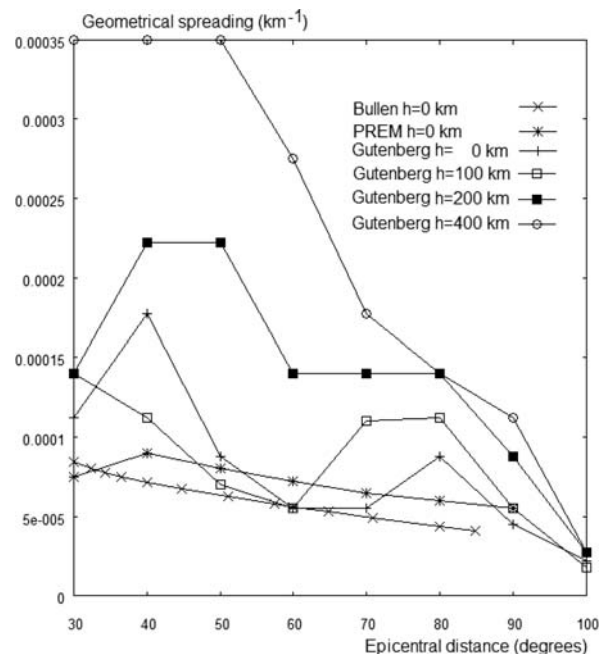


Fig. 8.6 Teleseismic geometrical spreading $1/g_d$ calculated by different methods. Bullen is from Bullen tables (Langston and Helmberger, 1975), PREM (Dahlen and Tromp, 1998) is from PREM model, Gutenberg curves are from Gutenberg and Richter attenuation tables for 0, 100, 200 and 400 km respectively

be 0.000056 at 60° using the Bullen attenuation curve (Fig. 8.6) and inserting above gives

$$\log(A) = -Q(\Delta, h) + 2.65 \text{ or} \quad (8.24)$$

$$A(\Delta, h) \equiv 1/g_d = 447/10^{Q(\Delta, h)} \quad (8.25)$$

Using $Q(\Delta, h)$ gives us both the geometrical spreading and also amplitude loss due to anelastic attenuation. However since the effect of attenuation is nearly a constant term, independent of distance (see discussion on t^* below), then (8.25) will give only the geometrical spreading under the assumption that the anchor point at 60° gives an accurate geometrical spreading.

Comparing the curves (Fig. 8.5), it is seen that they are quite similar for events up to a depth 100 km. At shorter distances, the geometrical spreading is less for a deep event than a shallow event. This can partly be explained by shorter travel path, but more likely the assumption used about constant t^* might not hold. Nevertheless, Fig. 8.6, gives a good idea of what to expect for geometrical spreading at teleseismic distances although the Gutenberg-Richter curves are more meant to be for illustration than to represent exact geometrical spreading. For the range $30\text{--}90^\circ$ we can approximate the geometrical spreading made with the Bullen tables with the function

$$1/g_g = 0.0048 / (27.0 + \Delta) \quad (8.26)$$

In further analysis, this simple relation will be used.

8.4 Self Similarity and Seismic Source Spectra

The generally accepted theory of self similarity (e.g. Stein and Wysession, 2003) predicts a constant stress drop for earthquakes of different size in the same tectonic environment. From equations (8.14) and (8.15) we have

$$\Delta\sigma = \frac{7}{16}M_0 \frac{1}{a^3} 10^{-14} = \frac{7 \times 10^{-14}}{16 \times (0.37v)^3} M_0 f_0^3 \quad (8.27)$$

If the stress drop is constant, then $f_0^{-3} \approx M_0$, and the corner frequency decreases when the moment increases. We can use (8.27) to calculate the relationship between the corner frequency and the moment magnitude. Inserting the definition of moment magnitude

$$M_w = \frac{\log(M_0)}{1.5} - 6.07 \quad (8.28)$$

in (8.27), we get

$$\log(f_0) = 1.32 + 0.33 \log(\Delta\sigma) + \log(v) - 0.5M_w \quad (8.29)$$

Stress drop is generally thought to be in the range 1–100 bar with an average of 30 bar for interplate earthquakes (Kanamori and Anderson, 1975) although there are reports of both higher (e.g. House and Boatwright, 1980) and lower stress drop (Horiuchi and Iio, 2002). Assuming a stress drop of 30 bar and an S-velocity of 3.5 km/s gives, for the S-spectrum

$$\log(f_0) = 2.35 - 0.5M_w \quad (8.30)$$

This relation should at least give a hint whether an observed corner frequency is “reasonable”. Table 8.1 shows some values of f_0 calculated using (8.29).

Table 8.1 S-corner frequency as a function of stress drop for different magnitudes calculated using (8.29)

Magnitude	Corner frequency (Hz) for fixed stress drop			
	1 bar	10 bar	30 bar	100 bar
0	72	155	223	331
1	23	49	70	105
2	7	15	22	33
3	2.3	5	7	10
4	0.72	1.5	2.2	3.3
5	0.22	0.49	0.70	1.0
6	0.072	0.15	0.22	0.33
7	0.0022	0.049	0.070	0.10
8	0.00072	0.0015	0.0022	0.0033
9	0.00022	0.00049	0.00070	0.0010

From the table it is seen that it will be very difficult to determine corner frequency of earthquakes with $M_L \leq 2$ unless the sample rate is very high (> 200) and the signal to noise ratio is very good and a compensation for κ can be made (see Fig. 8.8).

Using (8.30) to calculate the corner frequency for a given M_w , the corresponding Brune spectra can be calculated (8.8) and the theoretical source spectra can be plotted as a function of magnitude, see Fig. 8.7. This figure illustrates the phenomenon of magnitude saturation (see also Chapter 6). For m_b , the amplitude is read at around 1 Hz. From the figure it is seen that the amplitude at 1 Hz increases linearly with moment until the corner frequency reaches 1 Hz (around magnitude 6) and for larger events, the amplitude at 1 Hz is smaller than the amplitude of the flat level. Thus for events larger than 6, m_b will underestimate the magnitude. The same happens for M_s , but at the lower frequency of 0.05 Hz. Since broadband magnitudes m_B and M_S are determined at lower frequencies, they will saturate at higher magnitudes than the corresponding m_b and M_s . Neither magnitude is measured at a particular frequency. The smallest frequency to use for m_b is 0.033 Hz corresponding to a saturation

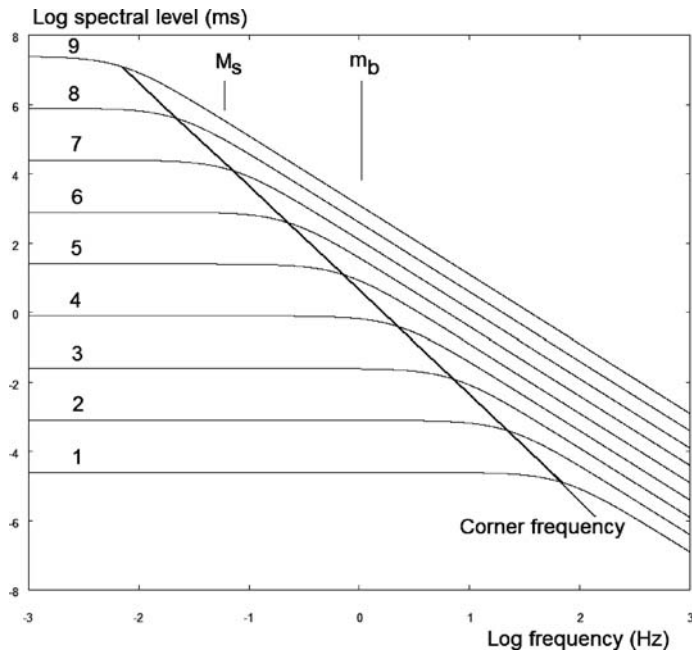


Fig. 8.7 Theoretical S-source spectra for different size earthquakes. The curves are calculated using (8.8) and (8.30) assuming a velocity of 3.5 km/s and a density of 3 g/cm³. The stress drop is 30 bar. The moment magnitude is indicated at each spectrum. A line indicates the corner frequencies where it crosses the spectra. The M_s and m_b lines indicate the frequencies of determination

starting around $m_b = 7.5$ (see also Bormann and Saul (2008)). For M_s , the lowest frequency used is 0.017 Hz corresponding to start of saturation around 8.5.

8.5 Spectral Analysis at Local and Regional Distances

Spectral analysis at regional and particularly local distances is very useful, and can be used to determine seismic moment and moment magnitude. The spectra must be corrected for geometrical spreading and attenuation as described above. The correction for attenuation is particularly important for getting the correct corner frequency. The attenuation has two effects on the spectrum: Change the shape which affects the determination of corner frequency and change the level which affects the seismic moment. Attenuation is particularly important for small earthquakes due to the high frequencies. Let us illustrate this with the “attenuation spectra”, which is the effect of attenuation on the source spectra (Fig. 8.8). See also Fig. 8.3.

It is seen that the near surface attenuation can seriously affect the spectrum making it difficult to get a correct corner frequency if no correction is made. The correction for κ is sometimes not possible, see below. The effect of Q has less serious

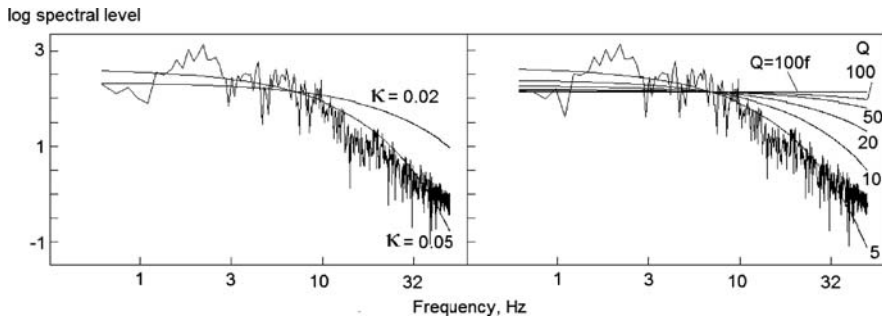


Fig. 8.8 A displacement spectrum of a local earthquake of magnitude $M_L = 3.4$. The spectrum has not been corrected for attenuation. The smooth curves are the contribution to the observed spectral shape as a function of different κ -values (left) and Q -values (right). The Q -values are constant except for the top line with $Q = 100f$. The data is from the Tanzania network, station ITB, vertical channel, origin time is 1992 10 09 6:53 and the travel time is 20 s

effect on the spectral shape, and in this example the spectrum is only seriously affected by a constant Q below 50. However, smaller events or events at larger distances would still be affected by this Q , see (8.32). If the corner frequency is high and if the effect of $Q(f)$ is not dominating the spectrum, the near surface attenuation will dominate the spectral decay and the real corner frequency cannot be seen, only the apparent corner created by the near surface attenuation. If we define the corner frequency f_κ as the frequency where the spectral level has reached 50% of the flat level, as a result of the effect of near surface attenuation, then f_κ can be calculated as

$$e^{-\pi\kappa f_\kappa} = 0.5 \quad \text{giving} \quad f_\kappa = \frac{0.221}{\kappa} \quad (8.31)$$

If e.g. $\kappa = 0.025$, $f_\kappa = 9$ Hz, and it will not be possible to obtain the true source corner frequency for small earthquakes ($M_L < 3.0$) without correction for κ . It might not be possible to correct for κ if the signal to noise ratio of the high frequency part of the spectrum is low, which could be due to a low magnitude, large distance and the effect of κ . Thus in order to get a reliable source corner frequency for small earthquakes, κ is a very critical parameter.

A similar effect will be obtained with Q , however since Q normally is frequency dependent, the effect will not be as dramatic, but more like a flattening of the spectrum. If α is near 1, no change in spectral shape occurs as illustrated in Fig. 8.8. We can similarly define f_Q as f_κ and get

$$e^{-\pi \frac{f_Q t}{Q_0^\alpha}} = e^{-\pi \frac{f_Q^{1-\alpha} t}{Q_0}} = 0.5 \quad \text{giving} \quad f_Q = \left(\frac{0.221 Q_0}{t} \right)^{\frac{1}{1-\alpha}} \quad (8.32)$$

For Norway, $Q = 440f^{0.7}$ (Table 8.5) which gives $f_Q = 93$ Hz if $t = 25$ s. In this case, the Q -correction is not critical for determination of f_0 . For the small ($M = -1$ to 1) very local earthquakes at Deception Island, $Q = 59f^{0.4}$ (Table 8.5)

and for a travel time of 2 s, $f_Q = 23$ Hz, so obviously in this case the Q -correction is critical to get the correct corner frequency. So if the source corner frequency is well under f_Q and f_κ , can we then forget about corrections for attenuation? For κ , the effect on the spectral level is negligible, however for Q , the level change also depends on the travel time. If we use the example of $Q = 440f^{0.7}$, then at a travel time of 100 s and at a frequency of 1 Hz we get that the spectral level has been reduced by a factor of 0.49. So correction for Q , even in a low attenuation area like Norway, is always important in order to get the correct seismic moment. Figure 8.9 shows an example of a spectrum of a small earthquake.

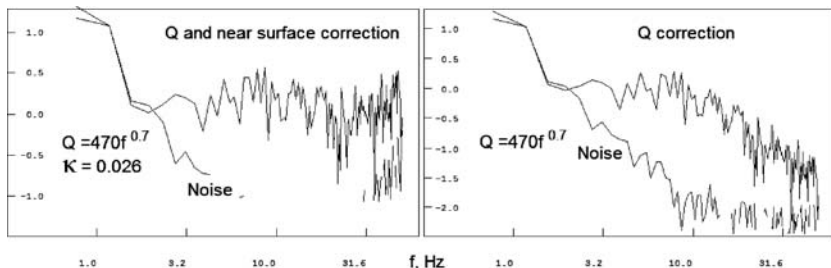


Fig. 8.9 S-wave displacement spectrum of a $M_L = 0.4$ earthquake in Northern Norway. The *right* hand figure has no correction for κ . The data is from vertical component of STOK, origin time is 2006 11 04 18:03. The attenuation values for Norway are taken from Table 8.4 and Table 8.5

The spectrum without κ -correction looks like a nice textbook example of a source spectrum with a corner frequency of about 10 Hz. From Table 8.1 we can see that a corner frequency of 10 Hz is rather low for a magnitude 0.4 earthquake. Correcting the spectrum for κ gives a nice flat spectrum and no corner frequency can be seen so the corner frequency must be higher than 50 Hz which is reasonable for a magnitude 0.4 earthquake (Table 8.1). The sample rate is 100 Hz and that is clearly not enough to resolve the corner frequency. On the other hand, near 50 Hz, the signal to noise ratio is close to 1, so a higher sample rate might not have helped in this particular case. It is however important that the sample rate is high enough to at least resolve the corner frequency, which means that the sample rate must be at least 4 times the corner frequency since only signals with frequency up to twice the sample rate can be resolved due to aliasing.

The mistake of not correcting for κ , when making spectra of small earthquakes, happens frequently. If the near surface attenuation is the dominating factor in shaping the spectrum, the corner frequency might appear to be constant for all earthquakes smaller than a certain magnitude. Recall (8.27)

$$\Delta\sigma = \frac{7 \times 10^{-14}}{16 \times (0.35v_s)^3} M_0 f_0^3 \quad (8.33)$$

If f_0 is constant, stress drop will scale linearly with seismic moment. Alternatively, it has been argued that when the magnitude goes down, the corner

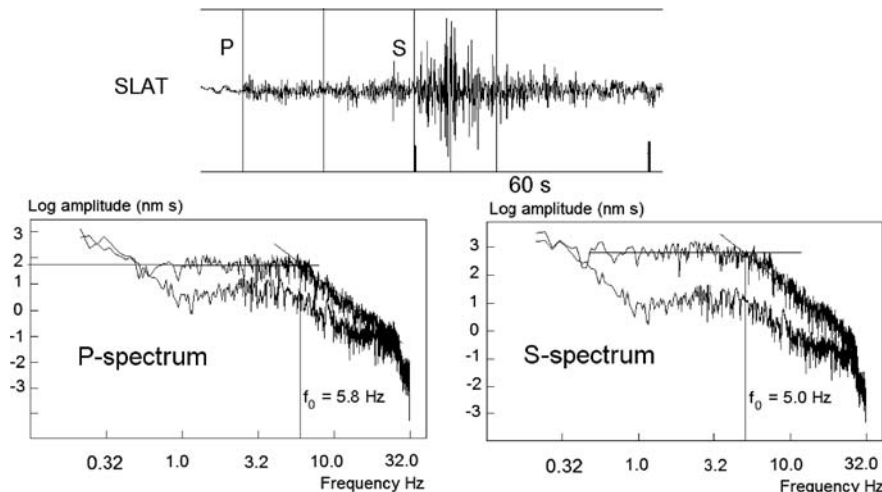


Fig. 8.10 Example of seismic displacement spectra of a local earthquake in Central Sudan. On *top* is shown the seismogram (vertical component) with the time windows used for spectral analysis. The *top* spectral curve is the signal spectrum while the *bottom* curve is the noise spectrum. The spectrum is corrected for attenuation $Q = 160f$. The epicentral distance is 413 km, depth 15 km and the origin time is 2006 06 23 09:11 and $M_L = 4.0$. Note that amplitude is in nm/Hz = nm s

frequency reaches some maximum frequency, however most studies seem to indicate that the principle of self-similarity holds down to very small magnitudes. For an overview of this topic, see Abercrombie (1995).

Figure 8.10 shows the seismogram and the corresponding P and S-wave spectra of a local earthquake in central Sudan. The spectrum shows that the signal to noise ratio is acceptable in the frequency band 0.5–15 Hz. Since we expect the corner frequency to be in the 1–5 Hz band, this is acceptable. Since no information about κ is available, no correction has been made for κ . However, for a typical κ -value, the spectrum will not be much affected for frequencies below 10 Hz (see (8.31)). The spectrum can thus be expected to represent a reasonably reliable spectrum.

The largest uncertainty is in the Q -value since at this relatively large distance, the Q -value will affect the spectral level. From the spectrum and the parameters above, the spectral parameter will be calculated. From the figure, the spectral flat level and corner frequency can be measured by the method of approximating the flat level and spectral decay with straight lines. The corner frequency is then measured where the two lines cross. Using this method we obtain the results listed in Table 8.2. The spectrum can also be fitted automatically through a grid search procedure (e.g., Ottemöller and Havskov, 2003) and the best fitting corner frequency and spectral level are found. In this example we obtain automatically a corner frequency of 6.1 Hz from the S wave spectrum, slightly higher than from the manual fitting and spectral flat level of 500 nm as compared to 600 nm found manually (Table 8.2), see also Exercise 8.1. Generally, the automatic fitting is regarded more consistent and thus preferable also in routine analysis.

Table 8.2 Spectral parameters for the spectra in Fig. 8.10. The parameters are obtained manually and the calculations assume $1/r$ spreading, $v_p = 6.4 \text{ km/s}$, $v_s = 3.6 \text{ km/s}$ and density is 3.0 g/cm^3

	Ω_0 nms	f_0 , Hz	a,m	$\Delta\sigma$, bar	M_0 , Nm	M_w
P	63	5.8	408	14	$2.1 \cdot 10^{14}$	3.5
S	600	5.0	266	84	$3.6 \cdot 10^{14}$	3.6

The details of for the calculation for S are: $\Omega_0 = 600 \text{ nm s} = 600 \cdot 10^{-9} \text{ ms}$, $f_0 = 5 \text{ Hz}$, then

$$M_0 = \frac{\Omega_0 4\pi \rho v_s^3 r}{0.6 \cdot 2.0} = \frac{600 \cdot 10^{-9} 4\pi 3000 \cdot 3600^3 \cdot 413 \cdot 10^3}{0.6 \cdot 2.0} \text{ Nm} = 3.6 \cdot 10^{14} \text{ Nm} \quad (8.34)$$

Using (8.28) we get the moment magnitude

$$M_w = \frac{\log(M_0)}{1.5} - 6.07 = 3.6 \quad (8.35)$$

A quick estimate can also be made using the standard spectral levels in Fig. 8.7. The spectral level of 600 nm has to be converted to units of m and referred to 1 m distance

$$\text{Spectral level at 1m distance} = 600 \cdot 10^{-9} \text{ (ms)} \cdot 413 \cdot 10^3 \text{ (m)} = 0.25 \text{ ms}$$

From Fig. 8.7, this also gives a magnitude around 3.6. This is a bit less than M_L and could be explained by Sudan using the Southern California M_L scale and/or a wrong Q . At 400 km, M_L probably has to be adjusted to the local conditions (see 6.14). Stress drop and source radius can now be calculated as

$$a = 0.37 v_s / f_0 = 0.37 \cdot 3600 / 5 = 266 \text{ m} = 0.266 \text{ km}$$

$$\Delta\sigma = \frac{7}{16} M_0 \frac{1}{a^3} \times 10^{-14} = \frac{7}{16} 3.6 \cdot 10^{14} \frac{10^{-14}}{0.266^3} = 84 \text{ bar}$$

This value of the stress drop is “reasonable” according to Table 8.1, however it is also very uncertain since it is critically dependent on the corner frequency being in the third power. In this example the corner frequency is quite well defined while in many other cases it might have a large error. By just changing the corner frequency to 6 Hz, the stress drop increases to 145 bar. The uncertainty is clearly seen when comparing to the P-spectrum where M_w for P is similar to M_w for S while the stress drops are very different.

Summary of procedures

- Attenuation: Use existing values. If no attenuation values are available for the area, then choose values for a similar tectonic area. A simple way of checking if values are reasonable is to check M_w for a consistent distance bias. If no bias, it

is likely that attenuation is reasonably correct. Alternatively attenuation can be determined, see Section 8.5. If no Q is available for P, use Q for S.

- Geometrical spreading: Start with $1/r$ and evaluate results to see if a more complicated relation is needed.
- P and or S- spectra: Expect similar values using P and S.
- Corner frequency: Check with Table 8.1 if “reasonable”. For small events, take the effect of κ into consideration.
- Stress drop: Expect stress drop to be associated with a larger error, at least a factor of 2.
- Using P only: Using only P can be very useful in case S is saturated, unclear or not seen at all. This last case can often happen for larger distances (> 200 km) or where S-waves are blocked by e.g. a graben structure.
- Corner frequency for small events: Do not expect to be able to recover corner frequency for small events since the effect of κ can make this impossible. Where corner frequency cannot be determined, spectra can be useful to get moment.
- Instrument types: Spectral analysis can be done using both seismometers and accelerometers provided sufficient frequency resolution.

8.6 Spectral Analysis at Teleseismic Distances

Source spectral analysis at teleseismic distances is less used than spectral analysis at local distances, partly because the seismic moment for larger events can be determined through moment tensor inversion, see Chapter 7. However, moment tensor inversion requires a good data set of globally distributed broadband stations and sophisticated setup of software which is not always available. Using spectral analysis of teleseismic events can quickly give an estimate of seismic moment, corner frequency and stress drop using a simple spectral analysis using both SP and broadband records. Using spectral analysis of the P- phases also has the advantage of being able to get a very quick estimate of seismic moment.

The spectral analysis can in principle be done for both P and S-waves. The spectral analysis is done the same way as for local distance with the main difference of using a global geometrical spreading and only correcting for t^* , as described in (8.5).

8.6.1 Attenuation

In the distance range $30\text{--}90^\circ$, t^* is rather constant although there is a tendency to increase in t^* with increasing distance (Stein and Wysession, 2003). There is some frequency and regional dependence (Der and Lees, 1985). The generally accepted value for t^* for P is 1.0 and for S it is 4.0 (e.g. Lay and Wallace, 1995). However t^* will depend on ray path. E. g. for a deep earthquake, t^* will be lower than for a shallow earthquake since the ray passes less time in the asthenosphere compared to the shallow event. Houston and Kanamori (1986) used a $t^* = 0.7$ for P in a global

study of source spectra, however it was argued by Singh et al. (1992) that a value of 1.0 would have been more appropriate. Correction for t^* is in general only valid for frequencies below 1 Hz (Stein and Wyssession, 2003).

8.6.2 Geometrical Spreading

The geometrical spreading for the distance range 30–90° for body waves (Fig. 8.6) for shallow earthquakes is well established. For events with $h < 100$ km and in the distance range 30–90° the approximate geometrical spreading curve (8.26) will be used.

Window length: Ideally only the direct P or S-wave should be used. However, the window length must be a few times $1/f_0$ in order to be able to determine the corner frequency. This means that for most shallow earthquakes, the time window will include the pP and sP phases, however the PP, PcP and ScS should not be included. In practice there is not much difference in the spectral level when different window lengths are used (remember the spectral density level is normalized with respect to window length) (e.g. Hanks and Wyss, 1972). In order to get a reliable moment, several stations and both P and S spectra should be used. For very large events ($M > 8.5$), which often consist of multiple ruptures, the corner frequency will not represent the whole length of the fault but only the largest sub-event and spectral analysis would underestimate both the source dimension and the seismic moment (Bormann and Saul, 2009a).

In order to compare spectral analysis at local and teleseismic distances, the large Mexican event used in Fig. 6.2 will be used. Figure 8.11 shows the spectra. Note that the t^* -correction overestimates the spectral values for $f > 0.3$ Hz, when the signal to noise ratio becomes bad and in general this will happen for frequencies > 1 Hz.

Table 8.3 compares the spectral parameter from the near field and far field spectra.

Comparing the spectral values in this limited example, it is seen that the local determination underestimates the magnitude and the teleseismic determination overestimates the magnitude. The differences are small and could be caused by radiation pattern effects, by only using single station measurements, wrong Q or geometrical spreading for the local spectrum. At both stations it seems, as predicted, that the P-corner frequency is higher than the S-corner frequency, however the corner frequencies do not agree at local and teleseismic distances which again could be caused by wrong attenuation (see also Singh et al., 1992). This example also demonstrates the difficulty in making P-spectral analysis of large events at short distances since the S-P time may be too short to get a long enough window to properly define the corner frequency and spectral flat level as it is almost the case for this event. The S-window can be made longer and it is seen that the S-corner frequency is better defined than the P-corner frequency.

Spectra at teleseismic distances are normally made with LP or broadband records in order to be able to define the spectral flat level and the corner frequency. However,

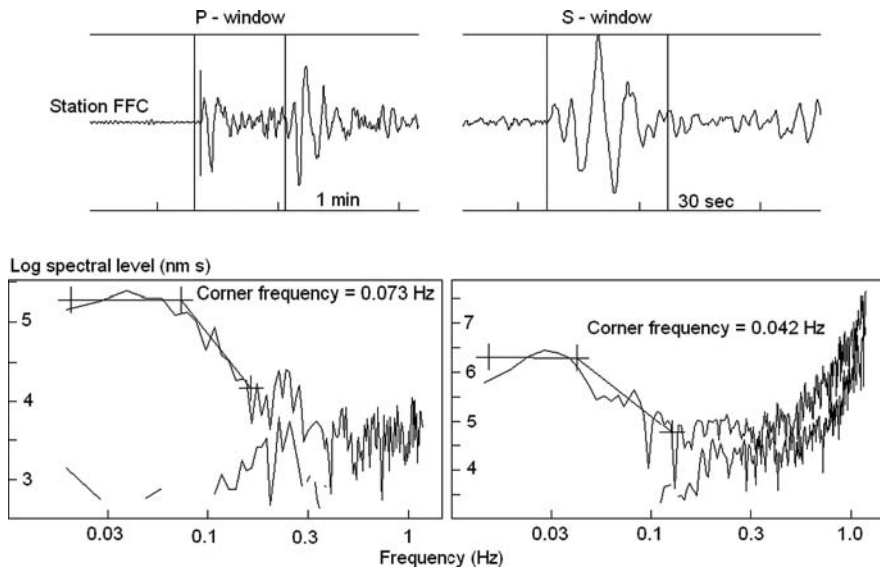


Fig. 8.11 P and S-spectra for a large Mexican event (*top*) recorded at an epicentral distance of 37° . The P-spectrum is shown to the left and the S-spectrum to the *right*. The lines indicate the manual selection of the spectral fitting. The P-spectrum has been corrected with a $t^* = 1$ and the S-spectrum with a $t^* = 4$. The *lower* curves are the noise spectra. Vertical channels are used. The origin time is 1996 0715 21:23

Table 8.3 Comparison of spectral parameters for near (hypocentral distance of 107 km) and far field spectra for the event shown in Figs. 8.11 and 6.2. The parameters for moment magnitude are also given for the Harvard (HRV) moment tensor solution and USGS solution

Station	Spectrum type	Corner frequency (Hz)	Stress drop (bar)	M_w
CAIG	P	0.13	6	6.5
CAIG	S	0.09	7	6.4
FFC	P	0.07	3	6.8
FFC	S	0.04	6	7.0
USGS				6.8
HRV				6.6

in some cases it is also possible to make teleseismic spectral analysis with SP records, see exercise 2 for an example.

Recommendations:

- In general broadband data is needed to get a good definition of the spectrum.
- Use distances $30\text{--}90^\circ$.
- Use for depth less than 100 km.
- Use a window length at least 2 times the expected $1/f_0$.
- Use standard values for t^* .

8.7 Determination of Q

Since determination of Q is a prerequisite for source spectral analysis at local and regional distances, it will be dealt with in this chapter.

In the following it is assumed that κ is frequency independent and Q is frequency dependent of the form

$$Q(f) = Q_0 f^\alpha \quad (8.36)$$

α is usually in the range 0.5–1.0 and Q_0 is a constant. Taking the natural logarithm of (8.7) gives

$$\ln(A(f,t)) = \ln(A_0) - \pi f \kappa - \pi f \frac{t}{Q(f)} \quad (8.37)$$

8.7.1 Determine κ

We will assume that the signals are generated by earthquakes following the Brune source model (8.8) and therefore have a source displacement spectrum of the form (8.8). If the signal is generated by an earthquake and we only use the part of the spectrum where $f_0 > f$, the spectral level will only depend on attenuation and (8.37) shows that plotting $\ln(A(f,t))$ vs. f , will give a straight line with slope $-\pi(\kappa + t/Q)$ if Q is frequency independent. If $Q = Q_0 f$, the slope becomes $-\pi\kappa$. If t/Q is small, the slope will also be directly proportional to κ . Thus to reliably determine κ by plotting the spectral level, for $f < f_0$, without knowing Q , short hypocentral distances should be used. If $Q(f)$ is known, the spectrum can first be corrected for $Q(f)$, and κ can be determined directly. A good test of the result is therefore to determine κ using different distances. If $Q(f)$ is correct, the value of κ obtained should be constant. A typical value of κ is 0.05. With a travel time through the near surface of 1 s, this corresponds to a $Q = 1/0.05 = 20$. Table 8.4 gives some κ – values for different regions and Fig. 8.12 shows an example of a calculation. This example shows an uncorrected spectrum. Since the magnitude is $M_L = 2.3$, we can expect a corner frequency in the 10–20 Hz band and the figure indicates that this is possible. The spectrum flat level shows a decay as frequency increases, probably caused by attenuation. The question is if this is a good event for determining κ . That can be checked by observing the effect of attenuation. As it is seen, a κ of 0.05 alone can explain the shape of the spectrum so κ must be smaller than 0.05 since the corner frequency also shapes the spectrum. On the other hand, the effect of Q , due to the relatively large distance (118 km hypocentral distance), can also explain the decay of the spectrum flat level. So the conclusion is that this is not a good event for determining κ unless Q is very well known since Q and κ will trade off with each other.

Figure 8.13 shows an example of a small near event. The event has magnitude $M_w = 1.1$ and the hypocentral distance is 21 km and can be expected to have a corner frequency larger than 30 Hz (Table 8.1). The uncorrected source spectrum

Table 8.4 κ for different regions using S-waves

References	κ (s)	Place
Anderson and Hough (1984)	0.04	Western US
Hough et al. (1988)	0.0003–0.0035	Anza, California
Singh et al. (1982)	0.027–0.047	Imperial fault, California
Frankel and Wennerberg (1989)	0.01–0.02	Anza, California
Abercrombie (1997)	0.049	Cajon Pass Scientific drill hole
Liu et al. (1994)	0.03 typical	New Madrid seismic zone
Margaris and Boore (1998)	0.035	Greece
Pacesa (1999)	0.026	Norway
Malagnini et al. (2000)	0.05	Central Europe
Akinci et al. (2001)	0.02	North Anatolian fault, Turkey
Motazedian (2006)	0.03	Northern Iran

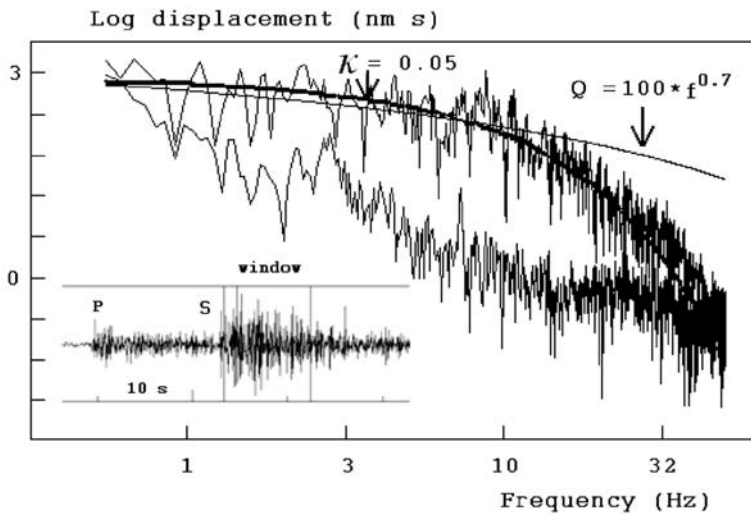


Fig. 8.12 S-spectrum of a local earthquake with magnitude $M_L = 2.3$. The *bottom* curve shows the noise spectrum. The hypocentral distance is 118 km. The spectrum has NOT been corrected for Q or κ . The effect of κ and Q is indicated with the curves. The inset below shows the signal and the window used for the spectrum. The station is PDH, vertical component from the Tanzania network, origin time is 1992 1007 11:35

clearly shows the effect of attenuation with an apparent corner frequency of 9 Hz. Making a similar test as above for the effect of Q , indicates that Q is not important due to the short hypocentral distance. We can therefore safely assume that the decay of the spectrum is due to near surface attenuation only.

The calculation of κ was now done in the 3–15 Hz range, which was selected to be lower than the expected corner frequency and also within a range of good signal to noise ratio (Fig. 8.13, left). The log smoothed spectral level is then plotted as a function of linear frequency (Fig. 8.13, right) and $\kappa = 0.037$ for S determined using

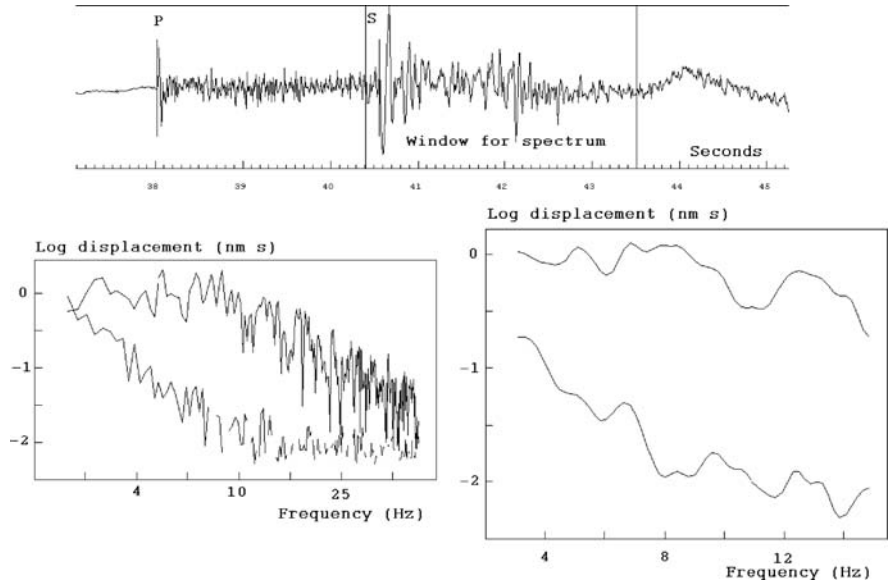


Fig. 8.13 S-spectra of a small local earthquake. The spectra are only corrected for instrument response. The *top* spectrum shows the signal and the *bottom* the noise. The *left* spectrum shows the log-log spectrum in a wide frequency range while the *right* spectrum gives the log-linear spectrum (smoothed) in a limited frequency range used for determination of κ . The station used is STOK, vertical component, origin time is 2006 1104 18:03, $M_w = 1.1$ and hypocentral distance is 21 km

(8.37). In practice, κ would be determined as an average using many events and stations. This method can be used for both P and S-waves.

The procedure to calculate κ is then:

- Select small events to get a high corner frequency.
- Select near events to be able to disregard Q , for longer distances Q must be known.
- Make the instrument corrected spectrum of P or S-waves.
- Fit a straight line to the “flat” part of the linear-log spectrum where $f < f_0$.
- Obtain the slope and calculate κ .

8.7.2 *Q* and κ from Spectral Modeling

The complete shape of the observed spectrum is proportional to

$$A(f, t) = K \frac{1}{1 + (\frac{f}{f_0})^2} e^{-\pi f \kappa} e^{\frac{-\pi f t}{Q_0 f^\alpha}} \quad (8.38)$$

where K is a constant. Given an observed spectrum, (8.38) can be modeled by trial and error, or better by automatic fitting, to determine f_0 , κ , Q_0 and α . This fitting, whether automatic or manual, will always involve trade-off between the different parameters and is best done if at least one of the parameters is known. Note that if $\alpha = 1.0$, the Q -term has no influence on the spectral shape since (8.38) becomes

$$A(f, t) + Ke^{-\pi f \kappa} e^{\frac{-\pi f t}{Q_0 f}} = A_0 e^{-\pi f \kappa} e^{\frac{-\pi f t}{Q_0}} \quad (8.39)$$

8.7.3 Coda Q

Coda waves constitute the end of the seismic signal for local and regional events (see Chapter 2). Determination of Q from coda waves is one of the most popular methods for determining Q since it only requires one station and no calibration information. Coda waves are thought to decrease in amplitude only due to attenuation (including scattering) and geometrical spreading and Aki and Chouet (1975) showed that, assuming that coda waves are single scattered S-waves, the coda amplitude decay can be expressed as

$$A(f, t) = t^{-\beta} A_0 e^{-\pi f \kappa} e^{\frac{-\pi f t}{Q(f)}} \quad (8.40)$$

where β is 1 for body waves and 0.5 for surface waves. Taking the natural logarithm, (8.40) can be written

$$\ln(A(f, t)) = \ln(A_0) - \beta \ln t - \pi f \kappa - \frac{tf\pi}{Q(f)} \text{ or} \quad (8.41)$$

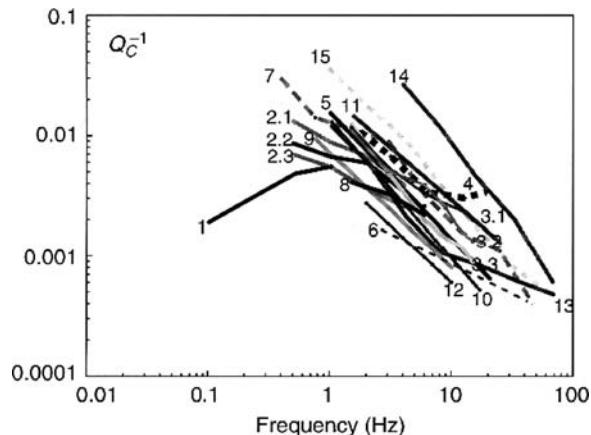
$$\ln(A(f, t)) + \beta \ln t = \ln(A_0) - \pi f \kappa - \frac{tf\pi}{Q(f)} \quad (8.42)$$

Plotting the envelope of $\ln(A(f, t)) + \beta \ln(t)$ as a function of t for a given frequency (by band pass filtering the signal), gives a straight line with slope $-\pi f/Q(f)$ and $Q(f)$ can be determined. As it can be seen, the Q -determination is not affected by κ . Q determined by the coda method is often named coda Q , Q_c and this might create the impression that it is a different kind of Q , while Q_c is Q for the wave types that coda waves are composed of, which is mostly thought to be S-waves (e.g. Sato et al., 2002; Rautian and Khalturin, 1978; Aki, 1980). See below for more discussion on this topic.

Figure 8.14 shows some typical coda Q relations from different parts of the world. It is seen that the coda Q -values are similar to Q_s (Fig. 8.1), further supporting that Q_c and Q_s are comparable, *provided the same volume is sampled*.

The figure shows that a typical Q_c at 1 Hz is 100 and at 1,000 at 10 Hz, see also Table 8.5. In practice there are several considerations to make. Rautian and Khalturin (1978) found that (8.42) only is valid for a lapse time t (time from origin time to start of coda analysis window) two times the S-travel time so it

Fig. 8.14 Coda Q for various regions. The numbers refer to different regions around the world. Details are given in Sato and Fehler (1998). Reproduced with kind permission of Springer Science and Business Media. Figure from Sato and Fehler (1998)



is important to ensure that the lapse time is long enough. Figure 8.15 shows an example.

In Fig. 8.15, the coda window is selected automatically from the origin time and the P or S arrival time and is selected at two times the S-travel time. The coda window used here is 15 s. The length will depend on the event size (smaller events must use smaller size since the end of the coda more quickly reaches the level of the noise). Using a value smaller than 10 s is not advisable since the window length

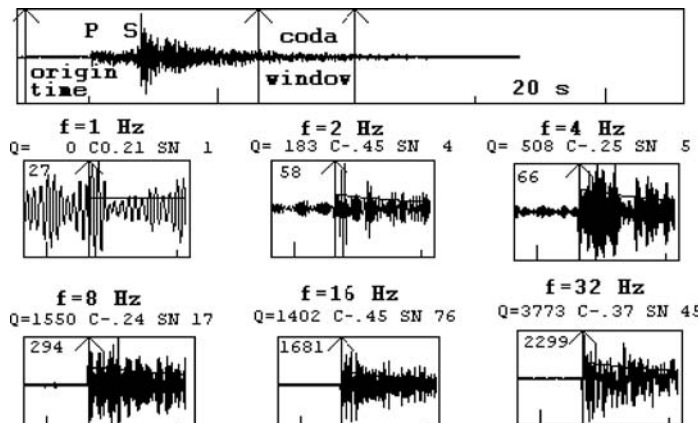


Fig. 8.15 Example of determining coda Q . The top trace shows the seismogram from a local earthquake. The first arrow shows the origin time, and the next 2 the window selected for analysis. The subsequent windows show the coda Q analysis for each frequency as indicated. For calculating Q , geometrical spreading $\beta = 1$. The abbreviations are: CO: Correlation coefficient and SN: Signal to noise ratio. Each coda analysis window show first 10 s of noise (same filter as coda signal) and 15 s filtered signal of coda window with the fitted envelope plotted. The number in the upper left hand corner is the maximum count. The data is from station TDM, Z-component in the Tanzanian network, origin time is 1992 1007 11:35, $M_L = 2.3$ and hypocentral distance 61 km

becomes too small to give a stable coda decay. 20–40 s seems to be a good size in practice. For each coda Q determination, the signals are filtered with the center frequency indicated. The bandwidth is increasing as the frequency increases to get constant relative bandwidth in order to avoid ringing. The envelope is calculated with a running RMS average in a 3 s window. The signal to noise ratio is calculated as the ratio between the filtered RMS values in the end of the coda window and in the signal before the P. For more details of the calculation method, see Havskov et al. (1989). It is seen that the signal to noise ratio and the signal level increase as the frequency goes up. This is often the case when using small earthquakes since the low frequency background noise is high compared to the signal level so it can sometimes be difficult to get reliable coda Q values for low frequencies (1–2 Hz). A signal to noise ratio of at least 3–5 should be required. For each frequency window, the correlation coefficient for the envelope is given and if the correlation coefficient is positive (envelope amplitude increases with time), Q is not calculated (as for $f = 1$ Hz). The lowest level of accepted absolute correlation coefficient should be 0.5 depending on window length. When using small windows, as in this case, it is often difficult to get a good correlation coefficient. With the values of Q obtained here, we can get the relation $Q_c = 113*f^{1.02}$, which is “reasonable relation” (see Table 8.5). In practice, Q_c would not be determined for only one earthquake and one station but rather as an average using many events for the same station to get Q_c near the station, or as a more stable estimate, an average Q_c for a group of nearby stations. This determination can also be done with one inversion of all the data, which also gives the possibility to determine β .

Coda Q is quite sensitive to choice of parameters like window length, lapse time, minimum correlation coefficient and filter width. It is therefore important when comparing coda Q result from different studies that the processing parameters are known and ideally identical. Numerous studies have shown that in particular the lapse times influences the results (e.g. Baskoutas, 1996; Hellweg et al., 1995; Kvamme and Havskov, 1989). When the lapse time increases almost all studies find increased Q and conclude that the longer lapse times means that deeper, high Q areas are sampled. This means that the differences between results as shown in Fig. 8.14 might partly be caused by using different lapse times. Note that always using a coda window start time of 2 times the S-travel time will result in different lapse times for different stations. In addition to Q varying as a function of the lapse time, it has also been observed that Q varies as a function of the window length (when lapse time is constant as measured to the center of the window) and this has been ascribed to a change in the scattering mechanism within the time window (Abubakirov and Gusev, 1990; Aki, 1991). However, it seems that this effect is most prominent for windows shorter than 30–40 s (Hellweg et al., 1995; Kvamme and Havskov, 1989). A very convincing explanation for lapse time dependence was given by Gusev (1995) who argues that the effect of scattering decreases with depth. He made a model where the contribution to scattering Q , Q_{sc} was proportional to h^{-n} where h is depth and n a constant, and got

$$Q_{sc} = 2\pi ft/n \quad (8.43)$$

where t is the lapse time. The total Q (coda Q measured) when also taking intrinsic attenuation Q_i into account is then

$$Q^{-1} = Q_{sc}^{-1} + Q_i^{-1} \quad (8.44)$$

This simple model with $n = 2$ or 3 and $Q_i = 2000$ seems to explain real observations very well, see Fig. 8.16.

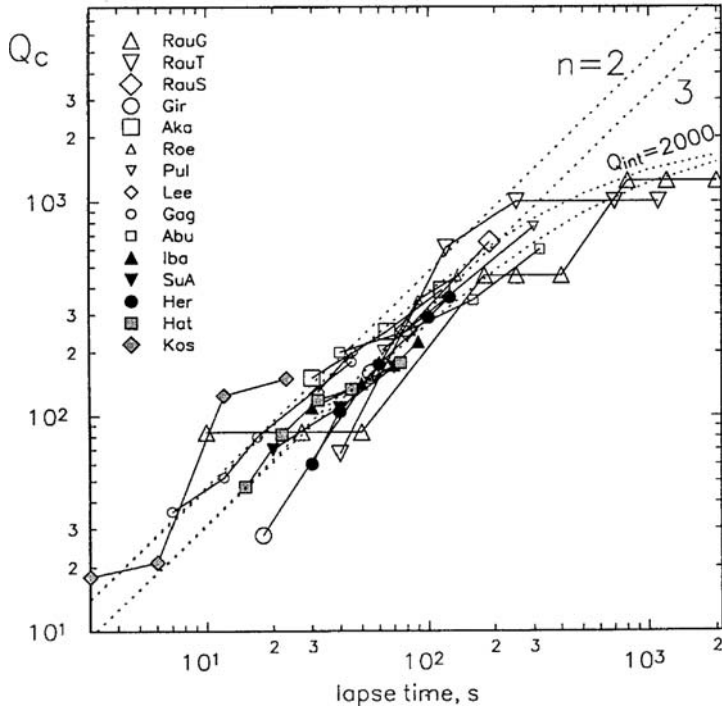


Fig. 8.16 Published observed coda Q versus lapse times for $f = 1.5$ Hz together with the predicted relationships for different n and $Q_i = 2,000$. Reproduced with kind permission of Wiley. Codes for Q-sources and figure are found in Gusev (1995), Fig. 1

Although the figure shows considerable variations, it convincingly explains the major differences in coda Q results due to lapse time. This explanation is of course the same as stating that Q increases with depth due to changes in scattering characteristics, however it also shows that this change is remarkable similar on a global scale. In the example above, we had a lapse time of 43 s and a $Q = 170$ at 1.5 Hz and this value fit within the observed results of Fig. 8.16. The scatter in the observations at particular lapse times is then probably due to real variations between different sites, which in general are smaller than the variation due to lapse time. Typical examples are volcanic areas, see Table 8.5.

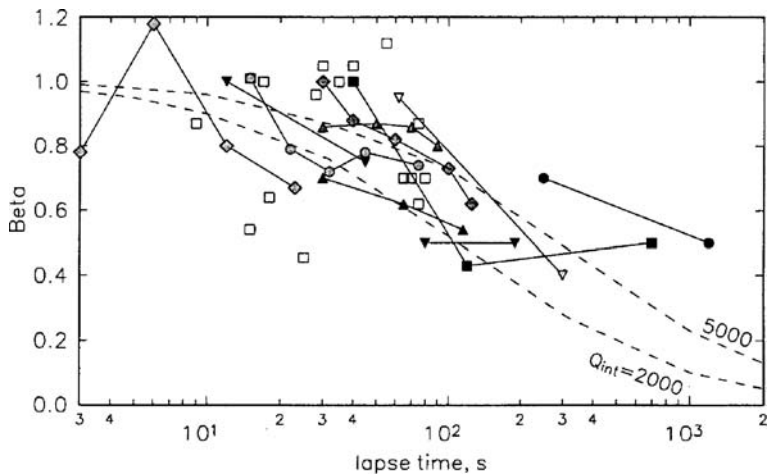


Fig. 8.17 Published observed α -values in $Q = Q_0 f^\alpha$ together with the predicted relationships for different n and Q_i (Q_{int} on figure). Reproduced with kind permission of Wiley. Figure and references from Gusev (1995), Fig. 3

Another consistent observation with coda Q is that increase in Q_0 leads to a decrease in α so attenuation at e.g. 10 Hz is less different than the Q_0 -values might indicate (Table 8.5). This trend can also partly be predicted by the Gusev model (Fig. 8.17).

The varying coda Q results raise a very important question: Which lapse time gives the correct Q to use for spectral analysis? The coda waves sample the crust within an ellipsoid with the foci at the event's hypocenter and the station. Assuming for simplicity that the hypocentral depth is 0 and the hypocenter and station are placed on the x-axis, then the surface projection of this ellipsoid is an ellipse, see Fig. 8.18

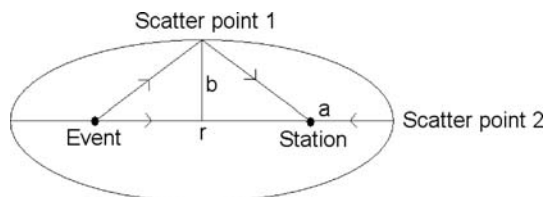


Fig. 8.18 The surface projection of the ellipsoid sampled by the coda waves. For simplicity a surface hypocenter is assumed. The station and epicenter are then in the foci. The epicentral distance is r , a and b are the ellipse major and minor axis, respectively. The two rays to scatter point 1 and 2 respectively, indicate the maximum distance the coda waves can travel in y and x directions respectively

Assuming single scattering, the maximum distance travelled from event to receiver is $v_s t$ which limits the ellipsoid volume. The major axis a can be calculated as

$$vt = r/2 + a + (a - r/2) = 2a \text{ so } a = vt/2 \quad (8.45)$$

and the minor axis b as

$$(vt/2)^2 = (r/2)^2 + b^2 \text{ so } b^2 = (vt/2)^2 - (r/2)^2 \quad (8.46)$$

and the equation for the ellipse on the surface is

$$\frac{x^2}{(v_s t/2)^2} + \frac{y^2}{(v_s t/2)^2 - (r/2)^2} = 1 \quad (8.47)$$

x and y are the surface coordinates. At $r = 0$, the depth of sampling would then be $v_s t/2$ and the volume would be a half sphere and less deep as r increases. The Q needed for spectral analysis is the Q along the path from the station to the hypocenter and that Q will depend on the hypocentral distance. For direct waves only the top part of the crust may be sampled (hypocentral depth dependent) while for larger distances (> 200 km), the whole (and particularly the deeper) crust is traversed. Coda waves and direct waves may not sample the same volume. Intuitively the lapse time should be of the same order or larger than the S-travel time used for spectral analysis in order for the two wave types to have samples the same part of the crust. This means, that for a particular area, a coda Q with a lapse time similar to the average S-travel for the events to analyze should be selected.

Summary of guidelines

- Select coda window at least at 2 times the S-travel time from the origin time and use the same lapse time, if possible, for all studies to be compared.
- Use at least 15 s coda window, use the same length window for all studies to be compared and ideally use a 30 s window.
- Use a signal to noise ratio of at least 3–5.
- Use a minimum absolute correlation coefficient of 0.4–0.6 depending on window length.
- When comparing results with different lapse times, use Fig. 8.16 to evaluate real differences.

8.7.4 Two Station Methods for Q-Determination

If seismic waves are recorded at two different stations at different distances, the difference in amplitude, at a given frequency, is due to attenuation and geometrical spreading. We can write

$$A_1(f, t_1) = t_1^{-\beta} A_0 e^{-\pi f \kappa} e^{\frac{-\pi f t_1}{Q(f)}} \quad (8.48)$$

$$A_2(f, t_2) = t_2^{-\beta} A_0 e^{-\pi f \kappa} e^{\frac{-\pi f t_2}{Q(f)}} \quad (8.49)$$

for the amplitudes recorded at station 1 and 2 respectively. If we observe the amplitudes at specific frequencies and travel times, assume a geometrical spreading, assume that κ is constant, chose the two stations along a great circle path to avoid the effect of radiation pattern, then the amplitude ratio at a given frequency at the two stations can be used to calculate $Q(f)$.

$$\frac{A_2(f, t_2)}{A_1(f, t_1)} = \left(\frac{t_2}{t_1} \right)^{-\beta} e^{\frac{-\pi f(t_2 - t_1)}{Q(f)}} \quad (8.50)$$

As it can be seen, $Q(f)$ is the only unknown in (8.50) and can be determined as

$$Q(f) = \frac{-\pi f(t_2 - t_1)}{\ln(A_2(f, t_2)/A_1(f, t_1)) + \beta \ln(t_2/t_1)} \quad (8.51)$$

This method is critically dependent on the absolute amplitudes so, if instrument response is not the same at both stations, the amplitudes must be corrected for instrument response. Soil amplification can also seriously affect the results for individual values of $Q(f)$ if they are not the same at both sites which is unlikely to be the case at all frequencies (see Section 8.6) so in general the spectra are smoothed before calculating Q . Figure 8.19 shows an example of calculating Q by spectral ratio using the data from the same area as for the coda Q calculation. It is seen that the variation of Q as a function of frequency is unstable, as discussed above, and for S it looks like Q it is almost constant. Note also that Q for P and S are very similar. Comparing this

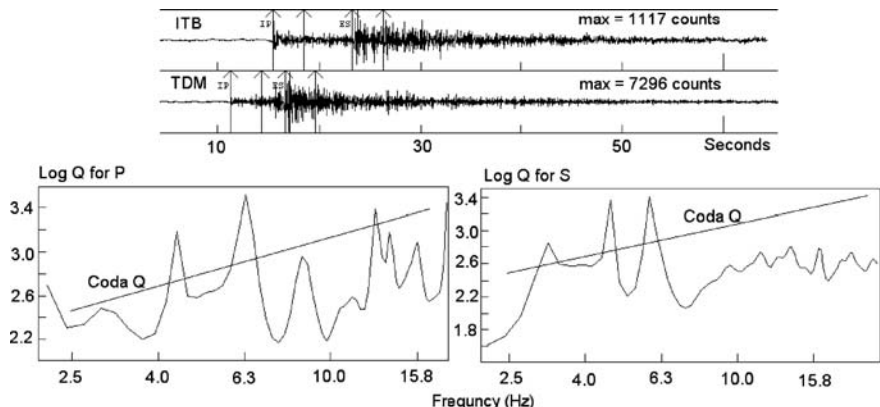


Fig. 8.19 Calculation of Q using relative spectrum. On top is shown the two stations used and the time windows (4 s) selected. Bottom left shows Q_P as a function of frequency and bottom right Q_S . The line on the Q_S figure shows Q_c as determined above. The lapse time to the start of the P and S-window is 13 and 20 s respectively. The data is from station ITB and PDH, Z-components in the Tanzanian network, origin time is 1992 1109 05:07, $M_L = 1.9$

to the results from the coda Q calculation, it is seen that the coda Q is slightly higher than Q_s determined by the spectral ratio and it is also more frequency dependent than Q_s . The spectral ratio method has many uncertain variables. It is assumed that we are only looking at one phase like Sg but the analysis might be done on a mixture of phases, or worse, the near station might have Pg while the far station has Pn and the travel paths would be different. The geometrical spreading is, in the above case assumed to be $1/r$ but could be different and even frequency dependent. We have also assumed that the radiation pattern is the same at the two stations which certainly is not the case. Thus in order to get reliable results, the analysis should be carried out using many events, stations and distances to average out some of the variation in the parameters.

It is seen that the spectral ratio and the coda Q methods give similar results. The lapse time for the S-window for the spectral ratio method is 20 s, while the coda Q lapse time was 40 s so the coda Q might sample a slightly deeper volume with corresponding higher Q , which also seem to be indicated from Fig. 8.19. In principle the spectral ratio method gives a Q -value using the same waves as used for spectral analysis and should therefore be used for correction. However, it is often easier to obtain stable results determining Q_c in which case one has to be careful with respect to processing parameters.

If Q is assumed independent of frequency, the ratio of A_2 and A_1 (8.50) can be written

$$\frac{A_2(f, t_2)}{A_1(f, t_{21})} = \left(\frac{t_2}{t_1}\right)^{-\beta} e^{-\frac{\pi f(t_2 - t_1)}{Q}} \quad (8.52)$$

and taking the natural logarithm gives

$$\ln\left(\frac{A_2(f, t_2)}{A_1(f, t_1)}\right) = \beta \ln\left(\frac{t_2}{t_1}\right) - \frac{\pi f(t_2 - t_1)}{Q} \quad (8.53)$$

In this case, the spectral ratio is linearly related to the frequency so Q can be determined from the slope of the curve $\ln(A_2/A_1)$ versus f . This can often be a good method to get a stable first estimate of Q , see exercise 3 for an example.

If κ is not constant, the spectra will have to be corrected for κ before analysis or κ will have to be determined in a multiple station-event inversion, see below. Note that we still assume that all site dependent effects are included in κ .

Summary of guidelines for calculation Q from relative spectra

- Select two stations as far apart as possible under the condition that the phase type is the same.
- Use a time window covering the major energy in the phases, typically less than 10 s.
- If possible, select two stations which are lined up with the event.
- Calculate constant Q to get a stable average value for comparison.

8.7.5 Multiple Station Method for Q -Determination

As a further development compared to the two-station method, we will now look at how Q can be determined with multiple stations. It is assumed, that we have k events recorded at i stations. Using the two-station method there was not enough information to determine local amplification and κ was assumed constant. With many stations and events, a site amplification term (correction to the amplitude, $L_i(f)$ at station i) is normally included. Using equation (8.48), including the site term and ignoring κ (would trade off with the site term) we get

$$\ln(A_{ki}(f, t_{ki})) = \ln(A_{0k}(f)) - \beta \ln t_{ki} + \ln L_i(f) - \frac{t_{ki} f \pi}{Q(f)} \quad (8.54)$$

where $A_{ki}(f, t)$ is the spectral amplitude of a particular phase at observation time t_{ki} . For a given frequency, there will be one equation for each station-event pair. The unknowns are k source terms $A_{0k}(f)$, i site terms $L(f)$ and $Q(f)$. This set of linear equations can be solved with standard methods and in addition to $Q(f)$, also the site terms are determined. The geometrical spreading term might have to be replaced

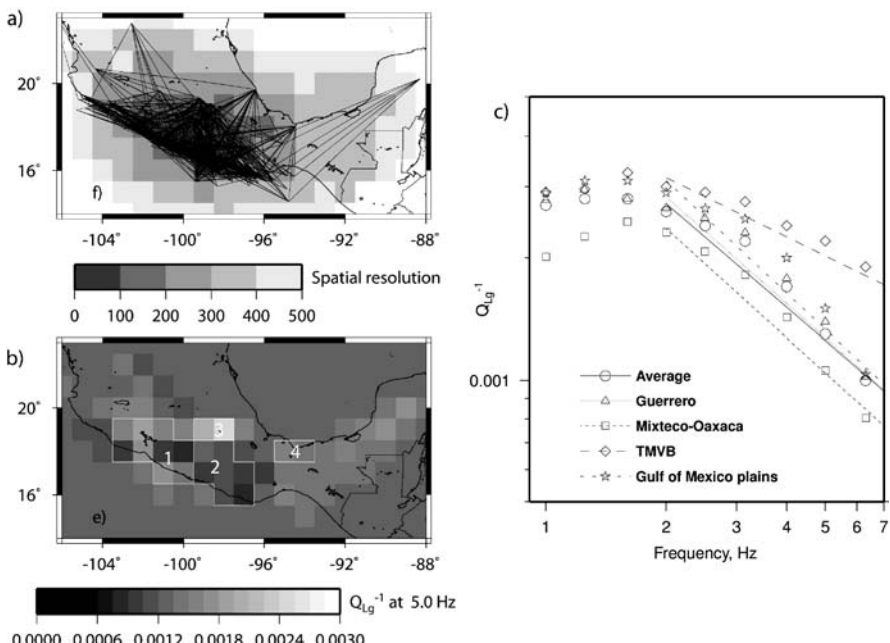


Fig. 8.20 Results from tomographic inversion for Q of Lg waves in Mexico: **a)** spatial resolution, **b)** lateral variation in Q_{Lg}^{-1} and **c)** Q_{Lg}^{-1} as function of frequency for a number of regions. Copyright 1998 American Geophysical Union. Reproduced by permission of American Geophysical Union. Figure is from Ottemöller et al., 2002. Processing is done with SEISAN program qlg

by a more detailed term or it can be assumed constant and determined during the inversion. However, this does not change the set up and solution to the equations.

The inversion for Q can be done for the common wave types P, S and Lg. The first step usually is to invert for an average Q for the whole or parts of the data set (e.g., Benz et al., 1997; Sereno et al., 1988). Often, attenuation is not constant throughout a region and determination of the variation can be used to map changes in rock properties. The changes in Q are typically resolved by formulating equation (8.54) as a tomographic problem (e.g., Menke, 1989; Tarantola, 2005). This has been done for P and S wave Q inversion by adopting an algorithm used for travel time tomography (Haberland and Rietbrock, 2001). When inverting for Q of Lg waves, the problem can be solved using a two-dimensional grid as Lg waves consist of multiple S wave reflections (e.g., Baumont et al., 1999; Phillips et al., 2000; Ottemöller et al., 2002). It is generally assumed that the attenuation of Lg waves is the same as the crustal average attenuation of S waves and Q_{Lg} can be used to correct S wave spectra at shorter distances. An example of inversion for the frequency dependence of Q and its lateral variation for Mexico is given in Fig. 8.20.

The following Table 8.5 gives Q -values for different regions of the world using different methods.

Table 8.5 Q from different regions. For some regions, several Q -values have been given and one considered typical has been selected. Abbreviations are Mult: Multiple stations method, Oth: Other method and Coda: Coda decay method

Region	Phase or average lapse time (s)	Q_0	α	Q at 10 Hz	Method	References
Eastern Canada	Pn	189	0.87	1401	Mult.	Zhu et al. (1991)
SE Australia	Pn	4571		1111	oth	Allan et al. (2007)
Mexico	Lg	204	0.85	1444	Mult.	Ottemöller et al. (2002)
Central Europe	S	400	0.42	1052	Mult.	Malagnini et al. (2000)
Northern Iran	S	87	1.46	2509	Oth	Motazedian (2006)
North Anatolian Fault, Turkey	S	40	0.45	112	Mult	Akinci et al. (2001)
Norway	S	470	0.70	2350	Mult.	Kvamme et al. (1995)
Deception Island volcanic area	4	58	0.40	146	Coda	Havskov et al. (2002)
State of Washington	20	63	0.97	588	Coda	Havskov et al. (1989)
Mount St Helens volcanic area	10	54	0.39		Coda	Havskov et al. (1989)
South-West Cameroon	40	65	1.0	650	Coda	Ambeh and Fairhead (1989)
Himalaya, India	30–60	126	0.95	1122	Coda	Gupta et al. (1996)
Southern India	80	535	0.59	2091	Coda	Kumar et al. (2007)

8.8 Soil Amplification

Under the discussion on calculation of seismic moment, the effect of the free surface was simplified to a constant amplification factor of 2.0. In addition to the free surface effect, a further increase in amplitudes measured on the surface will be observed at sites with low density/velocity surface layers due to the simple fact of energy conservation: A lower density requires a higher particle velocity to conserve the energy. The amplification factor can easily be up to a factor 10. It is frequency dependent and knowledge of soil amplification is of critical importance for seismic engineering as well as interpreting seismological results. A large amplification at a particular site means that the danger to buildings, in case of an earthquake, could increase dramatically and there are examples of identical buildings, one on soil and another on bedrock, where only the building on soil collapsed. There is therefore a large interest in calculating soil amplification and it has become a science in itself with many specialized methods, see e.g. Kudo (1995). The most popular methods are based on calculating spectral ratios and we essentially talk about 2 methods:

Amplification relative to a reference station: If we assume that the frequency dependent soil amplification $S(f)$ is identical to (8.50), we get

$$S(f) = \frac{A_2(f, t_2)}{A_1(f, t_1)} = \left(\frac{t_2}{t_1} \right)^{-\beta} e^{-\frac{\pi f(t_2-t_1)}{Q(f)}} \quad (8.55)$$

If station 1 is a reference station on hard rock and station 2 is on soft soil, β , t and $Q(f)$ are known parameters and station 1 and 2 are on line with the hypocenter (disregarding source effects), then $S(f)$ will give us the frequency dependent soil amplification at site 2 relative to site 1. Since it is assumed that there is no amplification at site 1, we in fact get the absolute amplification. This method has been used mainly with strong motion data in the near field and critically depends on having correct Q and geometrical spreading.

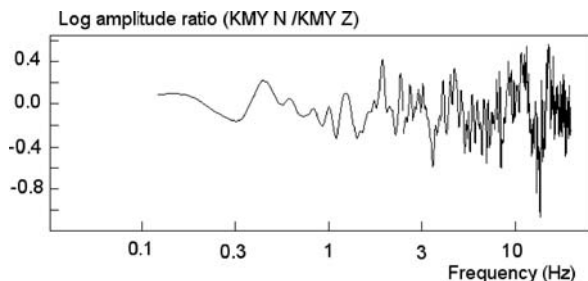
Since soil amplification is primarily affecting the horizontal motion, Nakamura (1989) developed an alternative method to determine soil amplification, the so-called Nakamura method. The method makes the spectral ratio of the horizontal channel over the vertical channel for the same station:

$$S(f) = \frac{A_H(f)}{A_Z(f)} \quad (8.56)$$

and the data used is either from an earthquake or natural background noise. This method has become extremely popular and a large number of publications and results are available and several specialized programs using the Nakamura technique are available (SESAME, 2004). See also Bard (1998), Lachette and Bard (1994), and Atakan et al. (2004a, b). However all programs essentially use (8.56) and have various options for smoothing the spectra and averaging the two horizontal components. Usually $S(f)$ is calculated using the average $S(f)$ for many time windows. In

addition to being used for seismic engineering, it can also be useful for the seismologist to investigate a particular site for abnormal amplification, which might explain unusual large amplitudes, particularly on the horizontal components. Figure 8.21 shows an example.

Fig. 8.21 Relative spectrum of noise for station KMY.
Made with SEISAN

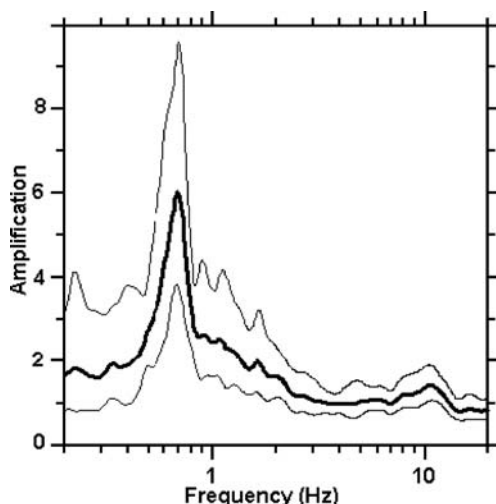


The figure shows relative spectra on a hard rock site in Norway (station KMY). It is seen that there is no overall amplification although there is some fluctuations. The average amplitude in the relative spectrum is 1.004 ± 0.6 . Figure 8.22 shows the relative spectrum made for a typical alluvial site.

At this site there is a clear fundamental frequency at 0.7 Hz where significant amplification occurs.

By comparing the Nakamura method to calculations based on known soil structure, it has been shown that the Nakamura method does not give the exact amplification but is quite good at detecting the frequencies at which amplification occur (SESAME, 2004).

Fig. 8.22 Relative spectrum made by the SESAME program from a sedimentary basin. The thick curve shows the average of many relative spectra and the thin curves the standard deviation. Basin geometry: Elongated alluvial valley, width~5 km, length~40 km, depth~200 m. Site Information: depth to bedrock: 196 m. Type of bedrock: Gneiss. Average shear wave velocity of deposits: 570 m/s. The Figure is modified from SESAME (2004)

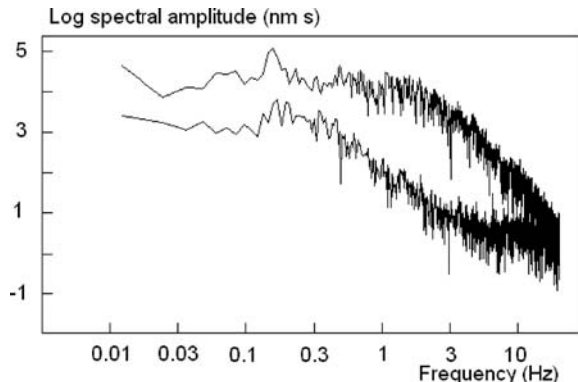


8.9 Exercises

Exercise 8.1 Spectral analysis of a local earthquake

Figure 8.23 shows an S-wave spectrum of a local earthquake recorded by the Andalucian network in S. Spain. The spectrum has been corrected for a $Q = 100 f^{0.7}$ and no correction has been made for near surface attenuation.

Fig. 8.23 S-wave spectrum for station VELZ from the Andalucian network, vertical component. The *top* curve shows the signal spectrum and the *bottom* curve the noise spectrum. The origin time is 2005 0702 12:58, the hypocentral distance is 239 km and the hypocentral depth is fixed to 10 km. PDE reports a magnitude $m_b = 4.3$



- From the spectrum determine the spectral flat level and the corner frequency.
- Calculate the geometrical spreading factor assuming a simple $1/r$ spreading and alternatively using the Herrmann-Kijko relation with $\Delta_x = 100$ km, see (8.19).
- Calculate the seismic moment, moment magnitude and stress drop for both types of geometrical spreading and compare the results.
- The spectrum has not been corrected for near surface attenuation. If we assume a value of $\kappa = 0.03$, how much will that change the moment?
- Determine the slope of the spectral decay above the corner frequency. It is supposed to be -2 . If it is not -2 , what does it tell us about the Q correction?

Exercise 8.2 Teleseismic spectral analysis

Figure 8.24 shows the P-phases from 2 stations and corresponding spectra for the largest earthquake occurring in Africa (Mozambique) in this century ($M_w = 7.0$). The spectra are shown for both a broadband station and a short period station and the aim of the exercise is to calculate spectral parameters from both stations and evaluate if an SP station can be used.

- Read spectral level and corner frequencies for the two spectra. Is the corner frequency “reasonable”, compare to what is expected for an earthquake of this size, see Table 8.1?
- Calculate the geometrical spreading factor using (8.26).

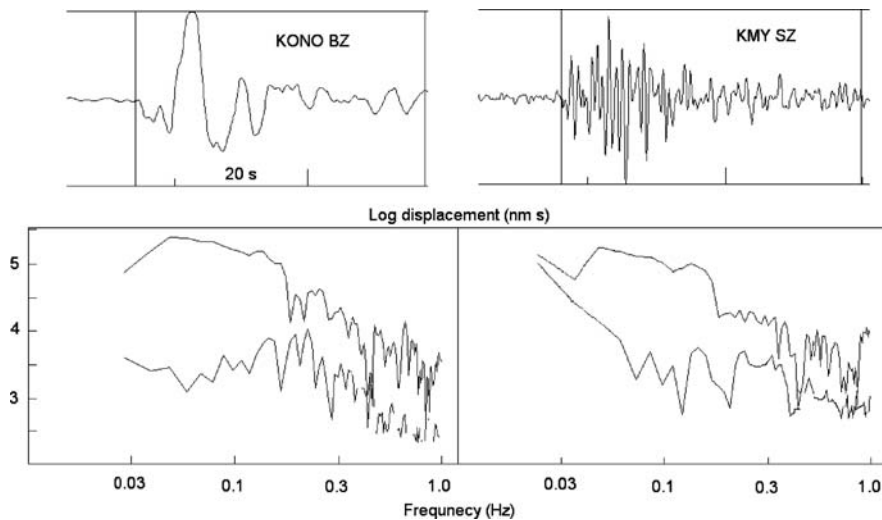


Fig. 8.24 P-phase from a teleseismic earthquake for two stations (*TOP*) in the Norwegian network. On the *bottom* is shown the corresponding spectra corrected for a $t^* = 1$. The *lower* spectra are the noise spectra. The origin time is 2006 0222 22:19. The epicentral distances are KMY: 83° and KONO: 82° . The magnitude is $M_w = 7.0$ (PDE)

- Calculate seismic moment, moment magnitude and stress drop. Does stress drop look “reasonable”?
- Compare the values for the 2 stations and evaluate the usefulness of using SP data.
- Read the period of the P-pulse on station KONO. Can that period be related to the corner frequency?

Exercise 8.3 Determine Q

Figure 8.25 shows the relative spectrum of the S-waves from 2 stations. From the figure it is clearly seen how the high frequency energy decreases at the far station (PDH) as the frequency increases (relative spectrum increases with frequency). The spectra have been checked for acceptable signal to noise ratio and the relative spectrum is smoothed.

It is seen that the relative spectrum is not quite a linear function of frequency but a linear approximation can be made, which indicates that a constant Q will give a good approximation to the attenuation in the area.

- Approximate the relative spectrum with a line and determine the slope, note that the y-axis is logarithmic to base 10.
- Use equation (8.53) to calculate a constant Q . The travel time difference between the two stations can be obtained from Fig. 8.25.
- If Q increases with frequency, how can the relative spectrum be expected to look?
- Estimate Q for the frequency band 5–15 Hz and 20–30 Hz.

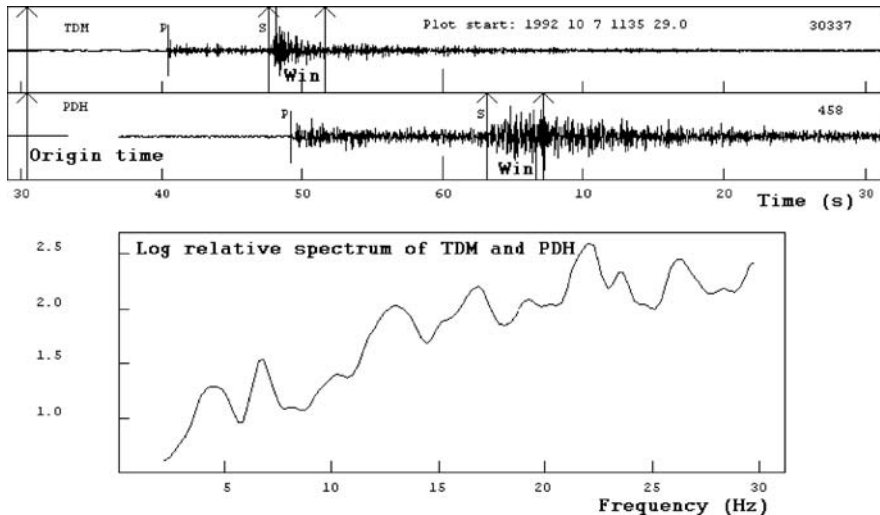


Fig. 8.25 Relative spectrum of the S-waves for two stations in the Tanzanian network. The *top* trace shows the near station and the *bottom* trace the far station and the origin time is indicated to the *left*. The number in *upper right hand corner* is the maximum amplitude in count. The *bottom* figure shows the relative spectrum

Computer exercises

- P and S spectra of local earthquakes.
- Acceleration spectra to check Q .
- P and S spectra of distant earthquakes.
- Compare spectra of local and distant stations.
- Effect of Q and kappa.
- Determine Q with various methods.
- Determine κ .
- Soil amplification.

Chapter 9

Array Processing

A seismic array consists of multiple sensors in a small enough area that signals are correlated and the seismic array is therefore also sometimes called a seismic antenna. The following general description largely follows Havskov and Alguacil (2006) and NMSOP.

The main advantages of using a seismic array instead of a single station are:

- Provide estimates of the station-to-event azimuth (back azimuth), and of the apparent velocity of different types of signals. These estimates are important both for event location purposes and for classification of signals, e.g., P, S, local, regional, or teleseismic.
- Improving the signal-to-noise ratio and detecting events otherwise masked by the background noise (e.g. Frankel, 1994).
- Location of seismic phases with onsets not well defined or the tracking of sources of almost-continuous signals such as a volcanic tremor (e.g. Almendros et al., 1997). This is not possible with conventional network methods.

Arrays can be divided into large fixed facilities, like the NORSAR arrays in Norway (NMSOP, Bungum et al., 1971; Bungum and Husebye, 1974), which are part of the International Monitoring System (IMS) with the purpose to monitor the Comprehensive Nuclear Test Ban Treaty (CTBT) for nuclear tests (see e.g. NMSOP and Dahlman et al., 2009). These facilities have their own software not generally available and it will not be described here. Many other arrays are used for research purposes and they vary in size from a couple of km's to a few hundred meters depending on the purpose and the available resources.

9.1 Basic Array Parameters

We will first look at some basic parameters for arrays. Figure 9.2 shows nine stations that are deployed in a rectangular array. Station s7 will record the wave arrival first, then s4, s8, s1, s5, s9 and so on. If the structure under the array stations is homogeneous, the waveforms recorded on all stations will be almost identical, except for a time delay and the added local noise. The waveform is moving horizontally across

the array with an apparent velocity v . We call this *apparent velocity* since it is what the velocity appears to be in the horizontal plane. The apparent velocity (do not confuse with the horizontal component of velocity!) is related to the true velocity c in the medium as

$$v = c/\sin(i) \quad (9.1)$$

where i is the angle of incidence as measured from the vertical direction. If e.g. the ray comes up vertically, the wavefront arrives at the same time at all stations and the apparent velocity appears to be infinite. This is also what we get from (9.1) since the angle of incidence is then 0° . A vector \mathbf{s} with the ray direction and with magnitude $1/c$ is called *slowness* (Fig. 9.1). Similar to apparent velocity, we define the *apparent or horizontal slowness* (the horizontal component of slowness) as

$$p = 1/v = \sin(i)/c \quad (9.2)$$

We can also define a horizontal vector \mathbf{p} with magnitude p (Fig. 9.2) as the horizontal projection of \mathbf{s} . If we assume that the arrival time to station S7 is $t=0$ and the coordinate system origin is also at S7, we can calculate the arrival time to the other stations knowing v and the azimuth α .

This is most simply done using the horizontal slowness vector \mathbf{p} . If the vector from S7 to S8 is called \mathbf{r} , then the travel time difference τ , between S7 and S8 is

$$\tau = \mathbf{p} \cdot \mathbf{r} = r \cos(\theta)/v \quad (9.3)$$

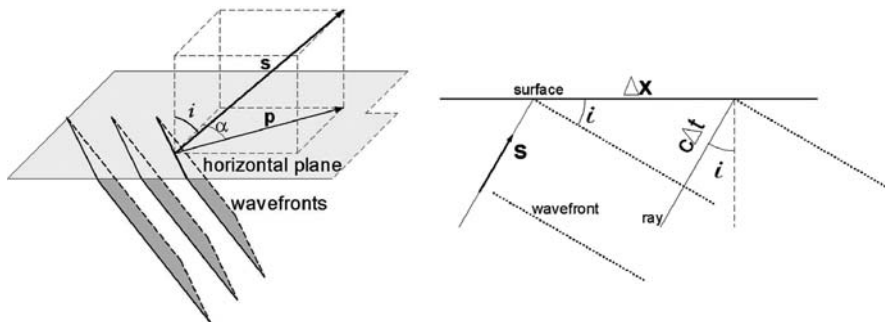


Fig. 9.1 Slowness definition. *Left:* Vector \mathbf{s} is normal to the plane wavefront and its angle with the vertical is the incidence angle i . The horizontal projection of \mathbf{s} is \mathbf{p} , the horizontal slowness, whose angle with the north direction is the ray azimuth α . *Right:* A projection on the incidence vertical plane. As the wavefront advances a distance $c\Delta t$, the intersection with the horizontal plane advances Δx , with apparent velocity v . Relation (9.1) between v and c can be seen from the geometry in the figure. Reproduced with kind permission of Springer Science and Business Media. Figure from Havskov and Alguacil (2006), Fig. 9.2

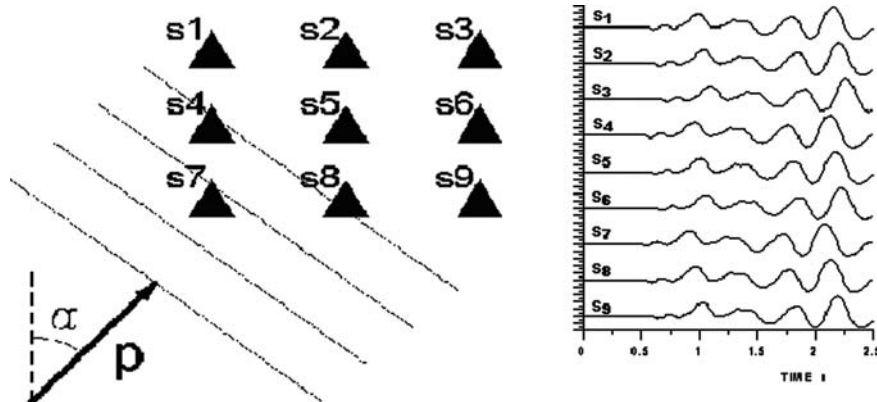


Fig. 9.2 *Left:* A plane wavefront arrives with apparent slowness \mathbf{p} to a rectangular shaped array (the intersection of the wavefront with the surface, where the array is installed, is shown). The angle α with respect to north defines the ray arrival azimuth. *Right:* The waveforms recorded are ideally identical, except for the relative delays. In practice, they present differences due to the added noise and to the local ground heterogeneity. Reproduced with kind permission of Springer Science and Business Media. Figure from Havskov and Alguacil (2006), Fig. 9.3

where θ is the angle between the vectors \mathbf{p} and \mathbf{r} . (9.3) contains two unknowns, θ and v , so two equations and 3 stations are needed to determine azimuth and apparent velocity. This means that an array must have at least 3 stations.

Equation (9.3) can be generalized to any pair of stations using an arbitrary origin for the coordinate system. This gives the time delay at any station with position vector \mathbf{r}_i and apparent slowness \mathbf{p} . Let $\tau_{ij} = t_j - t_i$ be the delay of the arrival at station j relative to station i . Then

$$\tau_{ij} = \mathbf{p} \cdot (\mathbf{r}_j - \mathbf{r}_i) \quad (9.4)$$

That is, if the horizontal coordinates of each station j are (x_j, y_j) with respect to the origin (normally one of the stations or the array center)

$$\begin{aligned} \tau_{ij} &= p_x (x_j - x_i) + p_y (y_j - y_i) \\ \text{with } p_x &= p \cdot \sin(\alpha) \\ \text{and } p_y &= p \cdot \cos(\alpha) \end{aligned} \quad (9.5)$$

If the array stations are not situated on a plane, their height has to be included in the equations, e.g. by using the 3D slowness vector \mathbf{s} instead of the 2D slowness vector \mathbf{p} . If the event is not far from the array, corrections might also have to be applied to account for the non linear wavefront, see NMSOP for more details. In the following, we will assume (9.5) to be correct.

9.1.1 Example of Calculating p from a Three Station Array

In its simplest form, a seismic array consists of 3 stations (Fig. 9.3). Considering a plane wave arriving at the 3 stations at times t_0 , t_1 and t_2 respectively, then, following (9.5), will give

$$\tau_{10} = x_1 \cdot p_x + y_1 \cdot p_y \quad (9.6)$$

$$\tau_{20} = x_2 \cdot p_x + y_2 \cdot p_y$$

where $\tau_{10} = t_1 - t_0$ and $\tau_{20} = t_2 - t_0$. Thus knowing the arrival times at the 3 stations, p_x and p_y can be determined (2 equations with 2 unknowns). From p_x and p_y , v and azimuth can be determined:

$$\tan(\alpha) = p_x/p_y \quad (9.7)$$

$$v = \sqrt{1/(p_x^2 + p_y^2)} \quad (9.8)$$

Note that the azimuth above is away from the event, while the direction (back azimuth) needed to find the epicenter is from the station to the event and 180° must be added to the azimuth. For local earthquakes, the distance to the event can be found from the S-P time, while for distant earthquakes, the distance can also be determined from the apparent velocity (see Fig. 9.11). Given the epicentral distance, a location can be made.

This simple example illustrates the principle behind determining the apparent velocity and direction to an earthquake using a 3 station array. So why use more

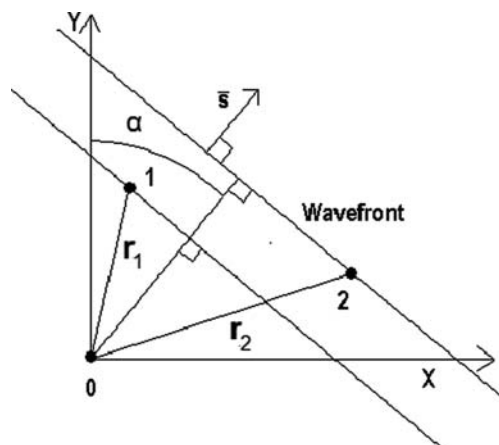


Fig. 9.3 A 3 station array. The stations are labeled 0,1,2 and station 0 is placed at the origin of the coordinate system. The vectors from the origin to station 1 and 2 are labeled $r_1(x_1,y_1)$ and $r_2(x_2,y_2)$ respectively and α is the azimuth of arrival

stations in the array? As we shall see below, the array is also used to determine weak signals in the presence of noise and in that case more sensors are needed. In addition, any small error in the arrival times for the 3 stations (reading errors, uncertain arrivals or time delays caused by local inhomogeneities) could affect the solution for small arrays. By having more stations, \mathbf{p} can still be determined using equations of type (9.6), however the equations must be solved by the least squares method. Generalizing (9.6) we can write

$$\tau_i = x_i \cdot p_x + y_i \cdot p_y \quad (9.9)$$

Rewriting gives

$$(\tau_i/x_i) = p_x + (y_i/x_i) \cdot p_y \quad (9.10)$$

so plotting (τ_i/x_i) versus (y_i/x_i) gives a straight line with slope p_y and intercept p_x .

9.1.2 Using a Seismic Network as an Array

A local or regional network can be used as an array in a similar way. This can be useful for an independent check of the consistency of the P-readings as well as actually determining the back azimuth and apparent velocity for earthquake location. In principle, S-readings can also be used, but since S-arrivals are much more uncertain than P-arrivals, it is less certain to use S. Relation (9.6) assumes a flat earth which is a reasonably good assumption up to a few hundred kilometers distance and, disregarding ellipticity, x_i and y_i (in km) can be calculated as

$$x_i = 111.2 \cdot (\lambda_i - \lambda_0) \cdot \cos(\theta_0) \quad (9.11)$$

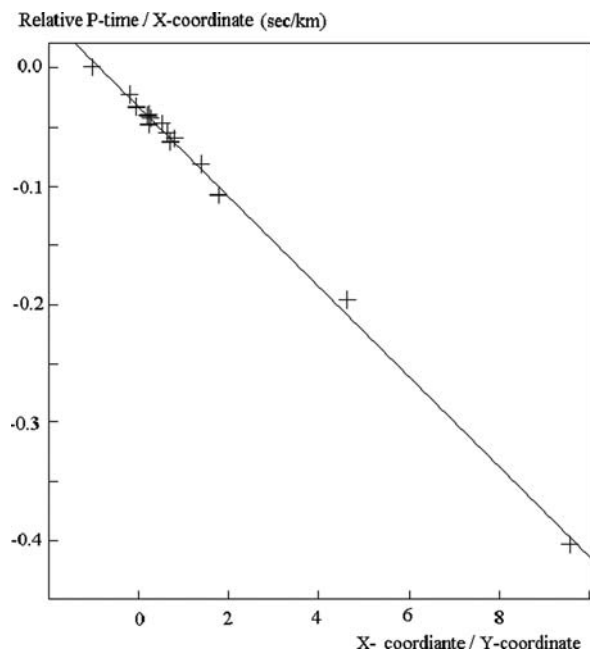
$$y_i = 111.2 \cdot (\theta_i - \theta_0) \quad (9.12)$$

where θ and λ are station latitude and longitude in degrees, respectively. The index zero refers to the reference station. Figure 9.4 gives an example

The NORSAR array determined back azimuth and apparent velocity for this event to 42° and 21 km/s while the plane wave solution gave 41° and 20 km/s respectively. The plane wave solution is thus almost identical to the array solution and could probably be improved by correlating the P-arrival waveforms in order to get more reliable relative arrival times (Chapter 4).

In practice, for small arrays, reading individual arrival times in order to determine α is not as accurate as signal processing methods where correlation between traces is done, see below.

Fig. 9.4 Fit of a plane wave to the routinely determined P-arrival times for stations in S. Norway. The reference station is NORSAR array station NB2 and the remaining stations are within 400 km of NB2. The event origin time is 2007 0308 05:03 and it is located at a distance of 80° from NB2. The magnitude m_b was 5.9 as determined by PDE



Details of array design is outside the scope of this book. More information can be fund in Havskov and Alguacil (2006) and NMSOP. Some basic principles for array design are:

- More sensors give an improved noise suppression.
- The size of the array must be as large as possible while maintaining signal coherence.
- Aliasing can occur in both time and space so the design must consider the dominant phases that should be detected. In general small arrays (hundreds of meters) with high sample rate can be used for local and regional studies while large arrays (1–100 km) are useful for teleseismic studies.

9.2 Beam Forming

The signal to noise ratio of a seismic signal can be improved by summing the signals of each station in the array using a delay as calculated by (9.6) for a given slowness vector. In this way the coherent seismic signal will be enhanced and the supposedly incoherent noise will cancel out. An N element seismic array with normal distributed noise amplitude will theoretically reduce the noise by a factor \sqrt{N} (NMSOP). Figure 9.5 shows an example.

Beam forming can thus be used to detect signals that otherwise would not have been detected on a single station. However, in the example above the trace delays

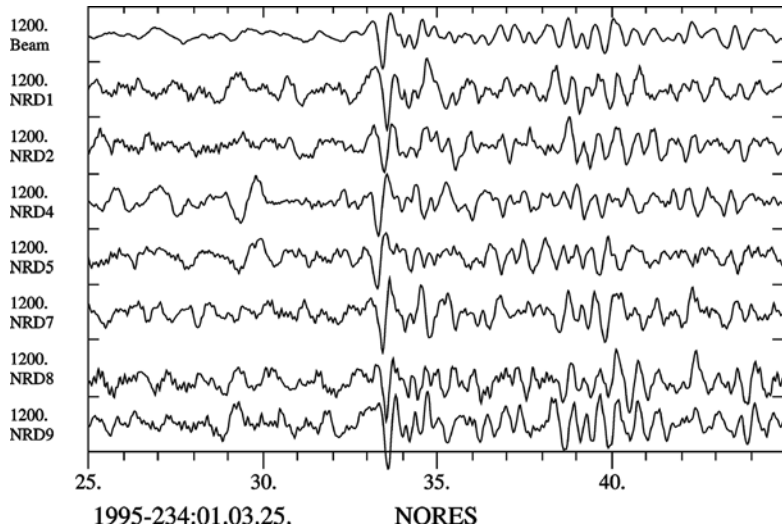


Fig. 9.5 Some NORES channels from an event in Greece. The beam is the *top* trace. All traces have equal amplitude scale. Copyright granted by IASPEI. From NMSOP, Fig. 9.13

were calculated from the known apparent slowness p . If we do not see the signal, how is it possible to use the correct p ? This brings us into how to process data from seismic arrays and intuitively the simplest way is to use beam forming. By taking a time window of the signal and summing the signals for all stations at all possible values of p , the power in the signal can be calculated and plotted as a function of p . In practice the apparent slowness is used. The beam forming is always done in a frequency band in order to obtain the best correlation. Figure 9.6 shows an example of beam forming.

9.3 Frequency – Wavenumber Analysis (fk)

Since the beam forming is always done in a frequency band, the result could also be expressed as a function of the apparent wavenumber $k = \omega p$ where ω is the center frequency of the filter. Thus by making a three-dimensional spectral analysis (time and 2D space), the power as a function of frequency and wavenumber $P(k,f)$, can be obtained as the Fourier transform of the autocorrelation function $\langle u(\mathbf{r},t) u(\mathbf{r} + \mathbf{r}',t + t') \rangle$

$$P(k,f) = \int \int \int \langle u(r,t) u(r + r',t + t') \rangle e^{-i(\pi kr' + 2\pi ft')} dr' dt' \quad (9.13)$$

where $u(\mathbf{r},t)$ is the amplitude as a function of location vector \mathbf{r} and time t . This is equivalent to beam forming in time domain considering that a time shift in time domain is equivalent to a phase shift in frequency domain. The output is similar to

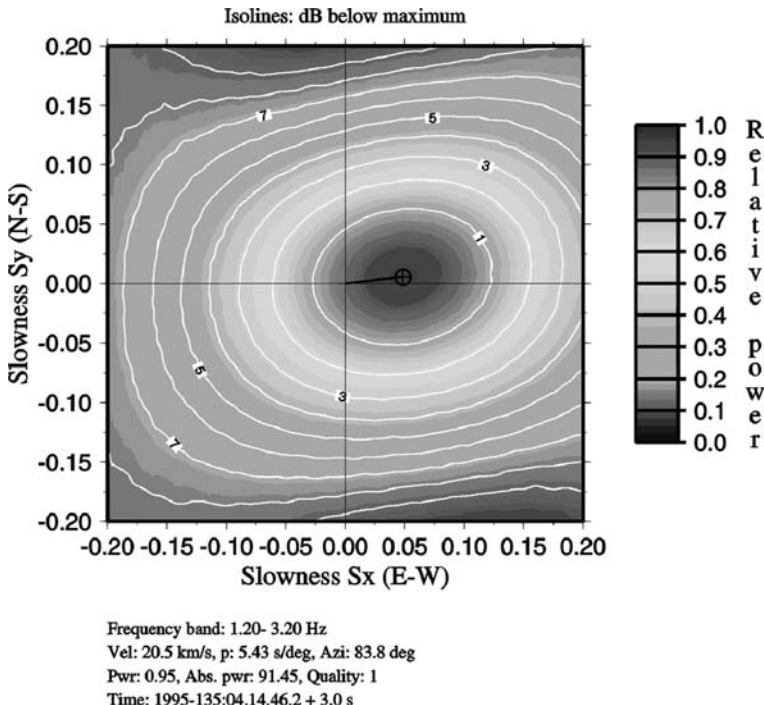


Fig. 9.6 Result from beam forming in the time domain (also called beam packing) of the NORES data in Fig. 9.5 in an equi-spaced slowness grid. The data were pre-filtered in the band 1.2–3.2 Hz. The isolines represent power of each beam within the 3-s window analyzed. Copyright granted by IASPEI. (Figure from NMSOP, Fig. 9.24)

the output of beam forming. For more details see e.g. Lacoss et al. (1969), Capon (1969), Harjes and Henger (1973) and Aki and Richards (2002).

9.4 Array Response

The beam forming assumes that the noise cancels out and the signal is enhanced by being in phase at the different sensors due to the delay. From Fig. 9.6 it is also seen that, within the slowness space searched, there is only one point where all signals are in phase. However, looking at Fig. 9.2, it is clear, that, due to the equal spacing of the sensors, we can imagine that with a near monochromatic input, for several different values of p , the signals are in phase and therefore several peaks in the slowness diagram will appear, see Fig. 9.7 bottom part. This is the result of spatial aliasing, which is particularly bad for regular spaced arrays, but something which must be taken into account with array analysis. It is therefore interesting to characterize the array ability for discriminating the true slowness among all the possible ones. This

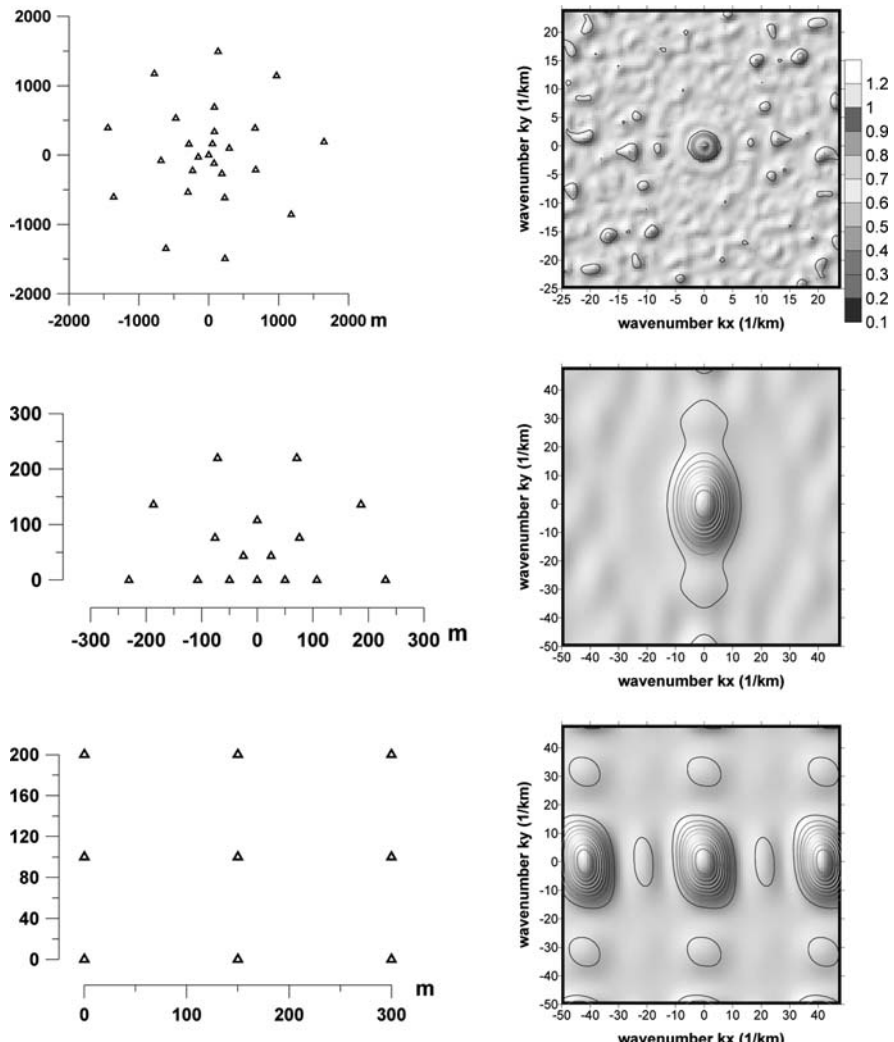


Fig. 9.7 Different examples of small aperture array shapes and their transfer functions. *Top*, the array ARCES with 25 stations and a diameter of 3 km, has a sharp almost ideal response. Next, there is a semicircular array, a rectangular one with a response showing spatial aliasing (ghost peaks). Reproduced with kind permission of Springer Science and Business Media. Figure from Havskov and Alguacil (2006), Fig. 9.5

can be calculated by inputting a signal that consists of a unit impulse approaching with true slowness p_t and the output of the beam forming using this signal can then be calculated (Havskov and Alguacil, 2006). This is called the array transfer function or the array radiation pattern. Some examples are seen in Fig. 9.7.

9.5 Processing Software

The software can be divided into two categories: Real time and offline.

Real time: In its simplest form, standard LTA/STA triggers are used to detect seismic events much like on conventional seismic stations and networks (see e.g. Havskov and Alguacil (2006) for an overview) and once an event is detected, array processing is done on the detected signal. This method does not enhance the S/N ratio so the alternative is to run the STA/LTA trigger on all the possible beams. This is the way the large arrays work and the software is mostly made only for these arrays and not generally available. Real time software is outside the scope of this book.

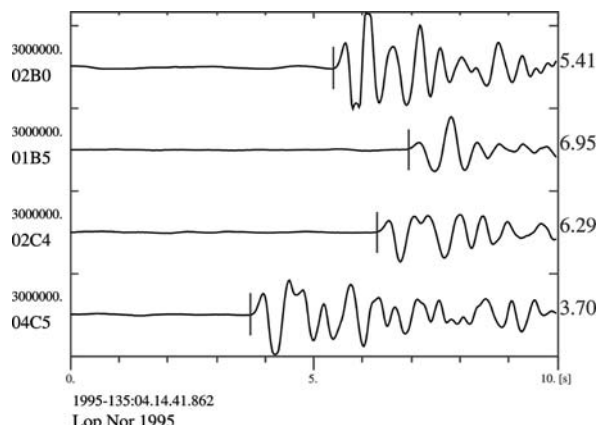
Off-line: The main purpose of the array is to determine the apparent velocity and azimuth for particular time segments in order to do further analysis of the events. For this kind of analysis several software packages are available and some examples will be given in the following.

9.5.1 Manual Processing

The slowness can be estimated by manually picking the onset times or any other common distinguishable part of the same phase for all instruments in an array as described above. We may then use (9.10) to estimate the slowness vector \mathbf{s} by a least squares fit to these observations. In order to make this method more accurate and automatic, cross correlation can be used to get accurate relative time arrivals. This is a standard procedure built into some processing systems. This method can also be used for small local networks recording teleseismic events. The example shown in Fig. 9.8 is from the large NORSAR array (aperture > 70 km), which has a similar size as many local seismic networks.

The results of the manual picking is comparable to both the beam forming and the fk-analysis, see NMSOP.

Fig. 9.8 NORSAR recording of the Lop Nor explosion of May 15, 1995. Vertical traces from the sites 02B0, 01B5, 02C4, and 04C5 of the NORSAR array are shown at the same amplitude scale. A plane wave fit to these 4 onset time measurements gives an apparent velocity of 16.3 km/s and a back-azimuth of 77.5°. Copyright granted by IASPEI. Figure from NMSOP, Fig. 9.26



9.5.2 FK Processing

The method of fk-processing is the simplest to use and is built into several processing systems. The procedure is to select the channels in an array to be used, select the time window and the filter and do the fk analysis on this data segment. We will use an example of a small array in Panama.

This array consists of eight 4.5 Hz sensors in an L-shaped array with a dimension of around 300 m. Its purpose is to analyze local events in the area. Figure 9.9 shows the signals from a magnitude 3.2 event located 65 km from the array. Since the array is so small, picking times manually is not practical and most likely would result in very inaccurate results. The first 0.5 s of the filtered signals look quite similar but after that the signals are surprisingly different considering the small size of the array. The result of the fk-analysis is seen in Fig. 9.10.

The result obtained will vary according to window chosen and filters used. Table 9.1 shows some examples. The table clearly shows that the processing parameters are important. So in this case, what is the most correct result? The event was also recorded by 3 other stations near the array and the location indicates that the hypocenter could be near or below Moho. In that case the high apparent velocity could be explained. A deep event should be expected to have sharp P-onsets which are also seen here. From the network location, the azimuth is expected to be 209° which is also closest to the results obtained with the short time window. A 10° “error” is acceptable for this kind of data, particularly when the earthquake location is uncertain in itself. No testing has been made to systematically check the array deviation due to local inhomogeneities, which is one more source of error. This discussion is not to prove which solution is correct, only to draw the attention to the problems involved when using fk-analysis for small arrays and that some testing and calibration must be made before using the results.

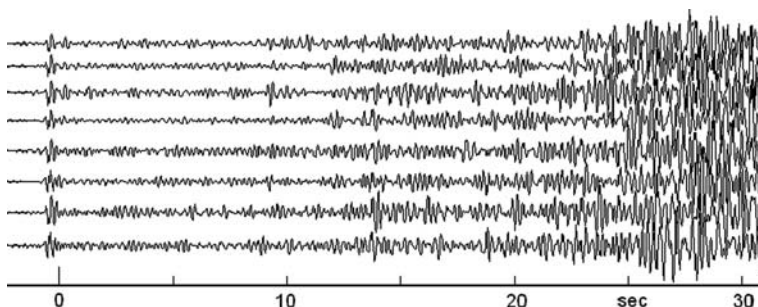


Fig. 9.9 Signals from the 8 station Chiriquí array. The signals have been filtered 1–5 Hz. The origin time is 2004 0204 15:00. For more information, see ftp://ftp.geo.uib.no/pub/seismo/REPORTS/CENTRAL_AMERICA/PANAMA_WORKSHOP_2004/PANAMA/ChiriNet/

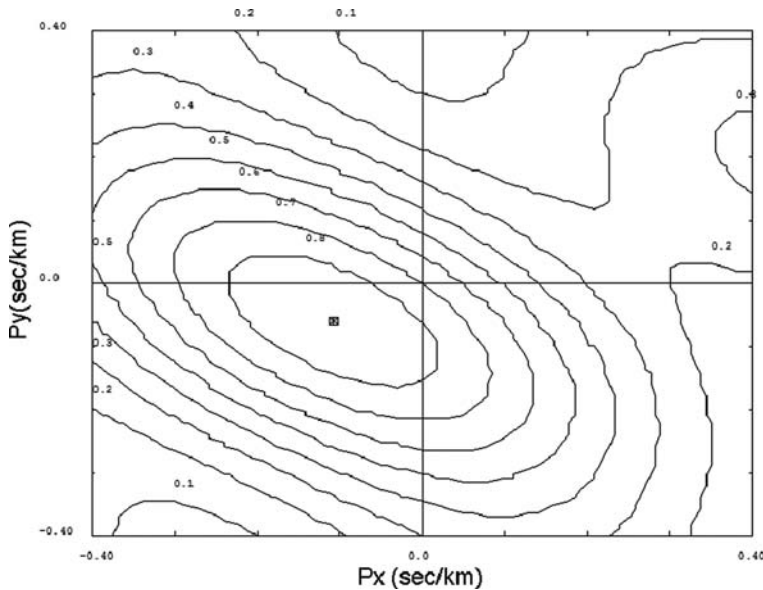


Fig. 9.10 The figure shows the output from the fk analysis for the signals seen in Fig. 9.9. A 0.6 s time window around the P was used and the filter was from 1 to 5 Hz. The axis' give the apparent slowness P_x and P_y (km^{-1}). The apparent velocity at the point of maximum power was 8.8 km/s and the azimuth 240°

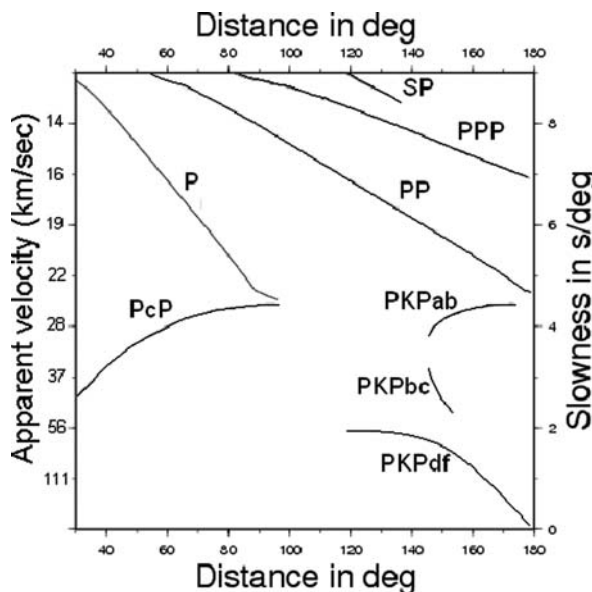
Table 9.1 Results of fk analysis with different input parameters. All examples had the same time window start as seen in the P-zoom in Fig. 9.9

Filter	Time window	Azimuth	Apparent velocity	Max power
1–5	0.4	219	12.0	0.90
	0.6	240	8.8	0.89
	1.0	239	8.2	0.87
2–4	0.4	222	10.9	0.93
	0.6	241	8.0	0.91
	1.0	254	9.3	0.89
3–6	0.4	219	12.0	0.90
	0.6	240	8.8	0.90
	1.0	236	9.0	0.83
4–8	0.4	217	12.2	0.87
	0.6	234	9.9	0.80
	1.0	224	9.9	0.74

9.6 Using Array Measurements for Identifying Phases

Identifying seismic phases can often be difficult and seismic arrays, whether small dedicated arrays or regional networks can determine the apparent velocity (or slowness). For local and regional phases, small purpose built arrays must be used to

Fig. 9.11 Apparent velocity and slowness as a function of phase type and epicentral distance for a shallow source. The calculation is made using the IASP91 model and the calculation and figure is made by Klaus Stamler



get the apparent velocity while for global distance, regional networks can reliably determine the apparent velocity as demonstrated above. Knowing the distance, and the apparent velocity, it is then possible to reliably determine the phase type using tables or figures of apparent velocity versus distance, see Fig. 9.11.

In the example in Fig. 9.4, the apparent velocity was 21 km/s. At the distance of 80° we can identify this as a P-phase. From Fig. 9.11, it is seen that particularly for the different branches of PKP, there is a clear separation of the different apparent velocities and consequently determining apparent velocity can be a very useful tool in identifying the correct PKP (see Exercise 9.2).

9.7 Exercises

Exercise 9.1 Azimuth and apparent velocity from a three station array

An array has the following station locations (coordinates in km):

- Station 0 (0,0)
- Station 1 (100,0)
- Station 2 (0,200)

A P-wave is arriving at times $t_0 = 0$ s, $t_1 = 4$ s and $t_2 = 11$ s at station 1, 2 and 3 respectively.

- Calculate the back azimuth and apparent velocity using (9.6).
- From the Bullen table (Table 2.2), get the distance to the earthquake. Remember that the Bullen table gives the apparent velocity in s/deg, so the easiest is to

convert from km/s to s/deg before looking up in the table ($1^\circ = 111.2$ km). Assume a depth of 33 km.

- Use Fig. 9.12 to get an approximate location assuming the array is located in Southern Norway.

Exercise 9.2 Azimuth and apparent velocity using a regional network

The P-arrival times for 5 stations in the Norwegian network is given in Table 9.2 together with the station coordinates.

- Select a reference station.
- Calculate the distances to the reference station using (9.11) and (9.12).
- Calculate the arrival times relative to the reference station.

Table 9.2 Station coordinates and P-arrival times for a distant earthquake recorded by some stations in S. Norway. The origin time is 2007 1209 07:28

Station	Latitude, deg. N	Longitude, deg. E	P-time (s)
NSS	64.525	11.967	27.6
MOL	62.569	7.542	32.9
SUE	61.057	4.761	37.0
ASK	60.483	5.195	38.8
SNART	58.353	7.206	44.8

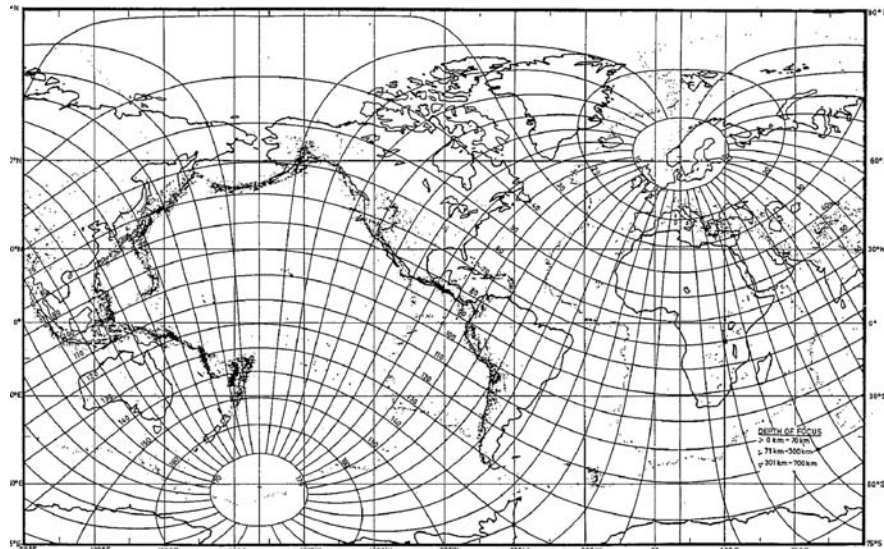


Fig. 9.12 Distances and back azimuth measured from S. Norway

- Plot the observations using (9.10) and calculate apparent velocity and back azimuth.
- Using Fig. 9.11, identify the type of P-phase.

Computer exercises

- Array processing using arrival time picks for more than 3 stations
- Array fk processing using 2 different arrays

Chapter 10

Operation

The preceding chapters in this book have described the main techniques for processing data in a typical network. In this chapter we will try to describe how the routine work can be organized using the described techniques. For many networks, data collection and processing is closely connected. The data collection has been described in NMSOP and Havskov and Alguacil (2006) and will not be repeated here. The processing can mainly be described as an interaction between the seismic data base and various processing programs (Fig. 10.1).

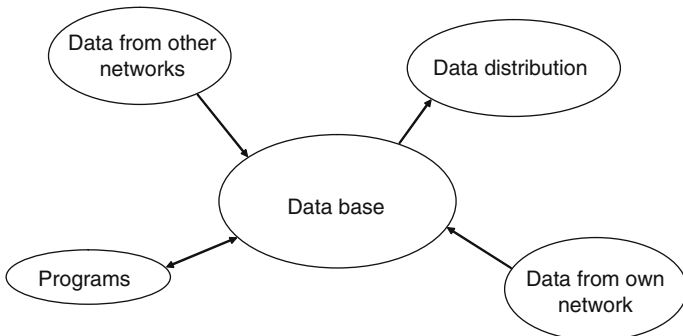


Fig. 10.1 Processing and storage of data

The way a processing system is set up has profound importance for the time spent on daily operation and the possibility of effective use of the data for information and research.

10.1 Data and Data Storage

The amount of data accumulating over the years will, for most networks, be very large and unless stored in a systematic way, it soon becomes a major task to find and work with specific data. Thus the first requirement to any processing system is to organize the data and make sure that all new data added is stored in the

organized system. Let us first look at the types of data stored in a typical processing environment:

Waveform data: This has been described in Chapter 3. Waveform data can either be file(s) for one event or it can be continuous data, which means that all the waveform data for a particular station is available. For the continuous data, the storage can be in files of various lengths from less than one hour to a month. The waveform filenames typically contain the date and time, but also the network or station and component names. Typical lengths are one hour or one day. The waveform data is by far the data occupying the most space. A station sampling at 100 Hz, three channels using a 24 bit digitizer will collect $24 \times 3600 \text{ s/day} \times 4 \text{ byte/sample} \times 3 \text{ (channels)} = 104 \text{ Mb/day}$. Compression (e.g., SEED format, see Chapter 3) will reduce this to less than half. However, even with compression, a 10 station, three-component network will collect $365 \times 104 \text{ Mb/2} \times 10 = 190 \text{ Gb/year}$.

Earlier, most systems would only store seismic events, meaning the waveform files corresponding to the event, while now more and more systems store the continuous data. Due to the availability of large disks, the data is usually available online, however a backup system is still needed.

Table 10.1 Example of file with observations in Nordic format as used by SEISAN

Input parameters:									
SIAT SP	:	Station and component							
IPHAS	:	Phase with onset							
W	:	Phase weight, HYP071 style							
HRMM SECON	:	Hour, minute and seconds							
CODA	:	Coda length (secs)							
AMPLIT PERI	:	Amplitude (nm) and period (sec)							
AZIM VELO	:	Azimuth (deg) and apparent velocity of arrival at station							
AIN	:	Angle of incidence							
Output parameters:									
AR	:	Azimuth residual							
TRES	:	Arrival time residual							
W	:	Weigh used in location							
DIS	:	Epicentral distance in km							
CAZ	:	Azimuth from event to station							
1993 1014 1638 24.1tL 58.285 6.356 16.0 BER 8 .8 2.6CBER 2.3LNAO									1
ACTION:UPD 97-03-25 21:28 OP:jh STATUS:							ID:19931014163824		I
1993-10-14-1638-01S.NSN_23									6
535 SOUTHERN NORWAY, this line is comment									3
STAT SP IPHASW D HRMM SECON CODA AMPLIT PERI AZIMU VELO AIN1 AR TRES W DIS CAZ7									
KMY SZ EP 1638 43.75 99							.010	122	328
KMY SZ ES 1638 59.09							.810	122	328
BLS5 SZ EP 1638 44.83 101							.210	127	3
BLS5 SZ ES 1638 59.60							-.210	127	3
ODD1 SZ EP 1638 53.18 122							.910	182	5
EGD SZ EP 1638 57.89 122							-.3	9	343
EGD SZ ES 1639 23.23							-.2	9	343
BER SZ EP 1638 59.23 105							-.3	9	346
ASK SZ EP 1639 0.91 113							-.2	9	344
ASK SZ ESG 1639 33.37							-1.9	9	344
SUE SN EP 1639 9.70 156							.2	9	343
NRA0 S EPn 1639 19.25	20.0	1.7	20.4	9.45	2.0	-8	-.1	9	401
NRA0 S EPg 1639 26.92			228.7	6.7	6.0	0	-1.9	9	401
NRA0 S ESn 1640 01.69			232.3	4.7	3.6	3	1.4	9	401
NRA0 S ELg 1640 15.09			222.4	3.4	6.2	-6	-.4	9	401

Calibration data: This has been described in Chapter 3. If the calibration data is not part of the waveform files, it must be stored in some way, usually in individual files corresponding to the seismic channels of the system.

Seismic observations: A large variety of parameters are obtained from the waveform data like phase arrival times, amplitudes, spectral parameters etc (see Chapters 2, Chapter 6, Chapter 7 and Chapter 8). These parameters are usually stored in files, typically one file per event. The format of these files (usually ASCII) varies depending on the programs used, for an example in Nordic format, see Table 10.1. Other popular formats are HYPO71 and IMS1.0.

Parameter files: Processing systems need parameters like station coordinates, travel time tables, crustal models etc.

All this parameter information is in most cases stored in files which have been organized in some user defined system. For large systems (like international data centers), the data is always organized in a relational data base, custom made for that organization, while for smaller systems this is seldom the case and the data is stored in a so-called flat file system.

Relational data base, advantages:

- Fast access to any part of the data.
- Secure, harder for users to unintentionally delete data, good backup.
- Keeping track of who is doing what and when.
- Very fast search using many parameters.

Relational data base, disadvantages:

- Complex to set up and maintain.
- Difficult to add new types of data or interface new programs, unless the user is experienced in data base set up.
- Hard to figure out what happens if something goes wrong.
- Might be difficult to move data and programs between different computer platforms.

Flat file system, advantages:

- Fast access to individual events.
- Easy set up and maintain for non specialists.
- Transparency to what happens and where data is located.
- Easy to move between computer platforms.

Flat file system disadvantages

- Slow search for large and complex data sets.
- Less secure than a relational data base, easier to accidentally delete data.
- Hard to keep track of who is doing what.
- Might be more primitive and therefore less flexible to work with than relational data bases.

There are few relational (commercial and public domain) data base systems that are used in seismology. In addition to storing the data, a data base system must also have all the common processing programs like phase picking and earthquake location integrated with the system and the system must allow for easy interfacing of new programs. The processing system, whether a relational data base or some user organized system should be able to:

- Store seismic events chronologically with all relevant data easily available for each event making addition and revision of data simple. Simple direct access to any one event.
- Provide simple access to continuous data so that any segment of any number of channels can be processed.
- Search for events fulfilling certain criteria like magnitude and area. Usually, a large number of parameters should be searchable. The selected events should then be directly accessible for further processing.

Storing the data in this way means creating one data base with all data from the network and the search software enables the user to select out any part of the data (e.g. distant events for one month) and work in the data base with only these events. Figure 10.2 shows the schematics of the SEISAN flat file data base system

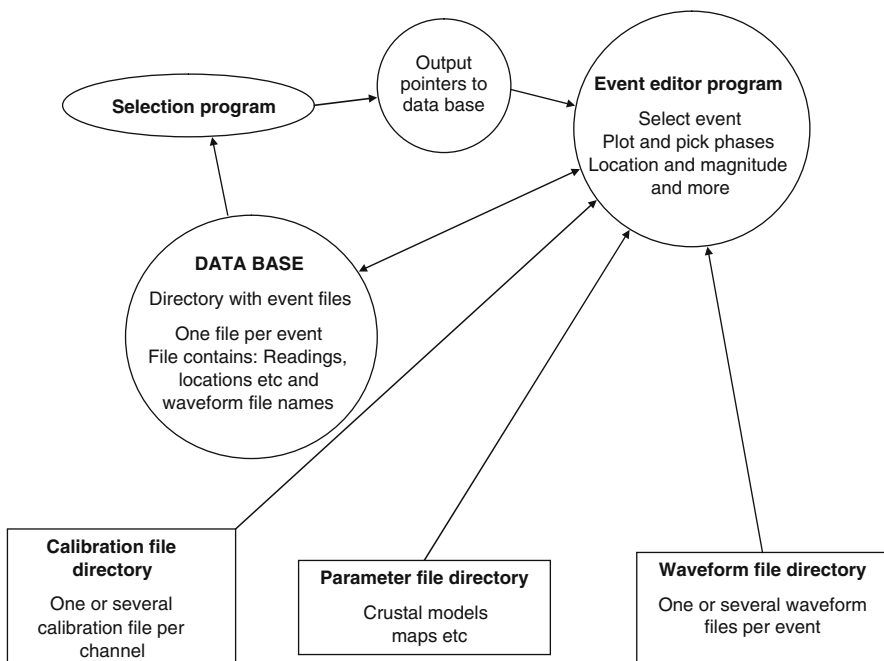


Fig. 10.2 Simplified schematics of the SEISAN data base and processing system

(Havskov and Ottemöller, 2000, 2002), which is able to do the above mentioned tasks and which has been used for most of the examples in this book.

If we look at SEISAN as an example, the data base consists of one file per event (Table 10.1 for an example) stored in one directory with subdirectories (not shown). The user can access any one of these events using the *event editor program*. E.g. giving the command *eev 200601201112*, the event editor program accesses the event nearest in time to 2006 0120 11:12 and the user can then scroll up and down to find other events nearby in time. Once an event has been selected, it can be plotted and phase readings are written back to the event file. Note that the waveform files are stored separately, however the waveform file name(s) are stored in the event file so the plotting program knows where to find them. Similarly, parameter files and calibration files are stored in separate directories known to the *event editor* and associated programs. Once phase picks have been made, the event can be located by the *event editor* and the results are written back to the event file (data base). The individual event files can be *manually edited* by the *event editor*, however most changes take place through programs. The data base (event files) can be searched by the *selection program* for a particular time period and given selection criteria and an output file is created with all the selected events in one file, which can be used for data exchange or processing by other programs, like mapping programs. The *selection program* also makes a file of pointers to the selected events (files) in the data base. This file can be used as input to the *event editor* to access only these events for further processing. Examples are to work only with all the events with a high RMS in order improve the locations or to select events with more than a certain number of polarity readings for making fault plane solutions.

10.2 Routine Processing

Most seismic networks will have procedures for automatically detecting seismic events which then become available for the analyst in the processing system. Alternatively, the analyst scans the continuous data and either extracts out desired waveforms for separate processing or works directly with the continuous data. Some systems will provide automatic arrival time picks and make corresponding hypocenter locations, which might be quite reliable for some networks and less so for networks badly configured relative to the seismicity. There is always a need for some manual processing as indicated in the following sections.

10.2.1 Screening of Detections

Any trigger system will provide false triggers, less so for large well distributed networks than for small networks with an uneven distribution. So the first task is to remove false triggers. It is an advantage to check the data with the same filter as was used for triggering since the event might not be seen otherwise.

10.2.2 Event Classification

Analysts looking at many events will often get a very good knowledge of some of the event characteristics and it is useful to classify the event immediately so it becomes easy to find particular types of events later.

A first and important classification is whether the event is local (0–1,000 km), regional (1,000–2,000 km) or distant (> 2,000 km) since different processing and travel time models are used in the two cases. A local event is easily identified by having clear P and S and if there is no doubt about the S-identification, the S-P time gives a good indication of the distance (distance in km close to 10 times the S-P time, see Chapter 5). An additional characteristic for a local event (magnitude < 4) is the high frequency signal ($f > 5$ Hz) (Fig. 2.18 and Fig. 2.19), while distant events typically have P-signals with $f < 5$ Hz (Fig. 6.11). However, without carefully checking the frequency, a distant event might be misidentified as a local event, see Fig. 2.28. Regional events ($1,000 \text{ km} < \Delta < 2,000 \text{ km}$) can sometimes be difficult to classify due to a complex crustal structure and rather low frequency content, see examples in Chapter 2.

A second important classification is whether an event is a likely explosion. Since explosions often occur at the same place and time of day, analysts quickly become able to identify explosions. There are automatic systems available for identifying small explosions based on frequency content and other parameters (Chernobay and Gabsatarova, 1999 give an overview), however analysts are more reliable, see NMSOP for a general discussion on this topic.

For some areas (like Scandinavia), there are more explosions than earthquakes, so explosion identification is important. See also Section 10.2.6.

Other classifications: Depending on the area, the event can also be classified as volcanic and volcanic events can have several sub groups (outside the scope of this book, see e.g. NMSOP or McGuire et al. (1995)). Other possibilities are sonic booms and rock-bursts. Or the user might simply want to make his own classification.

Storing classified events: Most systems store all events in one data base from which a subset can be extracted for special studies. Some local and regional networks store local and global data in separate data bases, partly because different programs have been used for the processing. This is not recommended since:

- The distinction between local and global data is not always unambiguous and there is therefore a risk of loosing data falling between the two categories.
- Data is not processed chronological and the operator does not get the complete picture of the network detection.
- Merging data from other networks becomes more difficult.
- Reporting data is not done in a systematic way.

10.2.3 Analysis

In the following we list some of the tasks which often are done routinely at a seismic network.

Picking phases, amplitudes, locating and calculating magnitudes: This operation is mostly done in an integrated process so phases (see Chapter 2) and amplitudes (see Chapter 6) are picked, then location and magnitude are calculated (see Chapters 5 and Chapter 6). If large residuals are found, phase picks and phase identification are checked (see Chapter 5). An important check here is to compare the amplitude based magnitudes from the different stations. The amplitudes themselves can be very different due to different distances (mostly with M_L , see Table 10.2) and it is hard to evaluate if they are correct unless magnitude is calculated. If magnitudes deviate more than 0.3–0.5 from the average magnitude, this may be an indication of a badly read amplitude or an incorrect calibration function for the particular channel, so reading amplitudes for both local and global events provides a good quality check. Table 10.2 shows an example for a local event and Table 10.3 for a distant event.

Table 10.2 Individual amplitudes and magnitudes for a small event in Western Norway. The average magnitude is 1.8. Abbreviations are: STAT: Station code, Amp: Amplitude (nm) and r: Hypocentral distance (km). The origin time is 2004 0511 00:50

STAT	EGD	BER	ASK	ODD1	KMY	BLS5	SUE	STAV	HYA	FOO	SNART	MOL
r	30	42	52	75	91	93	120	122	137	177	216	309
Amp	85	49	90	53	23	37	41	30	20	17	53	4
M_L	1.6	1.5	1.9	1.8	1.5	1.8	1.9	1.8	1.7	1.8	2.4	1.5

From the table it is seen that the amplitude generally decreases with distance. There can also be a large variation in amplitude at similar distances. However, the observation at SNART clearly stands out as too large indicating an error somewhere.

Table 10.3 Individual amplitudes and magnitudes for a distant event in Alaska. The average m_b is 5.9. Abbreviations are: STAT: Station code, Δ : Epicentral distance (degrees), Amp: Amplitude (nm) and T: Period (s). The origin time is 2007 1002 18:00

STAT	FFC	TLY	KURK	ARU	ESK	BFO	KAPI
Δ	34	53	63	64	69	77	87
Amp	313	332	377	389	482	331	485
T	2.4	1.3	1.7	1.2	1.2	1.7	1.8
m_b	5.6	5.9	5.9	6.0	6.2	5.9	6.1

This example of a distant event shows that the amplitude measurements for m_b are quite constant over a large distance range and the period measurements have a significant influence on the magnitudes (see station FFC). The variation in magnitudes is small indicated that observations and calibrations are ok. A similar analysis could be made for M_s .

Spectral analysis: It is recommended to routinely do spectral analysis (see Chapter 8). This will give the moment magnitude as well as other spectral

parameters. One advantage is that it is possible to calculate magnitude of most events based on P-waves. This is particularly useful for regional events where the distance is too short to get a reliable m_b and too far to get M_L (S might not be seen).

Doing fault plane solutions: For clear global events, it is important to read the polarity of P so the data can contribute to global fault plane solutions. The same is the case for local and regional events if enough stations are available. For a local or regional network, fault plane solutions should be made routinely for events with enough data (see Chapter 7).

Getting data from other networks or stations: Some networks are too small or badly configured to well locate their own events and it is often an advantage to add data (phase readings and/or waveform data) from nearby stations and/or networks. An example of this is Central Europe where events that occur between the countries. Norway is an example of a long narrow country with seismicity outside the station network (Fig. 5.6). It can also be useful to compare magnitudes. Data exchange can be manual or automatic in real time.

Getting data from global data centers: Local networks are often too small to accurately locate distant events (example in Chapter 5). By fixing the location to the global location, a valuable feedback can be obtained on the local reading practice. For this purpose, ISC cannot be used since it recalculates locations when all data has been obtained, which could be up to 2 years after the occurrence of the event. However, ISC does have preliminary locations from other agencies available. USGS gives out a PDE (Preliminary Determination of Epicenters) location within an hour of the occurrence of an event, and this location is gradually improved over the next hours and days, so the PDE solution is the most practical to use in day to day operation. In addition, the PDE location can be used to calculate arrival times of secondary phases to help identifying these phases. Most networks only report the first arrival P. It is a good practice to report all clear phases since these additional phases are important for global structure analysis. For many small networks, the purpose is not to locate events outside the network. This can result in many networks only reading phases for their own events. This is an unfortunate practice for the following reasons:

- When not contributing phases to the global data base at ISC, valuable data is lost and the global catalog is not as good as it could have been, which also will affect the region of the local network.
- The local network does not get proper credit on a global scale of its operation.
- When comparing the magnitudes M_s and m_b calculated locally with the values reported by global centers, a valuable feedback is obtained on local reading practices as well as providing a check on the local calibration functions (see example in Table 10.3).
- Distant events recorded locally can be used to get local crustal structure from both travel time tomography and receiver function analysis (see Chapter 2).

It is therefore strongly recommended to process ALL earthquakes recorded with a local or regional network.

10.2.4 Epi and Hypocenter Maps

For many events, a useful tool is to plot the individual location, both as a help to see where it is located in relation to the stations as well as the absolute location. A simple and quick routine, integrated with the processing software, is needed for this task. Figure 10.3 shows an example.

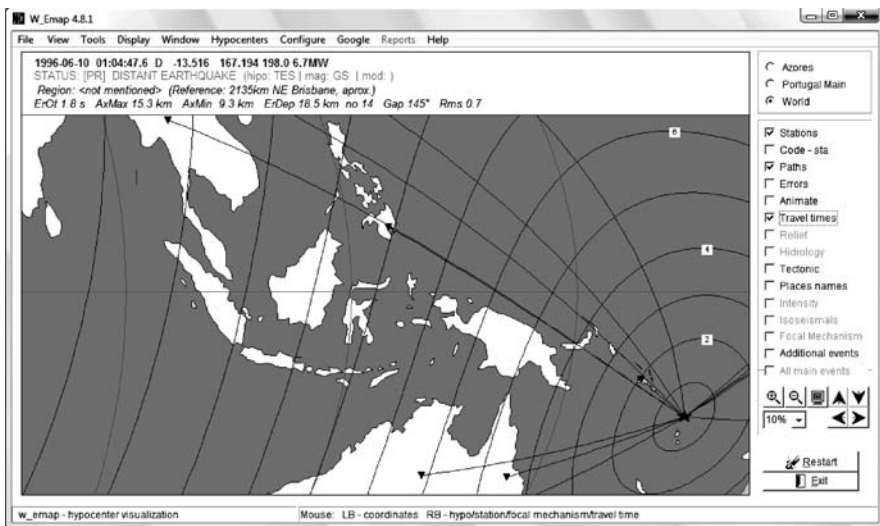


Fig. 10.3 Plotting on event with program w_emap (made by Fernando Carrilho, part of SEISAN). This program can show travel paths, travel times etc (see menu at left) and the top shows important information about the event. Note that Google can be used for plotting

Sometimes, particularly for felt events (see below) there is a need for quickly associating an event with a geographical map. This has traditionally been done with GIS (Geographical Information Systems). An alternative for many applications is now Internet based mapping software (e.g. Google Map) and many data centers use this for plotting earthquakes. The Generic Mapping Tools (GMT) (Wessel and Smith, 1991, 1998) is a common software used in seismology to produce non-interactive maps. For routine use with individual events, it is again important that the plotting function is integrated with the processing software (e.g. w_emap), see Fig. 10.4 for an example using Google Map.

The most common utility is to plot many earthquakes to get an idea of the epicenter distribution, see Figs. 10.8 and 1.5. Additionally, depth sections are useful in order to investigate e.g. subduction zones (see Fig. 1.6). Plotting the hypocentral location of aftershocks is particularly useful since the spatial distribution of aftershocks within the first days will show the extension of the ruptured surface. The aftershocks can therefore be used to get both the area ruptured as well as the orientation of the fault and thereby helping to resolve the ambiguity from the fault plane solution (see Chapter 7).

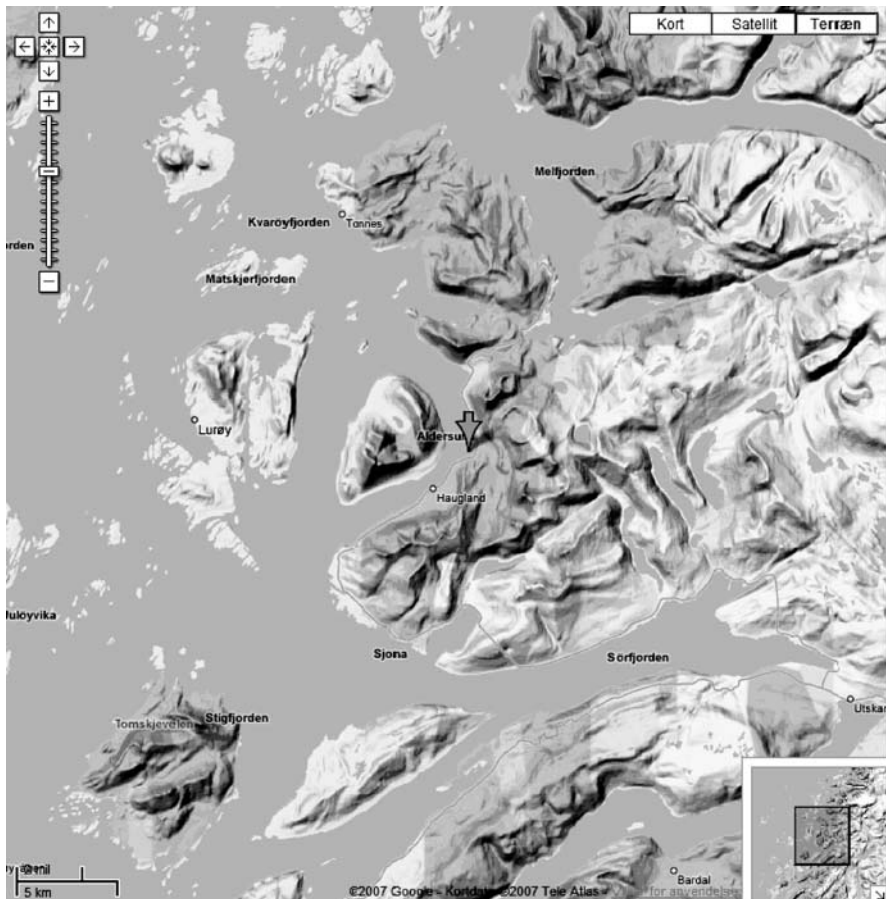


Fig. 10.4 GoogleMap with the epicenter of an earthquake. The epicenter is shown with the arrow

10.2.5 Felt Earthquakes

In most populated areas, there are felt earthquakes. In the past, information from felt earthquakes was very important and often the only information. Interest in macroseismic investigation declined with the increased instrumental coverage, however it is now understood that it is still important to collect macroseismic information in order to calibrate studies of historical earthquakes, study local attenuation and seismic hazard and risk. It can also sometimes be useful to compare the area of maximum intensity to the instrumental epicenter. The work related to felt events requires two actions: (a) Be able to quickly and accurately report location and magnitude. While the location usually is not a problem, it can be problematic to calculate larger magnitudes for a local or regional network, see Chapter 6, (b) Collect macroseismic information. This is the most time consuming and requires that the action has been

How many times have you ever felt an earthquake in the past ?

It is my first experience A few times Often

SECTION A - WHERE YOU WERE

1. At the time of the earthquake, where were you?

Outdoors Ground floor Upper floor if so, which floor?

Stationary vehicle Moving vehicle

Other

2. What were you doing?

Walking Standing Sitting Kneeling Lying down Sleeping Other

SECTION B - EARTHQUAKE SHAKING AND SOUND

3. What best describes the shaking

No shaking It was... Don't know

4. What best describes any sound heard?

No sound It was... Don't know

SECTION C - EFFECTS ON PEOPLE AND ANIMALS

5. Which best describes what happened where you were (your house, neighbours)?

I don't know whether other people noticed it or not

6. (Only for earthquakes that happened at night) Did the earthquake wake you up?

I wasn't asleep

Where other people where you were woken up?

Don't know

7. Was it difficult to stand or walk?

I wasn't standing

8. How would you best describe your reaction?

No reaction/Not felt

9. Where you were, did anybody run outdoors in panic?

Don't know

Fig. 10.5 Example of part of questionnaire used by EMSC (European-Mediterranean Seismological Center, www.emsc-csem.org) for collecting macroseismic information

planned beforehand. Options are e.g. collection by internet (see Fig. 10.5) or distribution of questionnaires by mail, e.g. to post offices, in which case the effected area must be known in order to make an adequate coverage.

Once the data has been received, it is processed, either automatically or manually and a macroseismic map produced, see Fig. 10.6 for an example. *Like other data, it is important that the macroseismic data forms part of the general data base.* Several parameters are usually stored like felt area, maximum intensity and macroseismic location and magnitude. For more information on collecting and processing macroseismic data, see the comprehensive description in NMSOP.

10.2.6 Quality Control

Quality check of data: Once all data for a month is available and possible data from other networks have been merged in, it is time for a final check of the data.

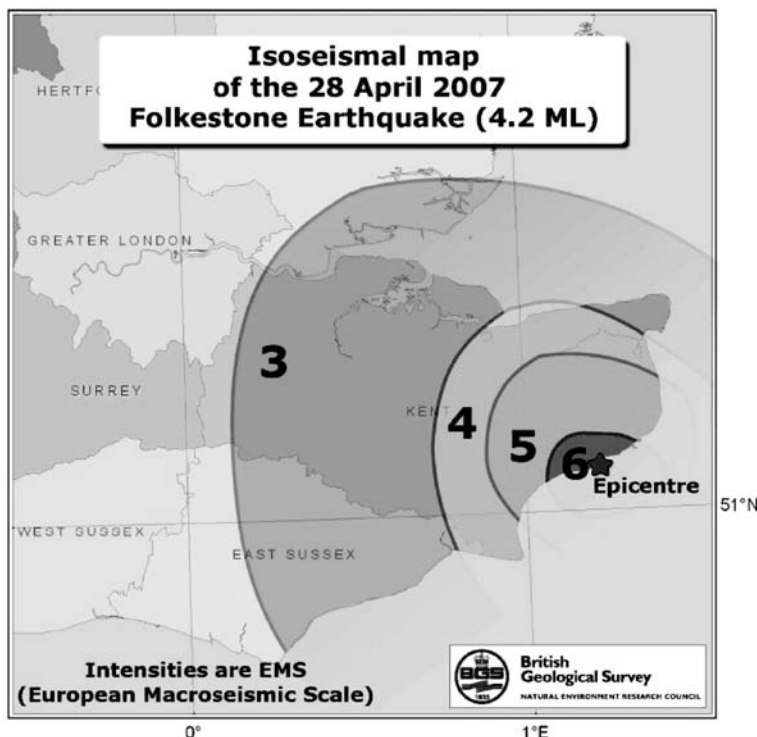


Fig. 10.6 Example of an isoseismal map for an earthquake of magnitude 4.2. The data is from the British Geological Survey. The numbers are intensities. (http://quakes.bgs.ac.uk/earthquakes/reports/folkestone_folkestone_28_april_2007.htm)

Residuals: Travel time residuals should all be below a network and event-dependent value. A small local network (~100 km) with events inside the network will typically have residuals < 0.5 s while a large regional network can have, particularly S-residuals, of 2–5 s due to inhomogeneities and difficulty in identifying secondary phases. For distant events, P-residuals from clear P-phases should be less than 2 s (typically less than 1 s) while secondary phases can have larger residuals. Like for regional events, secondary phases can be difficult to identify and are generally not used for location by large agencies. The network should have a clear policy on how large residual are accepted for particular events and weight out arrivals with larger residuals. However, the phases read should be left in the data base so the information of the phase arrival is retained.

RMS: All events should have an travel time residual RMS less than a certain value depending on the network configuration, number of stations and types of events. For a small local network, RMS should be less than 0.5 s, for a regional network less than 1–2 s and for global location less than 1–3 s. These values will strongly depend on how many secondary phases are used. Examples of residuals and RMS are seen in Tables 5.9, 5.10, 5.11, 5.12, and 5.13.

Hypocenters: Low residuals and RMS do not itself ensure a reliable location (see Chapter 5), so the hypocenter must be evaluated. *Depth:* Particularly a reasonable depth must be ensured. The local operator will often know what is reasonable in different areas and take appropriate action. For teleseismic events, a local or regional network cannot get reliable depths unless depth phases are read and the depth should be fixed to the known agency value. *Epicenter:* Location in unusual areas, according to the local knowledge, should be checked. This becomes evident when making an epicenter plot. Epicenters far outside the network should be checked against global locations and fixed to global locations if deviating too much (>100 km). *These checks of the hypocenters should ensure that the local data base of both local and global events presents an accurate picture of the seismicity and not just the seismicity as seen from the local network.* A particular problem which might create inconsistencies is the changing of location model depending of area and distance. A local flat layer model is usually used locally while a spherical global model is used for larger distances. See Chapter 5 for more discussion on this topic.

Explosions: Some networks reports are contaminated by explosions. Apart from trying to identify the event immediately when reading the phases (see Section 10.2.2), many networks also have agreement with mines, construction companies and the military to get reports of explosions. This means that an event can be marked as a confirmed explosion in the data base and forced to have zero depth. It is important to get as much information as possible for the explosion: Origin time, location and charge. Well identified explosions can be used to test location accuracy and also to improve crustal structure. Even with manual identification and reports, many explosions are not identified since they often look very much like earthquakes (see Fig. 10.7). In that case statistical analysis can help to identify probable explosions. Fig. 10.8 shows earthquakes and explosions in Norway.

The simplest method to identify explosions is to inspect the time of day distribution of the event catalog. Earthquakes occur randomly while explosion predominantly occur at certain hours, particularly in the working hours. Figure 10.9 shows an example.

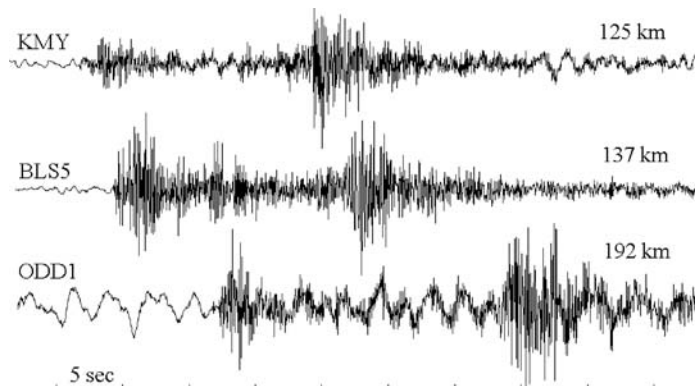


Fig. 10.7 An explosion in S. Norway as record on 3 stations. The epicentral distances are indicated on the traces. $M_L = 1.8$, origin time 2002 0411 13:16. The explosive charge was 43 T

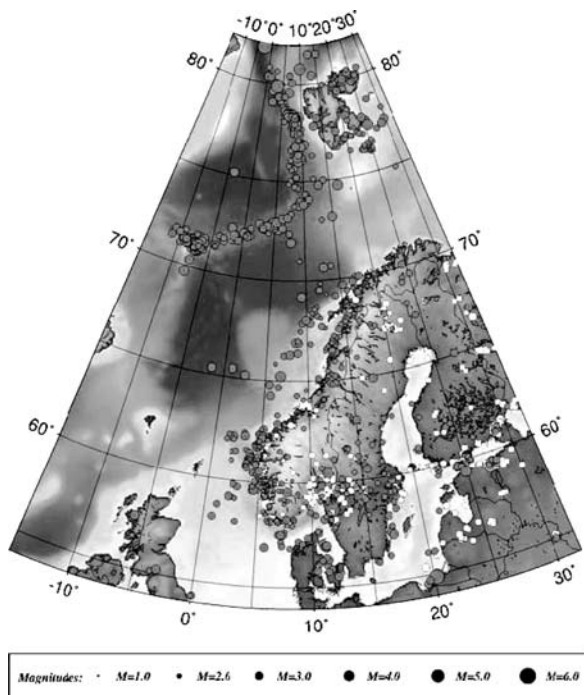


Fig. 10.8 Earthquakes and explosions in Norway for 2004. Explosions are indicated with the white symbols

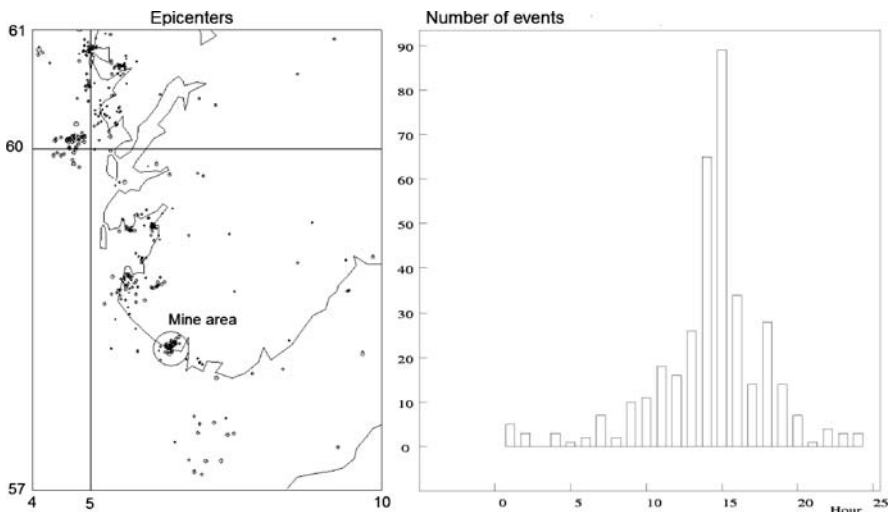


Fig. 10.9 Left: Epicenters for events in Southern Norway for 2006. A known mine area is indicated with a circle. Right: Time of day distribution for the events shown on the left. Time is GMT. Norway is 1–2 h ahead of GMT

The time of day distribution shows a very clear predominance for events to occur in the day and are therefore potential explosions. The known mine area to the south shows a clear clustering of epicenters, however the events do not occur at one point so the spreading of the epicenters give an indication of the location accuracy. Other known mines have explosions at night time so we cannot construct a filter for the whole area using one time of day distribution. A practical explosion filter can be constructed as follows (Ottemöller, 1995).

- Divide area into sub-areas where time of day distribution might be uniform, Fig. 10.10 shows an example.
- Calculate time of day distribution for different upper magnitude limits since it is likely that there is an upper limit on the size of the explosions.
- Construct the filter to mark all events as probable explosions when the magnitude is smaller than a given magnitude and the event occurs within the time interval indicated by the time of day distribution.
- Only filter for time periods of known explosion activity if this information is known (e.g. a road construction project).

This filter will also remove earthquakes if the magnitude is below the threshold magnitude and they occur at the “wrong time”, however, this kind of filtering is still better than doing nothing and may provide an initial indication of the problem.

A more sophisticated approach is to determine the signal characteristics of the explosions and then to use pattern recognition to identify new events as explosions.

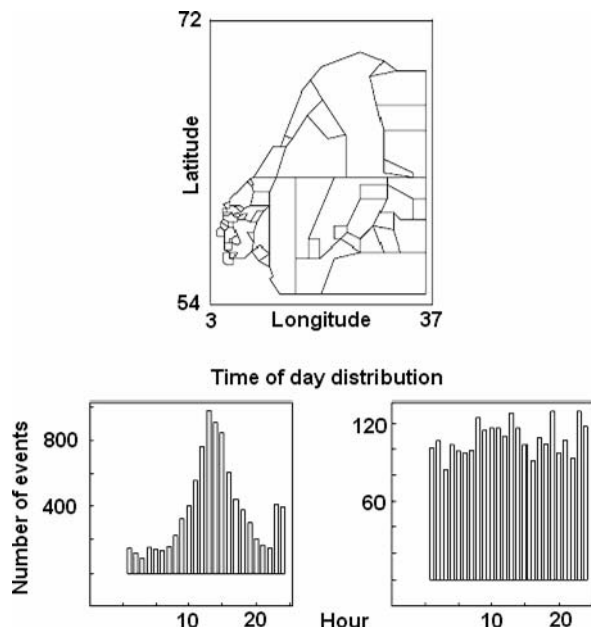


Fig. 10.10 Explosion filtering. The top figure shows the filter areas used for Scandinavia. The bottom left figure shows the time of day distribution for a 10 year Scandinavian catalog before filtering and the figure bottom right shows the distribution after filtering out probably explosions. Figure modified from SEISAN manual

Most explosions are very shallow and this has an effect on the seismograms. We also expect less generation of S-waves from explosions compared to earthquakes. However, generally the identification remains a complex task as there will be differences between a number of explosion sites, and even explosions from a single site may not be the same. There are also examples in which the difference between earthquakes and explosions is not obvious.

10.2.7 Seismic Bulletin

The majority of seismic stations and networks report their phase readings, locations and magnitudes to the international data centers like ISC (International Seismological Center), USGS (US Geological Survey), EMSC (European Mediterranean Seismological Center) and others on a monthly basis. Some also send phase readings as soon as they are available to be able to have them included in the rapid near real time locations of USGS and EMSC. The ultimate data center is the ISC since it receives the most data and waits up to 2 years for final processing in order to get as much data as possible. By combining all data, the ISC always detects events not found by any other agencies, mostly in far away places where no single network has location capability. The ISC will accept and organize, in its data base ALL data it receives irrespective of magnitude so ALL networks are encouraged to send all its data to the ISC. ISC will analyze events with minimum reported magnitude of 3.5 and larger, along with events with multiple network reports or stations reporting at distances more than 10 degrees. However, independently of ISC reprocessing, the local agency locations and magnitudes will be retained and can be found in the ISC data base. This is a good way to back up the local network data.

Bulletin: Most networks, local and global, distribute a bulletin. In the past, the bulletin was mostly printed, now it is mostly in electronic form. Making a bulletin is useful for reviewing and terminating the work for a month. Older data often do not exist in electronic form and bulletins have to be used. The ISC no longer prints its bulletin, but the printed version is available in PDF files (Table 10.4).

The bulletin also gives the Harvard moment tensor solution. Also notice that only a few stations give polarity (indicated with a \uparrow or \downarrow). The depth has been fixed to the standard 33 km, but using the 11 pP – P observations the more accurate depth of 41 km has been obtained. Unfortunately, the majority of stations only report P, while as mentioned earlier, other clear phases should also be reported.

10.3 Data Exchange

Seismology depends strongly on sharing data. In the early days of seismology this meant to send phase readings to a central agency, which could calculate location and magnitudes and the first such global collection of data was published as ISS (International Seismological Summary) and the work was mainly done at

Table 10.4 Example of part of an ISC bulletin with 216 observations. The event parameters are shown first with locations etc from different agencies. The prime solution from ISC is shown last. Then follows observations from stations in distance order.

	TIY	Taiyuan	55.99	322 eP	18 13 23	+0.1
NEIC $16^{\circ}18'03''$ $45^{\circ}0\pm0^{\circ}22$, $4^{\circ}26'S \times 152^{\circ}65'E$, $h3.3km$, Mb5.2/21,	TIY	[$1.5\mu m, 20^{\circ}E$][$1.5\mu m, 21^{\circ}0;Z,Ms5.0$]				
<i>M5.3/51, Error ellipse is semi-major=9.9 km</i>	XAN	X'an	56.11	316 P	18 13 22.5	-1.3
<i>semi-minor=5.2 km azimuth=85.0.</i>	XAN	[$1.3\mu m, 20^{\circ}E:N$]	pP	'AP'	18 13 35.4	0
<i>MOS $16^{\circ}18'03''$ $50^{\circ}3\pm3^{\circ}25$, $4^{\circ}25'S \times 152^{\circ}71'E$, $h3.3km$, Ms5.1/4,</i>	XAN	[$2.1\mu m, 20^{\circ}E$]	sP	'XP'	18 13 41	0
<i>Mb5.4/12, Error ellipse is semi-major=29.2 km</i>	XAN	[$Ms.3 2.7\mu m, 20^{\circ}E;Z,Ms5.3$]				
<i>semi-minor=12.3 km azimuth=12.7.</i>	KLR	Kul'da	56.28	344 eP	18 13 26	+1.3
<i>IDC $16^{\circ}18'03''$ $50^{\circ}7\pm2^{\circ}19$, $4^{\circ}35'S \times 152^{\circ}72'E$, $h7.3km \pm 17.8km$,</i>	KLR	[$1.2\mu m, 25^{\circ}$]	SP		18 21 20.5	-1
<i>M5.1/9, Mb4.5/18, Error ellipse is semi-major=25.8 km</i>	KLR	[$1.0\mu m, 6^{\circ}0$]				
<i>semi-minor=12.2 km azimuth=90.0.</i>	KMI	Kunning	56.54	304 eP	18 13 29.5	+2.5
<i>HRVD $16^{\circ}18'03''$ $50^{\circ}8\pm0^{\circ}1$, $4^{\circ}21'S \times 152^{\circ}84'E$, $h26km \pm 1km$, Mw5.7,</i>	KMI	[$70\text{ nm}, 1^{\circ}2, Mb5.6$]	pP	pP	18 13 34.8	-4
<i>Data Used: GSN; Centroid moment tensor solution. Data used:</i>	KMI	[$1.8\mu m, 26^{\circ};Z,Ms5.0 1.2\mu m, 18^{\circ};N,1.0\mu m, 18^{\circ};E,Ms5.1$]				
<i>GSN; LP body waves: s21, c25; Half duration: 354.</i>	CMAR	Chiang Mai Array	57.49	295 P	18 13 33.9	(.3)
<i>Moment tensor: Scale 10^{17} Nm, $M_w 0.19\pm.31$; $M_{eff} 3.48\pm.31$;</i>	CM31	Chiang Mai Array	57.49	295 eP	18 13 34.4	+0.6
<i>$M_{eff} \sim -3.67\pm.37$; $M_{eff} 0.59\pm1.11$; $M_{eff} -0.43\pm1.09$; $M_{eff} 0.95\pm.43$.</i>	CMAR	Chiang Mai Array	57.49	295 pP	18 13 42.9	(1.2)
<i>Principal Axes: $T 3.69, Plg9^{\circ}$, $Azm353^{\circ}$; $N 0.17, Plg79^{\circ}$,</i>	CD2	Chengdu	58.25	310 P	18 13 38.5	-0.5
<i>Azm133°; $P -3.86, Plg7^{\circ}$, $Azm262^{\circ}$; Best double couple:</i>	HHC	Hu-hao-te	58.50	324 eP	18 13 39.8	-0.8
<i>$M_{eff} 3.8 \times 10^{17}$ Nm, $NPJ, \phi: 37^{\circ}, \delta79^{\circ}$, $\lambda: 179^{\circ}$, $NP2, \phi: 128^{\circ}, \delta89^{\circ}$,</i>	HHC	[$1.7\mu m, 20^{\circ}E$]	S	S	18 21 38	-2
<i>$\lambda: 1^{\circ}$.</i>	HHC	[$3.3\mu m, 20^{\circ};Z,Ms5.3 1.9\mu m, 20^{\circ}0;N,Ms5.3$]				
<i>BII $16^{\circ}18'03''$ $53^{\circ}3$, $3^{\circ}42'S \times 152^{\circ}13'E$, $h3.7km$, Ms5.2, Ms5.1,</i>	BTO	Baotou	59.26	323 eP	18 13 45.5	-0.4
<i>mB5.7; mb5.1.</i>	HIA	Hailar	60.47	336 eP	18 13 55.2	+1.2
<i>DJA $16^{\circ}18'05''$ $35^{\circ}5\pm4^{\circ}89$, $4^{\circ}28'S \times 143^{\circ}56'E$, $h364km \pm 13.6km$,</i>	HIA	[$4mm, 6^{\circ}9, Mb4.5 1.94\mu m, 19^{\circ};Z,Ms5.0$]				
<i>Mb4.6/3, Error ellipse is semi-major=156.2 km</i>	LZH	Landzhou	60.72	316 eP	18 13 56	+0.1
<i>semi-minor=45.6 km azimuth=108.0.</i>	LZH	[$53\text{ nm}, 1^{\circ}8, Mb5.4$]	pP	sP	18 14 07.8	0
<i>ISC $16^{\circ}18'03''$ $45^{\circ}9\pm0.20$, $4^{\circ}26'S \pm 0.03$ $\times 152^{\circ}62'E \pm 0.049$,</i>	LZH	[$1.6\mu m, 20^{\circ}Z$]	PP	PP	18 16 16	+4
<i>b41km $\pm 2.2km$; pp-P-P, n216, o1305/129, Mb5.0/41, Ms5.2/69,</i>	LZH	[$Ms.2 1.4\mu m, 18^{\circ}E$]				
<i>3C-2D, New Britain region</i>						
PMG Port Moresby 7.46 226 eP 18 05 39.4 +4.5	MA2	Magadan	63.65	359 eP	18 14 17.7	+2.5
YOMI Yo Mokole 12.15 277 ceP 18 06 40.9 +1.6	MA2	[$90\text{ nm}, 1^{\circ}4, Mb5.6 1.1\mu m, 20^{\circ};Z,Ms5.1$]				
YOMI [$.29\mu m, 2^{\circ};1$] pP 18 06 45.9	GTA	Gaatoi	65.14	317 P	18 14 25.4	+0.3
MENI Mendum Tagoi 12.31 278 deP 18 06 41.5 (2.5) +0.1	GTA	[$16\text{ nm}, 1^{\circ}4;Z,Mb4.9 1.4\mu m, 20^{\circ}E 1.9\mu m, 20^{\circ}0;Z,Ms5.3$]				
CTAO Charters Towers 16.92 201 eP 18 07 40.4 (.8) -0.9	ULN	Ulaanbaatar	65.44	328 eP	18 14 26.7	(1.4)
CTA Charters Towers 16.92 201 P 18 07 43.0 +1.8	SHL	Shillong	65.88	300 eP	18 14 30	-0.1
CTA Charters Towers 16.92 201 S 18 10 58.1 +11	YAK	Yakutsk	68.41	349 eP	18 14 45.1	(1.1)
CTA Charters Towers 16.92 201 sP 18 07 56.9 (.6) CSY	Casey Station	68.49	197 eP	18 14 44	-1.8	
BKM Butte a Klehm 20.29 132 c/P 18 08 21.0 .0 TLY	TLY	Talaya	69.52	330		
KAKA Kakadu 21.67 246 eP 18 08 29.7 -.5.4	TLY	[$.89\mu m, 20^{\circ};Z,Ms5.0$]				
NOUC Port Laguerre 22.15 144 eP 18 08 38.9 -.0.9	IRK	Irkutsk	69.55	331 eP	18 15 04.1	+11.5
TANV Tanna 22.24 134 eP 18 08 38.0 -.2.6	IRK	[$.60\mu m, 1^{\circ}7;Ms.4.9$]			18 15 28	
WRAB Tennant Creek 23.66 227 P 18 08 54.6 -.0.1	IRK	[$.51\mu m, 16^{\circ}0$]				
ARMA Armidale 26.04 182 eP 18 09 17.7 +0.3	ODAN	Odare	70.12	300 P	18 14 55.2	(.9)
ARMA Armidale 18 12 09.1 MOY	MONDY	Mondy	70.86	329 eP	18 15 07.3	+6.8
ARMA Armidale S eS 18 13 48.1 +5 +5	MOY	[$28\text{ nm}, 1^{\circ}3$]				
ASAR Alice Springs Ar 26.43 221 P 18 09 19.8 (.14) -.1.3	PDYAR	Pededy Ar. Beam	71.13	340 P	18 15 00.8	(.7)
ASAR Alice Springs Ar 26.43 221 sP 18 09 34.4 -.2.6	PDYAR	Pededy Ar. Beam	71.13	340 pP	18 15 08.9	(1.4)
ASAR [$.11\mu m, 6^{\circ}77;1$] LR 18 19 34.8 GUN	GUMBA	Gumba	71.69	301 P	18 15 03.5	-2.4
ASAR [$1.6\mu m, 18^{\circ}24;Ms.4.6 SNR=19.9$] PKI	PULCHEK	Pulchoki	72.01	301 P	18 15 06.4	-1.4
ASPA Alice Springs 26.44 221 eP 18 09 20.6 -.0.5	KKN	Kakan	72.17	301 P	18 15 07.1	(.6)
ASPA Alice Springs S eS 18 13 53.2 +3 +3	DMN	Daman	72.28	301 P	18 15 08.6	-0.8
STKA Stephens Creek 29.36 199 P 18 09 46.3 (.15) -.1.1	BILL	Bilbii	72.77	5 eP	18 15 18.1	+6.5
RIV Riverview 29.45 182 eP 18 09 49.2 +1.0	BILL	[$.41\text{ nm}, 1^{\circ}3$]				
CNB Canberra 31.05 185 eP 18 10 02.5 +0.1	VNDA	Vanda	73.38	178 ↑P	18 15 14.2	-0.8
CNB Canberra eS 18 14 53.1 -.11	VNDA	Vanda	pP	pP	18 15 27	0
BUNI Buntu Taipa 32.23 270 ceP 18 10 13.4 (.14) +0.5	VNDA	Vanda	73.38	178 pP	18 15 27.7	(1.3)
ADE Adelaide 33.17 201 eP 18 10 21 +0.1	SBA	Scott Base	73.92	177 eP	18 15 18.2	-0.1
TANI Tanete Lipujang 33.17 270 ceP 18 10 20.6 -.0.5	SBA	[$6mm, 6^{\circ}8;Mb4.6 1.66\mu m, 21^{\circ};Z,Ms4.9$]				
TOO Toolangi 33.79 190 eP 18 10 26.7 +0.4	WMQ	Urumqi	75.22	317 P	18 15 25.5	-0.8
TOO Toolangi eS 18 15 35.6 -.11	WMQ	[$1.5\mu m, 28^{\circ}0;N$]	PP	PP	18 18 19	+2
FORT Forrest 35.10 218 eP 18 10 35.8 -.1.7	WMQ	[$.68\mu m, 28^{\circ}0;Z$]	PPP	PPP	18 20 06.5	+4
FORT Forrest 18 13 32 SKS	WMQ	[$Ms4.8j$]	SKS	SKS	18 25 29	+2
TSM Tawau 35.53 283 eP 18 10 47 +5.6	WMQ	Urumqi	SCS	SCS	18 25 34.5	+2
LQP Lukhban 35.83 301 eP 18 10 33.3 -.10.6	WMQ	Urumqi	SPP	PS	18 25 50	-3
CVF Callao Caves 37.41 307 eP 18 10 57 -.0.2	HYB	Hyderabad	76.15	289 iP	18 15 31.5	-0.6
RANI Rangndo 37.66 262 c eP 18 11 02.9 +3.6	TTA	Tatalina	77.33	21 eP	18 15 38.0	(.9)
KELI Kelakatan 38.10 262 deP 18 11 07.8 (.18) +4.9	TTA	Tatalina	77.33	21 eCP	18 15 46.8	(1.7)
SRDI Scraved 38.46 262 eP 18 11 07.8 (.17) +1.9	TIXI	Tiksi	77.34	352 P	18 15 39.7	+1.9
TAU Tasmania Univ. 38.78 186 P 18 11 09.2 +0.9	TIXI	[$10\text{ nm}, 1^{\circ}, Mb4.7 2.26\mu m, 21^{\circ};Z,Ms4.5$]				
JOW Kunigami 38.85 324 P 18 11 10.0 (.18) +0.9	TIXI	Tiksi	77.34	352 eCP	18 15 44.2	-4.3
JOW Kunigami 38.85 324 pP 18 11 17.4 (.19) -.3.1	DDI	Dehra Dun	78.91	302 eP	18 15 52.5	+5.3
QRZ Quartz Range 40.57 157 i/P 18 11 24.3 +1.1	PMR	Palmer	79.27	24 eP	18 15 47.6	-0.9
HBZ Hicks Bay 40.65 148 i/P 18 11 25.7 +1.8	NDI	New Delhi	79.30	300 eP	18 15 46	-3.4
PUZ Puketiti 40.98 149 i/P 18 11 26.2 -.0.4	IMA	Indian Mountain	80.01	20 eP	18 15 53.2	(2.0)
NOZ North Gisborne 41.28 149 i/P 18 11 29 -.0.1	IMA	Indian Mountain	80.01	20 eCP	18 15 57.9	(.9)
THZ Tophouse 41.52 157 ↑/P 18 11 31 .0 MCK	McKinley	80.43	23 eP	18 15 54.5	-0.2	
TCW Tory Channel 41.61 155 ↑/P 18 11 32.3 +0.5	MCK	[$12\text{ nm}, 1^{\circ}, Mb4.7 51\mu m, 20^{\circ};Z,Ms4.9$]				

Oxford University (Stoneley, 1970). This task was taken over by the International Seismological Center (ISC) in 1964. ISC is funded by its member organizations and a few large research agencies and is thus independent of any one country. In order to work with the original analog waveform data, researchers had to write to each individual agency to request copies. With the creation of WWSSN (World Wide Standard Seismic Network) in 1960, the situation was made simpler by having microfiche copies of all WWSSN records stored in one place at the USGS.

With the introduction of digital seismic stations and the internet, the situation has become much easier. All data from major broadband stations are stored at a few global data centers of which the IRIS (Incorporated Research in Seismology) data center in the US is the most important. However, these data centers only store a fraction of the data collected globally, since the centers mostly have data from broadband stations. Thus in order to get data from other networks and stations, the user must still in many cases, request data manually which implies sending a formal request. The trend is now for many networks to make all data available on the internet as soon as it has been recorded. Objection against this practice is that the local network users should get a chance to do research with the data before others and that the sponsors of the network want to control who gets the data. However, the local network also needs data from nearby stations so the benefits of completely open data access outweigh the disadvantages. Also, many networks are operated to also produce data for science, so science done by others or in collaboration can help to argue the case for network funding in the future. ***It is therefore strongly advised to share all data on the internet.*** There are 3 ways to do this:

- The simplest way is to put all data on an ftp server and this does not require any special software. The disadvantage is that the outside user must know exactly what data is desired since there is no search facility.
- Real-time exchange of waveform data allows for easy integration with the automated processing system and the associated interactive processing.
- Integrate a web based search system with the data base. This requires more work, unless it is already built into the data base system.

In order to share data, it is important that it is available in one of the recognized formats, see Chapter 3. Data can either be parameter data or waveform data.

From the ISC, data can be requested back to 1964. The user can request only hypocenters or hypocenters with associated information (headers) and readings. The data will be displayed on the screen and can then be saved by the user.

The most comprehensive data center for waveform data is the IRIS data center in Washington. The center has several options for selecting data in either the continuous data base or selecting waveform data associated with an event. A very user friendly interface for getting event data is Wilber, see Fig. 10.11. The event is selected interactively from the epicenter map and the user can then select, stations, channels and time window for data extraction. Several of the recognized formats are used. Selecting data for e.g. 10 stations only takes a few minutes. Wilber only have

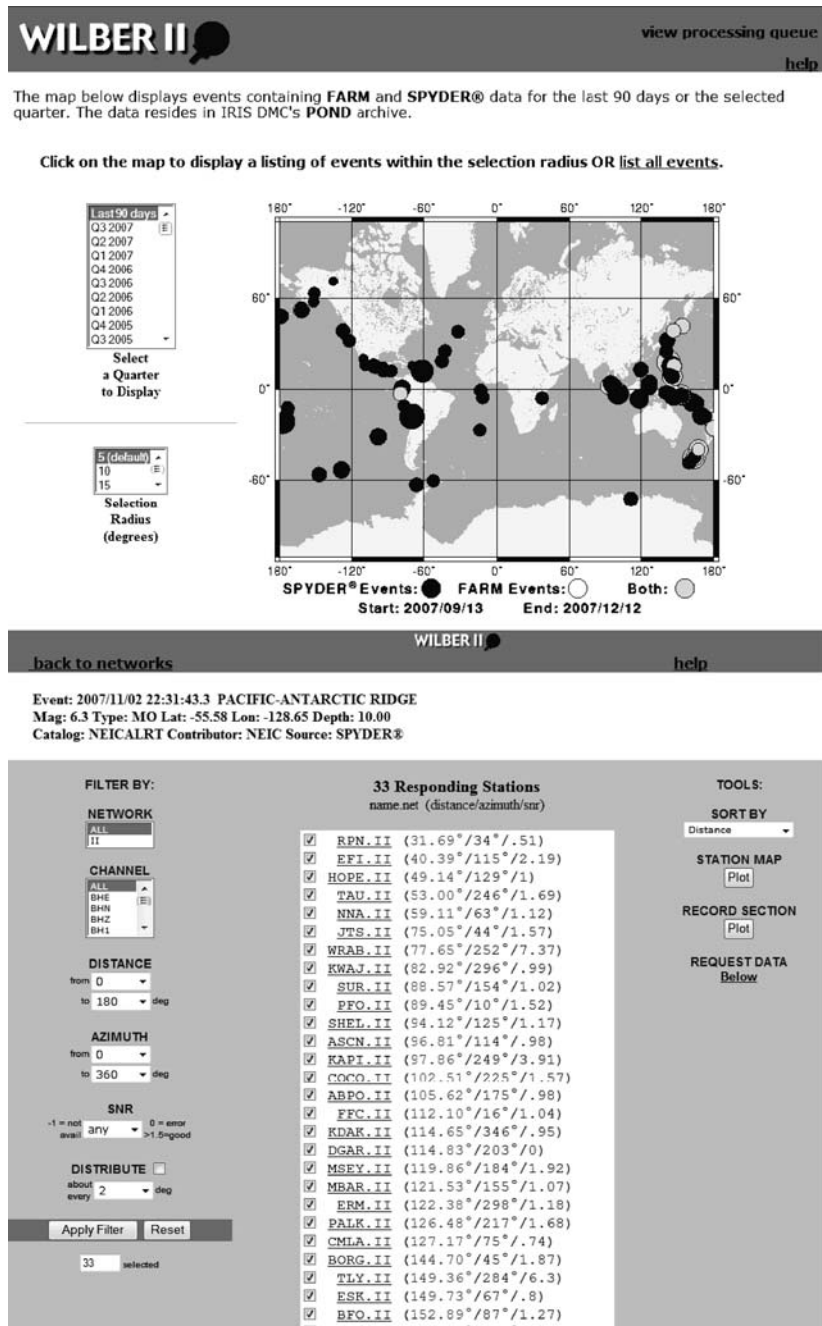


Fig. 10.11 The IRIS data center Wilber interface. On top is shown the initial event selection screen and on the bottom the station selection. Only GSN stations are shown

pre-selected events, mostly larger than 5, so smaller events must be extracted using a different software directly from the ring buffer system using start and stop times.

Selecting data from global data centers to augment the data available for a local region is a fast and simple method of improving the local data base.

10.4 Earthquake Statistics

Once a certain amount of data become available, the data can be checked for completeness and detection level.

Completeness and b-value: The number of earthquakes in a given time period occurring in different magnitude ranges can be described by the so-called Gutenberg-Richter linear relation

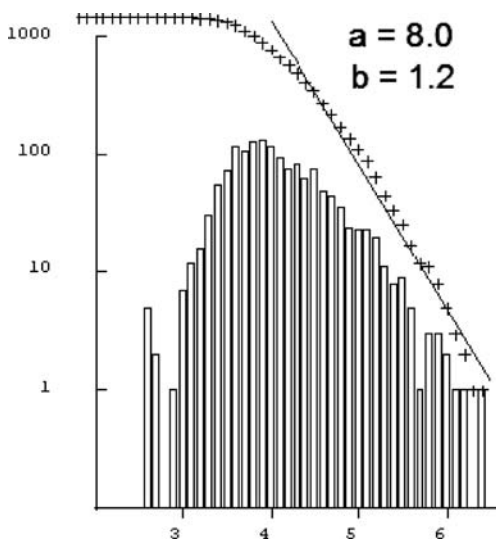
$$\log N = a - b M \quad (10.1)$$

where N is the number of earthquakes with magnitude greater than or equal to M (cumulative number) occurring in a the given time period. The constant a is the number of earthquakes with magnitude zero while b (so-called *b-value*) often is a constant near 1. This means e.g. that there should be 10 times more events with magnitude 3 than 4 etc. The empirical Gutenberg-Richter relation has turned out to be valid for both the global occurrence of earthquakes as well for smaller regions and can therefore be a useful tool for characterizing a particular region. The *a-value* is a quantitative measure of the level of activity while the *b-value* describes the relative number of small and large events in the time interval and it can be an indication of the tectonics of a region. A high *b-value* (~ 2) is typical of earthquake swarms while a low *b-value* indicates high stress conditions (Stein and Wysession, 2003). It has commonly been observed and theoretically argued that the *b-value* decreases before some large earthquakes (Mogi, 1985) is due to stress changes. The relation between stress and *b-value* can e.g. be observed in some subduction zones, see e.g. Katsumata (2006).

The values a and b are also important parameters in seismic hazard analysis (Reiter, 1990). The simplest way to determine a and b is then to calculate N for different magnitude intervals and plot $\log N$ as a function of M . Figure 10.12 shows an example. The number of events continues to increase until magnitude 4, but below magnitude 3.8, the number of events starts to decrease. When the cumulative number of events stops increasing linearly, we have reached the network detection threshold, which is defined as the lower magnitude limit by which the network no longer detects all the events. In this case it seems to be around 4.1. This method of finding the network detection threshold is very simple and can be used for all networks. The *b-value* is a bit higher than 1.0 and the linear fit is not very good. This is not unusual and in this case, taking a year of data might have smoothed out the curve. So what does the *a-value* of 8 mean? Simply that 10^8 events of magnitude 0 are expected to occur globally in one month. We can also use (10.1) to calculate how many events we expect statistically at any other

Fig. 10.12

Gutenberg-Richter relation for events located by ISC for January 2002. The magnitude is m_b determined by ISC. The bars are the number of events in each magnitude (interval 0.1) and the “+” are the cumulative number of events. The line is the least squares line for the magnitude interval 4 – 6.5



magnitude. Inserting e.g. $M = 8$ in (10.1) gives $N = 0.025$ events per month or 0.3 events per year. This means one $M = 8$ every 3. year, which is a bit less than expected. The a and b -values can also be determined by other statistical methods, for more details see e.g. Gibowicz and Kijko (1994). The most common other method is the maximum likelihood method (Aki, 1965). The ZMAP software by S. Wiemer allows to analyze the changes in b-value with time and space (Wiemer, 2001) (<http://www.seismo.ethz.ch/staff/stefan/ETHZ.html>).

Events in time: The seismicity rate on a global scale is almost constant in time while in smaller areas it can vary significantly, particularly due to earthquake swarms and aftershocks. So it can be useful to plot the seismicity as a function of time. If the detection threshold is constant in a particular area, all events can be plotted. However if the detection threshold is variable e.g. due to changing noise conditions or uneven reporting, only events above the largest detection threshold should be used to investigate the event distribution in time. Since we expect close to constant seismicity rate, checking the number of events with time can also detect obvious network down times. Figure 10.13 shows an example. Only events where ISC report one of the magnitudes larger or equal to 5 have been used. For January 2002, the seismicity rate is fairly constant with 4 events per day. This is also the case for December 2004 until December 26, when the $M_w = 9.3$ Sumatra event occurs, which gives numerous aftershocks. Notice the exponential decay of number of aftershocks per day after the occurrence of the main event. This is typical for aftershocks and can be modeled using Omori's law (Stein and Wysession, 2003)

$$n = \frac{C}{(K + t)^P} \quad (10.2)$$

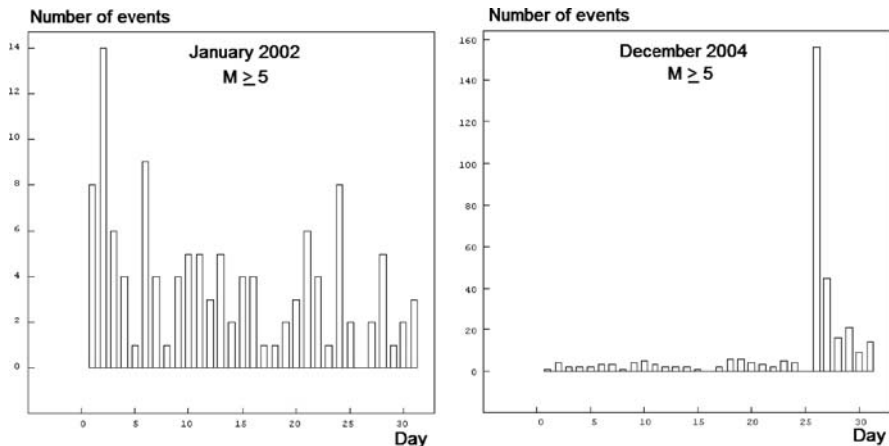


Fig. 10.13 Rate of seismicity (events/day) for 2 different months as reported using the ISC data base

where n is the frequency of aftershocks at time t after the mainshock and K , C and P are fault dependent constants. P is typically around 1. Searching a data set for aftershocks is used to clean catalogs for seismic hazard calculations, which should use data sets without aftershocks.

10.5 Software

There is a wealth of programs available, mostly in the public domain, for processing earthquake data. Most of the programs are open source and there are programs for several computer platforms. The dominant platforms are Unix (usually Sun Solaris) and Linux although many programs also are available for Windows. Most non graphical programs are written in Fortran or C, while graphical programs are mostly written in C, C++ or Java. It is not possible to mention all programs and therefore, at the end of the book, we list web sites where programs are available.

Major seismic instrument companies also have commercial software for processing, which range from rather simple to very sophisticated. Such systems could be very useful for new turnkey systems, however, it should be checked carefully that the system is able to do what is needed for a particular network. In particular, it is important that a processing system easily can integrate data, whether waveforms or parameters, from other networks. The description below of complete systems could be a guide to what is desirable and possible, also for a commercial system.

One of the obstacles for using different programs for processing earthquake data has been the many different formats used. Waveform formats have been standardized (see Chapter 3), while input and output parameter formats can vary between different programs making it necessary to make conversions between formats. For

daily processing, it is therefore desirable to use a group of programs which all use the same formats and/or share the same data base. This description of programs will therefore focus on program systems where most of the programs needed for daily processing are included and integrated into one system. Additionally, non-integrated mapping systems, location programs and phase picking programs in common use will also be mentioned. Only open source programs will be described.

The programs for location are described in Chapter 5 and for seismogram plotting in Chapter 4.

An overview of some seismological software is also given in the IASPEI International Handbook of Earthquake and Engineering Seismology (Lee et al., 2003a).

10.5.1 Processing Systems for Routine Operation

A processing system will be defined as an integrated system of programs which at least can

- Organize the data.
- Search in the data.
- Plot signals and pick phases.
- Locate the events and calculate magnitude.
- Do spectral analysis.
- Do fault plane solutions.
- Plot epicenters.

The system must easily be able to shift from one operation to the other. Table 10.5 gives an overview of public domain systems which can do part or all of this. Each system has a short description below. As it can be seen, there is not a lot of choice for integrated complete systems which have the capabilities needed for daily processing. While in our view it is desirable to have a well integrated system, it is also possible to combine individual tools depending on the requirements.

Formats: The systems might support other formats than indicated in the table, however only the most common formats are mentioned. For information about the waveform formats, see Chapter 3 and for parameter formats, see Chapter 10.

Continuous data: This means there is provision for handling continuous data for many channels. The software should be able to, seamlessly, display several channels, zoom, filter and extract out subsections.

Information about programs was taken from available public information and newer versions of the program might have enhanced capabilities not yet documented.

Some systems might have to download additional software so they are not installed in one go.

Table 10.5 Common public domain processing systems. Abbreviations are: Y: YES, N: No, Under platform: W: Windows, L: Linux, U: Unix. Data base: F: Flat file, R: Relational. X: X-graphics, Waveform formats: M: MiniSEED, G: GSE, S: SEISAN, C: CSS, A: SAC. Parameter formats: H71: HYPO71, S: SEISAN, C: CSS Magnitudes: C: Coda, L: Local, B: m_b , S: M_s , W: M_w , SEISAN can in addition calculate M_s and m_b

	GEOTool	Seismic handler	Giant-PITSA	SAC	SEISAN
Platform	LU	L	LU	LU	WLU
Data base	R	F	R	N	F
Search		N	Y	N	Y
Phase pick	Y	Y	Y	Y	Y
Local location	Y	Y	Y	Y	Y
Global location	Y	Y	N	N	Y
Ground simulation		Y	Y	Y	Y
Magnitudes		LBS	CL		CLBSW
Fault plane solution		N	Y		Y
Continuous data	Y	Y	N	N	Y
W formats	GC	MG	G	GCA	SMGA
Parameter formats	C	Local	H71		S
Graphics interface	X	X	X	X	X, W
Map programs	Y			Y	Y
Display t. times	Y	Y	Y	Y	Y
Three comp. analysis		Y	Y		Y
Rotation		Y	Y	Y	Y
Particle motion		Y	Y		Y
Spectral analysis	Y	N	Y	Y	Y
Fault plane solution		N	Y		Y
Array processing	Y	Y		Y	Y

GEOTool is an analysis system with strong visual capability. The software is released by the CTBTO (Comprehensive Testband Treaty organization) to national data centers, and thus not strictly open. However, it is open source and widely used within the CTBTO context. Being developed for monitoring at National Data Centers within CTBTO, GEOTool allows for easy integration of array with single station data, and analysis of data other than seismic. The strength of GEOTool is the modular design of the system and the link between the different components of the software such as data display and manipulation, mapping tool, array processing, display of travel times, spectra, etc. All data (parametric and waveform) can be stored in a CSS database either in files or a relational database.

SAC (Seismic Analysis Code) is a general purpose interactive program designed for the study of sequential signals, especially time series data. Emphasis has been placed on analysis tools used by research seismologists in the detailed study of seismic events. Analysis capabilities include general arithmetic operations, Fourier transforms, spectral estimation techniques, IIR and FIR filtering, signal stacking, decimation, interpolation, correlation, and seismic phase picking. SAC also contains an extensive graphics capability. SAC is the most used program for many special operations done in connection with seismological research like receiver function analysis and surface wave analysis, see Chapter 2. However, SAC is not made specifically for daily processing and in order to use it in this way, the user must

tailor the system for his needs, which involves writing of scripts and use of SAC macros.

GIANT is an analysis system for the consistent analysis of large, heterogeneous seismological data sets. It provides a GUI between a relational database and numerous analysis tools (such as HYPO71, FOCMEC, PREPROC, SIMUL, PITSA, etc.). The GIANT system is currently supported on Solaris and Linux and uses the X11 graphics system. The underlying concepts are discussed in Rietbrock and Scherbaum (1998). The system is mostly used for large data sets requiring automatic processing such as extensive aftershock recordings.

Seismic Handler SH. The main features are built around reading traces from continuous data streams in Seism-compressed MiniSEED files. Additionally supported formats are event data from GSE, AH and *Q* (private format of SH) files. The system can use a set of standard filters (simulation filters and Butterworth filters) on broadband input traces. For array processing there is computation of teleseismic beam traces using array-beamforming or fk-algorithm, determination of slowness and back-azimuth of an incoming wavefront. Location of teleseismic events can be done using global travel time tables based on array methods or relative travel times, determination of focal depth using depth phases. Location of regional and local events are using the LOCSAT program, and a flexible interface is provided for integration of other location programs. SH is particularly well suited for teleseismic data with many advanced features for trace manipulations and automatic or semiautomatic phase picks.

SEISAN. The SEISAN seismic analysis system is a complete set of programs and a simple database for analyzing earthquakes from analog and digital data. With SEISAN it is possible for local and global earthquakes to enter phase readings manually or pick them with a cursor, locate events, edit events, determine spectral parameters, seismic moment, azimuth of arrival from 3-component stations and plot epicenters. The system consists of a set of programs tied to the same database. Using the search programs it is possible to use different criteria to search the database for particular events and work with this subset without extracting the events. Additionally, SEISAN contains some integrated research type programs like coda *Q* and synthetic modeling. The data is organized in a database like structure using the file system. The smallest basic unit is a file containing original phase readings (arrival times, amplitude, period, azimuth, and apparent velocity) for one event. The name of that file is also the event ID, which is the key to all information about the event in the database. The programs are mostly written in Fortran, a few in C and almost all source codes are given, so the user should be able to fix bugs and make modifications.

10.5.2 Mapping Software

Epicenter and hypocenter plots are important elements of a processing system. Some programs are integrated with the system, some systems provide output for outside programs while others are completely free stranding. In the following, some system independent mapping programs will be described.

GMT (Generic Mapping Tools) is by far the most versatile and popular software system for plotting maps and associated information (<http://gmt.soest.hawaii.edu/>). GMT runs in the Unix environment including Cygwin (Unix simulation under Windows). There are many predefined GMT scripts available and also many program systems to create GMT scripts. Several systems provide output suitable for GMT or GMT scripts.

The description on the GMT home page is as follows: GMT is an open source collection of ~60 tools for manipulating geographic and Cartesian data sets (including filtering, trend fitting, gridding, projecting, etc.) and producing Encapsulated PostScript File (EPS) illustrations ranging from simple x-y plots via contour maps to artificially illuminated surfaces and 3-D perspective views. GMT supports ~30 map projections and transformations and comes with support data such as GSHHS coastlines, rivers, and political boundaries.

Geographic Information System (GIS): A number of open-source and commercial GIS software packages are available. The main functionality of these packages is the interactive display of geographic data. These packages are thus well suited to display earthquake data together with other geographic or geological data. The software can have built-in functionality to do geospatial processing and to perform searches to e.g. display subsets of data. It is also possible to write and add routines for a specific task. While it is possible to assemble one's own data sets, there are also a number of open data sets available through the Internet.

Google Map and Google Earth: Google provides an interface to their map systems which can be used in seismology to display epicenters and other information. The user simply has to provide an input file in a particular format and the seismic information is displayed on the Google maps, see Fig. 10.4 for an example. An internet connection is required. Some systems or programs will provide output files ready for Google.

SEISMICITY VIEWER (by A Lomax, <http://alomax.free.fr/seismicity/>) displays earthquake locations in 3D as probability density functions, maximum-likelihood hypocenters, Gaussian expectation hypocenters and Gaussian confidence ellipsoids. Station locations, associated P and S residuals, and geographic and geologic features are also displayed. The 3D image can be interactively rotated, zoomed and viewed along the coordinate axes in perspective or orthographic projections. The events can be viewed individually, all together, or sequentially as an animation.

10.6 Exercises

Exercise 10.1 Determine b-value

Table 10.6 gives a catalog of earthquakes in Western Norway.

- Calculate the number of earthquakes in 0.2 magnitude intervals (use coda magnitude), and the accumulative numbers N . Show table.
- Plot $\log N$ vs. M and determine the *b-value* using coda magnitude. Give the relation with both a and b .

Table 10.6 Earthquake catalog for Western Norway. Abbreviations are: HRMM: Hour and minute, s: Seconds and h: Depth (km)

Year	Date	HRMM	Sec	Latitude	Longitude	h	M _c	M _L
2003	7 2	1237	56.6	59.246	6.105	9.4	0.9	
2003	710	1303	7.0	59.292	5.616	11.5	1.4	1.2
2003	718	1930	22.1	60.871	5.005	0.0	1.4	1.1
2003	721	1428	57.4	60.952	1.437	15.0	2.5	1.5
2003	722	0335	26.3	60.927	1.627	15.0	2.2	1.4
2003	729	1542	37.7	60.696	3.744	15.0	2.3	2.5
2003	8 2	1912	41.6	60.108	7.204	19.7	1.1	1.0
2003	8 4	1943	52.6	60.692	5.507	0.1	1.0	0.6
2003	811	1349	42.5	60.291	4.894	52.3	0.8	1.5
2003	812	1537	15.1	60.192	2.486	15.0	1.8	1.3
2003	821	0723	1.4	60.086	4.791	0.0	2.2	2.0
2003	821	1159	3.0	60.839	5.029	0.6	1.4	
2003	825	1321	21.6	59.904	6.958	3.9	0.8	
2003	825	1823	18.0	59.281	5.298	20.0	1.3	1.1
2003	827	1621	32.5	59.075	5.812	0.0	1.8	1.8
2003	828	1501	42.5	60.694	5.594	0.0	1.3	
2003	9 3	1334	38.5	59.242	5.706	13.1	1.6	
2003	9 4	1402	21.2	60.863	4.987	15.0	1.2	0.8
2003	9 5	1440	2.0	60.567	4.966	0.0	0.6	0.7
2003	9 5	2117	57.1	59.474	5.675	15.0	2.2	1.9
2003	9 8	1027	15.2	59.646	5.581	0.0	1.5	1.0
2003	9 9	1332	36.6	59.211	6.178	15.6	1.3	1.0
2003	9 9	1803	53.0	60.691	5.378	0.1	1.6	0.8
2003	912	1619	11.9	60.443	4.815	0.6	1.3	1.4
2003	917	0155	30.4	59.604	7.316	15.3	1.7	1.4
2003	917	1435	41.7	59.349	6.077	0.3	1.5	1.1
2003	918	1806	38.7	59.759	7.061	17.5	1.3	
2003	919	0818	2.0	60.040	4.719	0.0	2.0	2.1
2003	920	1315	42.4	60.247	5.216	12.4	1.0	1.4
2003	920	1709	20.5	59.694	7.087	15.5	1.4	
2003	925	1131	45.7	60.466	5.407	0.0	0.8	
2003	928	1654	54.1	60.000	5.861	0.0	1.4	1.2
2003	928	2025	8.4	60.346	4.738	0.0	1.7	1.5
2003	929	1552	29.2	60.290	5.128	0.0	1.0	
2003	10 2	1330	35.3	59.153	6.200	15.0	1.3	
2003	10 2	1611	4.4	60.817	4.912	0.1	1.5	1.0
2003	10 9	0108	0.9	60.163	5.314	0.1	1.2	1.3
2003	1014	1355	39.1	60.501	4.919	0.0	1.5	0.9
2003	1020	0508	10.6	60.417	6.012	13.0	0.9	0.9
2003	1020	1331	16.0	59.378	6.034	13.8	1.4	
2003	1020	1620	21.0	59.150	7.611	11.3	1.7	
2003	1021	1432	41.3	60.674	5.460	0.0	1.6	0.9
2003	1022	1400	44.5	60.519	4.944	0.0	1.3	
2003	1023	1419	18.9	60.300	5.295	3.5	1.1	
2003	1028	1803	55.8	60.758	5.242	1.5	1.2	
2003	1031	1605	51.0	60.832	5.013	9.2	1.5	
2003	11 6	0343	50.8	60.747	4.573	0.0	0.9	1.1
2003	11 9	0459	58.9	59.619	7.105	12.6	1.6	0.8
2003	1110	2302	54.9	59.215	5.805	0.0	1.2	1.0
2003	1113	1301	3.6	60.512	5.349	0.0	0.7	1.4
2003	1113	1306	21.2	60.677	5.487	0.1	1.4	0.8
2003	1120	1109	31.8	59.333	5.657	2.3	1.6	1.2
2003	1121	1310	8.1	60.477	5.350	0.0	0.5	0.8
2003	1122	1908	58.2	60.218	2.545	15.0	2.6	2.2
2003	1125	1832	15.8	59.665	2.465	0.0	1.9	1.1
2003	1127	0317	49.6	59.914	6.215	0.0	0.7	0.6
2003	1128	1252	0.6	60.276	5.301	6.2	0.2	0.5
2003	1128	1529	31.3	60.189	5.312	11.4	0.8	0.8
2003	12 1	1404	6.6	60.713	5.339	0.0	1.6	1.1
2003	12 1	1501	52.0	60.162	5.237	16.1	0.7	0.4
2003	12 4	1449	16.1	60.544	4.959	0.1	1.4	1.3
2003	12 8	2353	9.8	60.323	7.252	3.1	1.8	1.7
2003	12 9	1400	1.2	59.492	4.473	0.1	1.2	1.6
2003	1211	1404	50.0	60.291	5.294	0.0	0.8	1.1
2003	1211	1454	29.8	60.695	5.568	1.8	1.4	0.8
2003	1212	0007	13.4	60.489	4.734	21.1	1.1	1.0
2003	1212	0315	6.7	59.857	6.523	0.0	1.5	1.3
2003	1212	1516	7.0	60.846	5.102	1.5	1.4	0.6
2003	1217	1433	40.9	59.315	5.675	0.0	1.5	1.1
2003	1219	1020	30.0	59.376	6.078	0.1	1.1	
2003	1219	1328	25.4	60.669	5.558	0.1	1.5	
2003	1225	1400	27.7	59.655	6.000	15.0	1.9	1.8

- How often will you statistically get a $M \geq$ earthquake?
- Can the detection threshold be estimated?

Exercise 10.2 Time of day distribution

Use the data in Table 10.6 to make a time of day distribution:

- Count the number of events for each hour.
- Plot the number of events as a function of the hour.
- Evaluate if the data contains explosions.

Computer exercises

- Data base manipulation (SEISAN).
- Epicenter and hypocenter plots, error ellipse.
- Get data from other agencies.
- Time of day, number per month.
- b-value.

References

- Abercrombie, R. E. (1995). Earthquake source scaling relationships from -1 to 5 M_L using seismograms recorded at 2.5 km depth. *J. Geophys. Res.* 100, 24015–24036.
- Abercrombie, R. E. (1997). Near-surface attenuation and site effects from comparison of surface and deep borehole recordings. *Bull. Seism. Soc. Am.* 87, 731–744.
- Abercrombie, R. E. (1998). A Summary of attenuation measurements from borehole recordings of earthquakes: The 10 Hz transition problem. *Pure Appl. Geophys.* 153, 475–487.
- Abubakirov, I. R. and A. A. Gusev (1990). Estimation of scattering properties of lithosphere of Kamchatka based on Monte-Carlo simulation of record envelope of near earthquake. *Phys. Earth. Planet. Inter.* 64, 52–67.
- Aki, K. (1965). Maximum likelihood estimate of b in the formula $\log N = a - bM$ and its confidence limits. *Bull. Earthq. Res. Inst. Univ. Tokyo*, 43, 237–239.
- Aki, K. (1980). Attenuation of shear waves in the lithosphere for frequencies from 0.05 to 25 Hz. *Phys. Earth. Planet. Inter.* 21, 50–60.
- Aki, K. (1991). Summary of discussions on coda waves at the Istanbul IASPEI meeting. *Phys. Earth Planet. Int.* 67, 1–3.
- Aki, K. and B. Chouet (1975). Origin of coda waves: Source, attenuation and scattering effects. *J. Geophys. Res.* 80, 3322.
- Aki, K. and P. G. Richards (2002). Quantitative seismology. Second Edition, ISBN 0-935702-96-2, University Science Books, Sausalito, 704 pp.
- Akinci, A. L., Malagnini, R. B., Herrmann, N. A., Pino, L., Scognamiglio and H. Eyidogan (2001). High-frequency ground motion in the Erzincan region, Turkey: Influences from small earthquakes. *Bull. Seism. Soc. Am.* 91, 1446–1455.
- Almendros, J., J. M. Ibáñez, G. Alguacil, E. Del Pezzo and R. Ortiz (1997). Array tracking of the volcanic tremor source at Deception Island, Antarctica. *Geophys. Res. Lett.* 24, 3069–3072.
- Allan, T. I., P. R. Cummins, T. Dhu and J. F. Schneider (2007). Attenuation of ground-motion spectral amplitudes in Southeastern Australia. *Bull. Seism. Soc. Am.* 97, 1279–1292.
- Alsaker, A., L. B. Kvamme, R. A. Hansen, A. Dahle and H. Bungum (1991). The M_L scale in Norway. *Bull. Seism. Soc. Am.* 81, 2, 379–389.
- Ambeh, W. B. and J. D. Fairhead (1989). Coda Q estimates in the Mount Cameroon volcanic region, West Africa. *Bull. Seism. Soc. Am.* 79, 1589–1600.
- Ambraseys, N. N. (1990). Uniform magnitude re-evaluation of European earthquakes associated with strong-motion records. *Earthq Eng Struct Dyn*, 19, 1–20.
- Ammon, C. J. (1991). The isolation of receiver effects from teleseismic P waveforms. *Bull. Seism. Soc. Am.* 81, 2504–2510.
- Anderson, K. R. (1981). Epicenter location using arrival time order. *Bull. Seism. Soc. Am.* 71, 541–545.
- Anderson, K. R. (1982). Robust earthquake location using M-estimates. *Phys. Earth. Plan. Inter.* 30, 119–130.
- Anderson, J. G. and S. Hough (1984). A model for the shape of the Fourier amplitude spectrum of acceleration at high frequencies. *Bull. Seism. Soc. Am.* 74, 1969–1994.

- Anderson, J., W. E. Farrell, K. Garcia, J. Given and H. Swanger (1990). Center for seismic studies version 3 database: Schema reference manual. Technical report C90-01, Science Applications International Corporation, Center for Seismic Studies, Arlington.
- Atakan, K., M. Ciudad-Real and R. Torres (2004a). Local site effects on microtremors, weak and strong ground motion in San Salvador, El Salvador. In: Bommer, J. J., W. I. Rose, D. L. Lopez, M. J. Carr, and J. J. Major (Eds.) Natural hazards in El Salvador. Geological Society of America, Special Paper SPE375, 321–328, ISBN No. 0-8137-2375-2.
- Atakan, K., A.-M. Duval, N. Theodulidis, P.-Y. Bard and the SESAME Team (2004b). The H/V spectral ratio technique: Experimental conditions, data processing and empirical reliability assessment. Proceedings of the 13th World Conference on Earthquake Engineering. Paper No.2268, 1–6 August 2004, Vancouver, Canada.
- Atkinson, G. M. (2004). Empirical attenuation of ground-motion spectral amplitudes in Southeastern Canada and Northeastern United States. Bull. Seism. Soc. Am. 94, 1079–1095.
- Bakun, W. H. and W. Joyner (1984). The M_L scale in Central California. Bull. Seim. Soc. Am. 74, 5, 1827–1843.
- Bakun, W. H. and A. G. Lindh (1977). Local magnitudes, seismic moments, and coda durations for earthquakes near Oroville, California. Bull. Seism. Soc. Am. 67, 615–629.
- Bard, P.-Y. (1998). Microtremor measurements: A tool for site effect estimation? Proceeding of the Second International Symposium on the Effects of Surface Geology on Seismic Motion. Yokohama, Japan, 3, 1251–1279.
- Baskoutas, I. (1996). Dependence of coda attenuation on frequency and lapse time in Central Greece. Pure Appl. Geophys. 147, 483–496.
- Baumbach, M., D. Bindi, H. Grosser, C. Milkereit, S. Paralai, R. Wang, S. Karakisa, S. Zünbüll and J. Zschau (2003). Calibration of an M_L scale in Northwestern Turkey from 1999 Izmit aftershocks. Bull. Seism. Soc. Am. 93, 2289–2295.
- Baumont, D., A. Paul, S. Beck and G. Zandt (1999). Strong crustal heterogeneity in the Bolivian Altiplano as suggested by attenuation of Lg waves. J. Geophys. Res. 104, 20287–20305.
- Benz, H. M., A. Frankel and D. M. Boore (1997). Regional Lg attenuation for the continental United States. Bull. Seism. Soc. Am. 87, 606–619.
- Bindi, D., D. Spallarossa, C. Eva and M. Cattaneo (2005). Local and duration magnitudes in Northwestern Italy, and seismic moment versus magnitude relationships. Bull. Seism. Soc. Am. 95, 592–604.
- Bormann, P. (2002). IASPEI new manual of seismological observatory practice. P. Bormann (Ed.) GeoForschungsZentrum, Potsdam.
- Bormann, P., R. Liu, Z. Xu, X. Ren, R. Gutdeutsch, D. Kaiser and S. Castellaro (2007). Chinese National Network magnitudes, their relations to NEIC magnitudes, and recommendations for new IASPEI magnitude standards. Bull. Seism. Soc. Am. 97, 114–127.
- Bormann, P. and J. Saul (2008). The new IASPEI standard broadband magnitude m_B . Seism. Res. Lett. 79, 698–705.
- Bormann, P. and J. Saul (2009a). Earthquake magnitude. In: Meyers, A. (Ed.) Encyclopedia of complexity and systems science, Vol. 3, Springer, Heidelberg - New York, 2473–2496.
- Bormann, P. and J. Saul (2009b). A fast non-saturating magnitude estimator for great earthquakes. Seism. Res. Let. 80, 808–816.
- Bormann, P., R. Liu, Z. Xu, K. Ren, L. Zhang and S. Wendt (2009). First application of the new IASPEI telesismic magnitude standards to data of the China National Seismographic Network. Bull. Seism. Soc. Am. 99, 1868–1891.
- Bouchon, M. (1981). A simple method for calculating Green's functions for elastic layered media. Bull. Seism. Soc. Am. 71, 959–972.
- Brune, J. (1970). Tectonic stress and seismic shear waves from earthquakes. J. Geophys. Res. 75, 4997–5009.
- Buland, R. (1976). The mechanics of locating earthquakes. Bull. Seism. Soc. Am. 66, 173–187.
- Buland, R. and C. H. Chapman (1983). The computation of seismic travel times. Bull. Seism. Soc. Am. 73, 1271–1303.

- Bullen, K. E. (1963). An introduction to the theory of seismology. Cambridge University Press, New York, 380 pp.
- Bungum, H., E. S. Husebye and F. Ringdal (1971). The NORSAR array and preliminary results of data analysis. *Geoph. J. R. Astron. Soc.* 25, 115–126.
- Bungum, H. and E. S. Husebye (1974). Analysis of the operational capabilities for detection and location of seismic events at NORSAR. *Bull. Seism. Soc. Am.* 64, 637–656.
- Bungum, H., A. Alsaker, L. B. Kvamme and R. A. Hansen (1990). Seismicity and seismotectonics of Norway and nearby continental shelf areas. *J. Geophys. Res.* 96, 2249–2269.
- Bødvarsson R., S. T. Rognvaldsson, R. Slunga and E. Kjartansson (1999). The SIL data acquisition system at present and beyond year 2000. *Phys. Earth Planet. Int.* 113, 89–101.
- Båth, M. (1979a). Introduction to seismology. Birkhäuser Verlag, Basel. 428 pp.
- Båth, M. (1979b). Earthquakes in Sweden 12951–1976. *Sveriges Geol. Und, C750, Årsbok* 72, 50 pp.
- Capon, J. (1969). High-resolution frequency-wavenumber spectrum analysis. *Proc. IEEE*, 57, 1408–1418.
- Carpenter, P. J. and A. R. Sanford (1985). Apparent Q for upper crustal rocks of the central Rio Grande Rift. *J. Geophys. Res.* 90, 8661–8674.
- Castellaro, S. and P. Bormann (2007). Performance of different regression procedures on the magnitude conversion problem. *Bull. Seism. Soc. Am.* 97, 1167–1175.
- Castello, B., M. Olivieri and G. Selvaggi (2007). Local and duration magnitudes determination for the Italian earthquake catalog, 1981–2002. *Bull. Seism. Soc. Am.* 97, 128–139.
- Červaný, V. and R. Ravindra (1971). Theory of seismic head waves. University of Toronto Press, Toronto, 312 pp.
- Chavez, D. E. and K. F. Priestley (1985). M_L observations in the Great Basin and M_0 versus M_L relationships for the 1980 Mammoth Lakes, California, earthquake sequence. *Bull. Seism. Soc. Am.* 75, 1583–1598.
- Chen, S. and G. M. Atkinson (2002). Global comparison of earthquake source spectra. *Bull. Seism. Soc. Am.* 92, 885–895.
- Chernobay, I. P. and I. P. Gabsatarova (1999). Source classification in northern Caucasus. *Phys. Earth Planet. Int.* 113, 183–201.
- Choy, G. L. and J. L. Boatwright (1988). Teleseismic and near-field analysis of the Nahanni earthquakes in the northwest territories, Canada. *Bull. Seism. Soc. Am.* 78, 1627–1652.
- Choy, G. L. and J. L. Boatwright (1995). Global patterns of radiated seismic energy and apparent stress. *J. Geophys. Res.* 100, 18205–18228.
- Choy, G. L. and J. Boatwright (2009). The energy radiated by the 26 December 2004 Sumatra-Andaman earthquake estimated from 10-minute P-wave windows. *Bull. Seism. Soc. Am.* 97, 18–24.
- Cipar, J. (1980). Teleseismic observations of the 1976 Friuli, Italy earthquake sequence. *Bull. Seism. Soc. Am.* 70, 963–983.
- Dahlen, F. A. and J. Tromp (1998). Theoretical global seismology. Princeton University Press, Princeton, 1025 pp.
- Dahlman, O., S. Mykkeltveit and H. Haak (2009). Nuclear test ban, converting political visions to reality. Springer, Dordrecht, 277 pp.
- Der, Z. A. and A. C. Lees (1985). Methodologies of estimating $t^*(f)$ from short period body waves and regional variations of $t^*(f)$ in the United States. *Geophys. J. R. Astr. Soc.* 82, 125–140.
- Di Giacomo, D., S. Parolai, P. Bormann, H. Grosser, J. Saul, R. Wang and J. Zschau (2010). Suitability of rapid energy magnitude determinations for rapid response purposes. *Geophys. J. Int.* 180, 361–374.
- Dindi, E., J. Havskov, M. Iranga, E. Jonathan, D. K. Lombe, A. Mamo and G. Tuttyomurugyendo (1995). Potential capability of the East African seismic stations. *Bull. Seism. Soc. Am.* 85, 354–360.
- Dineva, S. and R. Mereu (2009). Energy magnitude: A case study for Southern Ontario/Western Quebec (Canada). *Seism. Res. Let.* 80, 136–148.

- Doornbos, D. J. (Ed.) (1988). Seismological algorithms. Academic press, London, 469 pp.
- Douglas, A. (1967). Joint hypocenter determination. *Nature* 215, 47–48.
- Dreger, D. S. (2002). Time-domain moment tensor inverse code (TDMT_INV) version 1.1, user's manual, University of California, Berkeley.
- Dreger, D. S. (2003). TDMT_INV: Time domain seismic moment tensor INVersion. In: Lee, W. H. K., H. Kanamori, P. C. Jennings and C. Kisslinger (Eds.) International handbook of earthquake and engineering seismology. IASPEI, Academic Press, 81B, p. 1627.
- Dziewonski, A. M. and D. L. Anderson (1981). Preliminary reference Earth model. *Phys. Earth Planet. Int.* 25, 297–356.
- Dziewonski, A. M., T.-A. Chou and J. H. Woodhouse (1981). Determination of earthquake source parameters from waveform data for studies of global and regional seismicity. *J. Geophys. Res.* 86, 2825–2852.
- Ebel, J. E. and K. P. Bonjer (1990). Moment tensor inversion of small earthquakes in southwestern Germany for the fault plane solution. *Geophys. J. Int.* 101, 133–146.
- Engdahl, E. R., R. D. Van der Hilst and R. P. Buland (1998). Global teleseismic earthquake relocation with improved travel times and procedures for depth determination. *Bull. Seism. Soc. Am.* 88, 722–743.
- Eshelby, J. D. (1957). The determination of the elastic field of an ellipsoidal inclusion and related problems. *Proc. R. Soc. Lond. A* 241, 376–396.
- Evans, J. R., E. Eberhart-Phillips and C. H. Thurber (1994). User's manual for SIMULPS12 for imaging vp and vp/vs: A derivative of the "Thurber" tomographic inversion SIMUL3 for local earthquakes and explosions. USGS, Open-file Report 94-431.
- Frankel, A. (1994). Dense array recordings in the San Bernadino Valley of Landers Big Bear aftershocks: Basin surface waves, Moho reflections and three dimensional simulations. *J. Geophys. Res.* 96, 6199–6209.
- Frankel, A. and L. Wennerberg (1989). Microearthquake spectra from the Anza, California seismic network: Site response and source scaling. *Bull. Seism. Soc. Am.* 79, 581–609.
- Frohlich, C. (2006). Deep earthquakes. Cambridge University Press, Cambridge, 588 pp.
- Geiger, L. (1910). Herdbestimmung bei Erdbeben aus den Ankunftszeiten. Nachrichten von der Königlichen Gesellschaft der Wissenschaften zu Göttingen, Mathematisch-Physikalische Klasse, 331–349. (1912 translated to English by F. W. L. Peebles and A. H. Corey: Probability method for the determination of earthquake epicenters from the arrival time only. Bulletin St. Louis University 8, 60–71).
- Geller, R. J. (1976). Scaling relations for earthquake source parameters and magnitudes. *Bull. Seism. Soc. Am.* 66, 1501–1523.
- Gibowicz, S. J. and A. Kijko (1994). An introduction to mining seismology. Academic Press, New York, 399 pp.
- Goldstein, P., D. Dodge, M. Firpo, Lee Minner (2003). SAC2000: Signal processing and analysis tools for seismologists and engineers. In: Lee, W. H. K., H. Kanamori, P. C. Jennings and C. Kisslinger (Eds.) Invited contribution to, The IASPEI international handbook of earthquake and engineering seismology. Academic Press, London.
- Goldstein, P., A. Snoke, (2005). "SAC Availability for the IRIS Community", Incorporated Institutions for Seismology Data Management Center Electronic Newsletter. <http://www.iris.edu/news/newsletter/vol7no1/page1.htm>.
- Gordon, D. W. (1971). Surface-wave versus body-wave magnitude. *Earthquake Notes* 42, 3/4, 20–28.
- Greenhalgh, S. A. and R. Singh (1986). A revised magnitude scale for South Australian earthquakes. *Bull. Seism. Soc. Am.* 76, 757–769.
- Gupta, S. C., V. N. Singh and A. Kumar (1996). Attenuation of coda waves in the Garhwal Himalaya, India. *Phys. Earth Planet. Int.* 87, 247–253.
- Gusev, A. A. (1995). Vertical profile of turbidity and coda Q. *Geophys. J. Int.* 123, 665–672.
- Gutenberg, B. (1945a). Amplitudes of P, PP, and S and magnitude of shallow earthquakes. *Bull. Seism. Soc. Am.* 35, 57–69.

- Gutenberg, B. (1945b). Magnitude determination of deep-focus earthquakes. *Bull. Seim. Soc. Am.* 35, 117–130.
- Gutenberg, B. and C. F. Richter (1956). Magnitude and energy of earthquakes. *Annali di Geofisica*, 9, 1, 1–15.
- Haberland, C. and A. Rietbrock (2001). Attenuation tomography in the western central Andes: A detailed insight into the structure of a magmatic arc. *J. Geophys. Res.* 106, 11151–11167.
- Hanks, T. C. and M. Wyss (1972). The use of body-wave spectra in the determination of seismic source parameters. *Bull. Seism. Soc. Am.* 62, 561–589.
- Hanks, M. and H. Kanamori (1979). A moment magnitude scale. *J. Geophys. Res.* 84, 2348–2340.
- Hardbeck, J. L. and P. M. Shearer (2002). A new method for determining first-motion focal mechanisms. *Bull. Seism. Soc. Am.* 92, 2264–2276.
- Hardbeck, J. L. and P. M. Shearer (2003). Using S/P amplitude ratio to constrain the focal mechanisms of small earthquakes. *Bull. Seism. Soc. Am.* 93, 2434–2444.
- Harjes, H. P. and M. Henger (1973). Array Seismologie. *Zeitschrift für Geophysik*, 39, 865–905.
- Hauksson E. and P. Shearer (2005). Southern California hypocenter relocation with waveform cross-correlation: Part 1. Results using the double-difference method, *Bull. Seism. Soc. Am.* 95, 896–903.
- Havskov, J. and M. Macias (1983). A code-length magnitude scale for some Mexican stations. *Geofisica Int.* 22, 205–213.
- Havskov, J., S. Malone, D. McClurg and R. Crosson (1989). Coda Q for the state of Washington. *Bull. Seism. Soc. Am.* 79, 1024–1038.
- Havskov, J. and L. Ottemøller (2000). SEISAN earthquake analysis software. *Seis. Res. Lett.* 70, 532–534.
- Havskov, J. P. Bormann and J. Schweitzer (2002). Earthquake location. In: P. Bormann (Ed.) New manual of seismological observatory practice. GeoForschungsZentrum, Potsdam.
- Havskov, J. and L. Ottemøller (2002). SEISAN earthquake analysis and SEISNET network automation software. International handbook of Earthquake and Engineering Seismology, 81B, 15–16.
- Havskov, J. and G. Alguacil (2006). Instrumentation in earthquake seismology. Springer, Berlin, 358 pp.
- Havskov, J. and M. B. Sørensen (2006). New coda magnitude scales for mainland Norway and the Jan Mayen region. Norwegian National Seismic Network, Technical report No.19, University of Bergen.
- Havskov, J. and L. Ottemøller (Eds.) (2008). SEISAN: The earthquake analysis software for Windows, SOLARIS, LINUX and MACKINTOSH Version 8.2. Manual, Department of Earth Science, University of Bergen, Norway.
- Hellweg, M., P. Spudich, J. B. Fletcher and L. M. Baker (1995). Stability of coda Q in the region of Parkfield, California: A view from the US geological survey Parkfield dense seismic array. *J. Geophys. Res.* 100, 2089–2102.
- Herrmann R. B. and A. Kijko (1980). Short-period Lg magnitudes: Instrument, attenuation, and source effects. *Bull. Seism. Soc. Am.* 73, 1835–1850.
- Herrmann, R. B. and C. J. Ammon (2004). Computer programs in seismology, Source inversion, Saint Louis University.
- Horiuchi, S. and Y. Iio (2002). Stress drop distribution from micro-earthquakes at Ootaki, Nagano prefecture, Japan, obtained from waveform data by borehole stations. In: Fujinawa, Y. and A. Yoshida (Eds.) Seismotectonics in convergent plate boundaries. Terra Scientific Publishing Company, Tokyo. 381–391. <http://www.terrapub.co.jp/e-library/scpb/pdf/383.pdf>.
- Hoshiba, M. (1993). Separation of scattering attenuation and intrinsic absorption in Japan using the multiple lapse time window analysis of full seismogram envelope. *J. Geophys. Res.* 98, 15809–15824.
- Hough, S. E., J. G. Anderson, J. Brune, F. Vernon, III, J. Berger, J. Fletcher, L. Haar, T. Hanks and L. Baker (1988). Attenuation near Anza, California. *Bull. Seism. Soc. Am.* 78, 672–691.

- House, J. and J. Boatwright (1980). Investigation of two high stress drop earthquakes in the Shumagin seismic gap, Alaska. *J. Geophys. Res.* 85, 7151–7165.
- Houston, H. and H. Kanamori (1986). Source spectra of great earthquakes: Teleseismic constraints on rupture process and strong motion. *Bull. Seism. Soc. Am.* 76, 19–42.
- Hutton, L. K. and D. M. Boore (1987). The M_L scale in Southern California. *Bull. Seism. Soc. Am.* 77, 2074–2094.
- IASPEI (2005). Summary of magnitude working group recommendations on standard procedures for determining earthquake magnitudes from digital data. <http://www.iaspei.org/commissions/CSOI.html>.
- Jeffreys, H. and K. E. Bullen (1940). Seismological tables. British Association for the Advancement of Science, Burlington House, London.
- Jeffreys, H. and K. E. Bullen (1940, 1948, 1958, 1967, and 1970). Seismological tables, British Association for the Advancement of Science, Gray Milne Trust, London.
- Johnson, C. E., A. Bittenbinder, B. Bogaert, L. Dietz and W. Kohler (1995). Earthworm: A flexible approach to seismic network processing. *IRIS Newsletter* 14, 2, 1–4.
- Jost, M. L. and Herrmann, R. B. (1989). A student's guide to and review of moment tensors. *Seis. Res. Lett.* 60, 37–57.
- Julian, R. and D. L. Anderson (1968). Travel times. Apparent velocities and amplitudes of body waves. *Bull. Seism. Soc. Am.* 58, 339–366.
- Julian, B. R., A. D. Miller and G. R. Foulger (1998). Non-double-couple earthquakes. *Rev. Geophys.* 36, 525–549.
- Kanamori, H. (1977). The energy release in great earthquakes. *J. Geophys. Res.* 82, 2981–2987.
- Kanamori, H. (1983). Magnitude scale and quantification of earthquakes. *Tectonophysics*, 93, 185–199.
- Kanamori, H. and D. L. Anderson (1975). Theoretical basis of some empirical relations in seismology. *Bull. Seism. Soc. Am.* 65, 1073–1095.
- Kanasewich, E. R. (1973). Time sequence analysis in geophysics. The University of Alberta Press, Edmonton, 352 pp.
- Karnik, V., N. V. Kondorskaya, Yu. V. Riznichenko, Ye. F. Savarensky, S. L. Soloviev, N. V. Shebalin, J. Vanek, and A. Zatopek (1962). Standardization of the earthquake magnitude scales. *Studia Geophysica et Geodaetica*, 6, 41–48.
- Kasahara, K. (1981). Earthquake mechanics. Cambridge University Press, Cambridge, 248 pp.
- Katsumata, K. (2006). Imaging the high b-value anomalies within the subducting Pacific plate in the Hokkaido corner. *Earth Planet. Spa.* 58, 49–52.
- Keir, D., G. W. Stuart, A. Jackson and A. Ayele (2006). Local earthquake magnitude scale and seismicity rate for the Ethiopian Rift. *Bull. Seism. Soc. Am.* 96, 2221–2230.
- Kennett, B. L. N. (1991). IASPEI 1991 seismological tables. Australian National University, Research School of Earth Sciences, 167 pp.
- Kennett, B. N. L., S. Gregersen, S. Mykkeltveit and R. Newmark (1985). Mapping of crustal heterogeneity in the North Sea basin via the propagation of L_g -waves. *Geophys. J. R. Astr. Soc.* 83, 299–306.
- Kennett, B. L. N. and E. R. Engdahl (1991). Travel times for global earthquake location and phase identification. *Geophys. J. Int.* 105, 429–466.
- Kennett, B. L. N., E. R. Engdahl and R. Buland (1995). Constraints on seismic velocities in the Earth from traveltimes. *Geophys. J. Int.* 122, 108–124.
- Kennett, B. L. N. (2002). The seismic wavefield. Volume II: Interpretation of seismograms on regional and global scale. Cambridge University Press, Cambridge, 534 pp.
- Kikuchi, M. and H. Kanamori (1991). Inversion of complex body waves – III. *Bull. Seism. Soc. Am.* 81, 2335–2350.
- Kikuchi, M. and H. Kanamori (2003). Note on Teleseismic Body-Wave Inversion Program, User manual, <http://www.eri.u-tokyo.ac.jp/ETAL/KIKUCHI/>.
- Kissling, E., W. L. Ellsworth, D. Ebbart-Phillips and U. Kradolfer (1994). Initial reference model in local earthquake tomography. *J. Geophys. Res.* 99, 19635–19646.

- Klein, F. W. (2003). The HYPOINVERSE2000 earthquake location program. In: International handbook of earthquake engineering seismology. Academic press, Amsterdam, International Geophysics Series 81, 1619–1620.
- Kudo, K. (1995). Practical estimates of site response, state of the art report. Proceedings of the Fifth International Conference on Seismic Zonation, Nice, October 1995.
- Kulhánek, O. (1990). Anatomy of seismograms. Developments in Solid Earth Geophysics 18, Elsevier, Netherlands, 78 pp.
- Kumar, C. H. P., C. S. P. Sarma and M. Shekar (2007). Attenuation studies on local earthquake coda waves in the southern Indian peninsular shield. *Nat. Hazards* 40, 527–536.
- Kvamme, L. B. and J. Havskov (1989). Q in southern Norway. *Bull. Seism. Soc. Am.* 79, 1575–1588.
- Kvamme, L. B., R. A. Hansen and H. Bungum (1995). Seismic source and wave propagation effects of Lg waves in Scandinavia. *Geophys. J. Int.* 120, 525–536.
- Lacoss R. T., E. J. Kelly and M. N. Toksöz (1969). Estimation of seismic noise structure using arrays. *Geophysics* 34, 21–38.
- Lachette, C and P. Y. Bard (1994). Numerical and theoretical investigations of the possibilities and limitations of the “Nakamura Technique”. *J. Phys. Earth* 42, 377–397.
- Lahr, J. G. and J. A. Snoke (2003). The HYPOELLIPSE earthquake location program. In: International handbook of earthquake engineering seismology. Academic press, Amsterdam, International Geophysics Series 81, 1617–1618.
- Langston, C. A. and D. V. Helmberger (1975). A procedure for modeling shallow dislocation sources. *Geophys. J. R. Astr. Soc.* 42, 117–130.
- Langston, C. A. (1979). Structure under Mount Rainier, Washington, inferred from teleseismic body waves, *J. Geophys. Res.* 84, 4749–4762.
- Langston, C. A. (1982). Single-station fault plane solutions. *Bull. Seism. Soc. Am.* 72, 729–744.
- Langston, C. A., R. Brazier, A. A. Nyblade and T. J. Owens (1998). Local magnitude scale and seismicity rate for Tanzania, East Africa. *Bull. Seism. Soc. Am.* 88, 712–721.
- Lay, T. and T. C. Wallace (1995). Modern global seismology. Academic Press, San Diego, 521 pp.
- Lee, W. H. K. and J. C. Lahr (1975). HYPO71 (revised): A computer program for determining local earthquakes hypocentral parameters, magnitude, and first motion pattern. US Geological Survey Open-File Report 75-311, 100 pp.
- Lee, W. H. K., R. Bennet and K. Meagher (1972). A method of estimating magnitude of local earthquakes from signal duration. US Geol. Surv. Open-File Rep. 28 pp.
- Lee, W. H. K., H. Kanamori, P. C. Jennings and C. Kisslinger (Eds.) (2003a). International handbook of earthquake engineering seismology. Academic press, Amsterdam, International Geophysics Series, 81.
- Lee, W. H. K., J. C. Lahr and C. Valdez (2003b). The HYPO71 earthquake location program. In: International handbook of earthquake engineering seismology. Academic press, Amsterdam, International Geophysics Series, 81, 1641–1643.
- Lehmann, I. (1954). Characteristic earthquake records. *Geodætisk Instituts skrifter* 3. række bind XVIII, 33 pp.
- Lienert, B. R. and J. Havskov (1995). A computer program for locating earthquakes both locally and globally. *Seism. Res. Lett.* 66, 26–36.
- Liu, Z., M. E. Wuenscher and R. B. Herrmann (1994). Attenuation of body waves in the central New Madrid seismic zone. *Bull. Seism. Soc. Am.* 84, 112–1122.
- Lomax, A., J. Virieux, P. Volant and C. Berge (2000). Probabilistic earthquake location in 3D and layered models: Introduction of a Metropolis-Gibbs method and comparison with linear locations. In: Thurber, C. H. and N. Rabinowitz (Eds.) Advances in seismic event location. Kluwer Academic Publishers, Amsterdam, 101–134.
- Maderiaga, R. (1976). Dynamics of an expanding circular fault. *Bull. Seism. Soc. Am.* 66, 639–666.
- Malagnini, L., R. B. Herrmann and K. Koch (2000). Regional ground motion scaling in Central Europe. *Bull. Seism. Soc. Am.* 90, 1052–1061.

- Margaris, N., and D. M. Boore (1998). Determination of $\Delta\sigma$ and κ_0 from response spectra of large earthquakes in Greece. *Bull. Seism. Soc. Am.* 88, 170–182.
- McGuire, B., C. R. J. Kilburn and J. Murray (1995). Monitoring active volcanoes. UCL Press Limited, University College London.
- McNamara, D. E. and R. P. Buland (2004). Ambient noise levels in the continental United States, *Bull. Seism. Soc. Am.* 94, 4, 1517–1527.
- McNamara, D. E. and R. I. Boaz (2005). Seismic noise analysis system, power spectral density probability density function: Stand-alone software package, US. Geol. Survey Open File Report 2005-1438, 30 pp.
- Menke, W. (1989). Geophysical data analysis: Discrete inverse theory. Academic Press, New York, International Geophysics Series, 45.
- Mogi, K. (1985). Earthquake prediction. Academic press, New York, 355 pp.
- Molnar, P. B. E., B. E. Tucker and J. N. Brune (1973). Corner frequency of P and S-waves and models of earthquake sources. *Bull. Seism. Soc. Am.* 63, 2091–2104.
- Morelli, A. and A. M. Dziewonski (1993). Body wave traveltimes and a spherically symmetric P- and S-wave velocity model. *Geophys. J. Int.* 112, 178–194.
- Motazedian, D. (2006). Region- specific key seismic parameters for earthquakes in Northern Iran. *Bull. Seism. Soc. Am.* 96, 1383–1395.
- Muco, B. and P. Minga (1991). Magnitude determination of near earthquakes for the Albanian network. *Bollettino di Geofisica Teorico ed Applicata* 33, 17–24.
- Müller, G. (1977). Earth flattening approximation for body waves derived from geometric ray geometry – improvements, corrections and range of applicability. *J. Geophys.* 42, 429–436.
- Muir-Wood, R. (2000). Deglaciation seismotectonics: A principal influence on intraplate seismogenesis at high latitudes. *Quart. Sci. Rev.* 19, 1399–1411.
- Nakamura Y. (1989). A method for dynamic characteristics estimation of subsurface using microtremor on the ground surface. *Quarterly Report Railway Tech. Res. Inst.* 30–1, 25–30.
- Narcia-Lopez, C., R. R. Castro and C. J. Rebollar (2004). Determination of crustal thickness beneath Chiapas, Mexico using S and Sp phases. *Geophys. J. Int.* 157, 215–228.
- Okal, E. A. (1992). A student guide to teleseismic body wave amplitudes. *Seism. Res. Let.* 63, 169–180.
- Oppenheim, A. V., A. W. Schafer and J. R. Buck (1998). Discrete-time signal processing. Prentice Hall, New Jersey.
- Ottemöller, L (1995). Explosion filtering for Scandinavia. Norwegian National Seismic Network technical report #2. Department of Earth Science, University of Bergen, 209 pp.
- Ottemöller, L., N. M. Shapiro, S. K. Singh and J. F. Pacheco (2002). Lateral variation of Lg wave propagation in Southern Mexico. *J. Geophys. Res.* 107. DOI 10.1029/2001JB000206.
- Ottemöller, L. and J. Havskov (2003). Moment magnitude determination for local and regional earthquakes based on source spectra. *Bull. Seism. Soc. Am.* 93, 203–214.
- Ottemöller, L. and C. W. Thomas (2007). Highland boundary fault zone: Tectonic implications of the Aberfoyle earthquake sequence of 2003. *Tectonophysics*, 430, 83–95.
- Pacesa, A. (1999). Near surface attenuation in Norway and noise studies in Lithuania and Israel and status of seismology in Lithuania. M. Sc. thesis, University of Bergen, Norway.
- Payo, G. (1986). Introducción, análisis de sismogramas. Instituto Geográfico Nacional, Ministerio de la Presidencia, ISBN 84-505-4009-7, Spain, 125 pp.
- Peterson, J. (1993). Observations and modeling of seismic background noise. US Geol. Survey Open-File Report 93-322, 95 pp.
- Phillips, W. S., H. E. Hartse, S. R. Taylor and G. E. Randall (2000). 1 Hz Lg Q tomography in central Asia. *Geophys. Res. Lett.* 27, 20, 3425–3428.
- Press, W. H., S. A. Teukolski, W. T. Vetterling and B. N. Flannery (1995). Numerical recipes in C: The art of scientific computing. Cambridge University Press, New York, 994 pp.
- Pujol, J. (2000). Joint event location – the JHD technique and applications to data from local networks. In: Thurber, C. H. and N. Rabinovitz (Eds.) Advances in seismic event location. Kluwer Academic Publishers, Amsterdam, 266 pp.

- Rautian T. G. and V. I. Khalturin (1978). The use of coda for determination of the earthquake source spectrum. *Bull. Seism. Soc. Am.* 68, 923–948.
- Reasenberg, P. and D. Oppenheimer (1985). Fortran computer programs for calculating and displaying earthquake fault-plane solutions. US Geological Survey open-file report. 85-739, 109 pp.
- Reiter, L. (1990). Earthquake hazard analysis. Columbia University Press, New York, 254 pp.
- Richter, C. F. (1935). An instrumental earthquake magnitude scale. *Bull. Seism. Soc. Am.* 25, 1–32.
- Richter, C. F. (1958). Elementary seismology. W. H. Freeman, San Francisco, CA, 578 pp.
- Rietbrock, A. and F. Scherbaum (1998). The GIANT analysis system (graphical interactive aftershock network toolbox). *Seism. Res. Lett.* 69, 40–45.
- Ringdal, F. and B. L. N. Kennett (Eds.) (2001). Monitoring the comprehensive nuclear-test ban-treaty: Source location. Birkhäuser Verlag, Basel-Boston-Berlin, 420 pp.
- Roberts, R. G., A. Christofferson and F. Cassedy (1989). Real time event detection, phase identification and source location using single station 3 component seismic data and a small PC. *Geophys. J. Int.* 97, 471–480.
- Rögnvaldsson, S. T. and R. Slunga (1993). Routine fault plane solutions for local networks: A test with synthetic data. *Bull. Seism. Soc. Am.* 83, 1232–1247.
- Saari, J. (1991). Automated phase picker and source location algorithm for local distances using a single three-component seismic station. *Tectonophysics* 189, 307–315.
- Sato, H. and M. Fehler (1998). Seismic wave propagation and scattering in the heterogeneous earth. AIP Press/Springer Verlag, New York.
- Sato, H., M. Fehler and R. Wu (2002). Scattering and attenuation of seismic waves in the lithosphere. International handbook of earthquake and engineering seismology. Academic Press, San Diego, 81A, 195–208.
- Scherbaum, F. (2001). Of poles and zeros; fundamentals of digital seismometry. Kluwer Academic Publisher, Dordrecht, 256 pp.
- Scherbaum, F. and D. Stoll (1983). Source parameters and scaling laws of the 1978 Swabian Jura (southwest Germany) aftershocks. *Bull. Seism. Soc. Am.* 73, 1321–1343.
- Scholz, C. H. (1990). The mechanics of earthquakes and faulting. Cambridge University Press, Cambridge, 439 pp.
- Schwartz, S. Y., J. W. Dewey and T. Lay (1989). Influence of fault plane heterogeneity on the seismic behavior in southern Kurile Islands arc. *J. Geophys. Res.* 94, 5637–5649.
- Schweitzer, J. (2001). HYPOSAT – An enhanced routine to locate seismic events. *Pure Appl. Geophys.* 158, 277–289.
- Schöffel, H. J. and S. Das (1999). Fine details of the Wadati-Benioff zone under Indonesia and its geodynamic implications. *J. Geophys. Res.* 104, 13101–13114.
- SEED (2007). SEED reference manual. Standard for the exchange of earthquake data, SEED format version 2.4. International Federation of Digital Seismograph Networks Incorporated Research Institutions for Seismology (IRIS), USGS. www.iris.edu
- Seggern Von, D. H., J. N. Brune, K. D. Smith and A. Aburto (2003). Linearity of the earthquake recurrence curve to $M > -1$ from Little Skull Mountain aftershocks in Southern Nevada. *Bull. Seism. Soc. Am.* 93, 2493–2501.
- Sereno, T. J., S. R. Bratt and T. C. Bache (1988). Simultaneous of regional wave spectra for attenuation and seismic moment in Scandinavia. *J. Geophys. Res.* 93, 159–172.
- SESAME (2004). Guidelines for the implementation of the H/V spectral ratio technique on ambient vibrations measurements, processing and interpretation. SESAME European research project WP12 – Deliverable D23.12, European Commission – Research General Directorate, Project No. EVG1-CT-2000-00026 SESAME. Also found at <http://www.geo.uib.no/seismo/ SOFTWARE/SESAME/USER-GUIDELINES/SESAME-HV-User-Guidelines.doc>.
- Simon, R. B. (1968). Earthquake interpretations. Colorado School of Mines, Golden, 99 pp.
- Singh, S. K., R. J. Aspel, J. Fried and J. N. Brune (1982). Spectral attenuation of SH waves along the Imperial fault. *Bull. Seism. Soc. Am.* 72, 2003–2016.

- Singh, S. K., M. Ordaz and R. R. Castro (1992). Mismatch between teleseismic and strong-motion source spectra. *Bull. Seism. Soc. Am.* 82, 1497–1502.
- Sipkin, S. A. (2003). USGS Earthquake moment tensor catalogue. In: Lee, W. H. K., H. Kanamori, P. C. Jennings and C. Kisslinger (Eds.) *International handbook of earthquake and engineering seismology*. IASPEI, Academic Press, New York, 81A, 823–825.
- Slunga, R (1981). Earthquake source mechanism determination by use of body-wave amplitudes – an application to Swedish earthquakes. *Bull. Seism. Soc. Am.* 71, 25–35.
- Snoke, J. A., (2003a). FOCMEC: FOCal MEChanism determinations. In: Lee, W. H. K., H. Kanamori, P. C. Jennings and C. Kisslinger (Eds.) *International handbook of earthquake and engineering seismology*. Academic Press, San Diego, Chapter 85.12.
- Snoke, J. A. (2003b). FOCMEC: FOCal MEChanism determinations. A manual. www.geol.vt.edu/outreach/vtso/focmec/.
- Stange, S. (2006). M_L determinations for local and regional events using a sparse network in southwestern Germany. *J. Seism.* 10, 383–4649.
- Stein, S. and M. Wyession (2003). *Introduction to seismology, earthquakes and earth structure*. Blackwell Publishing, Oxford, 498 pp.
- Stoneley, R. (1970). The history of the International Seismological Summary. *Geophys. J. Int.* 20, 343–349.
- Storchak, D. A., J. Schweitzer and P. Bormann (2003). The IASPEI standard seismic phase list. *Seism. Res. Lett.* 74, 761–772.
- Takanami, T. and G. Kitagawa (Eds.) (2003). *Methods and applications of signal processing in seismic networks*. Springer Verlag, New York.
- Tarantola, A. (2005). *Inverse problem theory and methods for model parameter estimation*. Society for Industrial and Applied Mathematics, Philadelphia, US.
- Thurber, C. H. and N. Rabinovitz (Eds.) (2000). *Advances in seismic event location*. Kluwer Academic Publishers, Amsterdam, 266 pp.
- Urhammer, R. A. and E. R. Collins (1990). Synthesis of Wood-Anderson seismograms from broadband digital records. *Bull. Seism. Soc. Am.* 80, 702–716.
- Vaněk, J. A., A. Zátopec, V. Kárník, N. V. Kondorskaya, Y. V. Riznichenko, E. F. Savarski, S. L Solovév and N. V. Shevalin (1962). Standardization of magnitude scales. *Bull. Acad. Sci. USSR, Geophys. Ser.* 108–111.
- Veith, K. F. and G. E. Clawson (1972). Magnitude from short-period P-wave data. *Bull. Seism. Soc. Am.* 62, 2, 435–452.
- Viret, M. (1980). “Determination of a duration magnitude relationship for the Virginia Tech Seismic Network,” in Bollinger, G. A., Central Virginia Regional Seismic Report December 1, 1980, US Nuclear Regulatory Commission Contract No. NRC-04-077-034, 1-8.
- Wadati, K. (1933). On the travel time of earthquake waves. Part. II, *Geophys. Mag. (Tokyo)* 7, 101–111.
- Waldhauser, F. and W. L. Ellsworth (2000). A double-difference earthquake location algorithm: Method and application to the Northern Hayward fault, California. *Bull. Seism. Soc. Am.* 90, 1353–1368.
- Wang, R. and H. Wang (2007). A fast converging and anti-aliasing algorithm for Green’s functions in terms of spherical or cylindrical harmonics. *Geophys. J. Int.* 170, 239–248.
- Wessel, P. and W. H. F. Smith (1991). Free software helps map and display data, *EOS Trans. AGU*, 72, 441.
- Wessel, P. and W. H. F. Smith (1998). New, improved version of the Generic Mapping Tools released, *EOS Trans. AGU*, 79, 579.
- Wiechert, E. (1907). Über Erdbebenwellen. Theoretisches über die Ausbreitung der Erdbebenwellen. Nachrichten von der Königlichen Gesellschaft der Wissenschaften zu Göttingen, Mathematisch-physikalische Klasse, 413–529.
- Wiemer, S. (2001). A software package to analyze seismicity: ZMAP. *Seism. Res. Let.* http://www.seismosoc.org/publications/SRL/SRL_72/srl_72-3_es.html.
- Wiggins-Grandison M. D. and J. Havskov (2004). Crustal attenuation for Jamaica, West Indies. *J. Seism.* 8, 193–209.

- Yang, X., R. North and C. Romney (2000). CMR nuclear explosion database (revision 3), Center for Monitoring Research CMR-00/16.
- Zhu, T., K. Chun and G. F. West (1991). Geometrical spreading and Q of Pn waves: An investigative study in Eastern Canada. Bull. Seism. Soc. Am. 81, 882–896.
- Zobin V (2003). Introduction to volcanic seismology: Vol. 6 (Developments in volcanology), Elsevier Science, Amsterdam.
- Zuniga, F. R., M. Wyss and F. Scherbaum (1988). A moment magnitude relation for Hawaii. Bull. Seism. Soc. Am. 78, 370–373

Software References

- GIANT:http://www.geo.uni-potsdam.de/arbeitsgruppen/Geophysik_Seismologie/software/giant.html
- Various: <http://www.iris.edu/manuals/>
- Various: <http://earthquake.usgs.gov/research/software/index.php>
- The most complete: <http://www.orfeus-eu.org/Software/softwarelib.html>
- SEISAN and others: <http://www.geo.uib.no/seismo/software/software.html>
- EarthWorm: <http://www.isti2.com/ew/>,<http://folkworm.ceri.memphis.edu/ew-doc/>
- Various: <http://www.spice-rtn.org/library/software/>
- Modeling etc: <http://www.eas.slu.edu/People/RBHerrmann/CPS330.html>
- HYPOSAT: <ftp://ftp.norsar.no/pub/outgoing/johannes/hyposat/>
- GMT: <http://gmt.soest.hawaii.edu/>
- Google map. (<http://earth.google.com/>)
- FOCMEC fault plane solution program. www.geol.vt.edu/outreach/focmec/

Index

A

Absorption, 246
Acausal filter, 65, 85
Acceleration spectrum, 249
Accelerometer, 57
 poles and zeros, 65
Active filter, 60
Aftershocks, 319–320
AK135 model, 18
Aliasing, 60, 93
 plotting, 93
 in space, 290
Amplitude
 frequency response, 61
 ratio, fault plane solution, 219
 reading, 157
 spectrum, 87
 uncertainty, 222
Analysis, routine, 304–305
Angle of incidence, 22, 49, 220, 300
 apparent, 104
Anisotropy, 19, 98
Antenna, seismic, 283
Antialias filter, 60
Apparent velocity, 19, 33, 49, 104,
 295–297
 identify seismic phase, 33
ARCES, 291
Array, 9
 -beamforming, 323
 noise suppression, 288
 processing, manual, 303
 radiation pattern, 291
 response, 290–291
 seismic network, 287–288
 size and geometry, 279
 small, 293
 three stations, 295–296
Arrival time order, location, 148–149

Arrival time variance, 117–118
Asthenosphere, 17
Attenuation, 261–262
Auto-correlation, 94
Auxiliary plane, 201
Average magnitude, 184
Azimuth, 103
Azimuthal gap, 120

B

Back azimuth, 107–108, 296
 computer location, 114
Band code, 74
Bandpass filter, 83
Bar, 264
BB seismometer, 58
Beach balls fault plane solutions, 208
Beam forming, 288–289
Bimodal regression, 181
Bisquare weighting, 138
Body wave(s), 7
 magnitude, 11, 164, 169–170
 broadband, 152
 spreading, 252
Broadband
 body wave magnitude, 152
 seismometer, 73–74
 surface wave magnitude, 152
Brune source model, 265
Bulletin, 13, 314
Butterworth filter, 65, 92
b-value, 324
Byte order, 69

C

Calculate epicentral distance, 107–108
Calculate rake, 205
Calibration data, 301

- Centroid
 - hypocenter, 227
 - origin time, 103
- Channel naming, 73
- Check
 - magnitudes, 305
 - response, 67
- Chord, 108
- Circular fault, 250
- Classification of events, 304
- CLVD, 232
- CMB, 21
- CMT, 226, 240
- Coda
 - length, definition, 164
 - and noise, 164
 - waves, 28
- Coda magnitude, 164
 - derive scale, 187–188
 - scales, different regions, 162
- Coda Q, 268
 - and lapse time, 273
 - practical considerations, 268–269
 - processing parameters, 270
 - sampling volume, 275
- Code
 - instrument, 74
 - orientation, 74
- Compensated linear vector dipoles, 225
- Complex response, 65
- Component
 - code, 73
 - to read phase, 34
 - rotation, 94–98
- Composite fault plane solutions, 209–210
- Compression, 207, 219
 - data, 72
 - Steim, 70
- Conrad discontinuity, 16, 22
- Continuous data, 73, 321
- Convergent plate boundary, 5
- Convert gain, 62
- Convert poles and zeros, radian to Hz, 65
- Convolution, 60, 94
- Core, 15, 17
- Corner frequency, 263–264
 - caused by κ , 262
 - examples, 261
 - filter, 60, 84
 - and magnitude, 259
 - teleseismic, 262
- Correction
 - for instrument response, 61
 - for radiation pattern, 250
- Correlation, 94
- Cosine taper, 91
- Critical reflection, 18
- Cross correlation, 94
 - determine arrival times, 123
 - to get P, 106
- Crust, 15–16
- Crustal conversions, 47
- Crustal phases, 27
- Crustal surface waves, 27
- Crustal thickness, globally, 16
- CSS, 322
 - format, 72
- CTBT, 124, 283
- CTBTO, 322
- Cygwin, 71
- D**
- Damping constant, 54
- Data
 - centers, 322
 - compression, 72
 - exchange, 314
 - formats, 68
 - statistics, 318–320
 - storage, 299
- Data base
 - relational, 301
 - for seismology, 302
- dB, definition, 59–60
- DC level, 90
- Deconvolution, 89
- Deglaciation, 6
- Degrees of freedom, location, 111
- Demultiplexed, 70
- Depth
 - check with RMS, 142
 - hypocentral, 135
 - phases, 128
 - and Pn, Pg, 129
 - start, 135
- Detection threshold, 319
 - and noise, 319
- Determine structure, 45
- Determine v_p/v_s , 46
- Digital data, reading speed, 65
- Digitizer, 68
- Dilatation, 208, 219
- Dip, 204
 - measure, 206

- Dipole, 197
Dip-slip fault, 3
Discrete wave number representation, 236
Dispersion, 7, 46
Displacement
 spectrum, 265
 transducer, 56
Distance
 correction, magnitude, 154, 162
 on spherical earth, 101
 weighting, 141
Distant event, 34
 definition, 306
Divergent plate boundary, 5
Diving wave, 19
Double couple, 213
Double difference location, 126
Duration magnitude, 160
- E**
- Earthquake
 location, 10
 source, 2
 swarm, 319
Earth structure, 15
Elastic rebound, 3
Electronic noise, 63
Ellipticity, 102
EMSC, 309, 314
Energy, 159
 magnitude, 179–180
 release, 151
Epicenter, 4
 location by computer, 110
 location, grid search, 112
 location, manual, 110
 map, 316
Epicentral distance, 101
 calculate, 105
Error
 ellipse, 116–117
 ellipsoid, 120
 in location, 120
EVALRESP, 71
Event
 classification, 304
 completeness, 318
 reference, 120
 screening, 303
 statistics, 318
Explosion, 313–314
- example, 27
identify, 304, 313
- F**
- FAP, 65
Fault
 area, 11
 geometry, 194
 slip, 11
Fault plane solution, 11, 307
 automatic, 221
 composite, 209–210
 global data, 210–212
 grid search, 211
 local event, 209
 using amplitude, 212–213
 ratio, 217, 240
 using spectra, 222
FBA, 56
FDSN, 73
Felt earthquakes, 308–309
Filter
 active, 60
 causal, 85
 corner frequency, 84
 octave, 79
 passive, 60
 phase shift, 60, 92
 read phase, 168
 in recorder, 58
Filtering, 83
FIR filter, 60, 322
First motion, 104, 210
fk analysis, 294
fk and filter, 293
Flat earth, 114
Flat file system, 301
Focal mechanism, 198
Focal sphere, 209
Foot wall, 194
Force balanced accelerometer, 56
Format
 CSS, 72
 GSE, 69
 MiniSEED, 73
 SAC, 71
 SEED, 70
 SEISAN, 71
 waveform file, 72
Fourier
 computer, 90
 density spectrum, 86
 transform, 90

Free surface effect, 222

on spectrum, 221

Frequency

content, seismic phases, 30

dependence, geometrical spreading, 246

displacement response, 54

response, definition, 61

wavenumber analysis, 289–290

G

Gap, azimuthal, 120

Geiger method, 113

Geodistance, 252

Geometrical spreading, 221, 263–264, 268

head waves, 238

Lg, 252

teleseismic distances, 262

GEOTOOOL, 322

GIANT, 322–323

GIS, 307, 324

Global CMT Project, 239

GMT, 324

Google map, 307, 324

GPS, 59

Green's function, 228, 235

Grid search

epicenter location, 116

fault plane solution, 221

moment tensor, 228

Ground acceleration power, 78

GSE

format, 70

response, 67, 69

Guidelines

coda Q determination, 268

Q from relative spectra, 275

Gutenberg-Richter relation, 318

H

Hanging wall, 194

Harvard fault plane solution, 264

High pass filter, 83

Horizontal component of velocity, 284

Horizontal slowness, 284

HYPOT1, 126, 144

Hypocenter, 9–10, 110–111, 122–123, 134

check, 311

program, 143

Hypocentral depth, 127

and Pn and Pg, 128

and pP, 147

Hypocentral distance, 119

HYPOELLIPSE, 144

HYPOINVERSE, 144

HYPOSAT, 114, 124, 144

I

IASP91

model, 18

travel times, 31

IASPEI, 22

Identify explosion, 304, 311

Identify phase, apparent velocity, 50

IIR filter, 322

Impulse response, 89

IMS, 283

IMS1.0, 69

Incidence angle, true, 104

Inner core, 15

Instrument

codes, 73

correction, 63, 86–91

and noise, 63

response correction, 61–68

Instrumental noise, 76

International Monitoring System, 69

Interplate earthquake, 6

Intrinsic attenuation, 271

Intrinsic Q, 246–247

Inversion

of travel times, 46

using surface waves, 46

IRIS, 66, 316

data center, 316

ISC, 10, 22, 145, 316, 319

solution, 314

ISCLOC, 145

Isoseismals, 310

Iteration process, location, 113

J

JB

model, 18

tables, 49

JHD, 123

Joint hypocenter location, 122–123

K

κ determination, 265–267

κ , determine, example, 265–266

κ , effect on spectrum, 258

κ example values, 266

L

L1 norm, 111

Lapse time, 268–269

and coda Q, 270–273

- Lg
example, 33
magnitude, 178
velocity, 27
- Lithosphere Q, 246
- Local event, 34–38
definition, 304
- Localize by arrival time order, 148–149
- Local magnitude, 11, 150, 154–160
definition, 10
derive scale, 185
- Local minimum
depth, 129
location, 113
- Locating earthquakes, 9–10
- Location
code, 74
error, example, 127
iterative, 134
local minimum, 134
relative, 120
single station, 103–107
with S-P, 107
timing error, 139
- LOCSAT, 323
- Love waves, 7
- Low pass filter, 83
- LP seismogram, example, 50
- LP seismometer, 55
- M**
- Macroseismic information, 308
- Magnification, 62
- Magnitude, 10–11
average, 184–185
body wave, 152
broadband body wave, 152
check, 305
coda, 162
distance correction, 162
duration, 162
energy, 179–180
general definition, 154
- Lg, 178
- local, 152
- moment, 152, 178–179
- range, 152
- saturation, 153, 157, 256
- scale for local conditions, 151
- scales, compare, 162
- station correction, 155, 184–185
- surface wave, 152, 172
- Major and minor double couple, 225
- Make response file, 67–68
- Mantle, 15–16
- Manual epicenter location, 107
- Map, epicenter, 316
- Mapping software, 323–324
- Master event location, example, 121
- Master event technique, 120–122
- m_B , 167
- m_b and filter, 167
- m_b , IMS scale, 166
- M_c , 160–164
- M_e , 179–180
- Measure dip, 203
- Measure strike, 203
- Megapascal (MPa), 251
- Meridian, 203
- Microseismic noise, 63, 93
- Mid-oceanic ridge, 16
- Mid-oceanic spreading, 5
- MiniSEED format, 70
- M_L , 154–160
anchor scale, 156, 186
for California, 156
deep earthquakes, 159
example of scales, 156
filter, 154, 158
and M_S , 177
reference distance, 157
small event, 159
- M_L – M_w relations, 182
- Modeling, spectrum, 249
- Model seismogram, 193–243
- Moho, 15
reflection, 36
velocity, 16
- Moment magnitude, 11, 152, 178
- Moment rate, 238
- Moment, scalar, 222
- Moment, static, 178
- Moment tensor, 229
inversion, 11, 227–235
regional case, 229
- Moscow–Prague formula, 172
- MPa, 251
- M_s , 171–175
- M_S , 175–177
- M_s (BB), 172
- M_S and M_L , 176–177
- Multiple rupture, 178
- Multiple station location, 107–109
- M_w , 178–179
- M_w , adjust to local conditions, 185

- N**
- Nakamura method, 278
 - Near surface attenuation, 247–248, 280
 - Noise
 - electronic, 63
 - microseismic, 93
 - probability density, 79
 - reduction, array, 288
 - seasonal change, 79
 - seismic, 93
 - spectrum, 67, 79
 - suppression, array, 288
 - Non double couple source, 225
 - Nordic format, 300
 - NORES, 289
 - Normal fault, 203
 - Normalization constant, 64–65
 - NORSAR, 283
 - Nyquist frequency, 60, 99
- O**
- Octave, filter, 84
 - Omori's law, 319
 - ORFEUS, 14
 - Orientation code, 74
 - Origin time, 10, 102–103, 108
 - centroid, 227
 - Outlier, location, 111
 - Outlier, phase, 139
- P**
- P-amplitude, 213
 - P amplitude equation, 216
 - Particle motion, 94–98
 - Passive filter, 60
 - P axis, 205
 - PcP example seismogram, 41
 - PDE, 116
 - solution, 306
 - Pdif, example seismogram, 43
 - Period reading, 153
 - Peterson noise curves, 78
 - Pg, example seismogram, 37
 - Pg and Sg, example seismogram, 35
 - Phase(s)
 - conversions, 46
 - depth, 128
 - IASPEI approved names, 23–26
 - for locating local events, 142
 - for location, 126–127
 - most important, 33
 - names, 30
 - reading, 91–93
 - and filter, 91–93
 - Phase, FIR filter, 85
 - Phase response, sensor, 62
 - Phase selection for location, 133
 - Phase shift, 55, 91–93
 - Phase spectrum, 87
 - Phase weight, 127, 130
 - PITSA, 99, 323
 - PKP, example seismogram, 44
 - Plate boundary, 4
 - Plate motion, 4
 - Plotting resolution, 93
 - PmP, example seismogram, 36, 238
 - Pn, example seismogram, 37–38
 - Pn travel time, 32
 - Polarity, 12, 84–85, 104, 206–208
 - read, 206
 - of SV and SH, define, 215
 - Polarization, 94–95
 - Polarized P-waves, 103
 - Poles and zeros, 64
 - accelerometer, 65
 - units, 64
 - Wood-Anderson seismograph, 154
 - Power density spectrum, noise, 78
 - pPdif, example seismogram, 43
 - pP, example seismogram, 41
 - PPP, example seismogram, 42
 - pP read as S, 41
 - PQL II, 99
 - PQLX software, 79
 - Probabilistic earthquake location, 112
 - Probability density noise, 79
 - Procedure, coda magnitude determination, 164
 - Processing format, 68
 - Processing software, 292–294
 - PS, example seismogram, 43–44
 - P-spectrum, example, 178
 - P and S spectrum, 264
 - P and T, define, 198
 - P and T, measure, 206
 - P-waves, 7
 - polarized, 103
- Q**
- Q, 262
 - Q, coda, 268–273
 - Q component, 95
 - Q determination, 273–275
 - multiple stations, 276–277
 - two stations, 273–275
 - waves, 277
 - Q from different regions, 277
 - Q, frequency dependence, 246–247

- Q , intrinsic, 246
 Q of Lg waves, 277
 Q and spectral ratio, 275
Quality control
 residuals, 310
 seismic data, 310
 Q -variation, 274–275
- R**
Radiation effect on spectrum, 249
Radiation pattern, 184
 average corrections, 250
Rake, 194
 ambiguity, 205
 calculate, 205
Rayleigh waves, 7
Ray method, 236
 global case, 236–237
Ray parameter, 18–19
 location, 114
 spherical earth, 19
 unit, 19
R component, 215–216, 222
Reading amplitude, 153
Reading period, 153
Read polarity, 206
Receiver function method, 46–47
Recording format, 68
Reference events, 120
Reflected ray, 18–19
Refracted phase, 18
Regional event, 34
 definition, 304
Regression, bimodal, 181–182
Relational data base, 301–302
Relative location, 120–125
Relative P, determine by correlation, 94
Resampling, 98–99
Residual weighting, 138–139
Resonance frequency, 53
Response
 check, 67
 curve, 55
 file, make, 67–68
 GSE, 67, 69–70
 poles and zeros, 64
 SAC, 65
 SEED, 65–66
 SEISAN, 67
Rg velocity, 27
Richter magnitude, 151
RMS *versus* depth, 142
RMS, recommend value, 310
- RMS travel time residual, 129
Rotation, component, 94–98
Routine analysis, 304–306
Routine processing, 303–314
Rupture, 2
 area, determine, 307
 multiple, 178
 time, 237–238
 velocity, 2, 102, 237
- S**
SAC, 71, 99, 322–323
 format, 68
 response, 67
Sample rate, 60, 288
Scalar moment, 222
Scattering, 28
 volume, 273
SCNL code, 74–76
Sdif, example seismogram, 98
SEED
 format, 70
 response, 66
SEISAN
 data base, 302–303
 format, 71
 response, 67
SeisGram2K Seismogram Viewer, 99
Seismic array, 9
Seismic event definition, 2
Seismic Handler, 94, 322–323
Seismic instruments, 6
Seismicity rate, 319
SEISMICITY VIEWER, 324
Seismic moment, 11
Seismic network as array, 287–288
Seismic noise, 76–80
Seismic observations, 301
Seismic phases, 9, 21–28
 different distance, 33–45
 examples, 33–34
 frequency content, 30
Seismic ray, 18–20
Seismic recorder, 58–61
Seismic sensor, 53–58
Seismic source model, 248–251
Seismic waves, 7
Seismogram
 modeling, 235–240
 ray method, 236
 pP, 40
 synthetic, 235–237
Seismograph, 6

- Seismometer, LP, 55
 phase response, 56
 Self similarity, 255–257
 Sensors
 dynamic range, 57
 natural frequency, 54
 Sg, example seismogram, 35–36
 SH, 323
 and SV polarity, definition, 215
 Short period seismometer, 54
 SIMULPS, 46
 Single station location, 103–107
 error, 106–107
 SKS, example seismogram, 98
 Slip, 194
 on a fault, 3
 Slow earthquake, 3
 Slowness, 284
 estimate, 292
 Snell's law, 18
 Software, 13–14
 fault plane solution, 240–241
 mapping, 323–324
 for processing, 320–324
 Soil amplification, 278–279
 example alluvial site, 279
 example rock site, 279
 Source radius, 250
 Source time function, 237–238
 Spectral analysis, 321
 local earthquake, 258
 procedures, 261–262
 teleseismic distance, 262
 Spectral estimate, automatic, 178–179
 Spectral modeling, 267–268
 Spectral parameters, automatic determination,
 260
 Spectral ratio and Q, 274
 Spectrum
 acceleration, 249
 displacement, 258
 example, 86, 268
 local event, 276
 teleseismic, 273–274
 sP, example seismogram, 41
 Spherical earth, 114
 Spreading, 5
 body wave, 263
 SP seismograms, 27
 SP sensor, 55, 57–58
 SS, example seismogram, 42, 43
 S-spectrum, example, 179
 Starting depth, 135
 Starting location, 134–138
 Static stress drop, 251
 Station code, 73
 Station correction, magnitude,
 184–185
 Station elevation, 102
 Station geometry and error, 120
 Steim compression, 70
 Stereographic projection, 200–201
 Store response information, 65–66
 Strain energy, 2
 Stress drop, 251, 255
 example calculation, 261
 Stress orientation, 198
 Strike, 194
 definition, 203
 and dip, determine, 203
 measure, 203
 Strike-slip fault, 3, 196, 224
 Strip method, 51
 Structure, determine, 45–48
 Surface wave(s), 7
 crustal, 27
 inversion, 46
 magnitude, 11, 152, 172
 broadband, 152, 172
 velocity, 7
 S-wave(s), 7
 splitting, 98
 Synthetic seismogram, 235
 ray method, 236
- T**
 t^* , 247, 262
 t^* , amplitude ratio, 216
 Tapering, 91
 T axis, 205
 T component, 95, 215
 Teleseismic, 9
 Teleseismic event, depth, 127
 T, example seismogram, 39
 Three station array, 286
 Thrust fault, 204
 Time of day distribution,
 311–313
 Time gaps, 73
 Timing error, location, 139
 Timing problems, 72–73
 Total reflection, 19
 TPg, example seismogram, 32
 T phase, example, 37
 Transform fault, 4–5
 Transition zone, 16

- Travel time, 28
 inversion, 46
 Pn, 32
Trial location, 113
True incidence angle, 104
T-wave(s)
 location, 139
 velocity, 28
- U**
Unit, poles and zeros, 79
USGS, 67, 314
- V**
Variance, arrival times, 117
Variance–covariance matrix, location, 117
Velest, 46
Velocity
 apparent, 107
 Moho, 16
Velocity sensor, 55
Volcanic seismology, 6
Volcanic tremor, 283
Volcano, 6
- v_p/v_s**, 7, 46
v_p/v_s, determine, 108
- W**
Wadati diagram, 109
Waveform
 data, 316
 file format, 99
Wavefront, 18, 283–285
 array, 283–285
- Weight**
 phase, 138–139
 arrival, 126
 residual, 138
Weighting, distance, 141
Wilber data selection tool, 316
Wood-Anderson seismograph, 165
WWSSN, 55, 316
WWSSN LP response, 172
WWSSN SP response, 165
- Z**
ZMAP, 319